![U.S. NRC logo] **U.S.NRC**

United States Nuclear Regulatory Commission

Protecting People and the Environment

Pacific Northwest National Laboratory Investigation of Stress Corrosion Cracking in Nickel-Base Alloys: Behavior of Alloy 152 And 52 Welds

Office of Nuclear Regulatory Research

AVAILABILITY OF REFERENCE MATERIALS
IN NRC PUBLICATIONS

U.S.NRC

United States Nuclear Regulatory Commission

Protecting People and the Environment

Pacific Northwest National Laboratory Investigation of Stress Corrosion Cracking in Nickel-Base Alloys: Behavior of Alloy 152 And 52 Welds

Prepared by:
S. M. Bruemmer
M. J. Olszta
R.J. Seffens
R.A. Bouffioux
N.R. Overman
M. B. Toloczko

Pacific Northwest National Laboratory
Richland, WA 99352

Margaret Audrain, NRC Project Manager

Office of Nuclear Regulatory Research

ABSTRACT

This report summarizes experimental results evaluating the primary water stress corrosion cracking (PWSCC) susceptibility of high-chromium, nickel-base weld metals and interface regions in more complex dissimilar metal welds. The primary research objectives were to establish quantitative measurements of SCC growth rates and determine relationships among cracking susceptibility, metallurgical characteristics and environmental conditions. Crack-growth rates have been determined under cyclic loading and at constant stress intensity (K) in simulated PWR primary water environments for 21 weld metal specimens including tests on nine alloy 152, one alloy 152M, three alloy 52, seven alloy 52M and one alloy 52MSS specimens. In addition, SCC response was investigated from alloy 182/82 into alloy 52M for 4 alloy 52M/182 overlay weld specimens and 2 alloy 52M/82 inlay weld specimens. Finally, crack-growth behavior was evaluated at various regions in dissimilar metal (DM) welds including 9 tests at DM interfaces covering those between two alloy 152 and low alloy steel, one alloy 52M and low alloy steel, two alloy 152M and carbon steel, two alloy 52M and carbon steel, and two alloy 152 and stainless steel interfaces. Most test specimens were machined from industry mockups to provide plant-representative materials, while a few were produced at laboratories using industry recommended procedures. In all cases, crack extension was monitored in situ by direct current potential drop (DCPD) with an estimated length resolution of about ± 1 µm making it possible to measure extremely low growth rates approaching 5×10^{-10} mm/s. Most SCC tests were performed at 360°C with a dissolved hydrogen concentration of 25 cc/kg to establish an electrochemical potential (ECP) at the Ni/NiO stability line where many nickel-base alloys are most susceptible to SCC; however, environmental conditions were modified during a few experiments to evaluate the influence of temperature, water chemistry or ECP on propagation rates. Extensive characterizations have been performed on material microstructures and stress-corrosion cracks by optical and electron microscopy techniques and linked to crack-growth test results to help define material and environmental parameters controlling SCC susceptibility.

FOREWORD

This report describes a study sponsored by the NRC Office of Nuclear Regulatory Research (RES) to investigate the stress corrosion cracking (SCC) susceptibility of alloy 690 weld metals including alloys 152, 52 and its many variants. SCC of nickel-based weld metals, such as those used for reactor vessel head penetration nozzles and reactor coolant system nozzles, is a degradation mechanism that can affect the operational safety of pressurized water reactors (PWRs). For instance, through-wall cracking was detected in an Alloy 82 and 182 hot leg nozzle weld at the V.C. Summer plant in 2000. Alloys 52 and 152 are thought to be more resistant to SCC than Alloys 82 and 182 because of higher chromium content, and there is no operational experience of their cracking in service. In light of the positive service history and low crack growth rates measured in laboratory testing sponsored by the industry, utilities have submitted requests to the Office of Nuclear Reactor Regulation (NRR) for relief from the inspection requirements found in Title 10 of the Code of Federal Regulations, Part 50.55a, including a 10 year interval for volumetric examination of pressure vessel head nozzles.

In the course of reviewing the relief requests and test results from industry-sponsored research, RES and NRR staff raised questions with respect to the potential for SCC due to higher strains associated with the welds and the weld metal's complex microstructure. These higher chromium weld metals are also more susceptible to segregation and weld cracking including solidification cracking and ductility dip cracking. Very little testing has been performed on dissimilar metal (DM) welds where complex compositions and microstructure can be produced at interfaces between Fe-bases alloys (e.g., low allow steel, carbon steel and stainless steels) and the high-Cr, Ni-base weld metal.

This report has documented SCC results on a large number of industry-made alloy 152, 152M, 52, 52M and 52MSS weld mockups revealing low CGRs in 360°C simulated PWR primary water. Specialized tests performed on alloy 52M overlay and inlay mockups supported very low SCC CGRs in the alloy 52M weld metal. The main conclusion from these experiments on alloy 152, 152M, 52, 52M and 52MSS weld metals with typical Cr bulk concentrations (28-30 wt%) is that they are resistant to SCC crack growth. Some differences were observed for alloy 152 and 52M welds in regions where the local Cr concentration was found to equal to or below ~24 wt%. SCC propagation rates up to ~1.4×10^{-8} mm/s were measured in an alloy 52M weld pass for the Ringhals overlay (CT035) and within DM weld alloy 152 dilution zones adjacent to the LAS interface. The presence of aligned grain boundaries along the crack path were a key requirement for significant SCC growth in the dilution zone specimens and limited the extent of observed IGSCC to local areas. Overall, these results support the excellent SCC resistance of the high Cr welds in the as-welded condition.

The application of the test results to plant components is particularly challenging given the large number of potential variations in weld designs and configurations that are found in service. These tests are ongoing and will continue to inform the evaluations by NRR to determine whether inspection requirement for components with Alloy 52 and 152 welds provide a reasonable assurance of safety.

TABLE OF CONTENTS

LIST OF FIGURES

xxiii

LIST OF TABLES

EXECUTIVE SUMMARY

Primary water stress-corrosion cracking (PWSCC) is a degradation mechanism that can affect pressure boundary components made of nickel-base alloys and their welds in pressurized water reactors (PWR). Fabrication and welding processes and especially weld repairs leave residual stresses that promote cracking in susceptible materials. Undetected PWSCC has led to reactor pressure boundary leaks and boric acid corrosion in nuclear power plants worldwide.

PWSCC of high-chromium, nickel-base alloys has been evaluated in simulated pressurized water reactor environments. This report focuses on material characterizations and test results for alloy 690 weld metals (alloy 152, 52 and 52M) conducted at PNNL over the last decade for NRC projects JCN N6007 and JCN N6925 as well as recent work under the EWA agreement NRC-HQ-25-14-D-0001, Task Order NRC-HQ-60-15-T-0008. Stress-corrosion crack-growth rates have been determined for 11 alloy 152/52/52M weld metal specimens, 4 alloy 52M/182 overlay specimens, 2 alloy 52M/82 inlay specimens and 9 alloy 152/52M dissimilar metal (DM) weld specimens in simulated PWR primary water environments. Weld metal, overlay/inlay and DM dilution zone specimens were machined from industry mock ups to provide plant-representative materials for testing. Specimens have been tested for one alloy 152 weld, two alloy 52 welds and three alloy 52M welds. The overlay and the inlay specimens were prepared to propagate stress-corrosion cracks from the alloy 182 or 82 material into the more resistant alloy 52M. In all cases, crack extension was monitored in-situ by direct current potential drop (DCPD) with length resolution of about ± 1 µm making it possible to measure extremely low growth rates approaching 5×10^{-10} mm/s. Most SCC tests were performed at 360°C with a dissolved hydrogen concentration of 25 cc/kg, while environmental conditions were modified during a few experiments to evaluate the influence of temperature, water chemistry or electrochemical potential on propagation rates. In addition, low-temperature (~50°C) cracking behavior was examined for selected weld metal specimens.

This project has completed some of the first SCC crack-growth tests on alloys 152, 52 and 52M weld metals in PWR primary water and helped establish a basis for their SCC propagation behavior. Similar to the previous PNNL test results for the as-received alloy 690 materials, the high-chromium weld metals have consistently shown a high resistance to SCC. Several different weld mockup types have been tested including U-groove, V-groove, butt weld, and narrow gap welds. Unlike the thermally treated alloy 690 base metal, a higher degree of intergranular (IG) engagement is typically seen, but measured propagation rates have been $\leq 1 \times 10^{-8}$ mm with most being less than 2×10^{-9} mm at test temperatures from 325 to 360°C. Despite the higher degree of engagement, transitioning to SCC can be more challenging due to the interdendritic weld metal microstructure and large grain sizes making uniform IG engagement across the crack front difficult. Only a few weld metal specimens have exhibited significant crack propagation along grain boundaries during long-term tests suggesting an overall good resistance to IGSCC for the high-chromium weld metals.

In an effort to improve IG engagement, limited testing has also been conducted at 50°C in PWR primary water. Hydrogen-induced IG crack growth and higher growth rates were promoted during cycling steps for an alloy 152 weld, but much smaller effects were seen for alloy 52 welds. The environment-induced cracking at low temperature is believed to occur during dynamic straining, and much more experimentation is needed to properly assess this behavior. The influence of preexisting ductility-dip cracks on SCC response has also been evaluated in alloy 52M with preliminary results showing no enhancement of crack growth due to a low density of these preexisting defects. SCC tests were also performed on industry mockups for

an alloy 52M/182 overlay and an alloy 52M/82 inlay. For both, initial SCC propagation rates in the lower-chromium layer (alloy 182 or 82) were less than expected with only partial IG engagement. Although the growth decreased significantly as the alloy 52M interface was reached, this was due to isolated IGSCC fingers intersecting the interface. A simple assessment of chromium concentration on growth rates through the interface region was not possible without a straight crack front.

Additional SCC data was generated for alloy 52M from the overlay and the inlay welds with the highest crack growth rate at constant stress intensity (K) in weld metals detected for the alloy 52M overlay material. Final activities have focused on characterizations and SCC experiments on various DM welds including stainless steel to alloy 152, carbon steel to alloy 152/52 and low alloy steel to alloy 152/52M interface regions. Unique microstructures and microchemistries were developed in the weld metal dilution zones and local areas of IGSCC were detected within selected weld passes. However, overall sustained crack growth under constant K was not observed in the weld or along the interface for any of the DM weld specimens evaluated.

This report documents SCC results on a large number of alloy 690 weld metal mockups revealing low crack growth rates in 360°C simulated PWR primary water. In addition, specialized tests performed on alloy 52M overlay and inlay mockups supported very low SCC CGRs in the alloy 52M weld metal. Overall, these results support the excellent SCC resistance of the high Cr welds in the as-welded condition at PWR operating conditions.

ACKNOWLEDGMENTS

ABBREVIATIONS AND ACRONYMS

ANL	Argonne National Laboratory
APT	atom probe tomography
ASTM	American Society for Testing and Materials
ATEM	analytical transmission electron microscopy
AW	as welded
BSE	backscatter electron
BWR	boiling-water reactor
CIEMAT	Energy Environmental and Technological Investigations Centre
CF	cold forged
CGR	crack-growth rate
CM	carbide modified
CR	cold rolled
CRDM	control rod drive mechanism
CS	carbon steel
CT	compact tension
CW	cold worked
DCPD	direct current potential drop
DH	dissolved hydrogen
DM	dissimilar metal
DOE	Department of Energy
DZ	dilution zone
EBSD	electron backscatter diffraction
ECP	electrochemical potential
EDS	energy-dispersive x-ray spectroscopy
ENSA	Equipos Nucleares S.A.
EPRI	Electric Power Research Institute
FIB	focused ion beam
GEG	General Electric Global
GTAW	gas tungsten arc weld
H	hydrogen
HAZ	heat affected zone
HWC	hydrogen water chemistry
IG	intergranular
IGSCC	intergranular stress corrosion cracking
INSS	Institute of Nuclear Safety Systems, Incorporated
IPF	inverse pole figure
K	stress intensity factor
KAPL	Knolls Atomic Power Laboratory
LAS	low alloy steel

LOCA	loss of coolant accident
LOF	lack of fusion
LWR	light water reactor
MA	mill annealed
MHI	Mitsubishi Heavy Industries
MRP	Materials Reliability Program
NG	narrow groove
NRC	U.S. Nuclear Regulatory Commission
PEELS	parallel detection electron energy loss spectrometer
PNNL	Pacific Northwest National Laboratory
PWR	pressurized water reactor
PWHT	post weld heat treatment
PWSCC	primary water stress corrosion cracking
R	load ratio (minimum/maximum)
RCS	reactor coolant system
RPV	reactor pressure vessel
SA	solution annealed
SCC	stress corrosion cracking
SE	secondary electron
SEM	scanning electron microscopy
SGB	solidification grain boundary
SMAW	shielded metal arc weld
SS	stainless steel
SSGB	sub-solidification grain boundary
STEM	scanning transmission electron microscopy
TEM	transmission electron microscopy
TG	transgranular
TT	thermally treated
TTZ	transformation toughened zirconia
VG	V-groove

1   INTRODUCTION

Primary water stress corrosion cracking (PWSCC) is a degradation mechanism that can affect pressure boundary components made of nickel-base alloys and their welds in pressurized water reactors (PWRs). PWSCC preferentially occurs in components that operate at high temperatures and pressures. Fabrication and welding processes and especially weld repairs leave residual stresses that promote cracking in susceptible materials. The narrow cracks, which are often located in complex structures either within or adjacent to welds, are difficult to detect and characterize during in-service inspections. PWSCC that went undetected has led to reactor pressure boundary leaks and subsequent boric acid corrosion of low alloy steels at Arkansas Nuclear One-1 in 2001 and Davis-Besse in 2002. Extensive wastage of the Davis-Besse reactor head could have resulted in a loss of coolant accident (LOCA) had reactor operation continued and the damage gone undetected. Circumferential cracks discovered in the V.C. Summer reactor coolant system (RCS) piping welds in 2000 and in pressurizer nozzle welds at Wolf Creek in 2006 have raised concerns that PWSCC in PWR piping also could result in a LOCA.

Increasingly, industry has utilized alloy 690 and associated weld metals alloys 52 and 152 in both replacement components and in mitigation methods including weld inlays and overlays. Alloy 690 has been used in steam generators since 1989 and more than 30 PWR replacement heads using alloys 690/152/52 have been placed into service. The high chromium nickel-base alloys have also been used in RCS piping, nozzles, and instrument penetrations. While the service history has been favorable, significant industry and international efforts are underway to characterize the PWSCC susceptibility of alloys 690/152/52. Initial results have been reported in document MRP-237 Rev. 1 [1] and Rev. 2 [2]. Although the issue of PWSCC susceptibility is being addressed by industry, the U.S. Nuclear Regulatory Commission (NRC) has sought to obtain PWSCC growth rates of these crack resistant alloys and assess mitigation methods to determine the validity and acceptability of licensee flaw analyses and to support regulatory inspection requirements. In order to be successful, an improved understanding of the complex interrelations between stresses in the affected components, material microstructure, and the aggressive nature of the PWR environment is necessary.

In the original testing program (JCN N6007), three test systems were assembled. Initial testing was conducted on 300-series stainless steels, alloy 600 and alloy 182 in BWR and PWR simulated water chemistries. The effect of cold work, electrochemical potential, stress intensity and temperature were examined, and the results obtained were in good agreement with previously reported data. While limited tests were also conducted on alloy 690 and its weld metals, testing of the higher chromium alloys was the focus of the follow-up project (JCN N6782) at PNNL and two additional test systems were constructed. At the beginning of this project, very few quantitative SCC growth rate measurements had been reported on alloy 690 and even less on its weld metals. Additional SCC propagation data was (and still is) needed to define improvement factors for these materials when compared with alloy 600 and its weldments. One of the biggest challenges for quantitative measurements has been the difficulty in promoting and measuring SCC growth in the nickel-base, high-chromium materials. However, modern test systems, proper transitioning and considerable patience makes this possible for most alloys.

The effects of material microstructure, cold work, stress intensity, water chemistry, temperature and electrochemical potential on PWSCC growth rates were investigated in the first two NUREG/CR reports (Volume 1 [3] and Volume 2 [4]) from this project. This was followed by a

focused NUREG/CR report (Volume 3 [5]) dealing with SCC of cold-worked alloy 690. Crack-growth rates were measured in 37 different alloy 690 specimens exposed to simulated PWR primary water environments and detailed relationships were established among the degree of cold work, hardness, strain distributions, material microstructure and SCC response. Quantifying the influence of cold work and material strength on PWSCC growth rates was an important aspect of this NUREG/CR along with an assessment of many different alloy 690 product forms such as CRDM tubing, plate and bar materials.

The current Volume 4 report summarizes PNNL testing results completed by the end of 2016 on alloy 690 weld metals including alloys 152, 52 and its many variants. The higher strains associated with the welds and the weld metal complex microstructure provides more issues of concern. These higher chromium weld metals are also more susceptible to segregation and weld cracking including solidification cracking and ductility dip cracking. Finally, very little testing has been performed on dissimilar metal (DM) welds where complex compositions and microstructure can be produced at interfaces between Fe-bases alloys (e.g., low allow steel, carbon steel and stainless steels) and the high-Cr, Ni-base weld metal. Individual chapters will describe characterizations and SCC crack growth experiments for each of these interest areas: alloy 152/152M/52/52M/52MSS weld metals (Chapter 3), alloy 52M overlay and inlay welds (Chapter 4), and the interface regions in DM welds (Chapter 5). Results from 26 crack-growth tests on specimens from 16 different mockup welds are described in some detail and conclusions are made with respect to SCC susceptibility in these weldments.

2   SCC CRACK-GROWTH TEST SYSTEMS, TESTING APPROACH, AND MATERIALS SELECTION

The purposes of the crack-growth systems are to develop, control, and measure stress corrosion cracks under well-defined material and environmental conditions, and to ensure that the SCC growth rate response is reproducible and characteristic of the test conditions. Features expected in a good crack-growth system include active constant K load control, active temperature control, a sensitive crack length measurement apparatus, a recirculating high-temperature water system, control over all aspects of water chemistry, and continuous monitoring of all pertinent test parameters. The options for PNNL in creating a crack growth capability were for PNNL to design crack growth test systems, buy commercial systems, or copy a system at another research institute. It was determined very early in the previous program that the most advanced and reliable crack-growth systems in the world have been designed, developed, and run by Peter Andresen at General Electric Global Research (GEG). His crack-growth systems have been copied to various degrees by research institutes and commercial companies throughout the world. The decision was made to work closely with Peter Andresen and GEG staff on a crack growth system design. In the process of building the systems, some design aspects were improved, and more up-to-date parts were chosen when advantageous. GEG has incorporated some of these improvements and newer parts into their systems.

2.1   Overview of SCC Crack-Growth Test Systems

The key components of these systems are: (1) a servo-electric load control system capable of holding constant load for very long periods of time, (2) a high-pressure piston pump to pressurize and flow water through the high-temperature loop, (3) an autoclave, (4) a custom-made water board for water chemistry control, (5) a reversing DCPD system for crack length estimation, and (6) a continuous data acquisition system. Careful consideration went into the selection of each piece of equipment to optimize either test system control or test environment. Some of the most important optimizations were to: (1) make sure that all wetted components release no contamination into the water, (2) have a high water flow rate through the autoclave, (3) have uniform temperature through a large volume of the autoclave, (4) have consistent water pressure, (5) have highly accurate measurements of test environment (temperature, conductivity, pH, load, dissolved gas content), and (6) have a sensitive DCPD measurement system. Each of the subsystems will be discussed in further detail below.

The water flow design of the system is a loop within a loop as shown in Figure 2-1. One loop is at low pressure, and its purpose is to flow water through a water column where selected gases and ionic impurities are dissolved or injected into the water. A side stream is taken off this low-pressure loop and fed into a high-pressure piston pump. The large pressure pulses and flow surges created by the piston pump are dampened by the use of pulsation dampers both at the inlet and outlet of the pump. The high-pressure water flows into a regenerative heat exchanger where hot water leaving the autoclave is used to heat the incoming water. Just prior to the water entering the autoclave, the partially heated water is brought up to test temperature using a preheater. After the water flows through the heated autoclave, it goes back through the regenerative heat exchanger and then through a water cooler that brings the water back down to room temperature. The cooled water then passes through a back-pressure regulator and emerges at ~0.07 MPa (10 psi) of pressure. The water flows through a flow meter, a conductivity sensor, a mixed resin bed demineralizer, and is finally dumped back into the low-pressure chemistry control loop.

SCC System Block Diagram
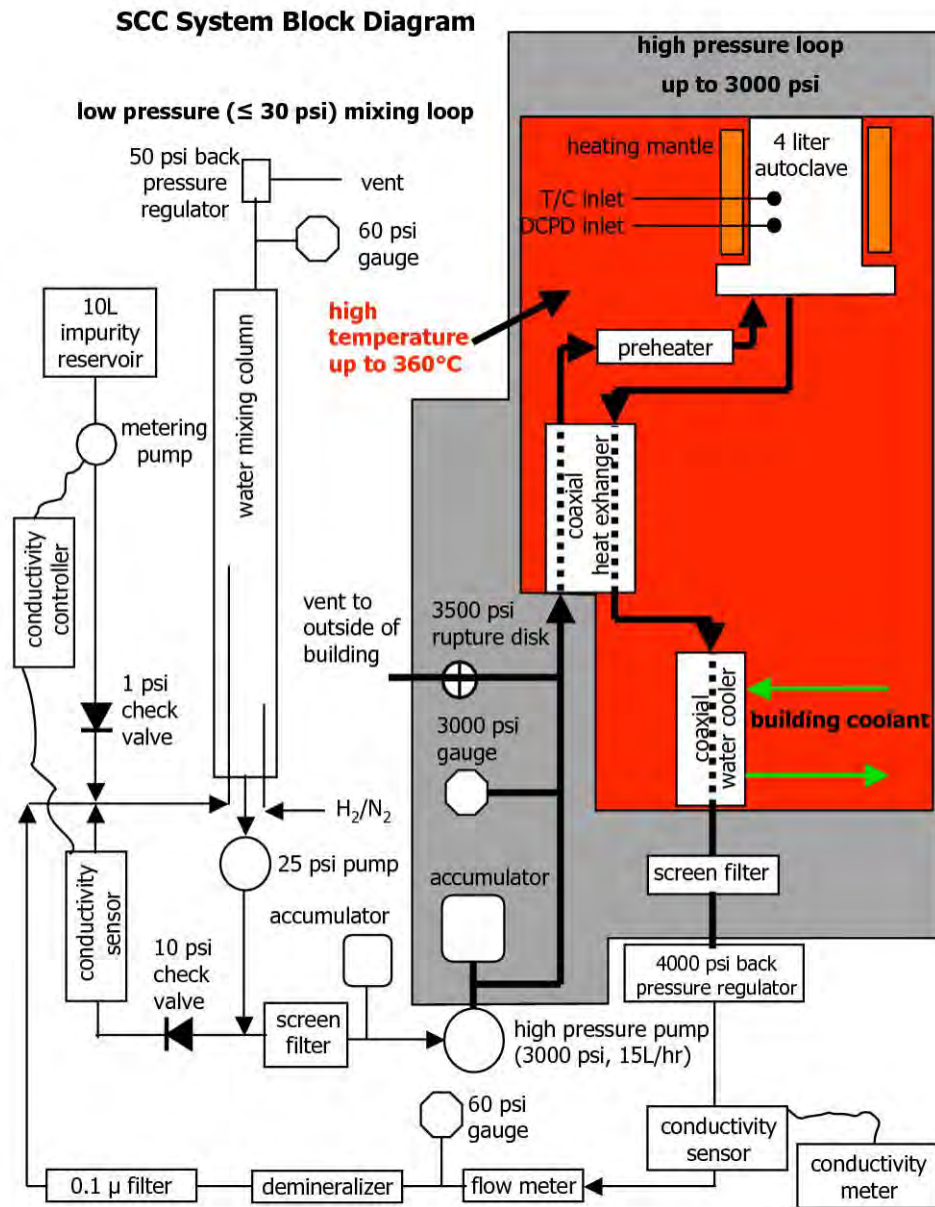
Figure 2-1   General Water Flow Diagram for PNNL SCC Crack-Growth Test Systems

Boron (B) and lithium (Li) levels for PWR water testing are controlled by pre-saturating the mixed resin bed demineralizer with boric acid and lithium hydroxide to specific levels that will result in tailored near-constant B and Li content in the water. There is some drift in the Li level in the water because it is singly ionized and is easily displaced from the demineralizer by more highly positively ionized species coming off the autoclave such as chromate. The displaced Li is removed by periodic partial replacement of water in the mixing loop with water having little or no Li (and some B). Boron and Li levels in the mixing loop are determined from measurements of water conductivity, pH, and temperature using pHSC4 software (obtained from Rick Eaker of Duke Power). Autoclave flow rate is held to at least 125 cc/min (approximately two autoclave exchanges per hour) to provide a consistent chemistry environment within the autoclave.

Load is applied to a sample using a servo-electric motor attached to the test frame. The servo-electric motor is controlled using proprietary software from GEG. The servo-electric motor can provide a smooth cyclic loading sine wave up to about 3 Hz, allowing in-situ pre-cracking of a test sample. Using DCPD data, the GEG software can continuously adjust the servo-electric motor to provide constant K loading conditions. As shown in Figure 2-2, the load from the servo-electric motor is transmitted into the autoclave with a pullrod, and the sample is braced from above by a top plate and 4-bar linkage that transmits load to the baseplate of the autoclave which is bolted to the test frame.

Crack length is estimated using a reversing DCPD system developed by Peter Andresen of GEG. A sketch of the system is shown in Figure 2-3. As with all DC potential drop measurement systems a constant current is run though the sample, and the voltage across the crack plane is measured and converted into a crack length by means of an empirically derived formula relating voltage to crack length. A referenced DCPD resistivity is monitored directly on the test specimen using a "back face" potential method developed at GEG. Using a solid-state polarity-reversing switch built into the current path, potential drop is measured in both a forward and reverse current flow condition. By measuring in both directions, the system eliminates contact voltages from the measurement.
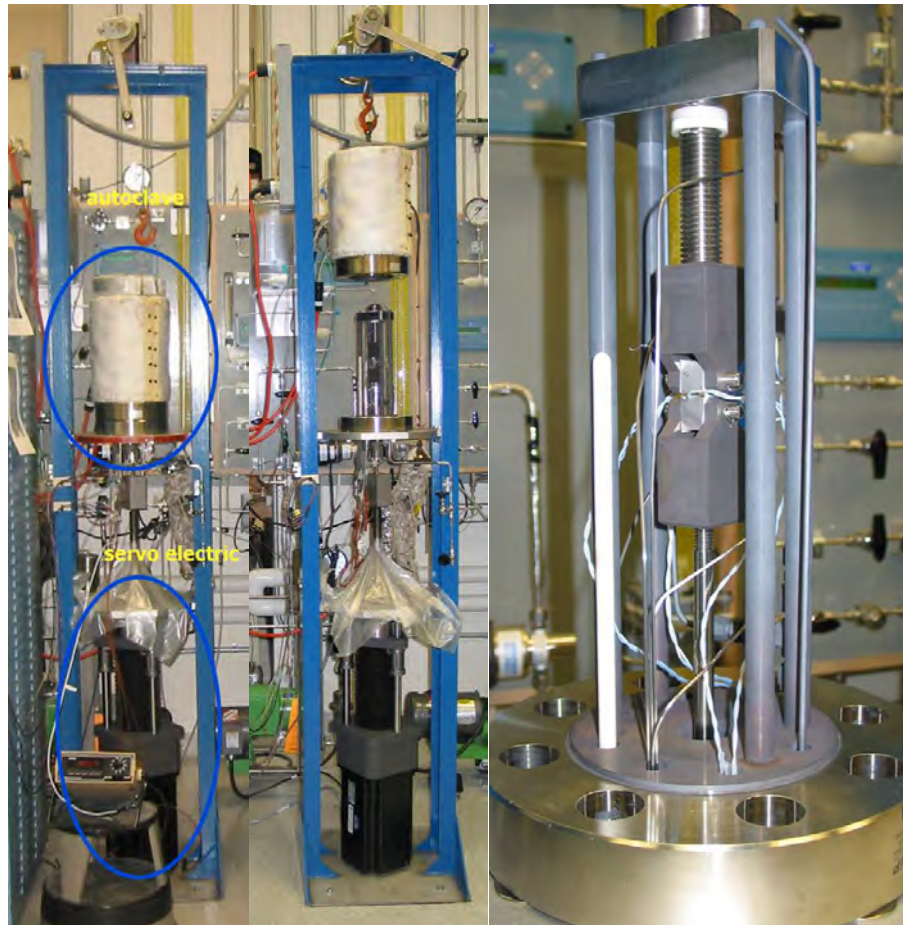
Figure 2-2   Typical Crack-Growth-Rate Test Frame Loading System Used at PNNL
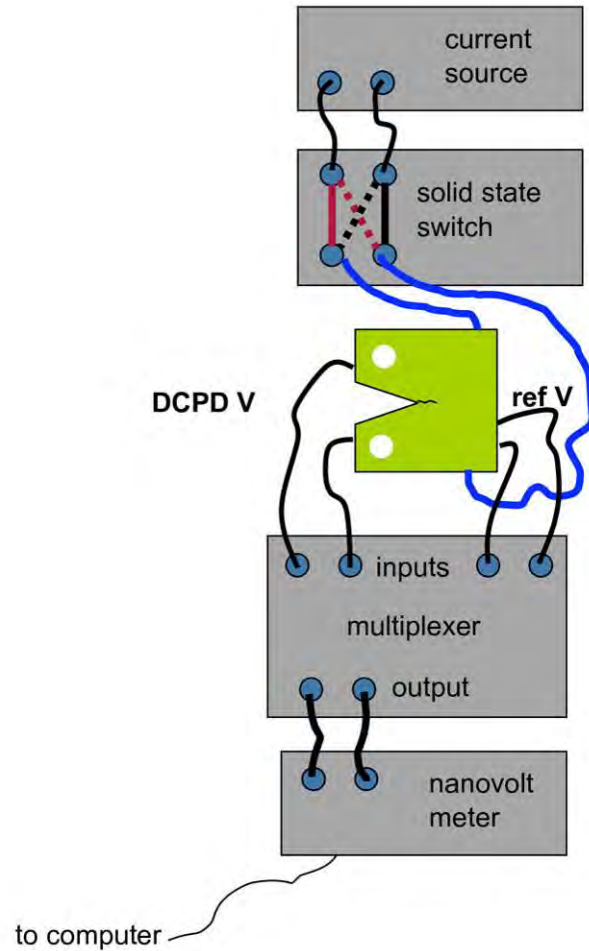
Figure 2-3 **Schematic Diagram Illustrating the DCPD System to Measure Crack Length in Situ**

The GEG software also controls the operation of the DCPD system and aggregates the data. Platinum wire is used for current and voltage feeds into the autoclave. For PWR water testing, segmented transformation toughened zirconia (TTZ) tubing is used to help prevent shorting of the Pt wires against other wires or any metal surfaces in the autoclave. Some crosstalk in the voltage wires occurs and is minimized by keeping the wires separated as far as reasonably possible from each other. In addition, the current wires are kept away from the voltage measurement wires. The sample is electrically insulated from the load train through a combination of ceramic spacers and sleeves. Spot welding is used to attach the platinum wires to a specimen. The spot weld locations are marked on the sample prior to inserting the sample into the load train.

The PNNL systems have the capability to monitor autoclave water outlet conductivity, mixing loop water conductivity, autoclave temperature, autoclave water flow rate, sample corrosion potential (via a ZrO_2 insulated Cu/Cu_2O reference electrode in the autoclave), dissolved oxygen, water pressure, DCPD current, and DCPD voltage. With the exception of water pressure and flow rate, these parameters are recorded in the test data file. Statistical information on temperature and current fluctuations are also recorded. Additionally, messages describing changes in test conditions and other issues are a permanent part of the data record.

2.2   General SCC Crack-Growth Testing Approach and Issues

Although systems have been designed for both 1T and 0.5T CT specimens, the primary specimen geometry used in this project is the 0.5T CT with side grooves. The details of the specimen geometry are shown in Figure 2-4. Prior to loading a specimen in the autoclave, the sample thickness, notch depth and width values are all measured and recorded into the data record for the test. Using the sample dimensions and the yield strength of the specimen at the test temperature, in accordance with American Society for Testing and Materials (ASTM) E-1681, an upper limit on the value of the stress intensity (*K)* is calculated using the formula:

$$K = \sigma_{ys}\sqrt{D/1.27} \tag{2.1}$$

where σ_{ys} is the yield strength at the test temperature and D is the smallest of the specimen thickness, the remaining uncracked specimen width and the crack length. In the case of materials with large amounts of work hardening (defined as $\sigma_{UTS}/\sigma_{ys} > 1.3$) such as annealed 300-series stainless steels and nickel-base alloys, the average of the yield and ultimate stress is used in place of the yield stress as per ASTM guidelines.

After the sample dimensions are measured and spot-weld locations are marked on the sample, it is cleaned and inserted into a test system. Pre-cracking of a sample is done in-situ at the test temperature when a single specimen is being tested. Initial pre-cracking of two or more specimens mounted in-series is not possible in-situ because the length of time needed to nucleate a pre-crack is not consistent, so precracking two specimens in series would likely lead to specimens with different precrack lengths. The differing precrack lengths would make it impossible to maintain and control the K level in both specimens during and after pre-cracking. Thus, the approach for testing at PNNL is to nucleate a crack individually on each of the two specimens under fatigue in air[1], followed by continued precracking of the two samples loaded together in-situ. Crack transitioning steps are carefully selected to grow the pre-crack in high-temperature water using the following stages: (1) fatigue, (2) corrosion fatigue and (3) SCC. Typically, this means producing initial precracks of ~1 mm in air followed by an additional ~1 mm by cycling in-situ before transitioning to slow cyclic loading plus hold times to promote SCC. An Instron servohydraulic test frame is used to precrack CT specimens in air, and the same DCPD electronics and system control software used for the crack-growth systems is also used for the Instron test frame.

---

[1] Practically speaking, CT samples slated for testing in series could be individually precracked in-situ. However, this would result in a significant increase in system set-up requirements, sample modifications, test time and expense. The initial precracking in air is now done without impacting the current operation of the available PNNL SCC test systems. This precracking is done under well-controlled conditions, and care is taken to make sure that samples, grips and other components are cleaned before testing.
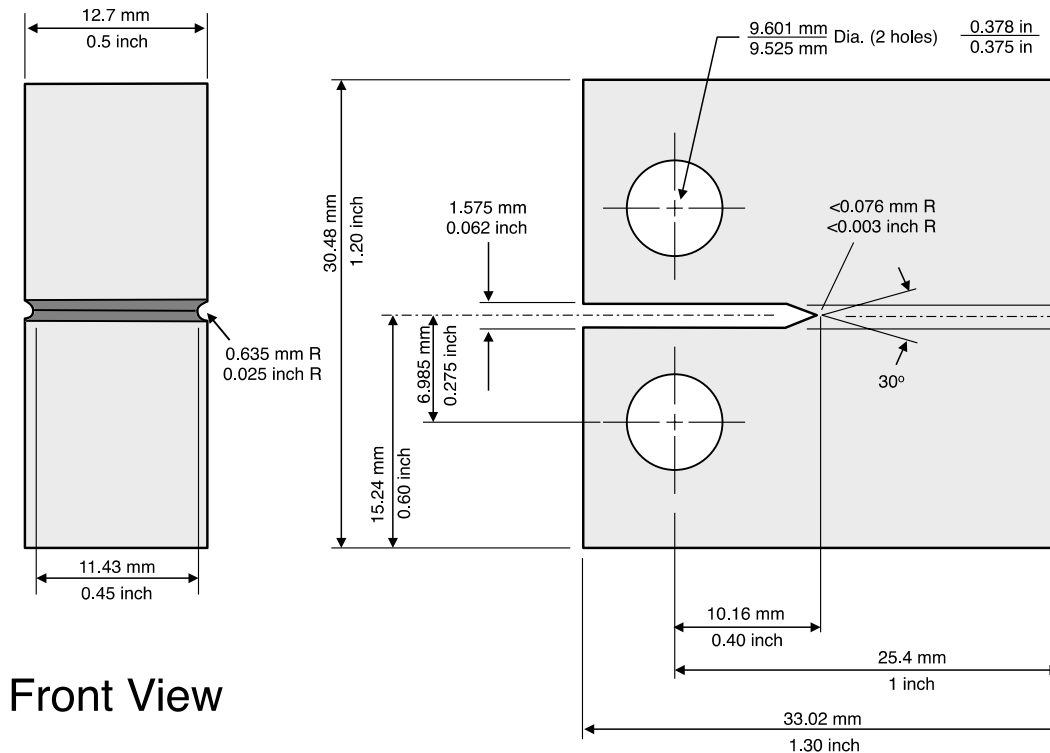
Figure 2-4   Schematic Drawing of a 0.5T CT Specimen. Dimensions for 1T CT Specimens Are Approximately Double

The first step in pre-cracking is to cycle the sample at a relatively high frequency (1–20 Hz) with a large load ratio and K_{max} less than the K level chosen for constant K. As the crack begins to grow from the notch, the load ratio and frequency are reduced while the K_{max} value is increased. By pre-cracking in this way, each pre-crack segment can grow beyond the plastic zone created by the previous segment. For all samples, cyclic loading steps at frequencies of 0.1 Hz down to 0.001 Hz are performed in high-temperature water. The final phase involves crack transitioning by very slow cycling with a hold time ranging from 1 h to 24 h. This grows the crack beyond the pre-cracking plastic zone and allows the crack to transition from transgranular (TG) fatigue to the crack growth mechanism that occurs for that material under constant K conditions.

For materials such as cold-worked (CW) 316SS that crack readily in LWR environments, obtaining a steady crack growth rate (CGR) after transitioning to constant K can easily be accomplished by following a standard procedure. However, determining a constant K CGR in highly SCC-resistant materials such as alloy 690 and its welds is more challenging with the main focus on giving the crack adequate opportunity to become an engaged IG crack. For these materials, the use of alternate cyclic and cycle + hold loading conditions, including various load ratio (R) values and modified rise/fall times, are often employed prior to reaching constant K. Tests conducted at PNNL have shown that an R of 0.5 usually produces the best engagement response, and in base metal materials, efforts are made to run the specimen under slow continuous cycling for several grain dimensions prior to the onset of cycle + hold loading. The much larger grain dimensions and more irregular shape of the grain boundaries in weld metals makes transitioning to an engaged crack front even more challenging. If extremely slow or inconsistent CGRs are observed, cyclic loading is typically restarted to move the crack forward (ten microns to several hundred microns) and then retransition to constant K. This retransitioning procedure may be performed several times. The constant K SCC response is

judged on the response of the material to these multiple observations at constant K. Observation of the propagation rate under selected cyclic loading and hold time conditions is also used to judge the crack growth resistance of the material.

The ideal increment of crack length over which to measure a steady CGR would be several grain diameters. However in alloy 690 and its weld metals, this is often an extremely impractical goal that could take more than two years to achieve and so it is necessary to choose an increment based on factors related to accuracy and resolution in the DCPD crack length data trend. The most easily quantifiable factor is noise or scatter in the DCPD crack length data. Each PNNL crack growth system has slightly different noise levels. The best system at PNNL has a noise level of 1.0 μm peak-to-peak while the "worst" system has ~3 μm peak-to-peak noise. Noise creates uncertainty in the measurement. Uncertainty is greatest when only a few measurements are performed, but as the number of measurements is increased, an average value can be resolved along with statistics on the goodness of fit. This is equivalent to fitting a trend line through the data. As long as the noise remains random (e.g., the residuals in the curve fit remain random), trends in the data down to the noise level can be resolved. Other factors contributing to the uncertainty in trends in the data are related to environment, crack morphology effects, and resistivity drift of the material. Environmental parameters such as water temperature, water conductivity, and dissolved hydrogen have been found to affect crack length, and it is important to limit deviations in these parameters. All environmental parameters on PNNL crack growth systems that can lead to phantom changes in crack length are monitored and tightly controlled. The factor affecting crack length accuracy and resolution that is most difficult to control is crack morphology. DCPD is based on the notion that there is no electrical current conduction behind the crack front. In stress corrosion crack-growth testing (especially in PWSCC testing), it has been found that there is almost always some feature in the crack morphology that allows current conduction behind the crack front. The most easily identifiable feature is an uncracked ligament in the wake of a crack as shown in Figure 2-5. Electric current bridging across very closely spaced crack walls is also thought to contribute to conduction behind the crack front. These features cause underprediction of DCPD-measured crack length and reduce the sensitivity of the DCPD system to detecting movement of the crack front. Crack ligaments can also cause large steps in crack extension when they break. Uneven growth along the crack front also causes crack length underprediction and reduced sensitivity in the same way as ligaments behind the crack front. It is important to recognize that all these morphology effects do not cause falsely high CGRs, but instead lead to underprediction of crack extension. The only phenomenon that leads to a falsely high CGR is resistivity change that occurs in Ni-base alloys such as alloy 600 and alloy 690. It is a well-known phenomenon that the resistivity of these alloys will slowly increase with time when testing at PWSCC temperatures. Without compensation, resistivity drift will give the appearance of a slowly increasing crack length. It is typical to compensate for resistivity drift by monitoring the resistivity of a piece of unstressed reference coupon placed in the autoclave environment. The resistivity change of the test specimen is normalized to the resistivity of the reference coupon. Looking at all these factors in aggregate, the test systems at PNNL are designed with a sufficiently high data acquisition rate to allow trends in crack extension to be detected down to the noise level of the DCPD system as long as test conditions are tightly controlled and resistivity drift is properly factored into the crack length measurement. Effects of current conduction behind the crack front and uneven crack extension will produce CGRs that are lower than what are actually occurring, so any CGR that is detectable by DCPD is expected to be an underprediction of the actual rate. There has yet to be a test where CGR has been overpredicted.
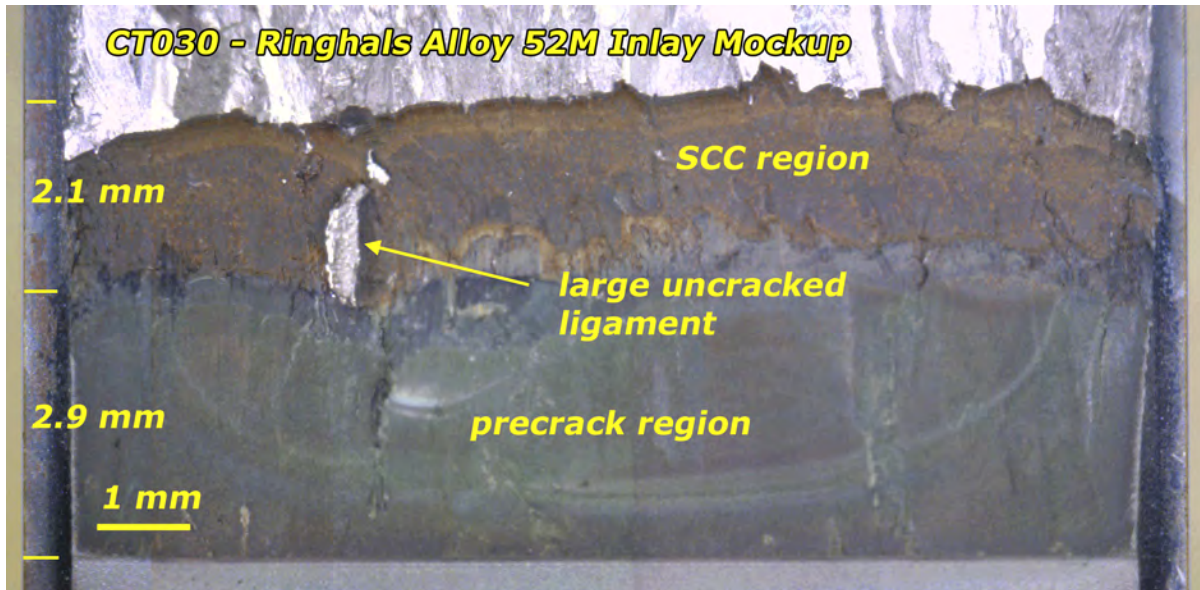
Figure 2-5   Example of Large Uncracked Ligament Detected in the Wake of a Crack

2.3   Specific SCC Crack-Growth Testing Approach

Unless noted otherwise, experiments were conducted in simulated PWR primary water with 2000 ppm B and 2 ppm Li. A prototypic simulated PWR primary water environment is considered to be 325°C with 29 cc/kg H_2. Tests conducted early in the program were often done at this temperature and hydrogen concentration, however as the program progressed, the desire to better understand the crack growth response of alloy 690 and its welds eventually led to testing at 350°C, and then later at 360°C. Testing now is typically conducted at 360°C. Dissolved hydrogen (DH) concentration also evolved over the course of the program with most testing now done at DH concentrations that place the corrosion potential of the material on the Ni/NiO stability line where crack growth response is known to be greatest in alloy 600 and its weld metals. Limited testing was also performed at 50°C under primary water conditions. The *K* was controlled to a value of 30 MPa√m under most conditions, however high K values were often evaluated up to ~40 MPa√m near the end of many SCC CGR tests. Crack growth tests were performed with two specimens in series allowing a greater range of material conditions to be examined in a shorter period of time.

Specimens were first precracked in air and followed by further crack extension using aggressive cycling in high temperature water. A variety of loading conditions were used to attempt to transition from the TG precrack to an IGSCC crack front. Loading conditions included R values ranging from 0.5 to 0.9, the addition of hold times up to 24 h, and various "periodic unload" schemes with a symmetric or a sawtooth wave form (e.g., rapid unload followed by a slow reload). Based on the current work and tests on alloy 690, a final cycling step at 0.001 Hz with R = 0.5-0.7 was often used and followed by the addition of hold times before determining CGRs at constant K.

The response of the material during transitioning was assessed continuously by comparing current propagation rates to results from earlier tests. As the database of observed CGRs and accompanying crack surface morphologies from previous tests grew, higher propagation rates during transitioning (particularly during cycle + hold loading) could be identified. If a CGR during

transitioning was indicative of a non-engaged crack front, then the crack would often be re-transitioned in an attempt to improve SCC engagement. For these SCC resistant alloys, several transitioning attempts were typically made before documenting constant K CGR response.

The general philosophy for assessing CGRs of alloy 690 and its weld metals is to first obtain baseline SCC behavior with the material in the expected plant thermomechanical treatment and then follow with tests on material in off-normal conditions. Testing typically begins in simulated PWR primary water environment, but at an elevated temperature and DH concentration at the Ni/NiO stability line). In some tests, these conditions would eventually be followed by systematic variations in environmental conditions to assess the effects of parameters such as temperature, stress intensity and DH on the SCC response of these materials.

Most weld metals were tested in the as-welded condition with the crack plane aligned along the dendrite growth direction (often referred to as the T-S orientation in weldments). For one case, the influence of a post weld heat treatment was evaluated and testing is also underway on 4 welds in the cold-forged condition with a reduction of 15% in thickness. The standard environmental condition for all tests has been 360°C simulated PWR primary water, however test temperature and hydrogen content has been varied to assess effects on crack growth response. With only five NRC test systems and test times ranging from 6 to 12 months, it has been challenging to study a wide range of welds even when testing two specimens in series.

From a testing perspective, several factors make determination of the IGSCC susceptibility of weldments particularly challenging. The first factor is that a relatively large amount of crack extension is required during transitioning to effectively sample the grain boundaries of the very large and elongated grains in these materials. A second factor is that these high-Cr welds appear to be resistant to IG growth in PWR primary water. This leads to a simultaneous need for aggressive cycling to sample grain boundaries in a reasonable time and gentle cycling to provide the best conditions for IG engagement. Our approach to dealing with these opposing requirements has been to frequently retransition and maintain gentle cycling conditions for long times. Another issue is that ligaments or contacts can form in these weld metals even when aggressive cycling is used during transitioning sequences. Not only can crack growth sometimes be slowed in the vicinity of these ligaments, but ligaments also affect the DCPD-based measurement of crack extension. The effect of ligament or contact formation during constant K crack growth has been assessed by observing the immediate crack growth response during cycling after constant K exposures. Ligaments or contacts that break will produce an initially high CGR for the given loading condition.

2.4   Materials Selection

Various alloy 152, 52 and 52M weld mockups have been obtained for SCC testing as part of this project. All of these materials were supplied by industry sources and were selected to represent industry practices of direct relevance to PWR service. In most cases, these mockups were produced specifically to qualify a welding approach to be used for plant replacement or repair. Alloy 152 and 52 U-groove welds produced by Mitsubishi Heavy Industries (MHI) were obtained from EPRI and were mockups for the pressure vessel head replacement at the Kewaunee plant. In addition, an alloy 52 butt weld was obtained from AREVA NP that was produced as part of a testing program. Alloy 52M and 152M welds were obtained from George Young at KAPL and supplied as part of an international cooperative program on alloy 690 led by EPRI and the NRC. Finally, alloy 52M/182 overlay and alloy 52M/82 inlay weld mockups produced by Ringhals-Vatenfall were obtained with the help of Pal Efsing. A brief description of the welds, their heat

numbers, and compositions are listed in Table 2-1. Weld fabrication method differed for each of the weldments and available information will be provided in the following sections.

Twenty-six SCC crack-growth tests on alloy 152/52/52M weldments were completed. Table 2-2 summarizes the various welds, specimen numbers and general test conditions for each of the weld metal tests. SCC results for these crack-growth tests will be described in detail along with characterizations of the welds.

Table 2-1   Alloy 152, 152M, 52, 52M and 52MSS Weldments at PNNL

Material - Source	Heat Number and Description	Weld Metal Composition, wt%
Alloy 152 – MHI	Heat 307380, U-groove mock-up weld for Kewanee, 304SS plate	Ni-28.7Cr-9.1Fe-0.03C-3.6Mn-0.33Si-0.15Al-0.12Ti-0.003S (independent analysis)
Alloy 152-ANL	V2 Dissimilar Metal Weld	
ANL 152-IHI	Butt Weld	
Alloy 152M - KAPL	Heat WC83F8, V-groove dissimilar metal weld, carbon steel (CS) and 316SS plate, no butter used on the CS and no PWHT applied	Ni-30.2Cr-8.7Fe-<0.005C-3.0Mn-0.22Si-<0.01Al-0.03Ti-1.176Nb-0.002S-0.03V (mill test report)
Alloy 52 – MHI	NX2686JK, MHI U-groove weld to 304SS plate, mock-up for Kewaunee plant	Ni-29.1Cr-10.0Fe-0.024C-0.25Mn-0.13Si-0.71Al-0.52Ti-0.01N$_2$ (standard comp)
Alloy 52M – KAPL	Heat NX5285TK, High constraint, narrow groove weld, alloy 690 plate	Ni-30.0Cr-7.9Fe-0.026C-0.19Mn-0.12Si-0.07Al-0.19Ti-3.83Mo-2.57Nb (mill test report)
Alloy 52M – KAPL	V groove weld	
Alloy 52M- ENSA	DPM 52M Butter	
Alloy 52MSS-Special Metals	NX77W3UK, V-groove weld, alloy 690 plate	Ni-29.9Cr-8.3Fe-0.014C-0.75Mn-0.13Si-0.11Al-0.21Ti-0.81Nb+Ta
Alloy 52 – AREVA NP	NX3926JK, Mockup butt weld, alloy 690 plate	Ni-29.1Cr-10.0Fe-0.024C-0.25Mn-0.13Si-0.71Al-0.52Ti-0.01N$_2$ (standard comp.)
Alloy 52M – KAPL	Heat NX5285TK, V-groove dissimilar metal weld, carbon steel and 316SS plate	Ni-30.0Cr-7.9Fe-0.014C-0.75Mn-0.13Si-0.11Al-0.21Ti-0.81Nb+Ta (mill test report)
Alloy 52M - KAPL	Heat NX5285TK, Narrow groove weld with modified weld conditions to create hot cracks	Ni-30.0Cr-7.9Fe-0.014C-0.75Mn-0.13Si-0.11Al-0.21Ti-0.81Nb+Ta (mill test report)
52M - EPRI	52M Temper Bead Repair Weld	
Alloy 52 - MHI	U groove weld	
Alloy 52M/182 Overlay - Ringhals	Mockup alloy 52M overlay on alloy 690 plate with alloy 182 overlay (heat numbers not available)	Ni-30.0Cr-8.4Fe-0.020C-0.81Mn-0.03Si-0.10Al-0.21Ti-0.85Nb+Ta (mill test report)
Alloy 52M/82 Inlay - Ringhals	Mockup alloy 52M inlay on alloy 82 weld and A533 pipe (heat numbers not available)	not available

Table 2-2   Summary of PNNL SCC Tests on Alloy 152, 52 and 52M Weldments

Specimen	Material	Test Description	Completion Date
CT013	Alloy 152 - MHI	PWR Primary Water, alloy 152	4/07
CT017	Alloy 152 – MHI, as welded	PWR Primary Water, Temp effects, alloy 152	6/08
CT018	Alloy 152 – MHI, stress relieved	PWR Primary Water, Stress relief effects, alloy 152	6/08
CT024	Alloy 52 – AREVA, as welded	PWR Primary Water, alloy 52	1/09
CT025	Alloy 52 – MHI, as welded	PWR Primary Water, alloy 52	1/09
CT028	Alloy 52M on Alloy 182 overlay – Ringhals	PWR Primary Water, alloy 182 into 52M, alloy 52M	4/09
CT029	Alloy 52M on Alloy 182 overlay – Ringhals	PWR Primary Water, alloy 182 into 52M, alloy 52M	4/09
CT030	Alloy 52M on Alloy 82 inlay - Ringhals	PWR Primary Water, alloy 82 into 52M, alloy 52M	10/09
CT031	Alloy 52M on Alloy 82 inlay - Ringhals	PWR Primary Water, alloy 82 into 52M, alloy 52M	10/09
CT032	Alloy 52 – AREVA as welded	PWR Primary Water, low temp on high temp CGR	10/09
CT033	Alloy 52 – MHI as welded	PWR Primary Water, low temp on high temp CGR	10/09
CT034	Alloy 52M on Alloy 182 overlay – Ringhals	PWR Primary Water, alloy 182 into 52M, alloy 52M	10/09
CT035	Alloy 52M on Alloy 182 overlay – Ringhals	PWR Primary Water, alloy 182 into 52M, alloy 52M	2/10
CT040	Alloy 52M narrow gap weld - KAPL	PWR Primary water, alloy 52M	7/10
CT041	Alloy 52M V-groove weld - KAPL	PWR Primary water, alloy 52M	7/10
CT042	Alloy 52M KAPL narrow gap weld with aligned hot cracks	PWR Primary Water, weld defects/cracks on SCC	7/10
CT043	Alloy 52M KAPL narrow gap weld with non-aligned hot cracks	PWR Primary Water, weld defects/cracks on SCC	7/10
CT049	Alloy 152 – As welded	PWR Primary Water, alloy 152	1/11-11/11
CT050	Alloy 52MSS – As welded	PWR Primary Water, 52MSS	1/11-11/11
CT051	Alloy 152 – AW+ 20%CF	PWR Primary Water, effect of cold work	1/11-8/11
CT052	Alloy 152 – As welded	PWR Primary Water, alloy 152	1/11-8/11
CT065	Alloy 52M/CS Interface dilution zone (no PWHT)	PWR Primary Water, CS interface	5/12
CT066	Alloy 152M/CS Interface dilution zone (no PWHT)	PWR Primary Water, CS interface	5/12
CT075	Alloy 152/SS Interface region	PWR Primary Water, SS interface	1/12-1/13
CT076	Alloy 152/SS Interface region	PWR Primary Water, SS interface	1/12-9/12
CT080	Alloy 152 – As welded	PWR Primary Water, alloy 152	6/12-6/13
CT081	Alloy 52M – As welded	PWR Primary Water, alloy 52M	6/12-6/13

Specimen	Material	Test Description	Completion Date
CT082	Alloy 152M/CS Interface dilution zone + PWHT	PWR Primary Water, CS interface	6/12-3/13
CT083	Alloy 52M/CS Interface dilution zone + PWHT	PWR Primary Water, CS interface	6/12-3/13
CT117	ANL Alloy 152/LAS interface	PWR Primary Water, LAS interface	8/14-4/16
CT119	ANL Alloy 152/LAS interface	PWR Primary Water, LAS interface	8/14-11/15
CT120	Alloy 52 – As welded	PWR Primary Water, alloy 52	8/14-6/15
CT134	Alloy 52M repair weld	PWR Primary Water, repair weld	9/15-11/16
CT135	Alloy 152 – As welded	PWR Primary Water, alloy 152	9/15-5/16
CT136	Temper bead repair weld, 52M/LAS interface	PWR Primary Water, LAS interface	11/15-11/16
CT137	Alloy 52M butter – As welded	PWR Primary Water, alloy 52M	11/15-11/16
CT138	Alloy 52M butter – AW + 15%CW	PWR Primary Water, effect of cold work	5/16-Ongoing
CT139	Alloy 52 – AW + 15%CF	PWR Primary Water, effect of cold work	5/16-Ongoing
CT140	Alloy 152M – AW + 15%CF	PWR Primary Water, effect of cold work	7/16-Ongoing
CT141	Alloy 152 – AW+15%CF	PWR Primary Water, effect of cold work	7/16-Ongoing

3   ALLOY 152/52/52M WELDS

3.1   Alloy 152 Welds

3.1.1   Early Tests on MHI Alloy 152 U-Groove Mockup Welds (CT013, CT017 and CT018)

Initial weld metal SCC testing started with the alloy 152 mockup weld obtained from EPRI, which was produced for the Kewaunee reactor pressure vessel head replacement by MHI. It was made using 6.1 mm (2.4 in.) thick plates of 304SS butted together with a U-groove as shown in Figure 3-1. Alloy 152 (heat 307380) butter passes were applied to each half of the U-groove (the ends of buttering were machined flat), and then the plates were welded together with alloy 152 (heat 307380). Both the buttering and the filler were applied by shielded metal arc welding (SMAW), of which the welding parameters for the alloy 152 SMAW filler material consisted of a deposition speed of 4-25 cm/min and a current of 95-145 A.

A portion of the weldment was sectioned at PNNL into 1.9 cm (0.75-in.) thick blocks (Figure 3-2), and metallographically prepared to reveal the individual weld passes and the butter zone as shown, for example, in Figure 3-1. Sections C, D, and E indicated in Figure 3-2 were selected for fabricating CT samples. After polishing, these blanks were marked for machining so as to locate the end of the pre-crack in a single weld pass and enable >1 mm of growth in that weld pass. A close examination was made to select a weld pass where the dendrites would be as parallel as possible to the pre-crack. The machined notch from section C is shown in Figure 3-3. Crack growth testing was performed in the weld pass below the pass where the machined notch is located. The precrack was located in the same weld pass for sections C and D, but the slight microstructural variability in the weld along the length of the mockup meant that it was necessary to use a different weld pass for crack growth testing (moving one up) for section E.
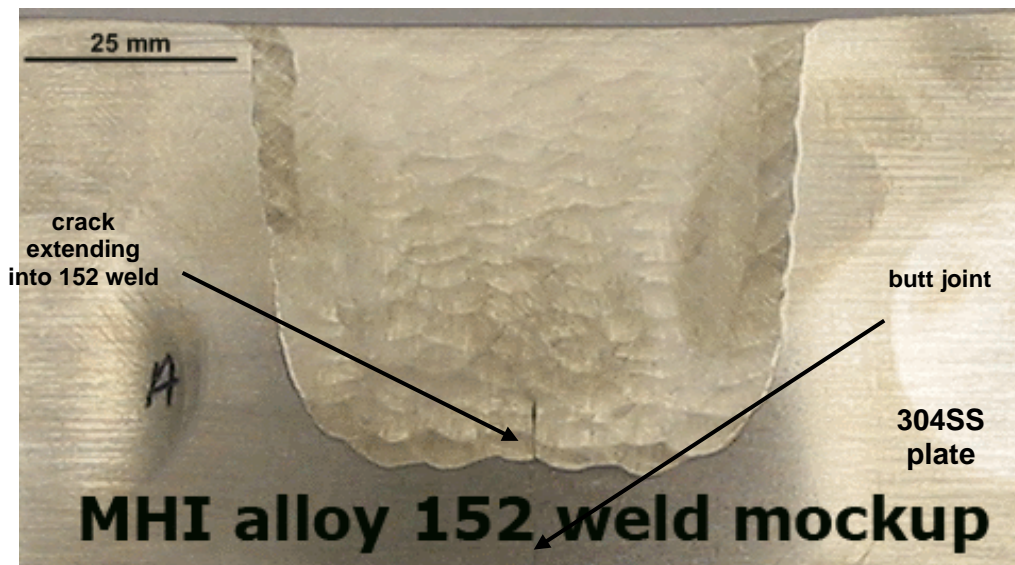
Figure 3-1   Optical Image of the MHI Alloy 152 Mockup Showing U-Groove Weld in Cross-Section
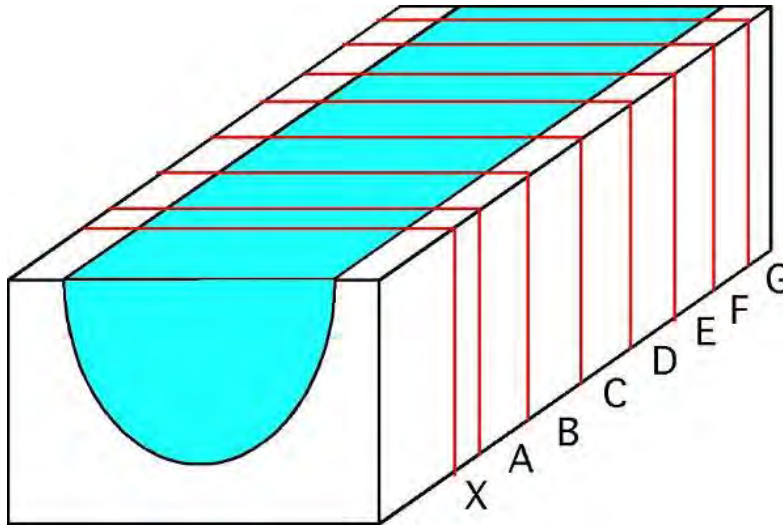
Figure 3-2   Sectioning Diagram for the Alloy 152 Welded Block. End Sections X and G Are 1.3 cm Thick and Were Used for Metallographic Observations While Sections A-F Are 1.9 cm Thick and Were Used for CT Samples. There Is ~7.6 cm of Welded Block in Front of Section "X"
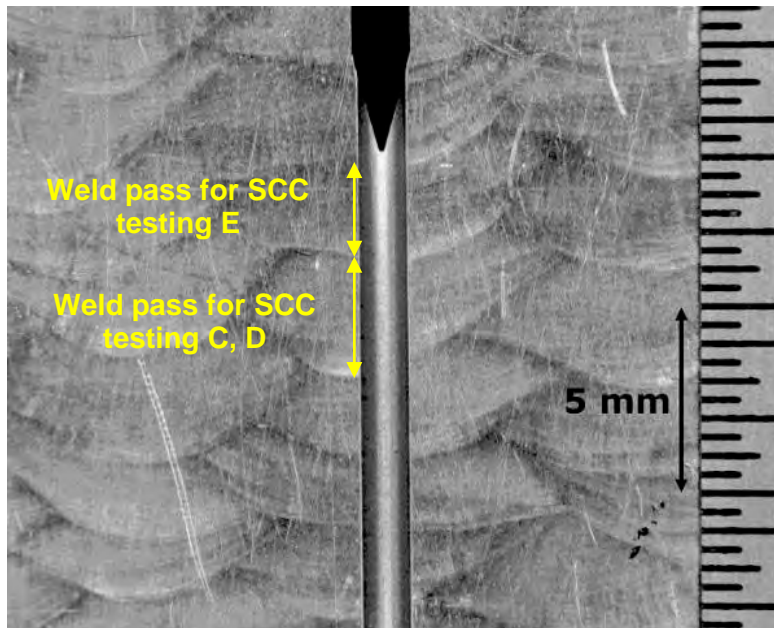
Figure 3-3   Optical Micrograph of Section C Showing the Location of the Machined Notch. This Same Weld Pass Was Selected in Section D, While the One Just Above and to the Left Was Selected in Section E

Scanning electron microscopy (SEM) examinations were carried out in section X and revealed a standard solidification and sub-solidification grain boundaries (SGB and SSGB, respectively). Examples of these are seen in Figures 3-4 and 3-5. Based on SEM examination of the microstructure of the alloy 152 weld, the weld is composed of a mixture of a cellular and columnar dendritic structure with heavy precipitation on both the SGB and SSGBs. The backscatter electron (BSE) images of the dendrites in Figure 3-4 reveal a mottled contrast that

is presumed to arise due to strain in the matrix. Carbides scattered throughout the dendrites show up as dark particles in the BSE images, whereas in the secondary electron (SE) images, the particles typically show up as bright particles because they are sticking out from the specimen surface. Some of the dendritic boundaries etched differently than the surrounding matrix, possibly due to either compositional changes or from precipitation on the boundaries. Perhaps the best method to illustrate the weld microstructure is by electron backscatter diffraction (EBSD) shown in Figure 3-5. Grain-to-grain orientation differences are highlighted identifying the elongated solidification grain boundaries.
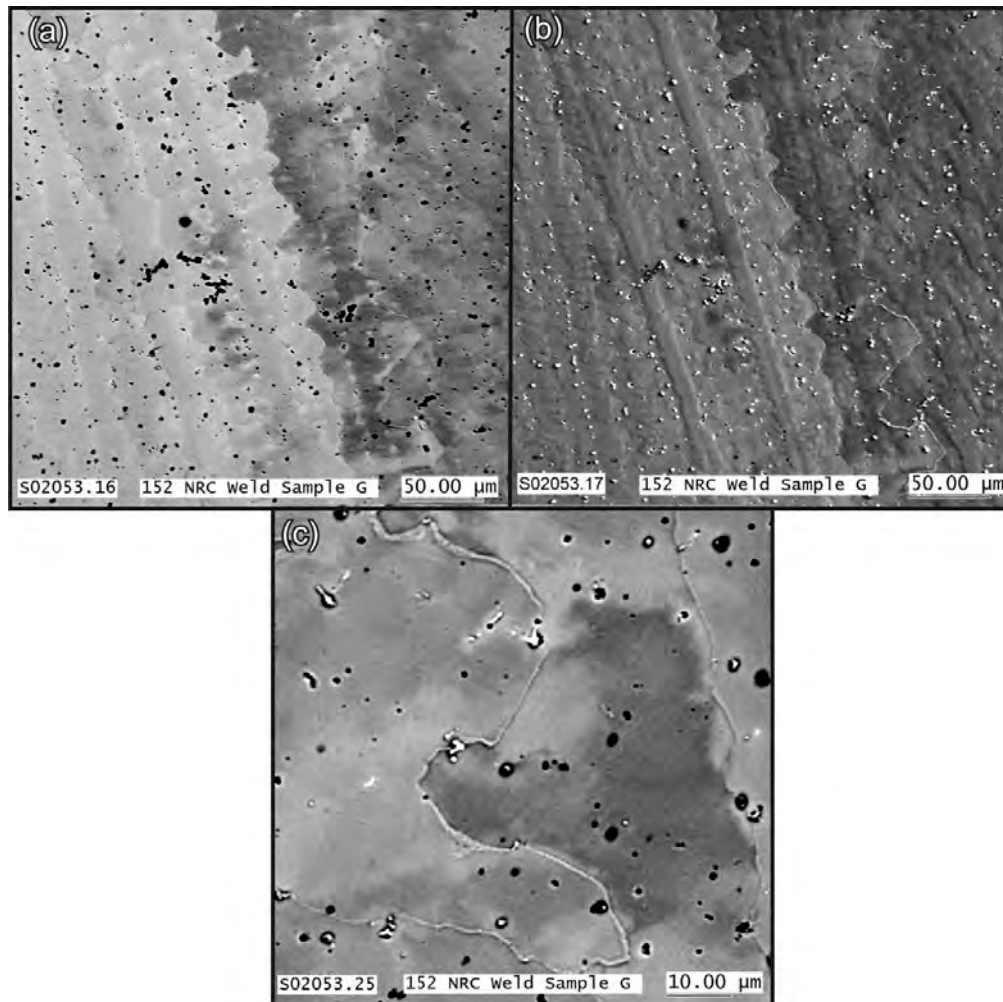
Figure 3-4   SEM (BSE (a), SE (b,c)) Images Are Shown from the Alloy 152 Weld Metal
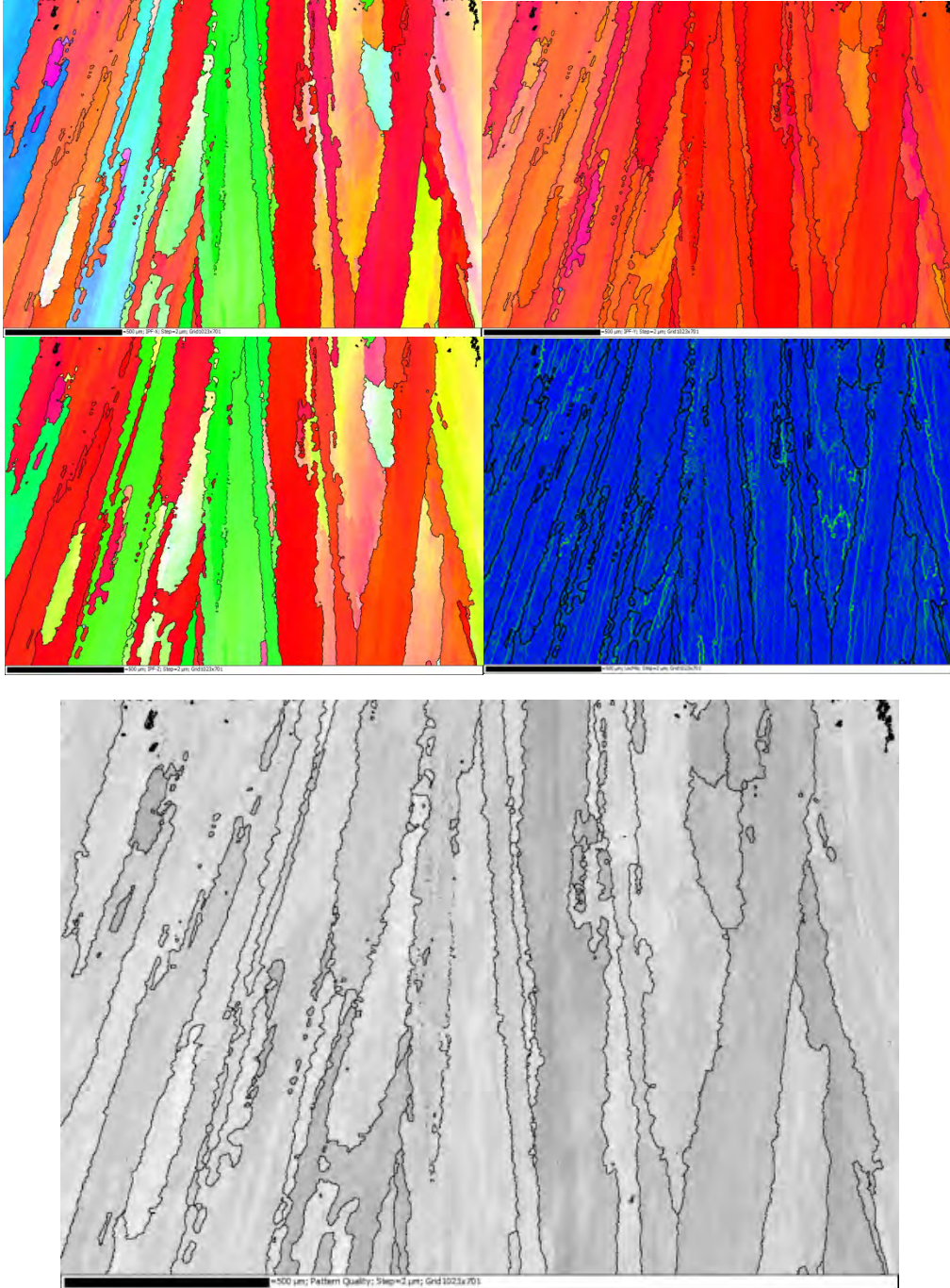
Figure 3-5 SEM-EBSD Micrographs of CT052 Showing the Inverse Pole Figure (IPF)-X, IPF-Y, IPF-Z and Local Misorientation Map of the General Microstructure in the MHI Alloy 152 Weld

Additionally, electron dispersive spectroscopy (EDS) composition maps were made to elucidate compositional inhomogeneities in the structure, and identify the major second-phase particles. As seen in Figure 3-6, there is a slight amount of coring indicated in the Mn map. Coring profiles in the Fe map (not shown) were complementary to the Mn map. The primary particles identified were rich in Nb (likely NbC) and Ti-Al-rich particles (likely a Ti-Al-O). TEM sample

preparation of a SGB (Figure 3-7) and SSGBs (Figure 3-8) was performed, and subsequent STEM/EDS maps were collected of each. Analysis of SGBs (Figure 3-7) indicates small (15-25 nm), semi-continuous Nb rich particles on the SGB as well as larger (100 nm), discontinuous Cr rich precipitates. Ti was not observed to be associated with the Nb carbides. On the SSGBs (Figure 3-8) large (100 nm), discontinuous Cr and Nb rich precipitates were observed on the boundaries. In this instance, Ti was observed to be associated with the Nb rich precipitation.
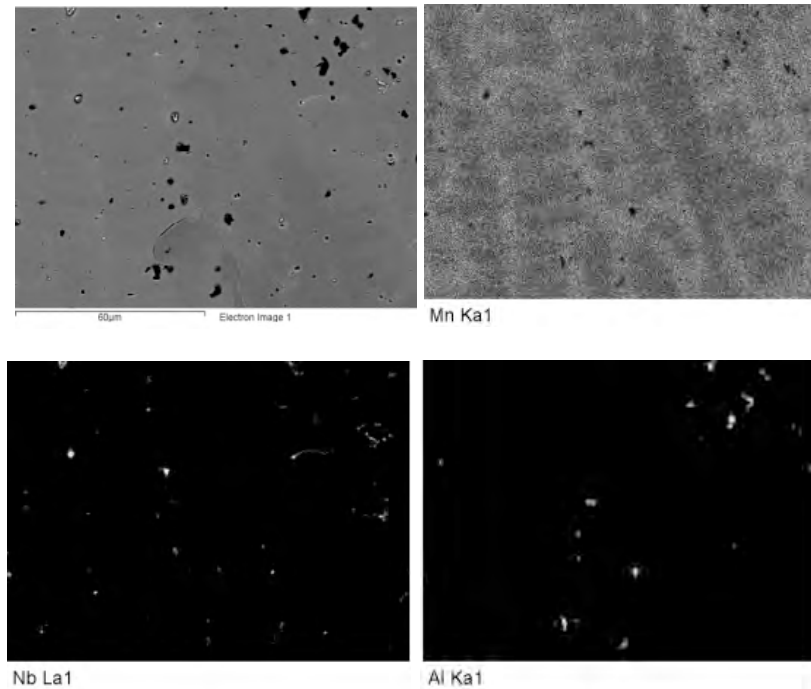
Figure 3-6   SEM-SE Micrograph Is Shown Along with Composition Maps for Mn, Nb and Al. The Mn Map Indicates a Slight Degree of Coring and the Other Two Maps Show the Locations of the Large NbC and the Ti-Al Particles in the Microstructure
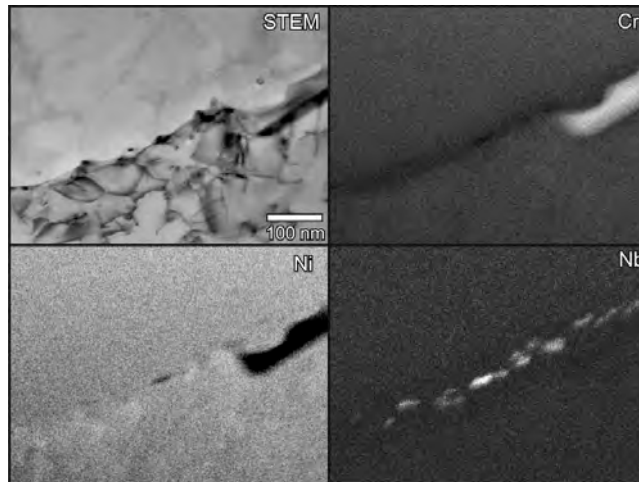
Figure 3-7   **An Example of a SGB That Shows a Single Large Cr-Carbide, with Numerous Smaller Nb Carbides Along the Boundary. In This Case, Ti Was Not Found Associated with the Nb Carbides**
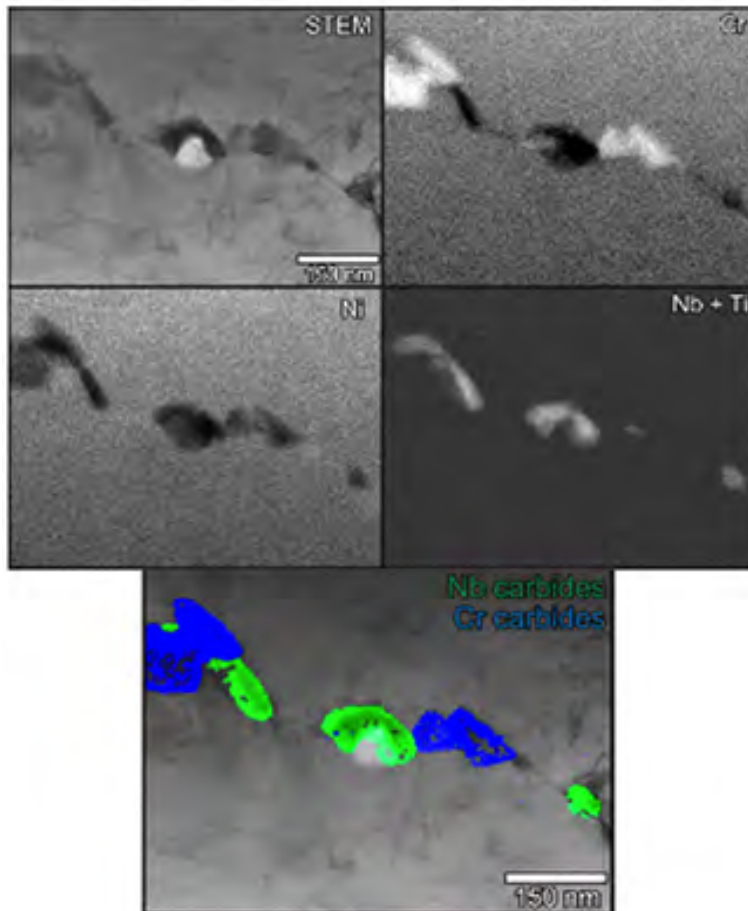
Figure 3-8   **Compositional Maps Taken in STEM Mode Revealed That Both Cr- and Nb-Rich Carbides Are Present on SSGBs. The Bottom Image Reveals That the Two Carbide Phases Can Sometimes Be Superimposed with Each Other. In This Example, Nb and Ti Were Associated with the Same Particles**

The welds were tested in the as-welded (AW) condition with the exception of one test that was performed on an MHI alloy 152 weld that had been given a low-alloy steel (LAS) stress relief heat treatment of 610°C for 12 h followed by air cooling. High-resolution SEM examinations did not indicate any significant effect of the heat treatment on the precipitate microstructures. Orientation of the specimens relative to the weld is shown in Figure 3-9. Specimens were machined from the blanks to target the desired crack growth path aligned with the elongated solidification grain boundaries shown in Figure 3-5.
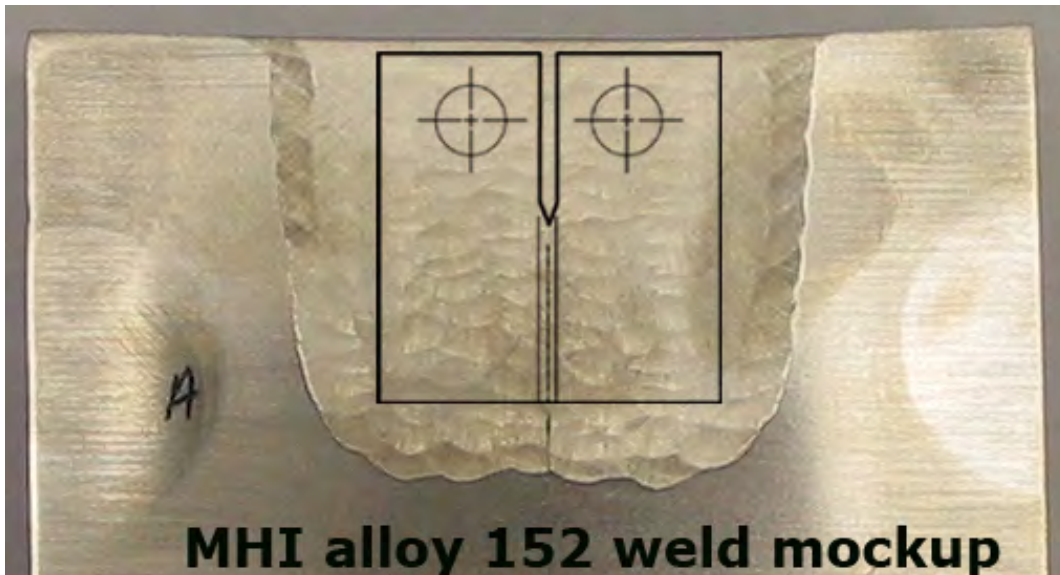
Figure 3-9   Image of MHI Alloy 152 Weld Showing Positioning of 0.5T CT Specimens

The first SCC crack-growth test was performed on a single CT specimen (CT013) of the MHI alloy 152 in the as-welded condition. Crack extension and transitioning were done in 325°C PWR primary water by cyclic loading at decreasing frequencies, with an R value of 0.7 and a K of 30 MPa√m. After >500 h cycling at 0.001 Hz, hold times of 2.5 h and then 24 h were added as shown in Figure 3-10. Extremely low, but stable CGRs were observed under these conditions decreasing to $3x10^{-9}$ mm/s after ~1000 h for the 24 h hold. Constant K was established and the measured propagation rate gradually decreased to $<5x10^{-10}$ mm/s over the next few months. After ~2200 h (3 months) at constant K, the test was ended. A summary table of test conditions and corrected specimen response for each test phase is shown in Table 3-1. Post-test examination started by sectioning of the specimen to obtain a crack side surface profile and then fatiguing the other piece of the CT specimen to expose the crack growth surface. The crack profile in Figure 3-11 shows that the crack growth direction was not as well aligned with the dendrites as appeared when marking the blank to cut the CT specimen. Nevertheless, regions of IG growth were found on the crack growth surface shown in Figure 3-12 during post-test examination. The SEM images indicate that the IG cracking is SGB. The IG growth appeared to begin during the cycle + hold steps and the final crack front was ~35% IG. Based on this degree of IG engagement, area-averaged propagation rates were determined and are reported in Figure 3-10. If only the maximum IG crack extension was considered, estimated local rates would be ~5X higher or $~1.5x10^{-9}$ mm/s at constant K.
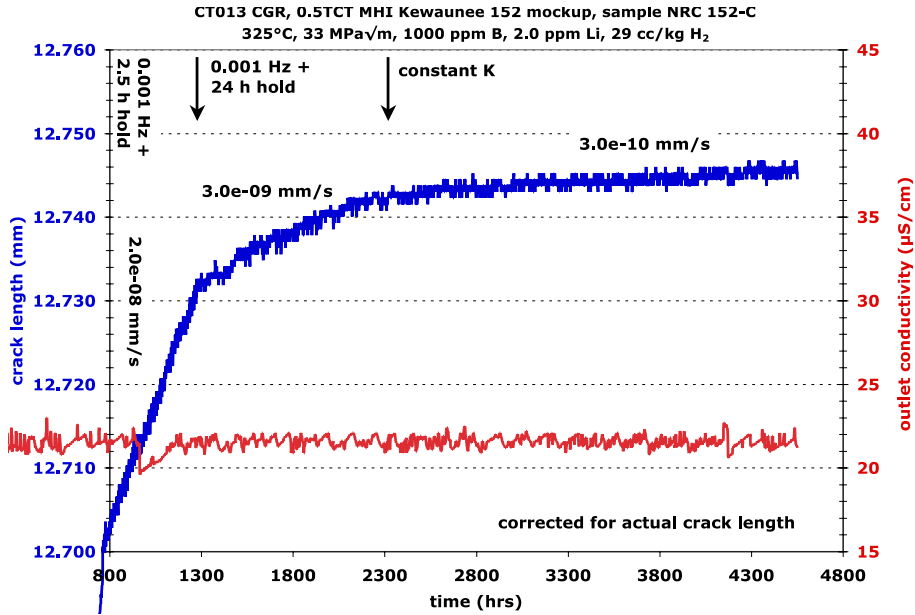
Figure 3-10   Crack Growth Response of MHI Alloy 152 Specimen CT013 During Transitioning and Constant K Steps

Table 3-1   Test Conditions and Corrected Specimen Response for MHI Alloy 152 Specimen CT013

Test Phase	Duration (h)	R	Freq (Hz)	Hold (h)	Water Chemistry Conditions	Temp (°C)	Kmax (MPa√m)	Avg. CGR (mm/s)	Approx. Crack Extension (mm)
1	8.1	0.3	1	0	29 cc/kg H_2	325	26	4.8E-05	0.936
2	4.4	0.5	1	0	29 cc/kg H_2	325	30	3.3E-05	0.526
3	4.6	0.6	1	0	29 cc/kg H_2	325	33	2.3E-05	0.361
4	6.8	0.7	1	0	29 cc/kg H_2	325	33	1.4E-05	0.335
5	26	0.7	0.1	0	29 cc/kg H_2	325	33	2.8E-06	0.289
6	161	0.7	0.01	0	29 cc/kg H_2	325	34	6.0E-07	0.353
7	552	0.7	0.001	0	29 cc/kg H_2	325	34	9.4E-08	0.171
8	520	0.7	0.001	2.5	29 cc/kg H_2	325	34	2.0E-08	0.032
9	855	0.7	0.001	24	29 cc/kg H_2	325	34	3.0E-09	0.010
10	2413	---	const	---	29 cc/kg H_2	325	34	3E-10	0.004
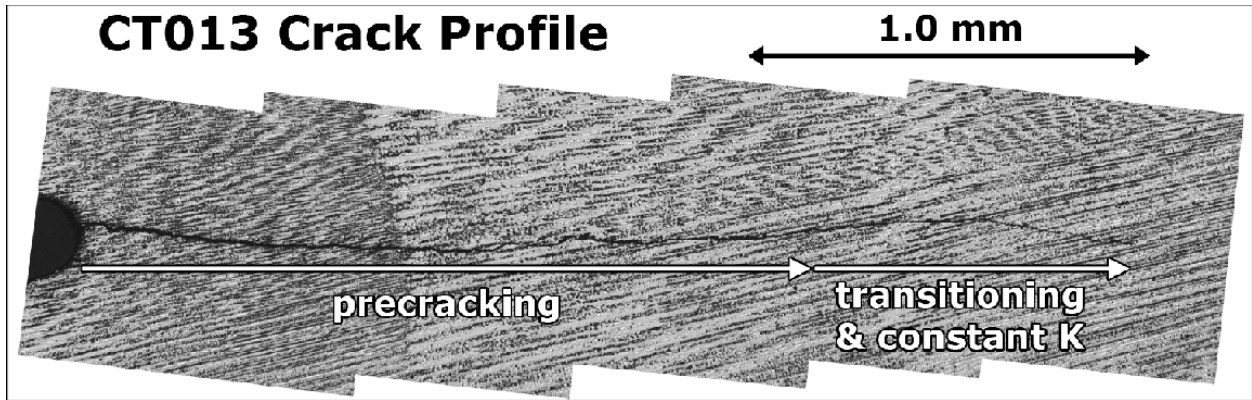
Figure 3-11   Side Surface Profile of MHI Alloy 152 Sample CT013 Showing Alignment of Crack Relative to Dendrite Structure
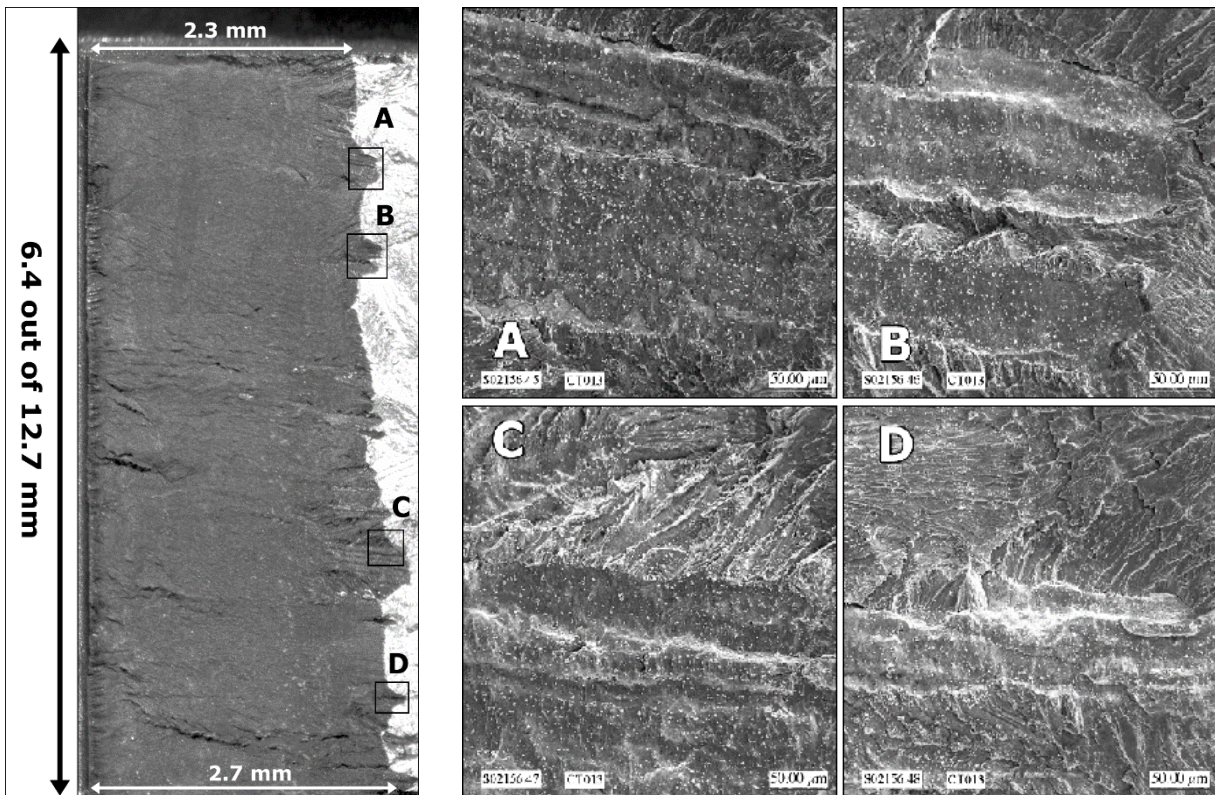
Figure 3-12   Crack Growth Surface of MHI Alloy 152 Specimen CT013. Optical Image on Left Reveals Local Areas of SCC Propagation and SEM Images on Right Illustrate IG Morphology

The next two alloy 152 specimens were tested in series with one in the as-welded condition (CT018) and one given a low alloy steel (LAS) stress-relief heat treatment (CT017). Overall crack growth response is shown in Figure 3-13 with testing performed both at 350°C and at 50°C. Unlike the CT013 test, shorter transitioning intervals were used with more emphasis on sampling the response of the material at several different regions in each specimen and on trying different methods to obtain a more engaged IG crack front. The transitioning conditions used in the first region of the specimen were identical to those in the first test on the MHI alloy 152 (CT013) with the exception of shorter duration. The initial crack growth during cycle + hold and constant K steps was essentially identical to that observed in the previous test (specimen CT013) as shown in Figure 3-14. Stable propagation rates were measured, and slowed to extremely low values under constant K conditions (<5x10^{-10} mm/s). A second region of the alloy 152 microstructure was then evaluated by extending the crack ~0.4 mm in both samples by moderate cycling.

CT017 & CT018 CGR, 0.5T CT Alloy 152 MHI for Kewaunee, samples D & E
1000 ppm B, 2.0 ppm Li, 29 cc/kg H$_2$
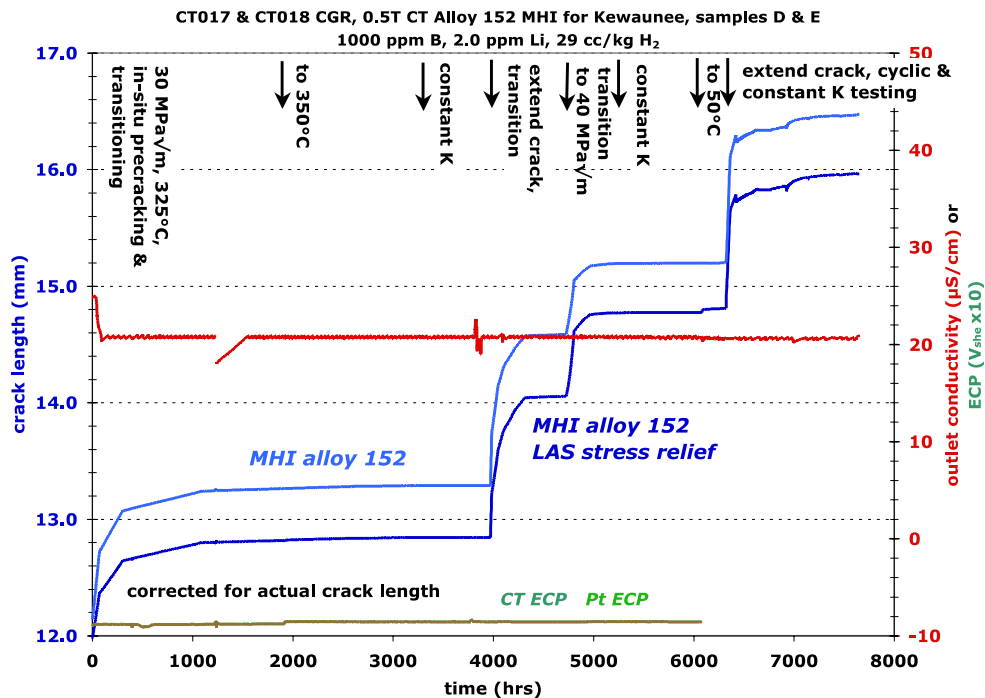
Figure 3-13   Overall Crack Growth Response of MHI Alloy 152 Specimens CT017 & CT018

CT017 & CT018 CGR, 0.5T CT Alloy 152 MHI for Kewaunee, samples D & E
350°C, 32-33 MPa√m, 1000 ppm B, 2.0 ppm Li, 29 cc/kg H₂

constant K

<5e-10 mm/s

MHI alloy 152

0.001 Hz + 24 h
R = 0.7

1.5e-09 mm/s

MHI alloy 152
LAS stress relief

<5e-10 mm/s

1.5e-09 mm/s

corrected for actual crack length

CT ECP   Pt ECP

time (hrs)

Δa from 0.001 Hz (mm)

Outlet conductivity (µS/cm) or ECP (V_she x10)
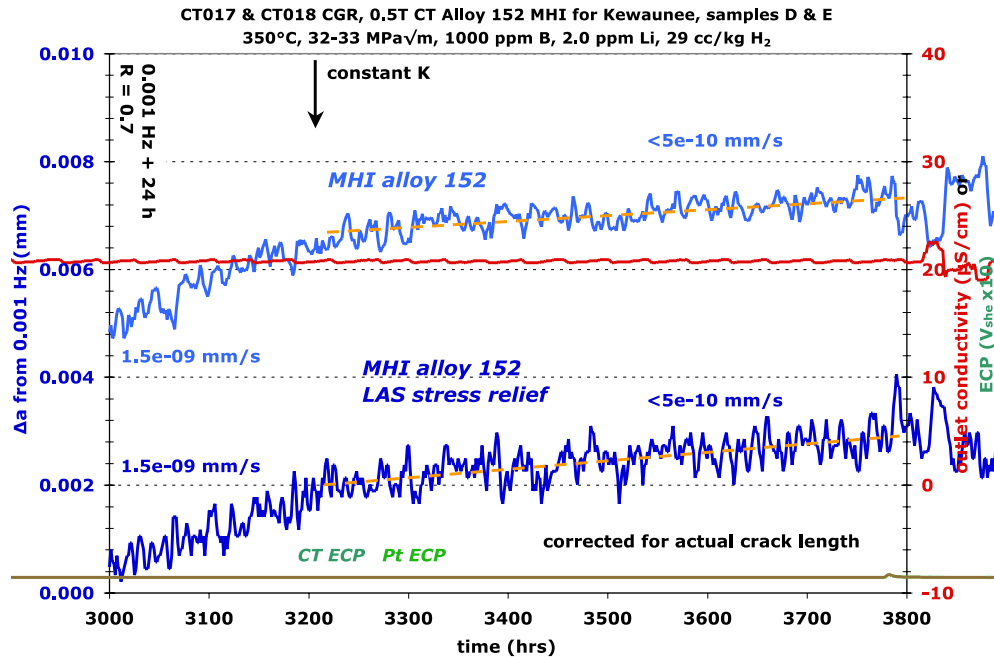
Figure 3-14   Constant K Crack Growth Response of MHI Alloy 152 Specimens CT017 & CT018 at 30 MPa√m.

An alternate SCC transitioning approach was then used with sawtooth waveforms during cycling with R = 0.5, a 12 s unload, and increasingly longer reload time ranging from 300 s to 1000 s. After ~100 µm of growth with the 1000 s reload time, the R value was then changed to 0.7 and a 2.5 h hold was added. Over ~200 h, the CGR was observed to slowly decrease to a rate below 1×10^{-8} mm/s as shown in Figure 3-15. The load cycle was then converted from a sawtooth waveform to a 0.001 Hz symmetric waveform while maintaining the same 2.5 h hold time and R value of 0.7. As shown in Figure 3-15, no change in propagation rate occurred upon converting to the symmetric waveform, and the CGR of ~6×10^{-9} mm/s was slightly less than that observed when this same cycle + hold condition was used earlier in the test. Since no SCC enhancement was indicated during the cycle + hold loading, it was decided to investigate the crack growth response at a higher K of 40 MPa√m. This was done for both specimens by extending the crack 0.4 mm using cyclic loading (0.01 Hz, R=0.6) and a dK/da value of 100 MPa√m/mm. Based on post-test correction of the crack length, the actual K value was ~48 MPa√m after the dK/da transition. After switching to 0.001 Hz (symmetric waveform) and an R of 0.7, propagation rates were evaluated after adding a 2.5 h hold and finally during constant K as shown in Figure 3-16. CGRs were 3-4X higher than seen at lower K levels with values of 1.7-2.1×10^{-8} mm/s and 1.0-1.7×10^{-9} mm/s for the cycle + hold and constant K conditions, respectively.
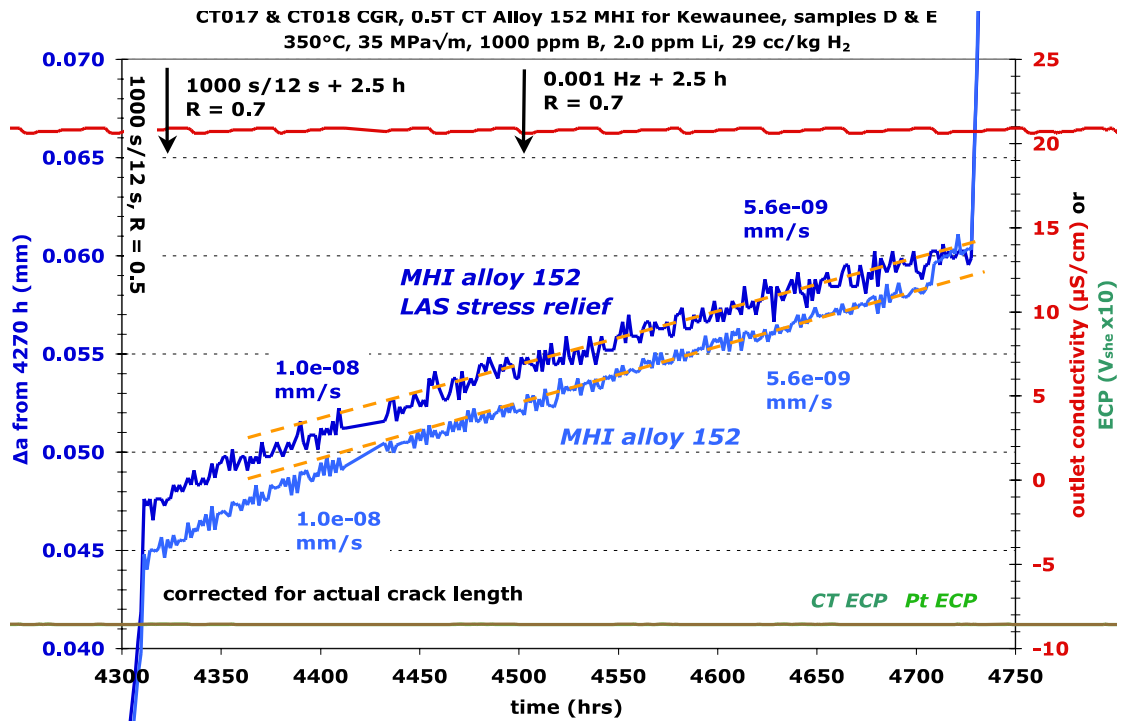
Figure 3-15   Crack Growth Response During Cyclic Loading Conditions of MHI Alloy 152 Specimens CT017 & CT018 in the Second Microstructural Region Examined
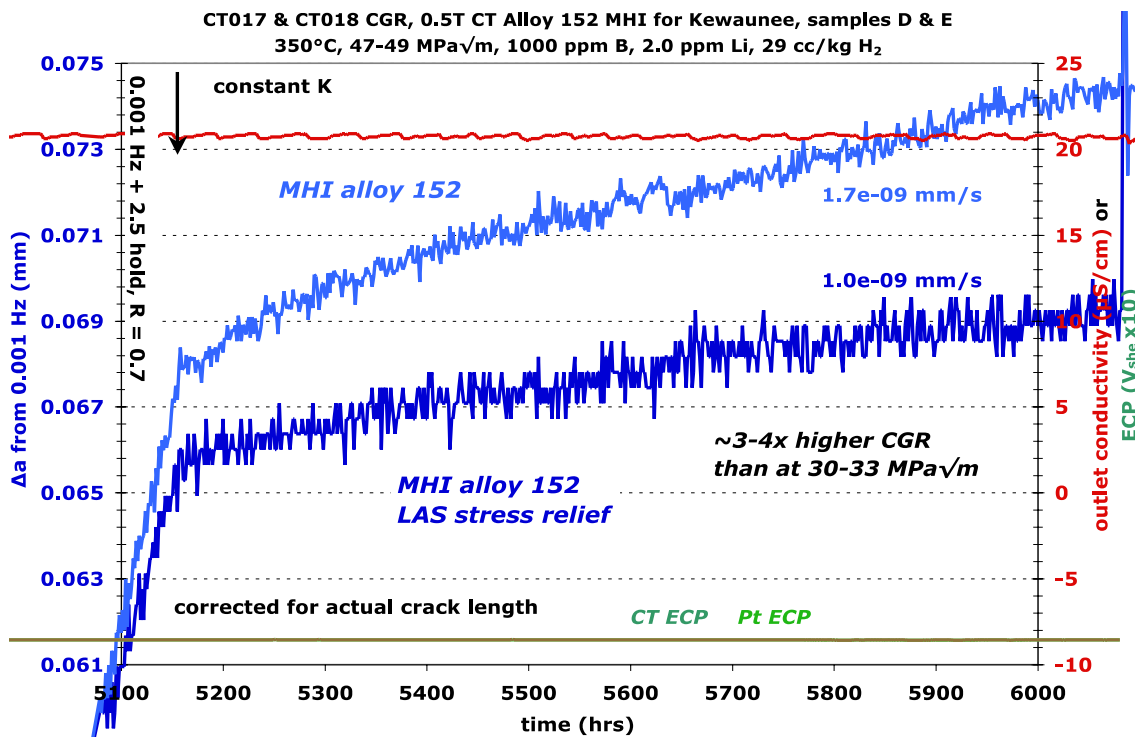
Figure 3-16   Constant K Crack Growth Response of MHI Alloy 152 Specimens CT017 & CT018 at ~48 MPa√m

The final stage of the test examined crack-growth response at 50°C while maintaining PWR primary water chemistry conditions, including a dissolved hydrogen content of 29 cc/kg. After extending the crack ~1 mm by cycling at 0.01 Hz, transitioning and constant K steps were performed as shown in Figure 3-17. The CGRs during cyclic and cycle + hold loading were found to be ~2-3X greater than rates observed at 350°C at the same K value and cycling conditions. However when the test was converted to constant K, the crack in both specimens ceased growing entirely, and when cyclic loading conditions were re-established, crack growth resumed. The test was later converted to constant K again with no crack advance. This suggests that dynamic strain during cycling is required for environment-assisted propagation at this low temperature.

One of the characteristic features of the crack growth response at 50°C was a relatively large systematic variation in the DCPD-measured crack length during low frequency cyclic loading. To better assess the cause of this, the DCPD response was examined in detail during cycle + hold loading conditions as shown in Figure 3-18. Large spikes in the DCPD-measured crack length were found to occur at the onset of each load cycle with the crack length decaying rapidly to a value slightly higher than existed prior to the load cycle. The spikes in the crack extension are clearly not a real phenomenon, but each load cycle does produce a small increment in crack length. The lack of growth during the hold time is consistent with the constant K response. It is thought that the spikes in crack length are due to the formation (during constant K loading) and destruction (during cycling) of "conducting" bridges behind the crack front. These bridges may form in the crack wake due to the electrochemical conditions of the PWR primary water at 50°C where Ni metal is stable. Enhanced electronic conduction across the crack will result in DCPD underestimating the actual crack length. Dynamic deformation during load cycling is apparently sufficient to break the bridges resulting in an immediate increase in DCPD-measured crack length. However, the bridges across the crack quickly re-form once the cycle is complete.

As a final phase of the test, the air fatigue CGR at 50°C of these specimens was measured and found to be 3-4X lower than in PWR primary water at the same temperature, further demonstrating that propagation at 50°C was an environment-assisted process. A summary of test conditions and corrected response of both specimens for each phase of the entire test is shown in Table 3-2. The specimens were then fatigue fractured in air to expose the crack growth surfaces. An optical image highlighting the crack growth surface created during high temperature testing is shown in Figure 3-19. Lines on the surface separate different phases of the tests. Regions of IGSCC are apparent, especially at the final high temperature crack front with the higher K level. SEM images in Figure 3-20 better illustrate the degree of IG engagement with the final crack front at 350°C having about 40% IG engagement. Somewhat surprisingly, more than 90% IG engagement was found to occur during the crack growth testing at 50°C. This IG growth is consistent with the higher CGRs observed during cycling loading of the specimens at 50°C in water.
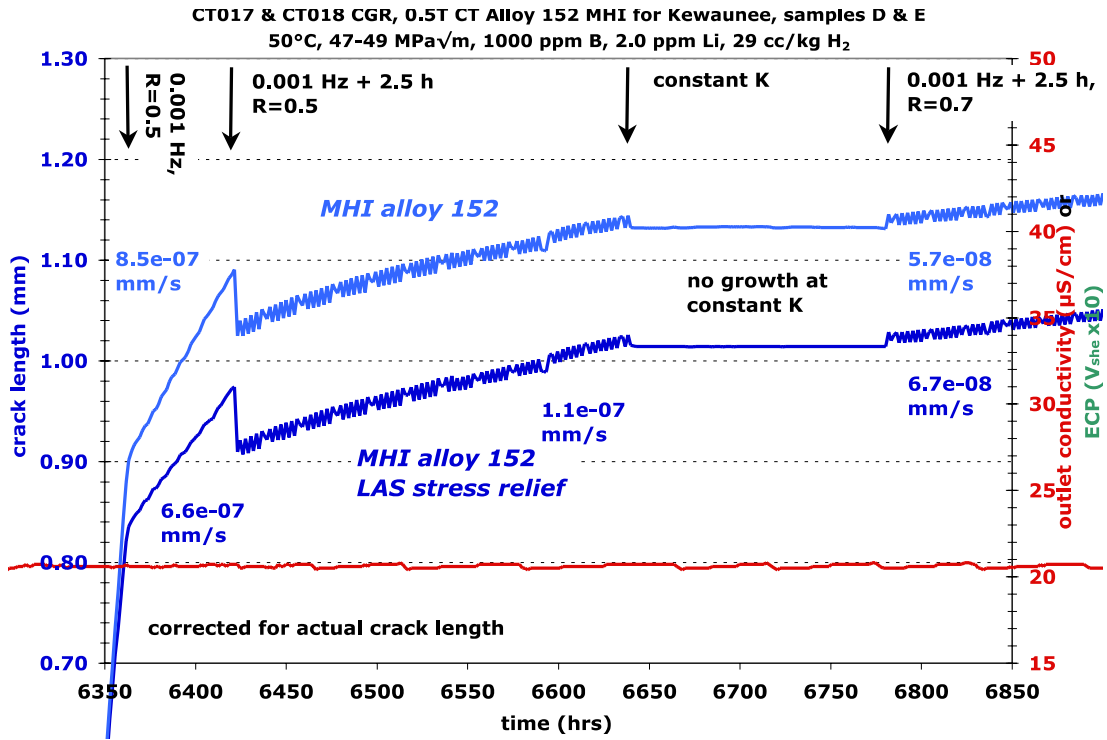
Figure 3-17 Crack Growth Response of MHI Alloy 152 Specimens CT017 & CT018 at 50°C in Simulated PWR Primary Water
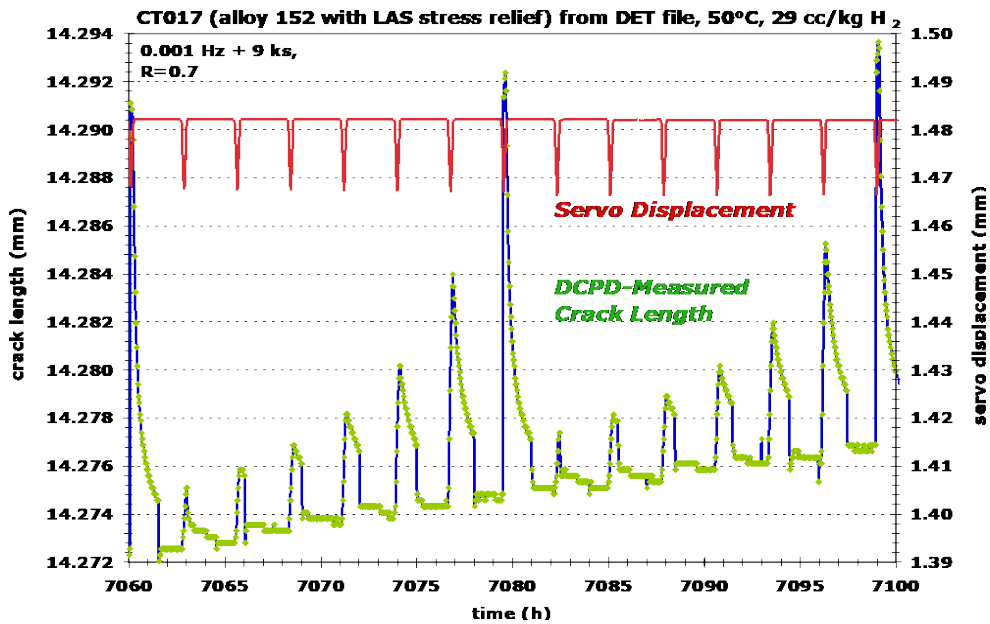
Figure 3-18 Detailed Plot Showing DCPD Measured Crack Growth Response During Cycle + Hold Loading Conditions at 50°C in MHI Alloy 152 Specimen CT017
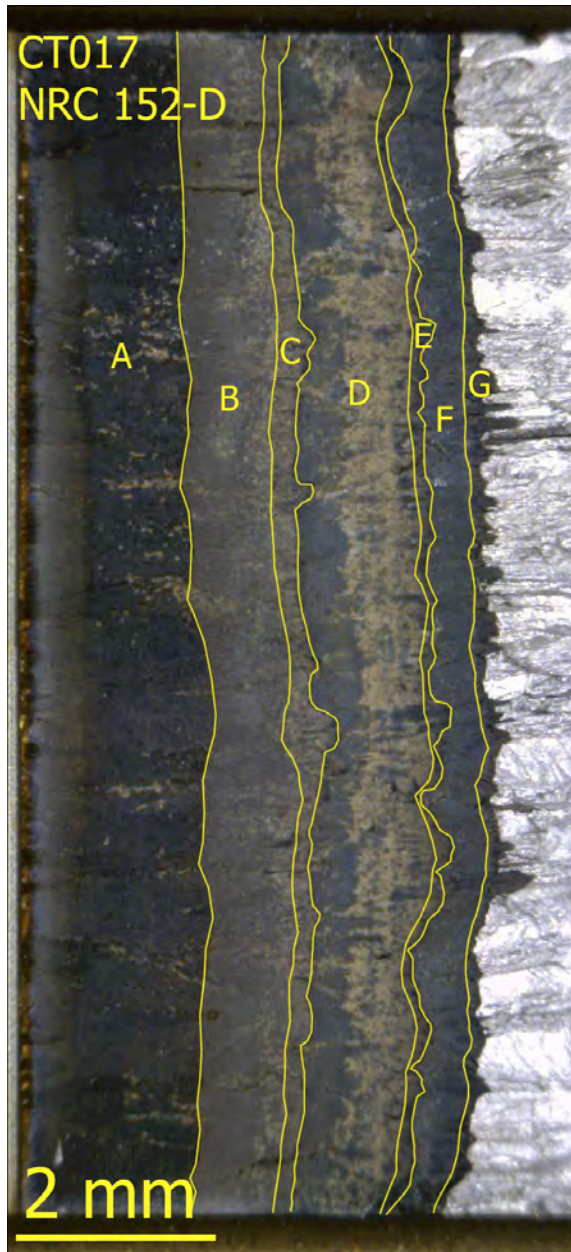
A: air precrack
B: rapid transitioning
C: SCC #1 (cycle+hold & constant K at 32 MPa√m
D: crack extension and transitioning
E: SCC #2 (cycle+hold & constant K at 34 MPa√m
F: dK/da (34->44 MPa√m) & transitioning at 44 MPa√m
G: SCC #3 (cycle+hold and constant K at 45 MPa√m

Figure 3-19   Optical Image of High Temperature Crack Growth Surface of the MHI Alloy 152 Specimen CT017

Table 3-2   Test Conditions and Corrected Response of MHI Specimens CT017 & CT018

Test Phase	Dur-ation (h)	R	Freq (Hz)	Hold (h)	Water Chemistry Conditions	Temp (°C)	CT017 MHI Alloy 152 Blank D - LAS Stress Relief K_{max} (MPa√m)	CGR (mm/s)	Approx. Crack Ext. (mm)	CT018 MHI Alloy 152 Blank E - As Welded K_{max} (MPa√m)	CGR (mm/s)	Approx. Crack Ext. (mm)
1	~3	0.3	3	0	air precrack	RT	25	9.3E-05	0.40	25	8.4E-05	0.40
2	~2	0.5	3	0	air precrack	RT	28	7.3E-05	0.35	29	6.1E-05	0.35
3	~2	0.6	3	0	air precrack	RT	30	5.2E-05	0.35	31	4.3E-05	0.35
4	~3	0.7	3	0	air precrack	RT	31	2.7E-05	0.20	31	2.0E-05	0.20
5	79	0.7	0.1	0	29 cc/kg H_2	325	31	1.6E-06	0.398	32	2.4E-06	0.589
6	227	0.7	0.01	0	29 cc/kg H_2	325	31	3.0E-07	0.264	33	4.3E-07	0.346
7	795	0.7	0.001	0	29 cc/kg H_2	325	31	5.8E-08	0.155	33	5.7E-08	0.169
8a	822	0.7	0.001	2.5	29 cc/kg H_2	325	31	7.0E-09	0.021	33	7.0E-09	0.023
8b	686	0.7	0.001	2.5	29 cc/kg H_2	350	31	6.2E-09	0.017	33	7.6E-09	0.019
9	633	0.7	0.001	24	29 cc/kg H_2	350	31	1.4E-09	0.006	33	1.5E-09	0.007
10	726	---	const K	---	29 cc/kg H_2	350	31	4E-10	0.001	33	3E-10	<0.001
11	15	0.5	0.1	0	29 cc/kg H_2	350	32	9.2E-06	0.337	34	1.1E-05	0.396
12	66	0.5	0.01	0	29 cc/kg H_2	350	32	1.6E-06	0.414	35	1.8E-06	0.464
13	55	0.5	300s/12s	0	29 cc/kg H_2	350	33	8.5E-07	0.167	35	8.3E-07	0.162
14	112	0.5	600s/12s	0	29 cc/kg H_2	350	33	4.7E-07	0.175	35	4.1E-07	0.160
15	97	0.5	1000s/12s	0	29 cc/kg H_2	350	33	2.9E-07	0.106	36	3.0E-07	0.103
16	190	0.7	1000s/12s	2.5	29 cc/kg H_2	350	33	7.9E-09	0.007	36	8.4E-09	0.008
17	225	0.7	0.001	2.5	29 cc/kg H_2	350	33	7.9E-09	0.006	36	8.4E-09	0.008
18	80	0.6	0.01	0	29 cc/kg H_2	350	33->46	1.4E-06	0.562	36->49	1.3E-06	0.466
19	84	0.65	0.001	0	29 cc/kg H_2	350	46	2.8E-07	0.090	49	2.4E-07	0.074
20	69	0.7	0.001	0	29 cc/kg H_2	350	46	1.8E-07	0.048	49	1.8E-07	0.046
21	200	0.7	0.001	2.5	29 cc/kg H_2	350	46	2.4E-08	0.015	49	3.1E-08	0.021
22	923	---	const K	---	29 cc/kg H_2	350	46	1.4E-09	0.004	49	1.0E-09	0.006
23	89	---	const K	---	29 cc/kg H_2	100	37	no growth	---	39	no growth	---
24	151	---	const K	---	29 cc/kg H_2	50	37	no growth	---	39	no growth	---
25	39	0.5	0.01	0	29 cc/kg H_2	50	49	5.7E-06	0.711	53	6.5E-06	0.865
26	59	0.5	0.001	0	29 cc/kg H_2	50	50	6.5E-07	0.139	55	8.8E-07	0.189
27	116	0.5	0.001	2.5	29 cc/kg H_2	50	50	1.3E-07	0.009	55	1.2E-07	0.016
28	100	0.7	0.001	2.5	29 cc/kg H_2	50	50	1.3E-07	0.031	55	1.2E-07	0.026
29	142	---	const K	---	29 cc/kg H_2	50	50	no growth	---	55	no growth	---
30	337	0.7	0.001	2.5	29 cc/kg H_2	50	50	5.4E-08	0.110	55	5.1E-08	0.108
31	339	0.9	0.001	2.5	29 cc/kg H_2	50	50	1.2E-08	0.018	56	6.0E-09	0.015
32	208	0.7	0.001	2.5	29 cc/kg H_2	50	51	2.0E-08	0.011	56	1.6E-08	0.017
33	197	0.7	0.001	2.5	air	50	51	1.1E-08	0.028	56	6.3E-09	0.015
34	122	0.5	0.01	0	air	50	51	8.0E-07	0.381	57	8.5E-07	0.402
35	191	0.5	0.001	0	air	50	52	8.3E-08	0.064	57	8.9E-08	0.065
36	146	0.5	0.001	2.5	air	50	52	8.2E-09	0.006	57	9.2E-09	0.005
37	112	0.7	0.001	2.5	air	50	52	1.2E-08	0.002	57	1.3E-09	0.001
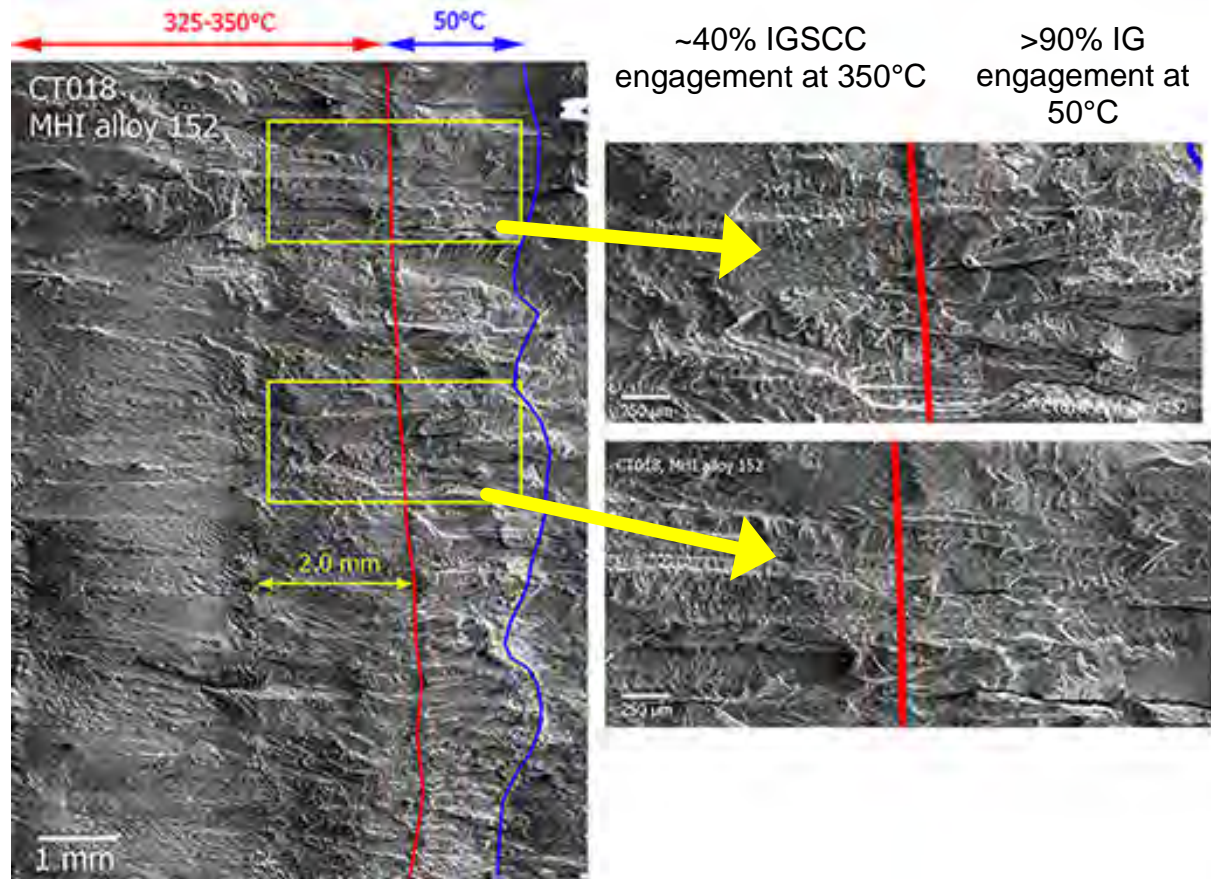
Figure 3-20   SEM Images of 350°C and 50°C Crack Growth Surfaces in MHI Alloy 152 Specimen CT018

3.1.2   More Recent Tests on MHI Alloy 152 U-Groove Mockup Welds (CT052, CT135)

Two additional specimens have been tested from the MHI alloy 152 U-groove weld with both as companions to more important controlling specimens. The first specimen CT052 was tested in series with a 20%CF alloy 152 specimen (CT051, reviewed in Chapter 5) where high CGRs were observed and limited the detailed evaluation of the as-welded CT052. The overall test summary for CT052 is listed in Table 3-3 and a slightly decreasing K value was obtained during the test driven by the faster crack growth in the cold-worked companion specimen. Transitioning was performed based on the CT051 specimen response and SCC response was assessed in step 15 under constant K loading. Crack growth behavior is documented in Figure 3-21 with a relatively stable (albeit a bit noisy) CGR of 2.6×10^{-9} mm/s. This is consistent with previous observations for the MHI alloy 152 weld metal described above.

The decision was made to remove this specimen and continue testing on the 20%CF specimen alone. Post-test characterizations were limited due to the short exposure of this specimen. An optical image in Figure 3-22 shows the initial air precrack (~1.3 mm) angled slightly upward followed by the crack growth in water (~0.5 mm). In addition, this region was examined by EBSD (lower images in Figure 3-22) and reveals TG cracking at the cross-section location. This TG crack is documented by SEM at higher magnifications as presented in Figure 3-23.

Penetrative oxidation off the crack walls can be seen to the crack tip. Finally, the crack-growth surface is presented in Figure 3-24 showing the short crack extension in water from the air precrack. No detailed analysis was performed to determine if any significant IG cracking was present.

Table 3-3   Data Summary for MHI 152 U-Groove Weld Specimen CT052

Test Phase	Start (h)	Duration (h)	R	Freq (Hz)	Hold (h)	Water Chem. (cc H_2 / kg)	Temp (°C)	Kmax (MPa√m)	CGR (mm/s)	Approx. Crack Extension (mm)
1	---	~3	0.3	5	0	air precrack	RT	21	---	0.40
2	---	~2	0.5	5	0	air precrack	RT	23	---	0.35
3	---	~2	0.6	5	0	air precrack	RT	25	---	0.35
4	---	~3	0.7	5	0	air precrack	RT	25	---	0.20
5	0	6	0.5	0.1	0	25	360	29	6.8E-06	0.121
6	6	50	0.5	0.01	0	25	360	29	1.3E-06	0.214
7	56	201	0.5	0.001	0	25	360	29	1.8E-07	0.117
8	257	45	0.5	0.01	0	25	360	28	4.1E-07	0.075
9	302	3	0.5	0.1	0	25	360	28	3.1E-06	0.027
10	306	12	0.5	0.01	0	25	360	28	4.2E-07	0.019
11	318	113	0.5	0.001	0	25	360	27	5.0E-08	0.022
12	431	160	0.5	0.001	2.5	25	360	27	9.3E-09	0.010
13	590	153	0.5	0.001	1	25	360	27	7.8E-09	0.002
14	743	158	0.5	0.001	2.5	25	360	27	3.7E-09	0.004
15	901	362	---	const K	---	25	360	27	2.6E-09	0.004
16	1263	297	0.5	0.001	1	25	360	27	3.9E-09	0.001
17	1560	208	0.5	0.001	2.5	25	360	27	2.1E-09	0.001
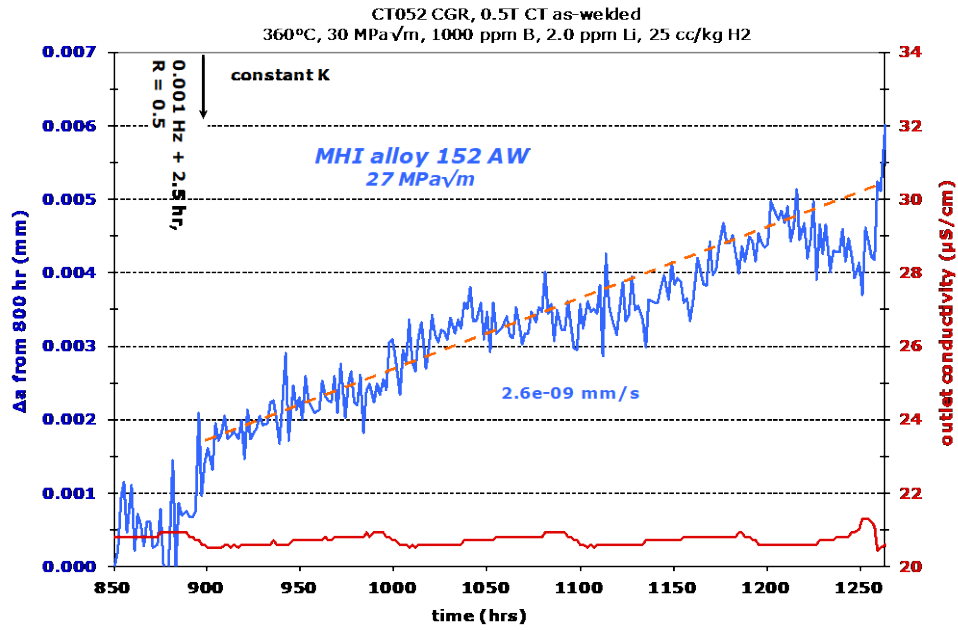
Figure 3-21   Crack Growth Response During Constant K Loading for Specimen CT052
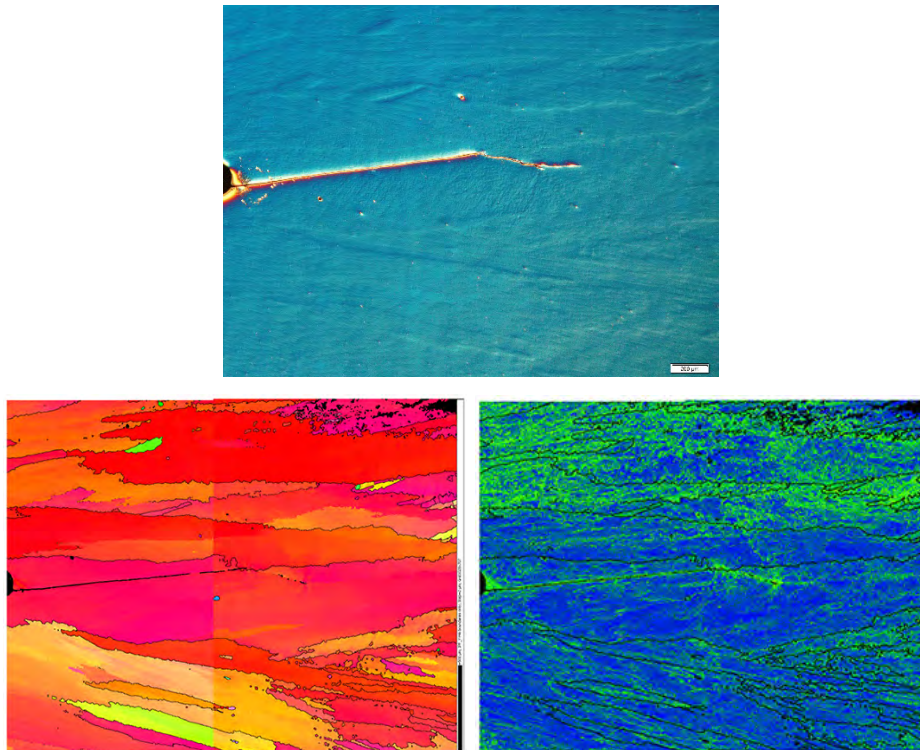
Figure 3-22   Optical (top) and SEM-EBSD (bottom) Micrographs of CT052 Cross-Section Showing the IPF-Y and Local Misorientation Map of the Crack from the Specimen Notch (left edge in top image, top center in bottom images)
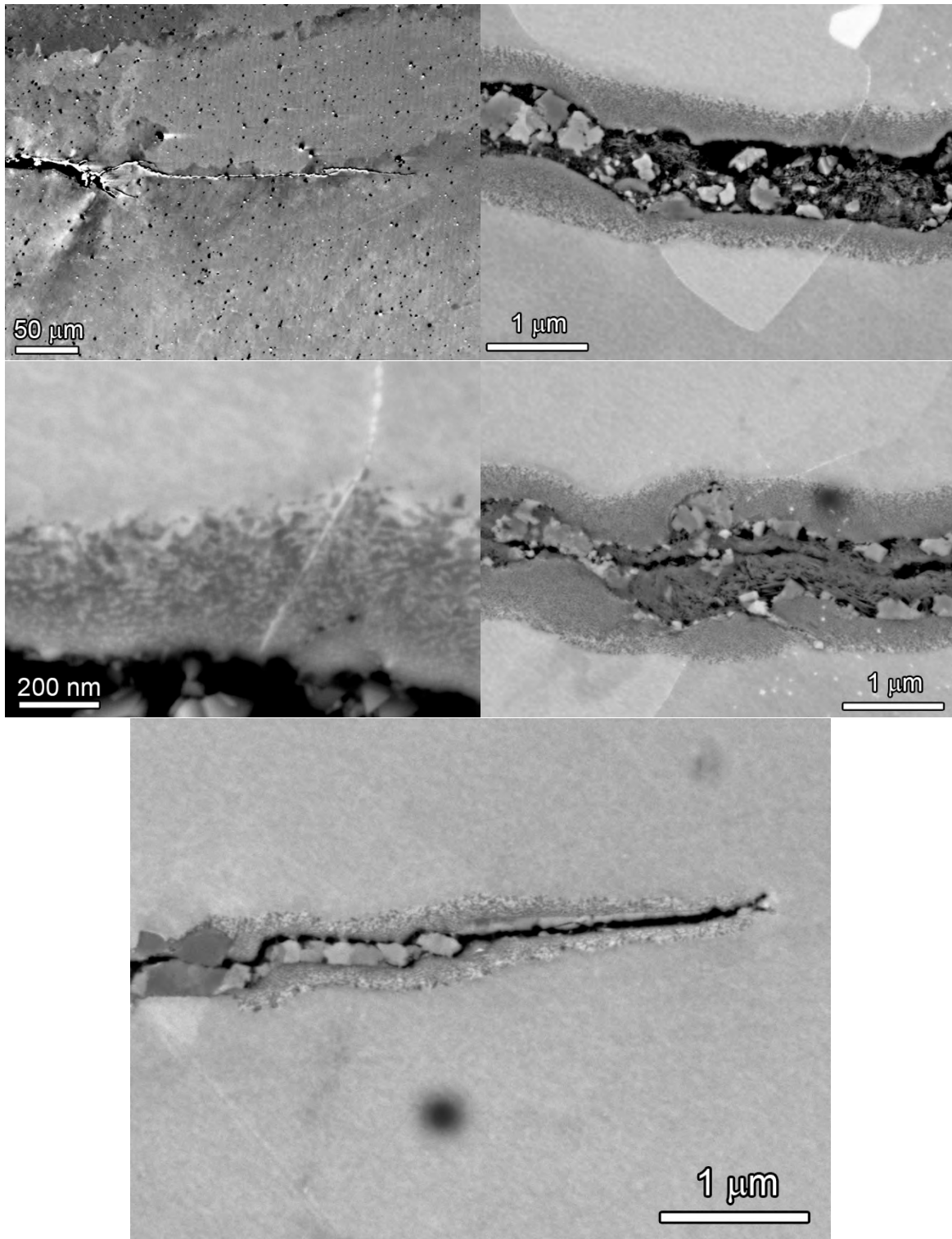
Figure 3-23   SEM-BSE Images from the CT052 Cross-Section Highlighting the TG Crack-Tip Region and Illustrating Oxidation at the Crack Walls to the Final Tip
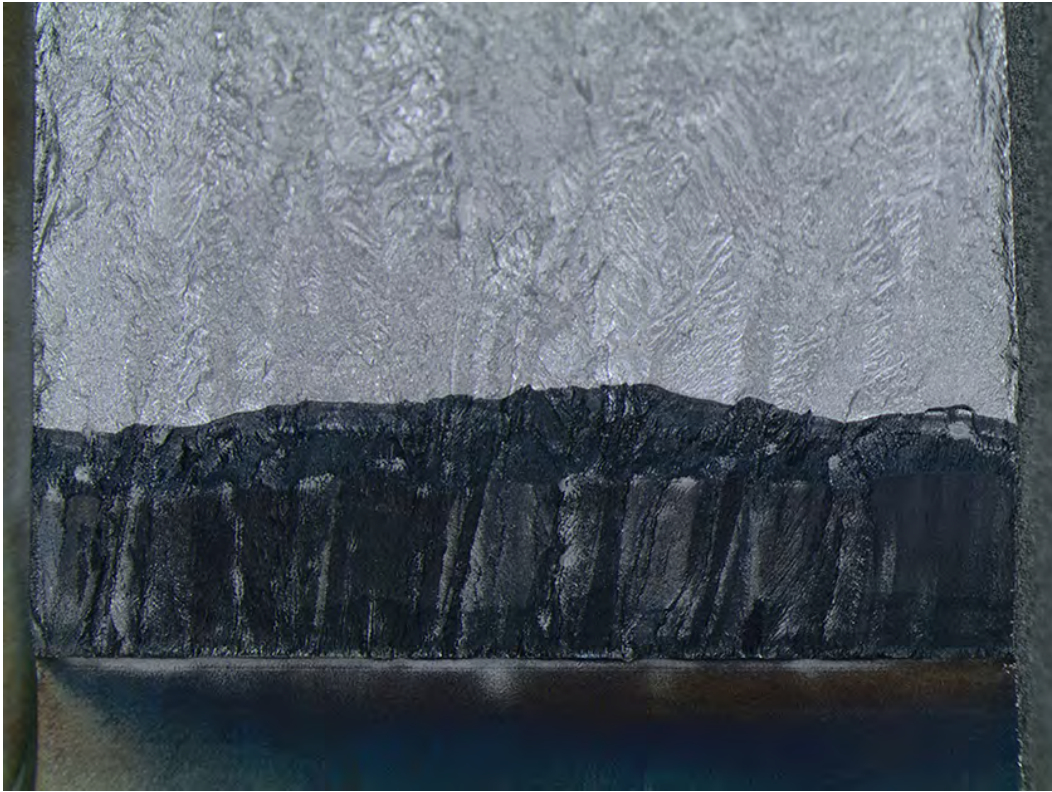
Figure 3-24   Optical Image of the Crack-Growth Surface on MHI Alloy 152 Specimen CT052

A final specimen (CT135) from the MHI alloy 152 U-groove weld was more recently tested in series with the EPRI alloy 52M repair weld specimen (CT134). Once again, the companion CT134 was the controlling specimen and testing steps were determined based on its response. The key difference for the CT135 specimen is that SCC response was investigated in the L-S orientation, while all the prior tests (CT013, CT017, CT018 and CT052) were performed in the T-S orientation. This modified orientation is illustrated in Figure 3-25 and it is important to note that the crack path is again aligned with the elongated solidification grain boundaries.

The testing sequence and response is summarized in Table 3-4, revealing that constant K behavior was evaluated twice along with a variety of cycle + hold loadings during transitioning. An early indication of limited SCC engagement was discovered during a 24h hold time as illustrated in Figure 3-26. Subsequent cycle + hold CGRs suggested an improved SCC response and constant K behavior was evaluated at two different K levels (33 and 38 MPa√m) as shown in Figure 3-27. In both attempts, the SCC propagation rate slowed with time at constant K and reached a value of $2\text{-}3\times10^{-9}$ mm/s.
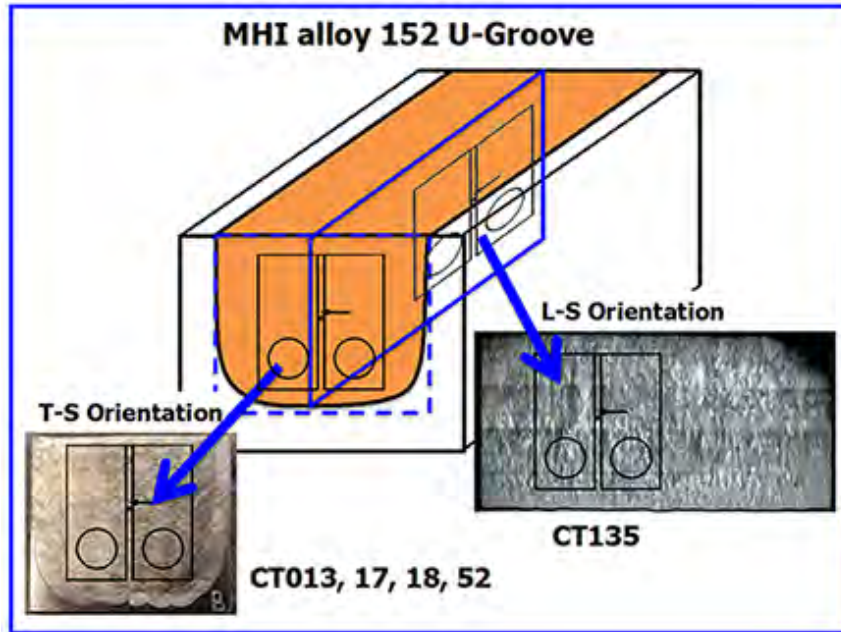
Figure 3-25   MHI Alloy 152 U-Groove Weld Showing the Standard T-S CT Specimen Orientation and Alternate L-S Orientation. For Both, the Target Crack Patch Is Aligned to the Long Axis of the Grains
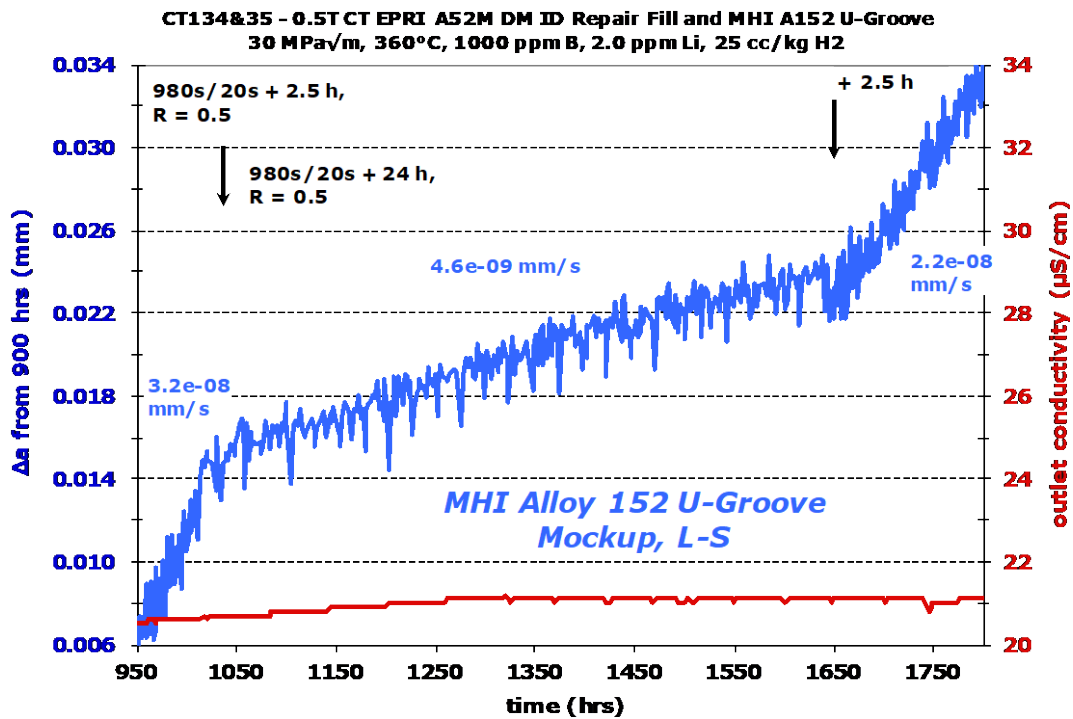
Figure 3-26   Measured Crack Growth During Cycle + 24h Hold Loading for CT135

Table 3-4   Data Summary for MHI 152 U-Groove Weld Specimen CT135

Test Step	Start (h)	Duration (h)	R	Freq (Hz)	Hold (h)	Water Chem. (cc H_2/kg)	Temp (°C)	Kmax (MPa√m)	CGR (mm/s)	Approx. Crack Extension (mm)
1	0	6	0.5	0.1	0	25	360	31	9.5E-06	0.236
2	6	28	0.5	0.01	0	25	360	31	2.0E-06	0.220
3	34	306	0.5	980s/20s	0	25	360	32	2.9E-07	0.323
4	340	668	0.5	980s/20s	2.5	25	360	32	3.2E-08	0.084
5	1008	635	0.5	980s/20s	24	25	360	32	4.6E-09	0.013
6	1643	182	0.5	980s/20s	2.5	25	360	32	2.2E-08	0.011
7	1825	394	0.5	980s/20s	0	25	360	33	3.1E-07	0.452
8	2219	137	0.5	980s/20s	2.5	25	360	33	4.5E-08	0.033
9	2356	618	---	const K	---	25	360	33	3.2E-09	0.008
10	2974	227	0.5	980s/20s	2.5	25	360	33	3.2E-08	0.027
11	3201	87	0.5	980s/20s	0	25	360	34	2.8E-07	0.084
12	3288	151	0.5	280/20s	0	25	360	35	9.8E-07	0.580
13	3439	190	0.5	980s/20s	2.5	25	360	36	4.2E-07	0.265
14	3629	210	0	980s/20s	2.5	25	360	36	6.5E-08	0.057
15	3839	264	0.5	980s/20s	24	25	360	36	1.1E-08	0.009
16	4103	159	0.5	980s/20s	0	25	360	38	7.5E-07	0.390
17	4262	95	0.5	980s/20s	2.5	25	360	38	8.0E-08	0.028
18a	4357	123	---	const K	---	25	360	38	4.4E-09	0.002
18b	4480	453	---	const K	---	25	360	38	2.3E-09	0.003
19	4930	120	0.5	980s/20s	2.5	25	360	38	6.5E-08	0.025
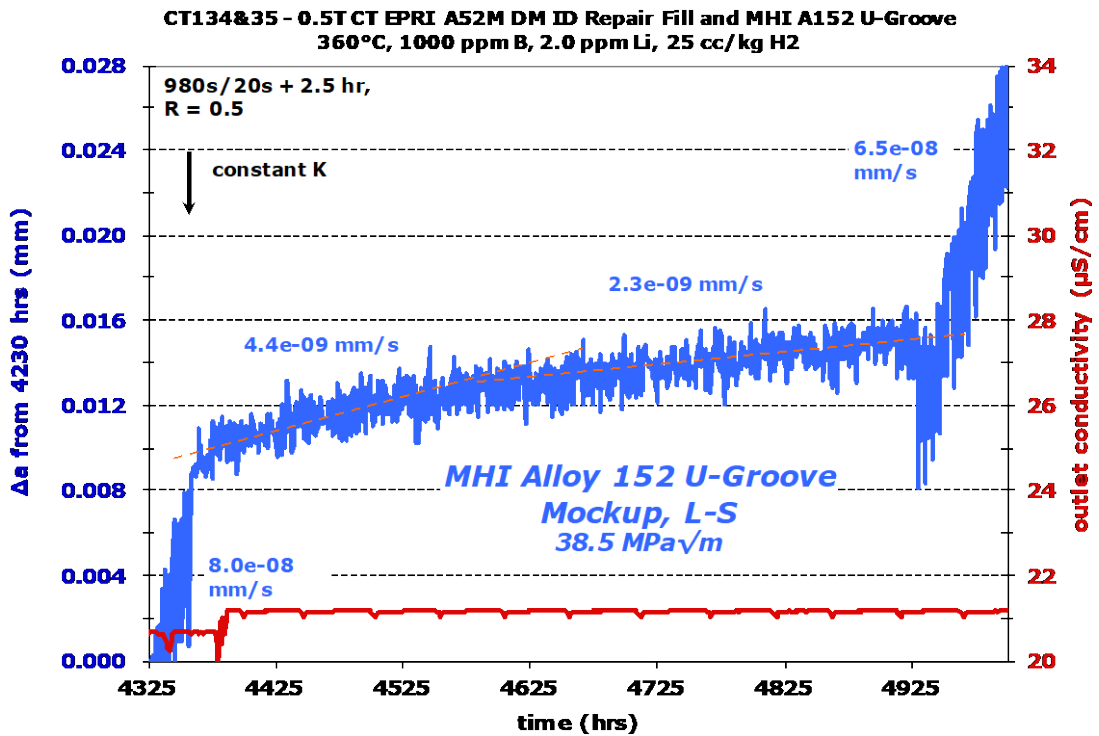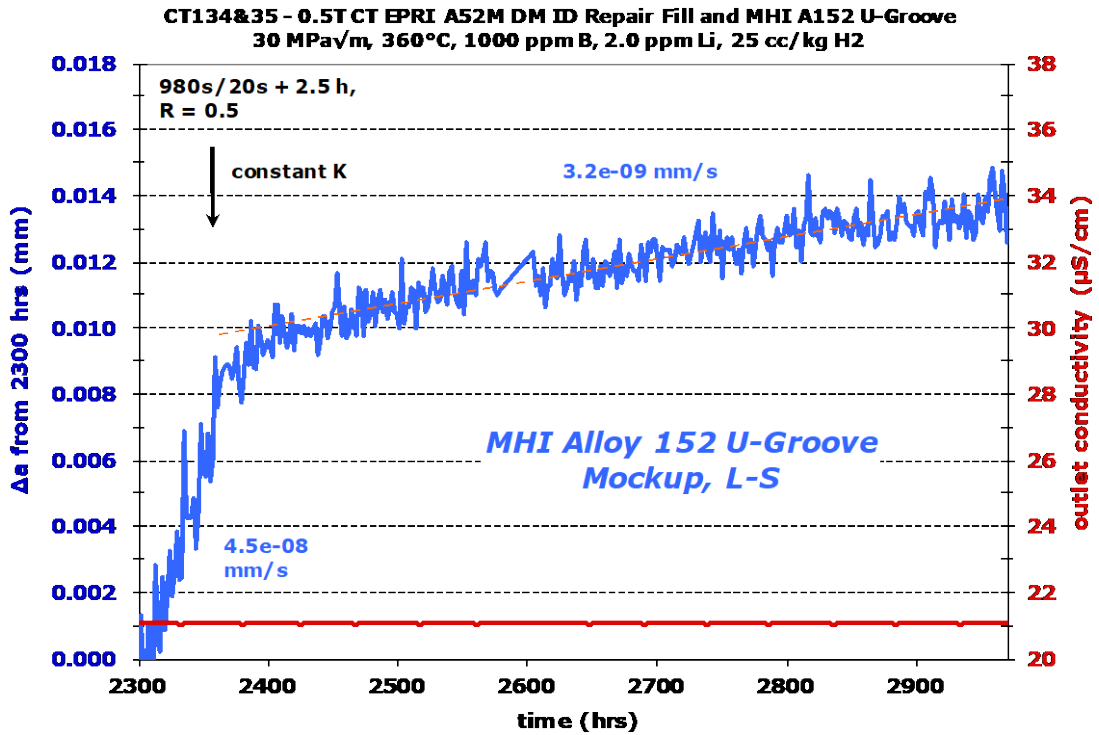
Figure 3-27 **Measured SCC Growth Rates During Constant K Loading for CT135 at Two K Levels: 33 MPa√m (Upper) and 38.5 MPa√m (Lower)**

3.1.3   ANL 152V2 DM Weld (CT049, CT080)

Material and Specimens

The composition of the alloy 152 heat WC04F6 weld filler metal used by ANL in their original, as well as in their new, alloy 152 weldment is listed in Table 3-5. PNNL received slices from the new (second) weldment, and it is referred here as the alloy 152 v2 weld. A diagram provided by ANL of the intended weldment geometry and weld-pass buildup plan is shown in Figure 3-28. It is a double bevel weld that joins alloy 690 to A533 steel. In preparation for the joint weld, the A533 steel plate was buttered with three layers of alloy 152 (not heat WC04F6), and this buttered A533 plate was given a post-weld heat treatment at 621°C for 3 hours. Due to limited quantities of heat WC04F6 weld filler metal, only a portion of the joint was fabricated using this filler metal. The remaining weld passes were made from two other heats of alloy 152. SCC testing at PNNL was confined to weld passes made from heat WC04F6.

As part of test preparation and during post-test analysis of the specimens, a variety of characterizations were carried out in the region of the WC04F6 weld passes. A rough polish and etch was first applied to the entire weldment as shown in

Figure 3-29. Since SCC susceptibility often scales with material strength, microhardness mapping was performed on the weldment. As shown in Figure 3-30, Vickers hardness was found to vary from ~200-260 kg/mm^2. In comparison, microhardness measurements on non-CW alloy 690TT, 17%CR alloy 690TT and 31%CR alloy 690TT yielded average values of 175, 240 and 300 kg/mm^2, respectively. Next, a variety of optical and SEM examinations were performed to characterize boundary structures and compositional variations within the weldment. Measured compositions by SEM-EDS are listed in Table 3-6 and were similar between the two welds using the WC04F6 filler.

Figure 3-31 shows grain boundaries and dendrite boundaries using optical differential imaging contrast, BSE imaging and EBSD. Both high angle and low angle grain boundaries were apparent and exhibited different contrast in EBSD imaging while optical imaging tended to detect only SGBs. SEM-BSE imaging did not clearly distinguish between high and low angle grain boundaries, but tended to most clearly show the SSGBs.

Table 3-5   Composition of the Alloy 152 Heat WC04F6 Weld Filler Metal Used by ANL in Their Original (V1) and New (V2) Alloy 152 Weldments. Values Are in wt%

Heat	Cr	Fe	Mn	C	Si	Nb+Ti	Al	Ti	P	S
WC04F6	28.7	10.4	3.5	0.048	0.41	1.54	0.06	0.09	0.003	0.003

Table 3-6   SEM-EDS Measurements of ANL Weld Metal Composition, Values Are in wt%

Sample/Region	Ni	Cr	Fe	Mn	Nb	Si	Al	Ti	Mo	Cu
Large Area Scan (0.75 x 0.5 mm^2) New V2 Weld	53.40	29.21	9.88	4.32	2.06	0.61	0.21	0.10	0.11	0.09
Large Area Scan Old V1 Weld	53.95	28.86	9.88	4.15	1.95	0.61	0.32	0.09	0.11	0.09
Average Grains New V2 Weld	53.38	29.04	9.87	4.35	2.13	0.63	0.23	0.11	0.15	0.13
Average Grains Old V1 Weld	53.85	28.94	9.72	4.20	2.16	0.63	0.24	0.11	0.11	0.03
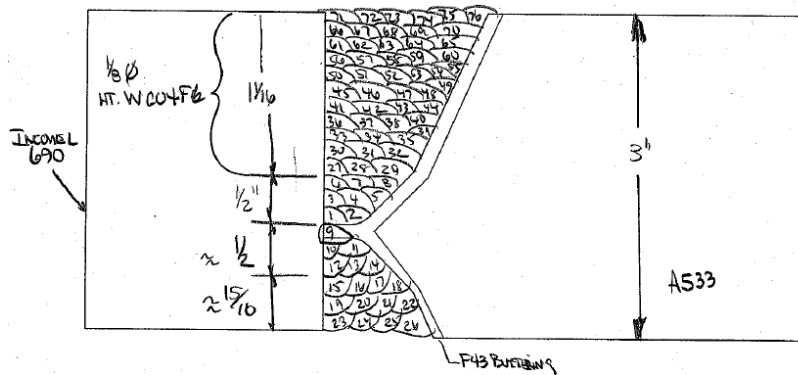
Figure 3-28   Weld Buildup Plan for the ANL Alloy 152v2 Weldment Fabricated Using Alloy 152 Heat WC04F6. PNNL Has Been Using the Name "Alloy 152 V2" for This Weldment

Figure 3-29   Optical Macro Image of a Weld Slice Taken from the ANL Alloy 152v2 Weldment. Note That the Weld Orientation Is Flipped from Drawing in Figure 3-28
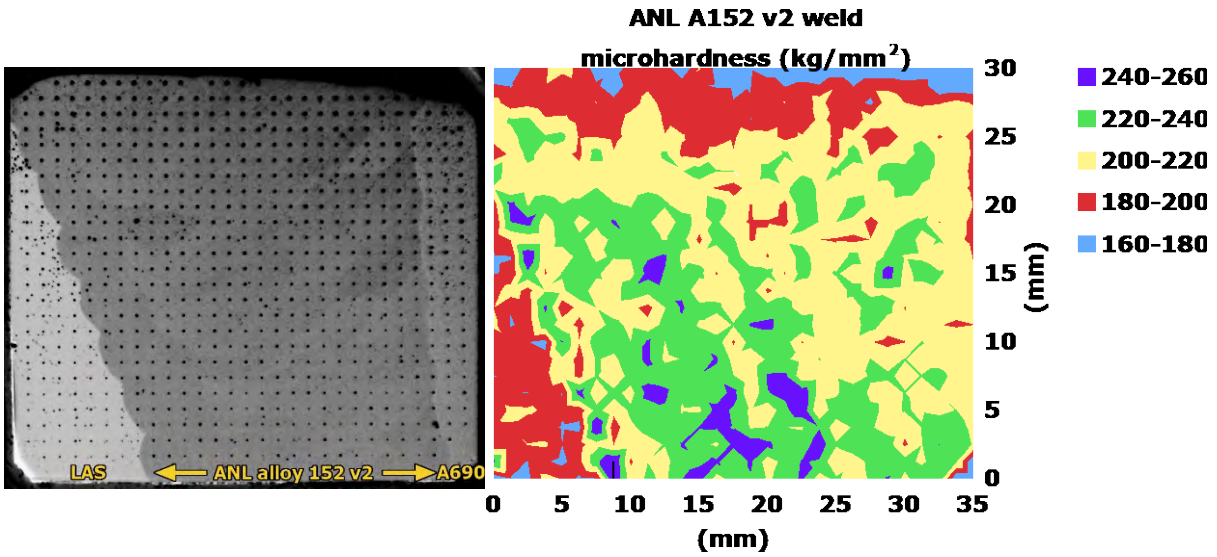
Figure 3-30   Microhardness Indent Pattern and Resulting Hardness Map for the Macro Slice of the WC04F6 Weld Region
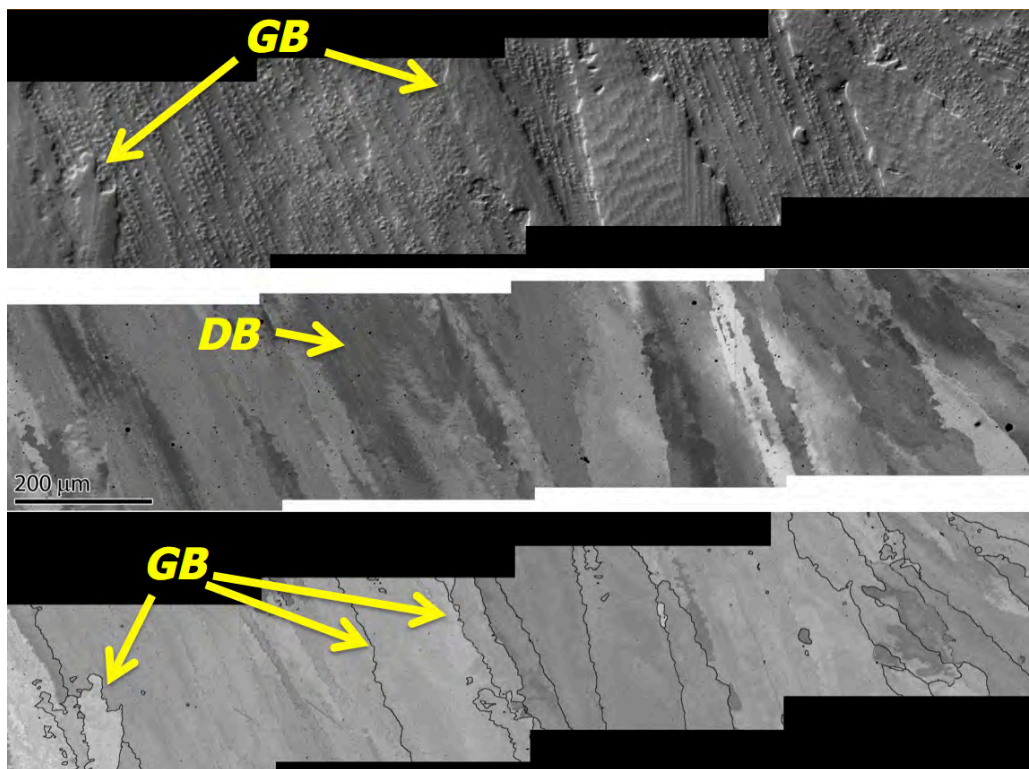
Figure 3-31   Comparison of SGB and SSGB Structures of the Alloy 152 V2 Weldment Using Optical Imaging (top), SEM-BSE Imaging (middle), and EBSD Pattern Quality Map (bottom)

Both lower (Figure 3-32) and higher (Figure 3-33) magnification SEM-EDS imaging of spatial elemental distributions was performed. The low magnification images indicate variations in Mn and Nb content consistent with the size and shape of the dendritic fingers. These EDS maps also showed a low density of Al- and Ti-containing particles dispersed throughout the matrix.

Higher magnification images revealed Nb- and Cr-rich carbides of the order of 50-100 nm decorating high-angle grain boundaries, while only NbC was found on the dendritic boundaries. These elemental distributions are similar to other alloy 152 weldments that have been characterized at PNNL.
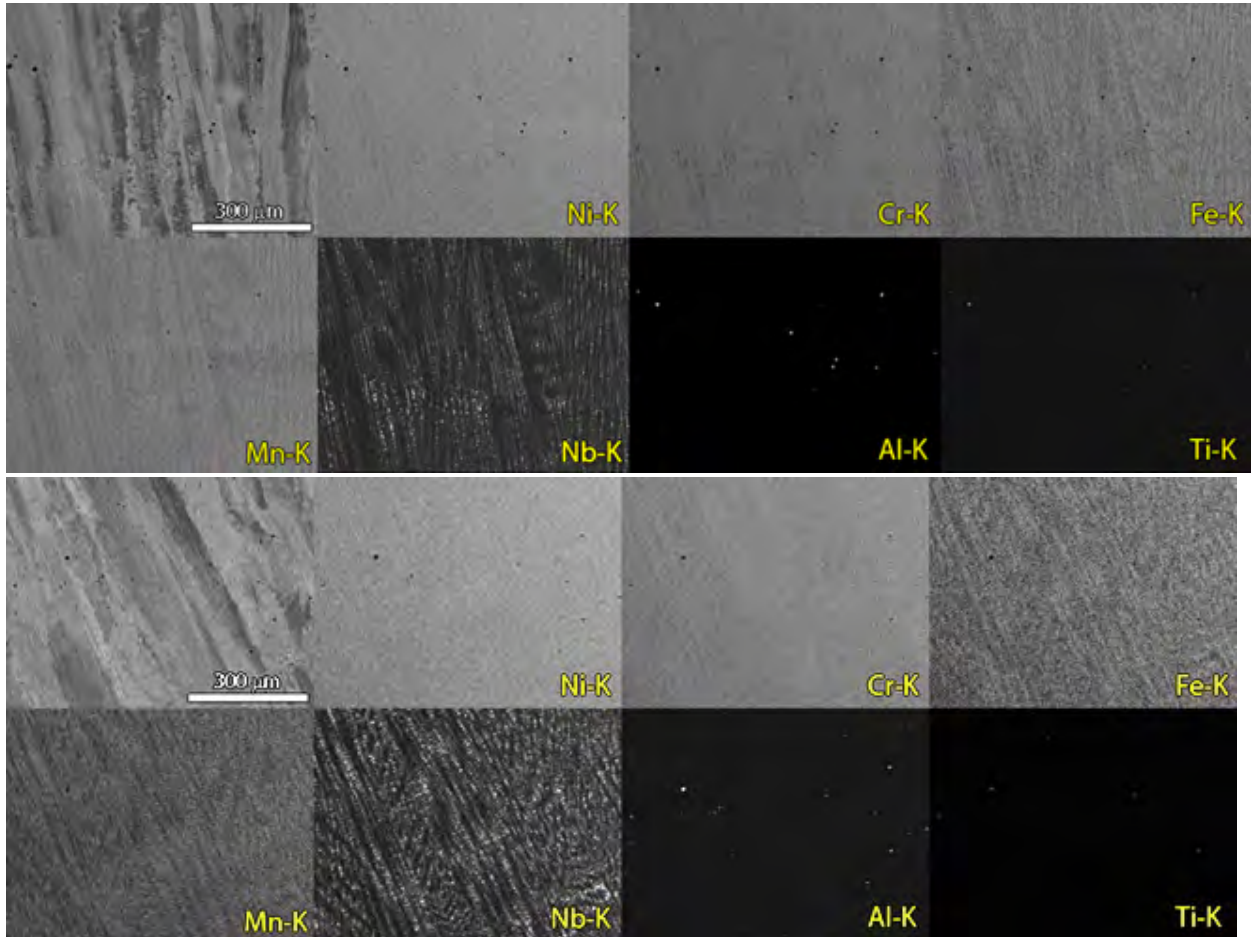
Figure 3-32   Low Magnification SEM-EDS Maps Provide an Overview of Composition Variations in the ANL Alloy 152 V2 Weldment. SEM-BSE Image in the Upper Left Shows the Grain and Dendrite Structure
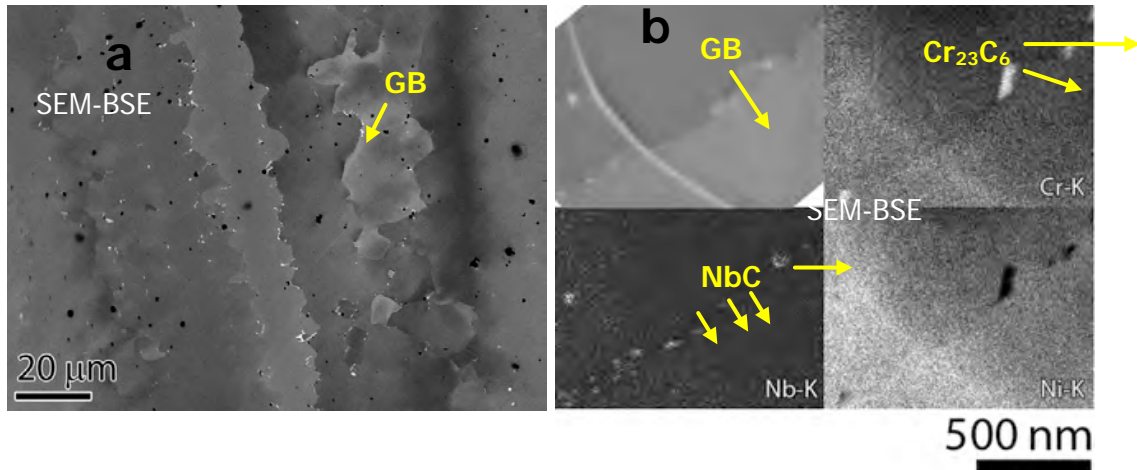
Figure 3-33   a) SEM-BSE Image Where Heavier Elements Produce Higher Brightness. Bright Precipitates Decorating SGBs and SSGBs Are NbC. Black Dot Contrast Is Polishing Debris. b) Higher Magnification SEM-BSE and EDS Images Showing NbC and Cr23C6 Carbides Decorating a Grain Boundary

Stress-corrosion crack growth tests were performed on 0.5T compact tension (CT) specimens with the orientation of the two specimens relative to the weld slices shown in Figure 3-34. Care was taken to position the geometric crack plane of each specimen parallel to the long axis of the weld grain boundaries because this was perceived to be the most susceptible crack path. The first specimen (CT049) was oriented to assess the SCC susceptibility of the third layer of weld passes from the alloy 152 butter on the LAS, while the second specimen (CT080) was positioned to assess the second layer of weld passes from the butter. The notch and precrack were positioned so that SCC evaluations would be made on weld pass regions of higher hardness (220-260 kg/mm^2 as shown in Figure 3-30). Detailed three-dimensional EBSD characterization of the grain structure was performed on specimen CT049 after testing. These results are shown here in Figures 3-35 and 3-36, and reveal that the grains have an overall acicular shape with an aspect ratio of roughly 5:1. The Test Plane A images in Figure 3-36 show ~200 µm sized grains with complex grain boundary shapes while the other images indicate that the long grain dimensions range from ~500 µm to >2000 µm. Many grains have been observed to run continuously from one weld pass to a neighboring weld pass. This combination of relatively large grains and complex grain shape is thought to represent a very tortuous IG cracking mode that cannot be easily maintained under crack-growth testing conditions.

After specimen fabrication, the specimen side grooves were polished and etched to indicate the level of success in specimen positioning within the weldment and also to give an idea of the microstructure sampled during SCC testing. Images of the side grooves for the two specimens are shown in Figure 3-37 (CT049) and Figure 3-38 (CT080). In both cases, the specimens appear to be well aligned with the grain boundaries.
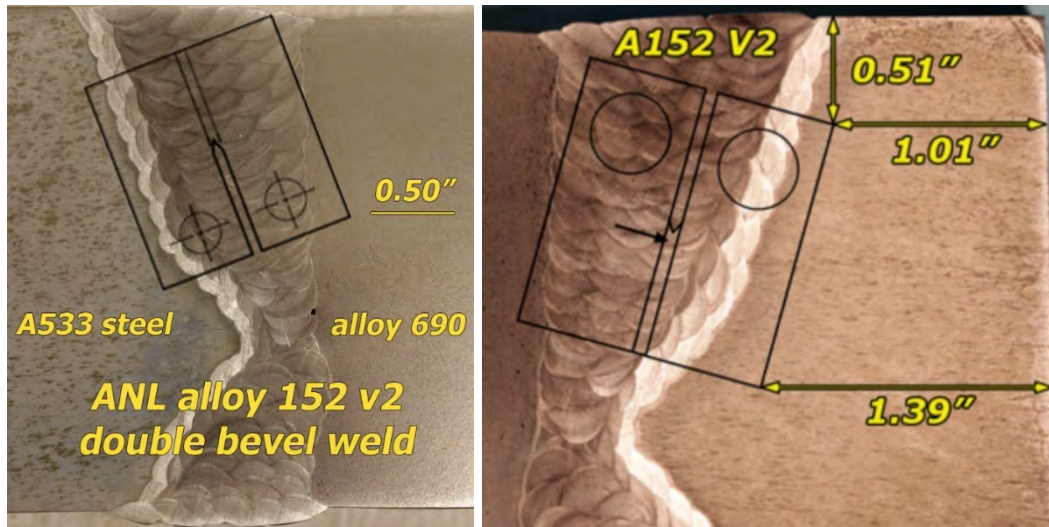
Figure 3-34   Locations of the 0.5T CT Specimens Extracted from Two Different Slices of the Alloy 152 V2 Weldment. Image on the Left Is for the First Test (CT049), While the Image on the Right Is for the Second Test (CT080). Both Specimens Were Oriented to Align the Elongated Grain Boundaries with the Geometric Crack Path and Within a Region of Higher Hardness Indicated in Figure 3-30
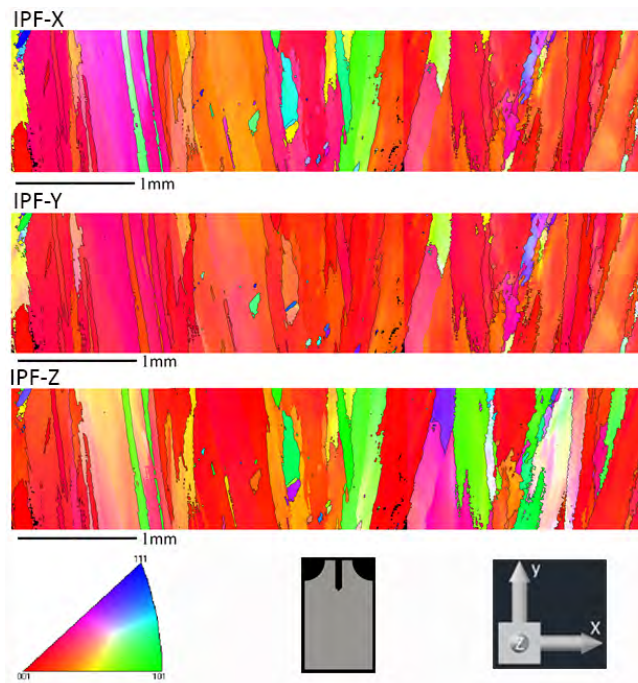
Figure 3-35   EBSD Inverse Pole Figures Illustrating the Grain Structure in the Alloy 152 V2 Specimen CT049 Specimen as Viewed from the Face of the Specimen
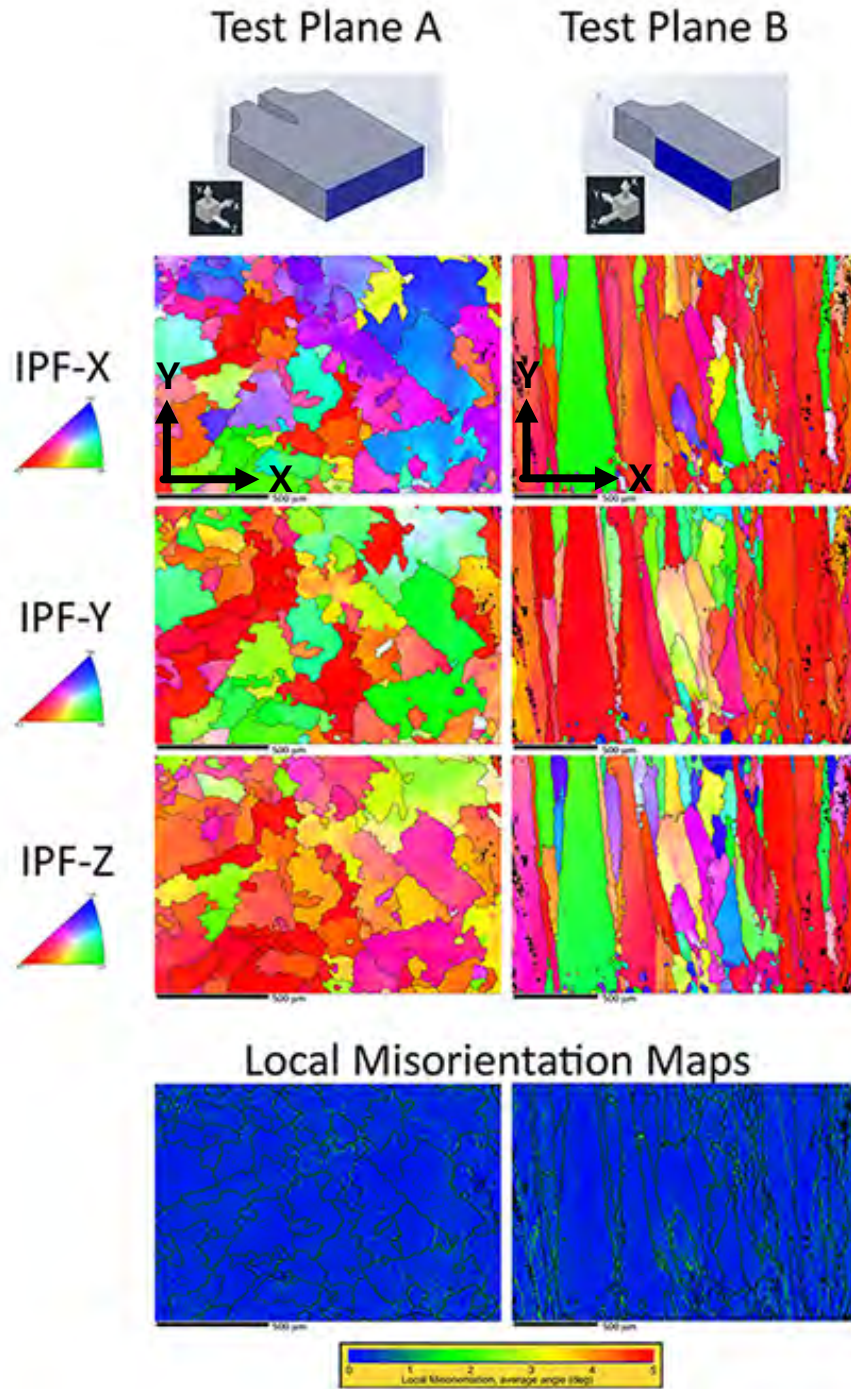
Figure 3-36   EBSD Inverse Pole Figures Illustrating the 3D Grain Structure in the ANL Alloy 152 V2 Specimen CT049 Specimen as Viewed from the End of the Specimen (Test Plane A) or on the Geometric Crack Plane (Test Plane B). The Z-Axis Is Normal to the Face of the Specimen

Figure 3-37 Optical Images of the Polished and Etched Side Grooves for the First Specimen (CT049) Cut from the ANL Alloy 152 V2 Weldment. Grain Shape Is Highly Variable, but Based on These Side-Groove Observations the Geometric Crack Path Is Well Aligned with the Grain Boundaries of the Elongated Grains
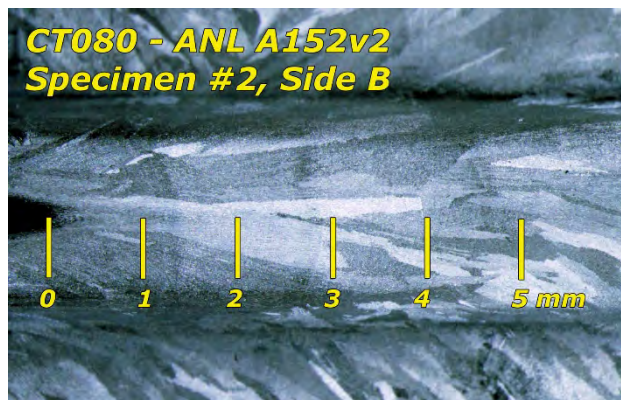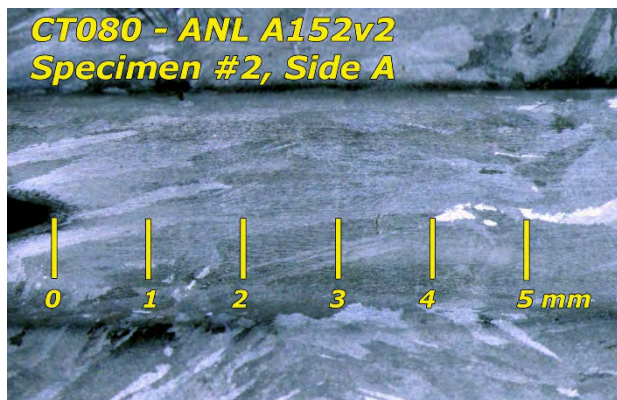
Figure 3-38 Optical Images of the Polished and Etched Side Grooves for the First Specimen (CT049) Cut from the ANL Alloy 152 V2 Weldment. Grain Shape Is Highly Variable, but Based on These Side-Groove Observations the Geometric Crack Path Is Well Aligned with the Grain Boundaries of the Elongated Grains

PWSCC Testing of Alloy 152 v2 Weld Specimen #1 (CT049)

An overview of the entire SCC test is summarized in Table 3-8 and in Figure 3-39. This test was conducted in 360°C primary water with a target K of 30 MPa√m, and five constant K

evaluations were performed. DCPD underestimated the actual crack length in this test resulting in actual K values that were up to 30% higher than the target value. The approach to this test was to evaluate SCC response in five separated microstructural regions. In each transitioning sequence, a different set of transitioning conditions (cyclic and cycle + hold loading) was used to attempt to promote IG engagement along the crack front prior to converting the test to constant K. The degree of IG engagement was determined from optical and SEM images of the crack growth surface after the test was completed (shown later), and the estimated percent engagement values are reported in Figure 3-39 where it can be compared to the crack position. Approximately 50% IG engagement was achieved at the onset of gentle cycling (estimated to be at 0.001 Hz) during the first transitioning sequence and was maintained over ~0.5 mm of crack extension during the first and second transitioning sequences. More aggressive cyclic loading conditions at the onset of the third transitioning sequence (at 2500 h) reduced engagement to ~20% IG, and this fraction increased during the fourth and fifth transitioning sequences to ~60%. The transitioning approaches for CT049 can be roughly grouped into two categories. Transitioning sequences #1-4 attempted to produce IG engagement using cyclic loading frequencies of ~0.001 Hz (using rise/fall times of 500s/500s, 980s/20s, 600s/12s, or 1000s/12s) at R = 0.5 with the addition of hold times, while transitioning sequence #5 attempts to produce IG engagement through slower continuous cycling down to much lower frequencies (5000s/12s and 25000s/12s) but at a more aggressive R value of 0.35. The highest amount of IG engagement (60%) was achieved in the final transitioning sequence where low frequency continuous cycling at an R of 0.35 was used, however as much as 50% IG engagement was measured where more typical frequencies of ~0.001 Hz (R = 0.5) were used.

Initial constant K CGRs can be grouped into the two categories of $<1 \times 10^{-9}$ mm/s or $2\text{-}6 \times 10^{-9}$ mm/s. Examples of these behaviors can be found in Figures 3-40 and 3-41. All constant K CGRs eventually dropped to $<1 \times 10^{-9}$ mm/s. No clear correlation exists between constant K CGRs and the degree of IG engagement with very little (if any) SCC growth observed during the final constant K exposure (Figure 3-40). Response for the five SCC evaluations is summarized in Table 3-8. The possibility of contacts behind the crack front or fingered crack advance were masking the DCPD measurement during constant K testing was often assessed by applying gentle cyclic loading after constant K. In cases of significant masking of DCPD response during constant K, gentle cycling will immediately produce a CGR that is temporarily an order of magnitude higher than expected rates. Testing of the ANL 152 v2 material showed no such response with CGRs immediately matching the expected values, thus reinforcing the notion that little or no crack advance occurred during loading at constant K.

Table 3-7   Summary of Test Conditions and Corrected Response for the ANL Alloy 152v2 Weld Specimens CT049

Test Phase	Duration (h)	R	Freq (Hz)	Hold (h)	Water Chem. Conditions	Temp (°C)	Kmax (MPa√m)	CGR (mm/s)	Approx. Crack Ext (mm)
1	~3	0.3	5	0	air precrack	RT	21	9.6E-05	0.40
2	~2	0.5	5	0	air precrack	RT	24	7.1E-05	0.35
3	~2	0.6	5	0	air precrack	RT	26	5.6E-05	0.35
4	~3	0.7	5	0	air precrack	RT	26	2.8E-05	0.20
5	8	0.5	0.1	0	25 cc/kg H_2	360	32	1.2E-05	0.279
6	85	0.5	0.01	0	25 cc/kg H_2	360	32	1.7E-06	0.540
7	258	0.5	0.001	0	25 cc/kg H_2	360	33	3.2E-07	0.287
8	119	0.5	980/20	0	25 cc/kg H_2	360	33	3.2E-07	0.129
9	480	0.5	0.001	2.5	25 cc/kg H_2	360	33	4.2E-08	0.072
10	310	---	const K	---	25 cc/kg H_2	360	33	4.3E-09	0.001
11	53	0.5	0.001	2.5	25 cc/kg H_2	360	33	- - -	0.004
12	114	0.5	600/12	0	25 cc/kg H_2	360	33	6.4E-07	0.222
13	220	0.5	600/12	1	25 cc/kg H_2	360	33	8.6E-08	0.075
14	93	0.5	600/12	2	25 cc/kg H_2	360	33	4.7E-08	0.020
15	367	0.5	600/12	1	25 cc/kg H_2	360	33	9.2E-08	0.126
16	134	0.5	600/12	2	25 cc/kg H_2	360	33	4.9E-08	0.020
17	267	---	const K	---	25 cc/kg H_2	360	33	<5E-10	0.001
18	156	0.5	0.01	0	25 cc/kg H_2	360	35	2.1E-06	1.095
19	65	0.5	0.001	0	25 cc/kg H_2	360	35	2.8E-07	0.067
20	93	0.5	600/12	0	25 cc/kg H_2	360	36	5.4E-07	0.168
21	76	---	const K	---	25 cc/kg H_2	360	36	<5E-10	0.012
22	115	0.5	600/12	0	25 cc/kg H_2	360	36	5.2E-07	0.203
23	172	0.5	1000/12	0	25 cc/kg H_2	360	37	3.5E-07	0.218
24	213	0.5	1000/12	2	25 cc/kg H_2	360	37	7.1E-08	0.048
25	380	0.5	1000/12	10	25 cc/kg H_2	360	37	1.4E-08	0.019
26	611	---	const K	---	25 cc/kg H_2	360	37	1.8E-09	0.004
27	116	0.5	600/12	0	25 cc/kg H_2	360	37	4.6E-07	0.220
28	70	0.35	600/12	0	25 cc/kg H_2	360	38	9.8E-07	0.248
29	95	0.35	1000/12	0	25 cc/kg H_2	360	39	6.6E-07	0.221
30	240	0.35	5000/12	0	25 cc/kg H_2	360	39	1.7E-07	0.150
31	348	0.35	25000/12	0	25 cc/kg H_2	360	39	4.9E-08	0.058
32	240	0.35	25000/12	3.5	25 cc/kg H_2	360	39	2.8E-08	0.026
33	849	---	const K	---	25 cc/kg H_2	360	39	4.6E-10	0.002
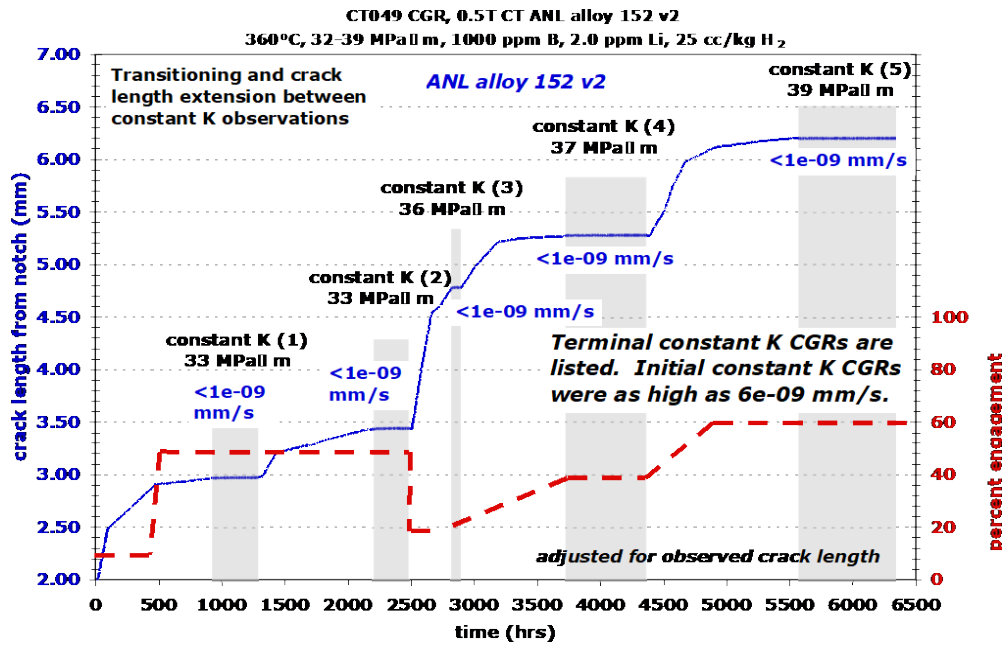
Figure 3-39 Overview of the Entire Test of the First ANL Alloy 152v2 Weld Specimen (CT049) Performed in 360°C Simulated PWR Primary Water. Dashed Red Line Indicates the Percent IG Engagement
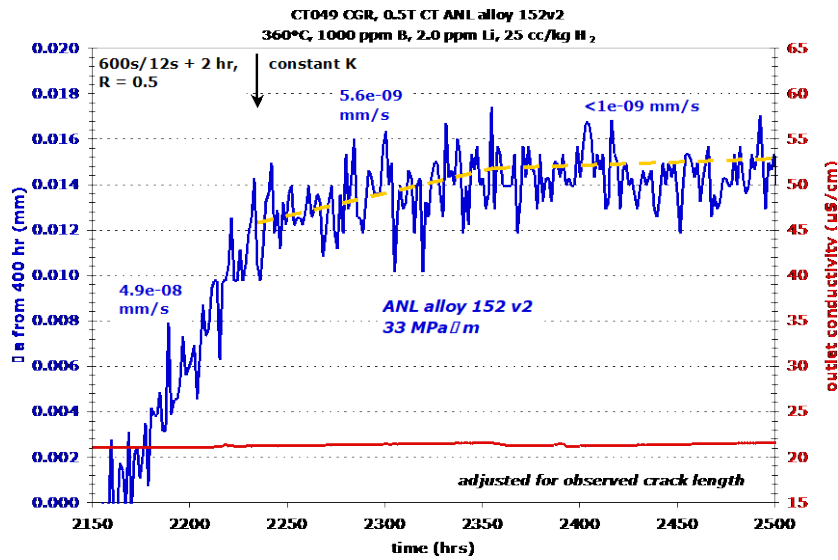
Figure 3-40 Crack Growth Response During the Second Constant K Evaluation of CT049 in 360°C Simulated PWR Primary Water. Stress Intensity Was ~33 MPa√m

CT049 CGR, 0.5T CT ANL alloy 152v2
360°C, 1000 ppm B, 2.0 ppm Li, 25 cc/kg H$_2$
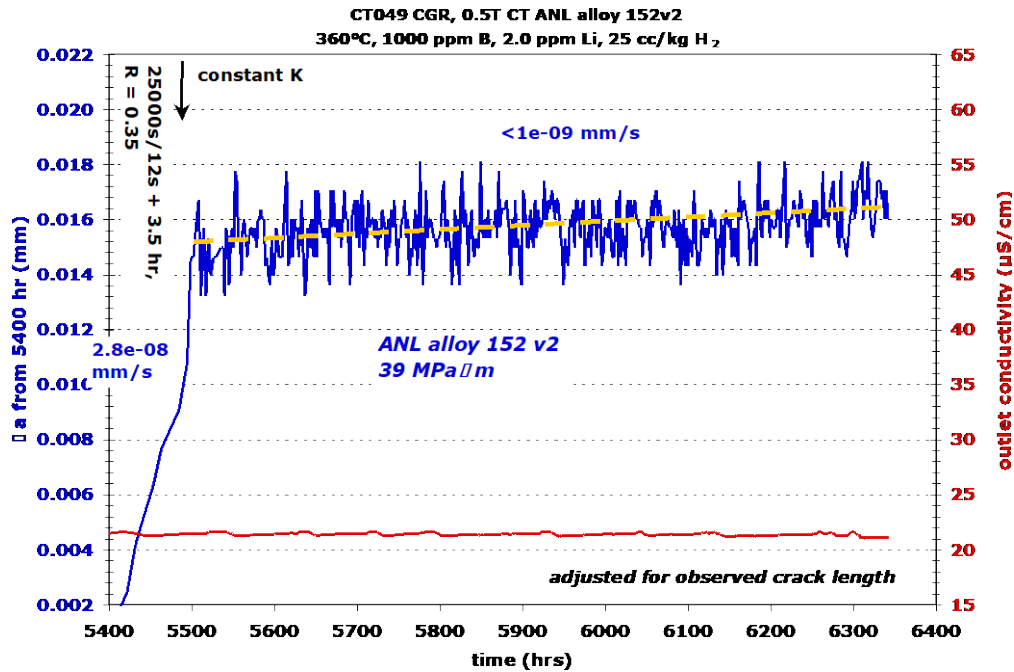
Figure 3-41   Measured Crack-Growth Response During the Fifth and Final Constant K Evaluation of CT049 in 360°C Simulated PWR Primary Water. Stress Intensity Was ~39 MPa√m

Table 3-8   Summary of Measured Constant K CGRs for the CT049 Specimen

Trans. Sequence	Stress Intensity (MPa√m)	% IG	Initial Const K CGR (mm/s)	Final Const K CGR (mm/s)
1	33	~50	2.8x10^{-9}	<1x10^{-9}
2	33	~50	5.6x10^{-9}	<1x10^{-9}
3	36	~20	<1x10^{-9}	<1x10^{-9}
4	37	~40	2.2x10^{-9}	<1x10^{-9}
5	39	~60	<1x10^{-9}	<1x10^{-9}

After SCC testing, the specimen was first sliced into two, producing slices that were 4 and 8 mm thick. The thicker piece was fatigued open for crack growth surface examinations, while the thinner piece was used for crack profile examinations. An optical image of the crack surface from the thicker piece is shown in Figure 3-42. Yellow lines were drawn where distinct changes in crack surface appearance were observed. In this optical image, areas of higher IG engagement have a rougher appearance than TG regions. IG cracking is responsible for the protrusions along the final crack front.

Detailed mapping of the IG/TG cracking morphology was performed using SEM imaging. SEM-SE images of regions within the four blue boxes in Figure 3-42 are shown in Figure 3-43. Significant amounts of IG cracking are present. The crenulated appearance clearly

distinguishes IG from TG cracking (see also Figure 3-44). Comparison of such images to the optical images permitted measurement of the degree of IG engagement throughout the test. However, additional efforts were put into analysis of the final ~1.5 mm of crack extension by analyzing SEM-BSE and SE montages across the width of the surface as shown in Figure 3-45.

Observations of the crack profile from the 4-mm-wide piece of CT049 are shown in Figures 3-46 and 3-47. In Figure 3-46, the air precrack can be clearly distinguished from the in-situ portion of the test. In this crack profile slice, the crack was entirely TG until the last ~1.4 mm, where it encountered and remained on a grain boundary. EBSD imaging shows that it is a high-angle grain boundary. The small branching cracks that formed near the final crack front are likely due to stresses driving the crack back down towards the geometric crack growth plane of the specimen. The final ~150 µm of IG crack extension shows nothing compositionally unique from SEM-EDS examinations (Figure 3-47). Major and minor elemental constituents appear compositionally similar to neighboring dendritic grain boundaries.

A key aspect of the crack growth morphology is very long sections of IG extension, often exceeding 1.5 mm. These long amounts of IG extension were probably made possible by having the geometric crack growth plane of the specimen well aligned to the long grain boundaries of the weld metal microstructure. IG extensions of this length clearly indicate that some grain boundaries in this weld are susceptible to environment-assisted cracking under a variety of cyclic loading conditions. The loading conditions during the last 1.5 mm of testing ranged from constant K to somewhat aggressive cycling at 600s/12s (R = 0.5) and 1000s/12s (R = 0.35) showing that IG cracking will occur in this weld metal even under continuous cyclic loading. However, these observations also show that despite "easy" IG cracking along some grain boundaries, full IG engagement across the crack front was not achieved despite the application of a variety of gentle cyclic loading conditions over very long crack extensions. This suggests that grain shape and boundary orientation to the crack path play a significant role in IG propagation along with possible variations in grain boundary susceptibility.
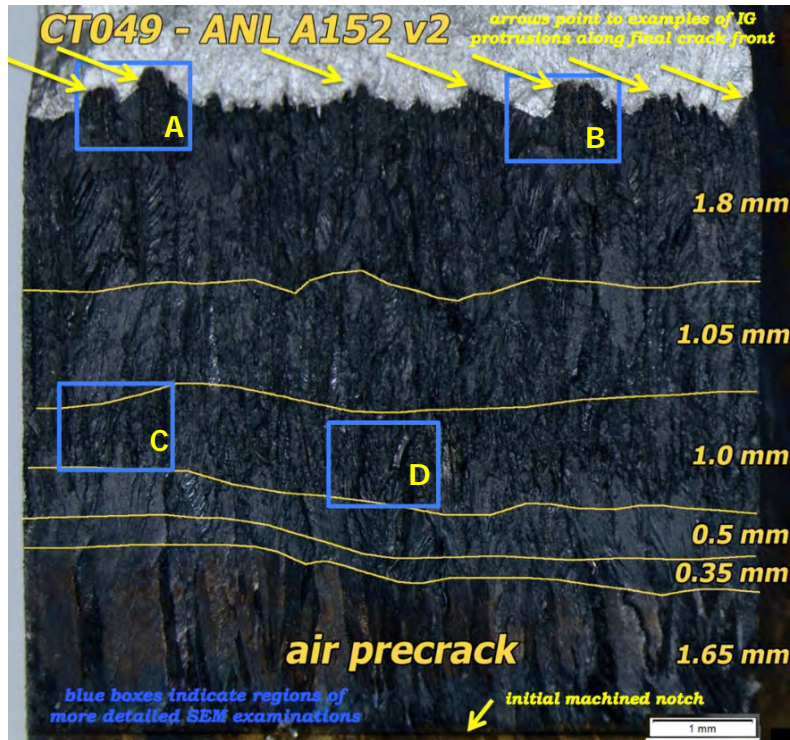
Figure 3-42   Crack-Growth Surface Optical Image of the 8-mm Wide Section of the CT049 Specimen. Yellow Arrows Indicate Examples of IG Protrusions Along the Final Crack Front. Blue Boxes Indicate Regions of SEM Examinations Presented in Figure 3-43
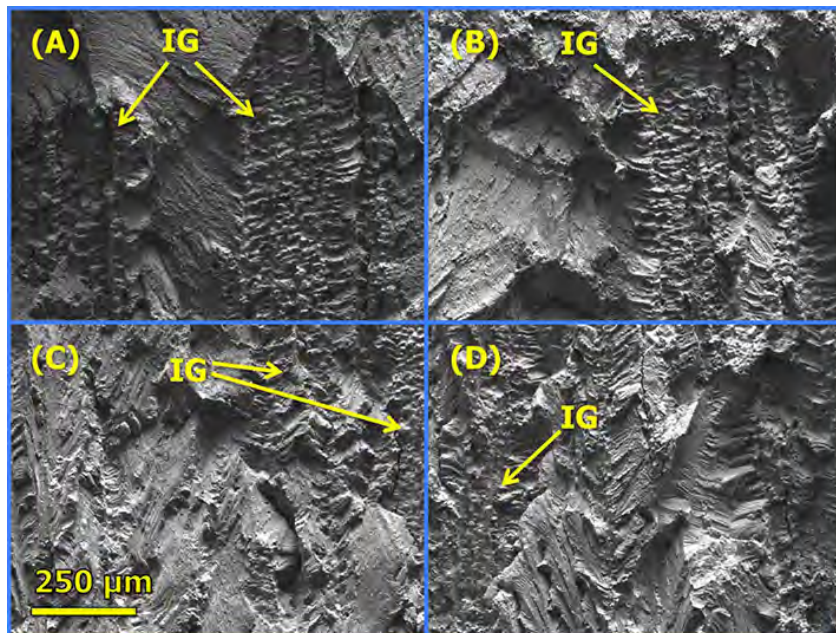
Figure 3-43   SEM-SE Images of Regions Within the Blue Boxes in the Optical Image of the Entire Crack-Growth Surface for the CT049 Specimen (Figure 3-42)
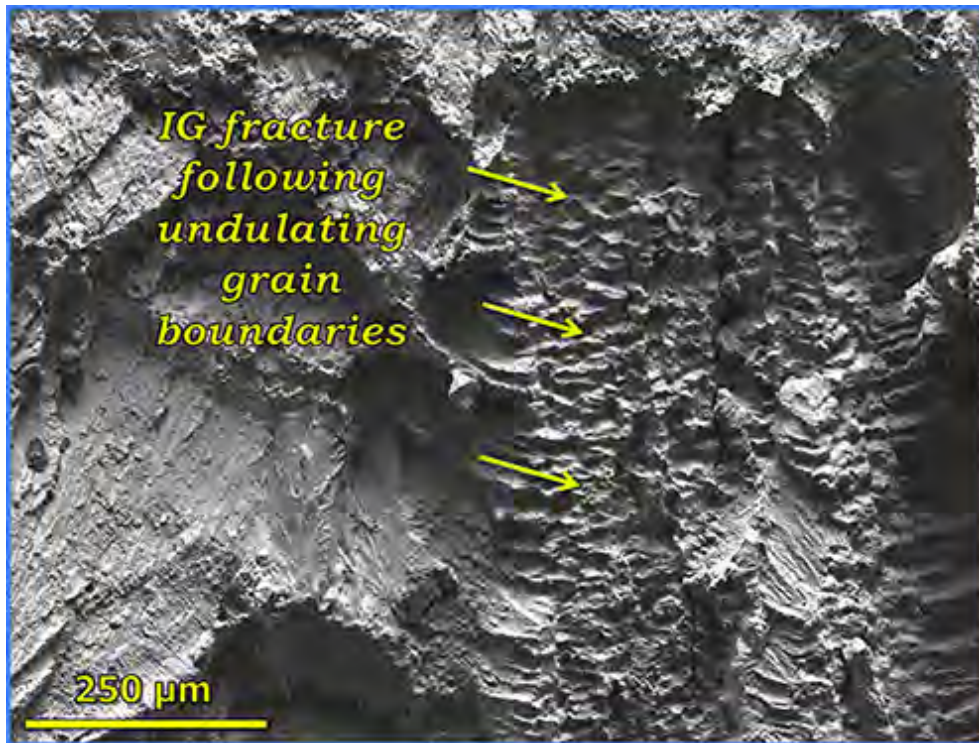
Figure 3-44 Higher Magnification SEM-SE Image Illustrating the IG Crack Surface Appearance in CT049
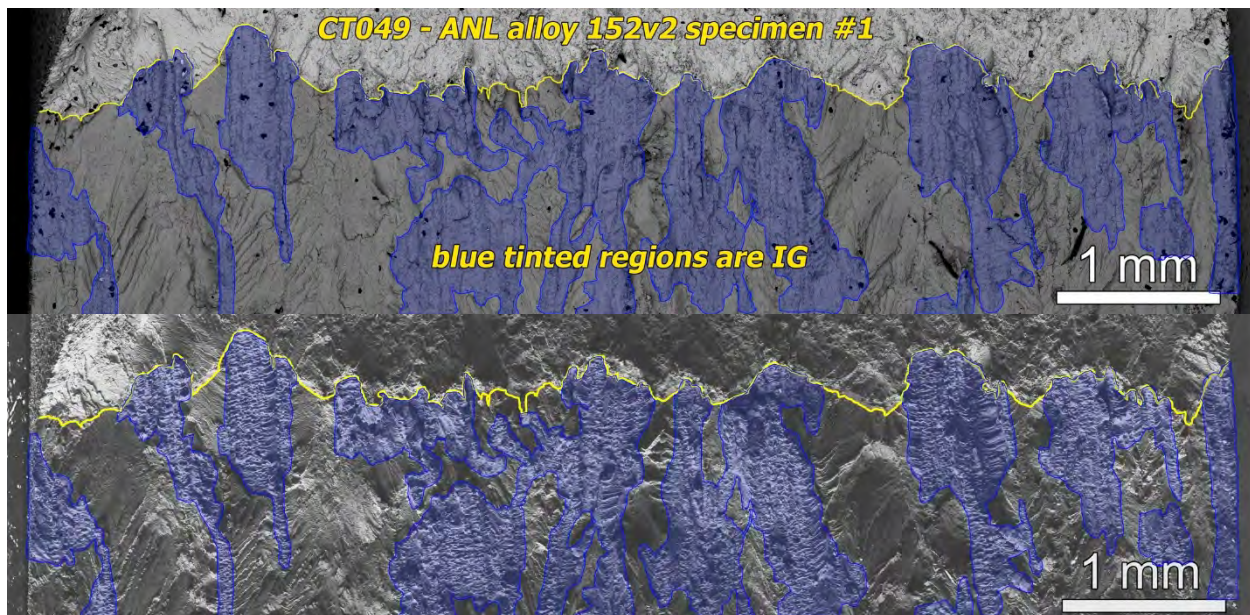
Figure 3-45 SEM-BSE (upper) and SE (lower) Images Showing IG Regions (blue tint) Along the Final ~1.5 mm of the SCC Test of CT049. Yellow Line Denotes the Final Crack Front at the Conclusion of the Test
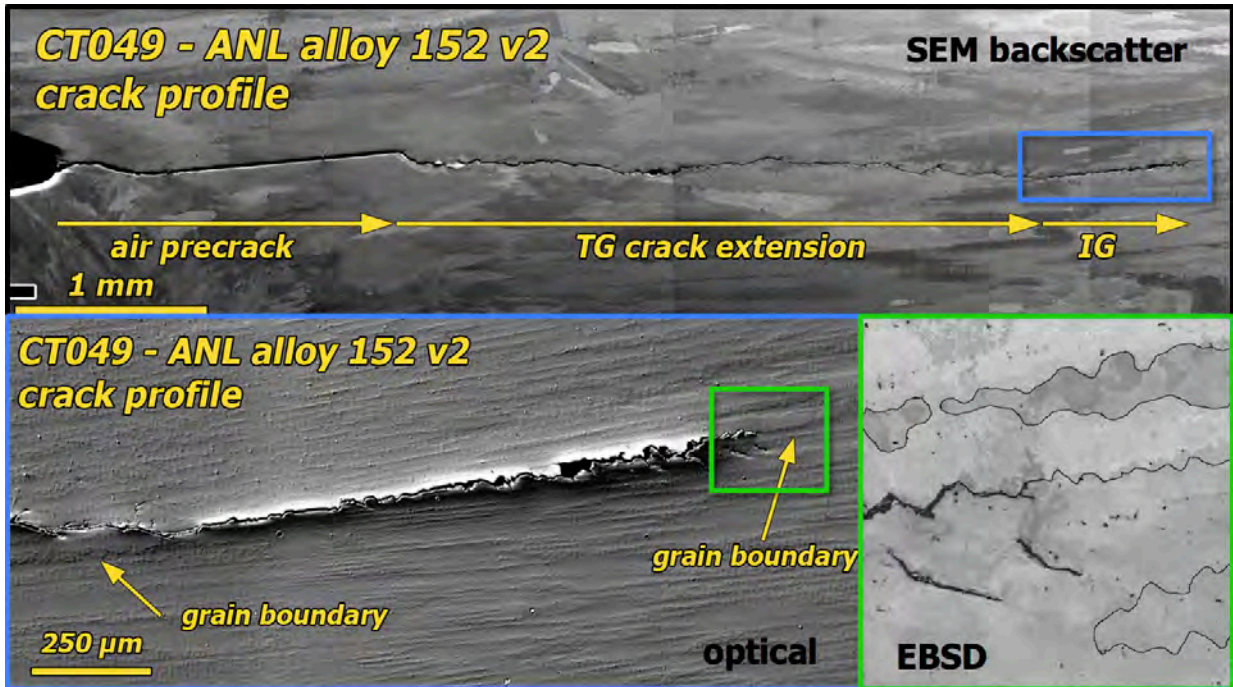
Figure 3-46   Compilation of SEM-BSE, Optical, and EBSD Images Showing the Crack Path in Profile from Notch to Final Crack Front in a Side-Surface Cross Section from the CT049 Specimen
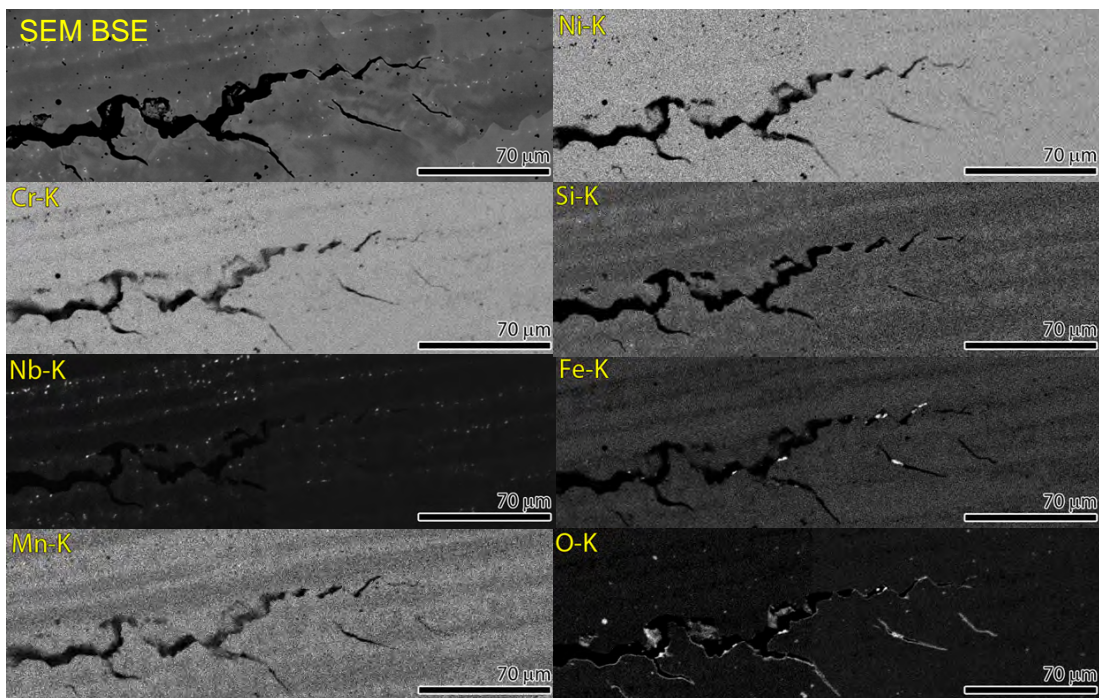
Figure 3-47   SEM-BSE and EDS Maps Showing Elemental Compositions Along the Final ~150 µM of the CT049 Crack Profile

With such long amounts of IG extension occurring over a wide range of testing conditions, a major challenge in assessing the SCC response of this material is determining what amount of crack advance occurred during constant K loading. DCPD clearly shows crack advance during cyclic and cycle + hold loading, but indicates very little (few µm) or no growth during constant K testing. The crack surface of this specimen contains extensive IG cracking and localized IG protrusions at the final crack front. At this point in time, a method to accurately isolate IG growth that occurs during constant K loading from what occurs during cyclic or cycle + hold loading has not been determined. On the possibility that some IGSCC is occurring during constant K that DCPD did not accurately capture, constant K CGRs were estimated from the IG protrusions along the final crack front. For this analysis, it was assumed that constant K IG extension is what occurred beyond TG tearing on either side of the IG cracking. This is illustrated in Figure 3-48 for two extreme examples (these are two of the same images in Figure 3-43) where the white dashed line indicates the postulated start of constant K IG growth, and the white arrows indicate the maximum extension. Following this method on all the protrusions along the final crack front in Figure 3-45, engaged constant K CGRs were calculated to be as high as $\sim 1\times 10^{-7}$ mm/s, however the majority of the measurements gave values closer to $\sim 2\times 10^{-8}$ mm/s.
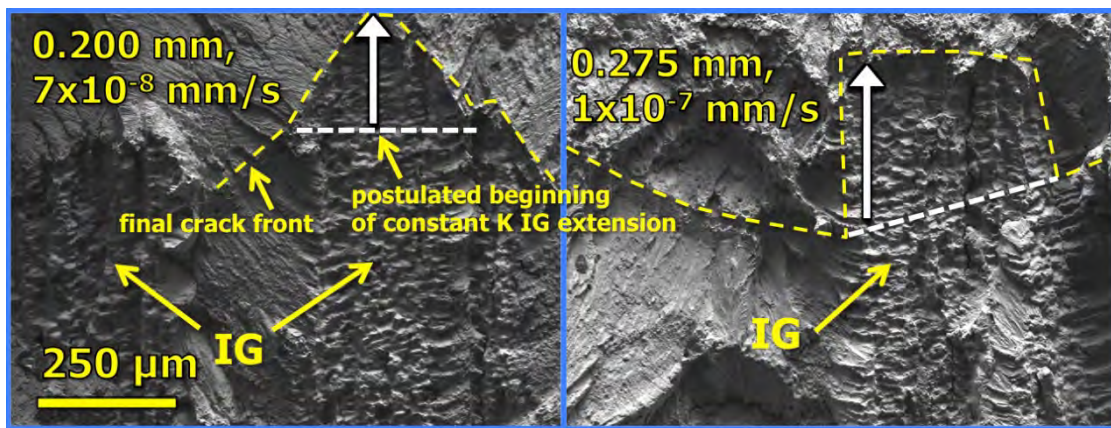
Figure 3-48   Illustration of Postulated Constant K IG Extension Along the Final Crack Front of CT049

It is important to recognize that while this analysis of the final crack front gives average constant K CGRs in the engaged regions of $\sim 1\text{-}3\times 10^{-8}$ mm/s, the shape of the final crack front shows no indication of a tendency for the crack to become progressively more IG during constant K loading. The only constant K IG cracking that may have occurred was from regions that were already engaged prior to setting the test to constant K. In addition, the morphology of the engaged regions of the final crack front shows no indication of IG expansion or ballooning. Instead, the IG regions typically have a pointed shape suggesting that the degree of IG engagement was decreasing as time progressed. The same resistance to achieving very high degrees of IG engagement was also observed during crack transitioning. While 60% engagement is higher than any other alloy 152/52 weld metal specimen tested at PNNL, there is no indication that full engagement would have been achieved if the transitioning had continued for much longer periods of time. The torturous grain boundary shape of this material favors the assessment that only limited engagement is likely.

The inability to obtain >60% IG engagement during transitioning or obtain an increase in IG cracking during constant K loading is somewhat in contrast to the ease at which portions of the specimen transitioned to (and maintained) IG growth for several millimeters at mildly aggressive

fatigue cycling conditions. The overall assessment of this specimen is that while significant IG crack advance is clearly possible, widespread sustained IGSCC is not.

PWSCC Testing of Alloy 152 v2 Weld Specimen #2 (CT080)

The observation of significant IG engagement, but with apparent low CGRs in the CT049 specimen prompted the decision to run a second test on this weldment. As described in the experimental section, this specimen was located in a slightly different position. The CT080 specimen was also rotated 180 degrees relative to CT049 so that cracking would progress towards the weld root rather than towards the crown. As with the first specimen, this one was again aligned parallel to the grain boundaries as best as possible (Figures 3-34 and 3-38). An overview of the entire DCPD-based crack growth response is shown in Figure 3-49. The first portion of the test was conducted under the same environmental conditions as the prior CT049 test (360°C at the Ni/NiO oxide stability). Similar transitioning techniques were also applied in this first part of this test, i.e., progressively more gentle cycling leading to gentle cycle + hold loading before assessing constant K response. The first constant K assessment that was started at ~1950 h produced very low CGRs of $<1\times10^{-9}$ mm/s as shown in Figure 3-50. After ~600 h at constant K, gentle cyclic loading was applied and produced typical CGRs for this loading condition, indicating that DCPD had not been masked by contact formation or fingered crack advance during constant K. The crack was then aggressively advanced to a new region where re-transitioning steps were started. CGRs during these transitioning steps were found to be identical to earlier in the test and similar to that in the prior test (CT049).

Having duplicated the crack-growth response during transitioning and constant K of the first test (360°C) based on in-situ DCPD, the environmental conditions and crack transitioning methods were altered to approximate those used by ANL on the two alloy 152 welds using the WC04F6 weld filler metal. Thus, test temperature was reduced to 320°C and the dissolved hydrogen concentration shifted to 29 cc/kg in the Ni-metal stability regime. Common ANL transitioning methods use progressively more-gentle cyclic loading steps and hold times just like PNNL and many other SCC testing laboratories, however the particular cyclic waveforms are slightly different. ANL tends to favor a 600s/12s (R = 0.5) load cycle for their most gentle continuous cyclic loading condition for this material and test temperature, and the most common hold time is 2 hours. As part of their crack-growth assessment, ANL also occasionally uses a periodic partial unloading step that consists of a 12s/12s (R = 0.5) load cycle every 1 or 2 hours. Since in-situ constant K correction is not done at ANL, this feature was turned off as well, and K was allowed to increase with crack length and SCC was evaluated under constant load conditions. Lastly, ANL assesses CGR response during transitioning by comparing the in-situ environmental CGR to a calculated air CGR that is an empirical fit to air fatigue tests on alloy 600, 182, and 690. Inputs into the air fatigue formula include K, load ratio and temperature. The ratio of the environment CGR to the calculated air fatigue CGR is used as a gauge for estimating the SCC engagement during transitioning. All these aspects of SCC testing were adopted for the second half of this test.
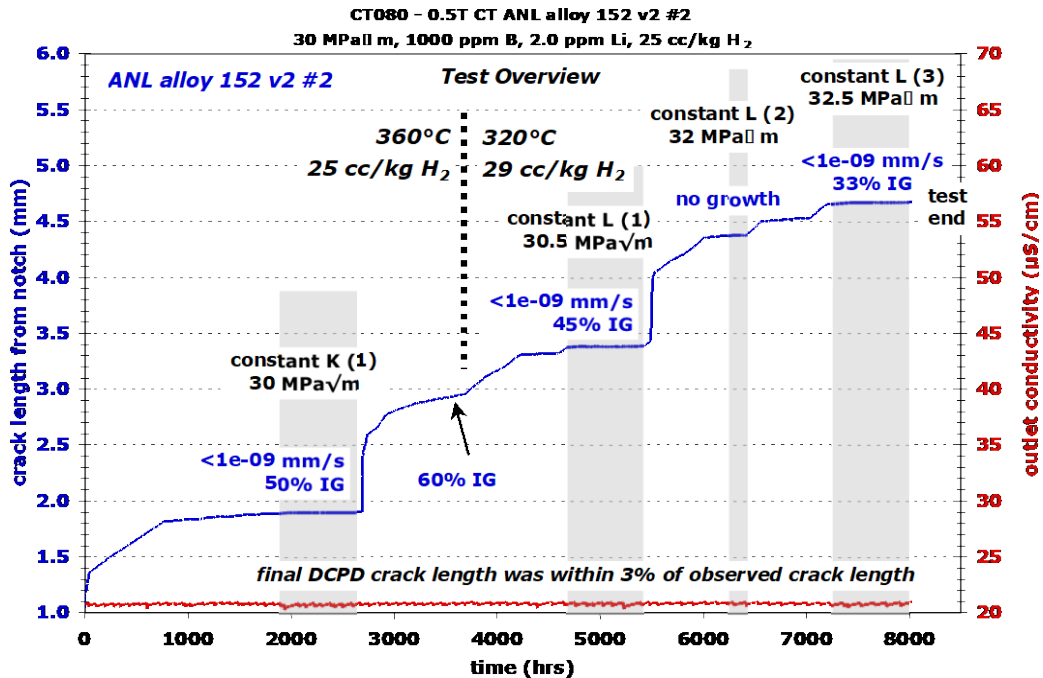
Figure 3-49 Overview of CGR Test on the Second Alloy 152 V2 Specimen (CT080) Performed in 360°C (0-3800 hours) and 320°C (3800-8000 Hours) Simulated PWR Primary Water. Terminal Constant K CGRs Are Listed
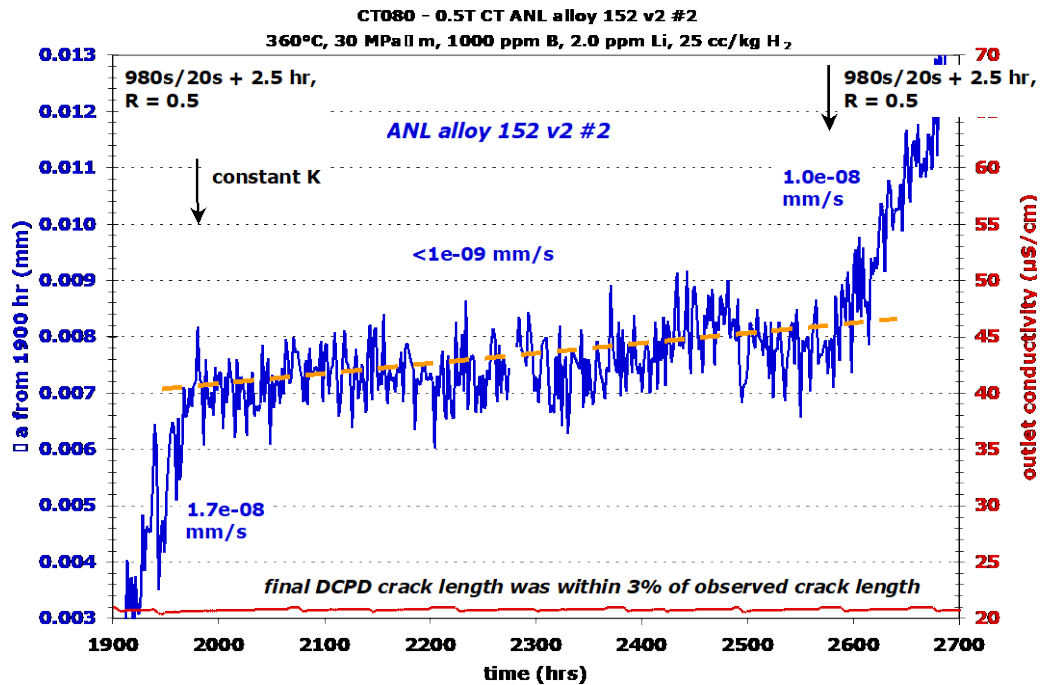
Figure 3-50 Constant K Crack Growth Response Following the First Transitioning Sequence on the Alloy 152 V2 Specimen CT080 in 360°C Simulated PWR Primary Water

During testing at 320°C, the CGR at 600s/12s (R = 0.5) cycling was frequently measured as suggested by the many small ramps in 320°C portion of the overview test plot (Figure 3-49).

The env/air CGR ratio consistently hovered between 2-3 for 600s/12s continuous cycling transitioning steps, and the addition of a hold time tended to increase this ratio by ~10%. The env/air CGR ratios for the first transitioning sequence at 320°C are shown in Figure 3-51, where they are compared to env/air ratios measured during the two transitioning sequences at 360°C. These ratios at the first 320°C transitioning sequence are typical of those in later transitioning sequences at 320°C, and they are similar or slightly lower than the values determined at 360°C. Constant load SCC evaluations were made three times at 320°C with all evaluations producing CGRs that quickly dropped below 1×10^{-9} mm/s, as illustrated by the last attempt shown in Figure 3-52. As with testing at 360°C, application of gentle cycling always showed no indication that DCPD was being masked during constant load exposures.
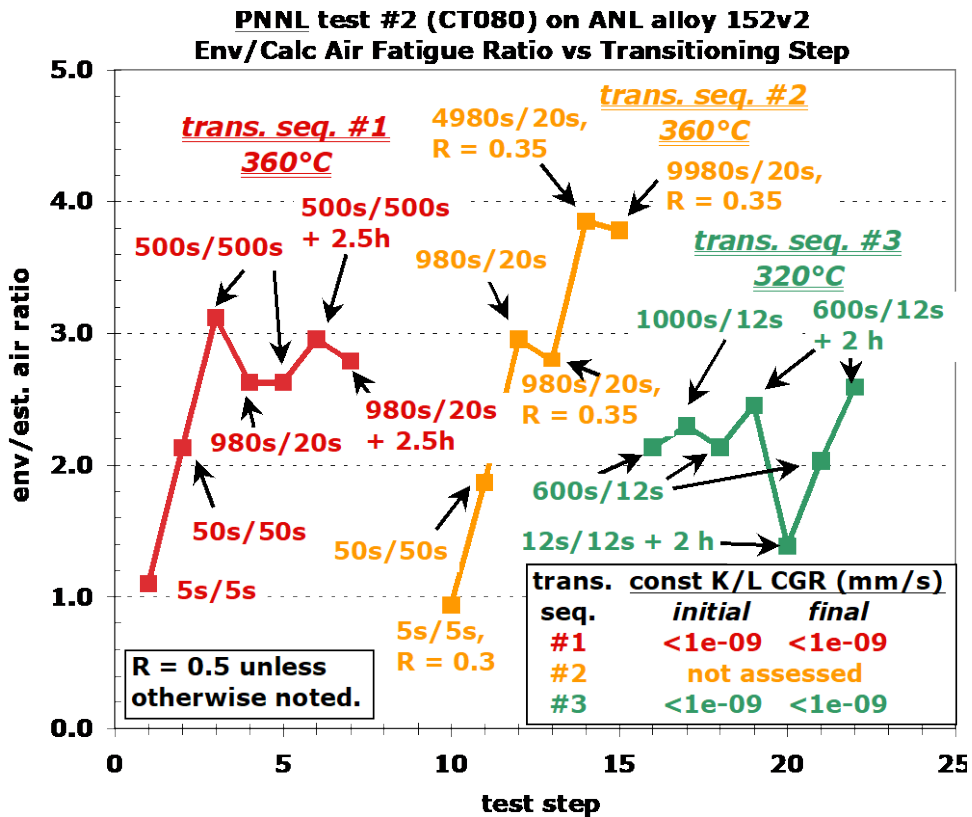
Figure 3-51   Env/air Ratio During the First Three Transitioning Sequences (two at 360°C and one at 320°C) for the Second Test on the Alloy 152 V2 Weldment (CT080)
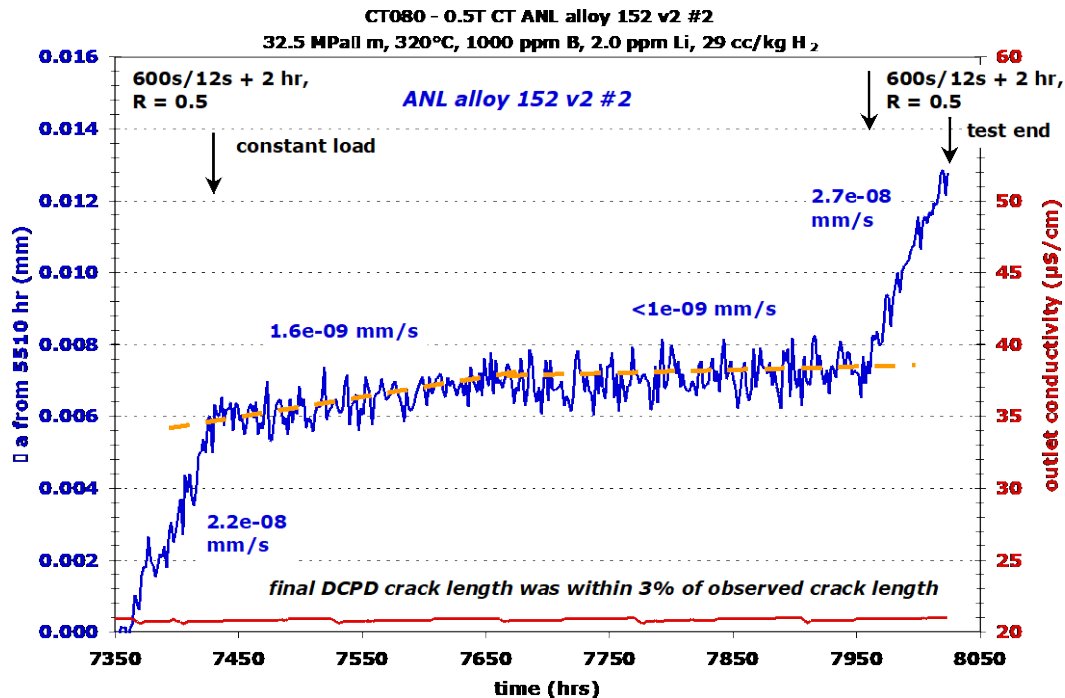
Figure 3-52 Third Constant Load Observation on the Alloy 152 V2 Specimen CT080. This Portion of the Test Was Conducted in 320°C Simulated PWR Primary Water

Post-test examinations were conducted in a similar fashion to the prior test on the CT049 specimen. The CT080 specimen was sectioned into an 8-mm-wide slice for crack-growth surface observations and a 4-mm-wide slice for crack profile observations. Optical imaging of the crack-growth surface (Figure 3-53) revealed differing appearances for the portions of the test at 360°C and 320°C. The degree of IG engagement was examined in detail along the final crack front using SEM-BSE imaging as shown in Figure 3-54 where regions of IG cracking are highlighted in blue. Complimentary SEM-SE images were also taken to confirm crack morphologies. The degree of IG engagement along the final crack front was estimated to be ~33%. Assessment of the remainder of the surface using the optical image produced a value of ~45% during the first constant load assessment at 320°C, while 50-60% peak IG engagement was measured at 360°C, consistent with the first test on this weldment. The crack profile image in Figure 3-55 (left side of the specimen in Figure 3-53) was found to have primarily TG cracking for this cross-section location.

The general conclusion for the test on this second alloy 152 v2 specimen (CT080) is that similar response was seen at 360°C, i.e., 50-60% IG engagement and terminal constant K CGRs were <1x10^{-9} mm/s. When the test temperature was lowered to 320°C, the degree of IG engagement decreased and constant load CGRs were again <1x10^{-9} mm/s.

Figure 3-53 Optical Image of the 8-mm-Wide Section of the Crack-Growth Surface of the Second Alloy 152 V2 Specimen (CT080) Tested in 360°C and 320°C Simulated PWR Primary Water

Figure 3-54 SEM BSE Image of the Final ~1 Mm of Crack Growth of the Second Alloy 152 V2 Specimen (CT080). This Portion of the Test Was at 320°C

Figure 3-55 Optical Image of the Side-Surface Cross Section Taken from the Second Alloy 152 V2 Specimen (CT080) After SCC Testing

3.1.4 Analysis of Multi-Lab SCC Tests Results on the ANL Alloy 152v2 Weld

Discussions among NRC, ANL and PNNL staff focused on multi-lab test results on the ANL alloy 152v2 weld (designated N152, double J, heat WC04F6) produced at ANL. A primary goal was to compare the testing approaches and measured crack growth responses during transitioning and under constant load or K conditions. The key issue is the observation by ANL of sustained crack growth during several of their constant load exposures versus the results at PNNL where sustained crack growth at constant stress intensity was not obtained. Peter

Andresen at GEG had also completed a test on this same weld with results similar to those found at PNNL. This section repeats some description of the two PNNL tests above then provides further analysis for the comparison of tests at all three laboratories.

PNNL Test #1 (CT049) on ANL Alloy 152v2 Weld

An overview of the entire SCC test curve was shown in Figure 3-39. This test was conducted in 360°C primary water with a target K of 30 MPa√m, and five constant K evaluations were performed. The approach to this test was to evaluate the constant K SCC response in five separated microstructural regions. In each transitioning sequence a different set of transitioning conditions (cyclic and cycle + hold loading) were used to attempt to promote IG engagement along the crack front prior to converting the test to constant K. The degree of IG engagement was determined from optical and SEM images of the crack growth surface after the test was completed and estimated values are reported as a function of test time and can be compared to the crack position also shown in Figure 3-39. Approximately 50% IG engagement was achieved at the onset of gentle cycling (estimated to be 0.001 Hz) during the first transitioning sequence and was maintained over ~0.5 mm of crack extension during the first and second transitioning sequences by gentle cycling. More aggressive cyclic loading conditions at the onset of the third transitioning sequence drove the crack down to 20% IG, and during gentle cycling in the fourth and fifth transitioning sequences, IG engagement increased to 60%. Initial constant K CGRs can be grouped into two categories of either ≤$1x10^{-9}$ mm/s or 2-6x10^{-9} mm/s. Final CGRs all dropped to ≤$1x10^{-9}$ mm/s. No clear correlation exists between constant K CGRs and the degree of IG engagement with the constant K CGR at 60% IG engagement remaining below $1x10^{-9}$ mm/s from the onset.

The ratio of the CGR in high temperature water to the estimated air CGR is presented in Figure 3-56. The dependency of the air fatigue formula on ∆K and R is identical to that used by ANL, but due to the wide scatter of the small amount of ANL air fatigue data at 360°C, the formula is normalized to produce an env/air ratio of ~1 at the relatively aggressive cyclic loading condition of 0.1 Hz where air fatigue response is expected to dominate in both air and water. Because the air values are simply estimates from a formula that has very little alloy 152 data to support it, not too much should be read into the values produced as a function of cyclic loading condition, however the env/air ratio does provide a means to compare response throughout a test for a particular loading condition. In concept, high env/air ratios are expected to correlate to a high degree of IG engagement and indicate the possibility of higher SCC growth rates when converting to constant K or load. In particular, the change in env/air ratio with the addition of a hold time may be an indicator of constant K CGRs.
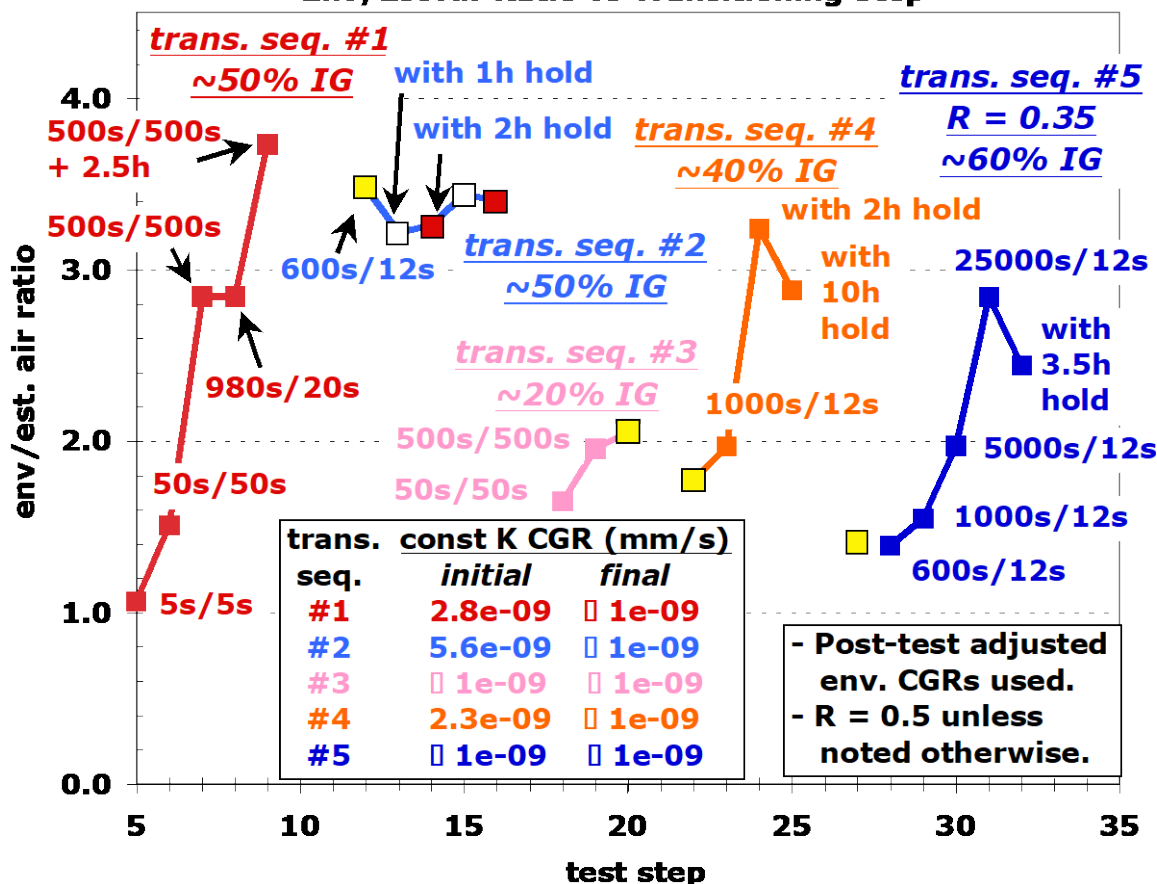
Figure 3-56 Ratio of CGR in High Temperature Water to Estimate Air Fatigue CGR for PNNL Test #1 on ANL Alloy 152v2 (CT049) Tested in 360°C Water

The transitioning approaches for the PNNL specimen CT049 can be roughly grouped into two categories. Transitioning sequences 1-4 attempt to produce IG engagement using minimum cycles of 500s/500s, 600s/12s, or 1000s/12s at R = 0.5 with the addition of hold times, while transitioning sequence #5 attempts to produce IG engagement through continuous cycling down to much lower frequencies (5000s/12s and 25000s/12s) but at a more aggressive R value of 0.35. As would be expected, the general trend during any one transitioning sequence is that lower cyclic loading frequencies where environmental effects are expected to play a bigger role in crack extension produced higher env/air ratios. The addition of a hold time was seen to either increase, decrease or have no effect on the env/air ratio. Peak env/air values remain at 3-4 throughout most of the test, but the env/air ratio for the 600s/12s cycle that was applied several times throughout the test continually decreases as the test progressed.

Transitioning sequences 1 and 2 where the addition of a hold time either increased or didn't lower the env/air ratio produced initial constant K CGRs that were in a higher category of 2-6x10^{-9} mm/s, and these sequences had approximately 50% IG engagement. Transitioning sequence #3 was applied after significant crack extension (~1 mm) at 0.01 Hz. The env/air ratios were ≤ 2 and a low initial constant K CGR along with low IG engagement were observed. Transitioning sequence #4 has relatively high final env/air ratios, but the addition of a hold lowered the env/air ratio slightly. This sequence produced initial constant K CGR in the higher

category of 2-6x10^{-9} mm/s and had ~40% IG engagement. Transitioning sequence #5 had a peak env/air ratio of ~3, but the ratio decreased with the addition of a hold time. Constant K CGR was ≤1x10^{-9} mm/s, but ~60% IG engagement was achieved.

An optical image of the crack surface (~8 mm of the width of the CT specimen, other 4 mm is used for crack profile exams) is shown in Figure 3-57. As indicated by the yellow lines mapped from variations in oxide appearance of the surface before it was sonicated, a relatively straight crack front was maintained throughout the test. Areas of higher IG engagement have a rougher appearance than TG regions. IG cracking is also responsible for the protrusions along the final crack front.
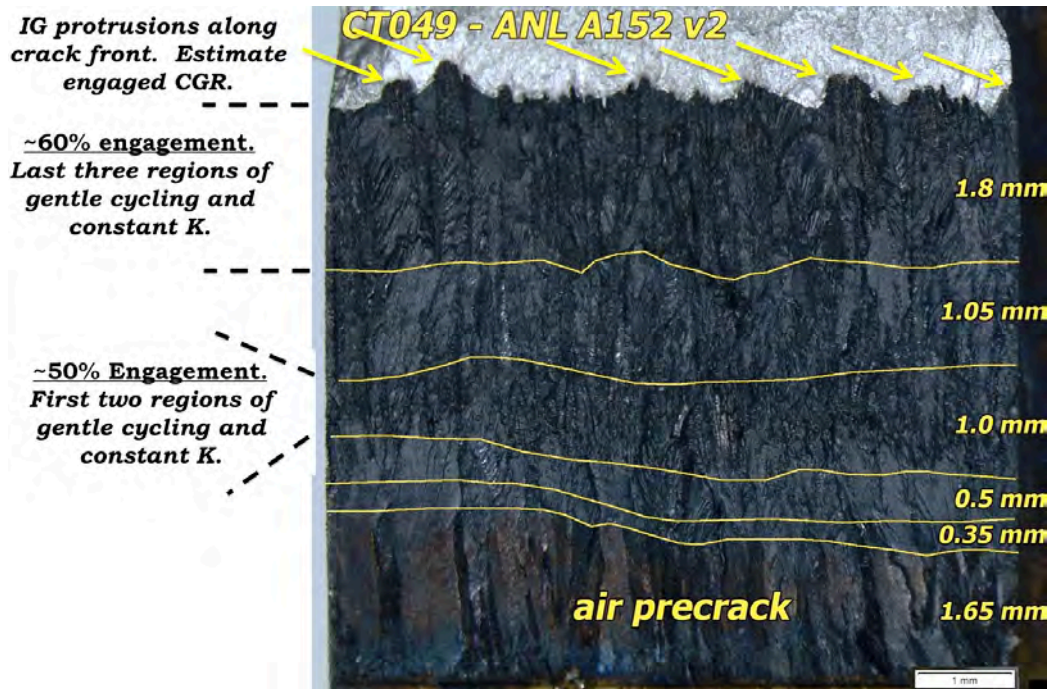
Figure 3-57   Optical Image of the Crack Surface from the First Test (CT049) by PNNL on ANL Alloy 152v2. Arrows Indicate Examples of Significant IG Protrusions Along the Final Crack Front

Detailed mapping of the IG/TG cracking morphology was performed using SEM montages (using both BSE and SE modes) across the width of the surface as shown earlier in Figure 3-45. A key aspect of the crack growth surface is very long sections of IG extension. This is made possible by having the geometric crack growth plane of the specimen well aligned to the long grain boundaries of the weld metal microstructure. IG extensions of this length (many mm) clearly indicate that certain grain boundaries are the preferred cracking path in this weld under a variety of cyclic loading conditions. An example would be the final ~1.5 mm of crack extension shown in Figure 3-45. This spans loading conditions ranging from constant K all the way down to 600s/12s at R = 0.5 and 1000s/12s at R = 0.35 showing that this weld will readily undergo IG cracking. However, these observations also show that despite "easy" cracking along certain grain boundaries, full IG engagement across the crack front is not achieved despite the application of a variety of gentle cycling conditions. This suggests grain shape and boundary orientation to the crack path play a significant role in IG propagation along with possible variation in grain boundary susceptibility.

Another challenge in assessing the SCC response of this material is determining what amount of crack advance occurred during constant K loading. DCPD clearly shows crack advance during cyclic and cycle + hold loading, but DCPD shows very little or no growth during constant K testing. The crack surface of this specimen reveals extensive IG cracking and localized IG protrusions at the final crack front. At this point in time PNNL has not found a method to isolate IG growth that occurs during constant K loading from that which occurs during cyclic or cycle + hold loading. It is intuitive to assume that IG protrusions mostly occur during constant K loading where fatigue advance is not happening, but it could simply be that during cyclic loading, IG cracks advance more readily along properly oriented grain IG boundaries than do TG portions of the crack front. Stress concentrations on the lagging TG portions of the crack may eventually limit how far the TG portions can lag behind the IG portions.

Comparisons of the various SCC "indicators" are summarized in Table 3-9. Transitioning sequences 1, 2 and 4 have the highest SCC indicators and also have initial constant K CGRs in the higher category. Transitioning sequence #3 has lower SCC indicators and a low initial constant K CGR. These sequences suggest a possible correlation between transitioning response, IG engagement and constant K CGR. However, transitioning sequence #5 does not have this consistency. The env/air values were reasonable and IG engagement is 60%, but the initial SCC CGR was below $1x10^{-9}$ mm/s and remains below that value. Post-test observation of the crack growth surface did not reveal any ligaments that could have affected the DCPD value.

Overall, while ≥50% IG engagement was achieved and encouraging env/air ratios were obtained during several of the transitioning sequences, initial constant K CGRs were no higher than $6x10^{-9}$ mm/s and always fell below $1x10^{-9}$ mm/s within 100 hours.

Table 3-9   Summary of CGR Indicators for the Test on CT049 at 360°C

Trans. Sequence	Peak Env/Air ratio for cont. cycling	Env/Air ratio with addition of hold time	% IG	Initial Const K CGR (mm/s)	Final Const K CGR (mm/s)
1	2.8	3.7	~50	$2.8x10^{-9}$	$≤1x10^{-9}$
2	3.5	3.4	~50	$5.6x10^{-9}$	$≤1x10^{-9}$
3	2.1	no hold time	~20	$≤1x10^{-9}$	$≤1x10^{-9}$
4	3.3	2.8	~40	$2.2x10^{-9}$	$≤1x10^{-9}$
5	2.8	2.4	~60	$≤1x10^{-9}$	$≤1x10^{-9}$

One other potential SCC indicator is the estimated CGR during the hold phase of cycle + hold loading steps. This is calculated by subtracting off the CGR that occurs during a pure cyclic loading condition with the same load cycle period and same R. Table 3-10 shows these results. Both positive and negative CGRs were obtained. The presence of both positive and negative values of the same order of magnitude suggest that on average, very little growth was occurring during the hold times, and this is consistent with CGRs measured during constant K assessments.

Table 3-10   Estimated CGR During the Hold Phase of Cycle + Hold Loading Conditions for CT049 Tested at PNNL

Trans. Seq.	Test Step	Load Cycle Period	Hold Time (s)	Total Period (s)	CGR (mm/s)	Estimated CGR During Hold (mm/s)
1	8	980s/20s	0	1000	3.2×10^{-7}	---
"	9	"	9000	10000	4.2×10^{-8}	1×10^{-8}
2		600s/12s	0	612	6.4×10^{-7}	---
"	12	"	3600	4212	8.6×10^{-8}	-8×10^{-9}
"	13	"	7200	7812	4.7×10^{-8}	-3×10^{-9}
"	14	"	3600	4212	9.2×10^{-8}	-1×10^{-9}
"	15	"	7200	7812	4.9×10^{-8}	-1×10^{-9}
"					*average:*	*-4×10^{-9}*
4	23	1000s/12s	0	1012	3.5×10^{-7}	---
"	24	"	7200	8212	7.1×10^{-8}	3×10^{-8}
"	25	"	36000	37012	1.4×10^{-8}	5×10^{-9}
"					*average:*	*2×10^{-8}*
5	31	25000s/12s	0	25012	4.9×10^{-8}	---
"	32	"	12600	37612	2.8×10^{-8}	-1.4×10^{-8}

GEG Test #1 (C541) on ANL Alloy 152v2 Weld

As part of the NRC-EPRI collaboration, GE Global Research (GEG) has provided to PNNL a full series of CGR plots and one half of the 0.5T CT specimen used by GEG for their first test (C541) on the ANL alloy 152v2 weld. Detailed exams of the crack growth surface have now been performed at PNNL enabling comparisons to the GEG measured crack growth response and to PNNL results.

An overview of the entire SCC test curve is shown in Figure 3-58. This test was conducted in 360°C primary water with an initial target K of 33 MPa√m, with three transitioning sequences and two constant K evaluations. The approach to this test was to evaluate the SCC response in three separated microstructural regions. Similar to the approach used by PNNL, in each transitioning sequence a different set of cyclic loading conditions were used to attempt to generate an SCC crack front prior to converting the test to constant K. Also shown in the plot is the estimated IG engagement as measured by PNNL from SEM and optical images (shown later in this section). Peak IG engagement was ~40% during transitioning prior to the first constant K assessment. This IG engagement was maintained during the first few steps of crack advance of the second transitioning sequence but fell off to ~30% IG by the start of the second constant K assessment. The third transitioning sequence appears to have forced the crack to predominantly TG fatigue, and IG cracking had increased only slightly prior to ending the test despite ~3000 hours of very gentle cycle + hold transitioning. However because of the very gentle cycling conditions and low CGRs, a total of only ~100 μm of material was covered during this final transitioning.
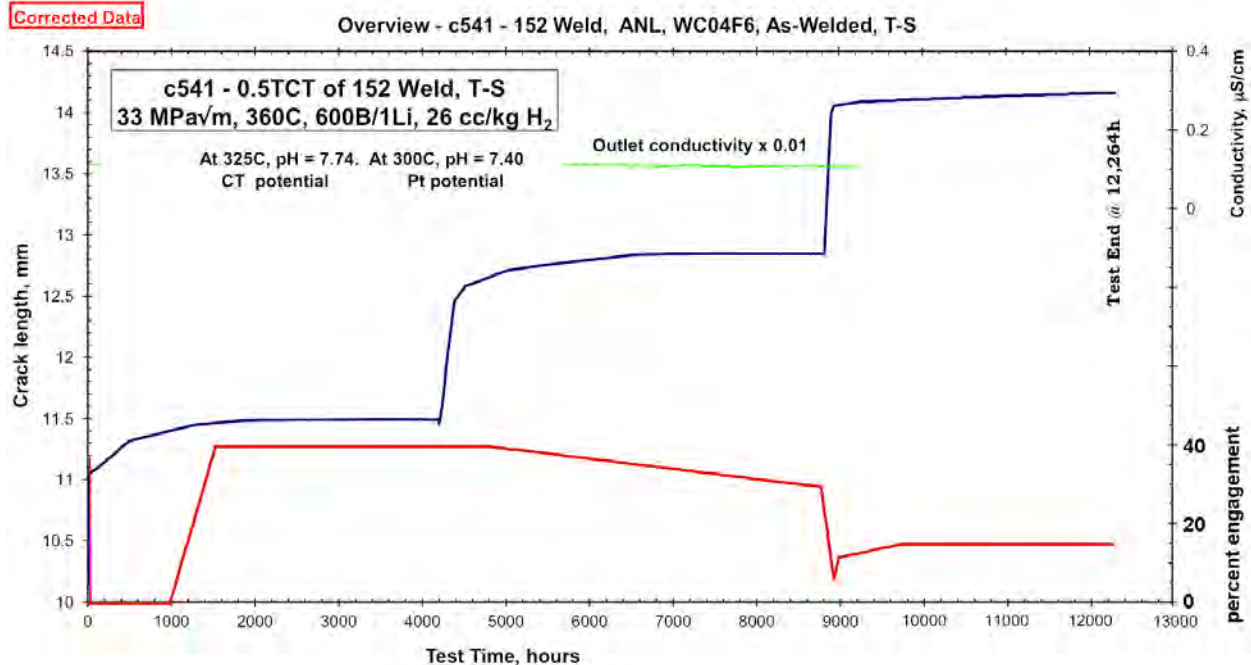
Figure 3-58   Overview of the Entire First Test (C541) by GEG on the ANL 152v2 Weldment Supplied by Peter Andresen. Percent IG Estimate Was Determined by PNNL

Figure 3-59 lists the cyclic loading conditions for all three transitioning sequences and plots the ratio of environment to estimated air response as a function of test step. Moderate env/air ratios (2.6-3.0) were achieved during the first transitioning sequence where the cyclic loading period was 1000 s with R=0.6. The second transitioning sequence started at R=0.4 produced an env/air ratio of 4.2. The remainder of this transitioning sequence utilized a 1000 s cycle but with R=0.5. The addition of increasingly longer hold times during the second transitioning sequence had no significant effect on the env/air ratio. Constant K assessment after these two transitioning sequences produced initial CGRs of no higher than 2×10^{-9} mm/s that fell off to $\leq1\times10^{-9}$ mm/s.

The third transitioning sequence utilized a base cyclic loading period of 475s/25s again at R=0.5. This produced an env/air ratio of 1 suggesting no environmental enhancement. Increasingly longer hold times were tacked onto this cycle to encourage IG engagement. The addition of the hold times had no effect on the env/air ratio. A constant K assessment was not performed after this transitioning sequence, but growth rates under cycle + hold loading were very low suggesting that constant K CGRs would also be very low.

Optical and SEM imaging performed at PNNL was used to document the GEG C541 crack growth surface and is summarized in the SEM secondary electron image shown in Figure 3-60. Note that a portion of the air precrack region is not shown in this figure. Blue lines indicate either the air precrack boundary or the final crack front produced in water, while yellow highlighted regions indicate areas of IG cracking. Two features of this crack growth surface worth noting are: 1) crack growth was somewhat uneven across the width of the crack with one side having a final length of ~3.9 mm and the other having a final length of ~3.0 mm, and 2) a

very long ligament reaching back to the air precrack boundary formed and remained intact through the entire test. Both of these features have the potential to diminish the accuracy of DCPD crack length measurement.
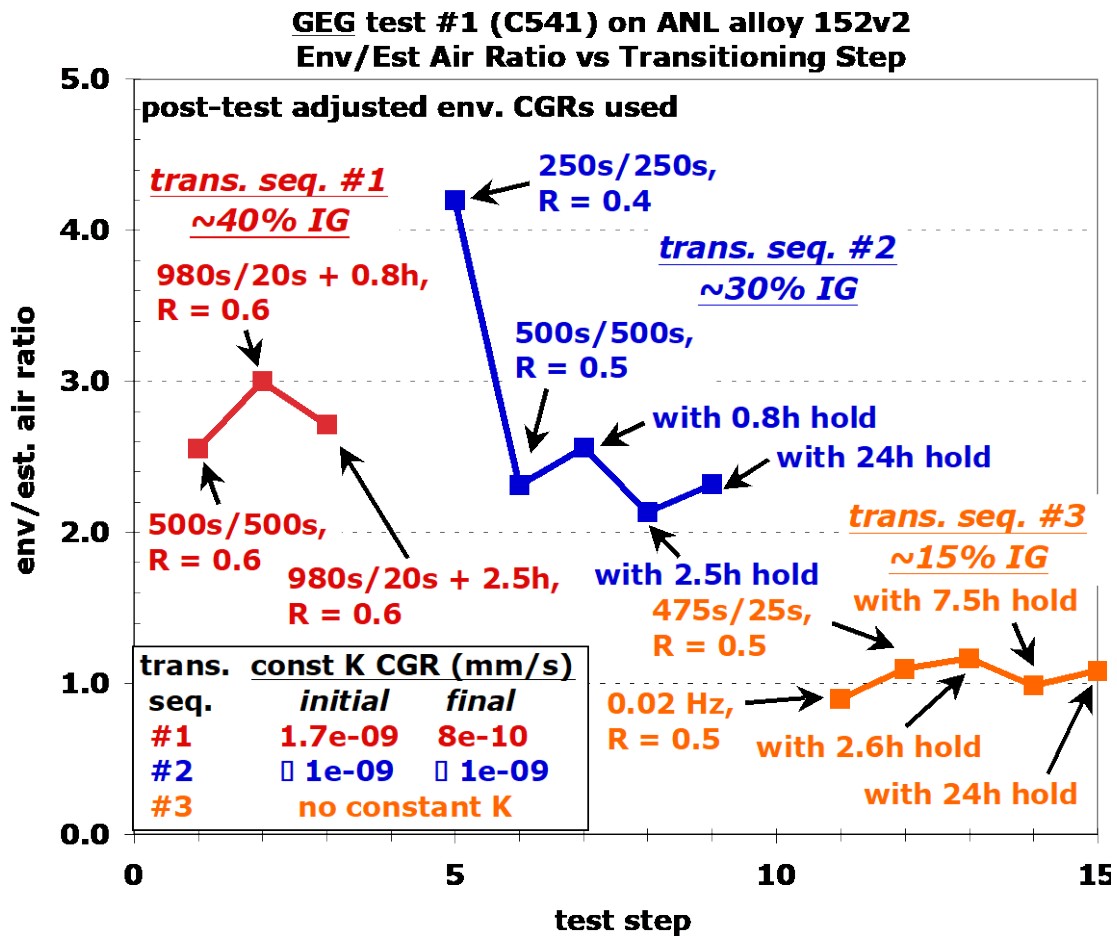
Figure 3-59 Ratio of Measured CGR in 360°C Simulated PWR Primary Water to Estimated Air Fatigue CGR for GEG Test C541 on ANL Alloy 152v2

A feature that stands out on this surface is that ~25% of the surface on the right side shows very little IG engagement throughout the test. This region is separated from the rest of the surface by the ligament mentioned above, and the difference in the degree of IG engagement between the two regions of the surface suggests there may have been some differences in the weld microstructural characteristics. Additional characterizations may be worthwhile to map weld characteristics across the weld in this specimen. Unless otherwise noted, the percentage of IG engagement will be quoted as relative to the entire width of the surface.

Focusing now on the left ~75% of the surface, the first ~0.5 mm of growth from the air precrack shows very little IG engagement. This corresponds to load cycling at 500s/500s with R = 0.6. Somewhat surprisingly, significant IG engagement of ~40% subsequently occurs very rapidly at distance of ~0.5 mm from the precrack. Due to the uncertainty in the correlation between DCPD crack length and actual crack length, two interpretations of the relationship between transitioning and IG engagement are possible. The first is that the step change in IG engagement corresponds to the onset of 980s/20s load cycling with either a 0.8 h or 2.5 h hold.

If this is the case, 40% IG engagement is then maintained during constant K and during the first steps of the second transitioning sequence that included load cycling at 250s/250s with R = 0.4 where the env/air value was 4.2. The IG engagement then diminishes slightly to ~30% by the start of the second constant K assessment.
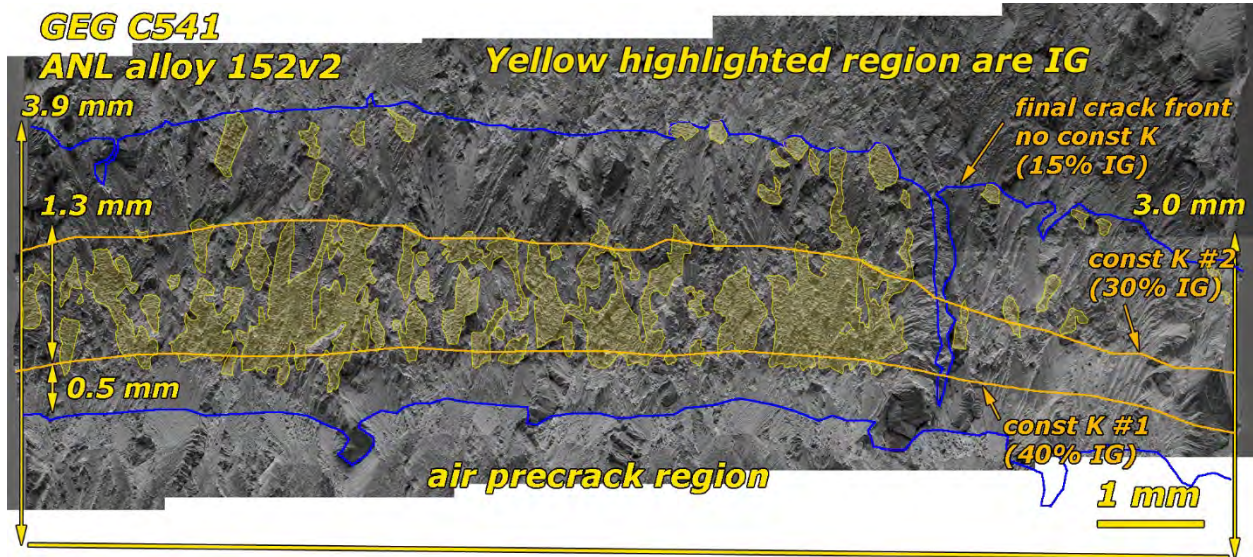
Figure 3-60   **SEM Secondary Image Obtained by PNNL of the GEG C541 Showing Various Features of the Crack Growth Surface**

The alternative interpretation of the IG engagement during the first and second transitioning sequences is that the step change in IG engagement took place at the start of second transitioning sequence at 250s/250s with R = 0.4 where the env/air ratio was 4.2. This interpretation has some compelling aspects in that 40% IG engagement occurs over a distance of roughly 1 mm consistent with the measured crack advance during this loading condition. The strong change in loading conditions also provides a palatable explanation for the step change in IG engagement. If this scenario is true, the first constant K measurement was conducted with 0% IG engagement, while the second would again be at ~30% IG engagement. Without clear evidence to point to one scenario or the other, it will be assumed that significant IG engagement occurred during the first transitioning sequence where gentle cycling is expected to produce IG cracking.

By the start of the second constant K assessment, IG cracking had diminished to ~30%. IG cracking is almost completely eliminated by the application of a 0.02 Hz cycle with R = 0.5 at the start of the third transitioning sequence. A small amount of IG engagement occurred in subsequent transitioning steps, reaching only ~5% by the end of the test. Table 3-11 summarizes the SCC indicators for this test. If IG cracking occurred during the final steps of the first transitioning sequence, then what is seen is that the env/air ratios are roughly consistent with the degree of IG cracking that occurred during cyclic loading. However, higher env/air ratios and higher degrees of IG engagement do not correlate to higher constant K CGRs.

One other SCC indicator that is reviewed here is the estimated CGR during the hold phase of cycle + hold loading steps. This is calculated by subtracting off the CGR that occurs during a pure cyclic loading condition with the same load cycle period and the same R. Table 3-12 shows these results. The positive and negative values reported here indicate that the CGR

during the hold is very low, and averaging the results together produces a CGR that is consistent with what GEG measured during constant K assessments.

Table 3-11   Summary of CGR Indicators for the First GEG Test (C541) on ANL 152v2 at 360°C

Trans. Seq.	% IG	Peak Env/Air Ratio for Continuous Cycling	Peak Env/Air Ratio with Addition of Hold Time	Initial Const K CGR (mm/s)	Final Const K CGR (mm/s)
1	~40	2.6	2.7	1.7×10^{-9}	$\leq 1 \times 10^{-9}$
2	~30	4.2	2.6	$\leq 1 \times 10^{-9}$	$\leq 1 \times 10^{-9}$
3	~15	1.1	1.1	no constant K	

Table 3-12   Estimated CGR During the Hold Phase of Cycle + Hold Loading Conditions of C541 Tested at GEG

Trans. Seq.	Test Step	Load Cycle Period	Hold Time (s)	Total Period (s)	CGR During Load Cycle (mm/s)	Estimated CGR During Hold (mm/s)
2	6	500s/500s	0	1000	2.6×10^{-7}	---
"	7	"	3000	4000	7.2×10^{-8}	9×10^{-9}
"	8	"	9000	10000	2.4×10^{-8}	-2×10^{-9}
"	9	"	85900	86900	3.0×10^{-9}	~0
"					*average:*	*2×10^{-9}*
3	12	475s/25s	0	500	4.9×10^{-7}	---
"	13	"	9500	10000	2.6×10^{-8}	2×10^{-9}
"	14	"	27000	27500	8.0×10^{-9}	-1×10^{-9}
"	15	"	85900	86400	2.8×10^{-9}	-4×10^{-11}
"					*average:*	*0.3×10^{-9}*

ANL Test #1 (N152-TS-1) on ANL Alloy 152v2 Weld

The measured CGRs, %IG engagement values and crack growth surface images for the N152-TS-1 specimen (1T CT as shown in Figure 3-61) were obtained from ANL reports. One feature of this specimen worth noting is that the geometric crack plane of the specimen is roughly at a 10-15 degree angle to the long grain boundaries in weldment. The post-test crack growth path indicated by the crack profile on the right half of the specimen in Figure 3-61(b) shows that not unexpectedly, cracking does go off the geometric crack plane in an attempt to follow the long grain boundaries.

Figure 3-61   1T CT Specimen That ANL Used for Their Test (N152-TS-1) on the ANL 152v2 Weldment

An overview crack growth plot of the entire test is not available to present here. The test can be broken up into four transitioning sequences with three taking place at 26-30 MPa√m and the fourth taking place at 46 MPa√m. An env/air vs test step plot was constructed based on the reported ANL data as shown in Figure 3-62. This plot serves to show the step-by-step response of the specimen from an env/air perspective. Transitioning appears to have been performed primarily with a 600s/12s waveform sometimes with a 1 or 2 h hold. Periodic partial unloading with a hold time of either 1 or 2 h was also used frequently during the testing. The env/air values hovered between 0 and 3 for all but two steps where values of 10.2 and 4.0 were observed for transitioning sequences #2 and #3b. Constant load SCC assessments immediately after these high env/air values produced initial rates of ~2-4x10^{-8} mm/s, but did not produce sustained high CGRs. In particular, the constant load response after the env/air value of 10.2 during transitioning quickly dropped from ~4x10^{-8} mm/s to $\leq$1x10^{-9} mm/s. The two highest sustained constant load CGRs (~2.0x10^{-8} mm/s) were obtained immediately after transitioning sequences #3a and #4 with low env/air values ($\leq$2).

ANL's optical image of the N152-TS-1 crack growth surface is shown in Figure 3-63 with their three SEM images overlaid by PNNL to show the regions of the detailed IG analysis (performed by ANL). Arrows on the sides of the optical image show the location of constant load assessment as taken from an ANL crack growth summary table. The contrast on the SEM images was inverted to allow easier determination of the position of these SEM images on the optical image. Yellow highlighted regions represent PNNL's attempt to determine the areas of IG engagement. This was guided by lines that ANL drew onto the SEM images to indicate regions of IG engagement. However, these lines were only drawn on two of the three SEM images, so it was necessary to estimate IG engagement on the third image (SEM image on the left). During the exams, it was noted that much of the IG cracking appeared to be piece-meal as if the crack was alternately growing through grains and then on grain boundaries as it traversed the microstructure. This is likely due to the inclined angle of the specimen relative to the grain boundary microstructure. It was extremely difficult to independently assess the %IG engagement and IG morphology from these images. Higher resolution SEM-SE and -BSE images covering this region as done for the PNNL and GEG crack growth surfaces are needed to enable accurate and consistent determination of the %IG engagement comparable to what is shown for CT049 (PNNL) and C541 (GE) in this report.
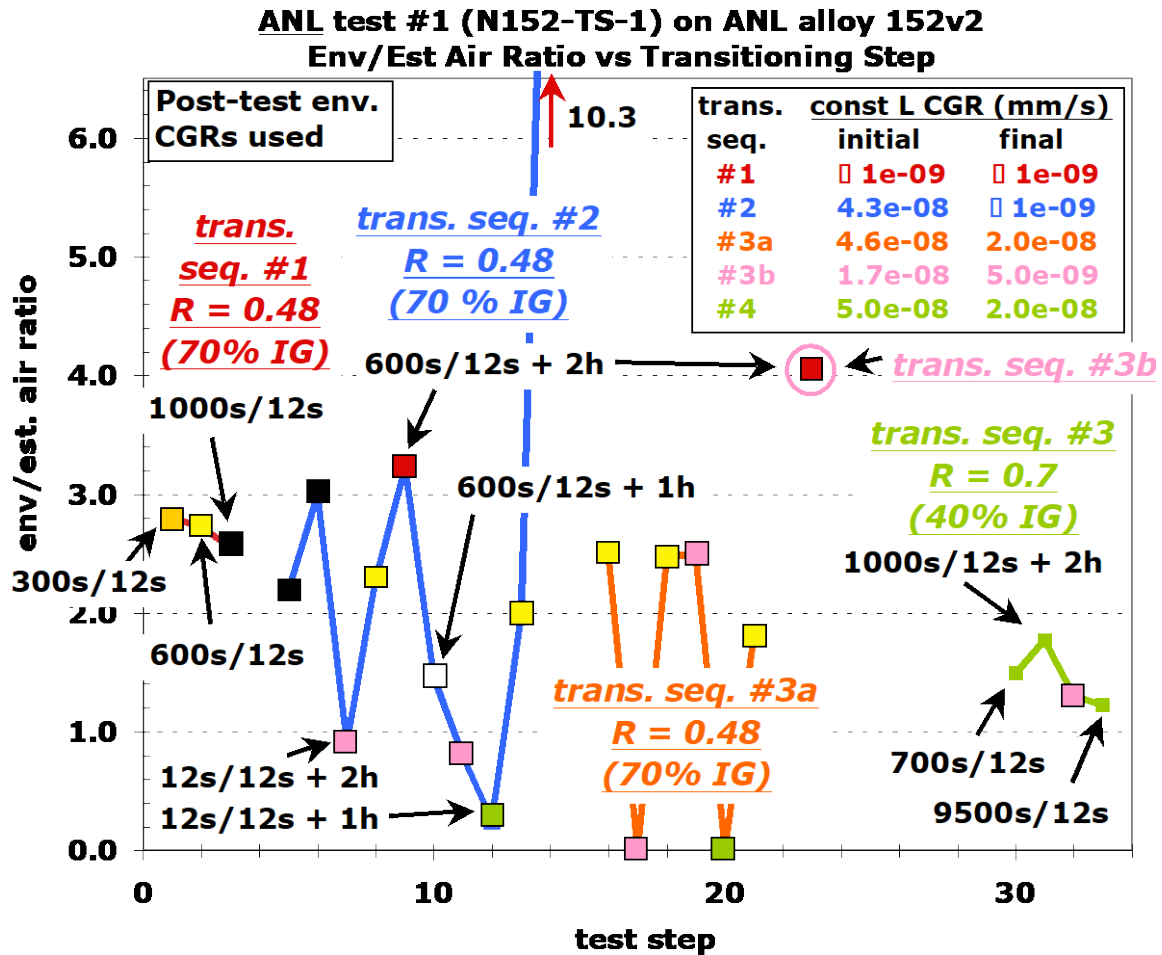
Figure 3-62   Ratio of CGR in High Temperature Water to Estimate Air Fatigue CGR for ANL Test on ANL Alloy 152v2 (N152-TS-1) Tested in 320°C Water

The red line in Figure 3-63 indicates ANL's method for determining the degree of IG engagement. In essence, a band across the surface is considered, and any IG that is found within that band adds to the fraction of IG engagement across the width of the specimen. ANL reports that 70% IG engagement was observed in the area covering the first four constant load assessments. The PNNL approach is somewhat different, the fraction of IG engagement is considered by drawing a line that is believed to best represent the crack front location at the time of the SCC assessment at constant load and then add up the fraction of the line length that intersects regions of IG growth. The blue line in the image represents PNNL's attempt at defining the crack front at the time of the third constant load assessment where a CGR of 2×10^{-8} mm/s was measured by ANL. IG engagement is measured to be <50%. This may be due, in part, to inaccuracies in locating regions of IG growth, but it is also due to the difference in the methods for calculating IG engagement. ANL's reported values for the %IG engagement (~70% early and ~40% at the end of the test) are used for comparison to the PNNL and GEG tests.
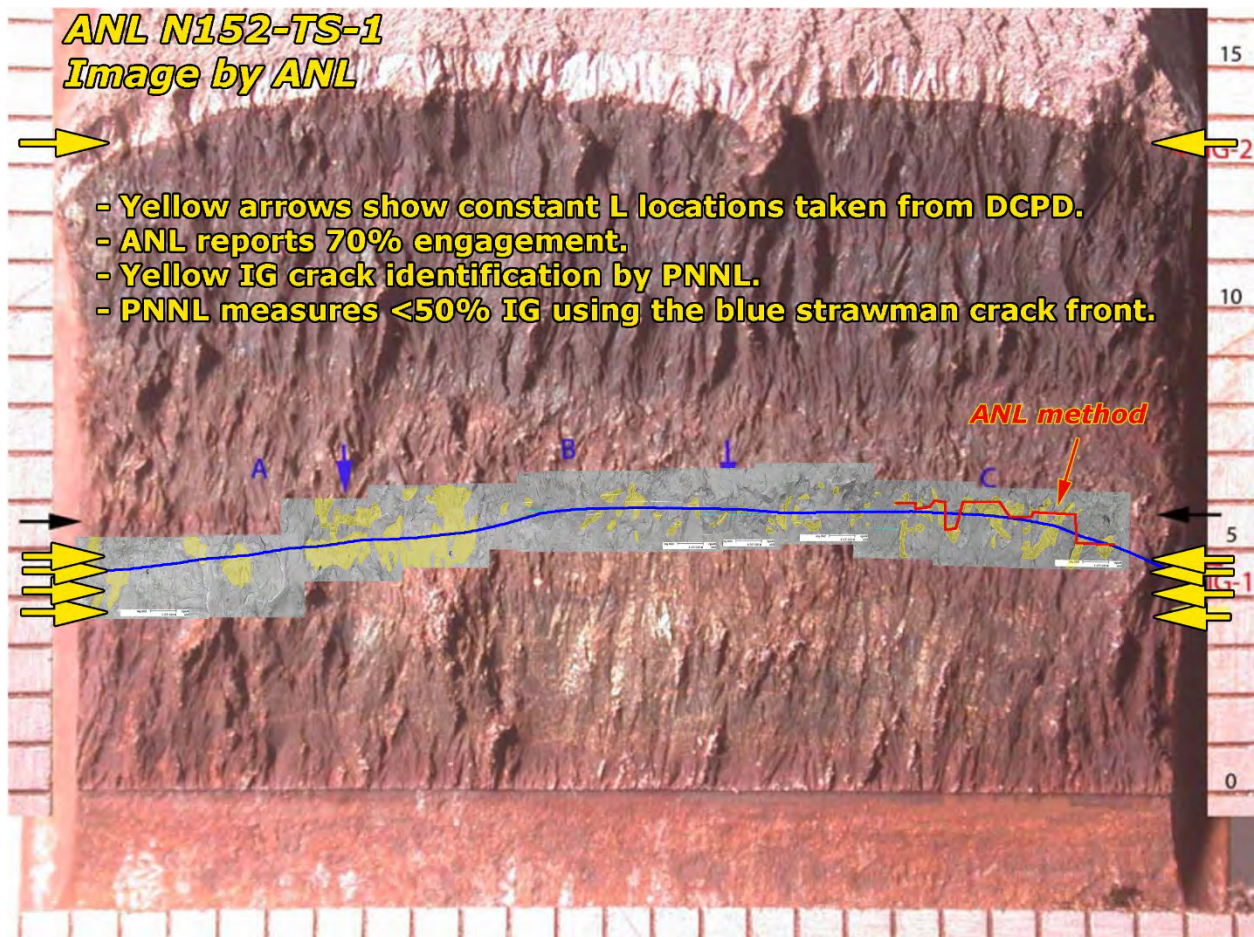
Figure 3-63   ANL Optical Image of the Crack Growth Surface of N152-TS-1. ANL's SEM Images Are Overlaid onto the Surface to Show Locations of IG Cracking Relative to the Entire Crack Surface and Indicated Crack Lengths at Constant Load

Table 3-13 summarizes the available SCC indicators for ANL's test on the alloy 152v2 material. The first four constant load assessments took place over ~0.5 mm of crack extension. The low CGRs obtained during the first two assessments are attributed by ANL as being due to the presence of a ligament that was either holding up crack advance or masking DCPD response. The sustained constant load CGR of 2.0×10^{-8} mm/s after transitioning sequence 3b was obtained over a period of ~1400 h and a DCPD indicated crack advance of ~100 µm. This assessment was ended by a 3-h power outage. Re-transitioning with a cycle + hold and converting back to constant load produced only a 5×10^{-9} mm/s CGR. Thus, a wide range of response was observed over a region that is reported to have 70% IG engagement. The K level was then increased to ~46 MPa√m while advancing the crack ~8 mm. Final transitioning took place through a series of continuous cycling steps with the final step being a 9500s/12s cycle at R = 0.3. Despite the low SCC indicators, a constant load CGR of 2.0×10^{-8} mm/s was obtained albeit the exposure time was limited to ~350 h.

Table 3-13   Summary of CGR Indicators for the First ANL Test (N152-TS-1) on ANL 152v2 at 320°C

Transitioning Sequence	Peak Env/Air ratio for continuous cycling	Env/Air ratio with addition of hold time	% IG	Initial Const K CGR (mm/s)	Final Const K CGR (mm/s)
1	2.8	no hold time	70	≤1x10^{-9}	≤1x10^{-9}
2	3.0	10.3	70	4.3x10^{-8}	≤1x10^{-9}
3a	2.6	2.6	70	4.6x10^{-8}	2.0x10^{-8}
3b	no cont. cycle	4.0	70	1.7x10^{-8}	5.0x10^{-9}
4	1.5	1.8	40	5.0x10^{-8}	2.0x10^{-8}

The last item to be covered is the estimated CGRs during hold times as shown in Table 3-14. Only two instances are present in ANL's testing where the CGR during a hold can be calculated. In one instance during the second sequence, a slightly negative CGR is calculated, while the second instance produced positive a CGR during a hold of 5x10^{-8} mm/s. This corresponds to the transitioning step that produced an env/air value of 10.3 and was followed by a low CGR at constant load.

Table 3-14   Estimated CGR During the Hold Phase of Cycle + Hold Loading Conditions of N152-TS-1 Tested at ANL

Trans. Seq.	Test Step	Load Cycle Period	Hold Time (s)	Total Period (s)	CGR During Load Cycle (mm/s)	Estimated CGR During Hold (mm/s)
2	6	600s/12s	0	612	2.6x10^{-7}	---
"	7	"	7200	7812	7.2x10^{-8}	4x10^{-9}
"	8	"	3600	4212	2.4x10^{-8}	-1x10^{-8}
"					*average:*	*-3x10^{-9}*
2	13	600s/12s	0	612	1.2x10^{-7}	---
"	14	"	7200	7812	5.2x10^{-8}	5x10^{-8}

Comparison of Results from PNNL, GEG, and ANL

Selected analyses have been performed on SCC growth rate test results for the same ANL alloy 152v2 weld tested at PNNL, GEG and ANL. It is important to note that no specimen is identical to another due to variations within a weld and how a specimen is aligned to the weld metal microstructure. Each lab has used some unique approaches in their attempt to generate sustained SCC propagation under constant K or load conditions. We believe some trends are apparent from the measured material response and the various analyses of SCC indicators.

Material Response

- IG engagement versus load cycling conditions: this weld will readily undergo IG cracking during continuous cycling under what could be considered mildly aggressive loading conditions with reasonable high growth rates (>10^{-7} mm/s). Example conditions

are 600s/12s with R=0.5, 1000s/12s with R=0.35, and 475s/25s with R=0.4. In addition, some of the highest degrees of IG engagement have been observed at the most aggressive R values, e.g. 0.4 and 0.35.

- Significant amounts of IG extension can occur without full engagement. Tests at PNNL and GEG show that 40-60% engagement can take place over fairly short distances and then persist at that level for as much as ~1.5 mm of crack extension without a further increase in IG engagement.

- High degrees of IG engagement do not consistently produce high DCPD-measured CGRs. The two highest sustained CGRs during testing at ANL were produced in regions of claimed 70% and 40% IG cracking. Testing at ANL in the same region of claimed 70% IG cracking more frequently produced constant load CGRs of ≤5x10-9 mm/s. Tests at PNNL with 50-60% IG engagement and at GEG with 40% IG engagement did not produce any sustained DCPD-measured propagation at constant K.

- There is nothing on the crack growth surface to clearly separate IG growth during constant K or load from IG growth during the prior transitioning steps.

The analysis of ANL's crack growth surface suggests a different cracking morphology. Whereas large amounts of IG crack extension were observed on the PNNL and GEG crack growth surfaces, much of the IG cracking that could be determined on the ANL crack growth surface was more piecemeal. The IG regions also tended to appear to be inclined to the crack growth surface. This suggests that the inclined orientation of the specimens produced interspersed TG and IG growth as the crack would alternately grow through a grain and then on grain boundaries.

In-Test SCC Indicators

- Cyclic CGRs from all three laboratories typically produced env/air ratios of 2-3. Several instances of higher values or lower values were not a consistent predictor of high or low constant K/load CGRs. The transitioning sequences that produced the two highest sustained CGRs at ANL had env/air ratios below 2.

- CGRs calculated from the hold phase of cycle + hold loading steps tended to have a high degree of scatter with negative values often being produced. Averaging several sequences together tended to produce a CGR that was generally consistent with the constant K response of the material but was not necessarily a representative value, i.e., -5x10-9 mm/s to +5x10-9 mm/s seemed to be representative of the average CGRs calculated from hold times where subsequent constant K or load assessments produced CGRs of ≤1x10-9 mm/s.

- Env/air ratios during cycling do seem to scale with the degree of IG engagement. There is some scatter in the trend, but a general trend does exist of higher degrees of IG engagement being found during portions of tests where higher env/air ratios are observed. Since it appears that all the IG engagement takes place during cyclic loading steps, this result perhaps should not be unexpected.

Conclusions from Analysis of Multi-Lab Tests on the ANL Alloy 152v2 Weld

SCC indicators as provided by ANL on their test on this material do not stand out in any way from those observed during tests at PNNL and GEG. However, PNNL's examination of the ANL crack growth surface indicates a more piecemeal IG cracking morphology and indicates a lower estimated degree of IG engagement than reported by ANL. The lower degree of observed IG engagement is due in part to the method used to calculate the fraction of IG engagement. A better understanding of ANL's result might be obtained if a more detailed SEM exam could be performed on the crack growth surface.

3.2   Alloy 52/52/52MSS Welds

3.2.1   Areva 52 Butt Weld and MHI 52 U Groove Weld

For the MHI alloy 52 weld, alloy 152 (heat 307380) was buttered onto the U-groove surface by SMAW, while alloy 52 (heat NX2686JK) was used as the filler and applied by gas tungsten arc welding (GTAW). Welding parameters for the MHI alloy 52 GTAW consisted of a deposition speed of 4-10 cm/min and a current of 150-300 amps. Welding parameters for the AREVA alloy 52 butt weld were not provided.

3.2.2   Alloy 52 Weld Samples (CT024, CT025, CT032 and CT033)

Duplicate tests have been performed on two alloy 52 welds, one made by AREVA (CT024 and CT032) and the other made by MHI (CT025 and CT033). Orientations of these specimens relative to the welds are shown in Figure 3-64. Before machining specimens, the blanks were etched to allow viewing the weld morphology, and a desired crack growth path through specific weld passes was determined. Specimens were again machined from the blanks to target the desired crack growth path, for example, as shown in Figure 3-64.

Two tests were performed with an AREVA alloy 52 sample paired with an MHI alloy 52 sample in both tests. An overview of the first test is shown in Figure 3-65 with CT024 being the AREVA material and CT025 being the MHI material. The test can be separated into three main phases. The first two phases evaluated crack growth response during transitioning and constant K at 350°C on two different regions in the specimens, while the third phase of the test examined the 350°C constant K crack growth response after extending the crack by cyclic loading at 50°C. This unusual transitioning method was based on the high degree of IG engagement observed in the MHI alloy 152 specimens during cyclic loading at 50°C (section 3.1.1).
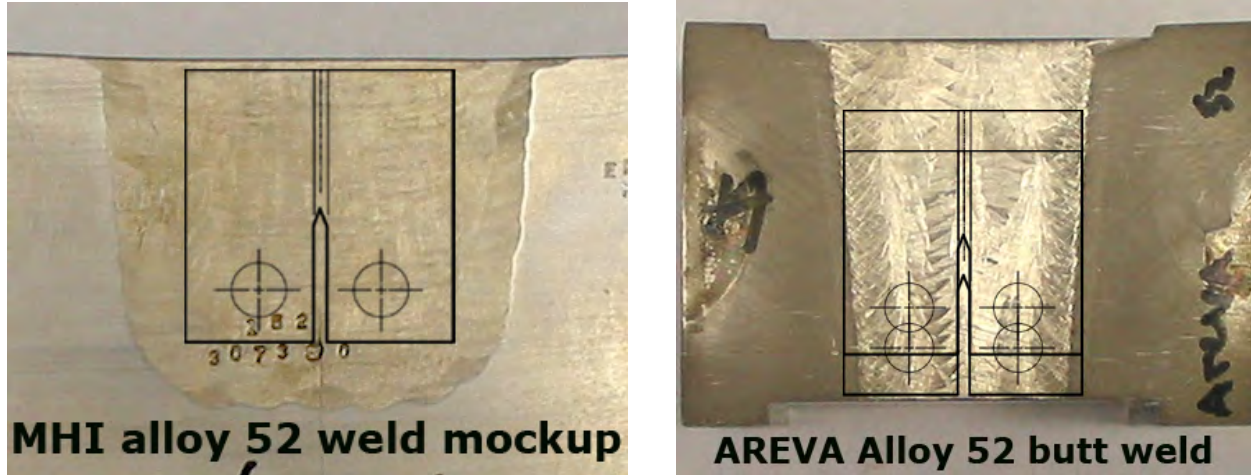
Figure 3-64 Image of the MHI Alloy 52 and AREVA Alloy 52 Welds Showing Positioning of the 0.5T CT Specimens
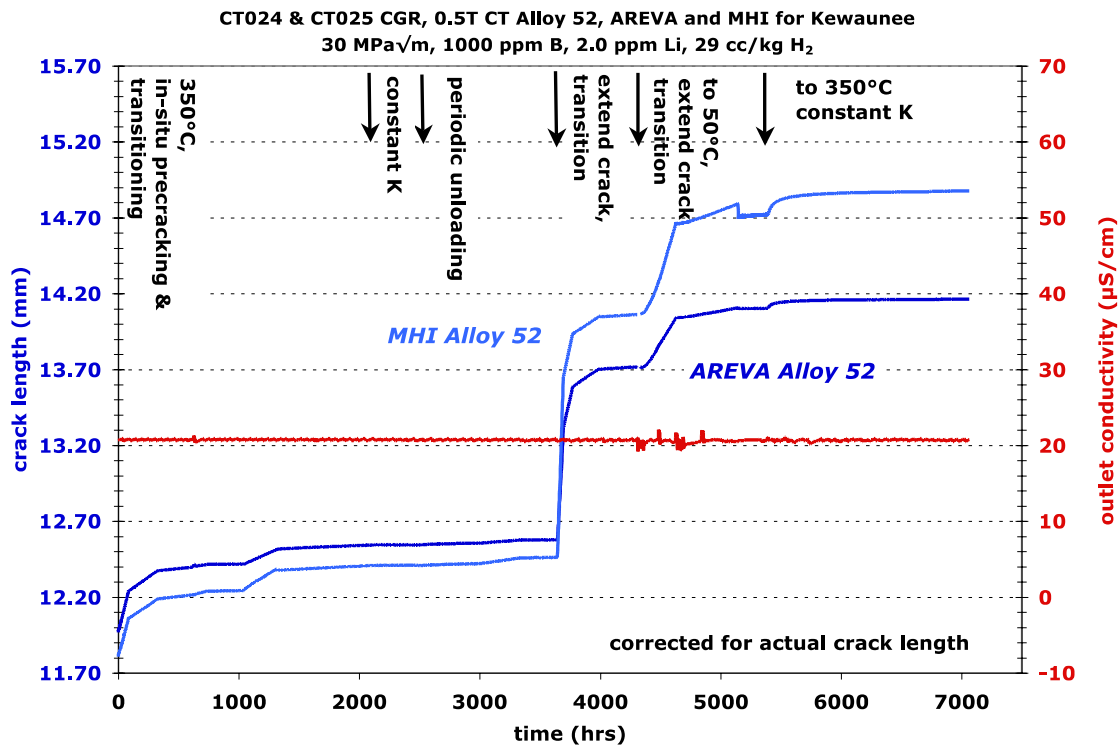
Figure 3-65 Overview of the Crack Growth Response of Two Alloy 52 Welds, One Made by AREVA (CT024) and One Made by MHI (CT025)

In the first region that was evaluated, CGRs during cycle + hold loading with R=0.7 were found to be a factor of 2-5X lower than transitioning CGRs in the MHI alloy 152 specimens from previous tests. Additional transitioning steps were applied using an R=0.5 and CGRs increased, however propagation rates in the alloy 52 specimens remained a factor of ~2X lower than for the alloy 152 specimens under equivalent gentle load cycling. Cycle + hold and constant K response was then determined as presented in Figure 3-66. The CGR during the extended time at cycle + hold loading was very linear with no suggestion of any change in the

degree of engagement. At approximately 2130 h, the loading conditions were set to constant K and no crack advance was measured over a period of approximately 500 hours. Transitioning was reinitiated using a series of different hold times and periodic unloading steps, but none gave any indication of an increase in engagement, and it was decided to advance the crack in the specimens to a new region. Using moderate cyclic loading conditions, the crack in each specimen was advanced over 0.5 mm, and transitioning was initiated using symmetric waveforms with R = 0.5. Propagation rates during subsequent cycle + hold conditions were found to be only slightly higher (40% higher with rates of ~1.4×10^{-8} mm/s) than the rates observed in the previous region suggesting that constant K CGR for the specimens would again be well below 1×10^{-9} mm/s.

For the final phase of the test, transitioning at 50°C was performed. In an attempt to generate an engaged IG crack front in the alloy 52 specimens, it was decided to perform similar cycling at 50°C in PWR primary water as was done for the alloy 152 specimens where extensive IG cracking was observed. The crack growth response of the alloy 52 specimens at 350°C is shown in Figure 3-65.
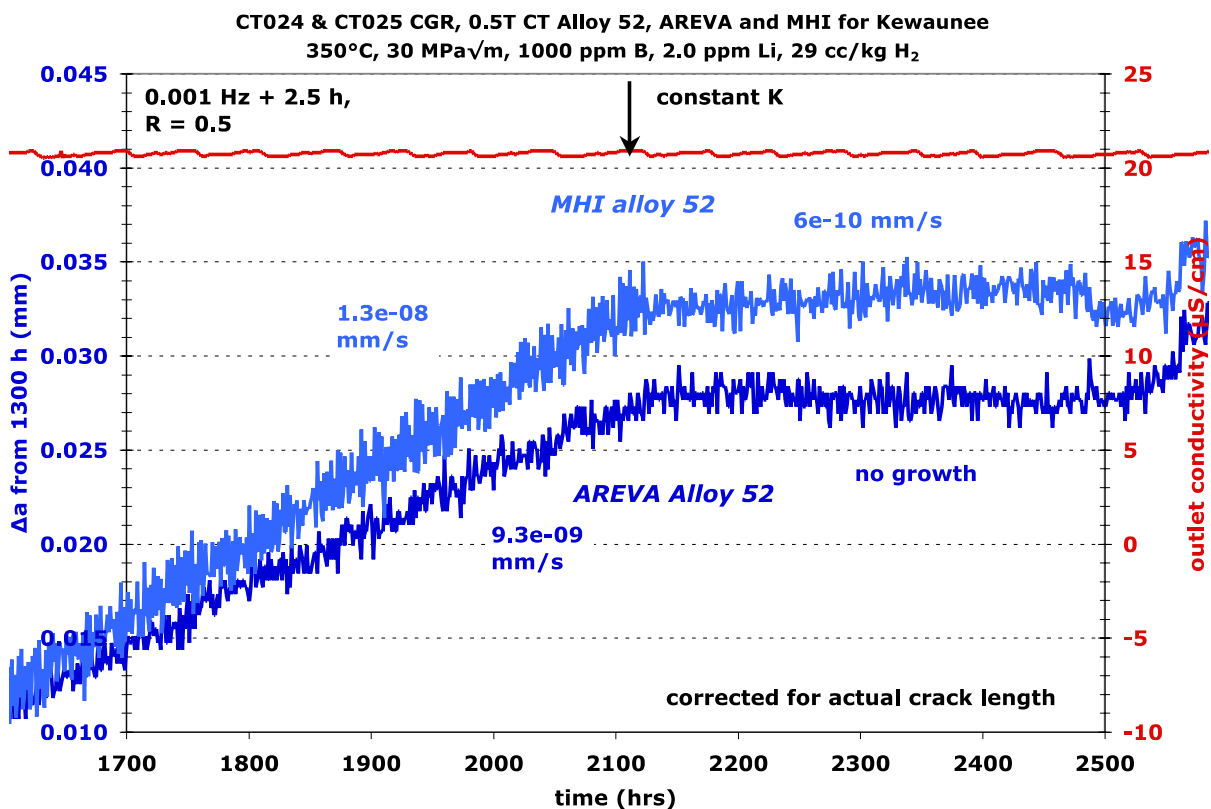
Figure 3-66   Cycle + Hold and Constant K Response of the AREVA and MHI Alloy 52 Specimens (CT024 & CT025) in the Second Phase of Each Specimen That Was Examined

While an increase in propagation rate with time during 0.001 Hz step is suggestive of an improvement in engagement, the CGR in each of the three cyclic loading steps was consistently lower than the rates observed at 350°C and much lower than measured for the alloy 152 specimens under equivalent cycling conditions. After ~1000 hours of crack extension at 50°C, the loading was converted to constant K, and the test temperature was brought back up to

350°C. DCPD fluctuations were allowed to settle out for 24 h before crack length measurements were resumed. The resulting crack length with time response at 350°C is shown in Figure 3-68. As can be seen, very high initial CGRs in excess of 1×10^{-7} mm/s were observed. Over the next 1400 hours (2 months), the propagation rates slowly decreased reaching levels below 1×10^{-9} mm/s similar to earlier high-temperature constant K response for these specimens. The high initial DCPD-measured growth rates is possibly due to the disruption of conducting bridges across the cracks formed at low temperatures and during the temperature increase to 350°C. As noted previously, electrochemical conditions are very Ni-metal stable at 50°C and move closer to the Ni/NiO potential as the temperature is increased to 350°C. The increase in DCPD-measured crack length may be due to oxidation or creep-induced fracture of these bridges in the crack at high temperature. It was not possible to separate this process from actual propagation, but it appears likely that the final constant K rates after 2 months are more representative of SCC growth rates. A summary of test conditions and corrected specimen response for each phase of the test is shown in Table 3-15.
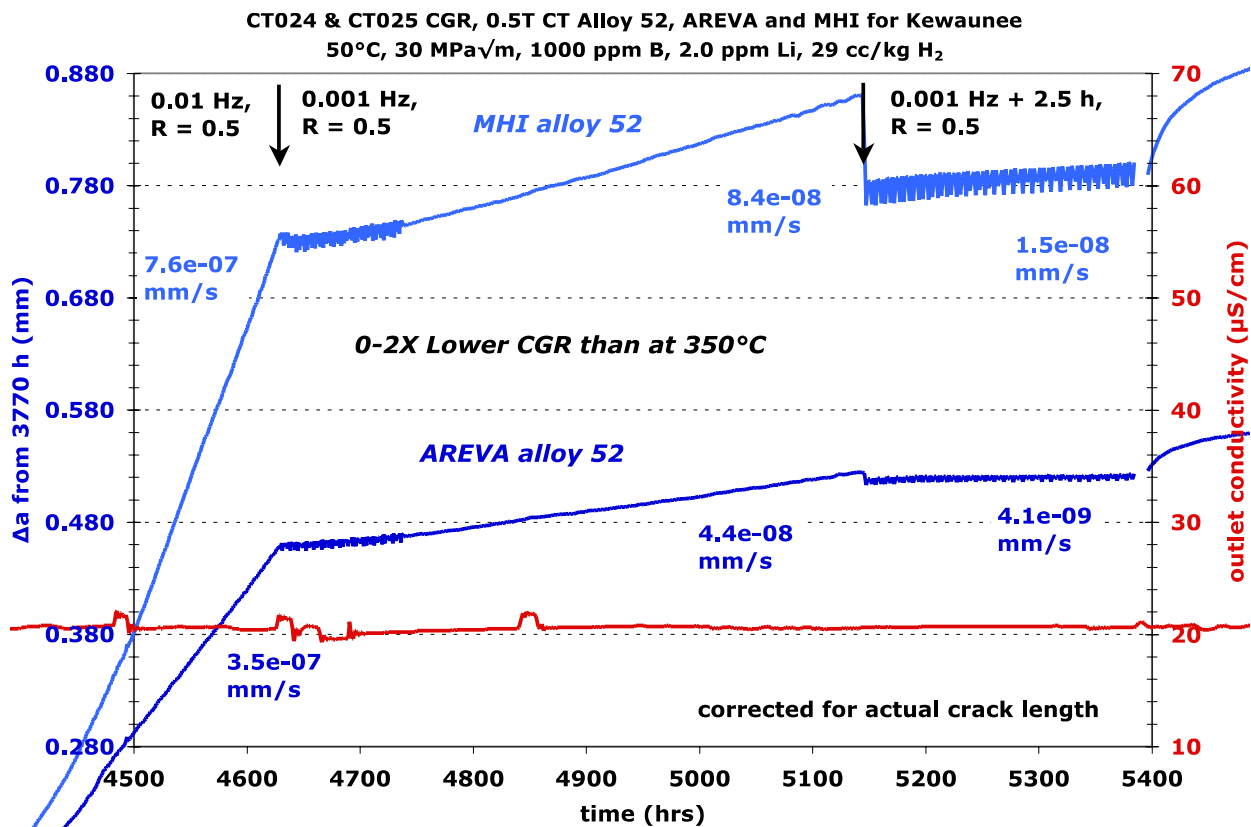
Figure 3-67   Overview of the Crack Growth Response of the AREVA and MHI Alloy 52 Specimens (CT024 & CT025) During Cyclic Loading Conditions at 50°C
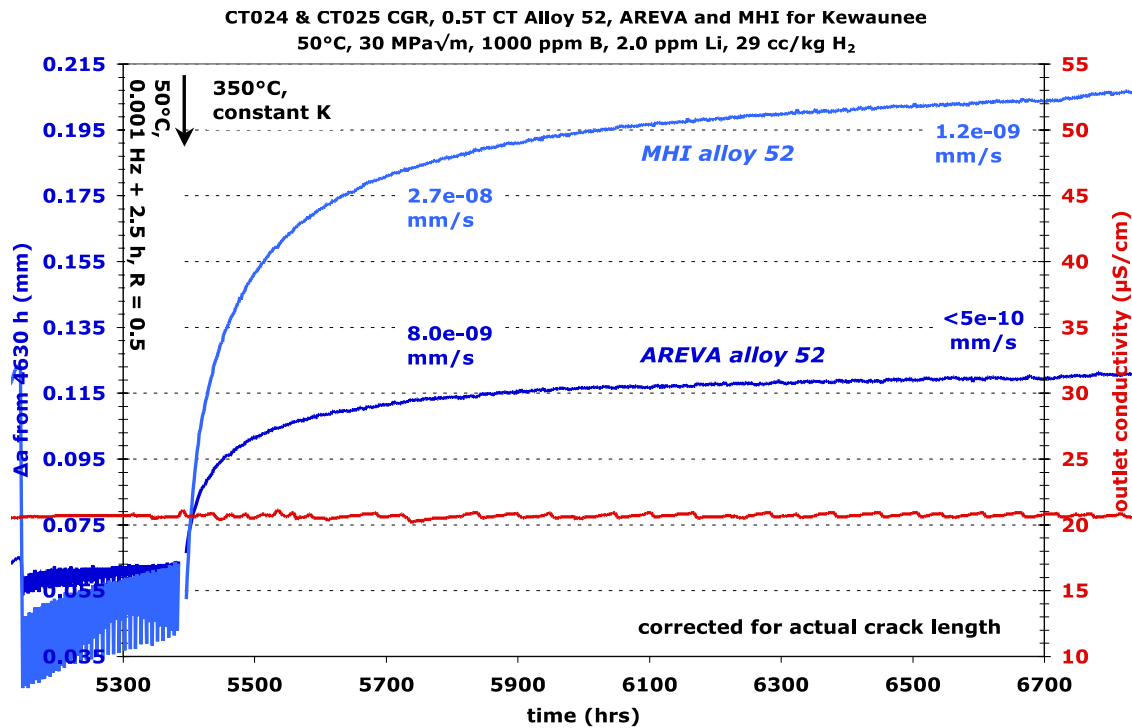
Figure 3-68   Constant K Crack Growth Response of the MHI and AREVA Alloy 52 Specimens (CT024 & CT025) at 350°C After Cyclic Loading Crack Extension at 50°C

The test was ended and the specimens were fatigued open in air to document the crack growth surfaces. Optical images of the crack growth surfaces for the AREVA and MHI alloy 52 specimens are shown in Figures 3-69 and 3-70, respectively. Several distinct bands are apparent on the surface, and are labeled as A through D in Figure 3-69. Band A corresponds to the transitioning and constant K testing in the first region that was examined. Band B corresponds to rapid crack extension performed to move the crack front forward to the next microstructural region of crack-growth testing while band C corresponds to the transitioning steps in this region. Finally, band D corresponds to crack extension at 50°C and during the subsequent constant K phase at 350°C. SEM examination determined that the crack-growth surface of the AREVA alloy 52 specimen was TG except for two small protrusions of IG growth within the yellow boxed region. An SEM example of this IG morphology is presented in Figure 3-71(left). This IG growth appears to have been initiated and propagated during 50°C cycling with no significant IG cracking produced during prior testing at 350°C. A higher fraction of IG cracking was discovered for the MHI alloy 52 specimen as indicated by the yellow-boxed regions in Figure 3-70. Whereas the AREVA alloy 52 specimen was less than 5% IG at the final crack front, the MHI alloy 52 specimen was ~35% IG. The cracking morphology in one of these IG regions for the MHI sample is documented in Figure 3-71(right) and again appears to have initiated and propagated during 50°C cycling.

3-65

Table 3-15   Summary of Test Conditions and Corrected Response for AREVA and MHI Alloy 52 Specimens CT024 & CT025

Test Phase	Dur-ation (h)	R	Freq (Hz)	Hold (h)	Water Chemistry Conditions	Temp (°C)	CT024 AREVA Alloy 52 Butt Weld Blank #1			CT025 MHI Alloy 52 U-groove Weld Blank #1		
							K_{max} (MPa√m)	CGR (mm/sec)	Approx. Crack Extension (mm)	K_{max} (MPa√m)	CGR (mm/sec)	Approx. Crack Extension (mm)
1	~3	0.3	3	0	air precrack	RT	25	1.2E-04	0.40	25	7.6E-05	0.40
2	~2	0.5	3	0	air precrack	RT	28	7.6E-05	0.35	28	4.6E-05	0.35
3	~2	0.6	3	0	air precrack	RT	31	5.1E-05	0.35	30	3.1E-05	0.35
4	~3	0.7	3	0	air precrack	RT	31	2.1E-05	0.20	30	1.5E-05	0.20
5	88	0.7	0.1	0	29 cc/kg H_2	325	31	8.0E-07	0.257	30	7.5E-07	0.235
6	237	0.7	0.01	0	29 cc/kg H_2	325	31	1.6E-07	0.133	30	1.5E-07	0.128
7	323	0.7	0.001	0	29 cc/kg H_2	325	31	2.2E-08	0.031	31	2.2E-08	0.033
8	82	0.7	0.001	0	29 cc/kg H_2	350	31	3.1E-08	0.011	31	5.3E-08	0.016
9	314	0.7	0.001	2.5	29 cc/kg H_2	350	31	1.4E-09	0.004	31	5.7E-09	0.015
10	272	0.5	0.001	0	29 cc/kg H_2	350	31	1.0E-07	0.098	31	1.5E-07	0.126
11	806	0.5	0.001	2.5	29 cc/kg H_2	350	31	1.2E-08	0.024	31	1.0E-08	0.028
12	365	---	const K	---	29 cc/kg H_2	350	31	no growth	---	31	9E-10	0.002
13	500	0.5	0.04	2.5	29 cc/kg H_2	350	31	4.3E-09	0.013	31	6.1E-09	0.012
14	343	0.5	0.04	0.5	29 cc/kg H_2	350	31	1.9E-08	0.022	31	3.1E-08	0.037
15	313	0.5	0.04	12.5	29 cc/kg H_2	350	31	8E-10	0.002	31	2.4E-09	0.004
16	49	0.5	0.1	0	29 cc/kg H_2	350	32	5.2E-06	0.718	34	7.2E-06	1.161
17	78	0.5	0.01	0	29 cc/kg H_2	350	33	9.7E-07	0.286	34	1.0E-06	0.308
18	225	0.5	0.001	0	29 cc/kg H_2	350	33	1.4E-07	0.119	34	1.5E-07	0.115
19	341	0.5	0.001	2.5	29 cc/kg H_2	350	33	1.4E-08	0.038	34	1.5E-08	0.042
20	297	0.5	0.01	0	29 cc/kg H_2	50	33	3.5E-07	0.306	36	7.7E-07	0.592
21	513	0.5	0.001	0	29 cc/kg H_2	50	34	4.3E-08	0.051	36	8.4E-08	0.018
22	250	0.5	0.001	2.5	29 cc/kg H_2	50	34	4.0E-09	0.012	36	1.6E-08	0.023
23	1327	---	const K	---	29 cc/kg H_2	350	34	1.4E-09	0.053	37	2.8E-09	0.151
24	352	---	const K	---	20 cc/kg H_2	350	34	1.2E-09	0.003	37	3.5E-09	0.006

Figure 3-69 Optical Image of the Crack Growth Surface of the AREVA Alloy 52 Specimen (CT024)
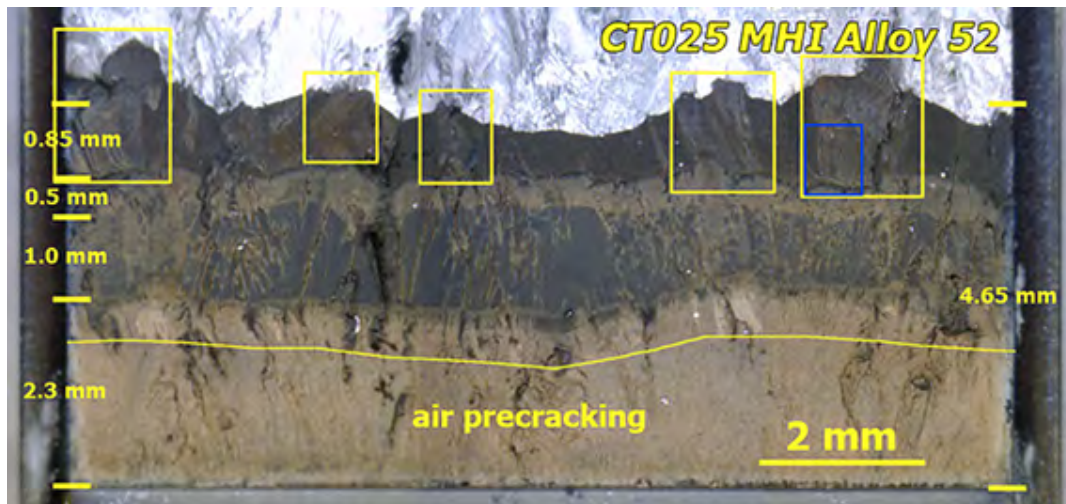
Figure 3-70 Optical Image of the Crack Growth Surface of the MHI Alloy 52 Specimen (CT025). Yellow Boxes Indicate Regions of IG Growth and the Blue Box Identifies the Area of the SEM Image Shown in Figure 3-71
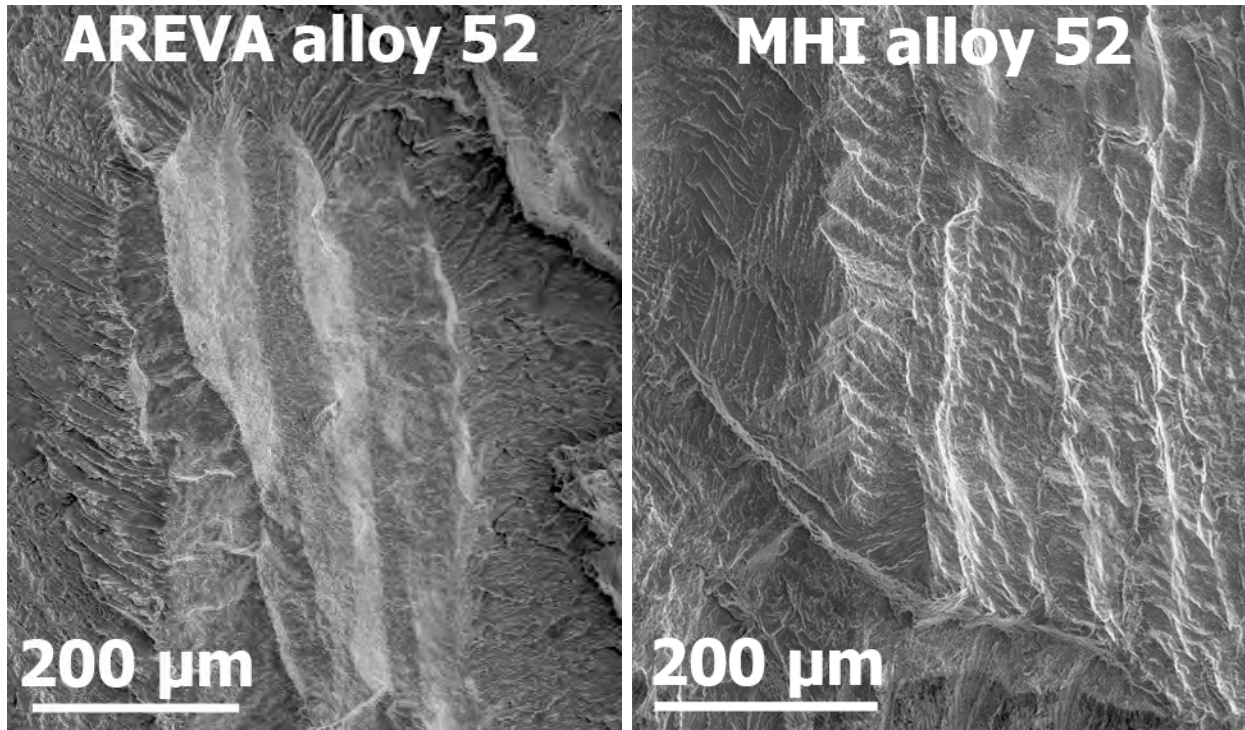
Figure 3-71   SEM Images Illustrating IG Regions on the Crack Growth Surface for the Alloy 52 Specimens: (left) Isolated IG Finger-like Area in AREVA Sample and (right) Typical IG Area in MHI Sample

Side surface images of the cracks were also obtained on these specimens with cut lines for both specimens shown in Figure 3-72. Side surfaces where polished and etched to reveal the dendrite and grain structure and are shown in Figures 3-73 and 3-74, respectively for the AREVA and MHI materials. The edge of the crack wall is feathered over making it somewhat difficult to determine TG or IG growth along the crack front, but comparison with the crack growth surfaces allows the start of IG growth to be identified. Of interest in looking at these side surfaces was the number of opportunities a crack had to intersect a grain boundary. The AREVA material has an extremely large grain size (500 to 2000 µm) that provides little opportunity for a TG crack to intersect a grain boundary while the MHI material has a wider range of grain size with some falling down into the 200 µm range. It is in a region of smaller grain size where the MHI alloy 52 material went IG.
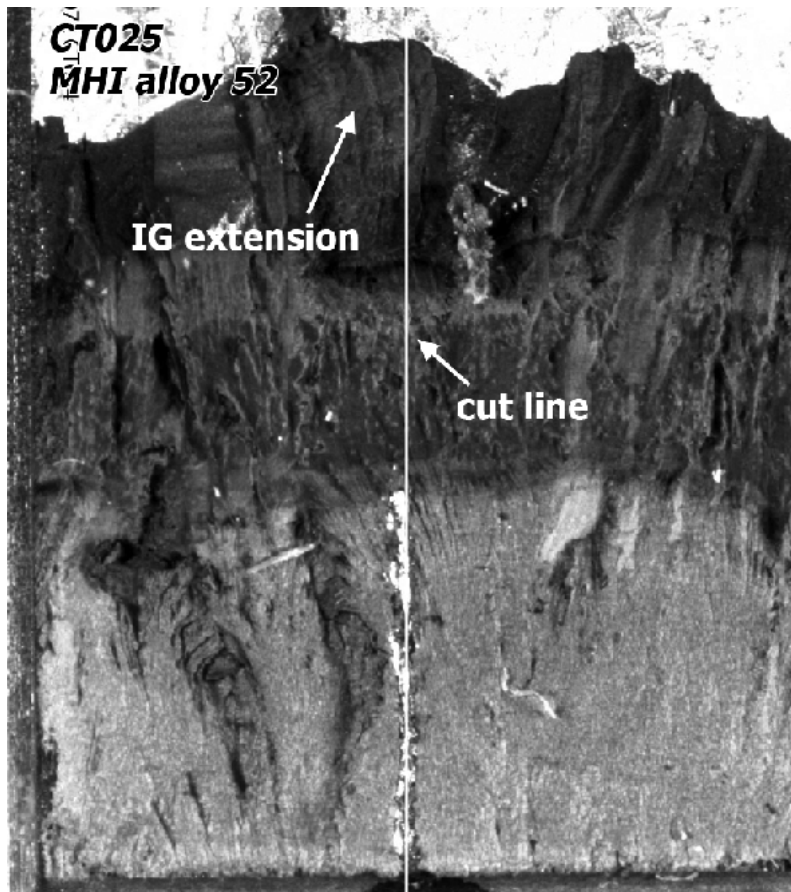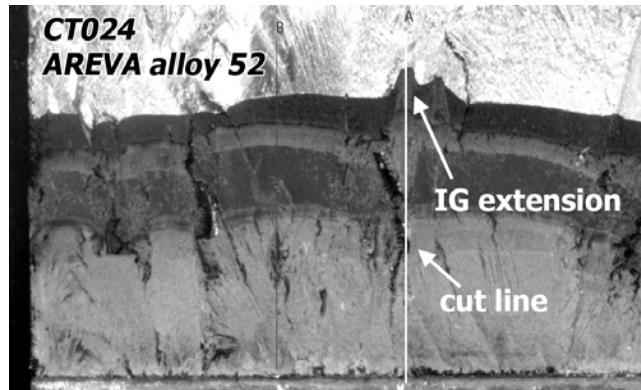
Figure 3-72   White Lines Indicate Where Crack Growth Surfaces Were Sectioned to Expose and Polish Crack Side Surfaces
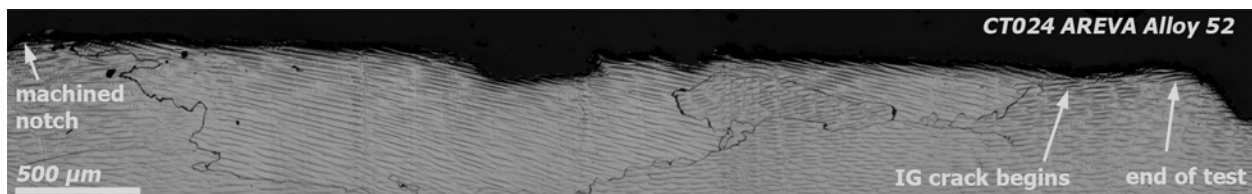
Figure 3-73   Side Surface Image of the AREVA Alloy 52 Specimen CT024
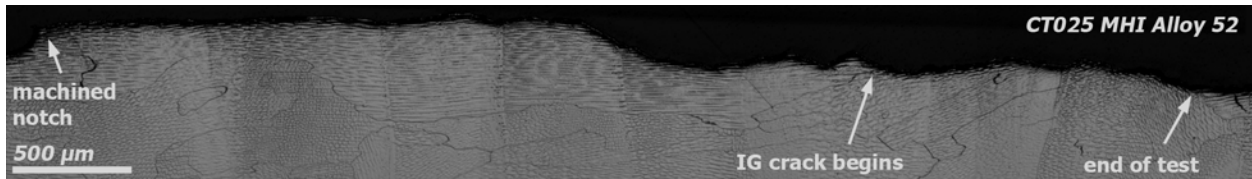
Figure 3-74   Side Surface Image of the MHI Alloy 52 Specimen CT025

A key issue that remained unclear was whether any significant IGSCC growth occurred during constant K testing at 350°C after crack extension at 50°C. In order to better assess the effects of the temperature change on the DCPD-measured crack length, tests were performed on a second pair of AREVA (CT032) and MHI (CT033) alloy 52 specimens in simulated PWR primary water. An overview of the entire crack growth test is shown in Figure 3-75. This time the test can be separated into four phases. During the first phase, the specimens were transitioned for several weeks at 350°C and displayed similar cyclic crack growth response as specimens CT024 and CT025 as illustrated in Figure 3-76. The temperature was then decreased to 50°C in the second phase and the crack extended by ~1 mm under cyclic loading conditions. This is documented in Figure 3-77. Conditions used were similar to those for the first set of alloy 52 specimens. Loading was then converted to constant K at a low value of 10 MPa√m and the temperature brought back up to 350°C in the third phase of the test. Considering the resistance of these materials, no crack growth was expected at this low K value. However, nearly identical DCPD crack growth response can be seen when comparing Figure 3-78 (CT032/33, low K) to Figure 3-68 (CT024/25, high K). The final phase of the test increased K values up to 30 MPa√m and then to 40 MPa√m using dK/da loading. Constant K SCC propagation rates increased slightly at the higher K values, but remained extremely low (corrected rates of 1.5×10^{-9} mm/s for the MHI alloy 52 and $<1 \times 10^{-9}$ mm/s for AREVA) as shown in Figure 3-79 and it was decided to end the test. A summary of test conditions and corrected data for each phase of the test is shown in Table 3-16.
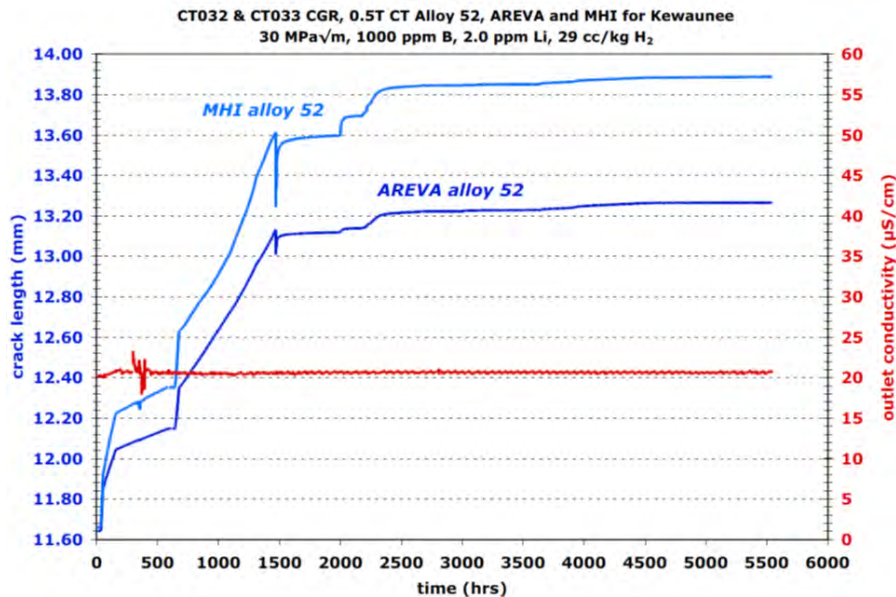
Figure 3-75   Overall Response for the Second Test on the AREVA and MHI Alloy 52 Specimens CT032 and CT033
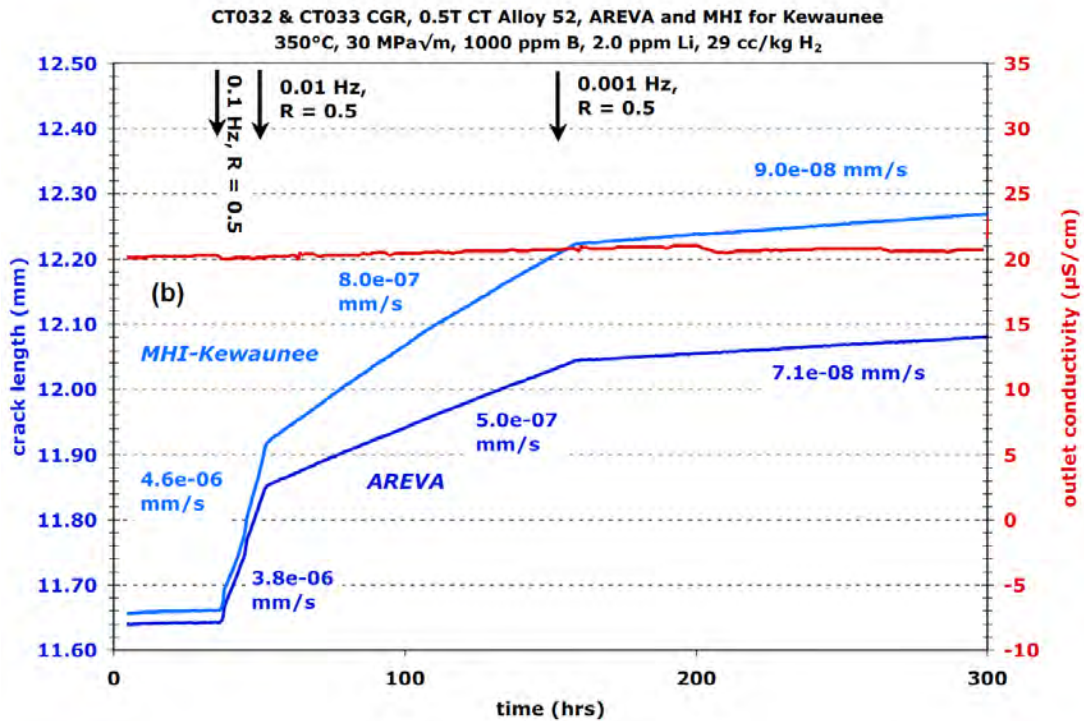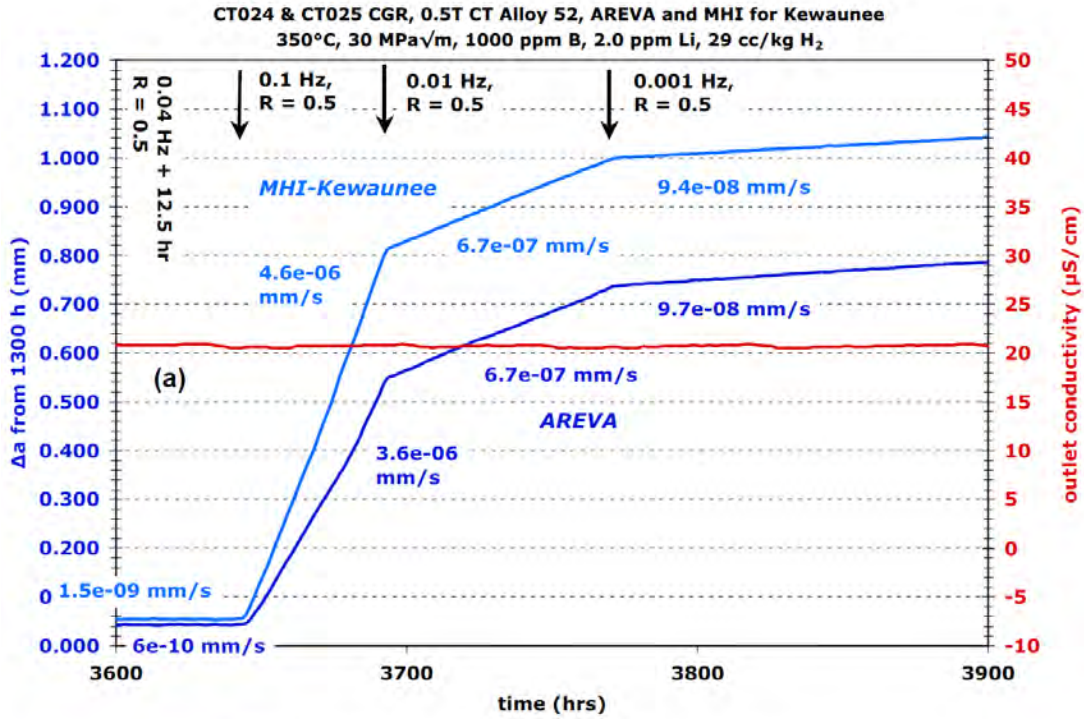
Figure 3-76   Similar CGRs Were Seen During Early Transitioning Between First Test (a) CT024/25 and Second Test (b) CT032/33 on the AREVA and MHI Materials
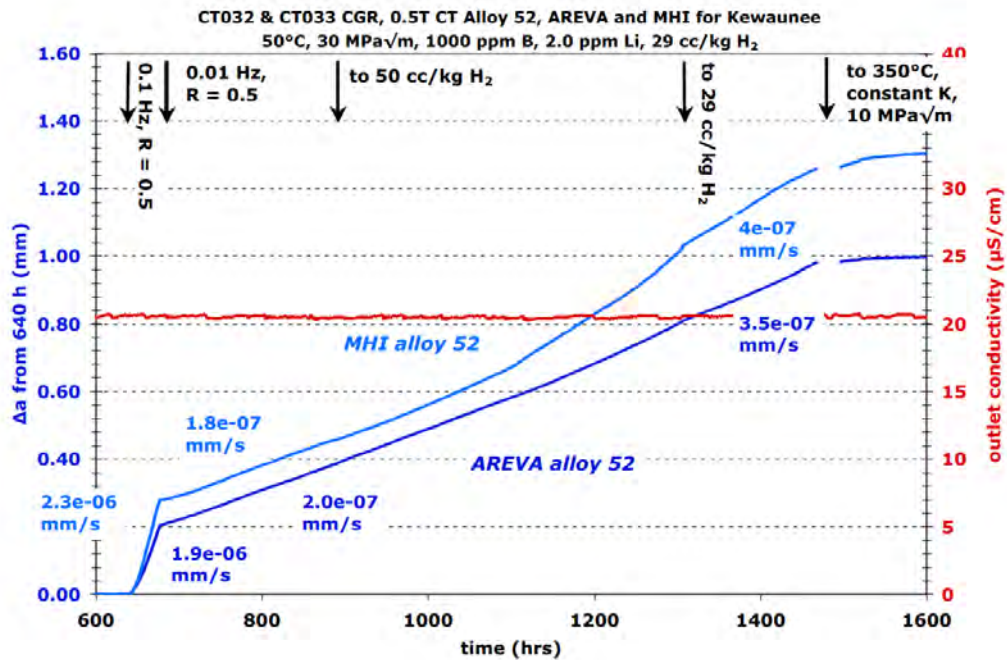
Figure 3-77   Cyclic Loading Response at 50°C of AREVA (CT032) and MHI Alloy 52 (CT033)
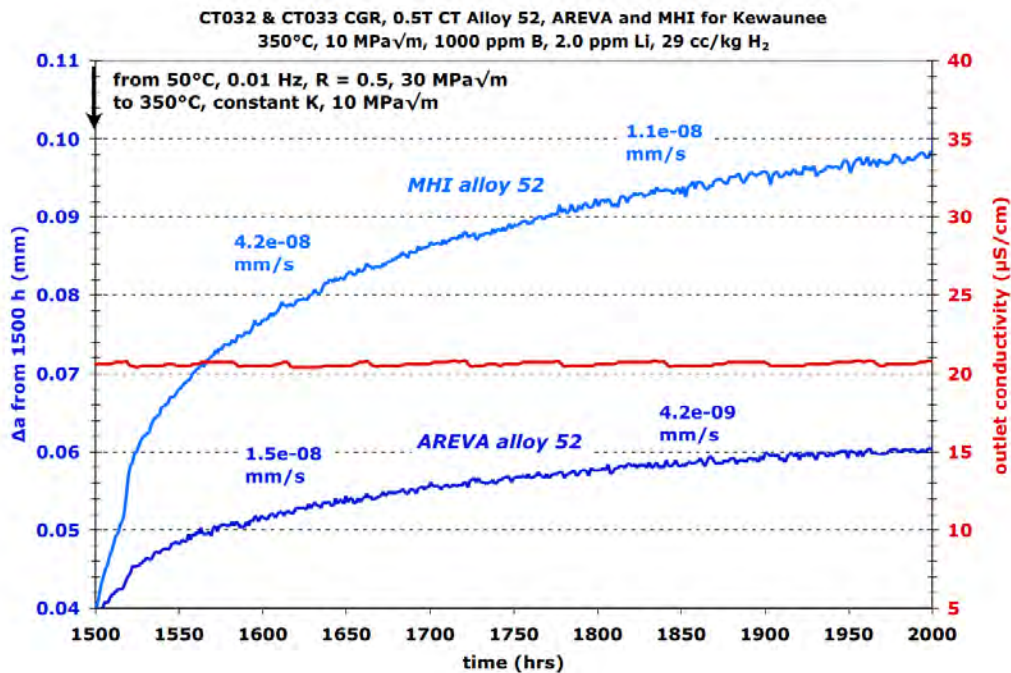
Figure 3-78   Crack Growth Response of a Second Set of AREVA and MHI 52 Specimens (CT032 & CT033) Tested at 350°C Following Crack Extension at 50°C
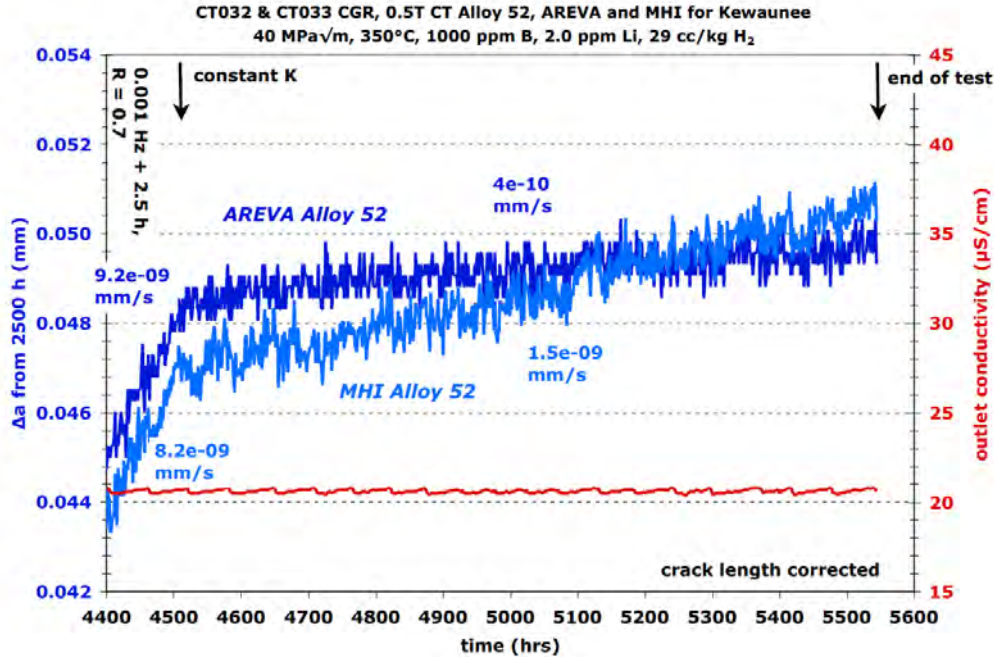
Figure 3-79   AREVA and MHI Alloy 52 Crack Growth Response at 40 MPa√m

After ending the test, the crack was sealed for crack-tip characterization by filling it with resin, and the specimens were each sectioned into two slices with one slice being fatigued open to reveal the crack growth surface, and the side of the other slice being polished to reveal the crack path through the material. The optical images of the crack growth surface, as shown in Figure 3-80, are somewhat difficult to discern because of resin coating the surface, but the large phases of the test are identifiable. It is also clear that there are regions of IG growth on the surface of both specimens. A side surface image of the AREVA (CT032) specimen is shown in Figure 3-81 revealing again that the material has very large grains. In this particular slice through the material, a significant amount of IG cracking was found; essentially the entire in-situ portion of the test appears to be IG along this section through the specimen. The side surface cut corresponds to a large protrusion on the crack growth surface in Figure 3-80. Several other protrusions are apparent indicating a higher degree of engagement than on the previous test (CT024). Figure 3-82 shows the side surface of the MHI (CT033) specimen with its smaller grains. Of interest in this photo is that while the crack eventually finds a grain boundary and cracks along it for some distance, it eventually goes off the boundary. Extensive cracking above and below the main crack is apparent. There is clearly some preference for IG cracking, but it appears that the grains must be well aligned for growth. Higher resolution SEM images of TG and IG cracks are presented in Figures 3-83 and 3-84. These micrographs reveal the shallow oxidation of the crack walls and extending to the crack tips.

Table 3-16   Summary of Test Conditions and Corrected Response for AREVA and MHI Alloy 52 Specimens CT032 & CT033

Test Phase	Dur-ation (h)	R	Freq (Hz)	Hold (h)	Water Chemistry Conditions	Temp (°C)	CT032 AREVA Alloy 52 Butt Weld Blank #1			CT033 MHI Alloy 52 U-groove Weld Blank #1		
							K_{max} (MPa√m)	CGR (mm/sec)	Approx. Crack Extension (mm)	K_{max} (MPa√m)	CGR (mm/sec)	Approx. Crack Extension (mm)
1	~2	0.3	3	0	air precrack	RT	25	1.5E-04	0.58	25	1.2E-04	0.48
2	~2	0.5	3	0	air precrack	RT	28	1.1E-04	0.46	28	8.1E-05	0.38
3	~2	0.6	3	0	air precrack	RT	31	6.8E-05	0.35	30	5.0E-05	0.29
4	~3	0.7	3	0	air precrack	RT	31	3.4E-05	0.35	30	2.3E-05	0.29
5	18	0.5	0.1	0	29 cc/kg H₂	350	31	6.0E-06	0.301	30	7.9E-06	0.457
6	106	0.5	0.01	0	29 cc/kg H₂	350	31	7.9E-07	0.303	31	1.4E-06	0.513
7	421	0.5	0.001	0	29 cc/kg H₂	350	32	1.0E-07	0.160	32	1.4E-07	0.219
8	60	---	const K	---	29 cc/kg H₂	50	32	not meas	0.015	32	not meas	0.007
9	37	0.5	0.1	0	29 cc/kg H₂	50	32	2.3E-06	0.234	32	3.4E-06	0.410
10	200	0.5	0.01	0	29 cc/kg H₂	50	32	2.5E-07	0.208	33	2.8E-07	0.254
11	425	0.5	0.01	0	29 cc/kg H₂	50	32	3.9E-07	0.522	33	6.5E-07	0.873
12	192	0.5	0.01	0	29 cc/kg H₂	50	33	4.4E-07	0.212	36	4.8E-07	0.357
13	504	---	const K	---	29 cc/kg H₂	350	11	decreasing	0.025	12	decreasing	0.085
14	186	0.78	0.001	2.5	29 cc/kg H₂	350	11	2.7E-09	0.024	12	8.3E-09	0.146
15	497	---	dK/da	---	29 cc/kg H₂	350	11->33	1.2E-08	0.059	12->38	1.3E-08	0.104
16	367	---	const K	---	29 cc/kg H₂	350	33	5E-10	<0.001	38	1.2E-09	<0.001
17	136	---	dK/da	---	29 cc/kg H₂	350	33->38	2.4E-08	0.002	38->44	2.9E-08	0.003
18	458	---	const K	---	29 cc/kg H₂	350	38	5E-10	<0.001	44	8E-10	<0.001
19	216	0.7	0.001	2.5	29 cc/kg H₂	350	38->39	1.1E-08	0.009	44->45	1.2E-08	0.010
20	86	0.7	0.001	2.5	29 cc/kg H₂	350	39->44	5.0E-08	0.009	45->51	5.4E-08	0.009
21	564	0.7	0.001	2.5	29 cc/kg H₂	350	44	1.1E-08	0.022	51	1.2E-08	0.024
22	1034	---	const K	---	29 cc/kg H₂	350	44	4E-10	0.001	51	1.5E-09	0.005

The crack growth results along with the crack surface observations support the conclusion that after going up to 350°C, slow oxidation of Ni-metal bridges is occurring in the crack produced at 50°C, and this is reducing or removing DCPD current conduction paths behind the crack front causing an artificially high CGR during this oxidation event. The very similar CGRs between the tests at 10 and 30 MPa√m suggest that very little IGSCC growth occurred after returning to 350°C even with ~35% IG engagement in the MHI specimen and ~20% IG engagement in the AREVA specimen produced by transitioning at 50°C.
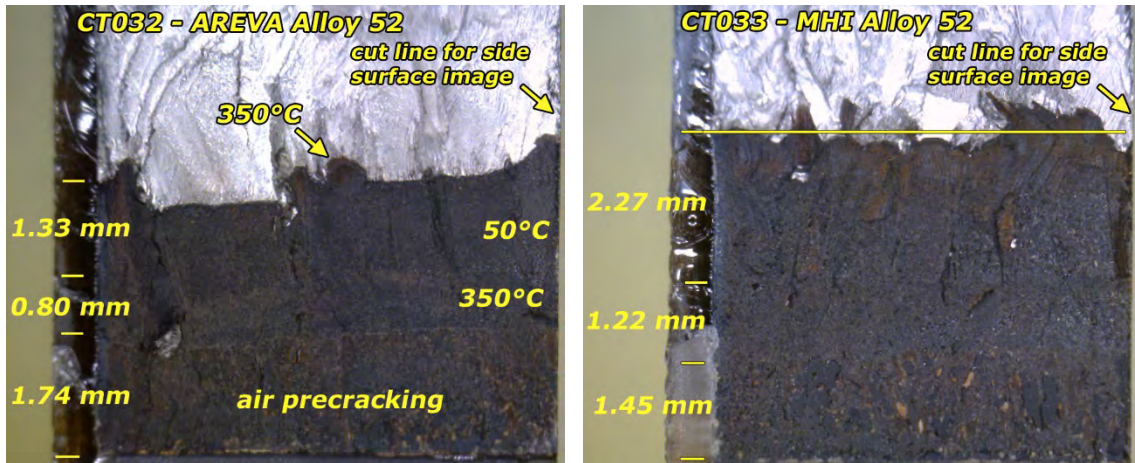
Figure 3-80   Optical Image of the Crack Growth Surface of the AREVA Alloy 52 Specimen CT032 (left) and the MHI Alloy 52 Specimen CT033 (right)
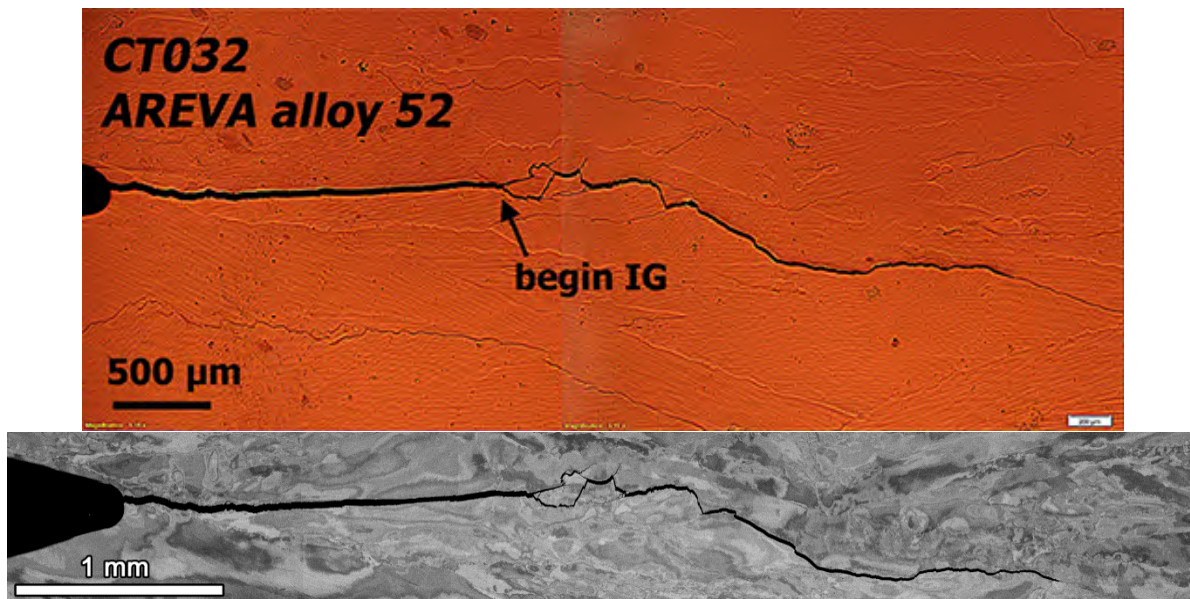
Figure 3-81   Side Surface Optical Image (top) and SEM-BSE Image (bottom) of Cracking in the AREVA Alloy 52 Specimen CT032 Showing Both TG and IG Growth
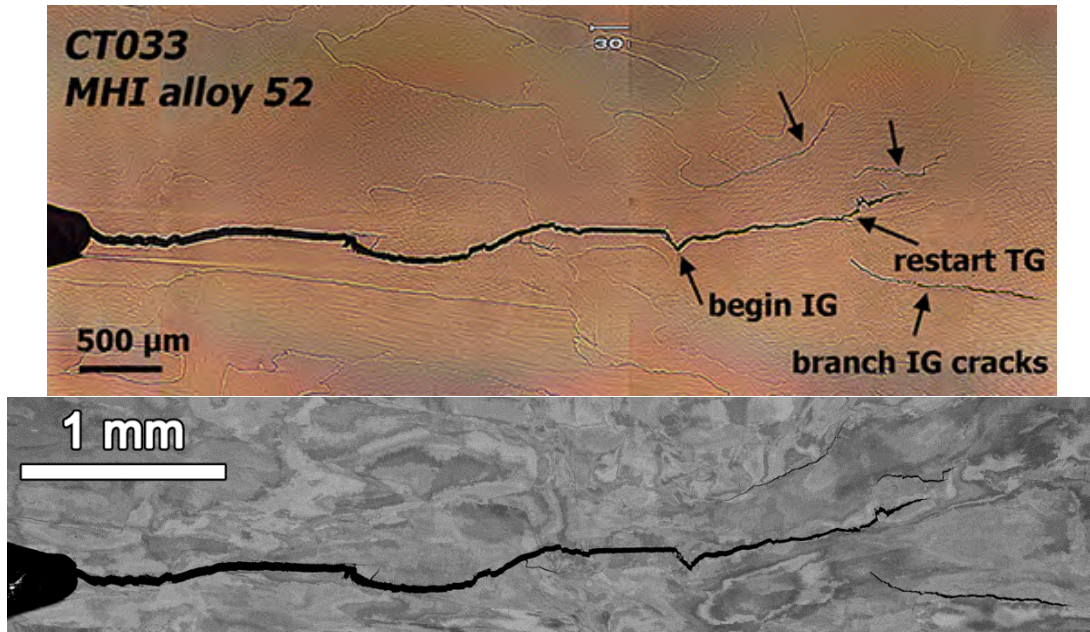
Figure 3-82   Side Surface Optical Image (top) and SEM-BSE Image (bottom) of Cracking in the MHI Alloy 52 Specimen CT033 Showing Both TG and IG Growth
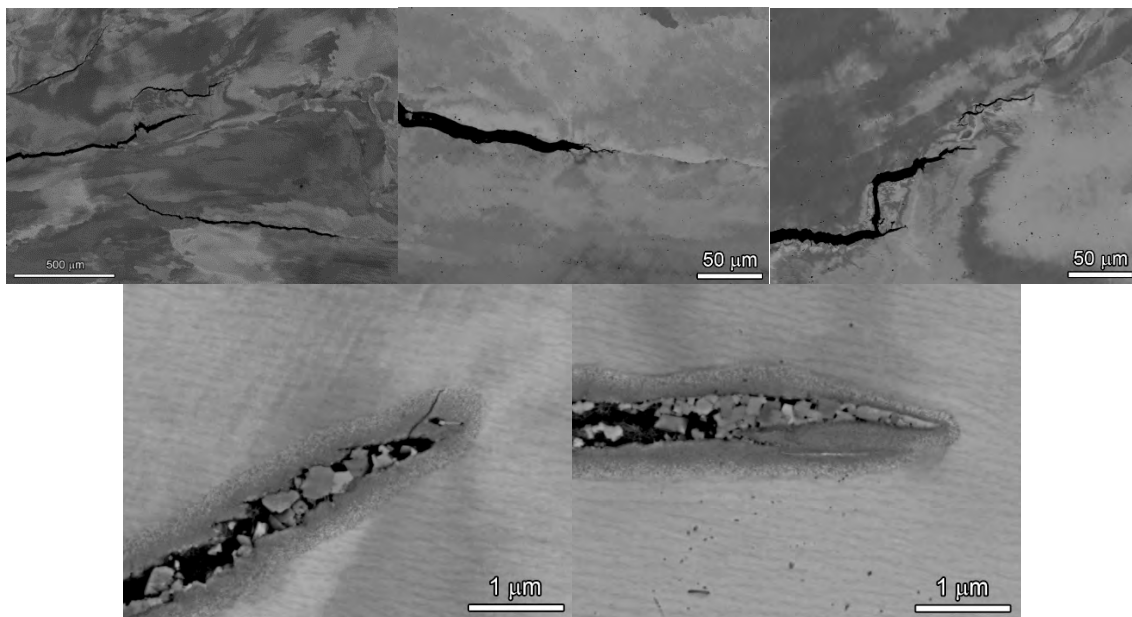
Figure 3-83   SEM-BSE of the Side Surface of the Leading Crack Growth Front of CT033 Showing Both IG and TG Cracking
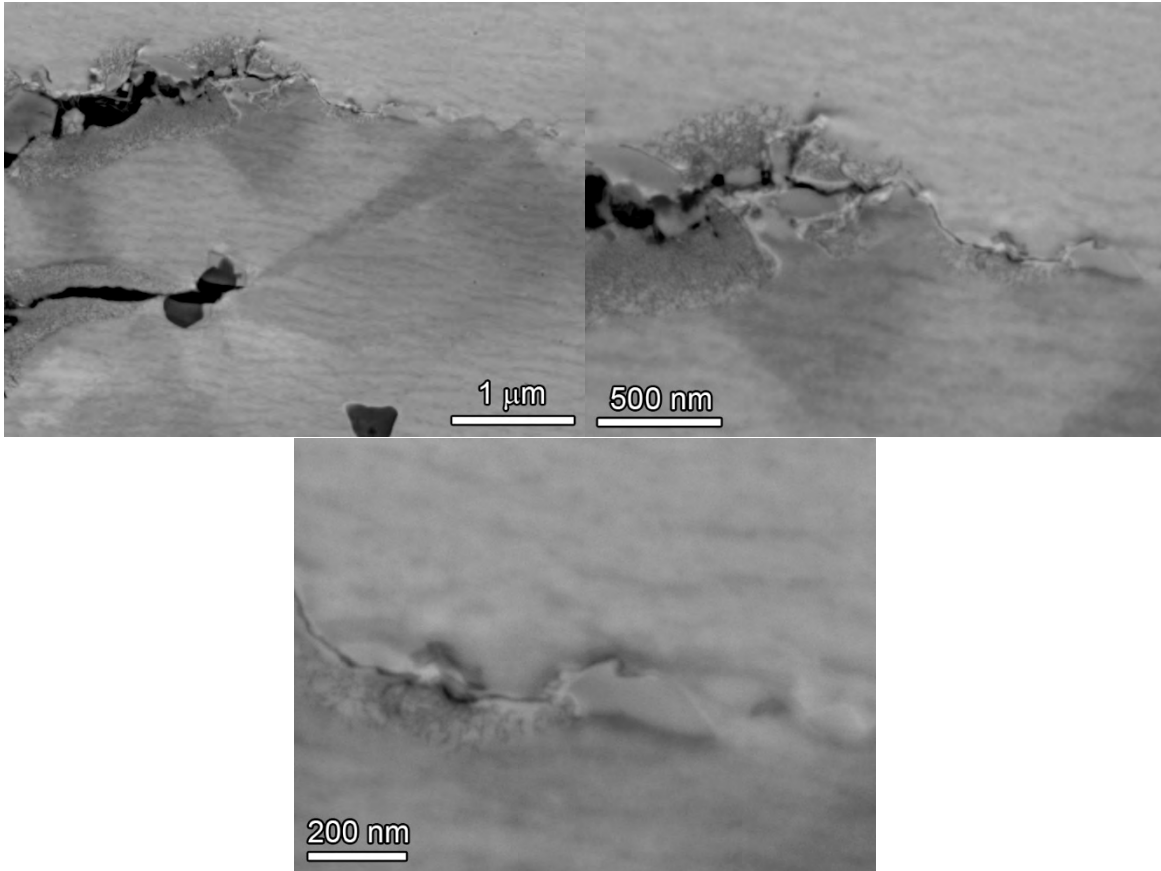
Figure 3-84   SEM-BSE of a Leading Crack Tip in CT033 Highlighting IG Cracking

3.2.3   KAPL Alloy 52M Welds

Characterizations, sample preparations and testing have been performed on three alloy 52M weldments received from KAPL. A brief description of the welds and weld metal compositions was given earlier in Table 2-1. Photographs of the V-groove and narrow gap mockups are presented in Figure 3-85. These welds were produced under prototypic best practice conditions and welding procedures. The third alloy 52M weldment was the same weld metal heat and narrow-gap configuration as the prototypic narrow gap weld, but re-fuse passes were applied between each weld pass to intentionally produce ductility dip cracks. Based on metallographic examinations, the individual weld blocks were sectioned by electro-discharge machining to create blanks for CT and thin sheets for more detailed microstructural examinations. Most characterization effort was placed on the alloy 52M weld with known weld cracks.

KAPL 304SS-carbon steel alloy 52M V-groove weld

(a)

KAPL alloy 690/52M/690 narrow gap weld

(b)
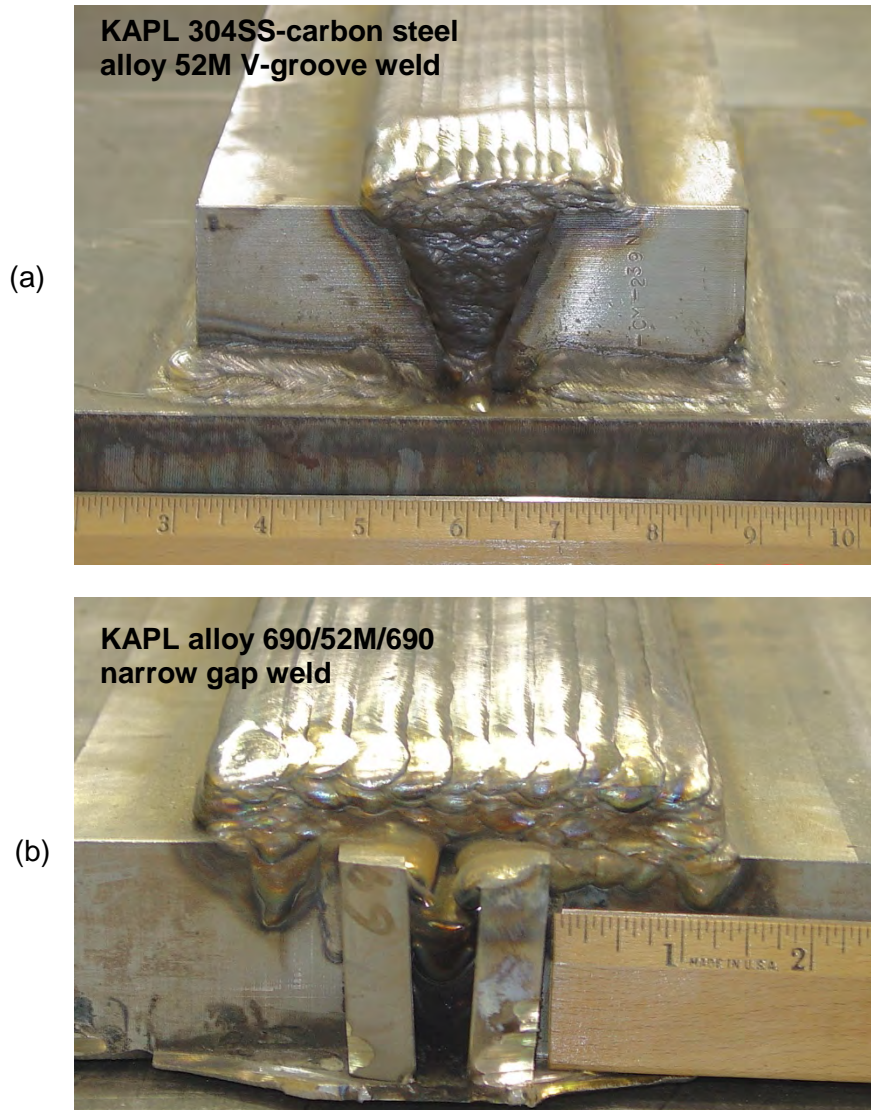
Figure 3-85   Alloy 52M Welds from KAPL: (a) Dissimilar Metal V-Groove Weld of Alloy EN52M Joining 304 SS and Carbon Steel and (b) Alloy EN52M Narrow Gap Weld Joining Alloy 690

Specimens CT040 and CT041 were machined from the center of the alloy 52M narrow-gap weld and alloy 52M V-groove weld, respectively. This is illustrated in Figures 3-86 and 3-87. Metallographic and SEM analyses were performed on the alloy 52M weld with hot cracks to determine the location of the ductility dip cracks. Optical imaging was useful in mapping out the location of defects across entire width of the CT blanks while SEM was used to study the defects in greater detail. As shown in Figure 3-88, the majority of the defects were short cracks along grain boundaries, and the density of these cracks was low. Because the cross-sectional area of the as-received weldment was only slightly larger than a 0.5T CT specimen, only a few regions of the weld could be selected for crack growth testing. Figure 3-89 shows the positioning of specimens CT042 and CT043 on the CT blanks, while the yellow boxes in Figure 3-88 show these CT locations relative to the observed weld defects in one of the metallography

specimens. Specimen CT042 is positioned off-center to intersect a higher density of weld cracks, while CT043 is positioned near the center where fewer cracks were observed. All four alloy 52M specimens were pre-cracked in air to a depth of ~1.2 mm.
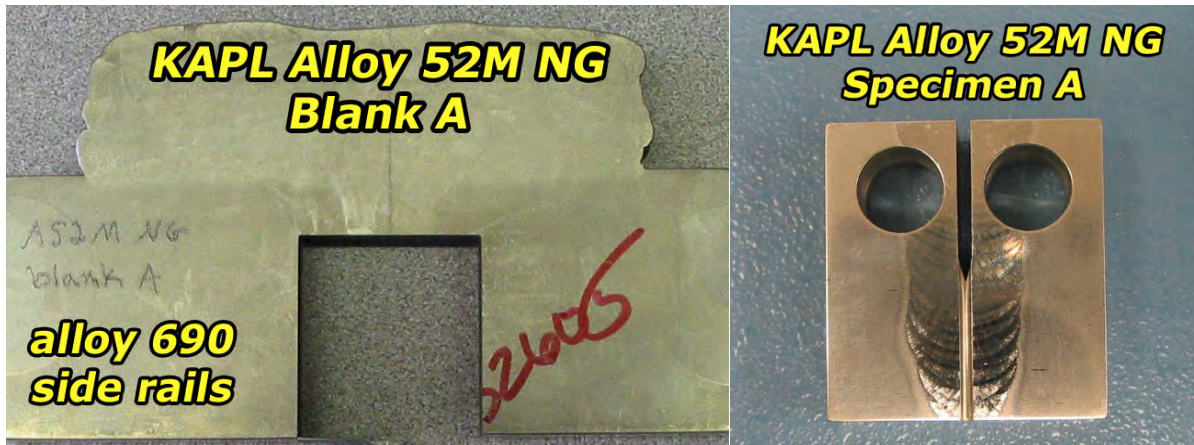
Figure 3-86   Photos of KAPL Alloy 52M Narrow Gap Weld Blank "A" and CT040 Specimen Machined from the Blank

Figure 3-87   Photos of KAPL Alloy 52M V-Groove Weld Blank "A" and CT041 Specimen Machined from the Blank
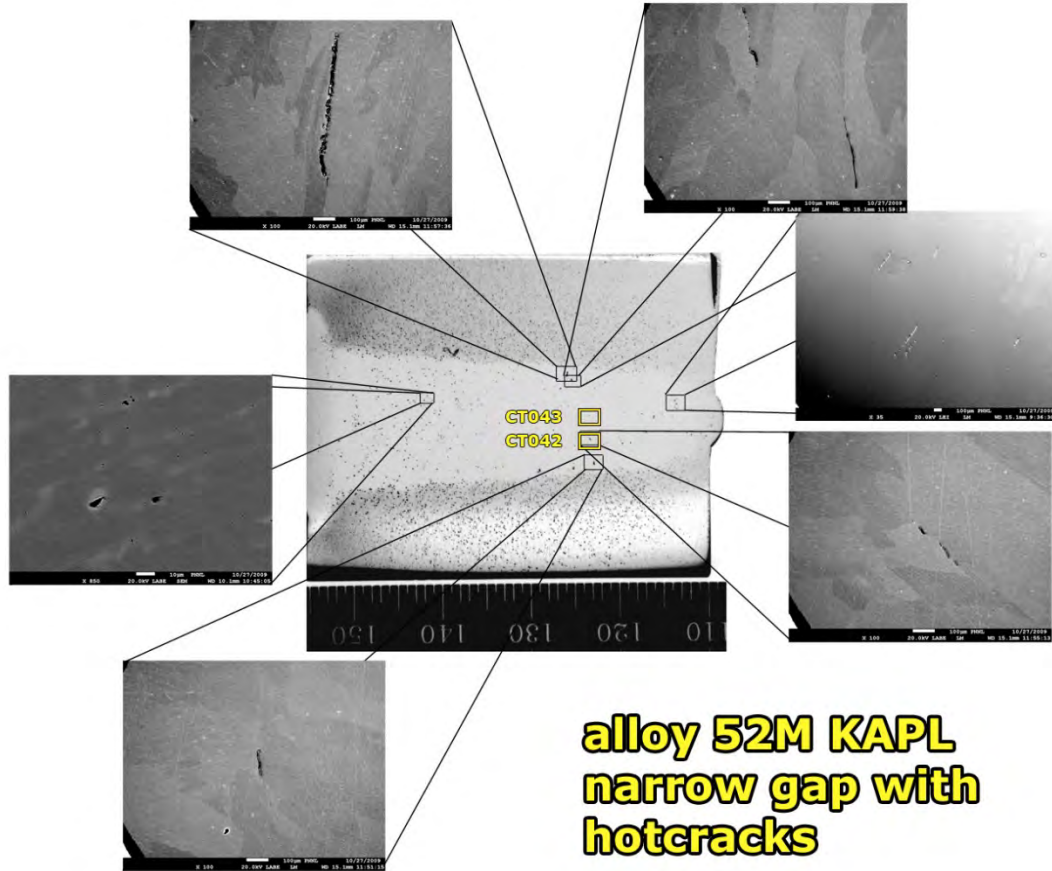
Figure 3-88   Overview of Defects in the KAPL Alloy 52M Weld with Known Weld Cracks

Figure 3-89   Photos of Specimens Cut from KAPL Alloy 52M Narrow Gap Weld Containing Hot Cracks. Blank a (CT042) Is Positioned Off-Center and near the Bottom of the Weldment to Insect a High Density of Weld Cracks, While Blank B (CT043) Is Positioned near the Center of the Weld Where No Weld Cracks Were Observed

Testing was performed in simulated PWR primary water at either 350°C with 20 cc/kg dissolved H_2 or, later in the test, 360°C and 25 cc/kg H_2. These hydrogen concentrations were selected to obtain ECP conditions at the Ni/NiO transition. An overview of the entire test is presented in Figure 3-90. During in-situ pre-cracking and initial transitioning steps at R = 0.7, low CGRs were observed, so steps were duplicated at a more aggressive R of 0.5 starting at ~180 h. CGR response increased significantly with both samples reaching rates >10^{-6} mm/s at 0.1 Hz. The V-groove weld sample exhibited higher CGRs than the narrow-gap weld as the cyclic frequency was reduced first to 0.01 and then to 0.001 Hz.

As transitioning steps continued, higher CGRs continued to be measured in the V-groove weld sample than for the narrow-gap weld sample. This is illustrated in Figure 3-91. Rates during cycle + hold were 1.6x10^{-8} mm/s for the V-groove weld, somewhat higher than identified for previous alloy 52 weld metal tests and ~2X higher than the narrow-gap weld. The decision was made to switch to constant K conditions at ~1130 h and investigate the SCC response. Crack-growth rates of 3.6x10^{-9} mm/s and ~7x10^{-10} mm/s can be seen for the V-groove and narrow-gap alloy 52M weld specimens, respectively. Stable SCC propagation is seen throughout the constant K period for the V-groove weld specimen in Figure 3-96, while growth, if any, appears to have stalled in the narrow-gap weld specimen.
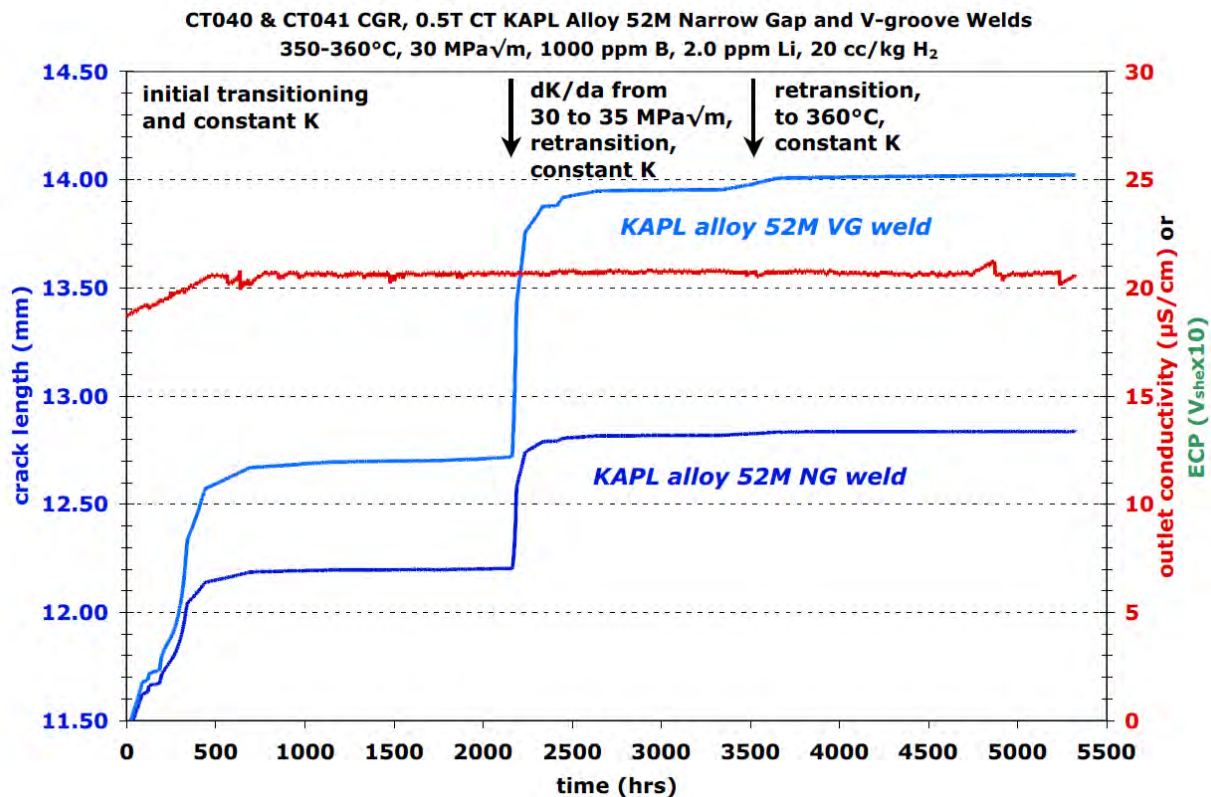
Figure 3-90   Overview of the Entire Test on the KAPL Alloy 52M Narrow Gap (CT040) and V-Groove (CT041) Specimens
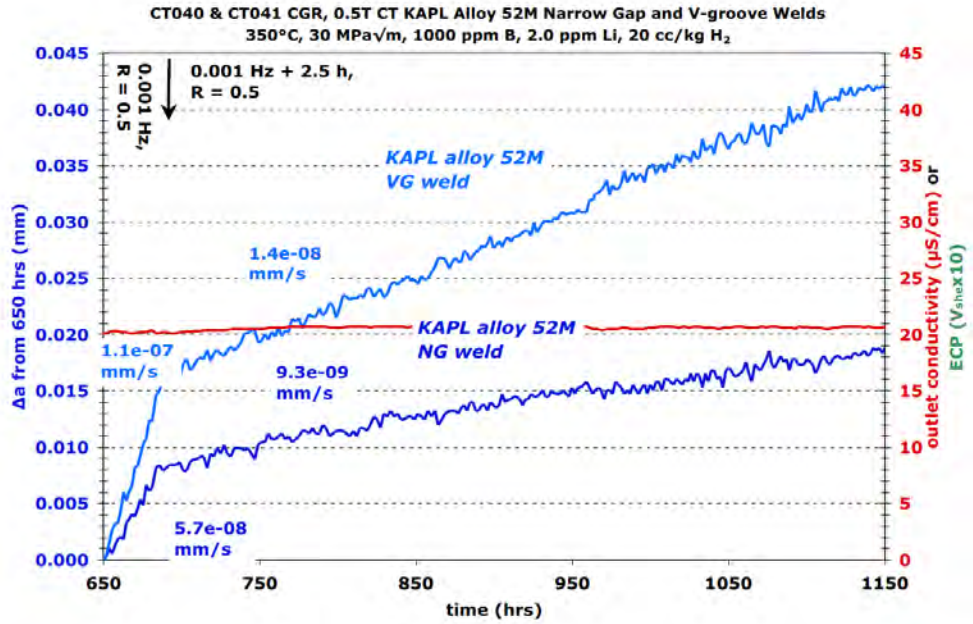
Figure 3-91   Response During Initial Cycle + Hold Transitioning Steps on the KAPL Alloy 52M Narrow Gap (CT040) and V-Groove (CT041) Specimens
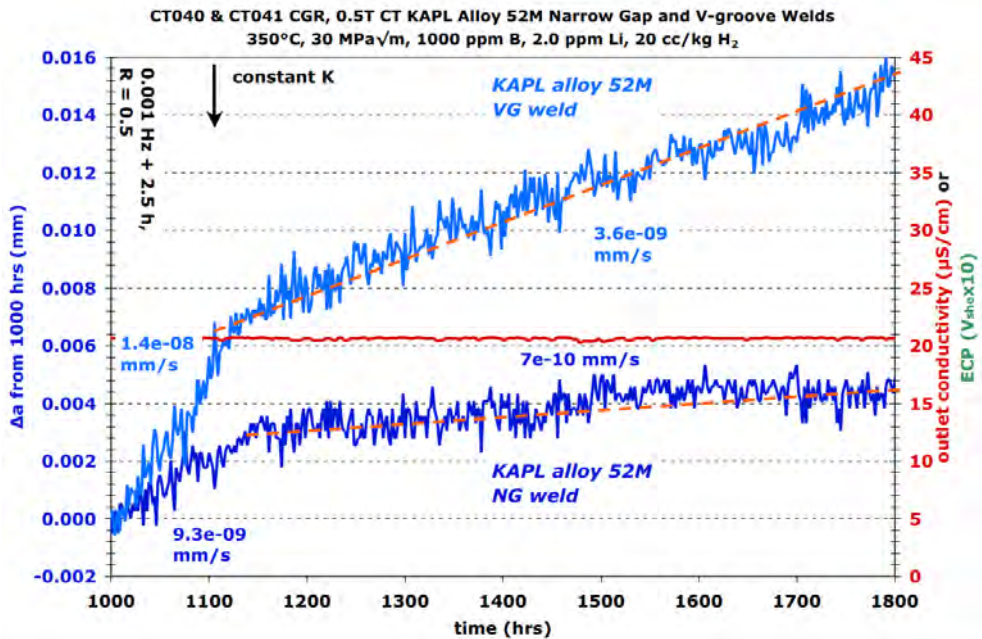
Figure 3-92   Response During Initial Constant K Step on the KAPL Alloy 52M Narrow Gap (CT040) and V-Groove (CT041) Specimens

Gentle cycling was restarted to move the crack front forward slightly and straighten the crack front, but since higher propagation rates were not observed during retransitioning, the decision was made to increase the K level for both specimens. Cycling at 0.1 Hz (R = 0.5) was established under dK/da loading at ~2165 h with the NG sample increasing from 30 to 35 MPa√m and the V- groove (VG) sample increasing from 32 to 39 MPa√m. The CGR

response during this step is documented in Figure 3-93 showing ~390 and 730 μm of crack extension respectively for the narrow groove (NG) and VG specimens over the 24-h period. Transitioning was then performed by decreasing the cyclic frequency and moving to a cycle + hold at ~2330 h. Higher CGRs were again observed during all loading conditions for the VG than for the NG sample. Transitioning steps were continued until constant K (35 MPa√m in the NG sample and 40 MPa√m in the VG sample) was established at ~2650 h as shown in Figure 3-94. Propagation rate for the NG specimen was initially stable at 1.3x10^{-9} mm/s, similar to what has been observed in previous alloy 52M materials tested at PNNL. The V-groove specimen exhibited a higher growth rate of ~3.0x10^{-9} mm/s for about 600 h and then appeared to slow down at ~3200 h. The initial CGR for the V-groove specimen is similar to the value measured at the lower K value.
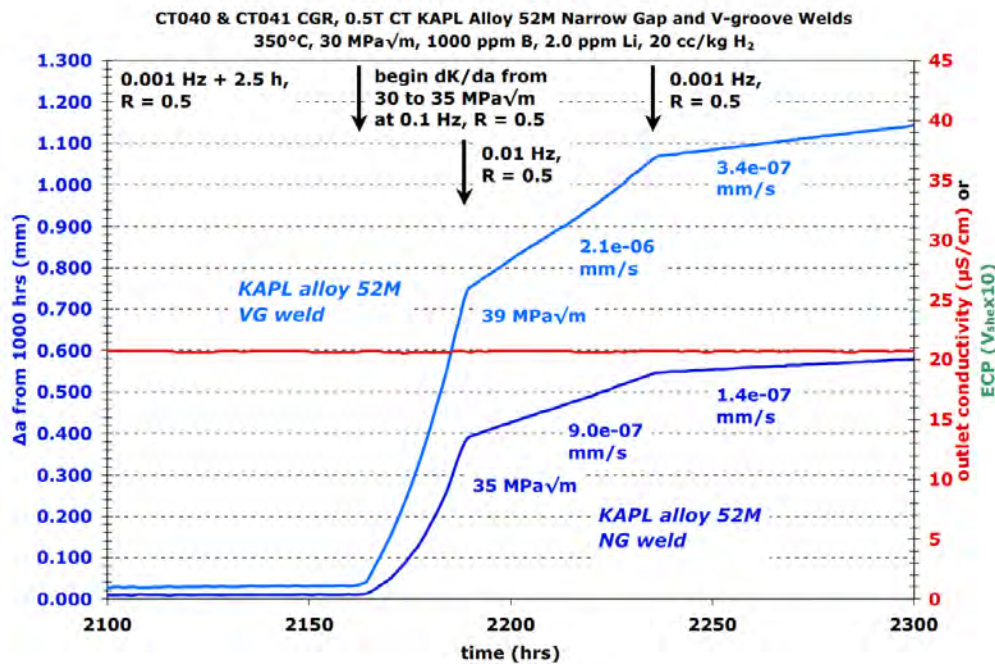
Figure 3-93   Crack-Growth Response During the K Increase by dK/da for KAPL Alloy 52M Specimens CT040 and CT041
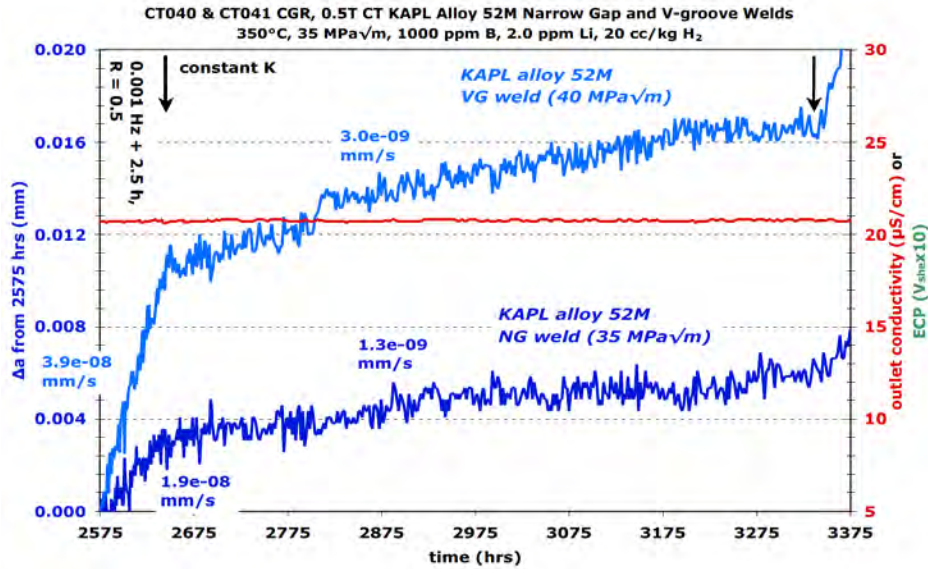
Figure 3-94   Crack-Growth Response from Cycle + Hold to Constant K for CT040 and CT041

To help promote SCC, a cycle + hold loading condition was re-established and the test temperature increased to 360°C while holding the ECP on the Ni/NiO line (25 cc/kg H_2). Once again, CGRs started higher when switching back to constant K but decreased after ~500 h. This is illustrated in Figure 3-95 with the VG specimen slowing from 3.5×10^{-9} mm/s to 2.3×10^{-9} mm/s. The rate for the NG specimen starts off at a low rate of ~6×10^{-10} mm/s and growth stops after 1000 h. This test was ended after ~1700 h under constant K (35-40 MPa√m) conditions at 360°C and 25 cc/kg H_2. The CGRs for both samples are similar to the previous measurements at 350°C with slightly lower K values. A summary of the corrected step-by-step data obtained during this test is presented in Table 3-15.
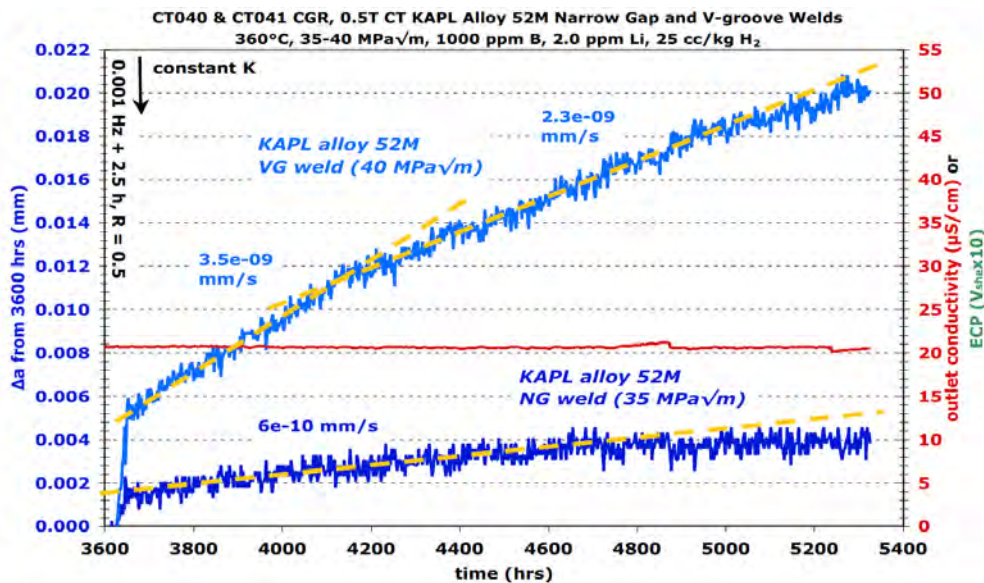
Figure 3-95   Crack Growth Response During Constant K at 360°C for the KAPL Alloy 52M Narrow Gap (CT040) and V-Groove (CT041) Weld Specimens

3-84

Table 3.8   Corrected Data Summary for KAPL Alloy 52M Specimens CT040 & CT041

Test Phase	Dur-ation (h)	R	Freq (Hz)	Hold (h)	Water Chemistry Conditions	Temp (°C)	CT040 KAPL A52M NG Blank A			CT041 KAPL A52M V-groove Blank A		
							Kmax (MPa√m)	CGR (mm/sec)	Crack Extension (mm)	Kmax (MPa√m)	CGR (mm/sec)	Crack Extension (mm)
1	~3	0.3	5	0	air precrack	RT	21	6.8E-05	0.40	21	6.2E-05	0.40
2	~2	0.5	5	0	air precrack	RT	23	4.0E-05	0.35	24	3.7E-05	0.35
3	~2	0.6	5	0	air precrack	RT	26	2.6E-05	0.35	26	2.6E-05	0.35
4	~3	0.7	5	0	air precrack	RT	26	1.3E-05	0.20	26	1.2E-05	0.20
5	86	0.7	0.1	0	20 cc/kg H_2	350	31	7.8E-07	0.241	32	9.8E-07	0.319
6	100	0.7	0.01	0	20 cc/kg H_2	350	31	1.3E-07	0.062	32	1.4E-07	0.078
7	153	0.5	0.1	0	20 cc/kg H_2	350	31	1.6E-06	0.443	33	3.5E-06	0.784
8	100	0.5	0.01	0	20 cc/kg H_2	350	31	3.5E-07	0.116	34	9.6E-07	0.302
9	242	0.5	0.001	0	20 cc/kg H_2	350	31	6.9E-08	0.055	34	1.4E-07	0.127
10	454	0.5	0.001	2.5	20 cc/kg H_2	350	31	1.1E-08	0.012	34	1.8E-08	0.033
11	647	---	const K	---	20 cc/kg H_2	350	31	~8E-10	0.002	34	4.6E-09	0.011
12	380	0.5	0.001	2.5	20 cc/kg H_2	350	31	1.8E-08	0.007	35	6.8E-09	0.021
13	26	0.5	0.1	0	20 cc/kg H_2	350	31->37	increasing	0.439	35->45	increasing	0.899
14	47	0.5	0.01	0	20 cc/kg H_2	350	37	1.1E-06	0.199	45	2.7E-06	0.436
15	94	0.5	0.001	0	20 cc/kg H_2	350	37	1.6E-07	0.061	46	4.5E-07	0.158
16	84	0.5	0.001	2.5	20 cc/kg H_2	350	37	1.3E-08	0.007	46	1.8E-08	0.017
17	32	0.5	0.001	0	20 cc/kg H_2	350	37	1.4E-07	0.013	46	4.2E-07	0.044
18	195	0.5	0.001	2.5	20 cc/kg H_2	350	37	2.3E-08	0.016	46	5.1E-08	0.041
19	704	---	const K	---	20 cc/kg H_2	350	37	1.6E-09	0.004	46	3.8E-09	0.010
20	159	0.5	0.001	2.5	20 cc/kg H_2	350	37	1.6E-08	0.008	46	5.3E-08	0.030
21	146	0.5	0.001	2.5	25 cc/kg H_2	360	37	2.1E-08	0.010	47	7.8E-08	0.037
22A	500	---	const K	---	25 cc/kg H_2	360	37	~1E-09	0.001	47	4.2E-09	0.009
22A	1176	---	const K	---	25 cc/kg H_2	360	37	~5E-10	0.001	47	2.8E-09	0.011

After testing, a slice was taken from each of the two CT specimens for preparation of an interior crack profile observation, and the other piece was fatigued open in air to reveal the crack growth surface. Figures 3-96 and 3-97 show optical and SEM-BSE micrographs of crack growth surface of CT040 and CT041, respectively. Strong changes in loading conditions are apparent along the crack growth surface of both specimens and are indicated by the yellow lines. In comparing the two surfaces the higher CGR of the VG specimen is apparent in each major region of the test. While the final crack front of the narrow gap specimen (CT040) is relatively straight with little or no strong SCC protrusions, the VG specimen (CT041) appears to have clear SCC protrusions along the entire crack front. The cut line for the crack profile specimens is shown on the crack growth surface images, and optical micrographs of the crack profile images are shown in Figures 3-98 and 3-99 for CT040 and CT041, respectively. The final crack front of the narrow gap specimen (CT040) is relatively straight with no obvious indication of IG engagement. The crack profile image shows that along the cut line, the precracking ended in the interior of a grain, and the subsequent crack growth appears to be essentially straight through the grain. Towards the end of the test, a grain boundary is encountered, but the cracking does not appear to be IG as it moves along the boundary. This suggests that the majority of the cracking in the narrow gap specimen is TG. While the precracking of the VG specimen (CT041) also ends in the interior of a grain, the crack does eventually find a grain

boundary and grow intergranularly. The crack does wander away from the boundary for a period, but it eventually finds the boundary again. The crack profile reinforces the observations of the crack growth surface that the cracking is significantly IG. The clear difference in CGR between the two types of welds made using the same wire is an interesting result that warrants further observations and supports the need to study welds made using production welding parameters.
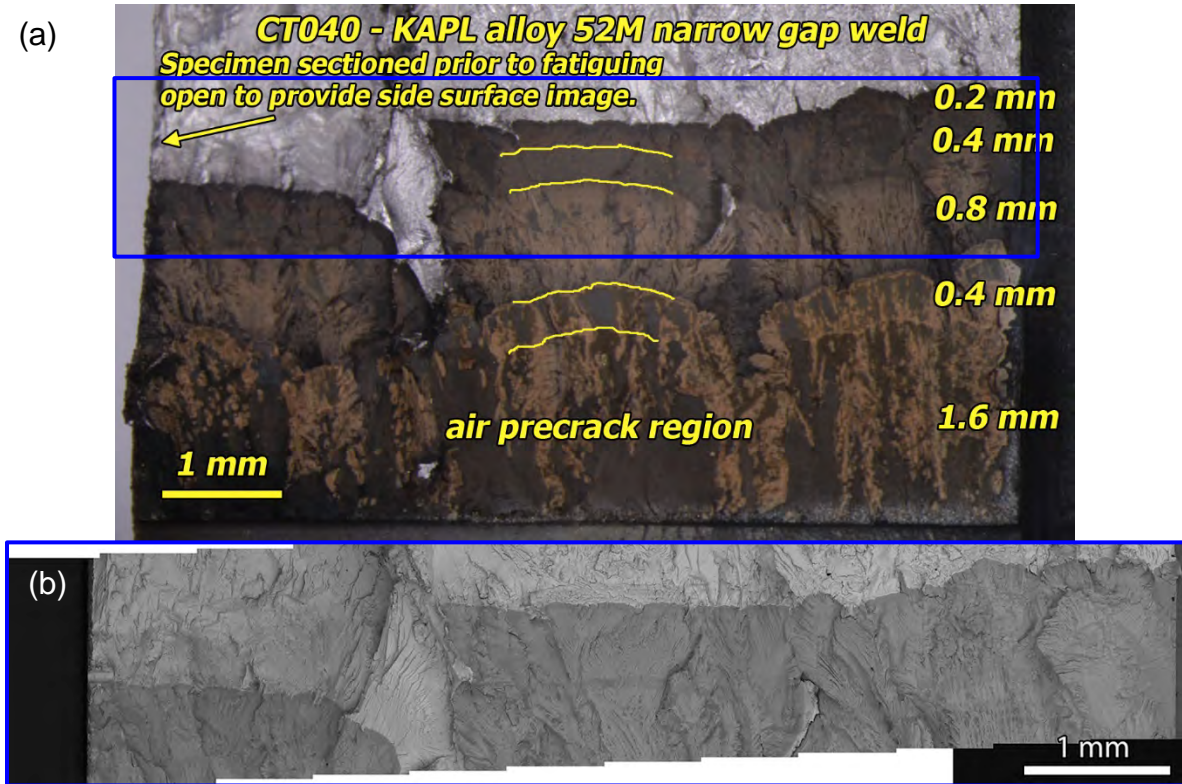
Figure 3-96   **Crack Growth Surface of the KAPL Alloy 52M Narrow Gap Specimen CT040: (a) Optical Image of the Overall Crack Growth Surface and (b) SEM-BSE Image of the Area Highlighted in (a)**
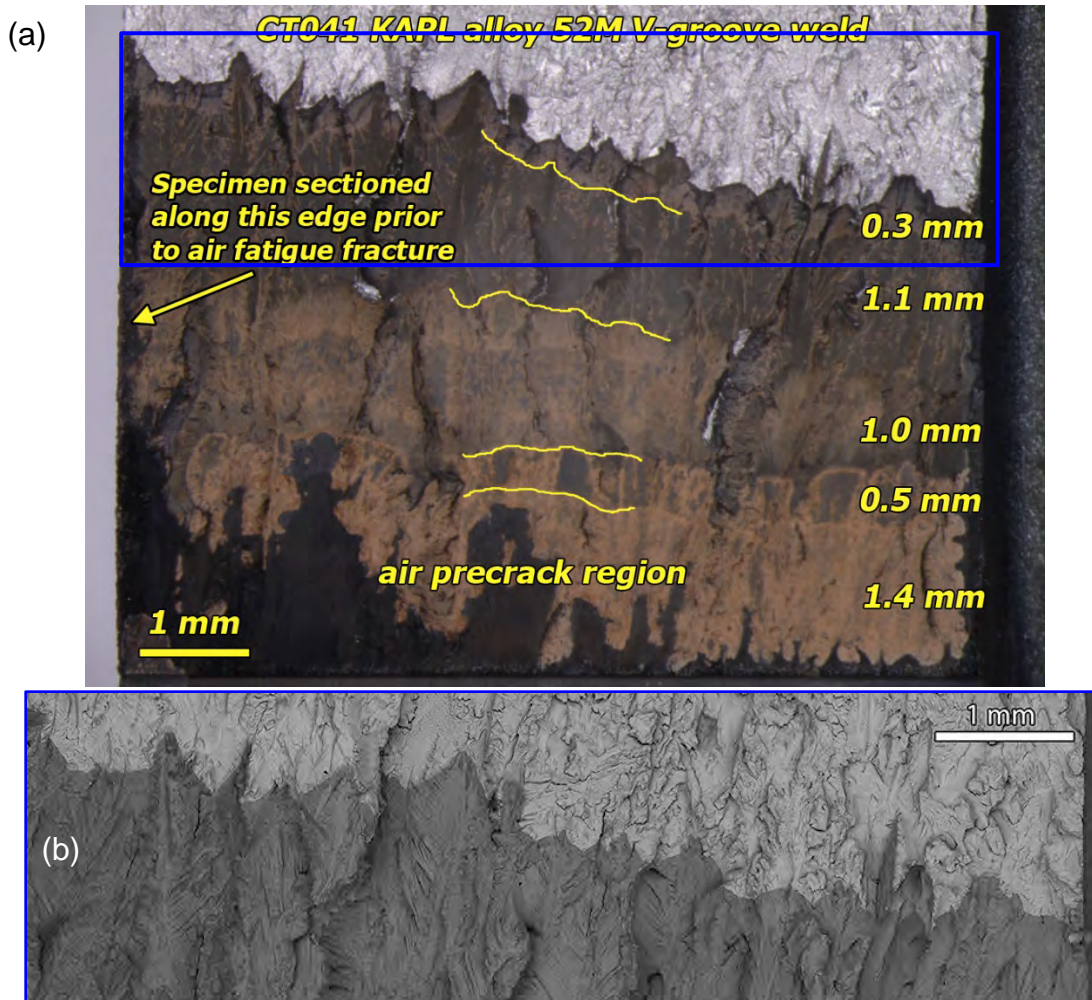
Figure 3-97   Crack Growth Surface of the KAPL Alloy 52M V-Groove Specimen CT041: (b) Optical Image of the Overall Crack Growth Surface and (b) SEM-BSE Image of the Area Highlighted in (a)
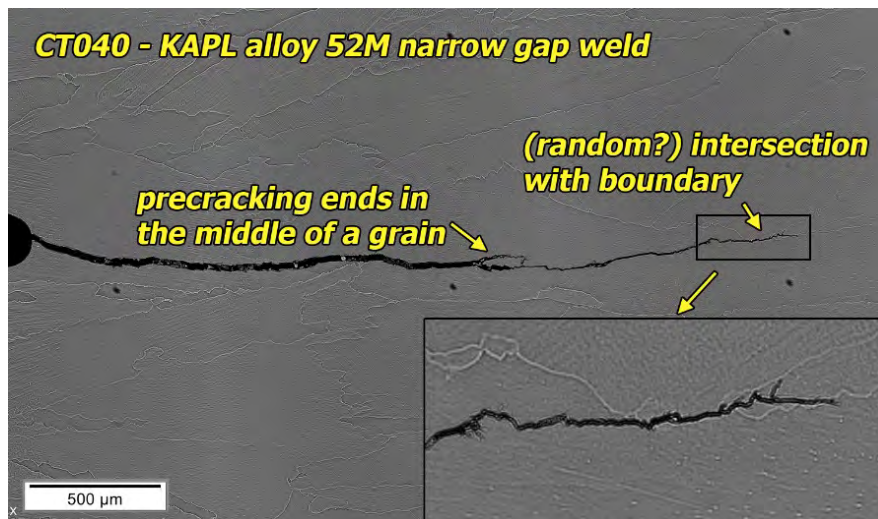
Figure 3-98   Crack Profile of the KAPL Alloy 52M Narrow Gap Specimen CT040

Figure 3-99   Crack Profile of the KAPL Alloy 52M V-Groove Specimen CT041

Analytical electron microcopy analysis was performed on both CT040 (Figures 3-100 to 3-103) and CT041 (Figures 3-104 to 3-107) to provide a better understanding of the crack morphologies. High magnification SEM-BSE imaging of the leading crack tip of CT040 (Figures 3-100 and 3-101) shows the TG nature of the crack even though it appears to be oriented with the aligned grains. At the highest magnification (Figure 3-101), penetrative oxidation accented the entire leading TG crack, suggesting the crack was not active for some time. The bright contrast along the crack wall is most likely a Nb-rich matrix carbide that the TG crack encountered. EBSD of the leading crack region (Figure 3-102) as well as of the base microstructure ~1-2 mm ahead of the leading crack tip (Figure 3-103) was performed to better illustrate not only the microstructure, but the local misorientation (which can be interpreted as a measure of strain) in the region of the SCC test. The solid yellow line in the pattern quality map in Figure 3-102 illustrates the TG nature of the SCC crack. The inverse pole figure (IPF) map shows in more detail the grain microstructure, and the local misorientation map provides an indication of a high amount of deformation in the grains surrounding the SCC crack. This microstructure and local misorientation can be compared to the base microstructure of the weld as seen in Figure 3-103 where the grains appear to be of similar shape and size, but with much less local deformation.

EBSD of the leading crack tip as well as base microstructure (~1-2 mm ahead of the leading crack tip) of CT041 is presented in Figures 3-104 and 3-105, respectively. The IPF figure indicates that propagation during part of the SCC test was IG, but eventually ended TG (Figure 3-104). Similar as for CT040, the local misorientation map of the leading crack-tip region in CT041 (Figure 3-104) shows a high density of deformation as compared to the base microstructure (Figure 3-105).

A transmission electron microscopy (TEM) sample was prepared by a focused-ion beam (FIB) system from a secondary IG crack tip (dashed yellow box in Figure 3-99) to ascertain the local grain boundary chemistry of the sample (Figure 3-106). SEM-BSE imaging of the sample shows no obvious secondary IG precipitation, but the bright contrast ahead of the leading tip suggests Cr depletion/Ni enrichment. Penetrative oxidation tapers to the leading secondary tip, which suggests this was an actively growing crack during the end of the test. Approximately 500 nm behind the IG crack tip, a TG crack can be seen without any contrast change ahead of the tip which would be associated with a chemistry change. Scanning TEM/EDS elemental maps taken of this crack region (Figure 3-107) confirm that there is Cr depletion/Ni enrichment ~1 μm ahead of the leading IG tip, and no chemistry change ahead of the TG crack (which is not as evident due to the thickness of the TEM foil). Interestingly, a small IG oxide particle which is Al and Zr rich is observed ahead of the crack tip which was not observed in the SEM-BSE image. Again, this is most likely due to the small interaction volume of the back-scatter

technique. No other secondary IG phases were observed. The penetrative oxidation along the crack walls was observed to be Cr rich with some Ni, but with a lower Fe content.
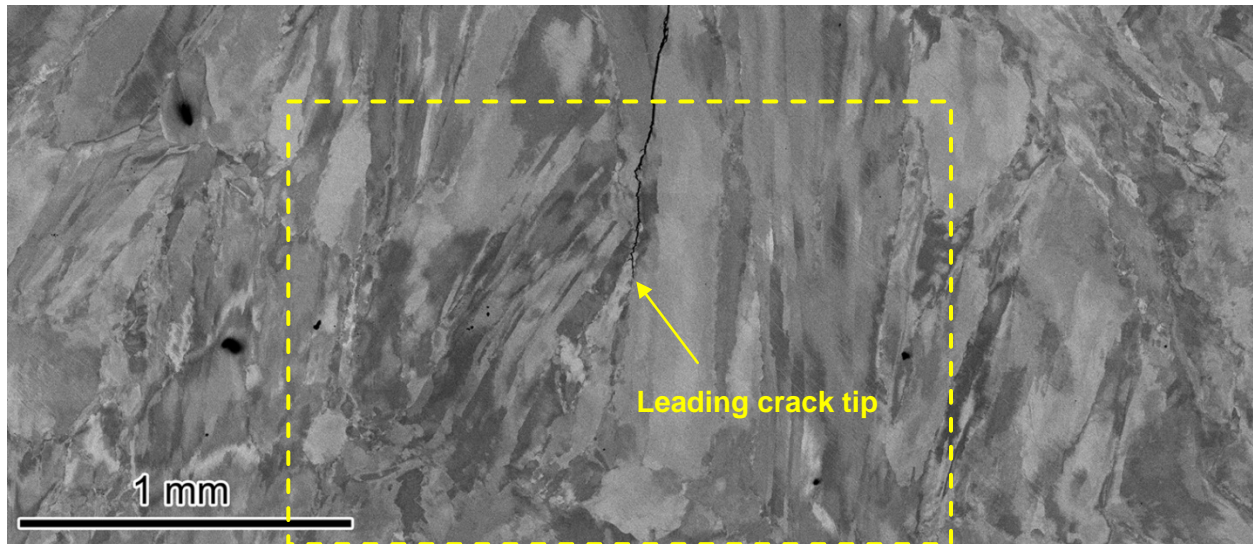
Figure 3-100 **SEM-BSE of the Leading Crack Tip in the CT040 Cross-Section Sample. Dashed Yellow Box Highlights the Region of Interest for EBSD Analysis in Figure 3-102**

Possible hot cracking

100 μm

1 μm

500 nm
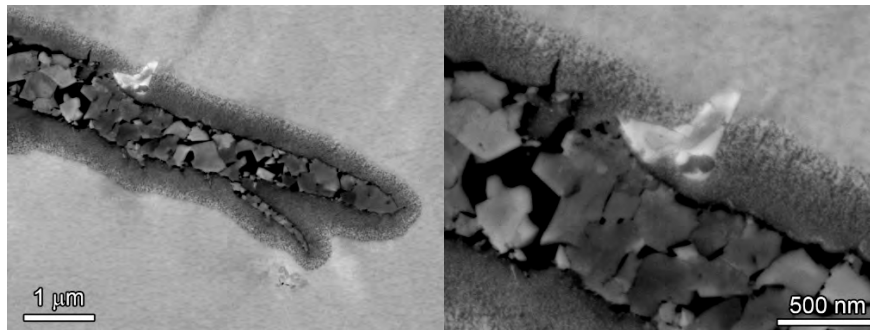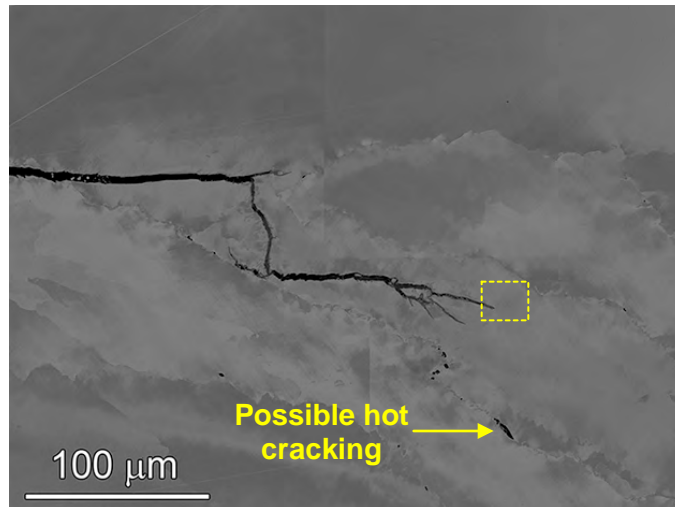
Figure 3-101 SEM-BSE High Magnification Micrograph of the Leading TG SCC Crack Tip in CT040 (higher magnification of the dashed yellow box shown in bottom figures). Note the Sample Is Rotated 90° from the Previous Figure
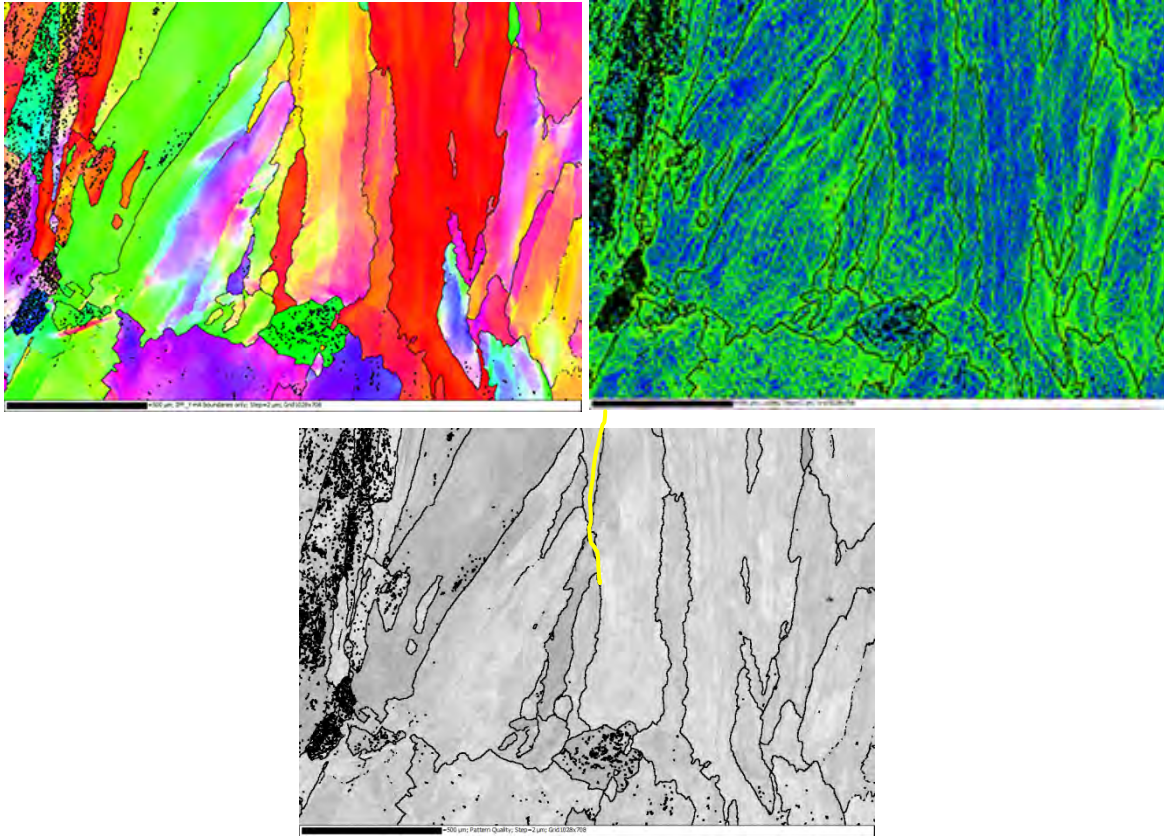
Figure 3-102 EBSD of CT040 (IPF, misorientation, and image quality maps) from the Yellow Dashed Box in Figure 3-100. The Yellow Line in the Pattern Quality Map Shows the Approximate SCC Crack
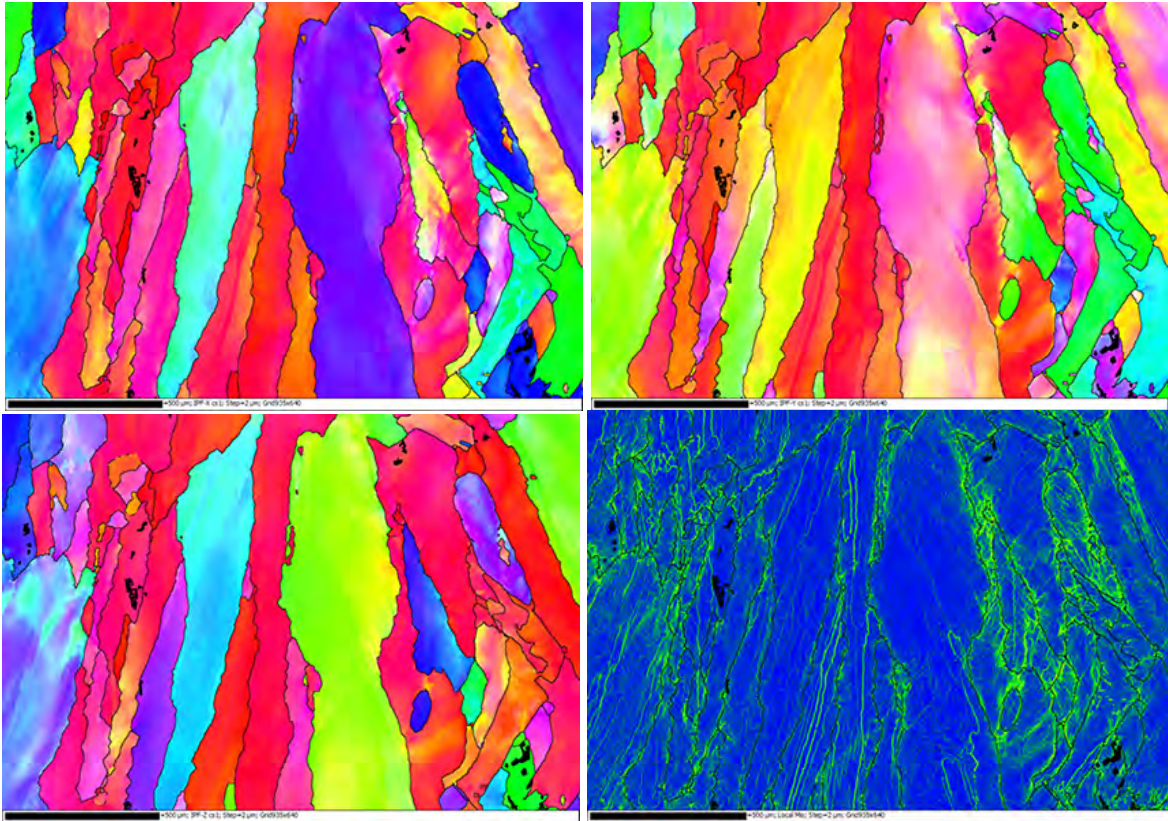
Figure 3-103   EBSD of CT040 (IPF maps and a misorientation map) from ~1-2 mm Ahead of the Yellow Dashed Box in Figure 3-100
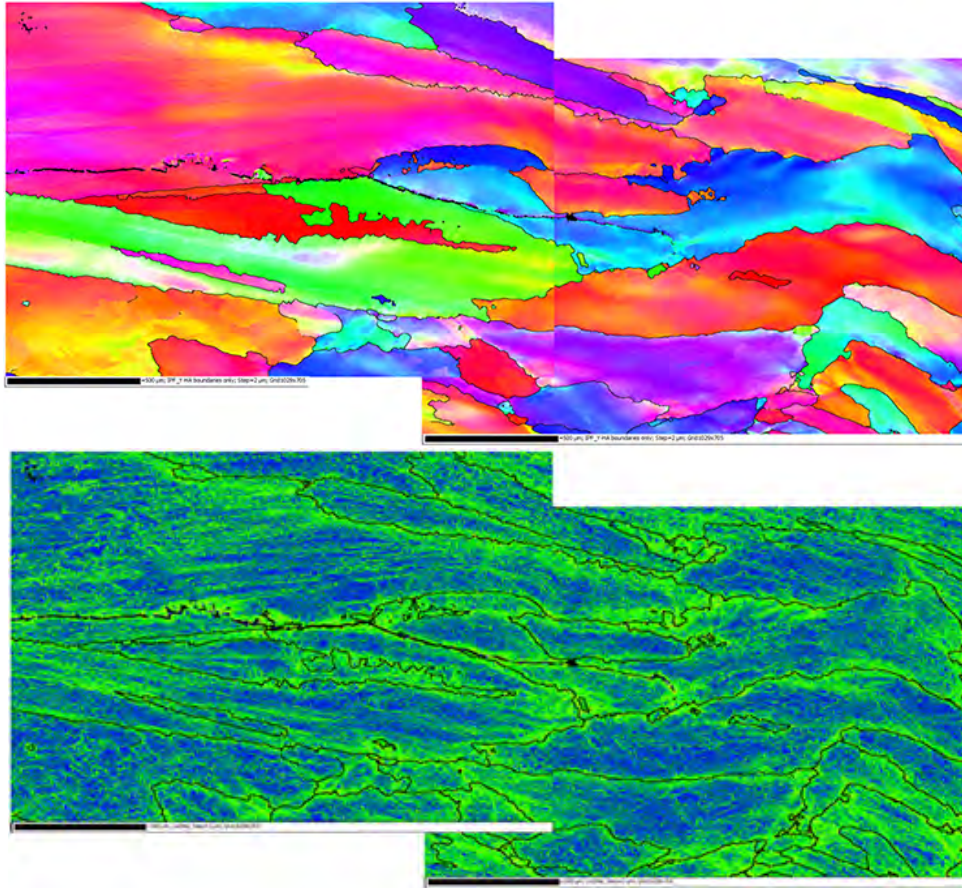
Figure 3-104 EBSD (IPF and misorientation density) of the Leading SCC Tip of CT041. Portions of the SCC Test Were Observed to Be IG, but the Leading Crack Tip Ended Transgranularly
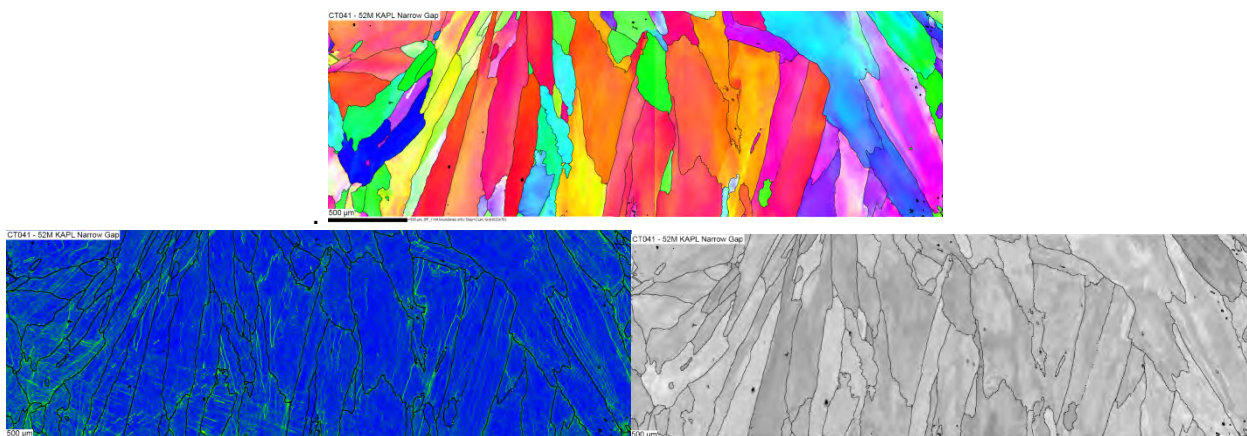
Figure 3-105 EBSD (IPF and misorientation density) ~1-2 mm Ahead of the Leading SCC Tip in CT041. Note That the Analysis Orientation Is Rotated 90 Degrees from the Previous Figure (i.e., the crack would be running top to bottom)
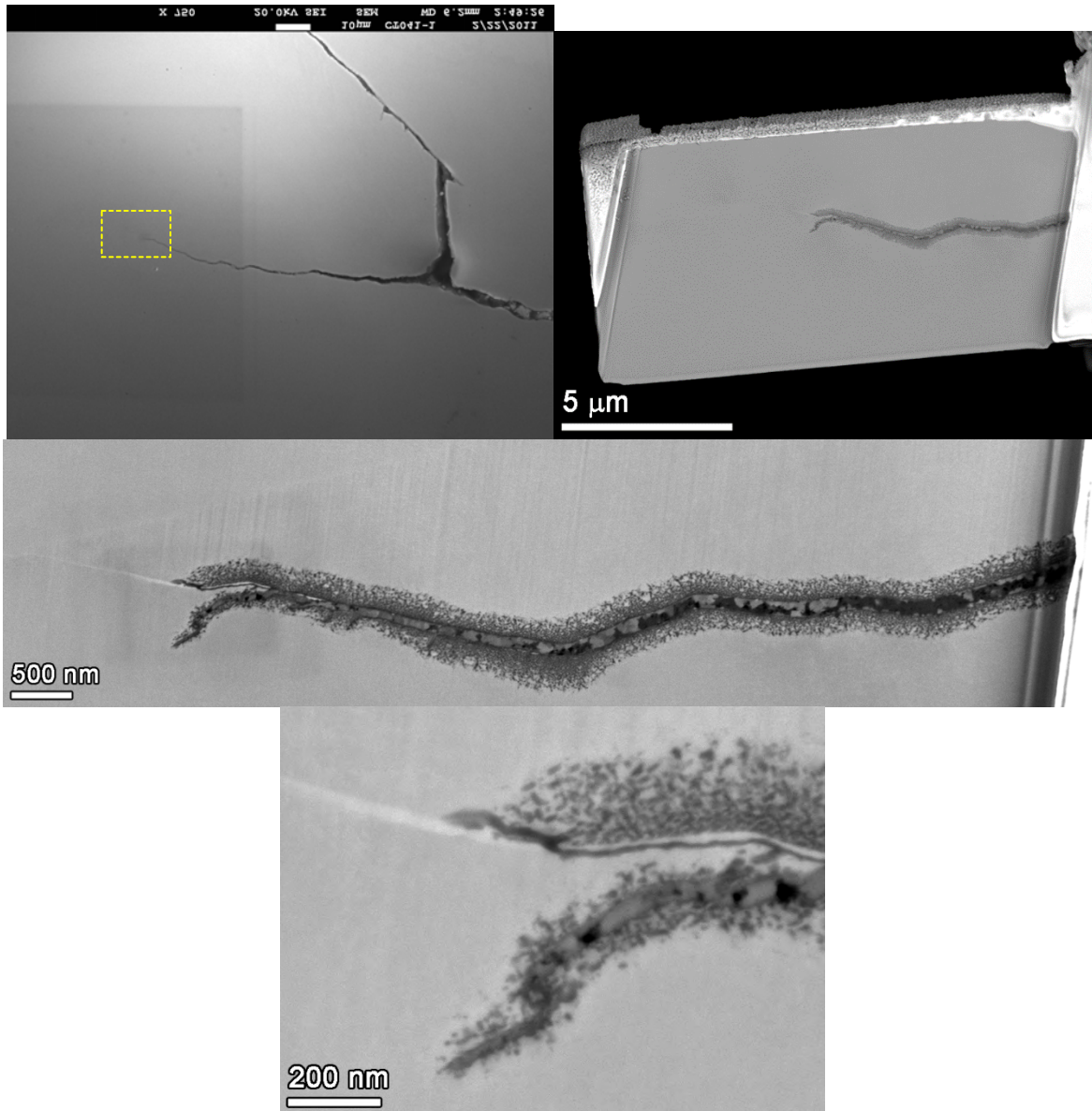
Figure 3-106 SEM Images of a Secondary Crack in CT041. A FIB-TEM Foil Was Prepared from This Region That Showed the IG Crack Split off into a TG Crack Before the End (identical orientation as Figure 3-99)
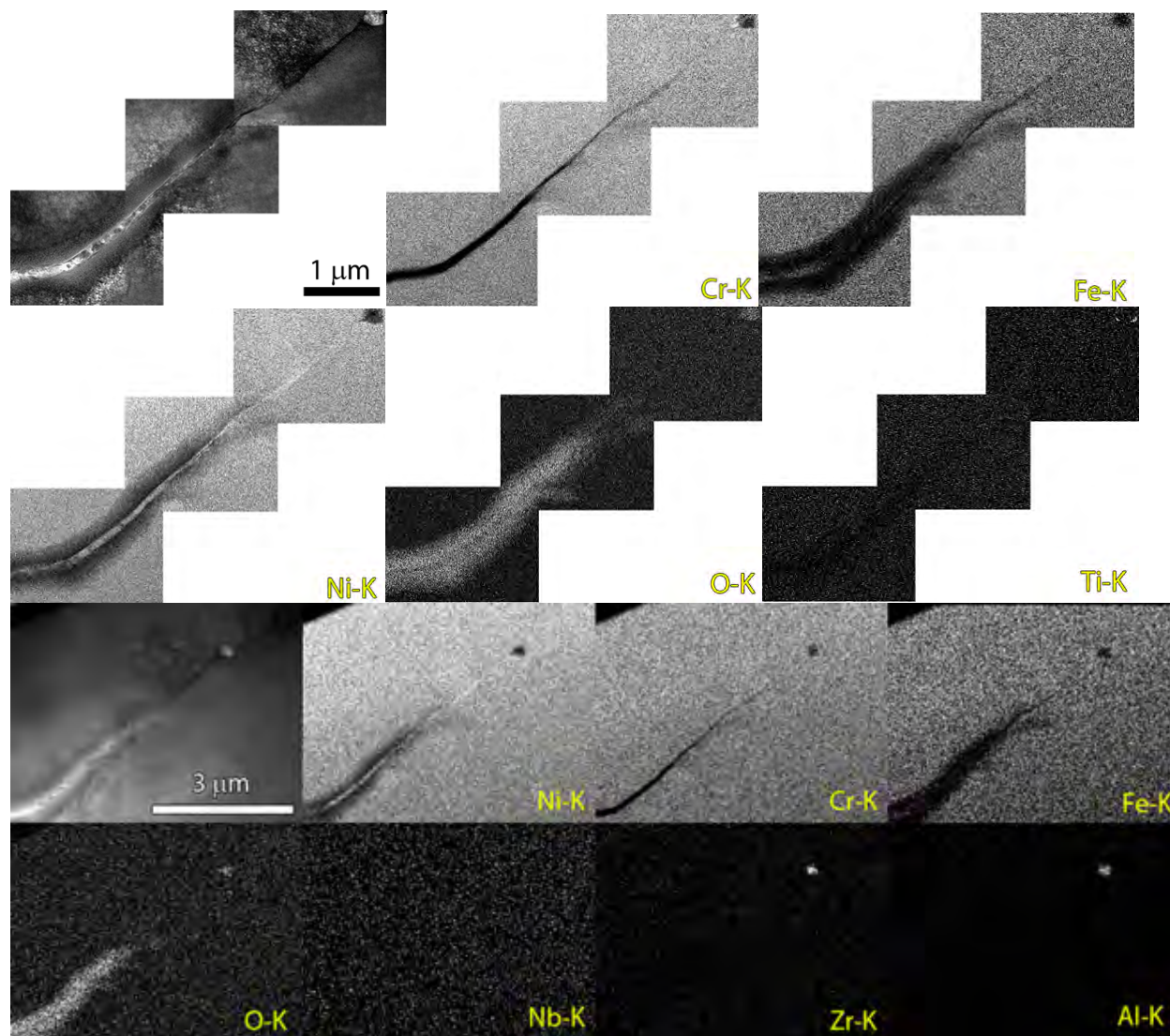
Figure 3-107 STEM (BF) and EDS Elemental Maps of the Secondary SCC Tip of CT041 Shown in Figure 3-106. Note That the Analysis Orientation of the SCC Tip Was Rotated from That Which Is Shown in Figure 3-106

3.2.3.2   KAPL Alloy 52M Narrow Gap Weld with Weld Cracks (CT042 and CT043)

The CT specimen aligned with the preexisting weld cracks (CT042) was cut from the weld blank so that the crack notch was ~2.8-3.0 mm from the region containing a low density of IG cracks. A standard precracking procedure in air was used to produce a precrack length of ~1.2 mm in both specimens, thus allowing ~1.6-1.8 mm of in-situ crack extension before reaching the region of material in CT042 containing cracks. The test was initiated in 350°C water, and an overview of the entire in-situ test is provided in Figure 3-108. As indicated by the overview plot, several different transitioning steps were applied in the first phase of the test. With no prior information about the cracking susceptibility of the material, it was decided to begin in-situ precracking and transitioning at a conservative R of 0.7, however low CGRs indicative of a highly resistant material were obtained and R was changed to a more aggressive value of 0.5 at 300 h as shown in Figure 3-109. CGR values measured at 0.001 Hz and at this same cyclic frequency with a 2.5 h hold were typical low values observed in other tests on alloy 152/52 as shown in

Figure 3-110. A higher CGR was not seen for the specimen aligned to intersect the preexisting weld cracks. Continuous cycling at 0.001 Hz was restarted at ~900 h and was followed by checking for an increase in susceptibility under two different sawtooth waveforms. The observed propagation rates were consistent with rates observed in prior steps, indicating typical response from both specimens.
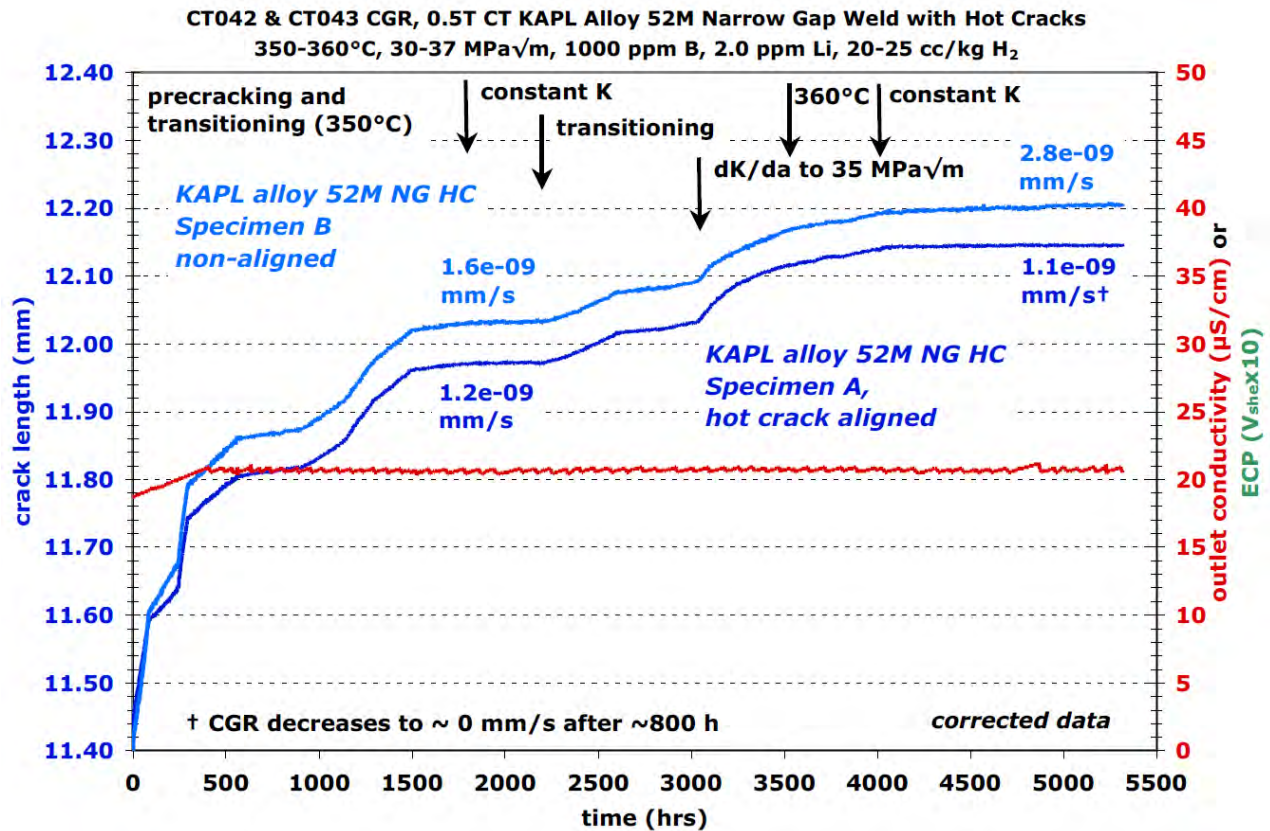
Figure 3-108 Overview of the Entire Test on the KAPL Alloy 52M Narrow Gap Weld Specimens (CT042 and CT043) with Preexisting Weld Cracks
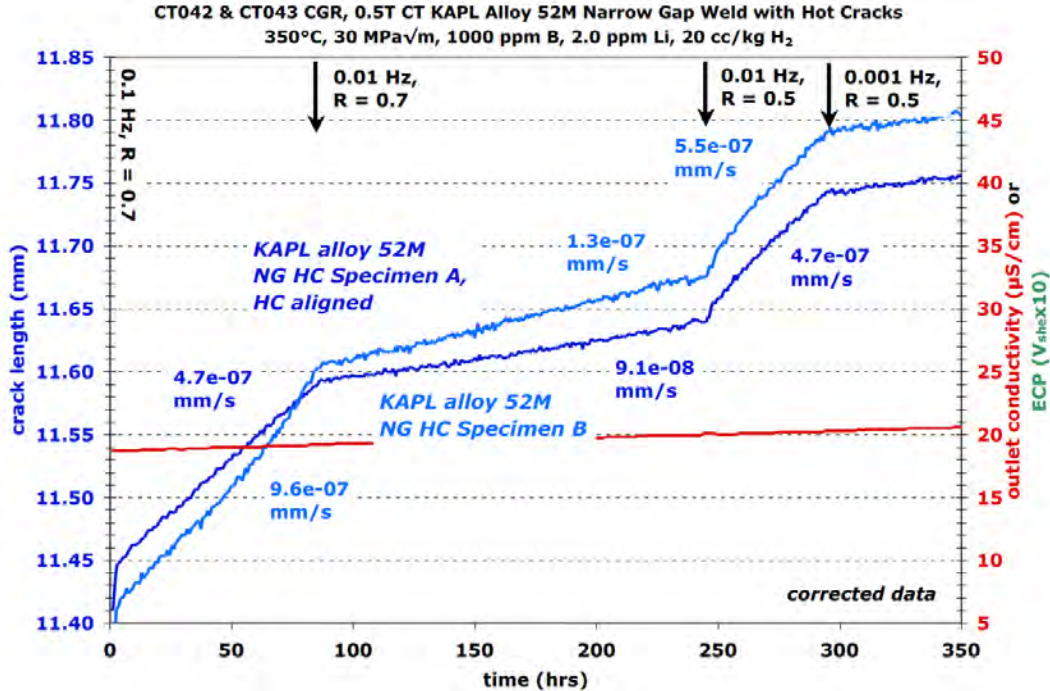
Figure 3-109 In Situ Precracking and Transitioning of the KAPL Alloy 52M Narrow Gap Weld Specimens (CT042 & CT043) with Known Hot Cracks
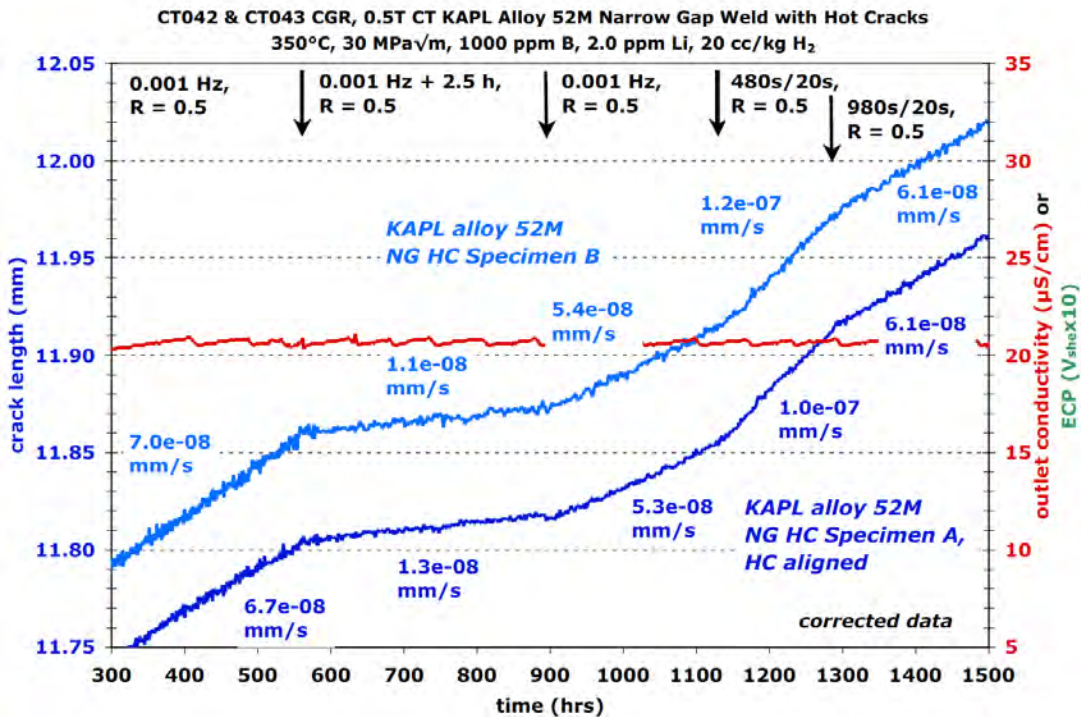
Figure 3-110 Continued Transitioning Steps Performed on the KAPL Alloy 52M Narrow Gap Weld Specimens (CT042 and CT043) with Weld Cracks

Having tried several different combinations of frequency and R during transitioning with typical alloy 152/52 crack growth response, and because the crack length was nearing the region in CT042 with aligned cracks, it was decided to transition to constant K. The sawtooth waveform

was converted to 0.001 Hz symmetric cycle + 2.5 h hold with R of 0.5 at 1500 h, and a steady rate of ~1.0x10^{-8} mm/s was observed in both specimens as shown in Figure 3-111. This rate was consistent with CGRs observed in other alloy 152/52 specimens, and the test was converted to constant K at ~1750 h. A steady propagation rate of ~1.4x10^{-9} mm/s was observed over the next ~400 h with no sign of increased propagation rate in the specimen aligned to intersect the IG weld cracks. Transitioning was restarted, and over the next several thousand hours of testing, cyclic loading conditions were varied, the K level was increase by 5 MPa√m (by dK/da), and the temperature was brought up to 360°C (see overview in Figure 3-108). Cyclic loading conditions were then returned to 0.001 Hz + 2.5 h hold where propagation rates of 1.6x10^{-8} and 1.9x10^{-8} mm/s were observed in the weld crack aligned and non-aligned specimens, respectively. These rates were ~1.7x higher than prior observations at these cyclic loading conditions, and the test was converted to constant K. Over the next 1300 h of testing, a relatively constant propagation rate of ~2.8x10^{-9} mm/s was observed (Figure 3-112) in the specimen not aligned with weld cracks while the specimen aligned to intersect preexisting cracks showed a steady rate of ~1.1x10^{-9} mm/s for 1000 hours and then no further growth was observed for the remaining 300 h. With lower propagation rates consistently observed in the aligned specimen, it was decided to end the test to examine the specimens. Table 3-17 lists a summary of the corrected step-by-step data obtained during this test.
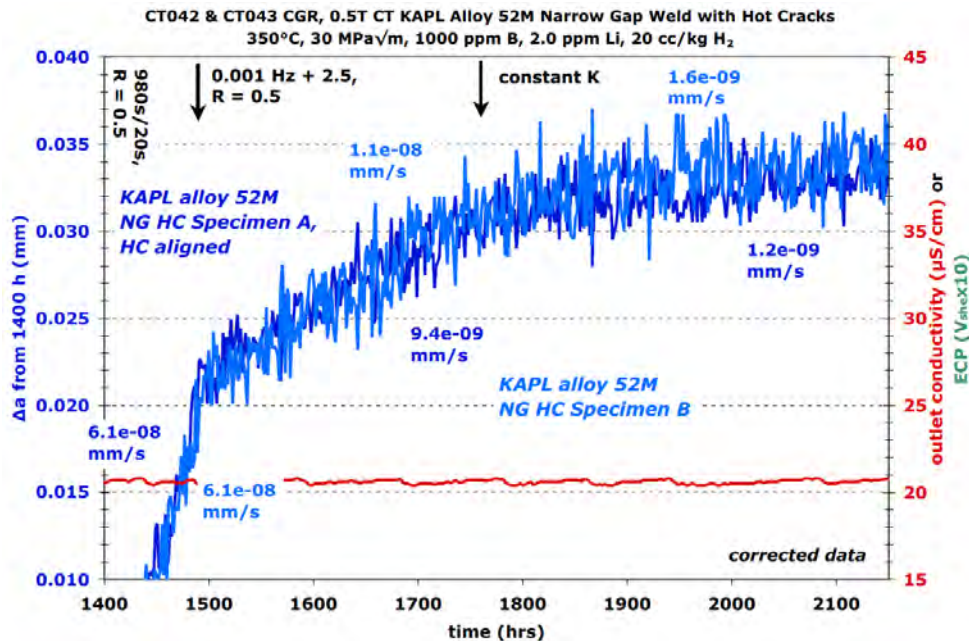
Figure 3-111 First Observation of Constant K Crack Growth Response on the KAPL Alloy 52M Narrow Gap Weld Specimens (CT042 & CT043) with Known Hot Cracks. Slightly Lower CGR in the Specimen Aligned to Intersect Hot Cracks
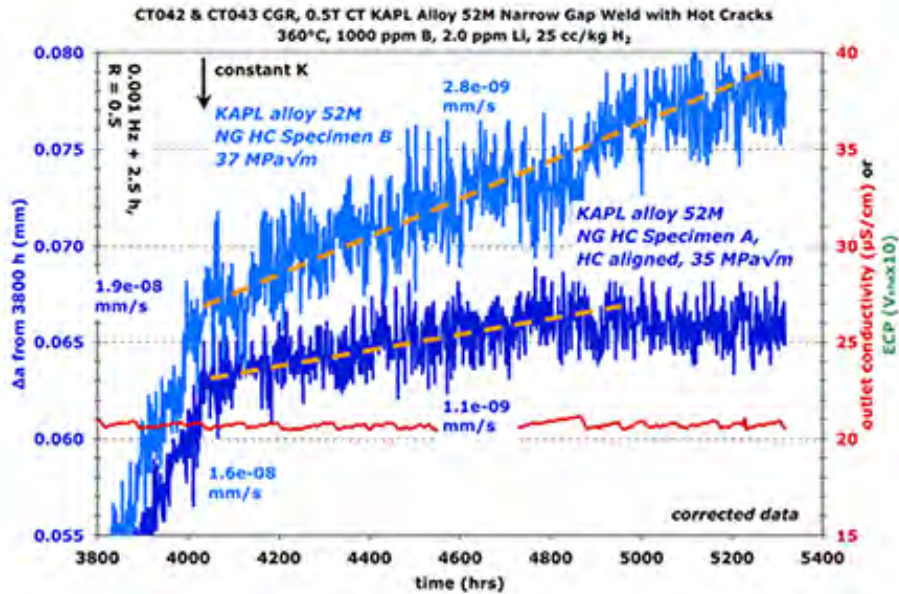
Figure 3-112 Second and Final Observation of Constant K Crack Growth Response of the KAPL Alloy 52M Narrow Gap Weld Specimens (CT042 & CT043) with Known Hot Cracks

Table 3-17 Corrected Data Summary for KAPL Alloy 52M Narrow Gap Weld Specimens CT042 and CT043 with Preexisting Weld Cracks

Test Phase	Dur-ation (h)	R	Freq (Hz)	Hold (h)	Water Chemistry Conditions	Temp (°C)	CT042 KAPL A52M NG HC aligned			CT043 KAPL A52M NG HC non-aligned		
							Kmax (MPa√m)	CGR (mm/s)	Approx. Crack Extension (mm)	Kmax (MPa√m)	CGR (mm/s)	Approx. Crack Extension (mm)
1	~3	0.3	5	0	air precrack	RT	21	3.7E-05	0.40	21	5.0E-05	0.40
2	~2	0.5	5	0	air precrack	RT	23	2.2E-05	0.35	24	3.2E-05	0.35
3	~2	0.6	5	0	air precrack	RT	25	1.3E-05	0.35	26	2.2E-05	0.35
4	~3	0.7	5	0	air precrack	RT	25	7.8E-06	0.20	26	1.3E-05	0.20
5	86	0.7	0.1	0	20 cc/kg H$_2$	350	30	4.7E-07	0.202	31	9.6E-07	0.281
6	159	0.7	0.01	0	20 cc/kg H$_2$	350	30	9.1E-08	0.049	31	1.3E-07	0.107
7	49	0.5	0.01	0	20 cc/kg H$_2$	350	30	4.7E-07	0.098	31	5.5E-07	0.145
8	261	0.5	0.001	0	20 cc/kg H$_2$	350	30	6.7E-08	0.060	32	7.0E-08	0.105
9	338	0.5	0.001	2.5	20 cc/kg H$_2$	350	30	1.3E-08	0.019	32	1.1E-08	0.051
10	241	0.5	0.001	0	20 cc/kg H$_2$	350	30	5.3E-08	0.040	32	5.4E-08	0.076
11	156	0.5	480/20	0	20 cc/kg H$_2$	350	30	1.0E-07	0.057	32	1.2E-07	0.093
12	193	0.5	980/20	0	20 cc/kg H$_2$	350	30	6.1E-08	0.042	32	6.1E-08	0.077
13	280	0.5	0.001	2.5	20 cc/kg H$_2$	350	30	9.4E-09	0.012	32	1.1E-08	0.048
14	420	---	const K	---	20 cc/kg H$_2$	350	30	1.2E-09	0.004	32	1.6E-09	0.038
15	405	0.6	0.001	0	20 cc/kg H$_2$	350	30	3.4E-08	0.040	32	3.6E-08	0.076
16	265	0.6	0.001	2.5	20 cc/kg H$_2$	350	30	6.3E-09	0.010	32	6.6E-09	0.044
17	175	0.5	0.001	1	20 cc/kg H$_2$	350	30	1.6E-08	0.009	32	1.6E-08	0.045
18	43	0.5	0.001	1	20 cc/kg H$_2$	350	30->35	1.0E-07	0.014	32->37	1.2E-07	0.045
19	413	0.5	0.001	1	20 cc/kg H$_2$	350	35	3.2E-08	0.067	37	3.7E-08	0.095
20	190	0.5	0.001	2.5	20 cc/kg H$_2$	350	35	1.4E-08	0.010	37	2.1E-08	0.047
21	355	0.5	0.001	2.5	25 cc/kg H$_2$	360	35	1.6E-08	0.019	37	1.9E-08	0.051
22	1289	---	const K	---	25 cc/kg H$_2$	360	35	1.1E-09	0.003	37	2.8E-09	0.047

3-99

Post-test examinations consisted of characterizing both the crack growth surface and a series of crack profiles obtained from side surfaces of the crack. To accomplish this, both specimens were serially sectioned as shown in Figure 3-113 prior to air fatiguing open the specimens. Five slices were obtained from the CT042 (weld cracks aligned), but due to a machining error, only four slices were obtained from CT043. The serial slices were placed in metallography mounts and polished to a high luster using colloidal silica as the final polishing agent. Crack profile images for CT042 and CT043 are shown in Figures 3-114 and 3-115, respectively. The crack profiles of CT042 show that the density of the preexisting IG cracks was too low and the distance from the SCC crack was too far for any cracks to be intersected by the crack front. In addition, the grain boundaries (and IG weld cracks) were at a steep angle to the geometric crack plane of the specimen, and the steep angle made it difficult for the SCC crack to grow favorably along the grain boundaries. Somewhat surprisingly, the crack profile images of the specimen that was not supposed to be aligned with weld cracks shows that a few IG cracks were in the vicinity of the crack path. However, as with the crack-aligned specimen, only a few weld cracks were present, and they were far from the SCC crack and at a steep angle to it. The grain boundaries are much better aligned with the geometric crack plane of the specimen. Instances of growth along grain boundaries are apparent, and the more favorable alignment is likely responsible for the higher constant K CGR in CT043.

Figure 3-113 Post-Test Serial Sectioning Plan for KAPL Alloy 52M NG Weld Specimens with Weld Cracks (CT042 and CT043)
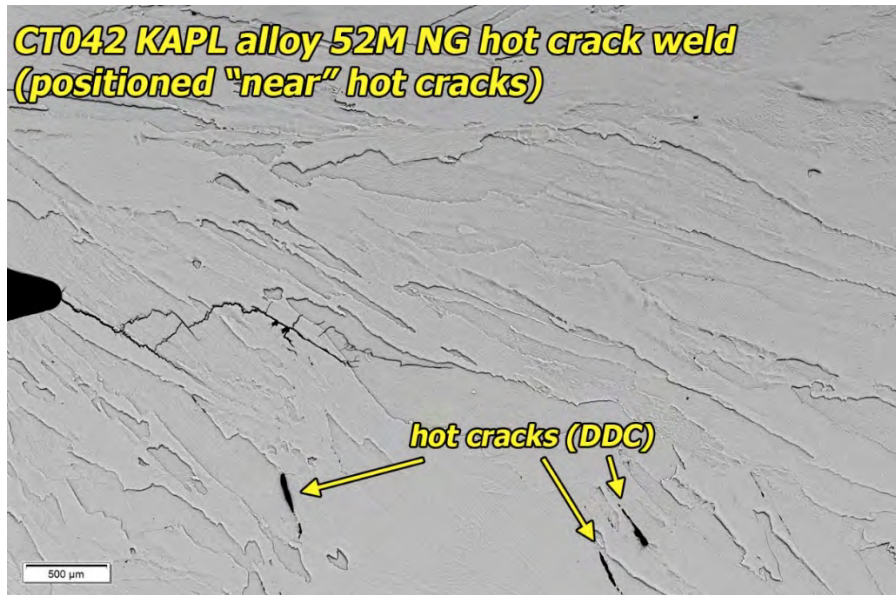
Figure 3-114 Crack Profile of Images from CT042, the Weld Specimen Aligned with Hot Cracks
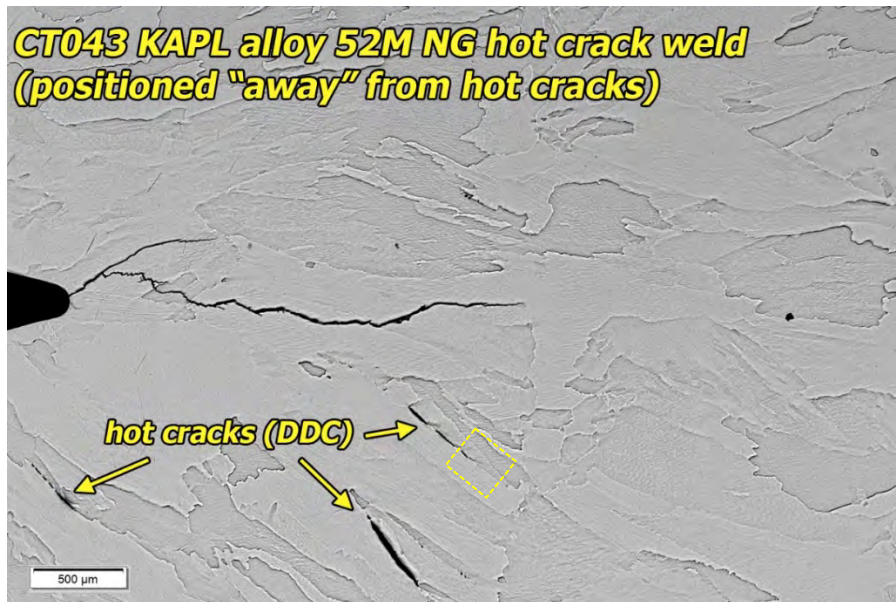
Figure 3-115 Crack Profile of Images from CT043, the Weld Specimen Not Aligned with IG Weld Cracks. The Profile Images Show Hot Cracks Below the SCC Test Plane

Figures 3-116 and 3-117 show the crack growth surface of the remaining piece of the CT specimens that was not used for crack profile observations. The edge of the specimen corresponding to the last serial section taken from the specimens is indicated, and the yellow line denotes the boundary between air precracking and in situ testing. The in-situ crack growth surface of the crack-aligned specimen (CT042, Figure 3-116) shows a lower amount of growth. A large number of ridges run along the length of the crack, and it is thought that these indicate jumps in crack growth plane. The areas inside the yellow boxes are the only regions along the crack surface that are clearly IG based on the optical images. No obvious indications of

3-101

intersected weld cracks are present. While there are no fingers of obvious SCC extension on the crack growth surface of the non-aligned specimen (CT043, Figure 3-117), the greater amount of in-situ crack extension and the fewer number of ridges are suggestive of better SCC engagement. As with CT042, there are no obvious indications of intersected weld cracks.

The post-test examination of these two specimens has revealed a density of weld cracks too low or too far from the SCC crack plane to provide any insight as to whether such preexisting IG cracks can affect SCC crack growth. An unintended outcome of the test on these two specimens is, however, a better understanding of the importance of grain boundary orientation relative to the geometric crack plane of the specimens. With these highly resistant welds that have very large, elongated grains with apparently low susceptibility to IG cracking, the difference in the CGR of the two specimens suggests that the highest possible CGR can only be determined if the grain boundaries are well aligned with the geometric crack growth plane of the specimen.

When considering the effect of poor welding conditions on CGR, there is also the possibility that unfavorable microstructure and/or segregation may be present in this weld containing hot cracks. One method to assess this affect is to compare the CGR of these specimens to the KAPL NG specimen that was fabricated without re-fuse passes (CT040). Since the grain boundaries in CT040 were favorably aligned with the geometric crack plane, CT043 with its favorable grain boundary orientation is the appropriate specimen with weld cracks to use for the comparison. Using the highest constant K CGR observed, CT043 exhibits a ~2x higher CGR than the standard specimen (CT040). This may indicate a small detrimental effect of chemistry or microstructure on SCC susceptibility for welds produced using parameters that promote weld cracks, however the current results are likely within the test reproducibility.
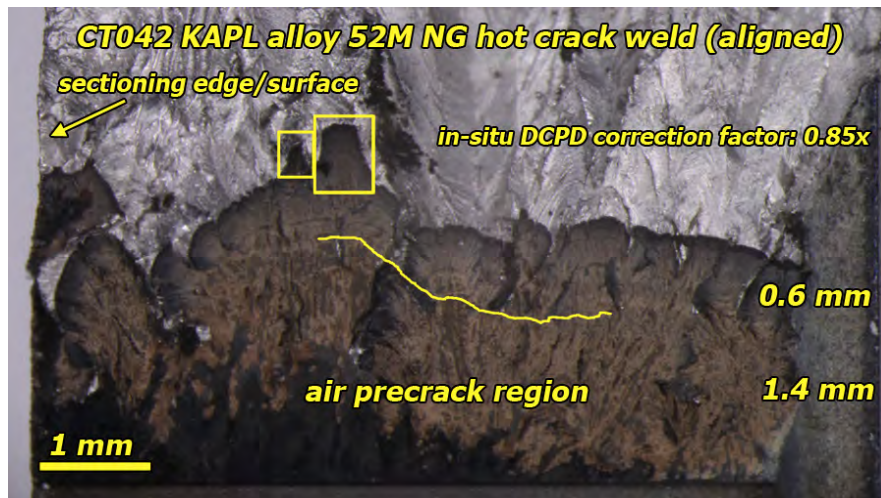
Figure 3-116 Crack Growth Surface from CT042, the Weld Specimen Aligned with Hot Cracks
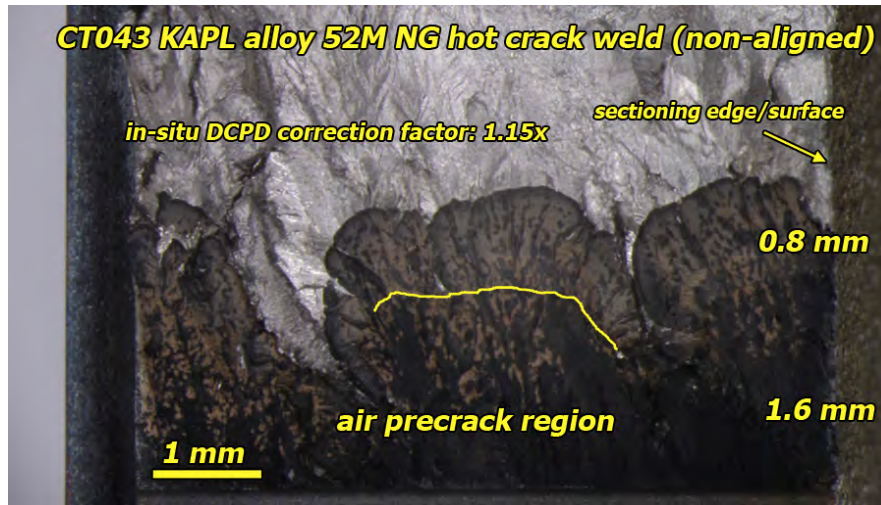
Figure 3-117 Crack Growth Surface from CT043, the Weld Specimen Not Aligned with Hot Cracks

SEM-BSE analysis of the leading SCC crack tip was performed (Figure 3-118) and illustrates the high level of local deformation as evidenced by the mottled contrast in the grains surrounding the tip. Higher magnification of the leading tip shows that it ended intergranularly, but the penetrative oxidation surrounding the entire tip suggests that it was not an active crack tip at the end of the test. As shown in Figure 3-115, a TEM sample was prepared from an IG weld crack adjacent to the SCC plane in CT043 (Figure 3-119) and was subsequently analyzed (Figures 3-120 and 3-121). The discontinuous nature of the weld cracks can be observed in the SEM-BSE image in Figure 3-119, as well as very small (75-100 nm), IG precipitation. No apparent penetrative oxidation is observed in conjunction with the hot cracks, which suggests no water reached these preexisting cracks during SCC testing. Higher magnification STEM/EDS elemental mapping of the IG cracks and the adjacent grain boundary shows the presence of small (less than 100 nm) Cr, Ti and Nb rich precipitates, but no unique chemistry associated with the cracks themselves.
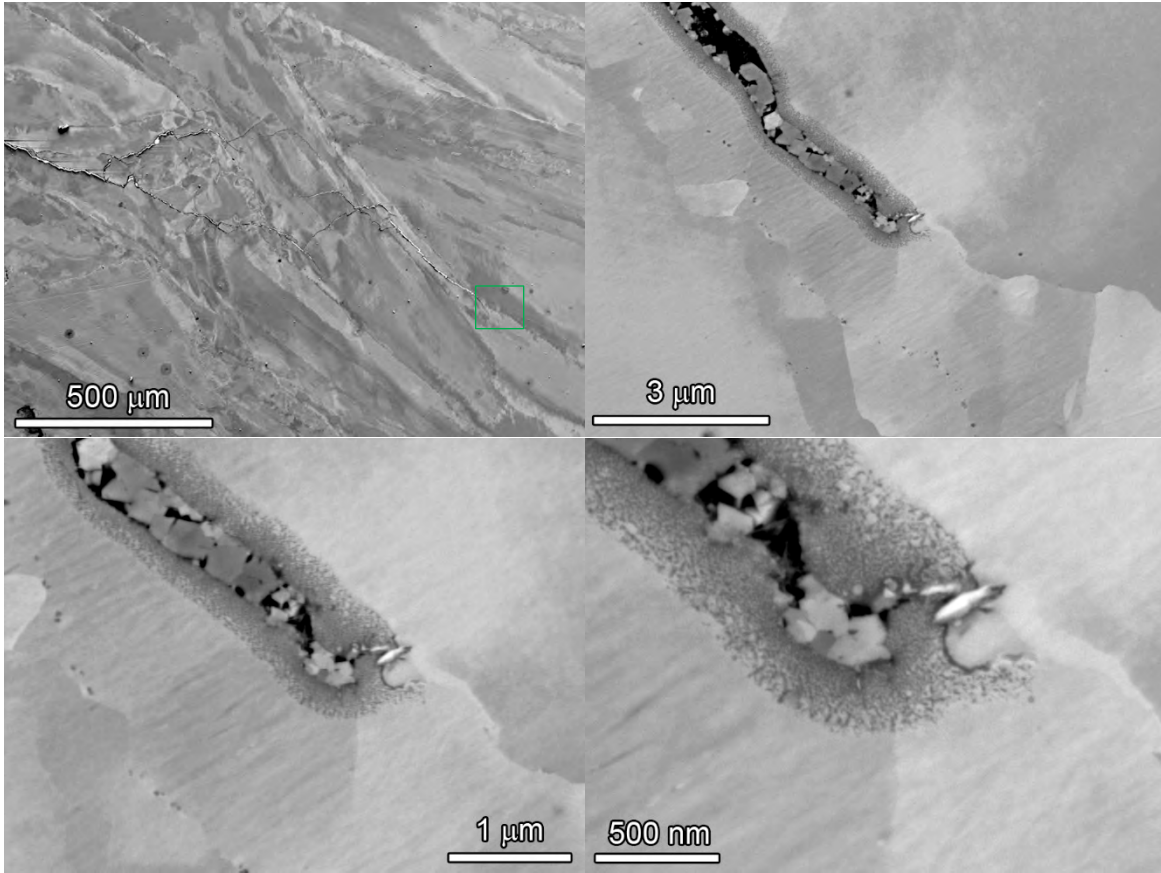
Figure 3-118 SEM-BSE Image of the Side Surface of the Leading Crack Growth Tip of CT043
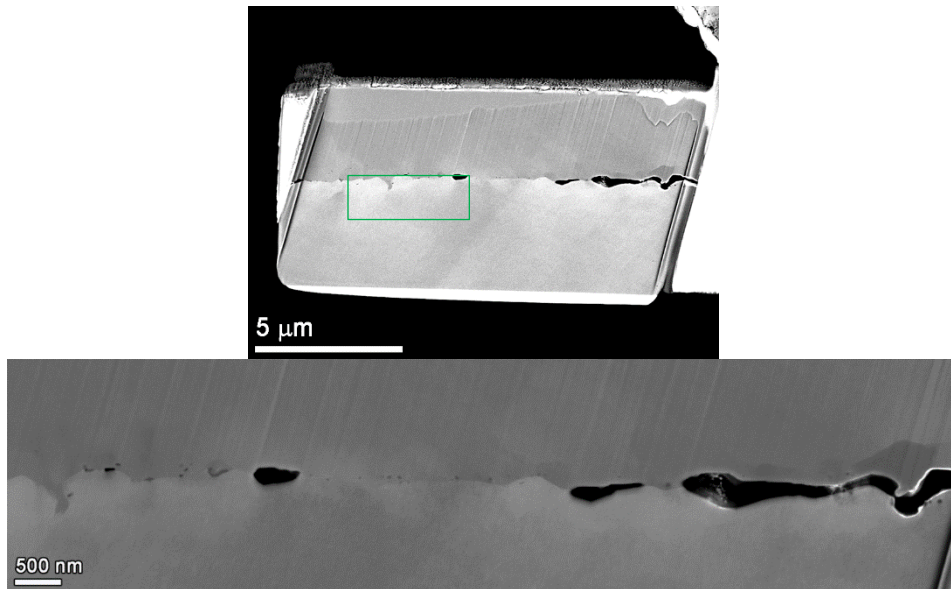
Figure 3-119 SEM-BSE Image of a TEM FIB Sample of a Weld Crack in CT043 Taken from the Dashed Yellow Box Region of Figure 3-115. The Solid Green Box in the Top Image Shows the Region of Interest in the Higher Magnification Image at the Bottom
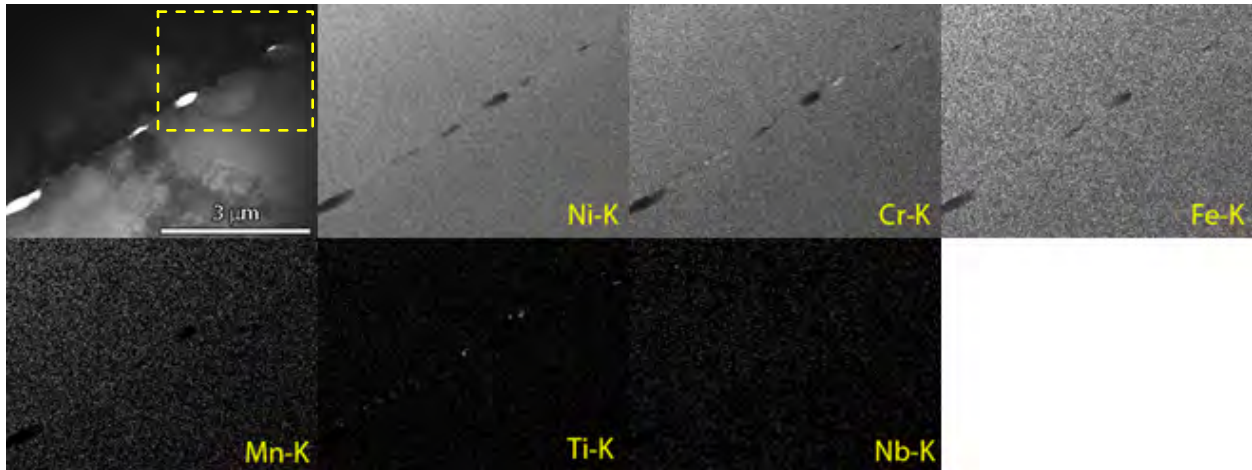
Figure 3-120 STEM BF Image and EDS Elemental Maps of the IG Weld Crack Region in CT043. A Higher Magnification Examination Was Taken of the Dashed Yellow Box and Is Shown in Figure 3-121. No O-K Signal Was Detected in These Cracks and Grain Boundary Precipitates Are Enriched in Cr and Ti

Figure 3-121 STEM-BF Image and EDS Elemental Maps of the Weld Crack in CT043 from the Yellow Dashed Box in Figure 3-120. At Higher Magnification, Small (100 nm) Nb-Rich Precipitates Are Observed on the Grain Boundary

3.2.4   Special Metals Alloy 52MSS Weld (CT050)

The alloy 52MSS weld was provided to PNNL and EPRI by Special Metals and was a V-groove weld (NX77W3UK) in alloy 690 plate. Alloy 52MSS is identified as ERNiCrFe-13 and has been proposed as a replacement for alloy 52M (ERNiCrFe-7A) primarily for its improved resistance to ductility dip cracking (DDC). A standard 0.5T CT specimen was machined and was tested in combination with an ANL alloy 152v2 specimen CT049 discussed earlier in the chapter. The alloy 152v2 CT049 was a higher priority specimen and was the control specimen during the experiment. A summary of test conditions and corrected response for the alloy 52MSS CT050 during each phase of the test is shown in Table 3-18 and an overview of the test highlighting constant K evaluations is presented in Figure 3-122. The measured SCC growth rates are also listed in Table 3-19 along with their corresponding K levels that were decreasing during the test because the cyclic CGRs were much higher for the controlling alloy 152v2 CT049 specimen. Load shedding to maintain a constant K for CT049 resulted in a lower applied K for CT050.

Table 3-18   Corrected Data Summary for SM Alloy 52MSS Narrow Weld Specimen CT050

Test Phase	Dura-tion (h)	R	Freq (Hz)	Hold (h)	Water Chem. Conditions	Temp (°C)	Kmax (MPa√m)	CGR (mm/s)	Approx. Crack Ext (mm)
1	~3	0.3	5	0	air precrack	RT	21	5.2E-05	0.40
2	~2	0.5	5	0	air precrack	RT	23	3.2E-05	0.35
3	~2	0.6	5	0	air precrack	RT	25	2.2E-05	0.35
4	~3	0.7	5	0	air precrack	RT	25	8.6E-06	0.20
5	8	0.5	0.1	0	25 cc/kg H_2	360	30	5.2E-06	0.141
6	85	0.5	0.01	0	25 cc/kg H_2	360	30	9.5E-07	0.274
7	258	0.5	0.001	0	25 cc/kg H_2	360	30	1.7E-07	0.147
8	119	0.5	980/20	0	25 cc/kg H_2	360	30	1.7E-07	0.066
9	480	0.5	0.001	2.5	25 cc/kg H_2	360	30	1.9E-08	0.039
10	310	---	const K	---	25 cc/kg H_2	360	30	1.9E-09	0.003
11	53	0.5	0.001	2.5	25 cc/kg H_2	360	30	Not Meas.	0.003
12	114	0.5	600/12	0	25 cc/kg H_2	360	29	2.4E-07	0.084
13	220	0.5	600/12	1	25 cc/kg H_2	360	29	3.3E-08	0.035
14	93	0.5	600/12	2	25 cc/kg H_2	360	29	2.5E-08	0.010
15	367	0.5	600/12	1	25 cc/kg H_2	360	29	4.4E-08	0.060
16	134	0.5	600/12	2	25 cc/kg H_2	360	29	2.7E-08	0.012
17	267	---	const K	---	25 cc/kg H_2	360	29	1.7E-09	0.001
18	156	0.5	0.01	0	25 cc/kg H_2	360	28	8.9E-07	0.489
19	65	0.5	0.001	0	25 cc/kg H_2	360	28	1.0E-07	0.027
20	93	0.5	600/12	0	25 cc/kg H_2	360	28	2.1E-07	0.064
21	76	---	const K	---	25 cc/kg H_2	360	28	<5E-10	0.006
22	115	0.5	600/12	0	25 cc/kg H_2	360	27	1.9E-07	0.073
23	172	0.5	1000/12	0	25 cc/kg H_2	360	27	1.1E-07	0.074
24	213	0.5	1000/12	2	25 cc/kg H_2	360	27	2.1E-08	0.016
25	380	0.5	1000/12	10	25 cc/kg H_2	360	27	5.7E-09	0.007
26	611	---	const K	---	25 cc/kg H_2	360	27	9.2E-10	0.003
27	116	0.5	600/12	0	25 cc/kg H_2	360	27	1.3E-07	0.049
28	70	0.35	600/12	0	25 cc/kg H_2	360	26	2.9E-07	0.072
29	95	0.35	1000/12	0	25 cc/kg H_2	360	26	1.7E-07	0.058
30	240	0.35	5000/12	0	25 cc/kg H_2	360	26	3.8E-08	0.035
31	348	0.35	25000/12	0	25 cc/kg H_2	360	26	1.2E-08	0.016
32	240	0.35	25000/12	3.5	25 cc/kg H_2	360	25	1.2E-08	0.009
33	849	---	const K	---	25 cc/kg H_2	360	25	3.9E-10	0.003
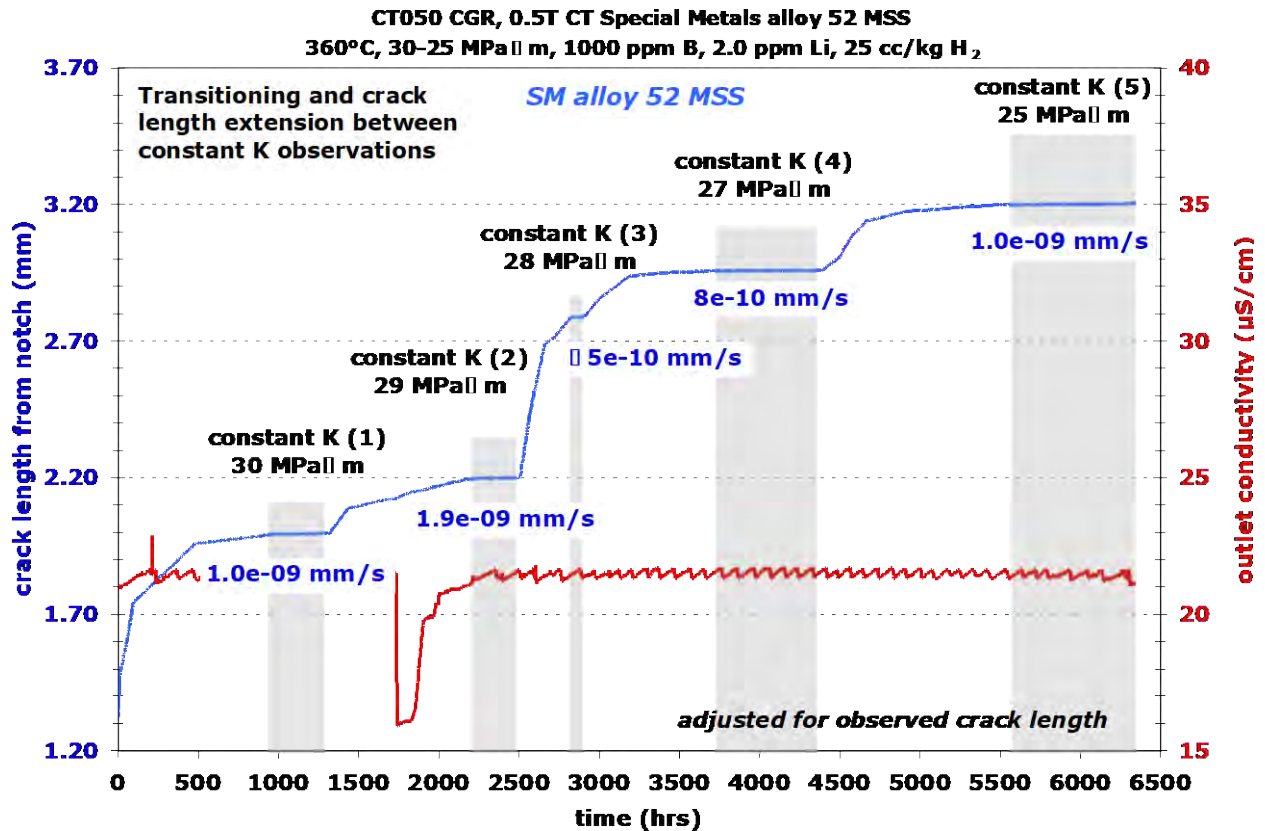
Figure 3-122 Overview of the Crack Growth Response of the Alloy 52MSS Specimen CT050

Table 3-19 SCC Crack Growth Test Conditions for CT050 Showing the CGRs for Each Constant K Evaluation

Loading Condition	K (MPa√m)	CGR (mm/s)
cyclic loading	30-25	Cyclic loading CGRs were comparable to prior tests on alloy 52/52M.
1st constant K	30	**1.0x10⁻⁹**
2nd constant K	29	**1.9x10⁻⁹**
3rd constant K	28	**≤5x10⁻¹⁰**
4th constant K	27	**~8x10⁻¹⁰**
5th constant K	25	**1.0x10⁻⁹**

Two examples of the low SCC growth rates measured at constant K are given in Figures 3-123 and 3-124 out of the five attempts made during the experiment. These evaluations revealed a reasonably stable crack growth response at ~1.9 and 1.0×10^{-9} mm/s over ~270 and 850 hours, respectively. It is important to note that the measured CGRs for various cycle + hold loading did not indicate SCC engagement or significant propagation during the hold times examined

between 1 and 10 hours. The SCC transitioning approach employed for this test was selected to match the cyclic loading (rise/fall times of 600/12 and 1000/12 seconds + hold times) previously used by ANL for tests on the alloy 152v2 material. This approach was specifically requested for the ANL alloy 152v2 control specimen CT049. As a result, transitioning was not optimized to promote SCC engagement in the alloy 52MSS, nor was the applied K. Nevertheless, crack growth response during the ~6400 h test suggested that this material is resistant to corrosion fatigue and SCC in PWR primary water. Supporting this conclusion is the lack of IG cracking produced during most of the test as illustrated by the crack growth surface in Figure 3-125 and cross-section images in Figures 3-126 and 3-127. However, somewhat surprisingly some evidence for localized IG crack growth was discovered at the end of the test perhaps promoted by the alternative transitioning in steps 28-32 where a low R value (0.35) was applied along with long rise times (5000-25000 seconds). This result suggests that transitioning tailored for the alloy 52MSS specimen may be effective to increase SCC engagement and a second test may be warranted to assess SCC behavior.
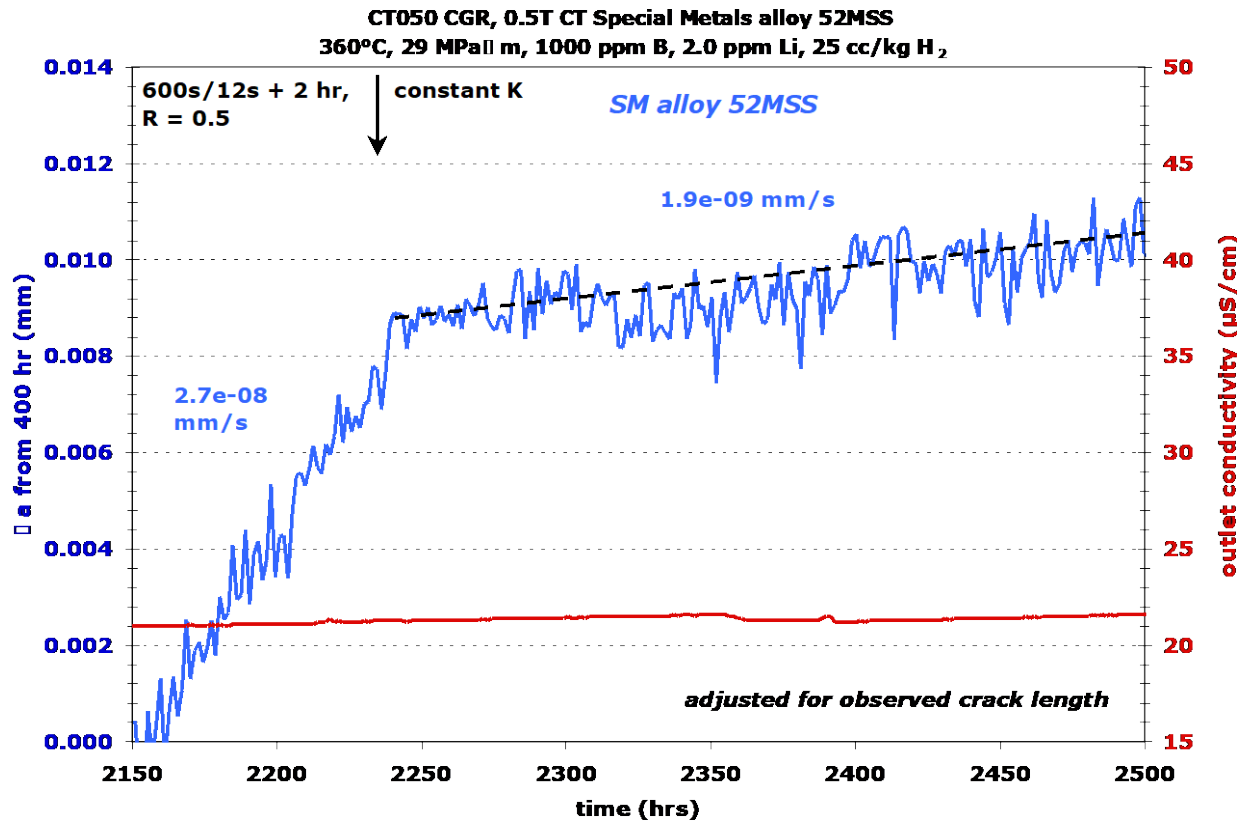
Figure 3-123 Second Observation of Constant K Crack Growth Response on the Alloy 52MSS Specimen CT050
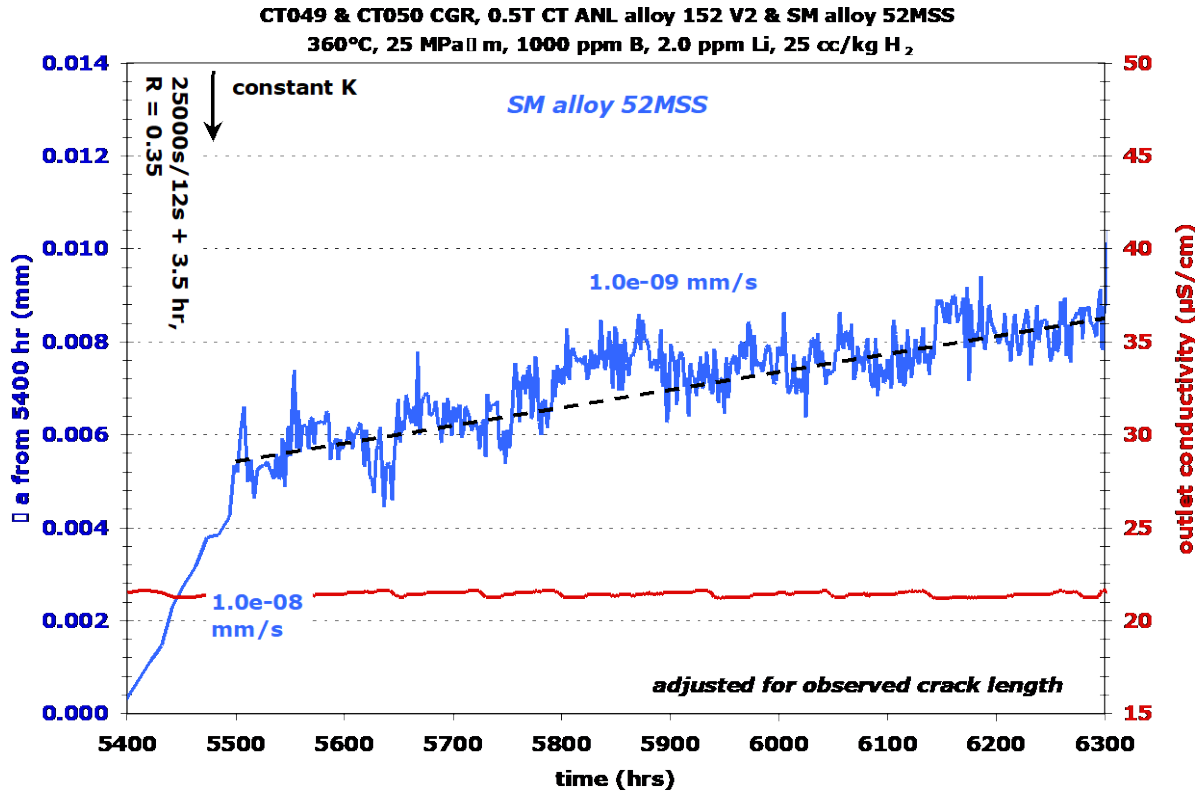
Figure 3-124 Fifth and Final Observation of Constant K Crack Growth Response on the Alloy 52MSS Specimen CT050
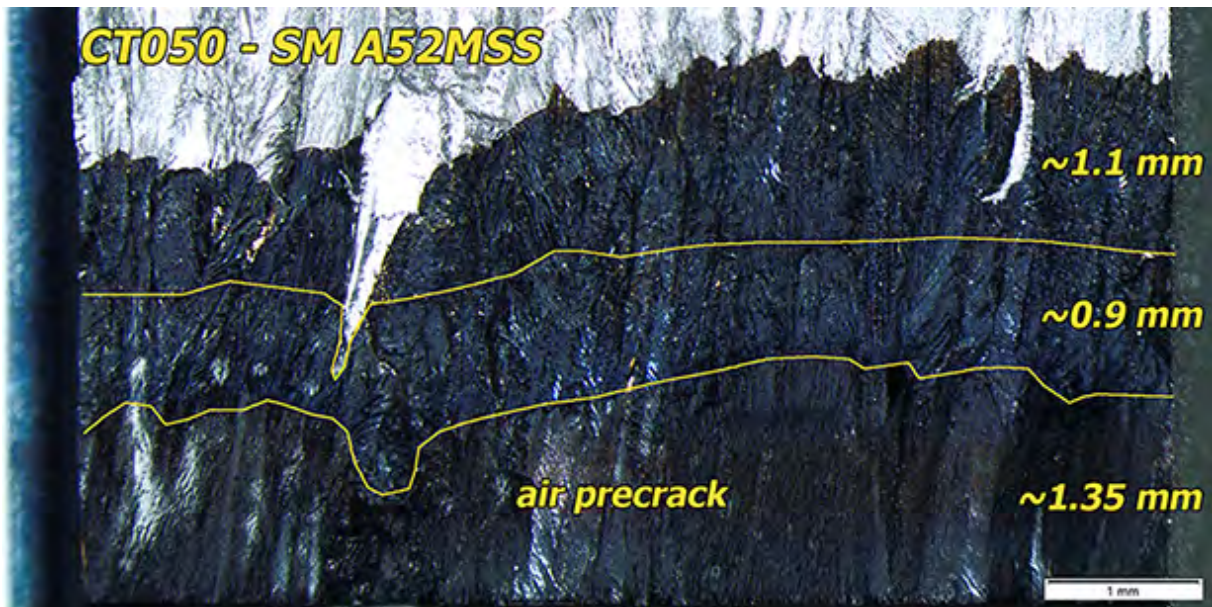
Figure 3-125 Optical Micrograph of the CT050 Crack Growth Surface Showing Primarily TG Cracking. Small Partially IG Protrusions Can Be Seen at the Crack Front
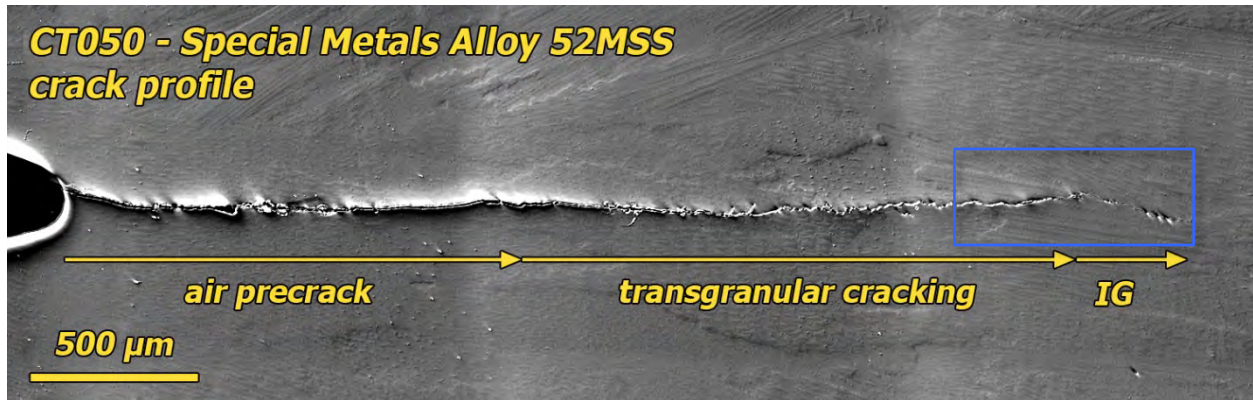
Figure 3-126 SEM-SE of the Cross-Section of CT050 Showing the First Part of the Crack Growth Test Being TG and the Last 250 µM of the Test Being IG
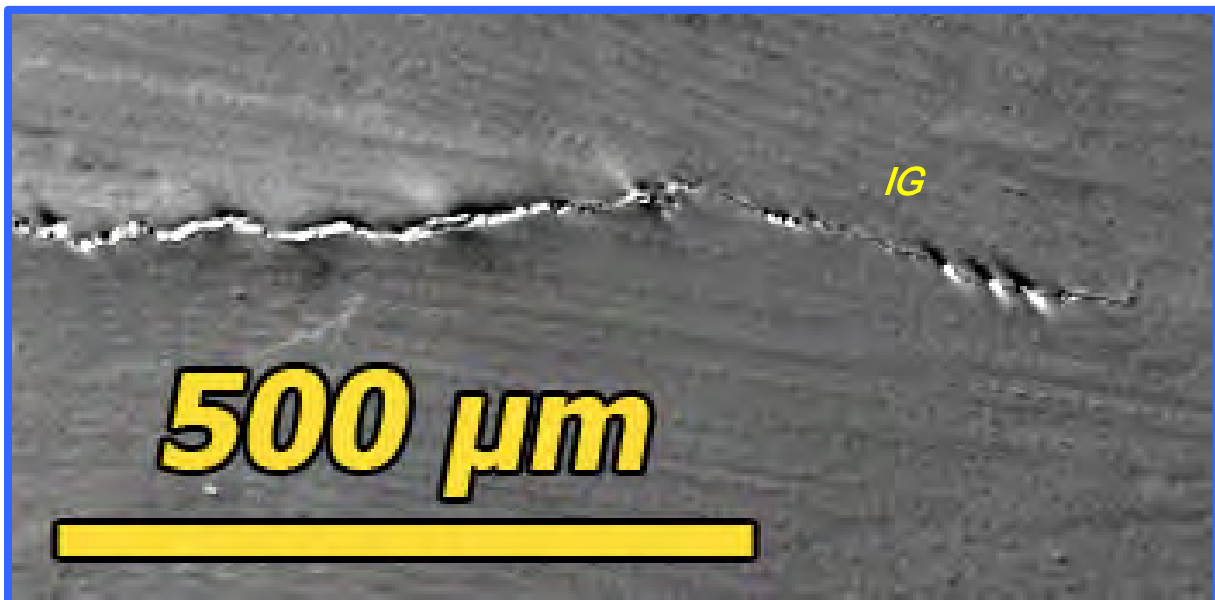
Figure 3-127 SEM-SE of the Cross-Section of CT050 Showing the Final 250 µm of the Crack Growth Test Being IG

3.3   Summary of SCC Behavior in High Cr, Ni Alloy Welds

The CGR response of industry-made alloy 152, 152M, 52, 52M and 52MSS weld mockups was investigated in simulated PWR primary water with most tests performed at 360°C with a dissolved hydrogen concentration of 25 cc/kg (corresponding to the Ni/NiO stability line). A summary of the measured constant K CGR response for the weld metal specimens at PNNL is shown in Figure 3-128. More than 60 measurements are identified with all CGRs $<5x10^{-9}$ mm/s and most $<2x10^{-9}$ mm/s. These SCC propagation rates for the high Cr weld metals are >100X lower than the alloy 182/132 disposition curve also shown in Figure 3-128. Specific information on the individual welds is provided in Table 3-20 so that the data points can be linked back to the reported test data earlier in this chapter. Interestingly, slightly higher CGRs can been seen for several of the alloy 52 and 52M welds, while our general experience found that the alloy 152

welds exhibited a higher degree of IG cracking on the post-test crack-growth surface. Estimated IG engagement is compared to the measured SCC CGRs in Figure 3-129 and demonstrates that the ANL v2 (alloy 152 B) and MHI (alloy 152 A) weld specimens did show more extensive IG cracking. Surprisingly, higher IG engagement did not result in a higher SCC CGR among the various weld specimens. Multiple evaluations of SCC on the ANL v2 weld specimens (Section 3.1.3) consistently revealed low propagation rates at constant K ending up at ~1x10^{-9} mm/s or less even though IG engagement was from 35 to 60%. Similar observations were observed for the MHI alloy 152 specimens where IG engagement was typically ~40%. The KAPL alloy 52M V-groove weld (Alloy 52M A) exhibited the most consistent and stable SCC CGRs (albeit only 2-5x10^{-9} mm/s) with an IG engagement of ~30% as indicated in Figure 3-129.
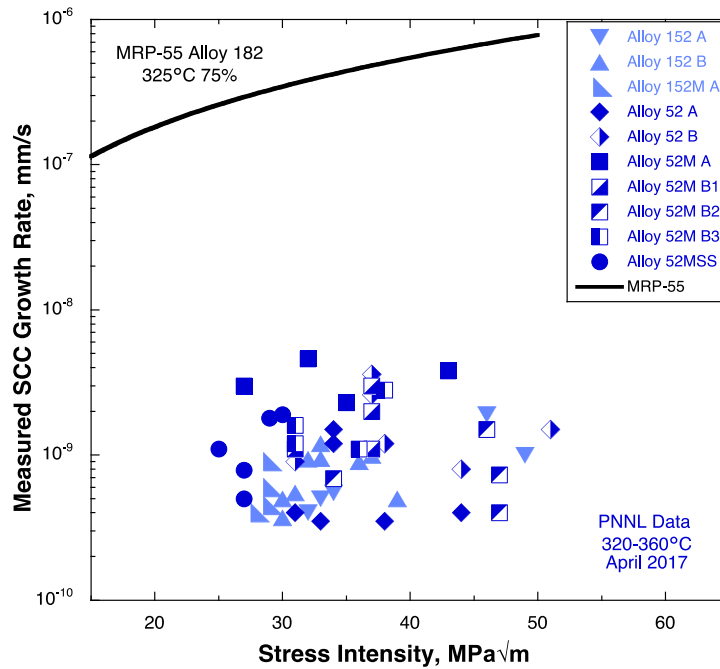
Figure 3-128   Summary of PNNL-Measured Constant K SCC CGRs for Alloy 152/152M/52/52M Weld Metal Specimens as a Function of Stress Intensity

Table 3-20   Weld and Specimen Information for Data Presented in Figures 3-128 to 3-132

Weld ID	Weld Information	CT Specimens
Alloy 152 A	MHI Alloy 152, heat 307380 U-groove weld	PNNL: CT013; CT017; CT018; CT052 ANL: MHI152-TS-1; MHI152-TS-11
Alloy 152 B	ANL Alloy 152, heat WC04F6 V2 dissimilar metal weld	PNNL: CT049; CT080 GEG: c541; c576 ANL: N152-TS-1
Alloy 152 B1	ANL Alloy 152, heat WC04F6 V1 dissimilar metal weld	ANL: A152-TS-2; A152-TS-4; A152-TS-5
Alloy 152 C/C1	ANL Alloy 152, heat 509528 High/normal current weld	ANL: HC152-CR-1; NC152-CR-1
Alloy 152 D	Alloy 152, heat 747136	GEG: c501 CIEMAT: E1W
Alloy 152 E	Alloy 152, heat WC51G0	GEG: c510
Alloy 152 F	Alloy 152, heat 146444	GEG: 525
Alloy 152 G	Alloy 152, heat 706447	GEG: c555
Alloy 152M A	KAPL Alloy 152M, heat WC83F8 V-groove dissimilar metal weld	PNNL: CT081 GEG: c577
Alloy 52 A	AREVA Alloy 52, heat NX3926JK butt weld	PNNL: CT024; CT032
Alloy 52 B	MHI Alloy 52, heat NX2686JK U-groove weld	PNNL: CT025; CT033 GEG: c511
Alloy 52 C	Alloy 52, heat NX6133JK	GEG: c502 CIEMAT: EW
Alloy 52 D	Alloy 52, heat NX6523JK	GEG: c542
Alloy 52 E	Alloy 52, heat NX4467JK	ANL: MC52-CR-1
Alloy 52M A	KAPL Alloy 52M, heat NX5285TK V groove weld	PNNL: CT041
Alloy 52M B1/B2/B3	KAPL Alloy 52, heat NX5285TK narrow groove weld	PNNL: CT040; CT042; CT043
Alloy 52M C	Alloy 52M, heat NX7859TK	GEG: c636
Alloy 52MSS	Alloy 52MSS, NX77W3UK Special Metals V-groove weld	PNNL: CT050

Comparisons were reported between SCC CGRs and IG engagement for PNNL tests on alloy 690 CRDM, plate and bar materials in our previous NUREG/CR report [5]. These results did show a positive correlation with SCC propagation rates increasing with the %IG measured on the crack-growth surface. However, it is interesting to note that higher SCC CGRs ($>1 \times 10^{-8}$ mm/s) were not observed for the cold-worked alloy 690 materials until the IG engagement was greater than ~70%. IG engagement levels of 20-50% corresponded to SCC CGRs of $2\text{-}5 \times 10^{-9}$ mm/s comparable to the highest SCC propagation rates measured on the weld specimens in Figure 3-129.

In order to better assess SCC behavior for the alloy 152/152M/52/52M welds, reported crack-growth test results from other laboratories have been obtained and plotted along with the PNNL data. General Electric Global Research (GEG) has evaluated the most different welds and have seen very similar behavior as illustrated in Figure 3-130. SCC has been evaluated on several welds at both laboratories including Alloy 152 B, 152M A and 52 B. The detailed comparison of

tests on the ANL v2 weld (Alloy 152 B) was described in Section 3.1.4. In addition, GEG also tested Alloy 152 A and found similar CGR response during cycle + hold loading.
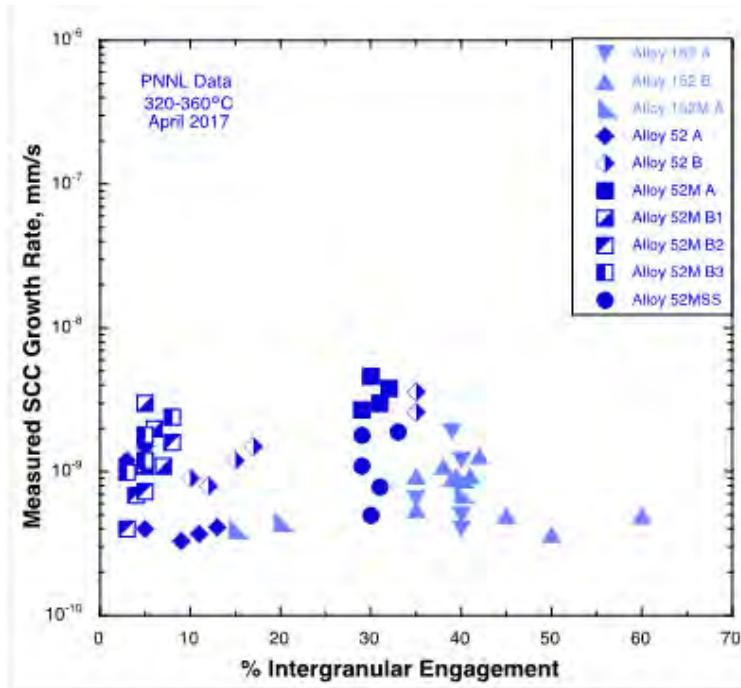
Figure 3-129   PNNL Measured Constant K SCC CGRs for Alloy 152/42/52M Weld Metal Specimens as a IG Cracking Observed on the Post-Test Crack Growth Surface
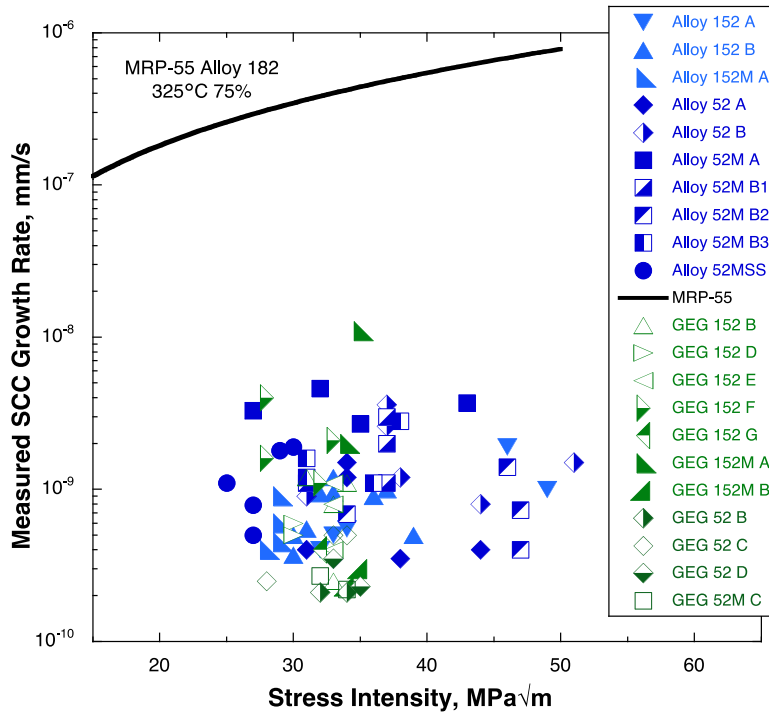
Figure 3-130 Summary of PNNL- and GEG-Measured Constant K SCC Crack-Growth Rates for Alloy 152/152M/52/52M Weld Metals as a Function of Stress Intensity

The other major laboratory comparison is to the SCC CGR data reported by ANL and is presented in Figure 3-131. Without question, reported measurements on the ANL v1 (Alloy 152 B1) and v2 (Alloy 152 B) welds are quite different showing higher CGRs from 1-5x10^{-8} mm/s in many cases along with much lower examples. The detailed comparison of tests at ANL, GEG and PNNL on the ANL v2 weld (Alloy 152 B) was described in Section 3.1.4. While the higher SCC susceptibility of these two ANL alloy 152 welds (same weld wire) could not be confirmed at other laboratories, the results were duplicated at ANL and suggests that the high Cr welds are not inherently resistant to SCC.

Even after characterizations and SCC tests on 18 different high Cr welds, it is not possible to directly link bulk composition or microstructure to SCC susceptibility for these weld metals. The key reasons for this stems from the limited observations of SCC growth for any of the alloy 152/152M or 52/52M weld metals tested and the variations in microstructure (e.g., inclusions, precipitates and local strain densities) throughout individual welds. It is important to note that microstructural effects on SCC susceptibility of alloy 690 heats were determined in highly cold-worked materials and could not be assessed in as-received alloy 690 because all heats were resistant to SCC. The current results on as-welded alloy 152/52 materials is entirely consistent with this behavior. In an attempt to improve understanding of compositional and microstructural effects on the SCC susceptibility of the high-Cr weld metals, crack-growth tests will be performed on cold-worked alloy 152/52 welds and will be reported in a future NUREG/CR report.
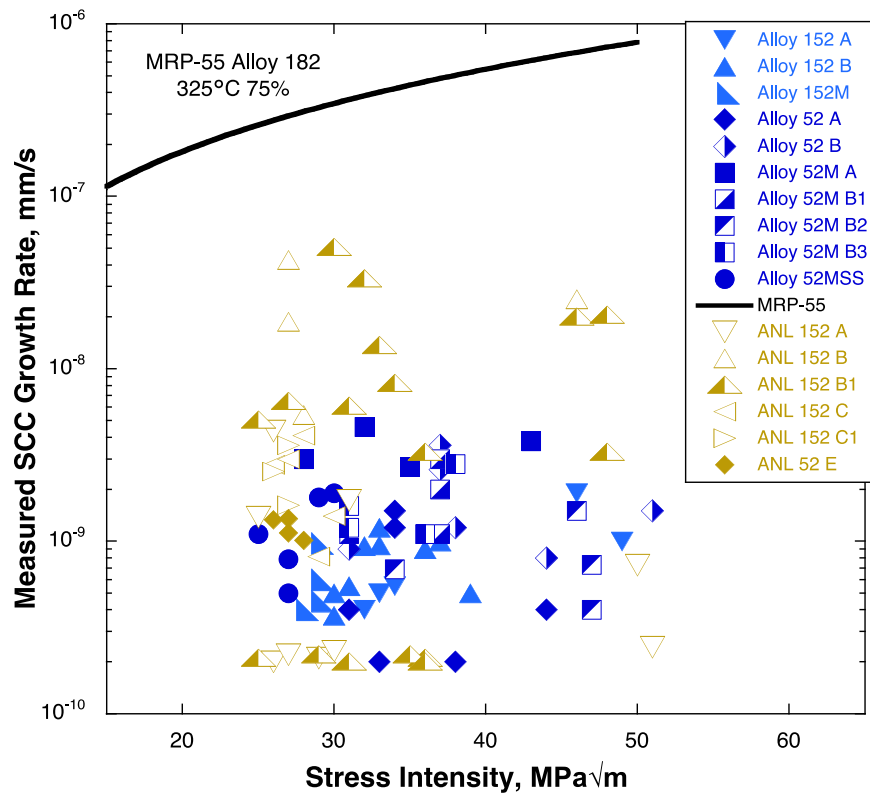
Figure 3-131 Summary of PNNL- and ANL-Measured SCC Crack-Growth Rates for Alloy 152/152M/52/52M Weld Metals as a Function of Stress Intensity
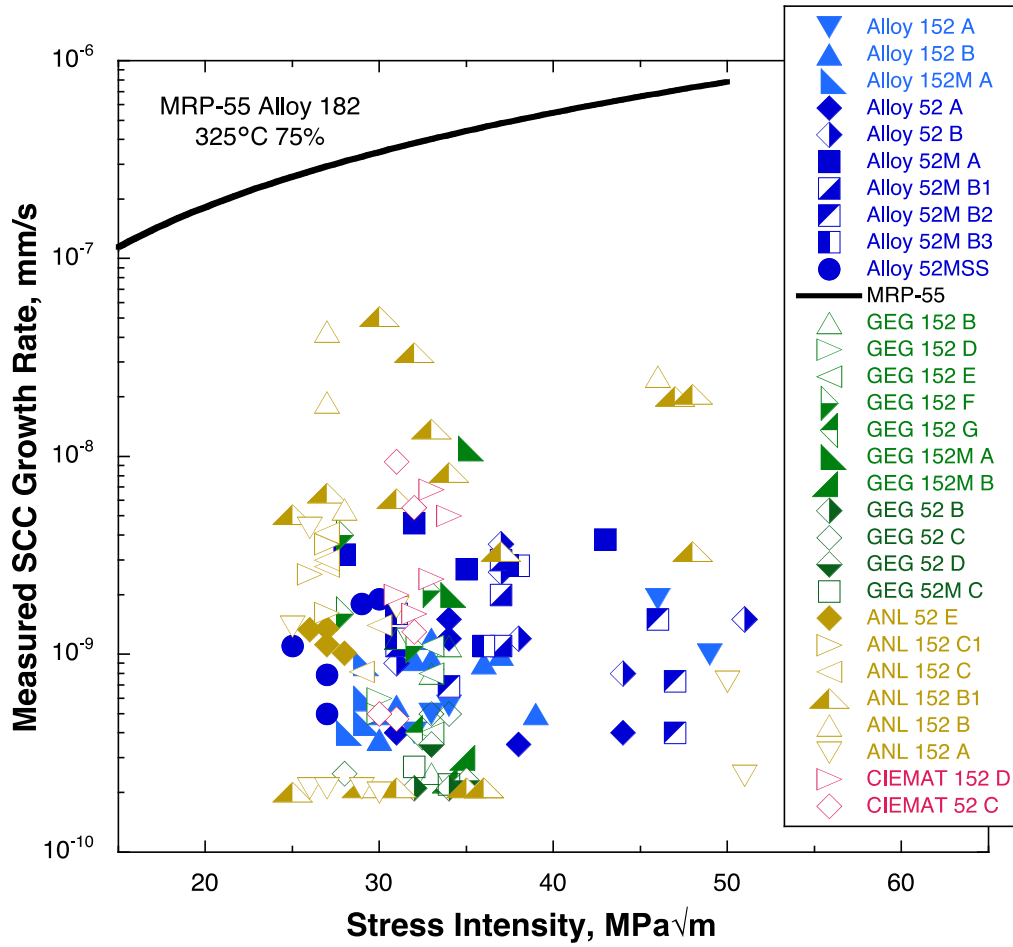
Figure 3-132 Summary of PNNL-, GEG-, ANL- and CIEMAT-Measured SCC Crack-Growth Rates for Alloy 152/152M/52/52M Weld Metals as a Function of Stress Intensity

4   ALLOY 52M OVERLAYS/INLAYS

Interactions with Pal Efsing of Ringhals made it possible to obtain both an overlay and an inlay mockup. The alloy 52M/182 overlay mockup was obtained directly from Ringhals and an overview of the mockup is shown in Figure 4-1(a). It was fabricated by robotically welding a 10-mm-thick alloy 52M layer onto an alloy 690 plate and then by manually welding alloy 182 onto the alloy 52M layer. The alloy 52M layer was applied by GTAW with a weld speed of 7.5 cm/min at a current of 130 A while the alloy 182 was applied by SMAW with a weld speed of 7-12 cm/min at a current of 95-125 A. The inlay mockup was obtained from Westinghouse and is from a full-scale inlay repair demonstration by Ringhals on a ring of A533 steel pipe. The inlay was fabricated first by carving a boat out of the inner surface of the ring as shown in Figure 4-1(b), and then alloy 82 filler was robotically welded onto the pipe section. This was followed by the robotic application of the alloy 52M inlay. Lastly, an alloy 152 weld layer was manually applied by Westinghouse to allow fabrication of compact tension specimens for SCC testing with an orientation allowing cracks to be grown from the alloy 82 into the alloy 52M.
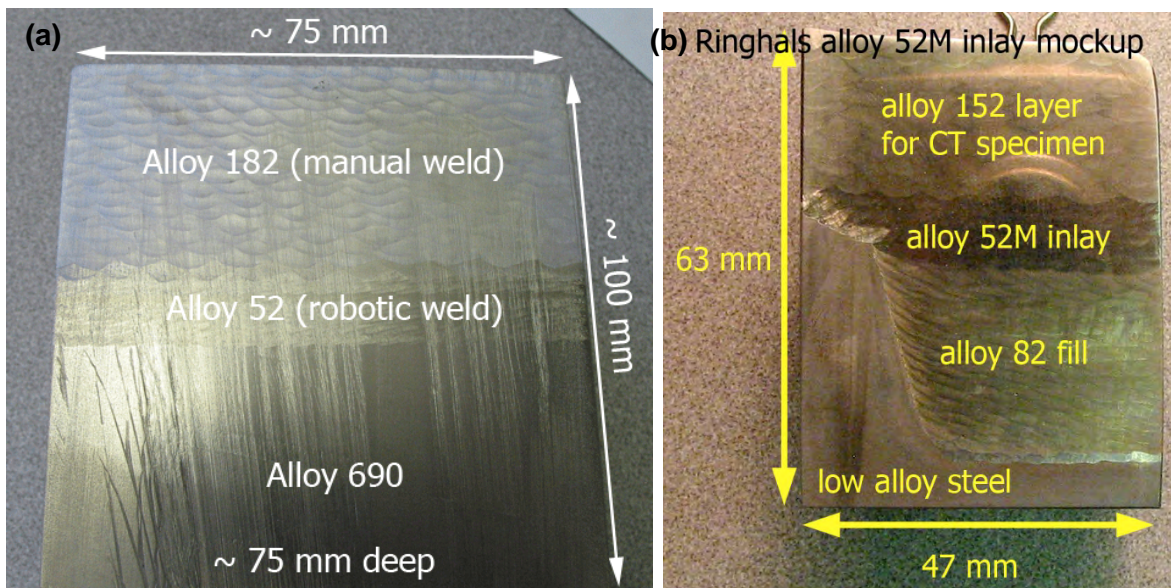
Figure 4-1   Overview of the Ringhals Alloy 52M Overlay (a) and Inlay (b) Mockups

4.1   Ringhals Alloy 52M/182 Overlay Welds

4.1.1   Alloy 52M/182 Overlay Weld Sample Pair #1 (CT028 & CT029)

Two 0.5T CT samples (CT028 and CT029) of the Ringhals alloy 52M/182 overlay were machined to locate the notch in the alloy 182 weld metal ~3 mm from the alloy 52M interface. The sample and notch locations are indicated in Figure 3.66. Composition measurements were performed using SEM-EDS at two locations along the interface between the 182 weld and alloy 52M weld as shown in Figures 4-3 and 4-4. Profile #1 was acquired at the bottom of an alloy 182 weld puddle while profile #2 was acquired at the saddle point between two alloy 182 weld puddles. The two profiles indicate a dilution zone width ranging from ~70 μm to 150 μm with dilution occurring in both the alloy 182 and alloy 52 welds. These measurements illustrate the complexity of the dilution zone at the alloy 52M/182 interface and suggest that a simple assessment of Cr concentration effects on SCC propagation rates will be difficult.
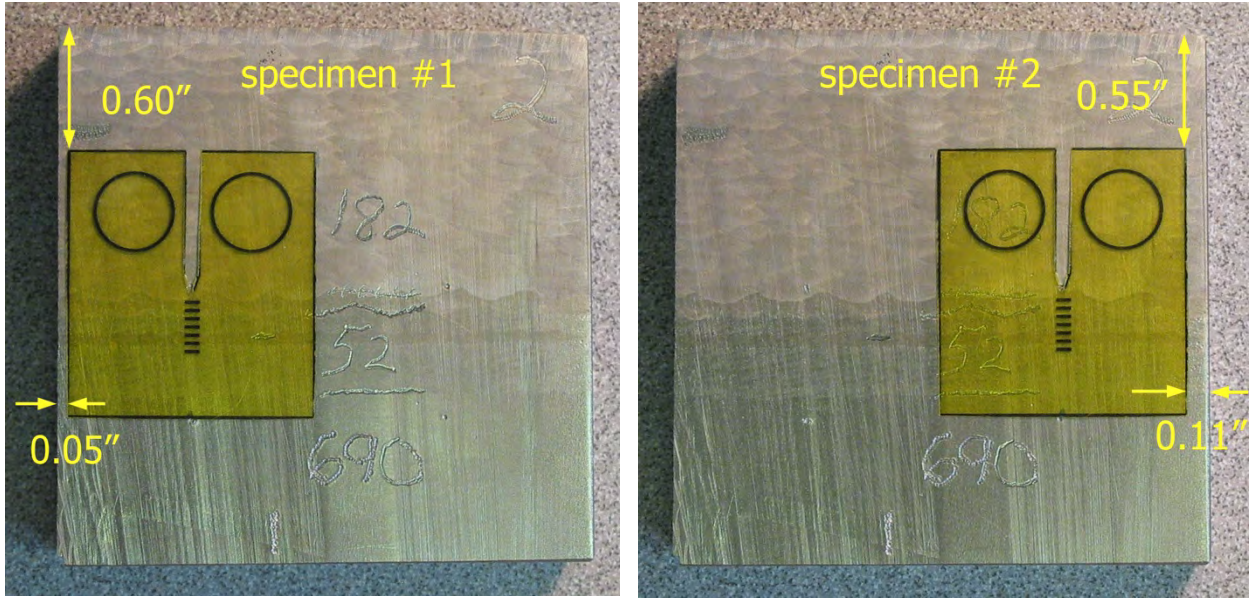
Figure 4-2 Photographs Showing Location of Specimens to Be Taken from Alloy 182/52/690 Overlay Received from Ringhals. Machined Notch Was ~3 mm from the Alloy 182 – Alloy 52M Boundary
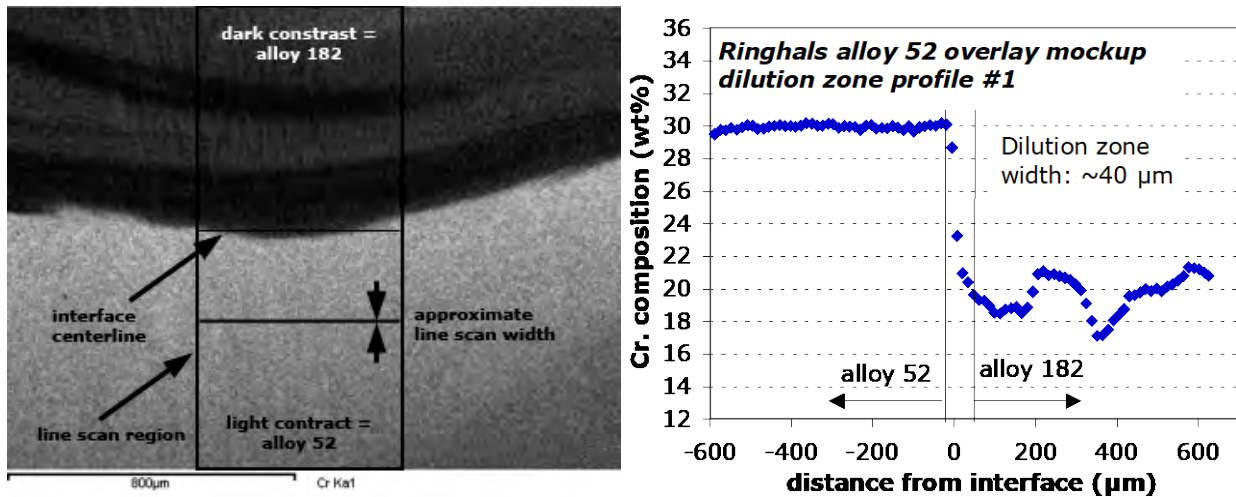
Figure 4-3 Compositional Profile #1 Across the Bottom of an Alloy 182 Weld Puddle and into the Alloy 52M of the Ringhals Alloy 52M/182 Overlay Material
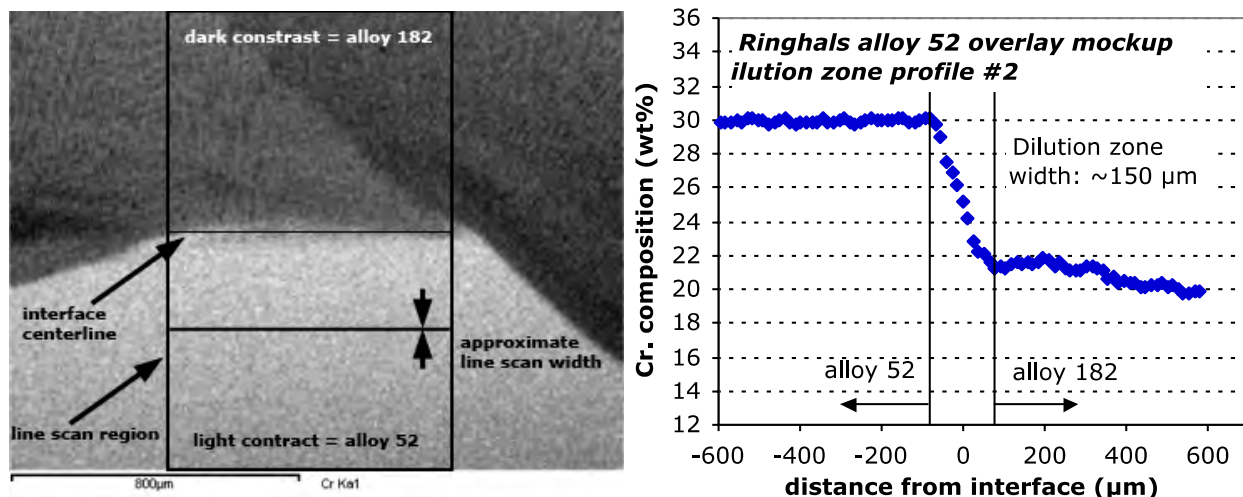
Figure 4-4   Compositional Profile #2 Across an Alloy 182 Weld Trough and into the Alloy 52M of the Ringhals Alloy 52M/182 Overlay Material

Fatigue precracking was performed in air to produce an initial crack extension of ~1.7 mm in the alloy 182 material. The overlay samples were mounted in series and tested in simulated PWR primary water at 350°C. A hydrogen concentration of 20 cc H_2/kg H_2O was maintained to produce an electrochemical potential at the Ni/NiO stability line in an attempt to promote maximum CGRs in the alloy 182 weld metal. An initial transitioning sequence was followed for crack growth through the alloy 182 weld metal similar to the test protocol used for two earlier alloy 182 CGR tests. The intent was to produce a fully engaged IGSCC crack front in the alloy 182 at a position that is ~400 μm from alloy 182/52M interface and monitor growth under constant K conditions as it approached the high Cr alloy 52M weld metal.

After crack extension at 0.01 and 0.001 Hz (R=0.7), the crack front is estimated to be ~550 μm from the interface and a hold time of 2.5 h was added at ~670 h. The CGR at 0.001 Hz with a 2.5 h hold was ~1.5×10^{-8} mm/s for both samples as shown in Figure 4-5. Because of this slower than expected CGRs, the R value was decreased to 0.5 to promote faster growth. Propagation rates increased to $2.5\text{-}3 \times 10^{-8}$ mm/s for both samples, and an initial attempt to evaluate constant K response was made starting at ~1240 h. Unfortunately, very slow SCC CGRs of ~2×10^{-9} mm/s were observed as illustrated in Figure 4-6.
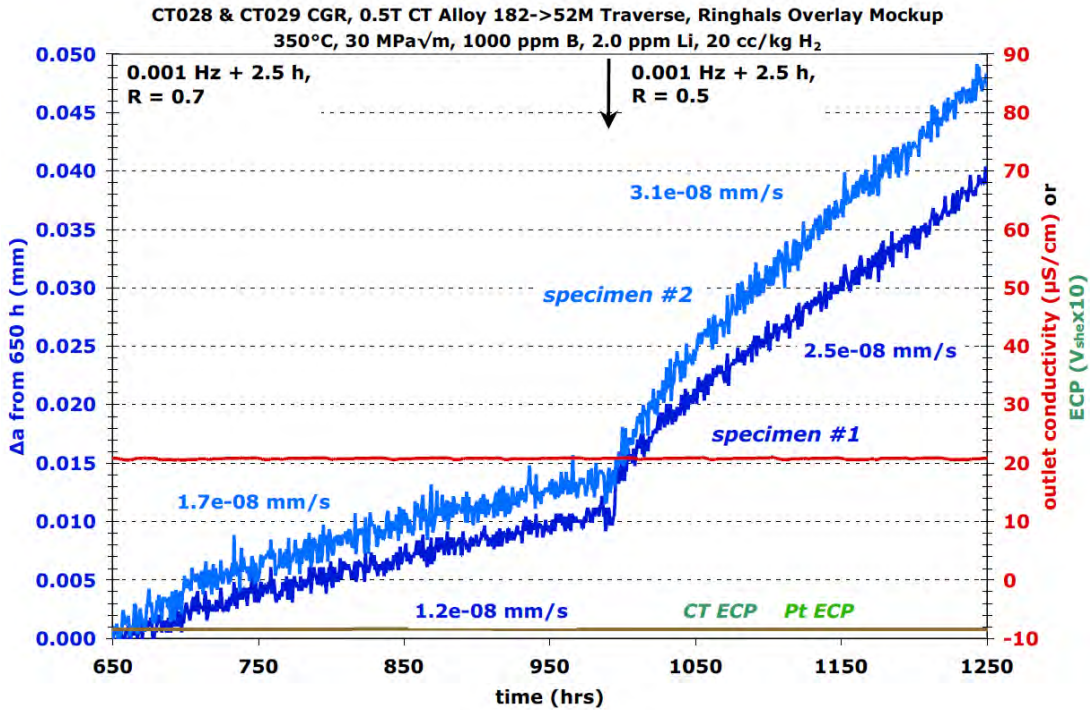
Figure 4-5 Initial Cycle + Hold Steps in the Alloy 182 Portion of the Ringhals Alloy 52M/182 Overlay Material
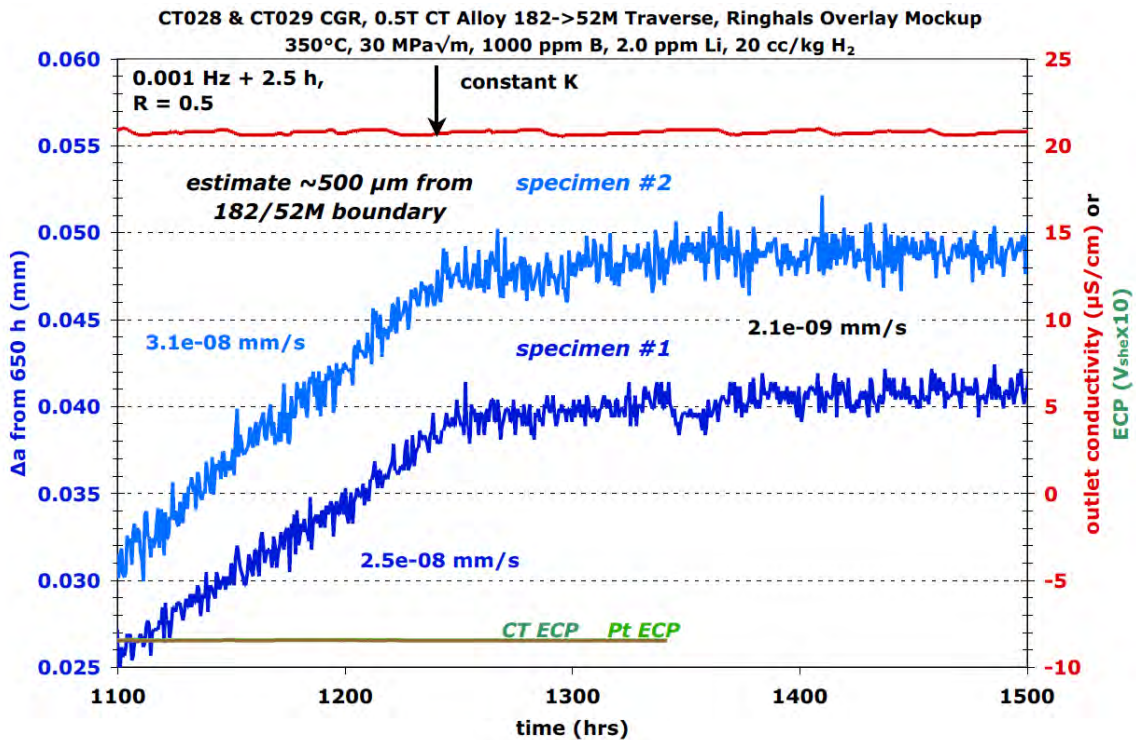
Figure 4-6 First Constant K Response of the Ringhals Alloy 52M/182 Weld Showing Very Low CGRs in the Alloy 182 Material

Since there was no indication of significant SCC growth under cycle + hold or constant K conditions, the decision was made to evaluate another microstructural region closer to the alloy 52M/182 dilution zone. Cycling at 0.01 and 0.001 Hz at R=0.5 was applied to straighten and extend the crack front by ~0.2 mm. This should have moved the crack front to within ~0.3 mm of the dilution zone. The R value was then increased back to 0.7 and cycling continued at 350°C until a test time of ~1750 h as shown in Figure 4-7. Unfortunately, crack-growth rates were found to be similar to those established previously.

The low crack growth response for the alloy 182 weld metal was unexpected based on prior SCC test results. Since most of this previous work on alloy 182 was performed at slightly lower temperatures, the decision was made to briefly assess response at 325°C at different DH concentrations (as in prior alloy 182 tests). In the end, constant K growth rates were extremely low (<1x10^{-9} mm/s) at 325°C, therefore the test temperature and H$_2$ level were increased back to 350°C and 20 cc/kg. Propagation rates were initially ~3x10^{-9} mm/s under these conditions (still slow for alloy 182) as shown in Figure 4-8, and decreased over the next two weeks to ~1x10^{-9} mm/s similar to what was observed previously.
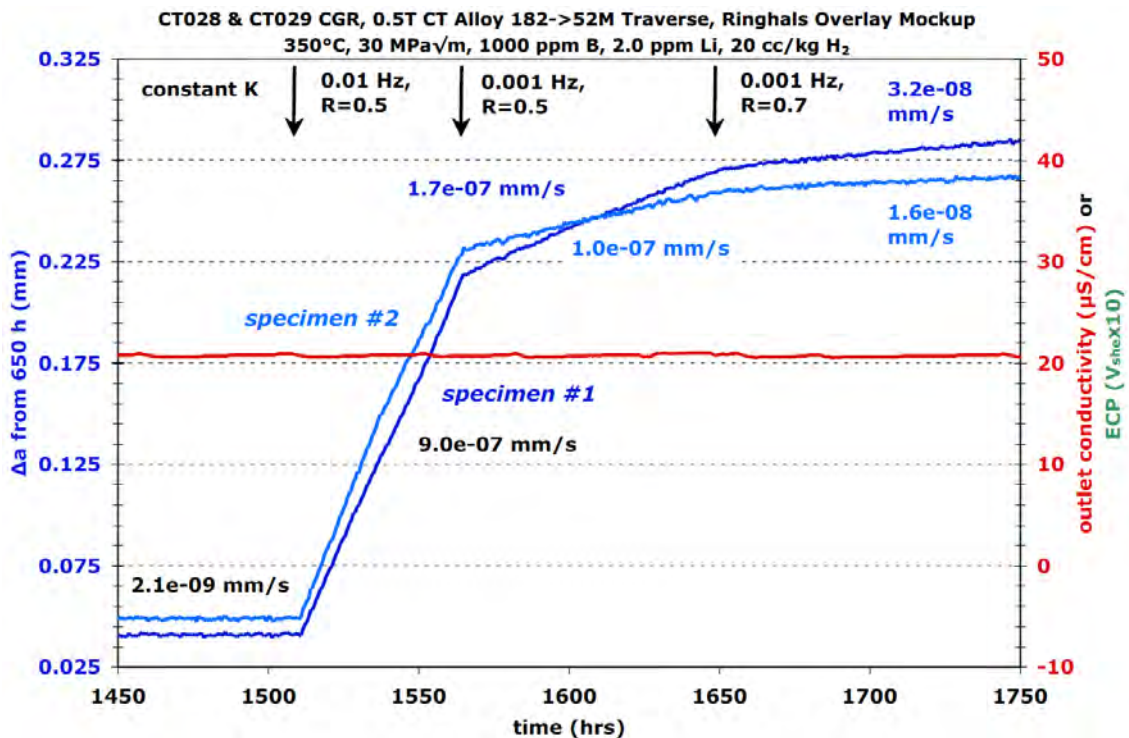
Figure 4-7 **Crack Extension into New Microstructural Region and Growth Response During Cycle + Hold Loading with R = 0.7 and R = 0.5**
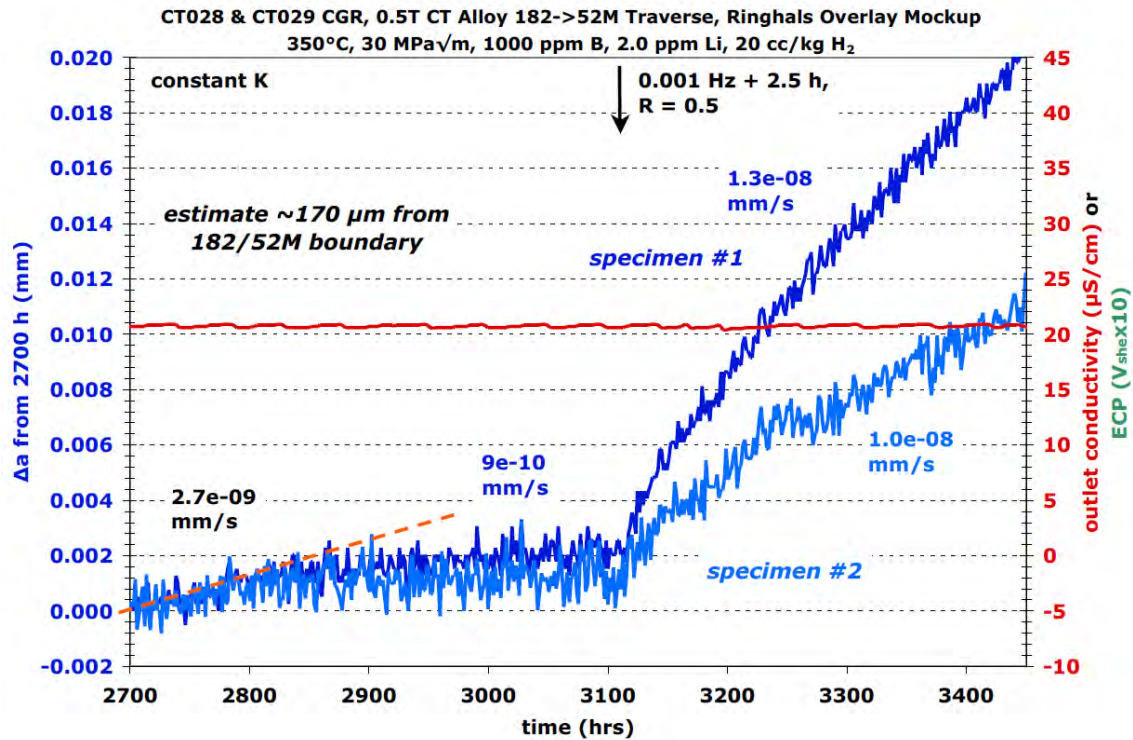
Figure 4-8 Repeat Observation of Constant K and Cycle + Hold Response at 350°C in the Ringhals Alloy 52M/182 Overlay. Very Low CGRs Suggest the Crack Had Entered into the Alloy 52M Weld

Based on DCPD-measured crack extensions, it was estimated that the alloy 52M should still be a distance of ~150 μm away. However, considerable uncertainty exists both for the actual crack length and the position of the interface. The only practical way to determine where the crack front currently is would have been to remove the samples and polish the side surfaces. It was decided to determine CGRs one more time under the standard 0.001 Hz + 2.5 h hold condition. As shown in Figure 4-8, this change was made at 3115 h and new rates stabilized at 1.0 and 1.3×10^{-8} mm/s. These rates are 3-4X slower than measured previously under identical conditions and suggested that the crack front has reached the alloy 52M interface even though it should be >100 μm away from the interface based on DCPD-measured crack extension.

Because of this uncertainty and the importance of evaluating SCC CGRs in the alloy 52M weld metal, the decision was made to drop the temperature and extend the crack well into the alloy 52M by cycling at 50°C. A similar cycling sequence was chosen as for the alloy 152 weld metal samples where extensive IG cracking was produced along the crack front. The low-temperature response of the two samples is presented in Figure 4-9. Surprisingly, aggressive cycling at 0.1 Hz and R=0.5 produced quite different behavior with much more crack extension in overlay specimen CT028 (~0.75 mm) than for specimen CT029 (~0.2 mm). This suggests that complex ligaments were present in the overlay specimen CT029 restricting crack growth or masking the true crack length. The decision was made to reduce the cyclic frequency to 0.001 Hz partially due to the significant crack length difference (~1.1 mm) between the samples. The applied K is maintained at 30 MPa√m based on the DCPD crack length for specimen CT028 and is estimated to be slightly lower for specimen CT029 (~26 MPa√m).
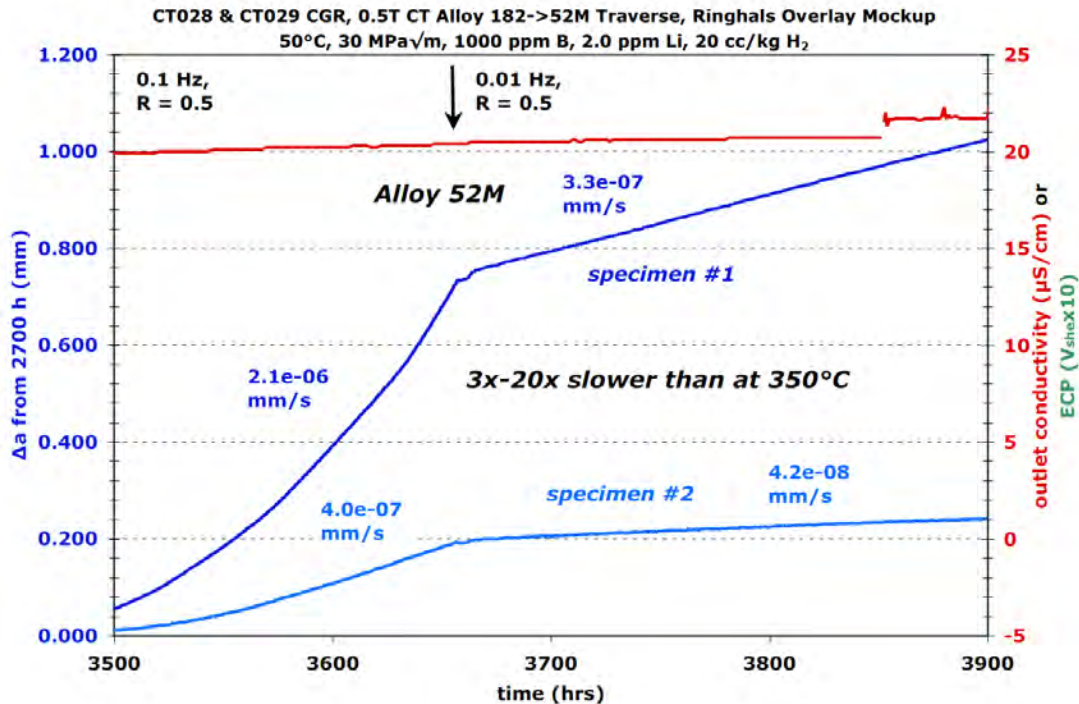
Figure 4-9   Crack Extension in Alloy 52M During Cycling at 50°C in the Ringhals Alloy 52M/182 Overlay

After a crack length increase of ~1.2 and 0.3 mm for the specimens CT028 and CT029 at 50°C, respectively, constant K conditions were established and the temperature was increased to 350°C. The crack-growth response at 350°C and 20 cc/kg is shown in Figure 4-10. As with the previous tests on alloy 152 and alloy 52, the propagation rates at 350°C decreased from relatively high values (>5x10^{-8} mm/s) to ~4x10^{-9} mm/s over the following 600 h (25 days). While the rates appeared steady over the last ~100 hours, it is expected that the rates would have continued to decrease slightly over time. In order to help assess the reason for the slowing growth rate, a periodic unload every 2.5 h was added at ~4750 h and an immediate jump in DCPD crack length was observed. Expanding the time scale to focus on this rapid increase in length revealed that most of the change (~0.2 mm for specimen CT028 and ~0.1 mm for specimen CT029) occurred during the first three 0.001 Hz cycles. This suggests that ligaments had developed and were broken by the initial cycles at an R of 0.5. Since the growth rate under the cycle + hold condition then reverted to the expected steady-state values, constant K conditions were resumed at ~4800 h. No indication of SCC propagation was observed over the next few days and the DCPD-measured crack length slightly decreased before the test was ended at 4936 h. A summary of testing conditions, crack extension, and CGR for each phase of the test is shown in Table 4-1. In order to better understand crack-growth response in the alloy 182 and alloy 52M regions, the specimens were removed, their side surfaces examined and then fatigue fractured in air to examine the crack growth surfaces.
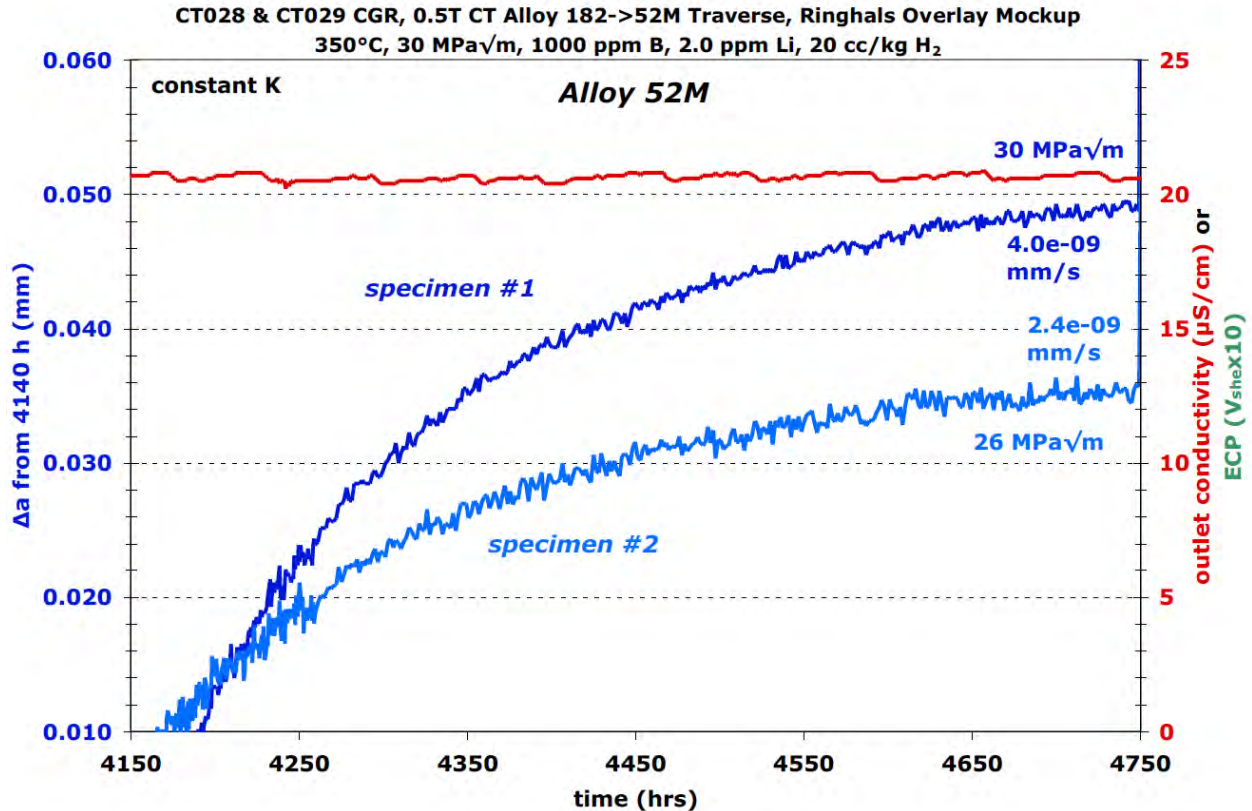
Figure 4-10   Constant K Crack-Growth Response in the Alloy 52M Weld Material After Temperature Increase from 50°C to 350°C

Side-surface examinations were performed to find the crack front as demonstrated in Figure 4-11(a). The crack can be identified within the side groove of the overlay sample CT028 and distance from the notch estimated as ~4.3 mm. This sample was subsequently removed from the system, the crack was resin impregnated, and then a slice was sectioned off to allow preparing a TEM crack tip specimen. The specimen was then air fatigue fractured and the resin burned off the crack growth surface by baking at 630°C followed by ultrasonic cleaning in DI water. The resulting, tinted crack growth surface is shown in Figure 4-11(b). The change from grey/gold to blue coloration on the crack growth surface results from the transition from crack growth in alloy 182 to alloy 52M. Consistent with the side-surface measurement, the overall crack length was 4.5 mm with ~2.9 mm in a water environment. This reveals an under prediction of crack length by DCPD, since it reported a total crack length of ~2.1 mm produced in 350°C and 50°C water.

Table 4-1   **Corrected Data Summary for Ringhals Alloy 52M/182 Overlay Specimens CT028 & CT029**

Test Phase	Dur-ation (h)	R	Freq (Hz)	Hold (h)	Water Chemistry Conditions	Temp (°C)	CT028 Ringhals Alloy 52M/182 Overlay Pair #1 Kmax (MPa√m)	CGR (mm/sec)	Approx. Crack Extension (mm)	CT029 Ringhals Alloy 52M/182 Overlay Pair #1 Kmax (MPa√m)	CGR (mm/sec)	Approx. Crack Extension (mm)
1	~3	0.3	3	0	air	RT	25	1.0E-04	0.71	25	8.1E-05	0.57
2	~2	0.5	3	0	air	RT	28	5.7E-05	0.49	28	5.4E-05	0.38
3	~3	0.6	3	0	air	RT	30	3.4E-05	0.30	30	3.1E-05	0.28
4	~5	0.7	3	0	air	RT	30	1.5E-05	0.30	30	1.4E-05	0.32
5	74	0.7	0.1	0	20 cc/kg H_2	350	30	1.0E-06	0.201	30	1.0E-06	0.236
6	214	0.7	0.01	0	20 cc/kg H_2	350	30	2.7E-07	0.200	30	2.6E-07	0.196
7	359	0.7	0.001	0	20 cc/kg H_2	350	30	5.3E-08	0.066	30	5.0E-08	0.074
8	345	0.7	0.001	2.5	20 cc/kg H_2	350	30	1.2E-08	0.011	30	1.7E-08	0.015
9	518	0.5	0.001	2.5	20 cc/kg H_2	350	30	2.5E-08	0.029	30	3.1E-08	0.033
10	267	---	const K	---	20 cc/kg H_2	350	30	2.1E-09	0.003	30	2.1E-09	0.002
11	55	0.5	0.01	0	20 cc/kg H_2	350	30	9.0E-07	0.177	30	9.0E-07	0.181
12	84	0.5	0.001	0	20 cc/kg H_2	350	30	1.7E-07	0.051	30	9.7E-08	0.028
13	119	0.7	0.001	0	20 cc/kg H_2	350	30	3.2E-08	0.017	30	1.6E-08	0.009
14	77	0.7	0.001	0	11 cc/kg H_2	325	30	2.6E-08	0.007	30	8.3E-09	0.004
15	410	0.7	0.001	2.5	11 cc/kg H_2	325	30	6.3E-09	0.009	30	2.4E-09	0.004
16	170	0.7	0.001	2.5	29 cc/kg H_2	325	30	3.3E-09	0.002	30	1.9E-09	0.000
17	181	0.7	0.001	2.5	11 cc/kg H_2	325	30	4.5E-09	0.003	30	2.4E-09	0.003
18	82	---	const K	---	11 cc/kg H_2	325	30	no growth	0.001	30	no growth	0.000
19	422	---	const K	---	20 cc/kg H_2	350	30	9E-10	0.004	30	no growth	0.000
20	365	0.5	0.001	2.5	20 cc/kg H_2	350	30	1.3E-08	0.034	30	1.0E-08	0.010
21	184	0.5	0.1	0	20 cc/kg H_2	50	30	2.0E-06	0.700	30	4.0E-07	0.179
22	249	0.5	0.01	0	20 cc/kg H_2	50	30	3.2E-07	0.302	30	4.4E-08	0.052
23	239	0.5	0.001	0	20 cc/kg H_2	50	30	4.3E-08	0.071	30	6.9E-09	0.010
24	602	---	const K	---	20 cc/kg H_2	350	30	4.0E-09	0.039	30	2.4E-09	0.027
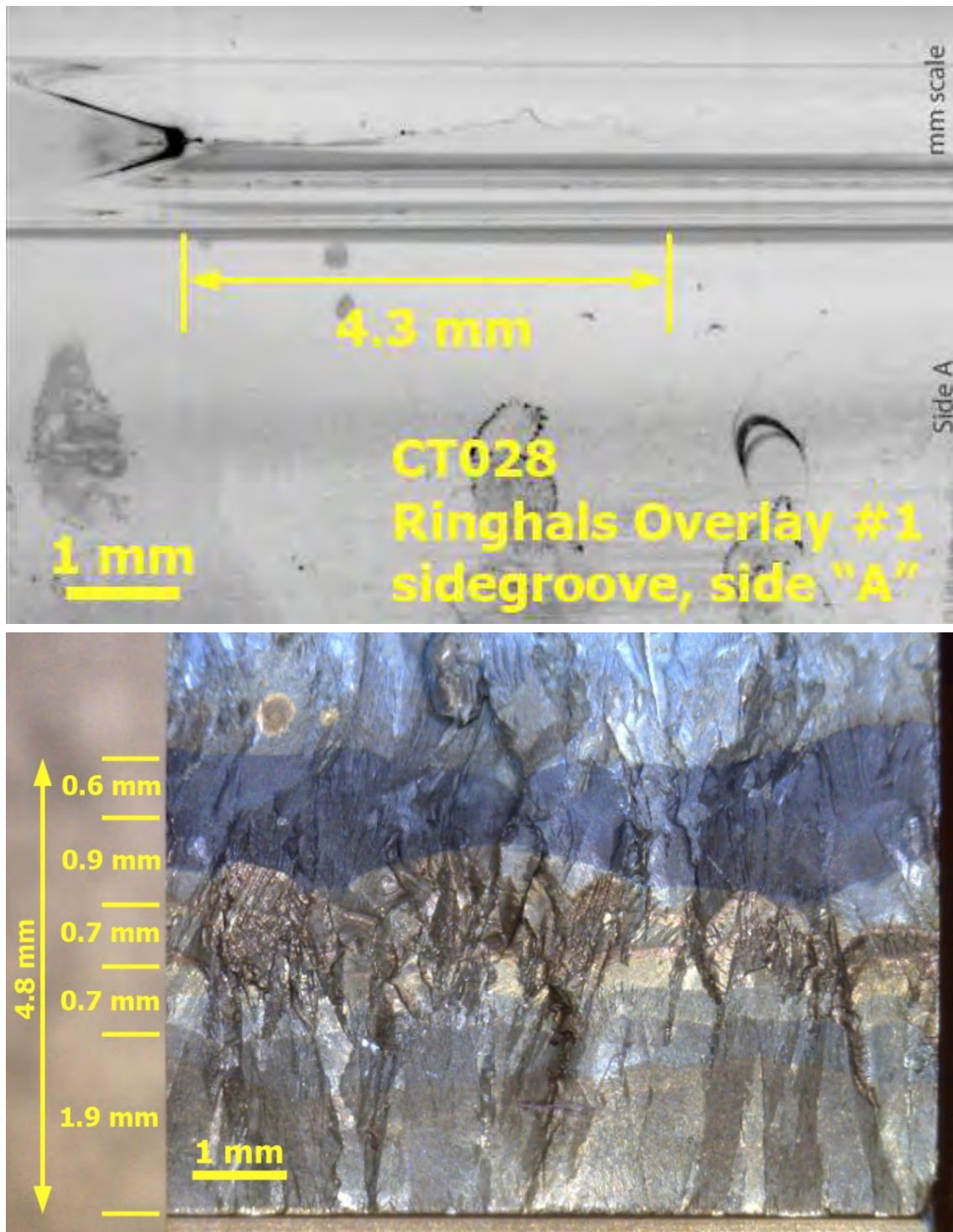
Figure 4-11 Optical Images Showing Crack in the Side Groove (top) and Fracture Morphology on the Crack-Growth Surface (bottom) for the Alloy 182/52 Overlay Specimen #1 (CT028)

4.1.2 Alloy 52M/182 Overlay Sample Pair #2 (CT034 and CT035)

Based on previous experience obtained with the alloy 182 weld metal in the overlay samples CT028 and CT029, the decision was made to begin SCC transitioning at 30 MPa√m under oxidizing BWR water conditions (288°C high purity water with 2 ppm O_2) with 30 ppb sulfate on the second alloy 52M/182 overlay specimens CT034 and CT035. This environment has been shown to give much more consistent SCC response for alloy 182 weld metals [7], and the intent was to promote maximum IGSCC crack-front engagement before switching to simulated PWR primary water. Initial transitioning steps were performed at an R value on 0.7 to reach constant K with the crack front a little more than 1 mm away from the alloy 182 - alloy 52M interface. The initial constant K growth rates were ~2x10⁻⁸ mm/s for both samples as shown in Figure 4-12. These rates were again lower than anticipated, but it was expected that the rate would increase with time as has been observed in previous tests on alloy 600 and alloy 182 under BWR oxidizing water conditions. However, the CGRs slowed slightly after ~300 h at constant K. A cycle + hold loading step with R = 0.7 was initiated at ~1220 h to explore whether crack ligaments in the wake of the crack were affecting the DCPD measurement of crack length. The lack of a significant jump in crack extension suggested little or no breakage of ligaments, and the test was returned to constant K. Unfortunately, the propagation rates remained at lower than expected values for this aggressive oxidizing environment, so a second application of cycle + hold loading, but at R = 0.5 was applied with similar results. While these rates indicate that IGSCC is occurring, the rates are 5-10X lower than other tests on alloy 182.
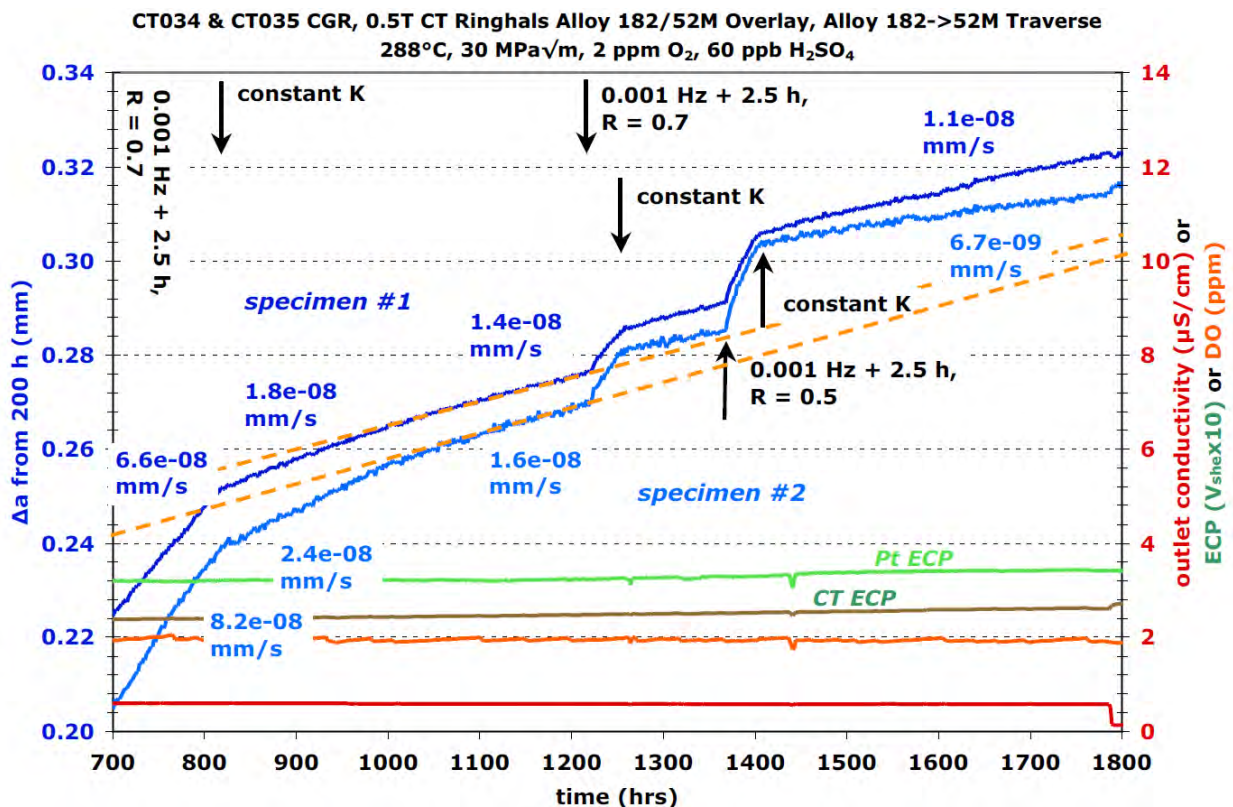
Figure 4-12 **Transitioning Steps to Constant K Response Under BWR Oxidizing Conditions of the Second Pair of Ringhals Alloy 52M/182 Overlay Specimens (CT034 & CT035)**

The decision was made to convert this test to PWR primary water conditions after the constant K CGRs were established in oxidizing BWR water conditions. As a first step, sulfate additions were stopped at ~1790 h and propagation rates slowly dropped by 25% in specimen #1 and 35% in specimen #2 over a period of ~375 h. Oxygen was then removed, hydrogen added, and the temperature increased to 350°C at ~2150 h. A dissolved hydrogen level of 20 cc/kg (near the Ni/NiO line) was used to promote maximum SCC susceptibility. Boron and Li were not added to fully simulate PWR primary water conditions, but this difference is not believed to have a strong influence on SCC. Over the following 3+ weeks, measured CGRs for the two overlay samples slowly decreased as illustrated in Figure 4-13. CT035 revealed a more significant drop by more than 3 times and appears to be approaching a steady-state CGR of $<1x10^{-9}$ mm/s. CT034 remained slightly higher, but its propagation rate was still extremely low. As was the case during the test of the first pair of overlay samples, the alloy 182 is very resistant to SCC. Even though transitioning in oxidizing water + sulfate should have promoted IGSCC, subsequent growth in hydrogenated water was difficult. As a result, it was again impractical to propagate SCC from the alloy 182 to the alloy 52M interface under these conditions. Even assuming a significant error (~40%) in the actual crack length, the required time to reach the interface under constant K or cycle + hold conditions in hydrogenated water would be greater than one year. Therefore, the decision was made to advance the crack front by 0.3-0.4 mm by aggressive cycling (hopefully removing any ligaments that may be present), then go through transitioning steps again in 288°C oxidizing water + sulfate.
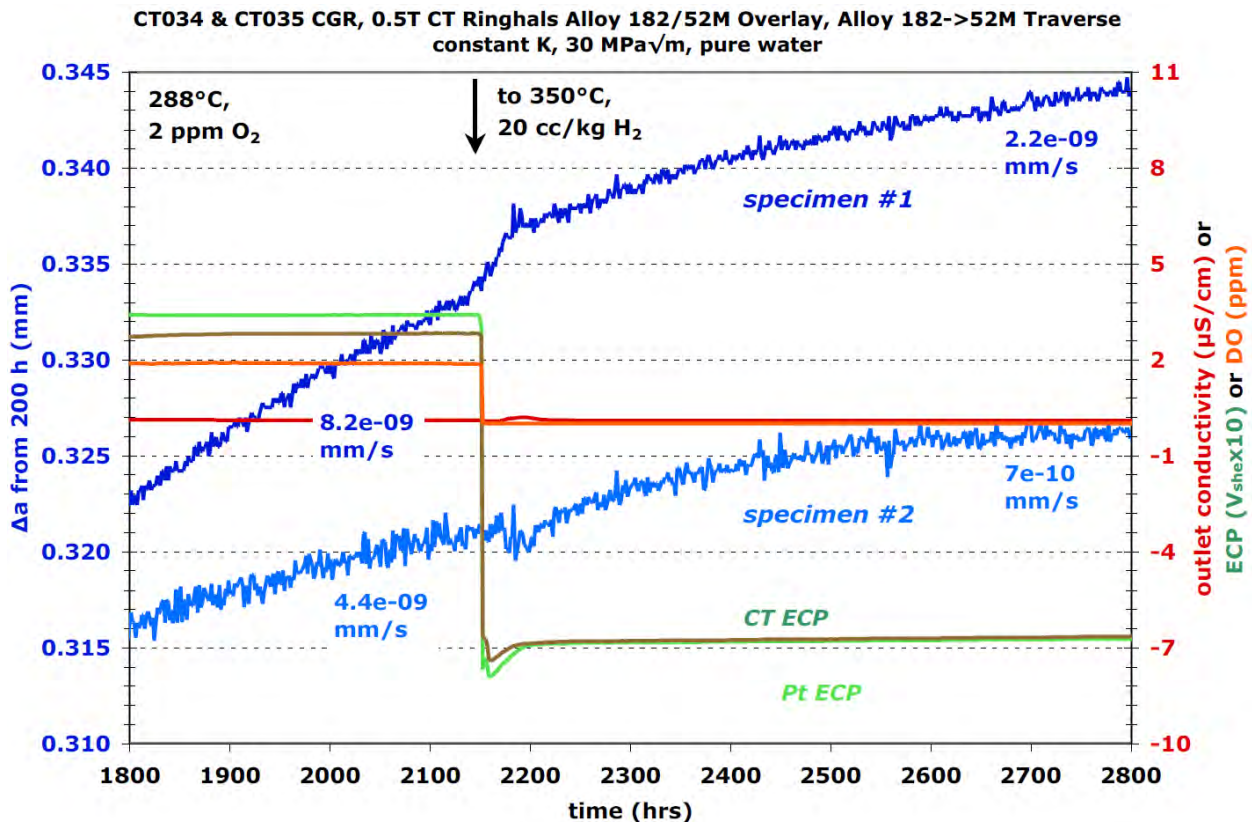
Figure 4-13   Crack Growth Response on Switching from BWR Oxidizing to Hydrogenated Water in the Second Pair of Ringhals Alloy 52M/182 Specimens (CT034 & CT035)

Initial cycling was conducted at 0.1 Hz with R=0.5 beginning at ~2960 h and revealed a reasonably rapid increase in DCPD-measured crack length of >100 µm in ~5 h before increasing the R value to 0.7 for another 50 µm. The transitioning sequence was continued at ~2975 h by decreasing the cyclic frequency to 0.01 Hz and then to 0.001 Hz at ~3015 h. Somewhat surprisingly, the measured cyclic CGRs were 2-4X lower than measured under identical conditions at the beginning of the test. To confirm this response, cycle + hold conditions were established at ~3180 h showing a CGR of ~3x10^{-8} mm/s in Figure 4-14. Once again, this is more than 2X lower than measured earlier in this test. Since the mockup was created by overlaying alloy 182 on top of alloy 52M, a compressive residual stress is not expected in the alloy 182. Therefore, a more likely explanation for the lower propagation rate is the presence of ligaments behind the crack front or a highly uneven crack front with areas already intersecting the alloy 52M interface. Loading conditions were briefly changed to a periodic unload at R = 0.3 producing a high ΔK of 21 MPa$\sqrt{m}$. The lack of a significant jump in crack length and the small increase in CGR suggests that no ligaments are being removed. Returning to the cycle + hold condition produced a similar CGR and indicates that the periodic unload had no effect. The test was converted to constant K at ~3660 h as shown in Figure 4-15. Specimen CT034 continued to exhibit low values with the propagation rate decreasing to 1x10^{-9} mm/s. However, specimen CT035 slowed only slightly, stabilizing at a rate of 1.0x10^{-8} mm/s and is comparable to the constant K propagation rates measured in earlier steps of the test.
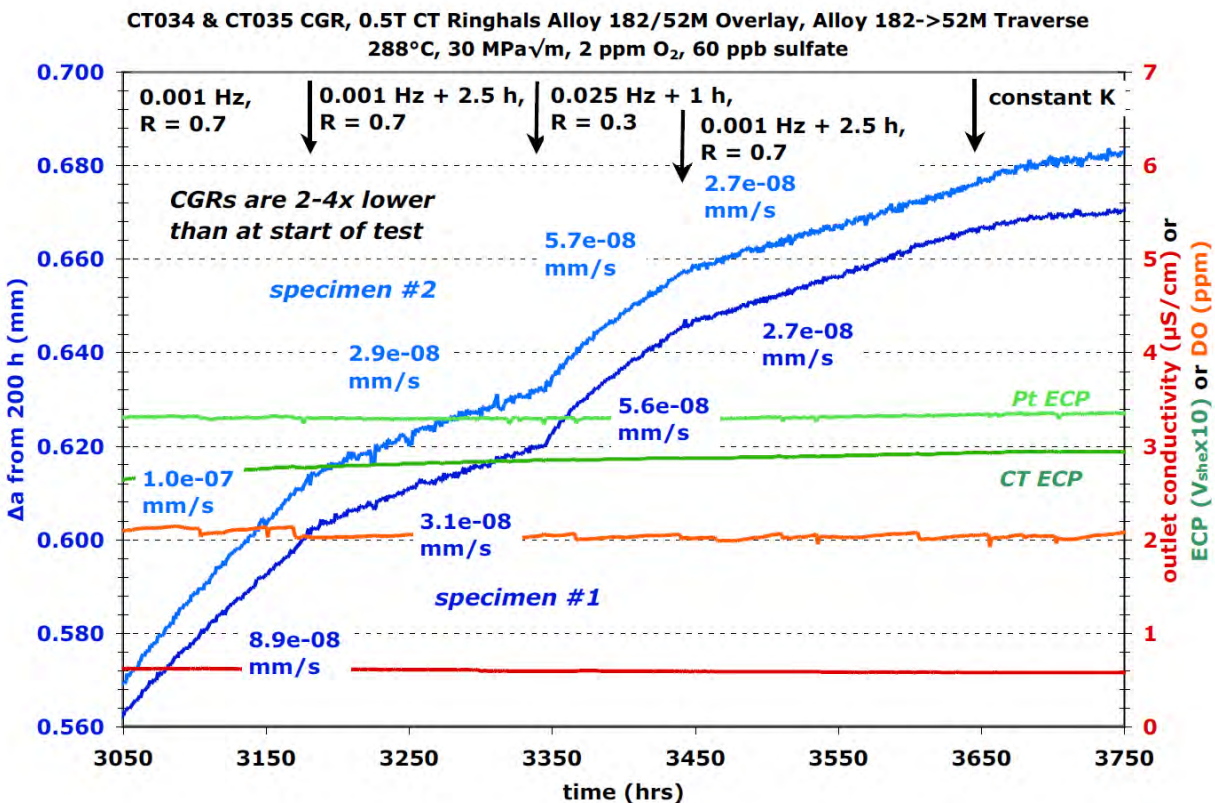
Figure 4-14   Response During the Second Transitioning Phase in BWR Oxidizing Water of the Second Pair of Ringhals Alloy 52M/182 Specimens (CT034 & CT035)
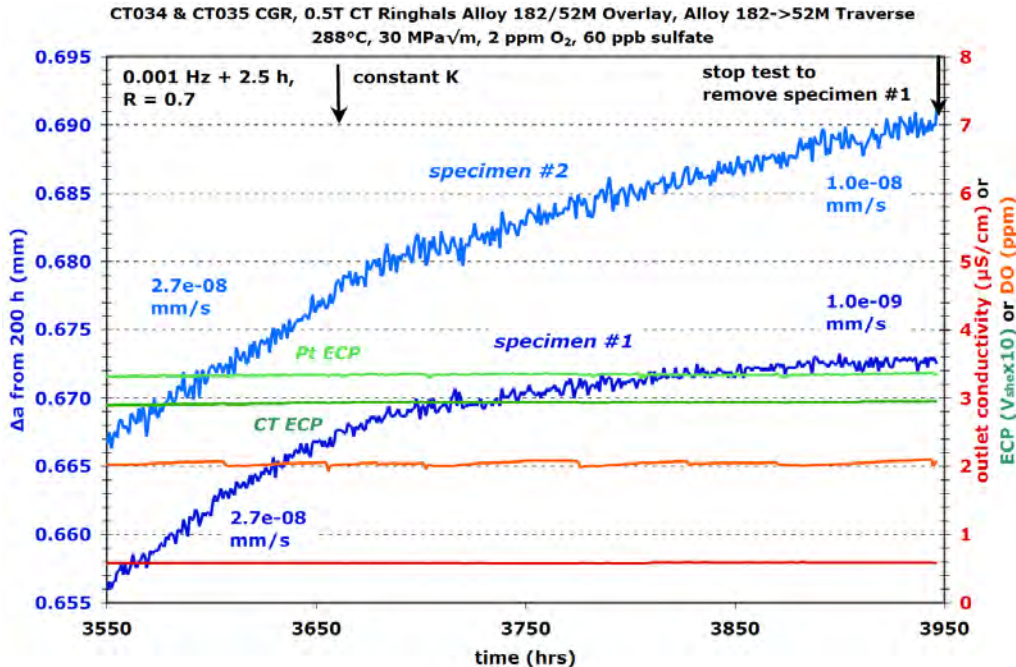
Figure 4-15   The Second Observation of Constant K Response for the Second Pair of Ringhals Alloy 52M/182 Specimens in BWR Oxidizing Water with Sulfate

The lower SCC CGRs being observed in the alloy 182 under aggressive oxidizing conditions creates even more doubt whether a useful evaluation of the alloy 182/52M interface can be obtained. If sustained higher SCC CGRs cannot be produced in alloy 182, it will be impossible to assess CGR changes during the approach to the interface. PNNL results on the four Ringhals overlay mockup samples clearly demonstrated the high SCC resistance of this alloy 182 in hydrogenated water. It also revealed that the alloy 182 is somewhat resistant to SCC in oxidizing BWR water. While the measured CGRs suggest that IGSCC is occurring, rates are still >5X lower than expected in oxidizing water plus sulfate.

After discussion with the NRC project manager, it was decided to stop the test to remove specimen CT034 for examination the crack front location at side surfaces and then document the crack-growth surface. These characterizations clearly showed that the crack front had intersected the alloy 52M prompting the decrease in propagation rates. The decision was made to restart the test on specimen CT035 under simulated PWR primary water conditions and apply aggressive cycling to advance the crack front moving it completely into the alloy 52M.

After crack extension at 0.1 Hz and 0.01 Hz, a number of transitioning steps were applied with variations in R and hold time. A rate of 3.2×10^{-8} mm/s was eventually established under cycle + hold loading at R = 0.5 as shown in Figure 4-16. This rate is approximately 3X higher than has been observed in the previous tests on alloy 152/52/52M, and decision was made to evaluate constant K at this time. A small step increase in DCPD-measured crack length (~10 μm) was detected when constant K was established at 5825 h, similar to that seen when switching from cycling to cycle + hold conditions previously. A stable CGR of 9.4×10^{-9} mm/s was seen over the first 300 h at constant K and then decreased slightly to 7.6×10^{-9} mm/s over the next 400 h. This final constant K response is shown in Figure 4-17. A summary of test conditions, crack extension, and growth rate for each phase of the test is shown in Table 4-2. These SCC propagation rates are 6-20X higher than those previously measured for alloy 52 welds.
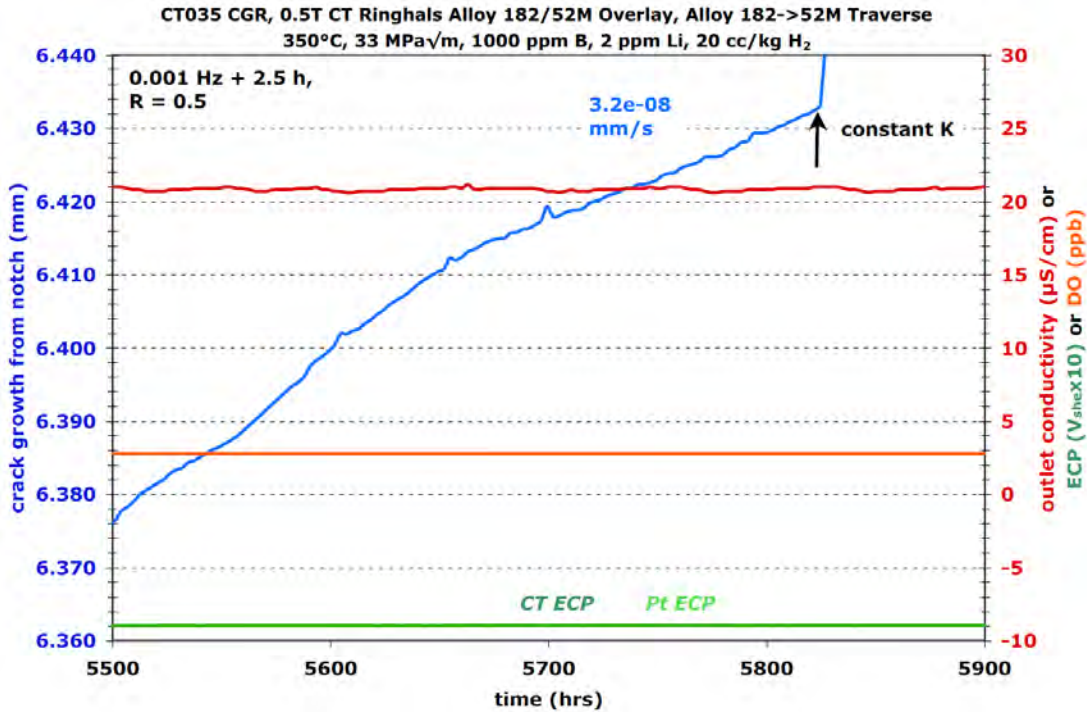
Figure 4-16   Final Cycle + Hold Loading Response of Ringhals Alloy 52M/182 Specimen CT035 Showing a Relatively High Rate of 3.2x10-8 mm/s
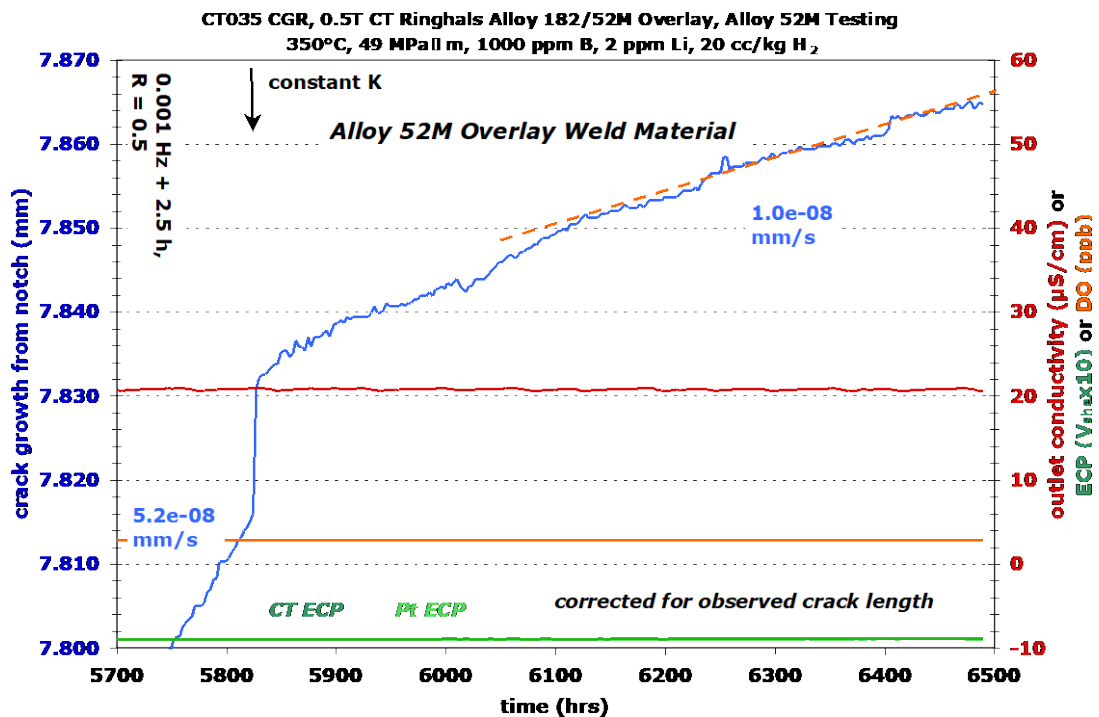
Figure 4-17   Final Constant K Response of Ringhals Alloy 52M/182 Specimen CT035 with Final Propagation in the Alloy 52M

Table 4-2 Data Summary for Ringhals Alloy 52M/182 Overlay Specimens CT034 & CT035

Test Phase	Dur-ation (h)	R	Freq (Hz)	Hold (h)	Water Chemistry Conditions	Temp (°C)	CT034 Ringhals Alloy 52M/182 Overlay Pair #2 Kmax (MPa√m)	CGR (mm/sec)	Approx. Crack Extension (mm)	CT035 Ringhals Alloy 52M/182 Overlay Pair #2 Kmax (MPa√m)	CGR (mm/sec)	Approx. Crack Extension (mm)
1	~2	0.3	5	0	air precrack	RT	25	2.3E-04	0.50	25	9.5E-05	0.50
2	~2	0.5	5	0	air precrack	RT	28	6.0E-05	0.30	28	6.5E-05	0.30
3	~2	0.6	5	0	air precrack	RT	30	4.3E-05	0.20	30	4.3E-05	0.20
4	~2	0.7	5	0	air precrack	RT	30	2.2E-05	0.20	30	2.1E-05	0.20
5	8	0.7	0.1	0	O2 + SO4 [A]	288	30	2.1E-06	0.057	30	3.8E-06	0.090
6	69	0.7	0.01	0	O2 + SO4 [A]	288	30	6.4E-07	0.163	30	1.3E-06	0.311
7	138	0.7	0.001	0	O2 + SO4 [A]	288	30	2.2E-07	0.135	30	4.2E-07	0.269
8	415	0.7	0.001	2.5	O2 + SO4 [A]	288	30	7.1E-08	0.176	30	6.6E-08	0.127
9	23	0.5	0.001	2.5	O2 + SO4 [A]	288	30	- -	0.012	30	- -	0.015
10	140	0.7	0.001	2.5	O2 + SO4 [B]	288	30	6.6E-08	0.033	30	8.2E-08	0.039
11	402	---	const K	---	O2 + SO4 [B]	288	30	1.4E-08	0.025	30	1.6E-08	0.030
12	31	0.7	0.001	2.5	O2 + SO4 [B]	288	30	6.1E-08	0.009	30	7.5E-08	0.011
13	116	---	const K	---	O2 + SO4 [B]	288	30	1.3E-08	0.006	30	1.1E-08	0.005
14	32	0.5	0.001	2.5	O2 + SO4 [B]	288	30	1.1E-07	0.014	30	1.2E-07	0.018
15	387	---	const K	---	O2 + SO4 [B]	288	30	1.1E-08	0.018	30	6.7E-09	0.011
16	363	---	const K	---	2 ppm O2	288	30	8.1E-09	0.012	30	4.4E-09	0.006
17	813	---	const K	---	20 cc/kg H2	350	30	2.2E-09	0.013	30	6.9E-10	0.001
18	5	0.5	0.1	0	O2 + SO4 [B]	288	30	7.7E-06	0.110	30	9.3E-06	0.134
19	7	0.7	0.1	0	O2 + SO4 [B]	288	30	2.6E-06	0.042	30	2.3E-06	0.043
20	43	0.7	0.01	0	O2 + SO4 [B]	288	30	3.1E-07	0.050	30	3.8E-07	0.056
21	160	0.7	0.001	0	O2 + SO4 [B]	288	30	8.9E-08	0.050	30	1.0E-07	0.059
22	168	0.7	0.001	2.5	O2 + SO4 [B]	288	30	3.1E-08	0.018	30	2.9E-08	0.018
23	95	0.7	0.025	1	O2 + SO4 [B]	288	30	5.6E-08	0.026	30	5.7E-08	0.026
24	218	0.7	0.001	2.5	O2 + SO4 [B]	288	30	2.7E-08	0.020	30	2.7E-08	0.020
25	288	---	const K	---	O2 + SO4 [B]	288	30	1.0E-09	0.006	30	1.0E-08	0.013
26	52	0.7	0.001	0	20 cc/kg H2	350	specimen removed from test			32	6.9E-09	0.016
27	21	0.3	0.2	0	20 cc/kg H2	350	"			33	1.9E-05	2.049
28	230	0.5	0.1	0	20 cc/kg H2	350	"			33	6.0E-06	0.461
29	184	0.7	0.01	0	20 cc/kg H2	350	"			33	5.8E-07	0.396
30	395	0.7	0.001	0	20 cc/kg H2	350	"			33	6.7E-08	0.032
31	64	0.7	0.001	2.5	20 cc/kg H2	350	"			33	5.9E-09	0.008
32	115	0.5	0.001	2.5	20 cc/kg H2	350	"			33	-	- -
33	427	0.5	0.001	0	20 cc/kg H2	350	"			33	4.9E-07	0.168
34	332	0.5	0.001	2.5	20 cc/kg H2	350	"			33	5.2E-08	0.081
35	660	---	const K	---	20 cc/kg H2	350	"			49	1.0E-08	0.034

[A] 2 ppm O_2 + 30 ppb SO_4^- ; [B] 2 ppm O_2 + 60 ppb SO_4^-

After testing was completed, CT035 was cut into two slices (1/3 and 2/3 of the thickness, respectively) of which the 2/3 section was fractured open, and the 1/3 section polished in cross-section to analyze the crack growth morphology using analytical microscopic analysis. Figure 4-18 shows the section of CT035 that was fractured open, illustrating the location of the 182/52M interface as well as the IG cracking within the 52M near the leading crack front when the test was transitioned to constant K. At the leading crack front, fingers of IG cracking appear consistent along solidification grain boundary packets, hence the entire front is not engaged at the the same time.

Figure 4-18   Optical Micrograph of the Crack Growth Surface of CT035

Optical micrographs of the side surface (which were highly polished and etched, Figure 4-19a) show the crack morphology of the entire test, with the first portion of the crack propagating through the A182 and the second through various weld passes of 52M. Higher magnification (the yellow box in the Figure 4-19b) shows the portion of the test within various weld passes of 52M and the approximate cycling regimes. The final ~1.25 mm of the test was run under constant K conditions, and the light surface etching revealed that it propagated intergranularly through a weld pass. The majority of the crack growth past the 182/52M interface was determined to be TG, with some incidental IG cracking most likely due to aligned boundaries.

EDS elemental mapping (Figure 4-20) of the SCC test between the 182/52M interface and the end of the test shows the variability in the composition of each of the 52M weld passes. To better illustrate the differences, color maps of Ni (in green), Cr (in red) and Fe (in blue) were overlaid on the SEM-BSE images to form a montage (Figure 4-21). Elemental linescans were taken along either side of the crack (as indicated in the overlay image), and are also presented in Figure 4-21. The elemental maps and linescans clearly indicate the transition from the 182 to 52M as well as the different 52M weld passes through the Ni and Cr-K signals. In the 52M, the first two passes have Cr content close to 30 wt% (Ni ~60 wt%), whereas in the third weld pass (of which the majority of the constant K testing was performed) the Cr content dropped to ~25 wt% and the Ni composition rose to close to ~70 wt%. In the final portion of the test, the SCC crack grew through a weld pass that was closer in composition to the first two weld passes.

While the slightly etched cross-sections (Figure 4-19) provided some grain boundary relief, EBSD performed on the last 2 mm of the test (Figure 4-22) clearly highlights the microstructure and crack growth path. Traces taken from the EDS elemental maps of the various weld passes

in the alloy 52M are overlaid on the EBSD maps to show the chemistry in relation to the microstructure. In weld pass #2 the majority of the crack is TG continuing on through half of weld pass #3 where the crack becomes IG. The transition to IG could be coincidental with the grain boundary being oriented almost perfectly with the growing crack. Approximately 500 µm before the final weld pass the crack becomes TG as it passes through a smaller grain packet, but quickly becomes IG again through the end of the test. A higher magnification EBSD pattern quality map of the end of the crack growth test is presented along with a trace of the crack (red line) to better illustrate the IGSCC cracking. Local misorientation maps of the final crack growth test show higher misorientations around the propagating crack, and possibly higher misorientation in weld pass #2 as compared to passes #3 and #4.
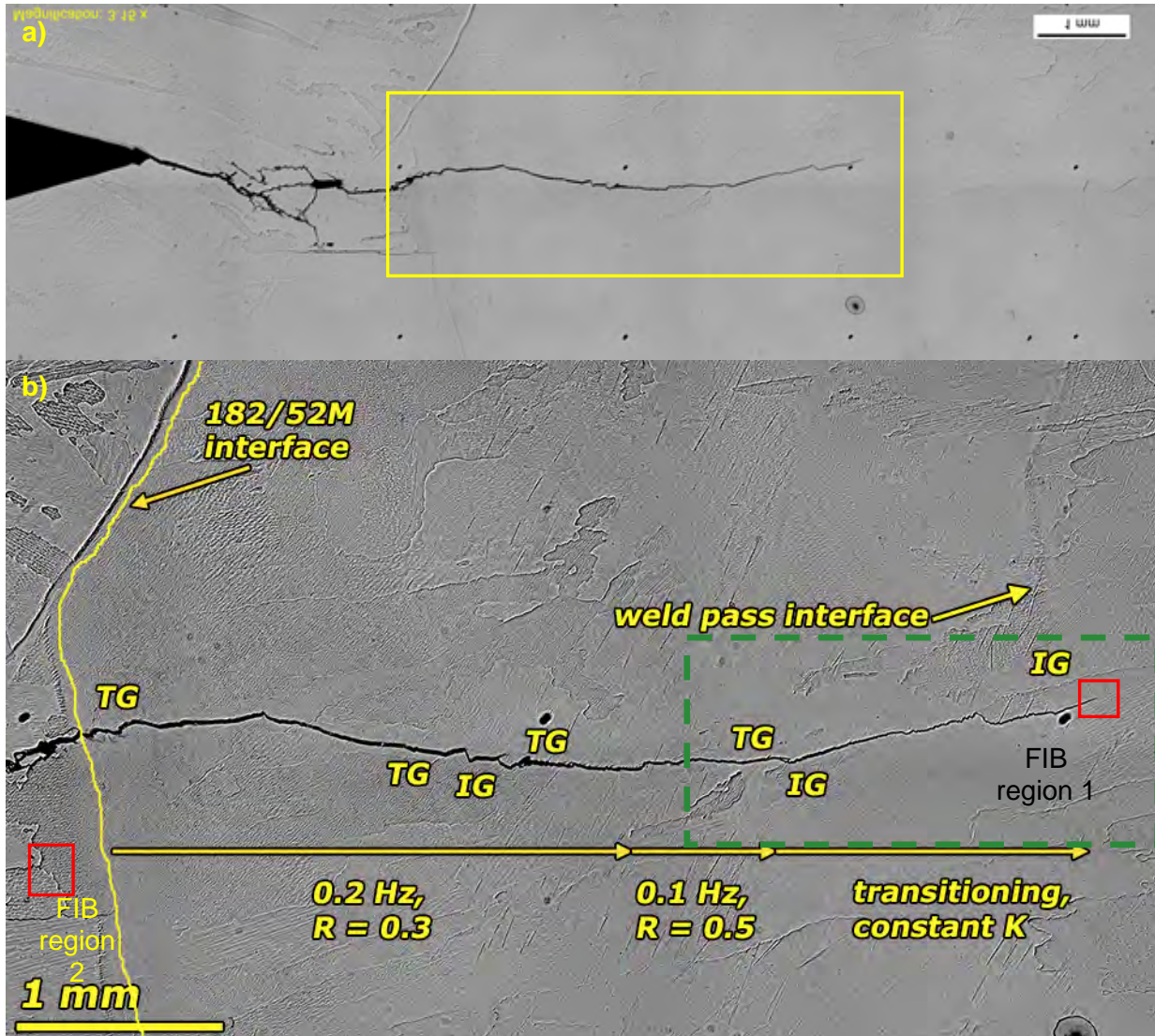
Figure 4-19   **Optical Micrographs (low and high magnification with solid yellow box showing high mag region of interest) of the Side Surface of CT035. The Dashed Green Box Shows the Location of EBSD Analysis. Two FIB Samples (Regions 1 and 2) Were Prepared from This Cross-Section and Are Highlighted by the Solid Red Boxes**
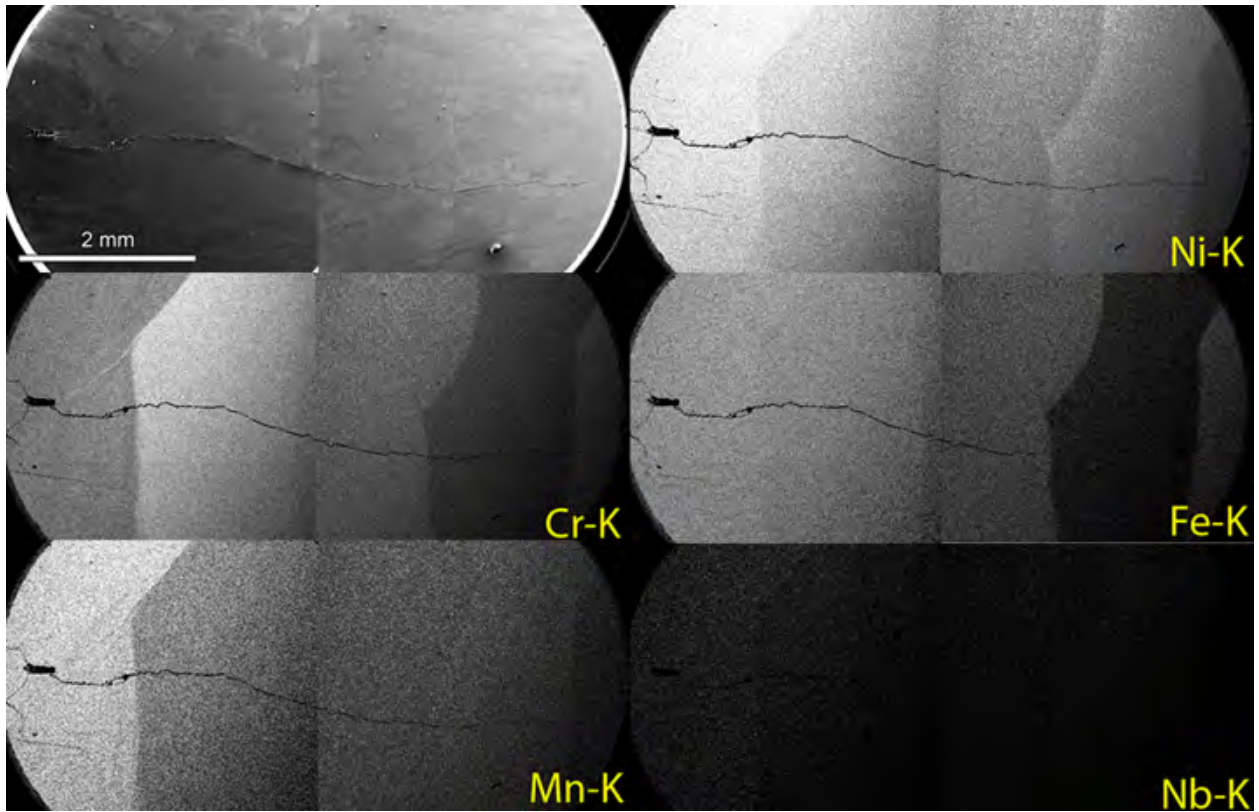
Figure 4-20 **SEM-BSE Image and EDS Elemental Maps of the CT035 Cross-Section Following the SCC Crack Path from the Alloy 182 Through Several Weld Passes of the Alloy 52M (approximately the same region as solid yellow box in Figure 4-19a). The Crack Ends in an Alloy 52M Region of Distinctly Different Composition (higher Ni, lower Cr and Fe)**
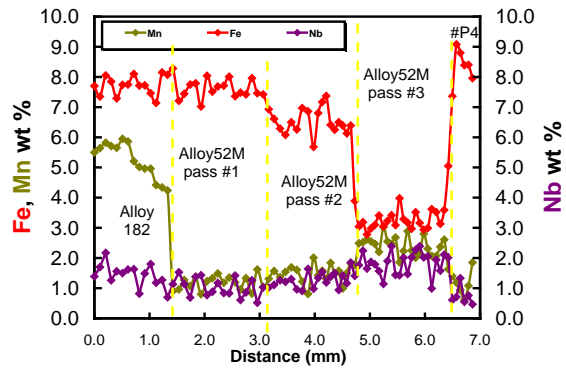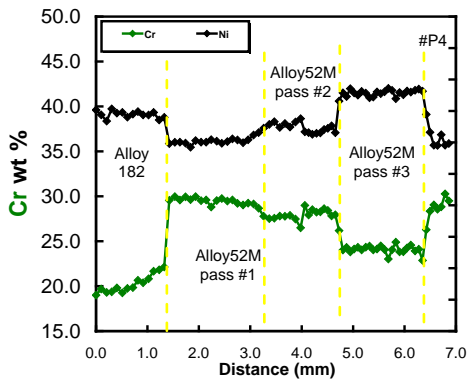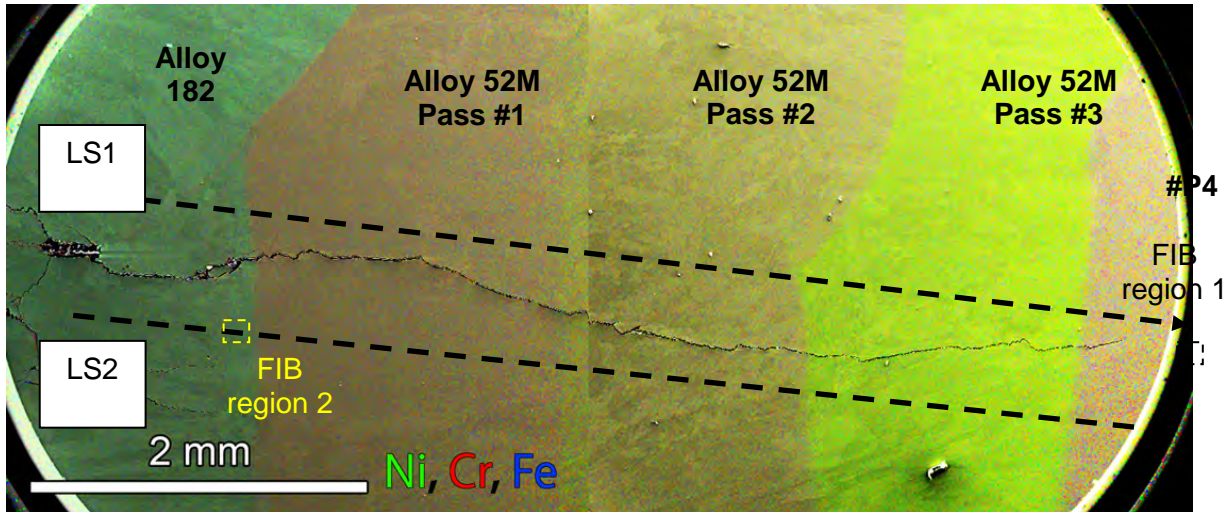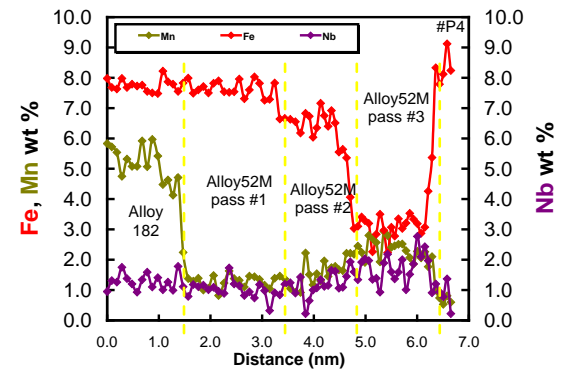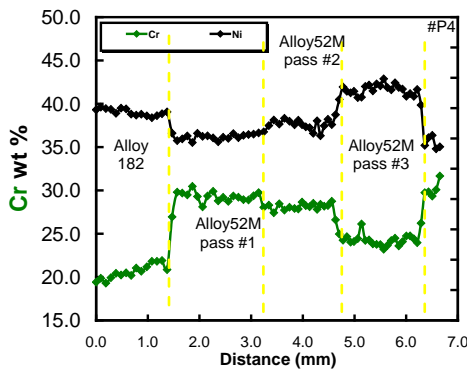
Figure 4-21   SEM-BSE Image with an Overlaid Composite EDS Elemental Maps for the CT035 Cross-Section Following the SCC Crack Path from the Alloy 182 Through Several Weld Passes of the Alloy 52M. EDS Line Scans Are Shown Illustrating the Composition Changes from the Alloy 182 to Alloy 52M and into the Ni-Rich Pass
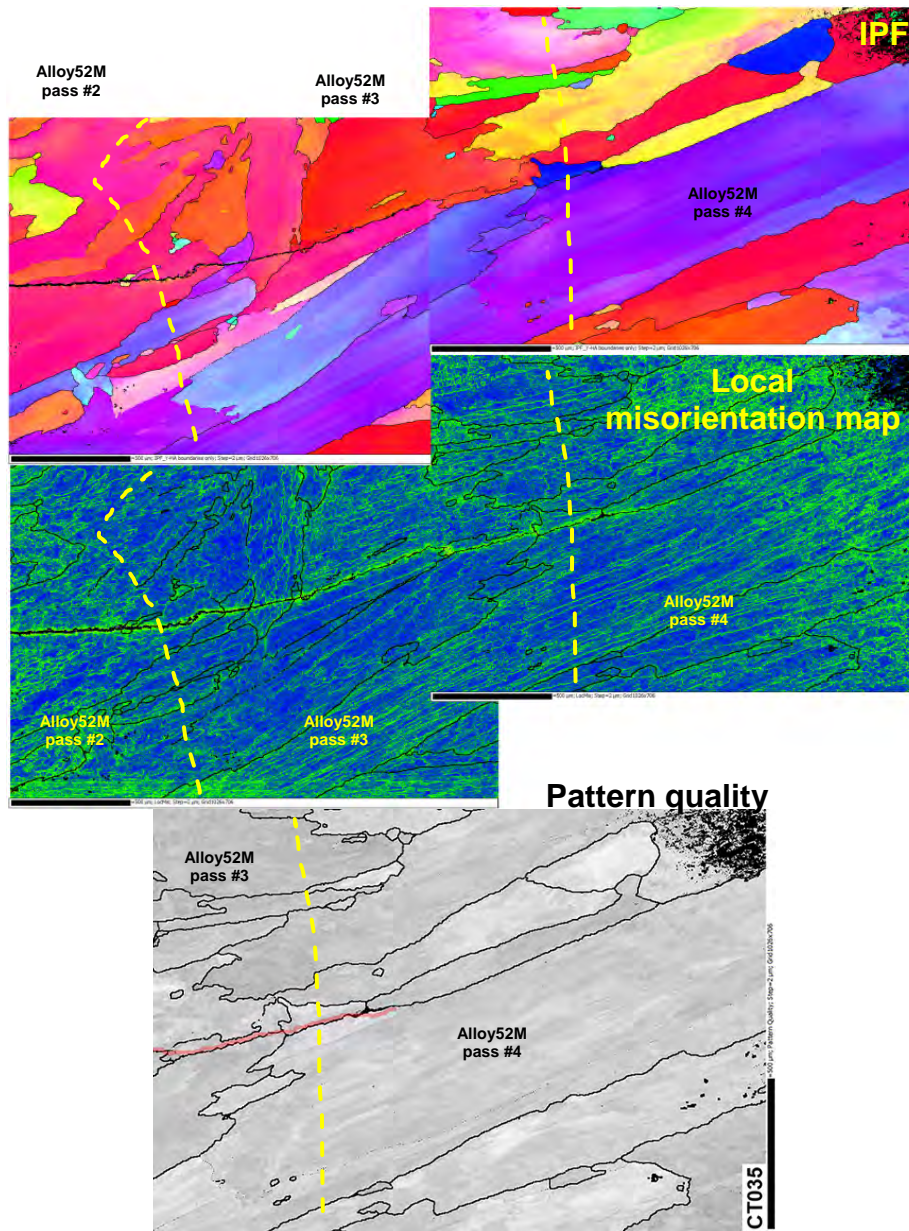
Figure 4-22   SEM-EBSD Pattern Quality Map, IPF Images and Local Misorientation Maps for the Final Length of the SCC Crack on the Side Surface of Specimen CT035. The Pattern Quality Map Is Shown for the Leading SCC Crack Tip (with a red line overlay to show approximate location of the crack)

In order to ascertain as to whether the local chemistry could be affecting the SCC crack growth, two plan view FIB samples were prepared (see locations in Figure 4-19 and Figure 4-21) from CT035, one from the leading SCC tip (52M weld pass#4) and one from a secondary crack in the A182.

Figure 4-23 shows medium (a) and high (b) magnification SEM-BSE and SE images of the leading IGSCC tip that corresponds to FIB Region #1. While the medium magnification image appears to corroborate previous images (Figures 4-19 and 4-22) showing the leading SCC tip is IG, at higher magnification it appears there are both IG and TG components to the tip. The plan

view FIB sample prepared from the dashed yellow box in Figure 4-23b was examined in SEM (Figure 4-24), illustrating this IG and TG appearance of the final tip. The crack appears to be traveling along the grain boundary, but there are TG offshoots at least near the crack front. The extensive penetrative oxidation around the primary and TG cracks suggests that the crack tip had been exposed to water for an extended period of time, therefore this is not an active crack. STEM/EDS elemental maps of this TEM sample were collected, but did not show any unique chemical segregation along the grain boundary. The penetrative oxidation is mostly Cr rich with some increased Ni content. Ni-rich oxide was observed to be deposited on the crack walls. A higher magnification STEM/EDS elemental map was collected at the end of the IG crack (Figure 4-25) and illustrates that there are small (75-100 nm) Cr-rich precipitates ahead of the crack.
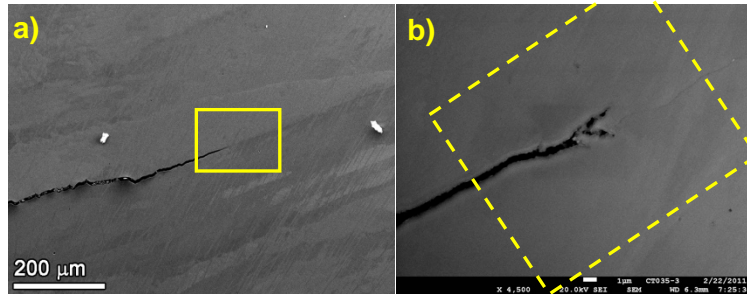
Figure 4-23   SEM-BSE Micrographs of the Leading SCC Crack in CT035 Corresponding to FIB Region 1 in Figures 4-19 and 4-22. The Solid Yellow Box in a) Shows the Location of b), and the Dashed Yellow Box in b) Indicates the Location of the Plan View FIB Sample

Figure 4-24   SEM-BSE Images of the Leading IGSCC Crack Tip in the Alloy 52M Pass of Altered Composition
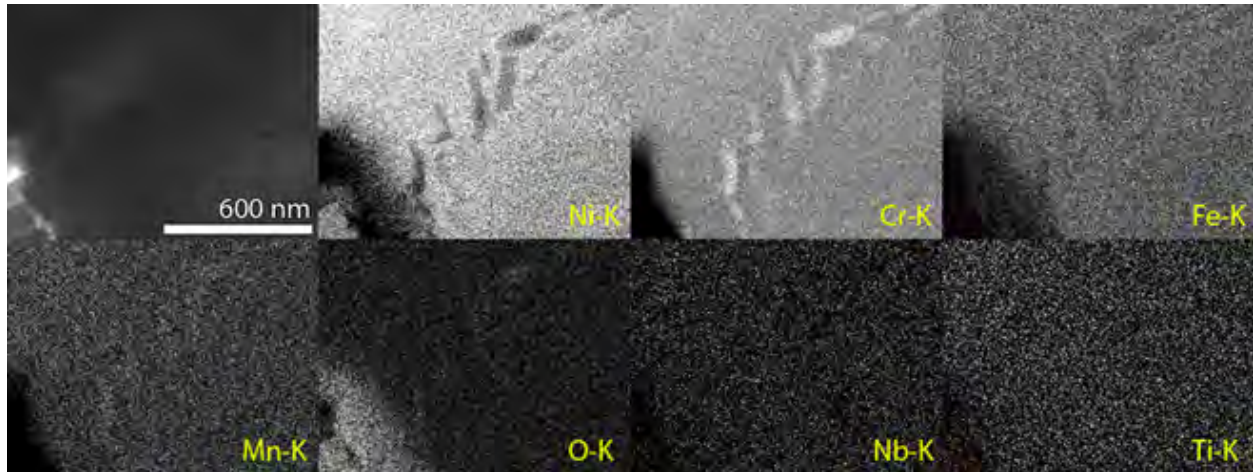
Figure 4-25   STEM/EDS Elemental Maps of an IG Crack Tip from the Dashed Yellow Box in Figure 4-24

A second FIB sample from a secondary IGSCC tip in the A182 region close to the A182/52M interface was prepared (see Figures 4-19, 4-21, and 4-26). In this instance, the secondary SCC was moving in a plane ~400 µm below the main crack, but still in the same direction as the main crack. From Figure 4-26, it can be observed that the secondary crack encountered a triple point and began moving along a grain boundary interface in a direction towards the main crack. The location of the plan view FIB sample is shown in the dashed yellow box in Figure 4-26b, and should be noted that the presentation of data in further figures re-aligns the crack orientation laterally instead of vertically as in Figure 4-26.

High resolution low kV SEM-BSE imaging of the plan view FIB sample better illustrates the microstructure of the secondary IGSCC tip (Figure 4-27). From this image, the penetrative oxidation along the crack walls is sparse, and appears to taper towards the front of the crack suggesting that this was an active secondary crack. The crack appears to be primarily IG, with one small TG offshoot. The density of IG precipitation can be observed ahead of the leading crack tip, with precipitates on the order of 50-100 nm. STEM/EDS elemental mapping of the leading tip (Figure 4-28) indicates that the IG precipitates are a mixture of Cr, Nb and Ti rich particles. The penetrative oxidation is mostly Cr rich, with some enrichment of Ni as indicated by the colored elemental map (Fe in red, Cr in green, and Ni in blue). As well, in both the Ni-K and colored map, there is slight Ni enrichment ahead of the crack tip. The FIB sample was slightly too thick to get a good indication of this Ni enrichment, and hence projection issues convoluted the oxide signal with the adjacent Cr depletion/Ni enrichment.
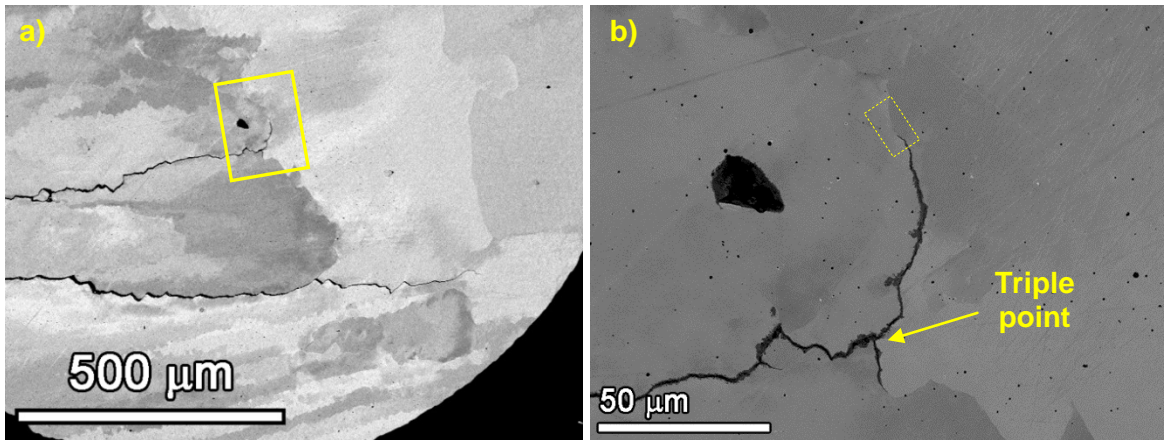
Figure 4-26 SEM-BSE Image of Secondary IGCSCC Cracks in the Alloy 182 Weld Metal for CT035. Solid Yellow Box in a) Provides the Location of b), and the Dashed Yellow Box in b) Illustrates the Location of the Plan View FIB Sample. Note the Orientation of These Images Is Identical to Those Shown Earlier in This Section
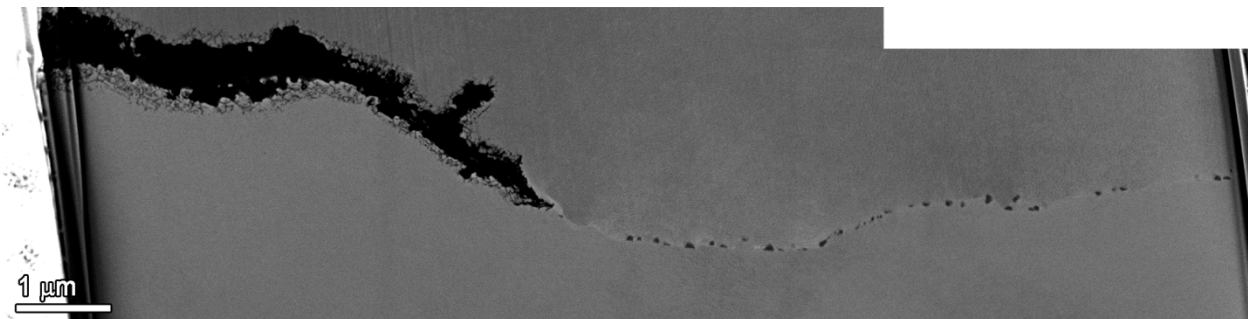
Figure 4-27 SEM-BSE Images of Secondary IGSCC Cracks (FIB region 2 in Figures 4-19 and 4-22) In the Alloy 182 Weld Metal for Specimen CT035. Note the FIB Orientation of the Sample Has Changed (crack orientation is now left to right instead of bottom to top) From the Previous Figures
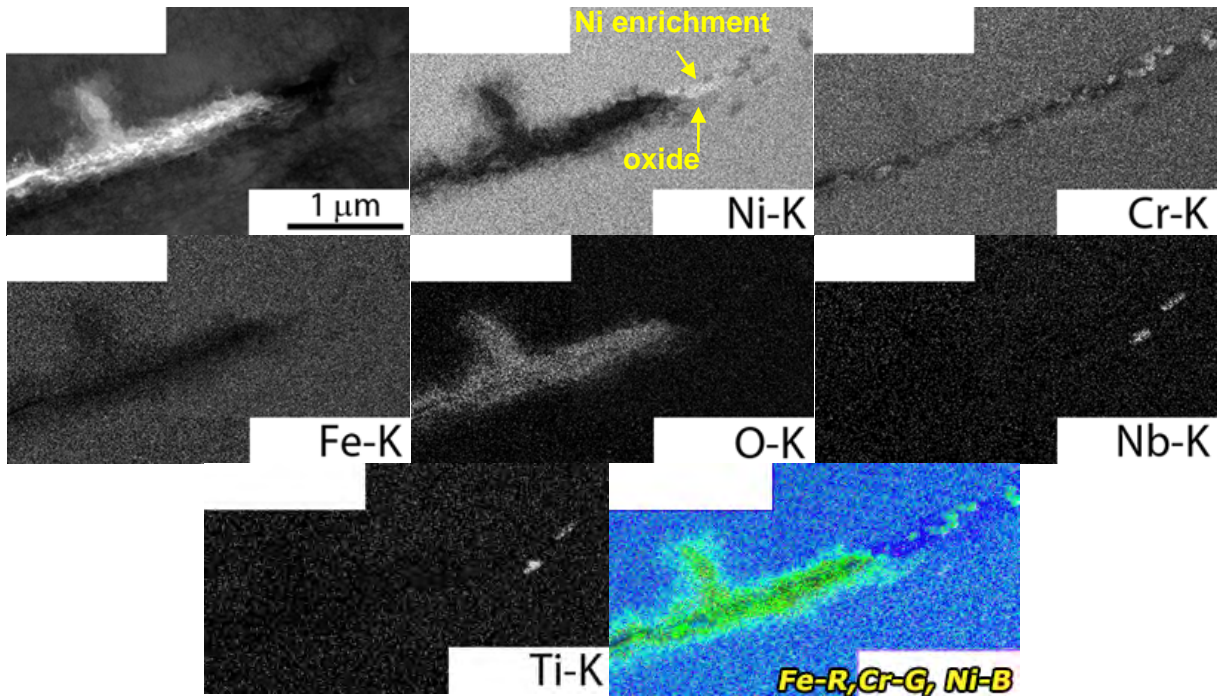
Figure 4-28   STEM/EDS Elemental Maps of a Secondary IGSCC Crack Tip in the A182 Region of the CT035 Sample

4.2   Ringhals Alloy 52M/82 Inlay Mockup (CT030 & CT031)

As mentioned in the beginning of this chapter, a section of an alloy 52M weld inlay mockup produced for Ringhals was obtained from Rich Jacko of Westinghouse. It consists of alloy 82 robotically deposited onto a low-alloy steel ring followed by a robotically deposited 10 mm thick inlay of alloy 52M. A layer of alloy 152 was manually welded on top of the inlay by Westinghouse to provide sufficient material to obtain CT specimens from the mockup. The approximate location of the 0.5T CT specimens (CT031 and CT032) is shown in the Figure 4-29. The notch was positioned to enable the precrack to be placed in the alloy 82 at a distance of ~0.5 mm from the alloy 52M interface. Side grooves of the machined samples were polished and etched to reveal the alloy 52M inlay and the alloy 82 weld. Examples of these regions are shown in Figure 4-30.
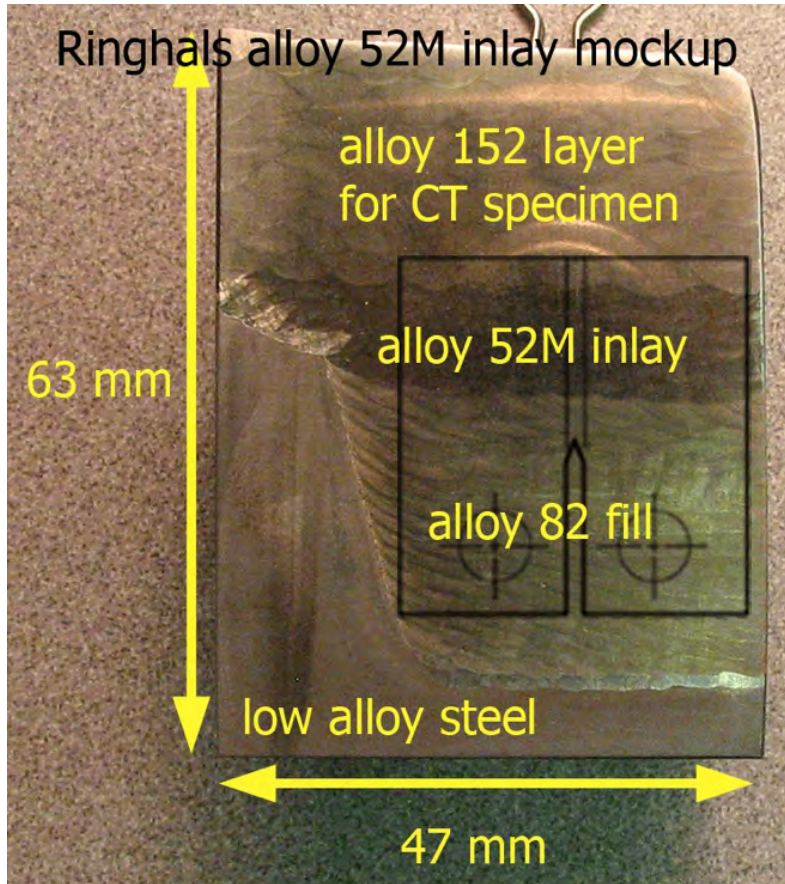
Figure 4-29 **Profile of Ringhals Alloy 52M Inlay Mockup Weld Received from Westinghouse. Alloy 52M Inlay Is 10 mm Thick**
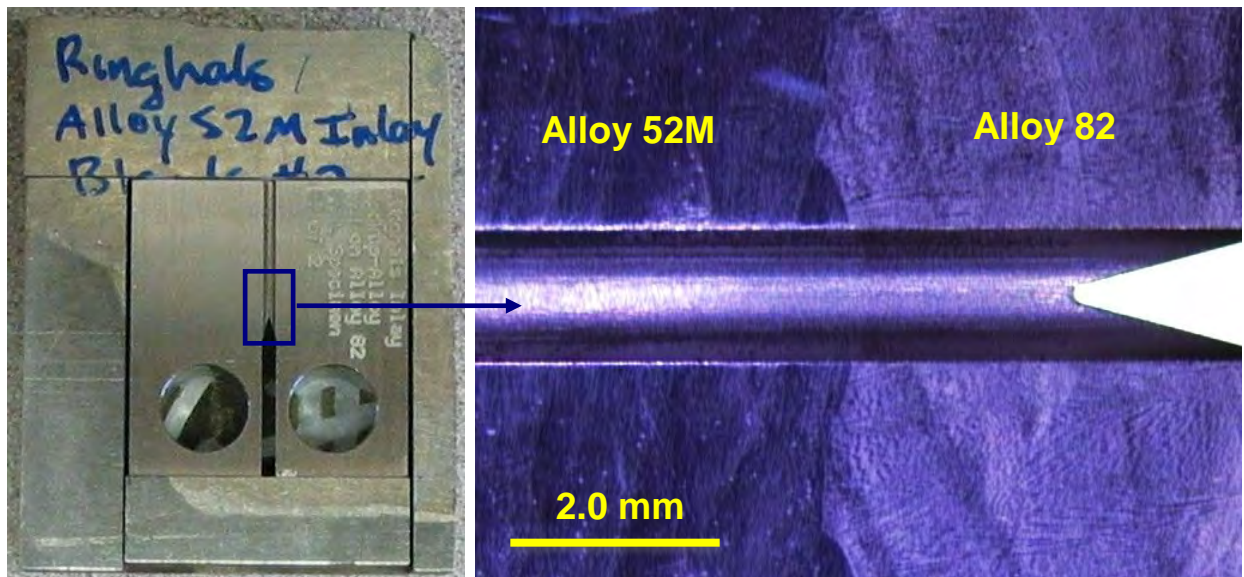
Figure 4-30 **Optical Images of the Alloy 52M/82 Inlay Sample CT031**

The goal of this test on the inlay samples was similar to that for the overlay samples; produce a fully engaged IGSCC crack front in the more susceptible alloy 82 and monitor growth under

constant K conditions as it approaches the alloy 52M interface. An overview of the entire test is shown in Figure 4-31. Testing began at 350°C and 29 cc/kg H_2 and was switched to 20 cc/kg (ECP at Ni/NiO line for expected maximum SCC growth rate) at ~130 h during the gentle cycling at 0.001 Hz. Surprisingly, the change to a hydrogen level near the Ni/NiO line prompted a small decrease in propagation rates. A 2.5-h hold time was added at ~220 h and the propagation rates dropped to ~5.4 and 2.2×10^{-8} mm/s for the two inlay specimens. After ~100 h in this cycle + hold condition, the rates stabilized at 2.9 and 2.1×10^{-8} mm/s. Based on prior alloy 82 results by GE Global, the R value was increased from 0.5 to 0.7 to help promote SCC. Propagation rates decreased by 2-3X after this change to values $<10^{-8}$ mm/s suggesting limited SCC engagement across the crack front. Consistent with this interpretation, rates further decreased to ~3×10^{-9} mm/s or lower when switching to constant K conditions as illustrated in Figure 4-32.

CT030 & CT031 CGR, 0.5T CT Ringhals Alloy 52M Inlay Mockup, Alloy 82->52M Traverse
350°C, 30 MPa√m, 1000 ppm B, 2.0 ppm Li, 29 cc/kg H_2
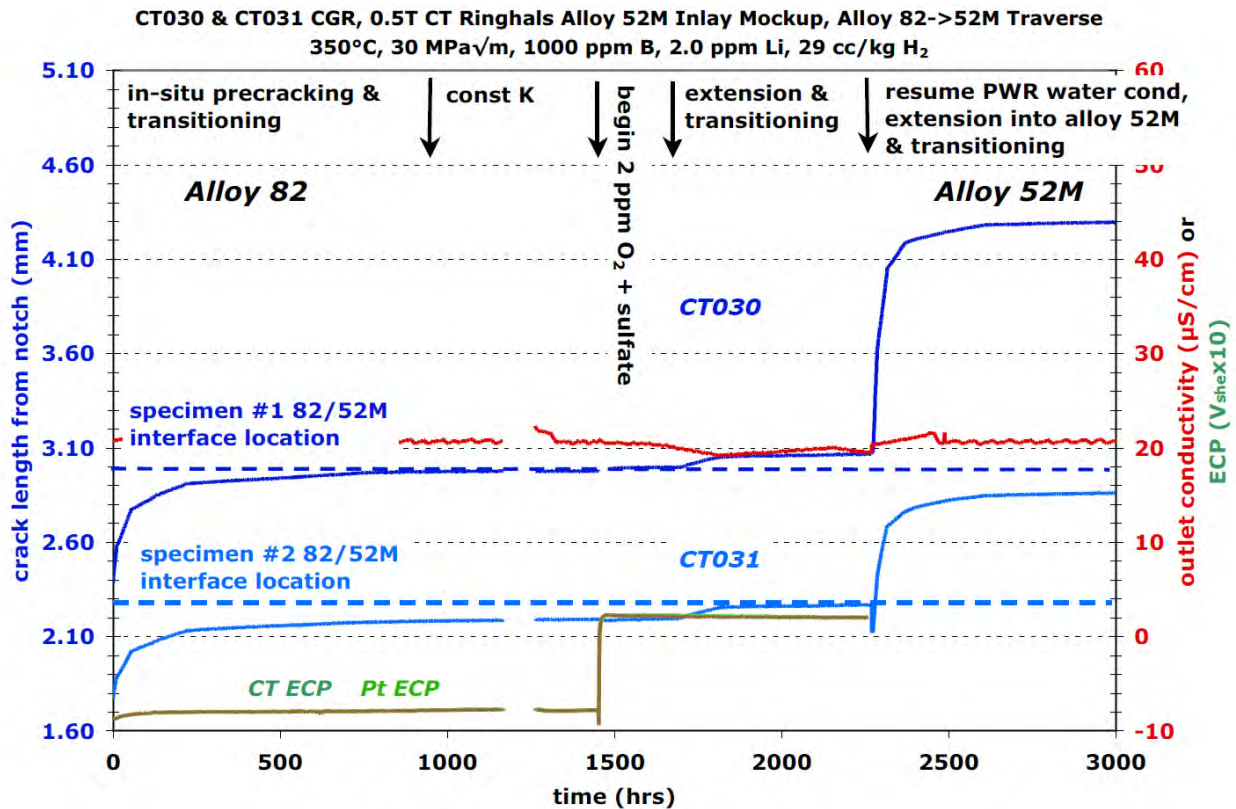
Figure 4-31   Test Overview for the Ringhals Alloy 52M/82 Inlay Mockups (CT030 & CT031)
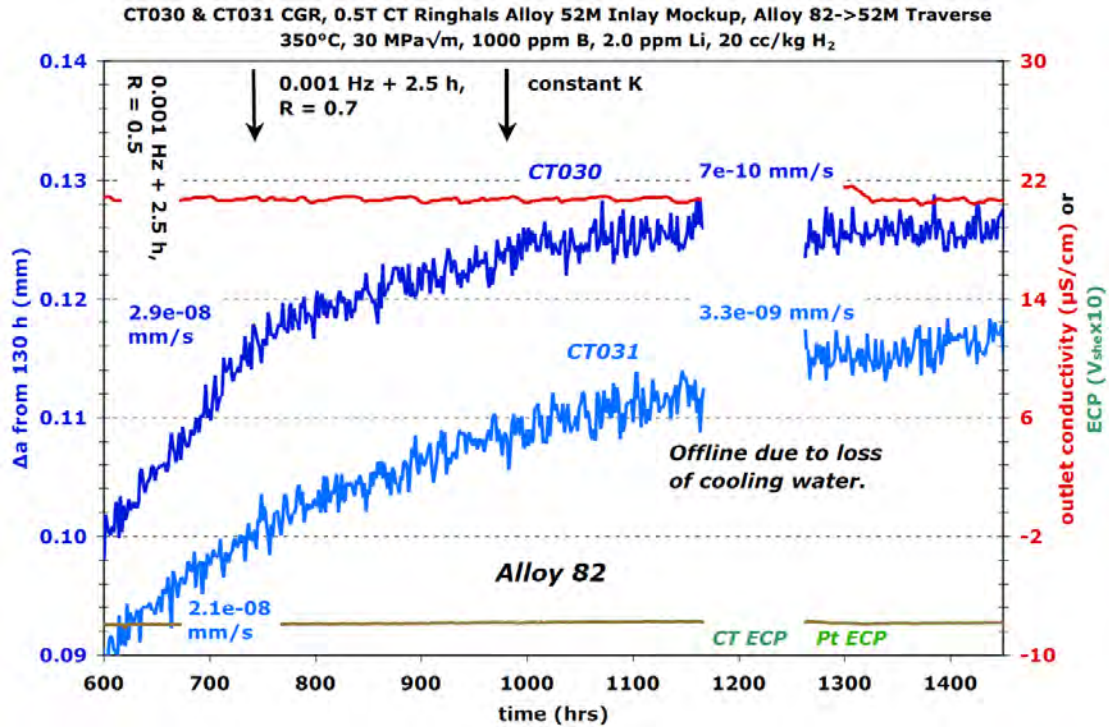
Figure 4-32   Initial Cycle + Hold and Constant K Response in PWR Primary Water of the Ringhals Alloy 52M/82 Inlay Mockup (CT030 & CT031)

In an attempt to promote IGSCC, environmental conditions were switched from hydrogenated to oxygenated and the temperature reduced to 290°C. Under these BWR-like water conditions, a higher IGSCC susceptibility has been observed for alloy 82 particularly with a low level sulfate addition. The goal was again to improve SCC engagement across the crack front under oxidizing conditions and then determine whether more rapid IGSCC rates could be maintained after returning to PWR primary water. Figure 4-33 shows that the CGR was relatively unaffected by the more BWR-like water conditions. At 1700 h, ~60 ppb sulfate was introduced to the water and gentle cycling was performed at 0.01 and 0.001 Hz (R = 0.7) to help restart crack advance followed by the addition of a 2.5 h hold. Unfortunately, CGRs during these transitioning steps were significantly lower than anticipated based on reported alloy 82 behavior in BWR oxidizing water with sulfate additions. The decision was made to stop the test and exam side surfaces to estimate the crack front location. Surprisingly, the cracks were determined to have reached the alloy 52M interface.
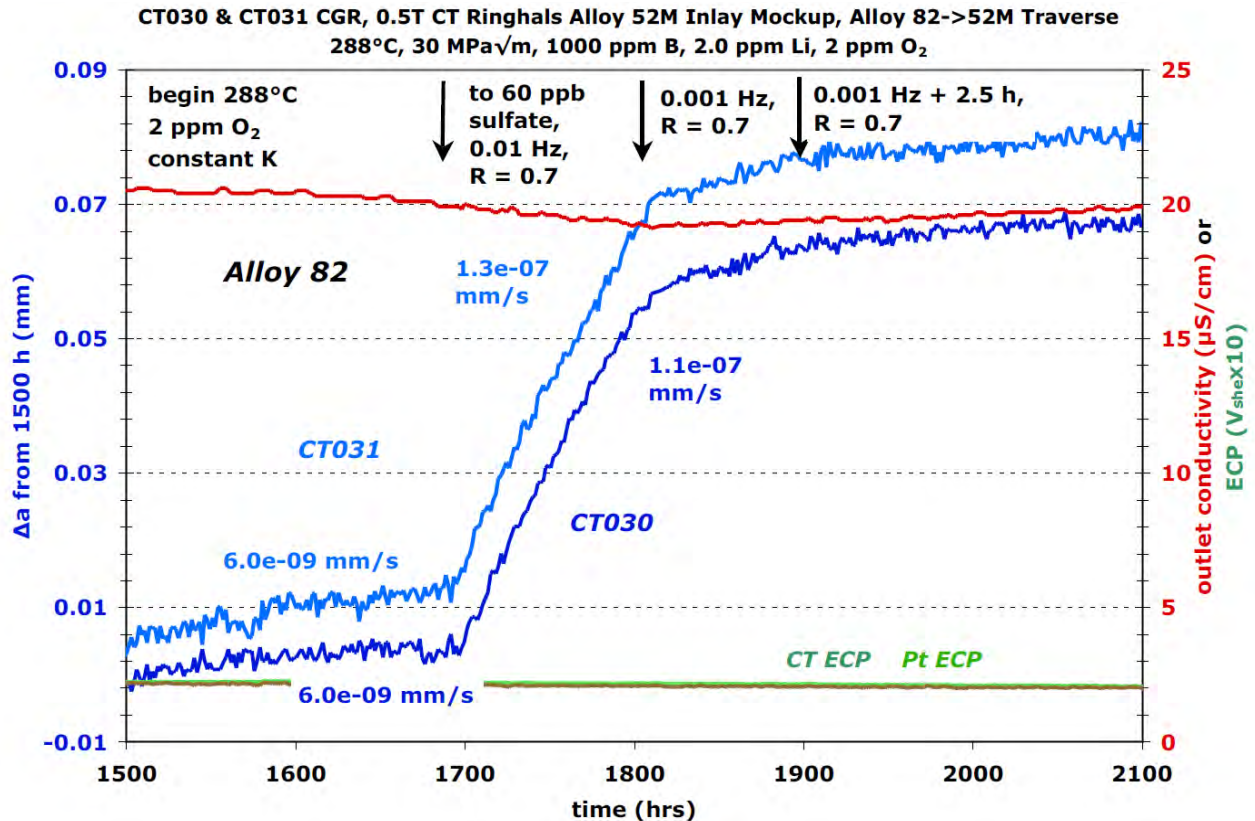
Figure 4-33 Constant K and Cyclic Loading Response of the Ringhals Alloy 52M/82 Inlay Mockup (CT030 & CT031) After Switching from PWR Primary Water to BWR Oxidizing Water

Crack-growth testing continued for the two Ringhals alloy 52M/82 inlay mockup samples after the restart at an accumulated test time of ~2275 h. Aggressive cycling was initiated to extend the crack well into the alloy 52M inlay region and evaluate SCC CGR response in the alloy 52M weld metal. A typical transitioning sequence was used and the cyclic frequency was reduced over multiple steps. Propagation rates during cycling at R = 0.5 were very similar to those measured previously for the alloy 52 weld metal samples (CT024, CT025, CT032 and CT033) and somewhat lower than seen for the alloy 82 weld metal under identical loading and environmental conditions. A 2.5-h hold time was added at ~2600 h and a CGR of $1x10^{-8}$ mm/s was observed (Figure 4-34). Once again, this propagation rate matched that documented previously for the alloy 52 samples, suggesting that limited SCC engagement had been created and constant K propagation rates would probably be $\leq 2x10^{-9}$ mm/s. It was then decided to examine the crack growth response with a less aggressive load ratio. Cyclic loading was changed to continuous cycling at 0.001 Hz, R = 0.7 for ~200 h, and then a 2.5 h hold was added. Propagation rates for both specimens under these loading conditions are similar to the MHI alloy 52 material (CT025 and CT033) where limited (if any) IGSCC was observed at 350°C.

Loading was changed to constant K at ~3820 h and low propagation rates of ~$1x10^{-9}$ mm/s were observed for both samples as illustrated in Figure 4-35. Since limited crack-growth data exists for alloy 52M, the test was continued at constant K to help build confidence in the measured rates. For these low rates, the measured crack extension under constant K loading was ~5 μm after testing for ~1 month.
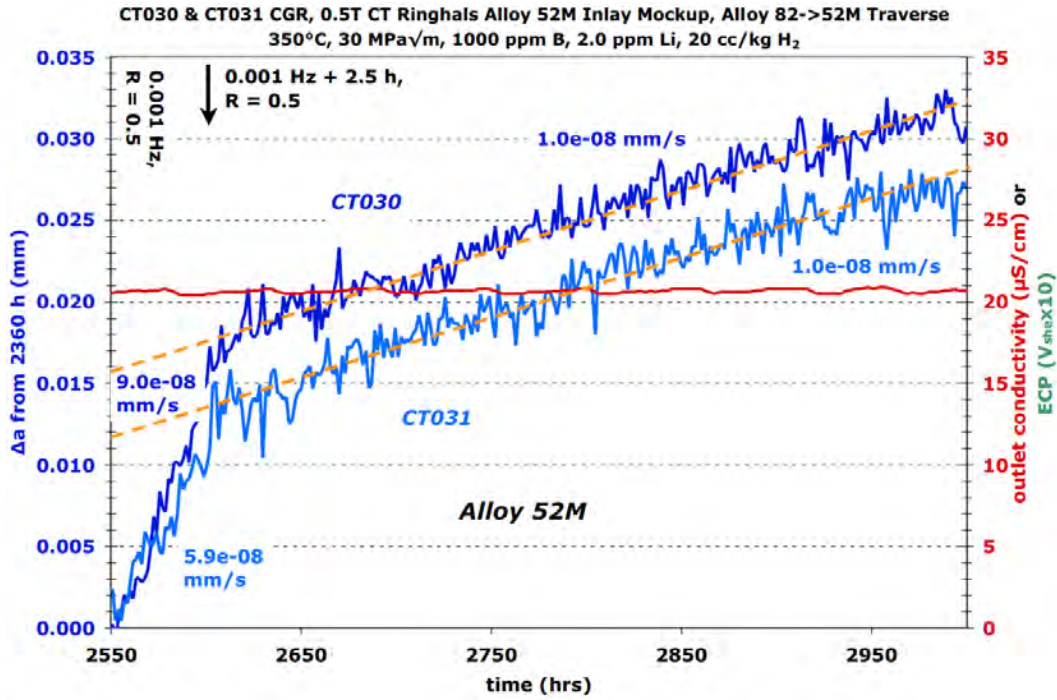
Figure 4-34   Alloy 52M Response During Cycle and Cycle + Hold Loading at R=0.5 in the Ringhals Alloy 52M/82 Inlay Mockup Specimens (CT030 & CT031)
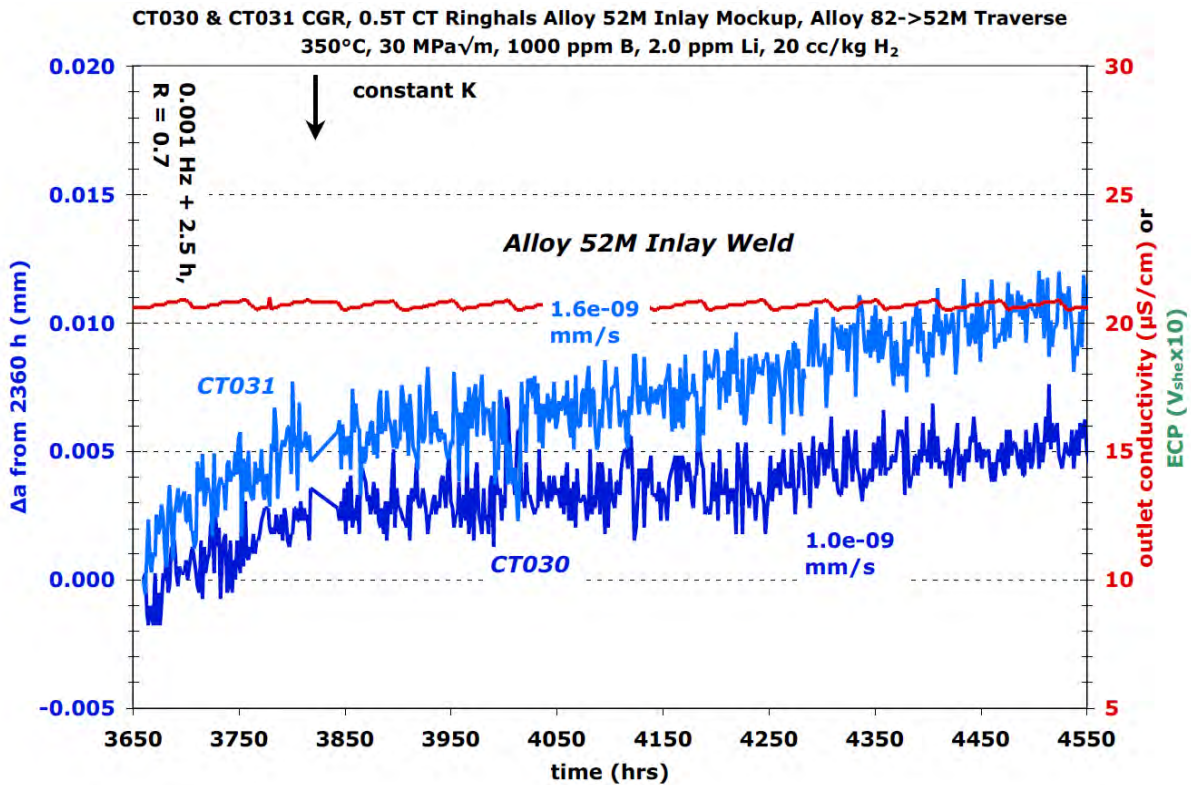
Figure 4-35   Alloy 52M Response During Constant K Loading in the Ringhals Alloy 52M/82 Inlay Mockup Specimens (CT030 & CT031)

The decision was made at ~4600 h to change back to cycle + hold loading and increase the applied K value from 30 to 40 MPa√m using a programmed dK/da response. The initial dK/da rate was ~0.05 MPa√m/μm, giving growth rates of ~6.5x10⁻⁹ mm/s during the 0.001 Hz cycle + 2.5 h condition with R = 0.7. At these slow propagation rates, the increase to 40 MPa√m would have taken months, and therefore, the dK/da was changed to 0.80 MPa√m/μm at ~4950 h producing a ~5 times increase in rate (to ~3x10⁻⁸ mm/s) as documented in Figure 4-36. Although systematic evaluations of dK/da effects were not being attempted, it is clear that the gradual increase in K and delta-K accelerates crack growth. It is important to note that while K is slowly increasing with time, the actual dK/da is high compared with what may be expected in actual piping components. In this case, K is being changed over μm dimensions whereas similar changes in K might be expected over mm dimensions in a component.

Final steps for this test were to evaluate SCC CGRs in the alloy 52M inlay at a higher K level of 40 MPa√m. The cycle + hold response was 1.3x10⁻⁸ mm/s for the two samples as shown in Figure 4-33. This compares to rates of 4.5 and 2x10⁻⁹ mm/s (3-4X lower) under this loading condition at 30 MPa√m earlier in this test. The higher CGRs at 40 MPa√m are similar to that measured for the MHI alloy 152 weld metal where localized regions of IGSCC were observed. Constant K conditions were established at ~5495 h and steady growth was observed in both specimens during this period with CGRs of 1.0x10⁻⁹ and 1.6x10⁻⁹ mm/s as shown in Figure 4-37. These rates are identical to those obtained on these specimens at 30 MPa√m, and the test was ended at 6500 h. A summary of test condition and corrected specimen response for each phase of the test is shown in Table 4-3.
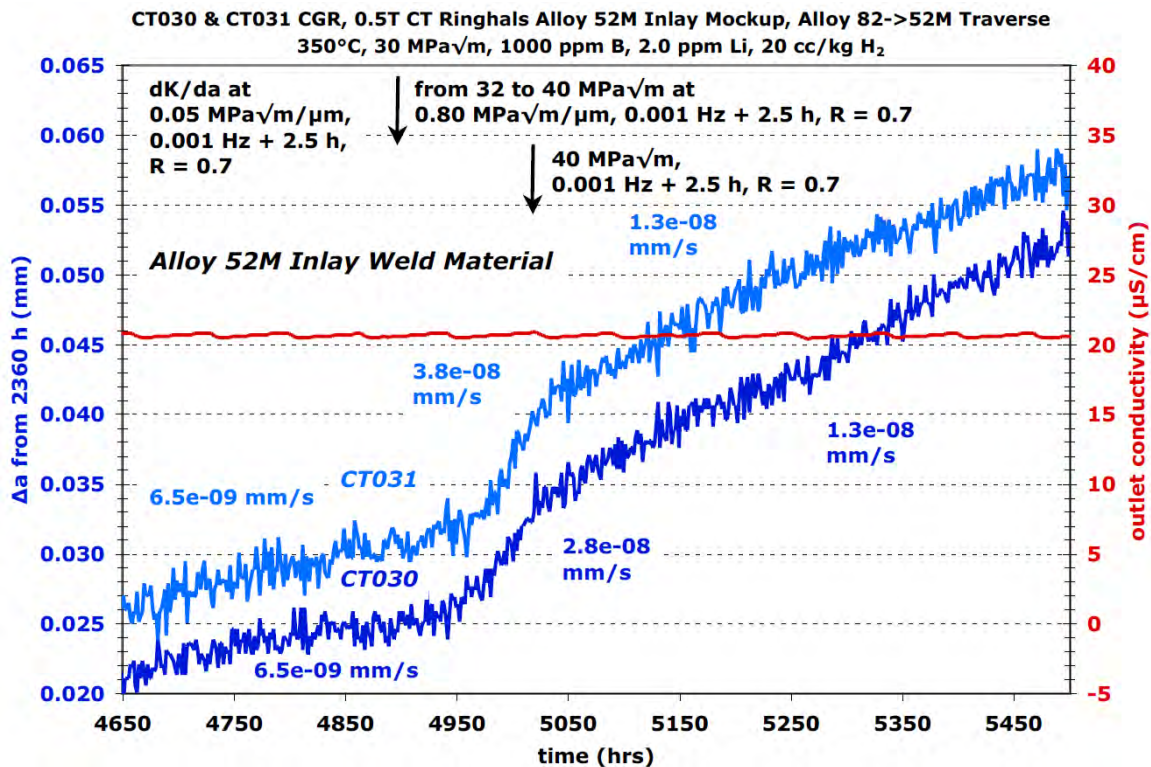
Figure 4-36   dK/da Response Going from 30 to 40 MPa√m of the Ringhals Alloy 52M/82 Inlay Mockup Specimens (CT030 & CT031)
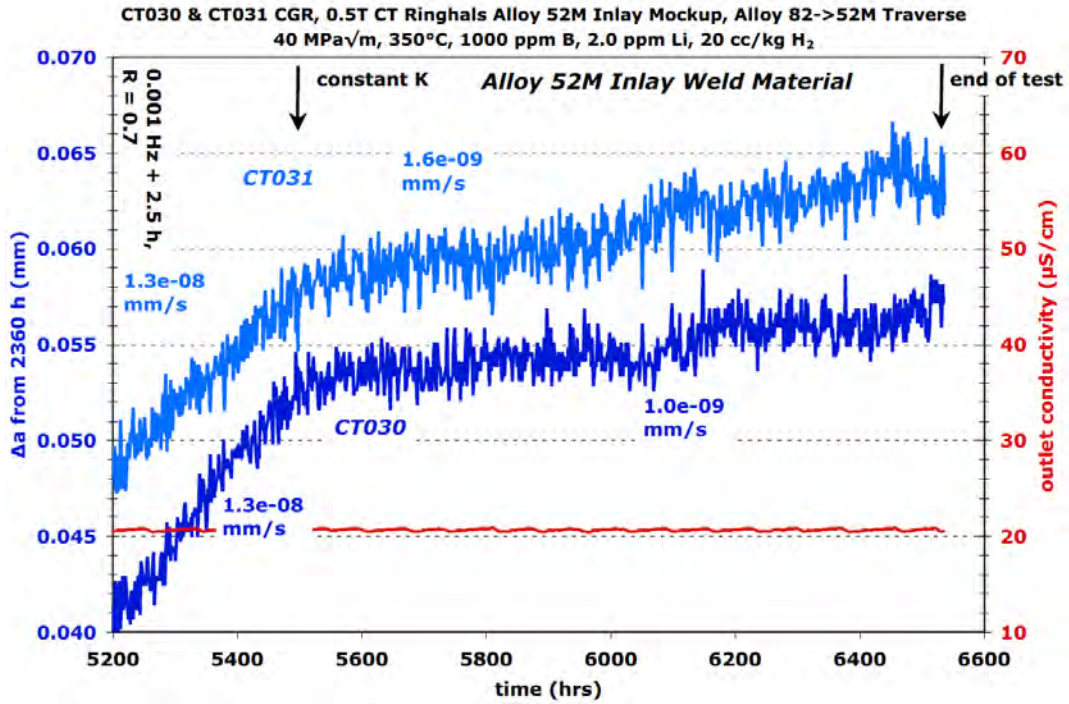
Figure 4-37   Constant K Response at 40 MPa√m of the Ringhals Alloy 52M/82 Inlay Mockup Specimens (CT030 & CT031)

Table 4-3   Corrected Data Summary for Ringhals Alloy 52M/82 Inlay Specimens #1 and #2 (CT030 & CT031)

Test Phase	Dur-ation (h)	R	Freq (Hz)	Hold (h)	Water Chemistry Conditions	Temp (°C)	CT030 Ringhals Alloy 52M/182 Inlay Specimen #1			CT031 Ringhals Alloy 52M/82 Inlay Specimen #2		
							Kmax (MPa√m)	CGR (mm/sec)	Approx. Crack Extension (mm)	Kmax (MPa√m)	CGR (mm/sec)	Approx. Crack Extension (mm)
1	~3	0.3	5	0	air precrack	RT	25	2.1E-04	0.40	25	1.7E-04	0.40
2	~2	0.5	5	0	air precrack	RT	29	1.2E-04	0.35	28	9.7E-05	0.35
3	~2	0.6	5	0	air precrack	RT	31	8.1E-05	0.35	31	5.6E-05	0.35
4	~3	0.7	5	0	air precrack	RT	31	2.4E-05	0.20	31	2.2E-05	0.20
5	11	0.5	0.1	0	29 cc/kg H_2	350	31	5.5E-06	0.218	29	3.4E-06	0.108
6	43	0.5	0.01	0	29 cc/kg H_2	350	31	1.4E-06	0.209	28	1.1E-06	0.173
7	60	0.5	0.001	0	29 cc/kg H_2	350	31	2.8E-07	0.067	28	2.5E-07	0.052
8	101	0.5	0.001	0	20 cc/kg H_2	350	31	1.8E-07	0.086	28	2.5E-07	0.084
9	568	0.5	0.001	2.5	20 cc/kg H_2	350	31	3.2E-08	0.063	28	2.7E-08	0.058
10	183	0.7	0.001	2.5	20 cc/kg H_2	350	31	3.2E-08	0.006	28	2.7E-08	0.007
11	534	---	const K	---	20 cc/kg H_2	350	31	7.3E-10	0.021	28	4.3E-09	0.006
12	197	---	const K	---	2 ppm O_2	288	31	6.6E-09	0.006	28	7.7E-09	0.011
13	111	0.7	0.01	0	2 ppm O_2 + SO_{4-}	288	31	1.2E-07	0.055	28	1.6E-07	0.072
14	95	0.7	0.001	0	2 ppm O_2 + SO_{4-}	288	31	2.4E-08	0.010	28	2.8E-08	0.008
15	209	0.7	0.001	2.5	2 ppm O_2 + SO_{4-}	288	31	5.2E-09	0.005	28	6.0E-09	0.005
16	161	0.5	0.001	2.5	2 ppm O_2 + SO_{4-}	288	31	1.3E-08	0.008	28	1.3E-08	0.006
17	14	0.4	0.2	0	29 cc/kg H_2	350	32	1.2E-05	0.640	27	7.7E-06	0.198
18	31	0.5	0.1	0	29 cc/kg H_2	350	32	4.2E-06	0.445	27	2.9E-06	0.339
19	52	0.5	0.01	0	29 cc/kg H_2	350	32	7.6E-07	0.148	27	4.9E-07	0.097
20	232	0.5	0.001	0	29 cc/kg H_2	350	32	9.9E-08	0.100	27	7.6E-08	0.109
21	390	0.5	0.001	2.5	29 cc/kg H_2	350	32	1.1E-08	0.018	27	1.3E-08	0.016
22	163	0.7	0.001	0	29 cc/kg H_2	350	32	3.4E-08	0.015	27	2.3E-08	0.007
23	649	0.7	0.001	2.5	29 cc/kg H_2	350	32	4.6E-09	0.019	27	4.4E-09	0.021
24	846	---	const K	---	29 cc/kg H_2	350	32	1.1E-09	0.021	27	2.0E-09	0.027
25	257	0.7	0.001	2.5	29 cc/kg H_2	350	32->34	7.1E-09	0.004	27->28	8.3E-09	0.006
26	112	0.7	0.001	2.5	29 cc/kg H_2	350	34->43	3.1E-08	0.010	28->35	4.8E-08	0.012
27	484	0.7	0.001	2.5	29 cc/kg H_2	350	43	1.4E-08	0.021	35	1.6E-08	0.024
28	1033	---	const K	---	29 cc/kg H_2	350	43	1.1E-09	0.005	35	2.0E-09	0.005

After ending the test, CT030 was fatigue fractured in air whereas CT031 was first backfilled with resin, sectioned into two pieces, and then one side was fatigue fractured in air while the other side was set aside for crack tip examinations. The most apparent feature of the crack growth surface of CT030 in Figure 4-38 is the very large uncracked ligament in the wake of the crack. This ligament formed at the onset of high temperature water testing, and was never broken during the entire test. Another feature of interest in the crack growth surface of CT030 is the rather uniform tan layer along the final crack front. This is likely representative of the final transitioning and constant K at 40 MPa√m. The jagged, uneven final crack front suggests a relatively high degree of engagement (but still with a very slow CGR). The side surface image

of the crack growing in the CT031 alloy 52M material in Figure 4-39 shows evidence of a large crack resulting from rapid extension with a narrower cracking extending out. The narrower crack, likely formed during cycle + hold and constant K, shows some preference for cracking along dendrites. This can be better seen in the SEM image of the same region in Figure 4-40.

Figure 4-38   Crack Growth Surface of Ringhals Alloy 52M/82 Specimen CT030

Figure 4-39   Optical Image of Side Surface of Crack Growing into Alloy 52M in the Ringhals Alloy 52M/82 Specimen CT031
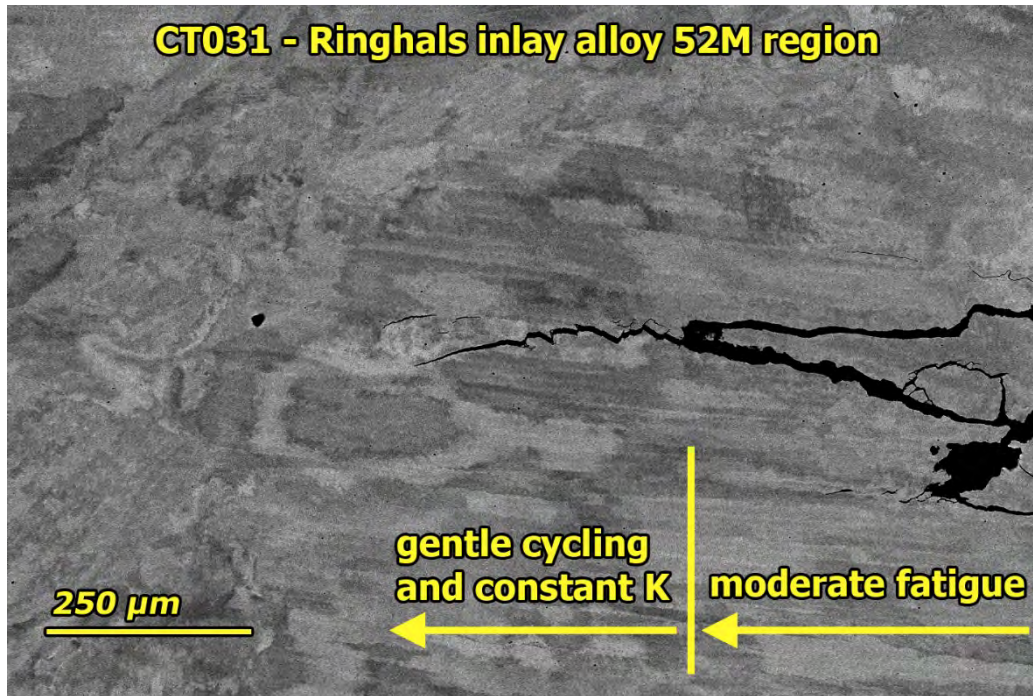
Figure 4-40   SEM Image of Side Surface of Crack Growing into Alloy 52M in the Ringhals Alloy 52M/82 Specimen CT031

4.3   Summary of SCC Tests on Alloy 52M Overlay and Inlay Mockups

Four SCC crack growth tests were performed on an alloy 52M/182 overlay mockup weld and two tests on an alloy 52M/82 inlay mockup weld. The intent for all tests was to first establish stable IGSCC growth in the more susceptible, alloy 182 or 82 weld metal then to evaluate SCC propagation response through the transition region and into the more resistant alloy 52M weld metal. Unfortunately, step 1 turned out to be extremely difficult with limited SCC growth rates produced in the alloy 182 and 82 weld metals plus propagation rates decreased even further as the crack front approached the alloy 52M interface. Multiple attempts were made in simulated PWR primary water at 350°C and in more aggressive oxidizing BWR water conditions with sulfate additions. While localized IG cracking was promoted particularly in the alloy 182 weld metal, the SCC growth rates under constant K loading were typically $<3 \times 10^{-9}$ mm/s in PWR primary water and only reached $\sim 1 \times 10^{-8}$ mm/s in oxidizing BWR water with high sulfate impurity additions. As a result, it was not possible to effectively assess the effect of the alloy 52M interface on the propagation of a highly engaged, rapidly growing IGSCC crack front. However, the crack growth response during periodic unloading and at constant K decreased significantly as crack front approached the alloy 52M interface. This may be due to local fingers of IG growth reaching and slowing at the alloy 52M as well as due to residual stresses near the interface influencing the applied crack-tip stresses and slowing growth at the crack front. In either case, the beneficial effect of the alloy 52M overlay or inlay to impede SCC propagation was observed.

A final step in all tests was to use aggressive cycling to move the crack front into the alloy 52M weld metal and evaluate SCC response under PWR primary water conditions. In nearly all cases, the measured SCC growth was limited with propagation rates at or below $\sim 4 \times 10^{-9}$ mm/s. The one exception was for the alloy 52M overlay specimen CT035 where a weld pass was discovered with a much lower bulk Cr concentration of ~ 24 wt%. In this region, an SCC growth

rate of 1×10^{-8} mm/s was measured at the high K level of 49 MPa√m. Since this was an off-normal and lower Cr weld metal composition, the observation of a moderate SCC propagation rate is not considered of practical importance. Overall, the alloy 52M weld metal employed for the overlay and inlay mockups were quite resistant to SCC in PWR primary consistent with the weld metals discussed in Chapter 3.

Additional tests on high-Cr weld overlays and inlays are clearly warranted and plans are in place to fabricate at least two alloy 52M overlays on alloy 182 pipe welds. Detailed microstructural characterizations will be performed followed by crack-growth tests investigating and quantifying SCC propagation from the alloy 182 weld metal into the alloy 52M weld metal. Selected experiments may also be conducted evaluating SCC growth along the interface region between the alloy 182 and the alloy 52M overlay.

5   INTERFACES AND DILUTION ZONES IN DM WELDS

Part of this effort to investigate SCC susceptibility in alloy 152/52/52M welds has included studying the response of these materials in DM weld mockups where there is a potential for dilution zones, high fabrication-induced stresses/strains and hardening that may increase SCC susceptibility. Studies of DM weld dilution zone, fusion line, and heat affected zone (HAZ) SCC response have been subject of investigation for BWR reactor conditions. The primary focus of these studies has been to assess the CGR as a crack grows through the weld dilution zone and/or along the interface between the Ni-alloy weld metal and the steel. In some cases, the crack path has crossed the fusion line and propagates into the steel. The effect of dilution on SCC CGR in these studies utilizing alloy 182 has been indeterminate which is not surprising because alloy 182 is an SCC-susceptible material, but cessation of constant load crack growth has consistently occurred when the crack reaches the bulk low alloy steel (LAS). Studies have attempted to assess fusion line or LAS HAZ response of DM welds by positioning specimens parallel to the fusion line. These studies have shown no accelerated SCC growth in these regions that were made using prototypic fabrication methods that included a post weld heat treatment (PWHT).

Alloy 152/52 is a much more SCC resistant material than alloy 182, and the possibility of increased susceptibility in weld dilution or fusion line regions of DM welds is of greater concern. This chapter describes the primary water SCC response at or near the fusion line of four DM weldments (alloy 152/304SS, alloy 152M/carbon steel (CS), alloy 52M/CS and alloy 152/LAS) where specimens have been aligned for crack growth to occur parallel to the fusion line in either the weld dilution zone, on the fusion line, or in the HAZ.

5.1   Dissimilar Metal Welds: Materials and Specimens

The fabrication and composition of the alloy 152/304SS U-groove weld (made by MHI for Kewaunee, supplied by EPRI) and the alloy 52M-CS V-groove weld (provided by George Young of KAPL) have both been described earlier in this report. The alloy 152M/CS V-groove weld is identical in geometry to the alloy 52M/CS V-groove weld. However, manual welding was employed for the alloy 152M instead of automated welding for the alloy 52M. The compositions of these weld materials are listed in Table 5-1, while the compositions of the 304SS and the A516 CS were not available. The alloy 152 U-groove weld was fabricated using buttering applied to the 304SS, but neither of the V-groove welds were made with butter weld steps, and neither were given a PWHT that is part of standard practice for nuclear reactor component joining of CS or LAS to nickel-base alloys. A slice was also obtained from ANL of an alloy 152 – LAS DM weld designated as V2. This weld used two different alloy 152 weld wire heats (WC04F6 and 146444) with reported compositions given in Table 5-1. The final DM weld evaluated was an alloy 52M temper bead repair weld produced by EPRI and no PWHT was required or applied.

Table 5-1   Composition of the Alloy 152/152M/52M Used for the DM Welds

Material - Source	Heat Numbers and Description	Weld Metal Composition (wt%)
Alloy 152/SS - MHI	Filler and Butter: heat 307380 U-groove mock-up weld using 304SS plate for Kewaunee reactor used for specimens CT075 and CT076.	Ni-28.7Cr-9.1Fe-0.03C-3.6Mn-0.33Si-0.15Al-0.12Ti-0.003S
Alloy 152M/CS - KAPL	Filler: heat WC83F8 V-groove weld, carbon steel and 316SS plate, no butter used on the CS, no PWHT applied to the CS used for specimens CT066 and CT082.	Ni-30.2Cr-8.7Fe-<0.005C-3.0Mn-0.22Si-<0.01Al-0.03Ti-1.18Nb
Alloy 52M/CS - KAPL	Filler: heat NX5285TK V-groove weld, carbon steel and 316SS plate, no butter used on the CS, no PWHT applied to the CS used for specimens CT065 and CT083.	Ni-30.0Cr-7.9Fe-0.014C-0.75Mn-0.13Si-0.11Al-0.21Ti-0.81Nb+Ta
Alloy 152/LAS - ANL	Filler and Butter: heat WC04F6 (1) top portion, specimen CT117 and heat 146444 (2) bottom portion, specimen CT119	(1) Ni-28.7Cr-10.4Fe-0.048C-3.48Mn-0.41Si-0.06Al-0.09Ti-1.54Nb+Ta (2) Ni-29.0Cr-9.4Fe-0.040C-3.56Mn-0.46Si-0.24Al-0.15Ti-1.84Nb+Ta
Alloy 52M/LAS temper bead repair- EPRI	Filler: heat NX8956TK used for specimen CT136	Ni-29.9Cr-8.6Fe-0.020C-0.72Mn-0.03Si-0.13Al-0.21Ti-0.81Nb+Ta

Two alloy 152/304SS DM weld fusion line specimens (CT075 and CT076) were cut from blanks as shown in Figure 5-1. After machining, the side grooves of the specimens were polished and etched to reveal the fusion line region to confirm the target location and to provide information on the microstructure that the crack would encounter (Figures 5-2 and 5-3). Based on these side-groove images, the geometric crack growth plane is very well aligned with the fusion line in both specimens. Specimen #1 appears to be exactly on the fusion line, while specimen #2 is in the 304SS at no more than 100-150 um from the fusion line.
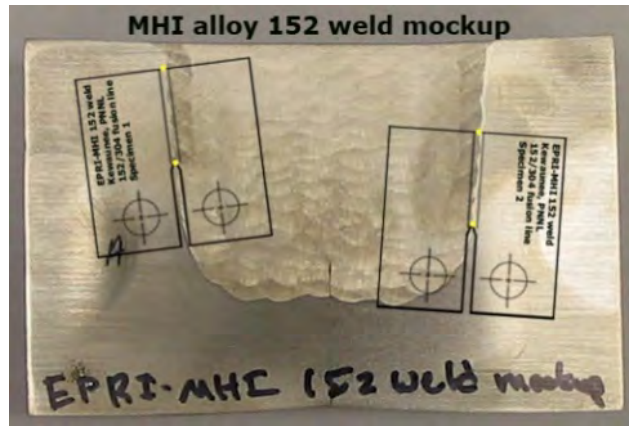
Figure 5-1   Photograph Showing the Target Orientation of the Two Alloy 152/304SS DM Weld Fusion Line Specimens (CT075 and CT076)
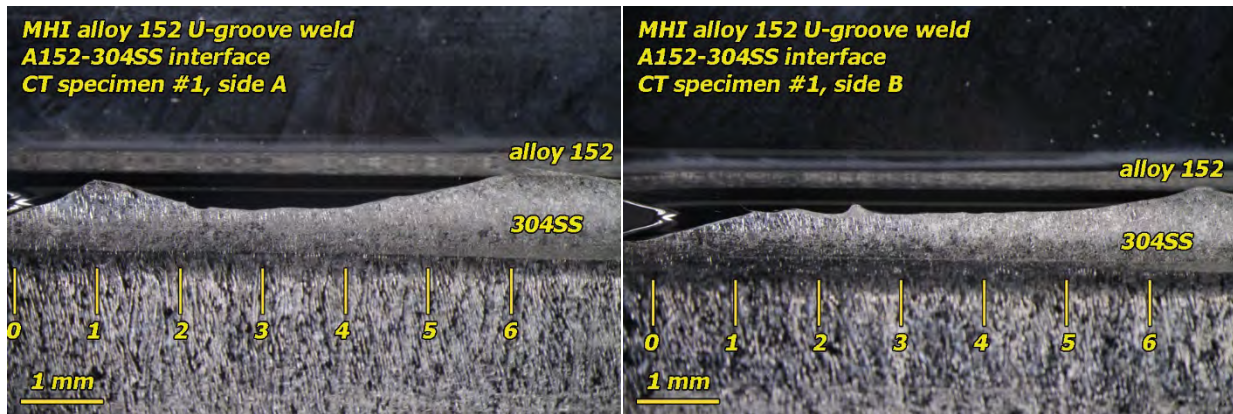
Figure 5-2   Polished and Etched Side Grooves of the MHI Alloy 152/304SS DM Weld Fusion Line Specimen #1 (CT075). Notch Can Be Seen on the Left Edge of the Optical Image
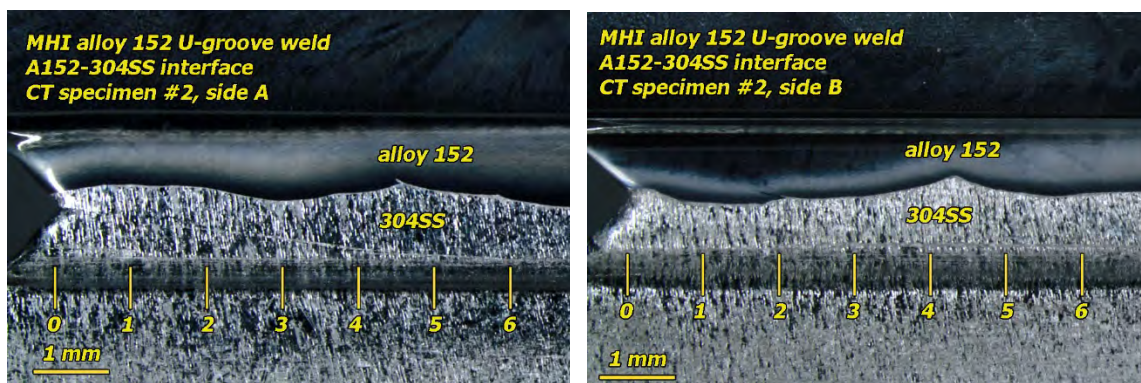
Figure 5-3   Polished and Etched Side Grooves of the MHI Alloy 152/304SS DM Weld Fusion Line Specimen #2 (CT076). Notch Can Be Seen on the Left Edge of the Optical Image

Two alloy 52M/CS and two alloy 152M/CS weld specimens were machined and SCC tested. The target SCC test region in the first pair of specimens (one alloy 52M and one alloy 152M) was the weld dilution zone and the fusion line was the target for the second pair. Photos showing the orientation of the first specimens relative to the welds are shown in Figure 5-4, while higher magnification images of the polished and etched side grooves are shown in Figure 5-5 for the alloy 52M (CT065) and Figure 5-6 for the alloy 152M (CT066). Based on these images, the notch of the alloy 52M specimen was well positioned at ~0.5 mm offset from the fusion line in the weld metal. The notch in the alloy 152M specimen was positioned somewhat further away at 0.5-1.5 mm offset from the more undulating fusion line of the manually joined weldment. Examination of the side-groove images (most easily seen in the images of the alloy 52M), shows that the grain boundaries are at a ~60 degree angle to the geometric crack growth plane. This is clearly not an optimal geometry for IGSCC testing, and other geometries were considered such as aligning the specimens so that notch was in the alloy 152M or 52M and the crack was aligned to grow towards the fusion line on a trajectory parallel to the weld grain boundaries. While this produces the best possible alignment to the grain boundaries for IG cracking, assessment of the dilution zone is limited to just that one region where the crack can grow. The orientation selected for this study allows for a much greater amount of material to be tested, and if a dilution zone is susceptible, IG cracking will occur even at this suboptimal orientation relative to the grain boundaries.
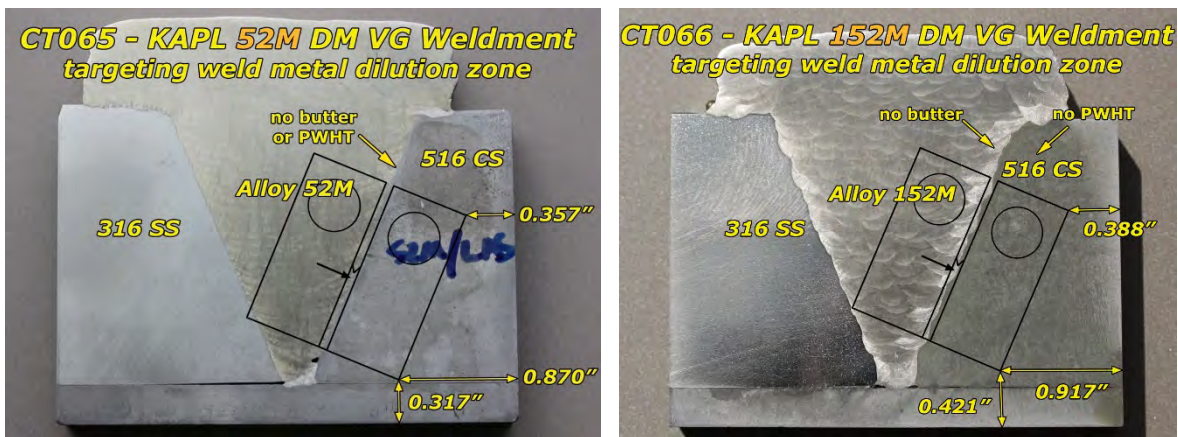
Figure 5-4   Optical Images Showing the Target Location of the Alloy 52M and Alloy 152M Dilution Zone CT Specimens (CT065 and CT066)

Figure 5-5   Polished and Etched Side Grooves of the Alloy 52M/CS Dilution Zone Specimen (CT065) Showing That the Crack Growth Plane Is ~0.5 mm into the Alloy 52M

Figure 5-6 **Polished and Etched Side Grooves of the Alloy 152M/CS Dilution Zone Specimen (CT066) Showing That the Crack Growth Plane Is ~0.5-1.5 mm into the Alloy 152M**

The second pair of specimens was oriented to specifically target the fusion line and CS HAZ. The specimens were again positioned parallel to the fusion line, but in this case, the goal was to line up the geometric crack path with the fusion line or slightly into the CS. Figure 5-7 shows that geometric crack path of the alloy 152M fusion line specimen (CT082) was very well aligned with the fusion line in side groove A, while side-groove B was slightly further into the CS than was desired. Figure 5-8 shows that the alloy 52M fusion line specimen (CT083) was very well aligned in both side grooves with the geometric crack path starting exactly on the fusion line and drifting no more than ~0.4 mm into the CS.
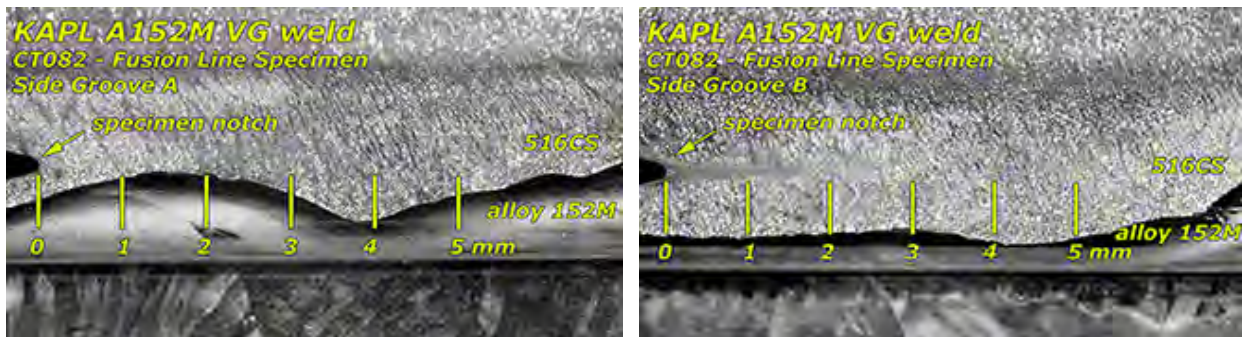
Figure 5-7 **Polished and Etched Side-Grooves of the Alloy 152M/CS Fusion Line Specimen (CT082) Showing That the Crack Growth Plane Is ~0.5-1 mm into the A516 CS**
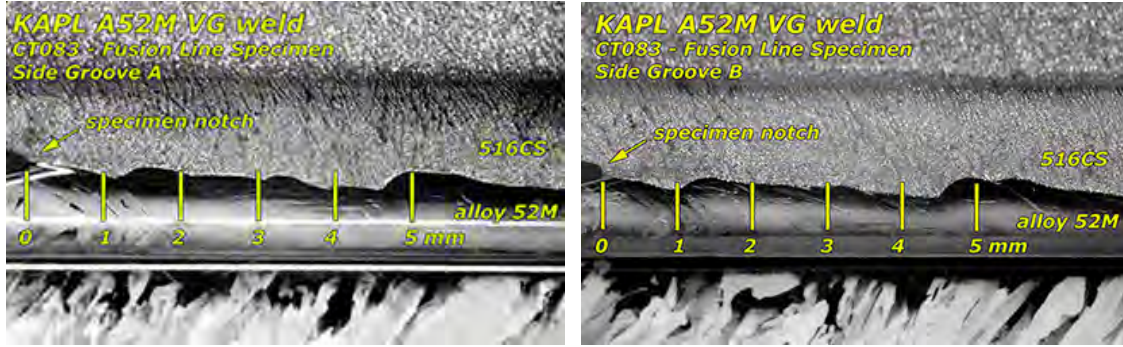
Figure 5-8 Polished and Etched Side-Grooves of the Alloy 52M/CS Fusion Line Specimen (CT083) Showing That the Geometric Crack Growth Plane Starts on the Fusion Line and Drifts ~0.4 mm into the A516 CS

The next two tests were conducted on an alloy 152 – LAS DM weld received from ANL designated as v2. This followed prior crack growth experimentation at ANL that revealed high SCC propagation rates in the alloy 152 dilution zone adjacent to the LAS. A metallographic slice was taken from the weld enabling detailed characterizations to be performed on the alloy 152 – LAS regions of interest. As expected, the weld microstructure in the dilution zone contained large solidification grain oriented perpendicular to the 152/LAS interface and the crack-growth path in the CT specimens. However, isolated areas were also found where grain boundaries aligned with the crack path were discovered along with Type II boundaries as illustrated in Figure 5-9. The dilution zone composition was mapped by SEM EDS and revealed bands of Fe enrichment and Cr depletion near several of these aligned boundaries in Figures 5-10 and 5-11.
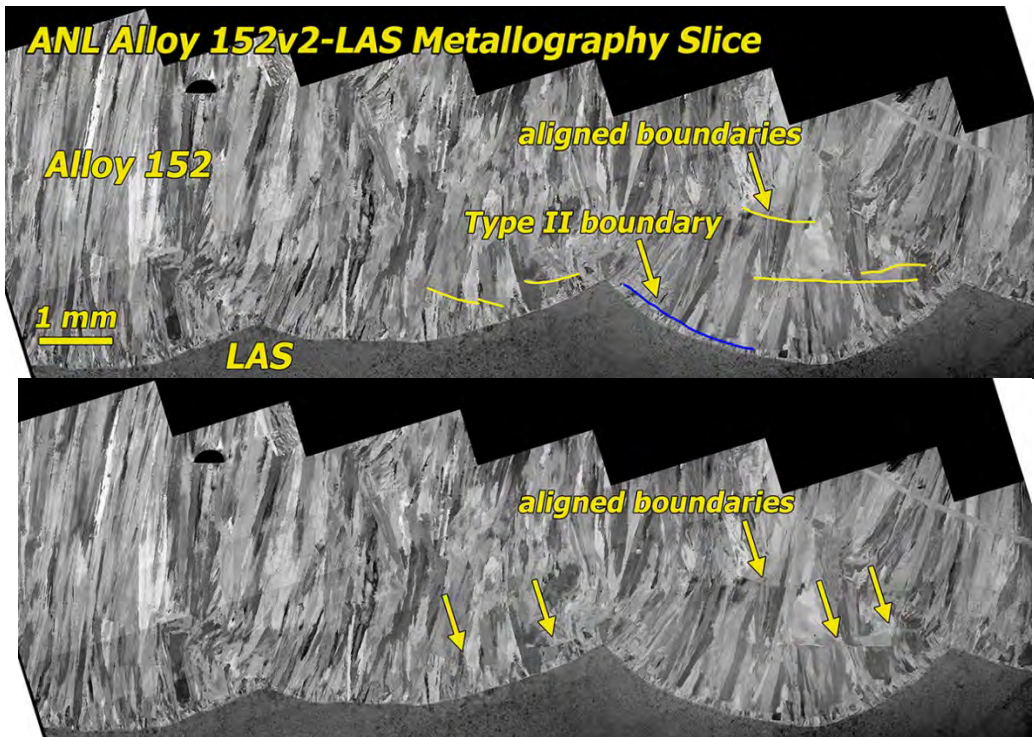
Figure 5-9 SEM-BSE Image Highlighting the Microstructure in the Alloy 152 – LAS Dilution Zone of the ANL V2 Alloy 152 DM Weld

Figure 5-10   SEM-EDS Composition Maps from the Area near Aligned Grain Boundary #1
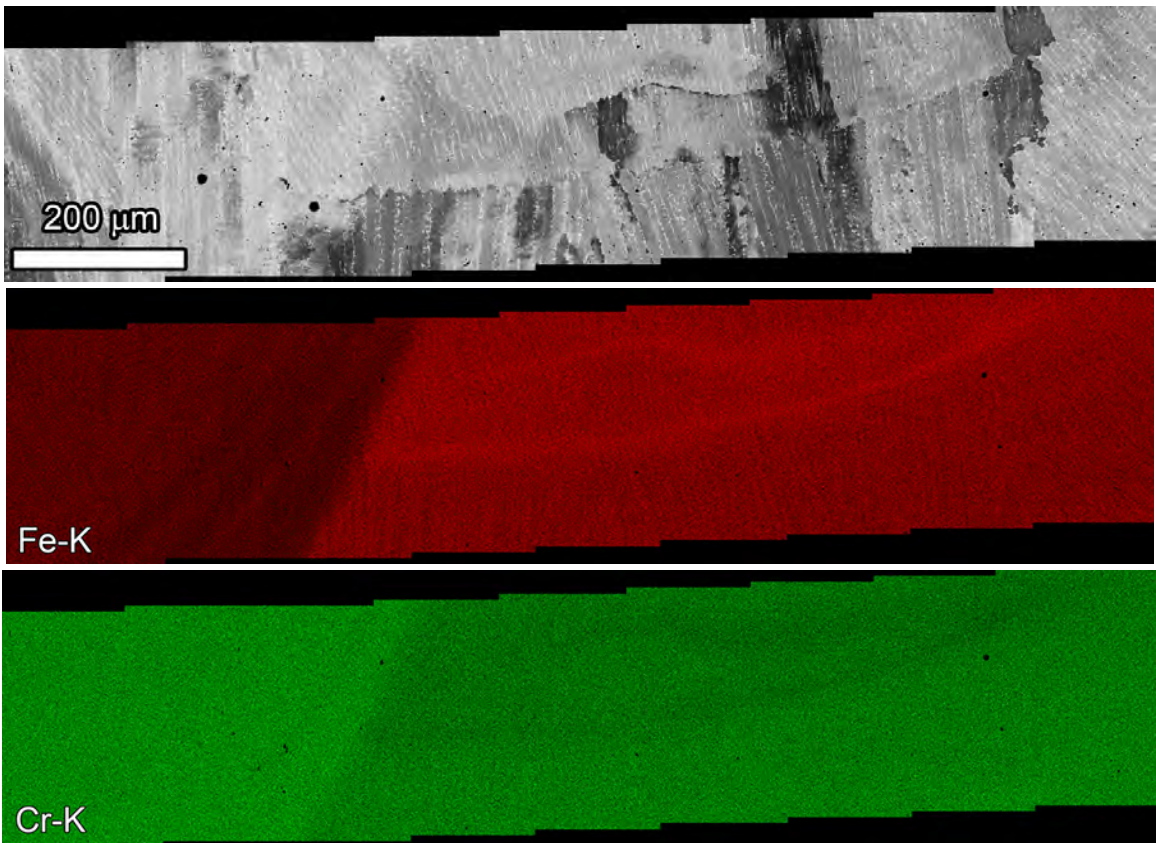
Figure 5-11   SEM-EDS Composition Maps from the Area near Aligned Grain Boundary #2
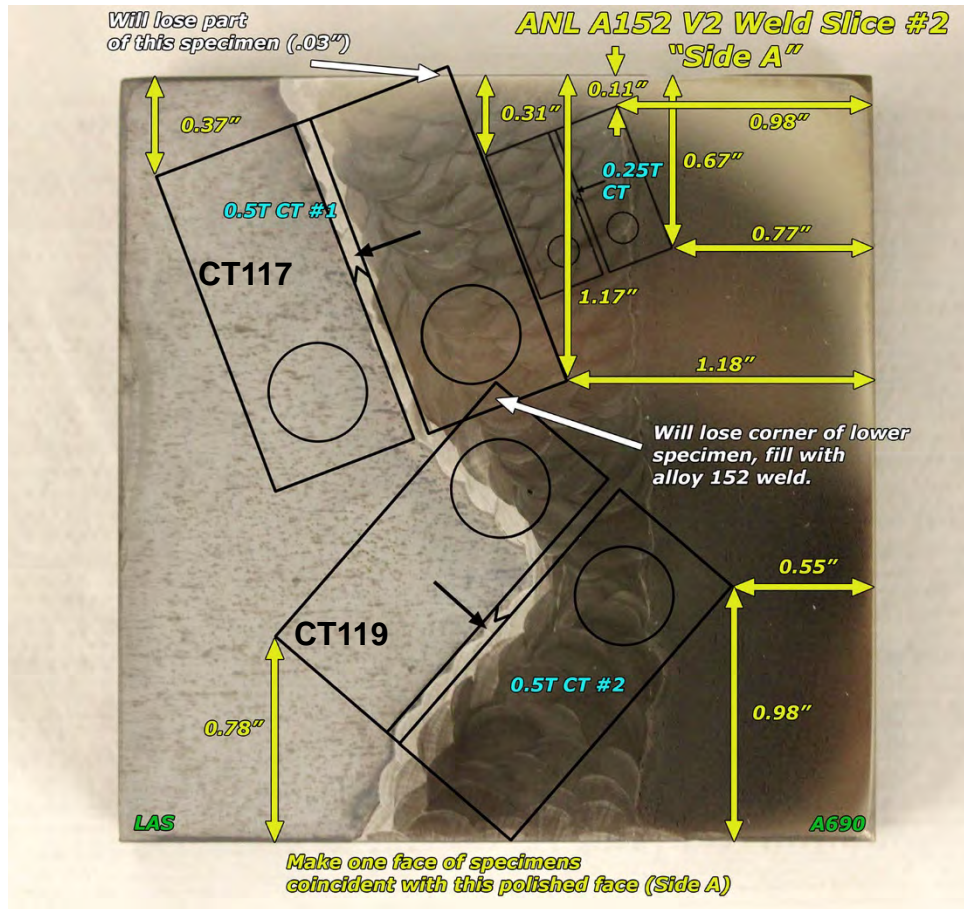
Figure 5-12   Optical Image Showing the Location of the Alloy 152 - LAS Dilution Zone CT Specimens (CT117 and CT119). Alloy 152 Weld Metal in Upper Portion Is Heat WC04F6 and in Lower Portion Is Heat 146444

Specimens CT117 and CT119 were machined from the slice as shown in Figure 5-12 and macro images of the CT specimens presented in Figures 5-13 and 5-14. Higher magnification side groove images illustrating the position of the notch and crack growth plane for CT119 are given in Figure 5-15 along with a SEM/EDS composition map for Fe in Figure 5-16. Significant Fe enrichment (and Cr depletion) is present before and after the first and second weld passes with a particularly high Fe concentration just entering the second pass along the crack growth plane. Polished and etched side-groove images for specimen CT117 are presented in Figure 5-17. Side B etching revealed very distinctive Fe-rich regions before and after the transition from the first to second weld pass. Much less compositional change is apparent from the etched appearance for Side A.

Figure 5-13   Macro Images of the Alloy 152v2 DZ CT117 Specimen
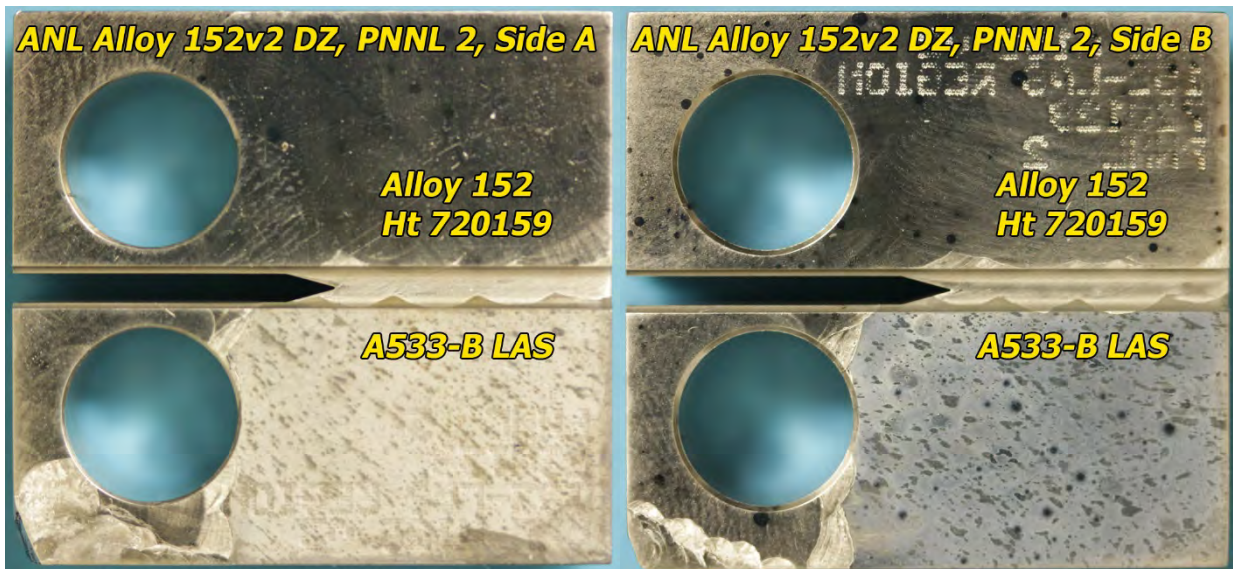
Figure 5-14   Macro Images of the Alloy 152v2 DZ CT119 Specimen
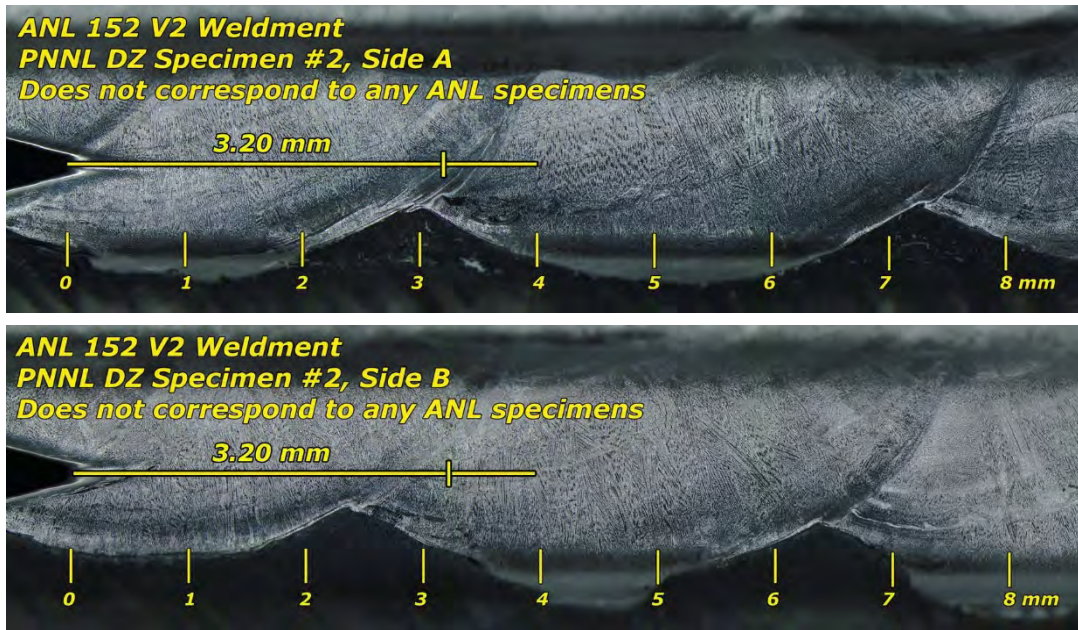
Figure 5-15   Polished and Etched Side-Grooves of the ANL 152v2 Specimen CT119
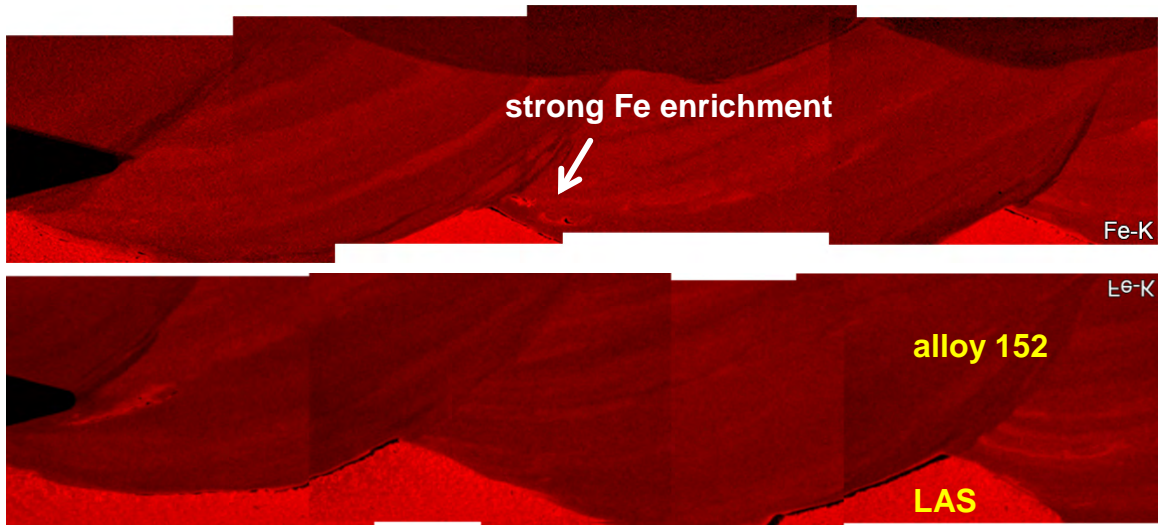
Figure 5-16   SEM-EDS Elemental Maps of Fe-K on Side-Grooves of the ANL 152v2 Specimen CT119
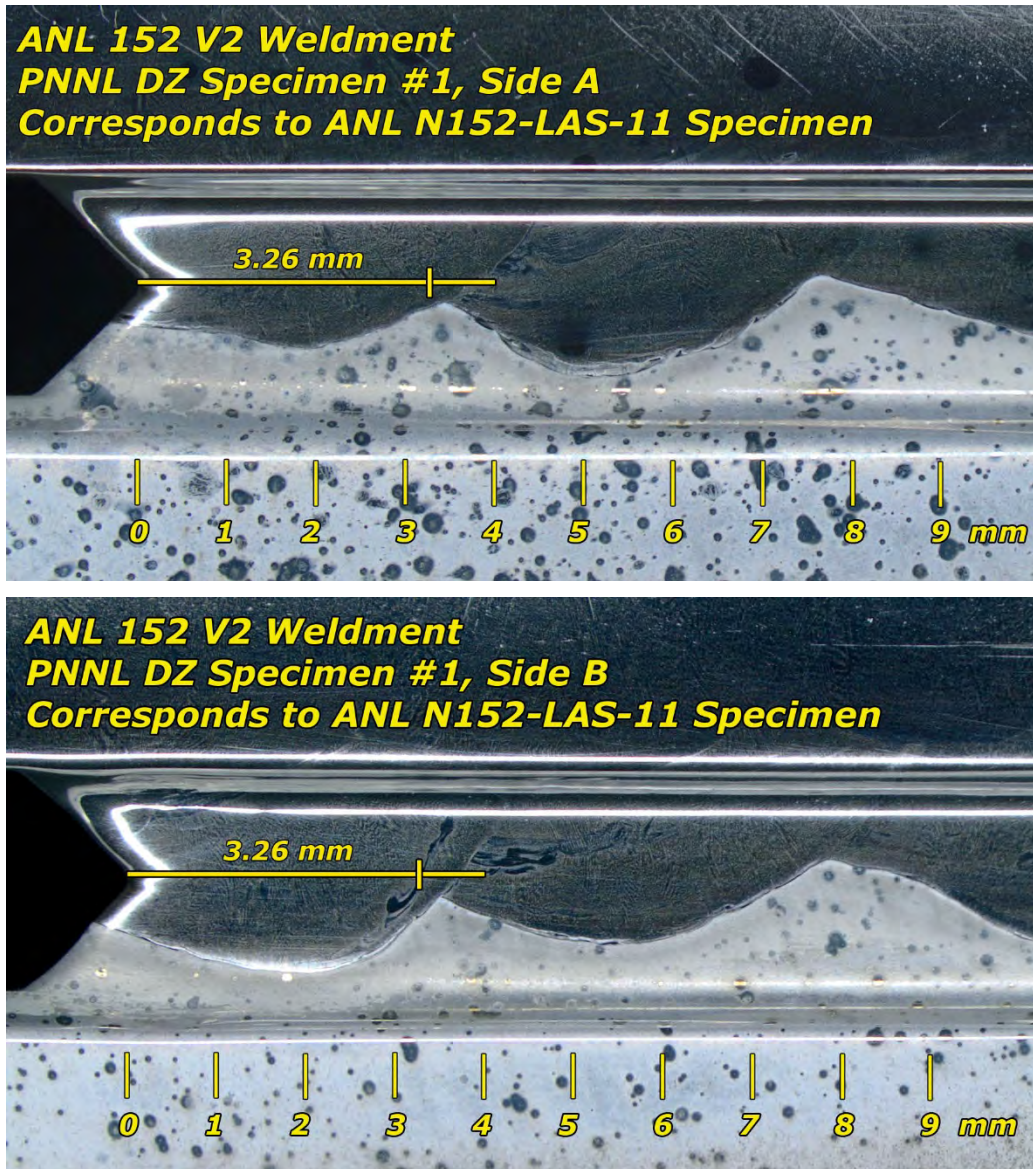
Figure 5-17   Polished and Etched Side-Grooves of the ANL 152v2 Specimen CT117

The final weld examined within this chapter is the EPRI temper-bead, alloy 690 – alloy 52M – LAS DM repair weld and a cross-section picture of the slice obtained at PNNL is presented in Figure 5-18. Detailed SEM and hardness characterizations were performed at several locations including the alloy 52M – LAS dilution zone region where CT specimen 136 was machined as documented in the lower image in Figure 5-18. Once again, side grooves for the CT specimen were polished to reveal the crack growth path (Figure 5-19) and higher resolution SEM exams identified local areas with aligned grain boundaries and Fe enrichment (Figure 5-20, side A). This region started at ~2 mm from the specimen notch and continued for more than 1 mm. However, such areas were isolated and were not found on side B side groove in Figure 5-20. Beyond the microstructural and microchemical features in the dilution zone, lack of fusion (LOF) cracks were discovered at a few local 52M/LAS interface regions. One of the LOF regions was positioned immediately ahead of the notch, providing an opportunity for its effect on SCC growth to be assessed. Two small cracks can be seen at identical locations on the Side A and B side grooves shown in Figures 5-21 and 5-22, respectively.
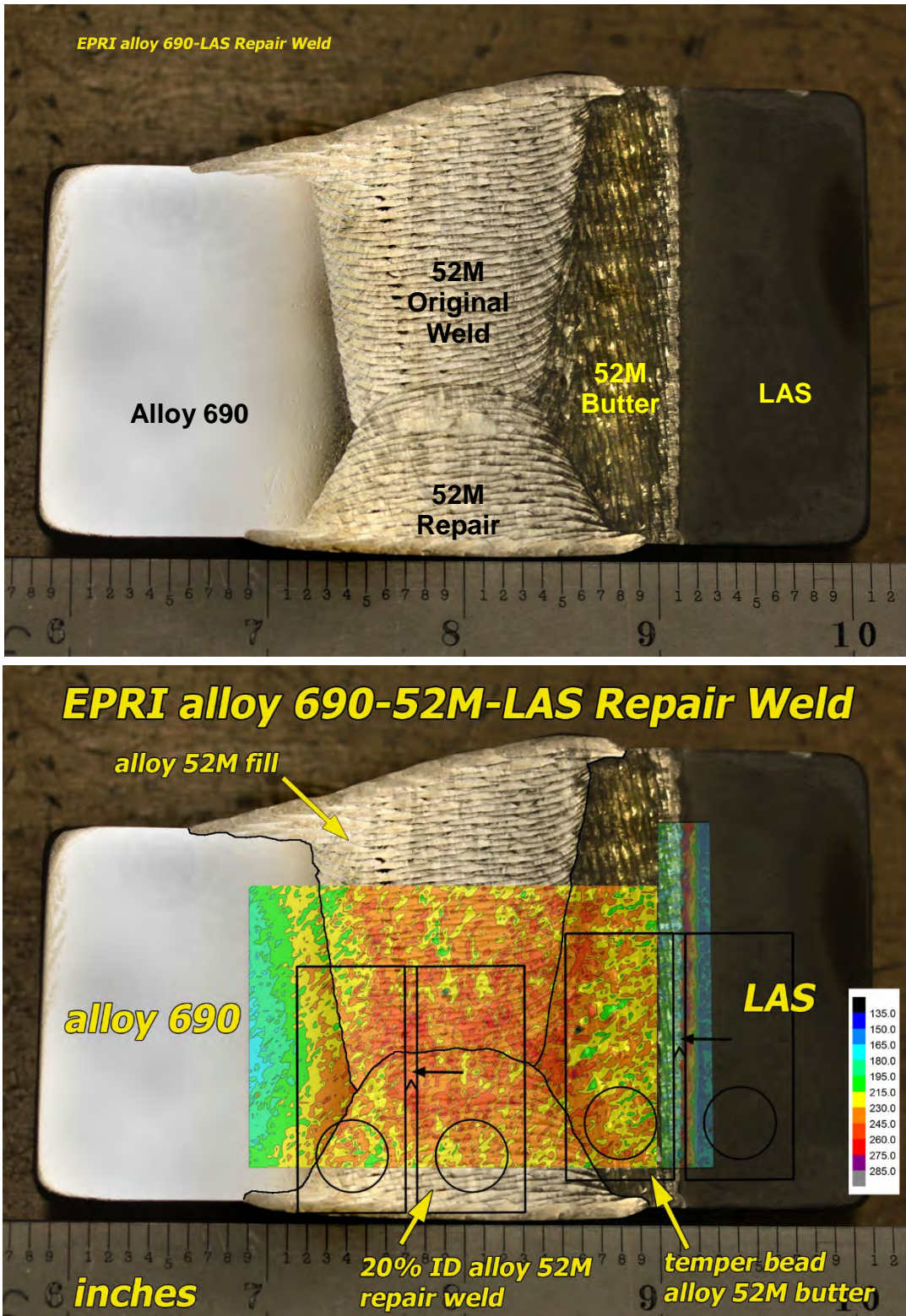
Figure 5-18 Etched Cross-Section Slice from the EPRI Temper Bead DM Repair Weld, Measured Hardness Maps and CT Specimen Layout Positions Are Superimposed in the Bottom Image. The Alloy 52M – LAS Dilution Zone Specimen CT136 Is on the Right

Figure 5-19 Polished and Etched Side-Grooves of the EPRI Temper Bead DM Repair Weld Specimen CT136
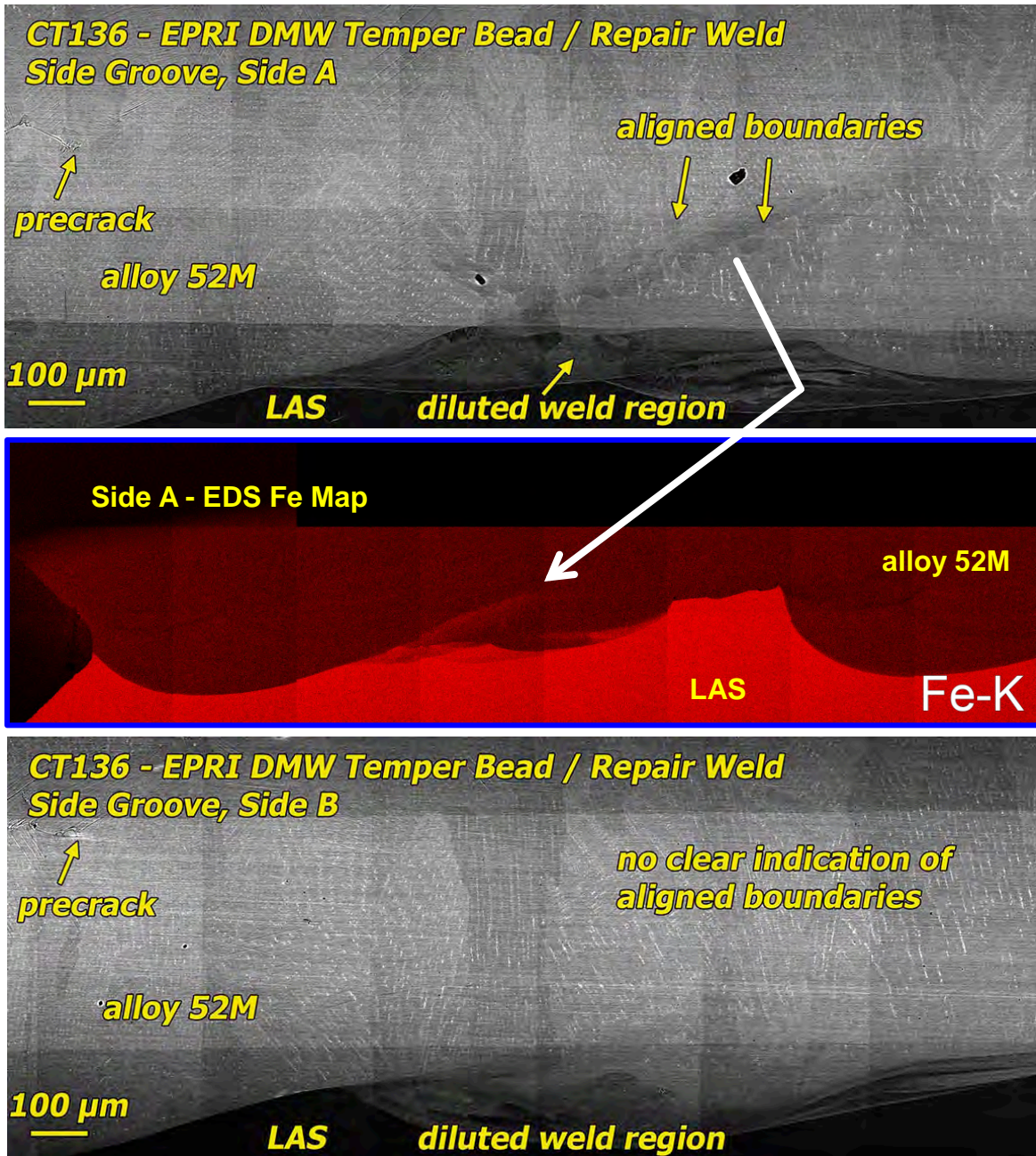
Figure 5-20   Highlighted Area of Fe Enrichment (and Cr depletion) Region Corresponding to the Presence of Two Aligned Grain Boundaries in the First Weld Pass of Side A for the EPRI Temper Bead DM Repair Weld Specimen CT136

Composition maps for Fe and Cr are included to confirm the interface location and indicate small regions in the weld metal where Fe ingress has occurred causing Cr depletion. A minor dilution zone can be identified near the LAS interface immediately before the LOF cracks. Higher magnification SEM images and composition maps document that two small cracks are present and there is a sharp transition from the LAS to the 52M weld metal without any dilution. Additional details on the LOF defect morphologies can be seen in Figure 5-22 where the cracks are primarily along the 52M/LAS interface, but do extend a small distance off the interface.
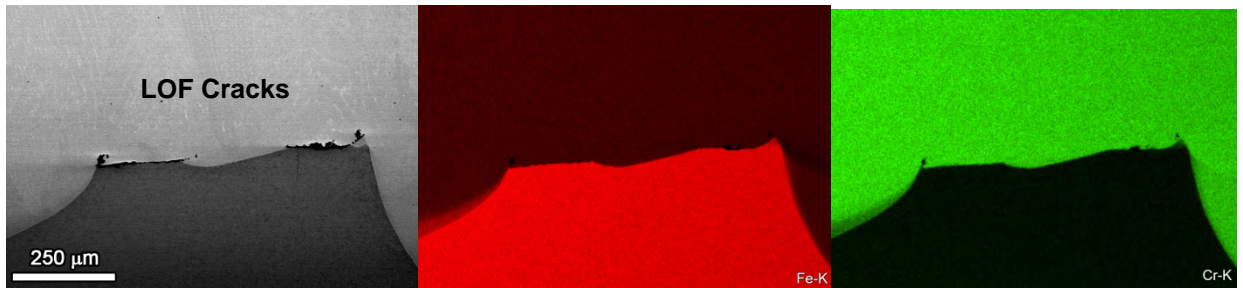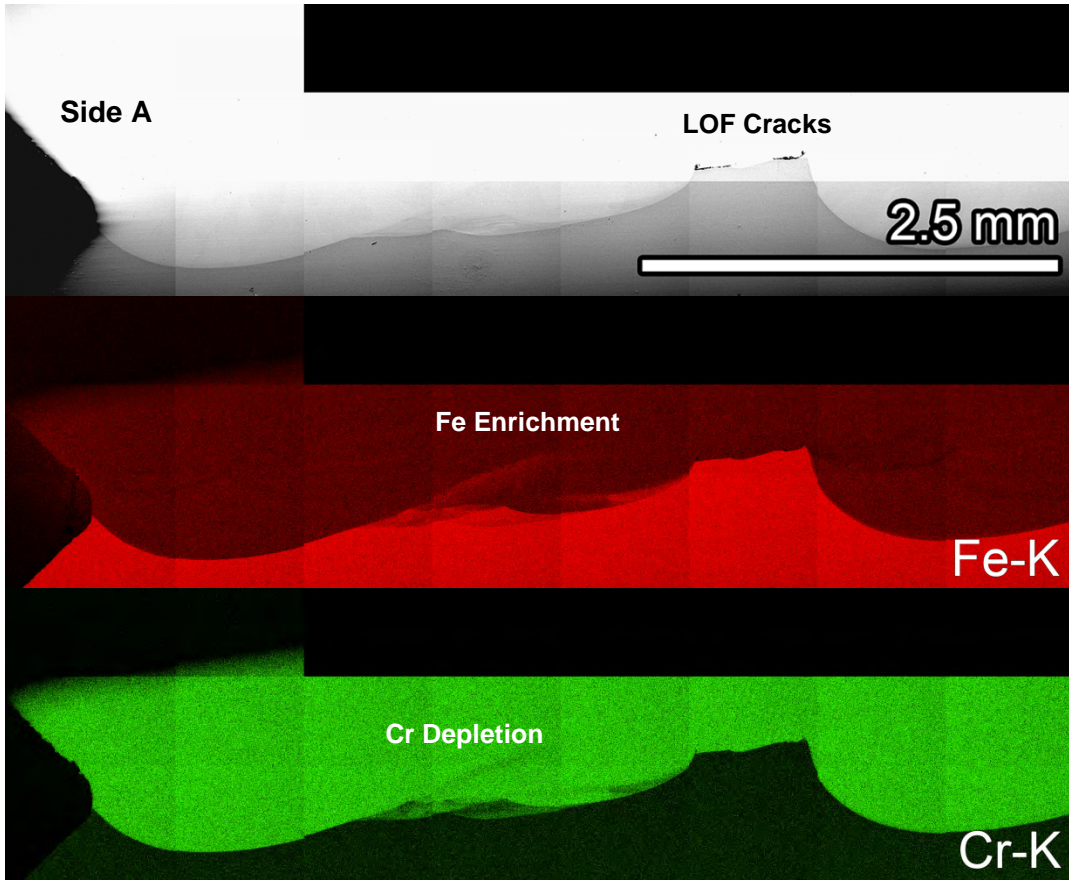
Figure 5-21 **SEM-BSE Images and EDS Elemental Maps Showing the 52M/LAS Interface Ahead of the Notch in the Side A Side Groove for the CT136 Specimen. Bottom Images Highlight the Local LOF Cracks**

Figure 5-22   SEM-BSE Images and EDS Elemental Maps Showing the 52M/LAS Interface Ahead of the Notch in the Side B Side Groove for the CT136 Specimen. Bottom Images Highlight the Local LOF Cracks

5.2   MHI Alloy 152-SS DM Weld Interface Specimens (CT075 and CT076)

SCC testing was initiated in January 2012 on two specimens made from MHI alloy 152 mockup U-groove weld (heat 307380) joining two pieces of 304SS plate. As noted in Section 1.1, CT specimens were machined to evaluate the fusion line and dilution zone regions between the alloy 152 butter (also heat 307380) and the stainless steel. An overview of the entire test on these two specimens is shown in Figure 5-23 and summarized in Table 5-2. As can be seen in the plot, CT076 exhibited much higher CGRs during aggressive cycling at ~1700-1900 h and ~3000-3250 h. As a result, the K value increased for CT076 during the test and slightly decreased for CT075. A total of four constant K crack growth assessments were made in three separated microstructural regions that were selected based on side-groove images (Figures 5-2 and 5-3). The crack growth response for the first and second constant K assessments (when CT076 was still at moderate K level) is shown in Figure 5-24. Variations in hold time from 1 to 10 h were applied during the final transitioning steps in attempt to improve IG engagement, but it did not obviously affect the constant K crack growth response with all measurements lying between 1.9 and 3.8×10^{-9} mm/s. When considered on a per specimen basis, the constant K CGRs are suggestive of a very small dependency on stress intensity. Application of gentle

cycle + hold loading after constant K assessments did not produce transient high CGRs that would be suggestive of ligament/contact formation or an uneven crack front during constant K.
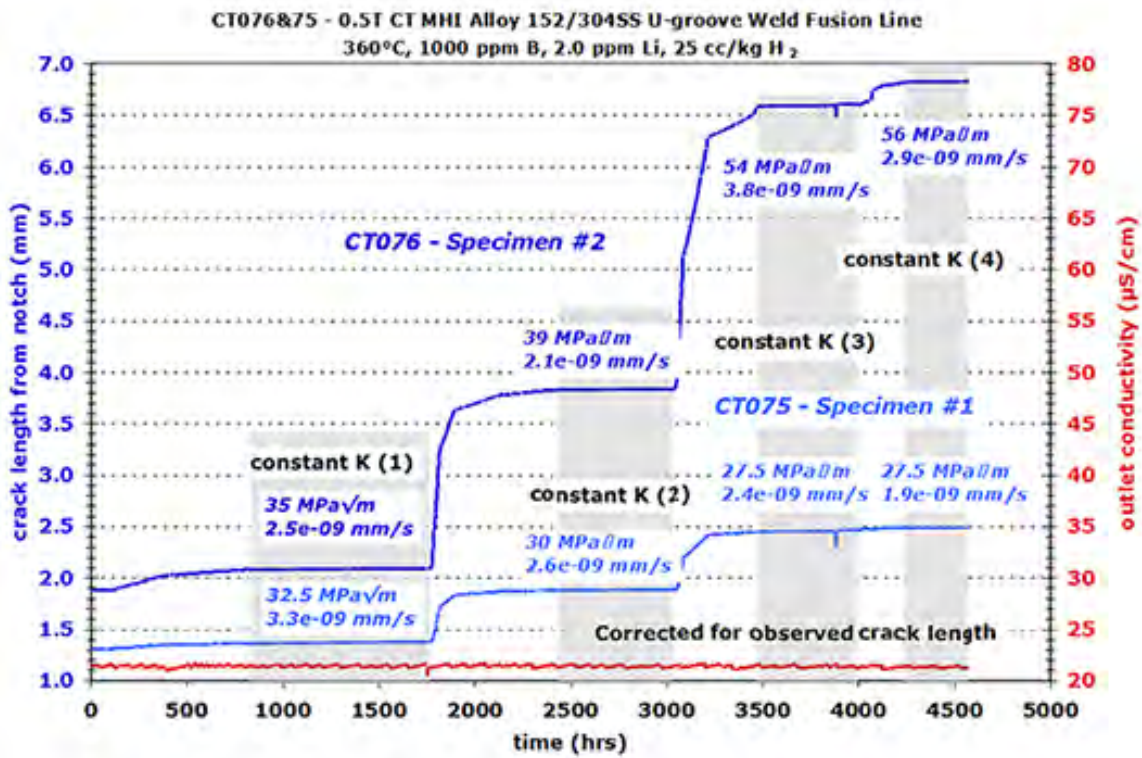
Figure 5-23   Overview of the Entire Test on the Two Alloy 152/304SS Fusion Line Specimens

Table 5-2   Test Summary for MHI Alloy 152/304SS Weld Fusion Line Specimens CT075 and CT076

Test Phase	Start (h)	Time (h)	R	Freq. (Hz)	Hold (h)	Diss H$_2$ (cc/kg)	T (°C)	CT076 MHI A152 UG/304SS FL #2			CT075 MHI A152 UG/304SS FL #1		
								Kmax (MPa√m)	CGR (mm/s)	Crack Ext (mm)	Kmax (MPa√m)	CGR (mm/s)	Crack Ext (mm)
0	0	123	---	const K	---	25	360	35	---	---	32.5	---	---
1	123	239	0.5	0.001	2.5	25	360	35	1.1E-07	0.093	32.5	1.9E-08	0.019
2	361	448	0.5	0.001	10	25	360	35	3.1E-08	0.045	32.5	7.4E-09	0.012
3a	809	615	---	const K	---	25	360	35	4.0E-09	0.005	32.5	3.3E-09	0.006
3b	1424	351	---	const K	---	25	360	35	2.5E-09	0.005	32.5	2.6E-09	0.003
4	1775	42	0.5	0.01	0	25	360	36	5.3E-06	0.813	31.5	1.3E-06	0.199
5	1817	75	0.5	0.001	0	25	360	38	8.9E-07	0.264	31	1.8E-07	0.057
6	1892	235	0.5	980s/20s	2.5	25	360	39	1.3E-07	0.118	30	3.4E-08	0.029
7	2127	315	0.5	980s/20s	10	25	360	39	3.7E-08	0.041	30	2.0E-08	0.008
8	2442	605	0.5	const K	---	25	360	39	2.5E-09	0.004	30	2.6E-09	0.005
9	3047	38	0.5	0.01	0	25	360	44	7.1E-06	0.937	29	1.8E-06	0.179
10	3085	125	0.5	0.001	0	25	360	50	1.9E-06	0.844	28	3.1E-07	0.128
11	3210	268	0.5	980s/20s	2.5	25	360	54	2.2E-07	0.292	27.5	2.6E-08	0.031
12	3478	524	---	const K	---	25	360	54	3.8E-09	0.019	27.5	2.4E-09	0.010
13	4002	118	0.5	980s/20s	2.5	25	360	55	2.0E-07	0.144	27.5	2.4E-08	0.010
14	4120	140	0.5	980s/20s	10	25	360	56	5.7E-08	0.032	27.5	3.9E-09	0.004
15	4260	314	---	const K	---	25	360	56	2.9E-09	0.001	27.5	1.9E-09	0.000
Total	4574									3.748			0.702

After SCC testing, the side grooves of the specimens were again photographed as shown in Figure 5-25 for CT075 and Figure 5-26 for CT076 to document crack length and crack path. Cracking on the fusion line is clearly evident in CT075 in the latter part of the test. With such good alignment to the fusion line, it is unclear whether the crack has a preference to stay on the fusion line. Also notable is that the crack length in side-groove A is ~3.0 mm, while it is ~2.1 mm in side-groove B. The side-groove images of CT076 show that it reaches the fusion line part way through the test, but then continues to follow a straight path back into the 304SS suggestive of no preference to stay on or near the fusion line. Crack length is essentially identical on both sides of the specimen. The large crack opening for CT076 is due to the very high K later in the test.
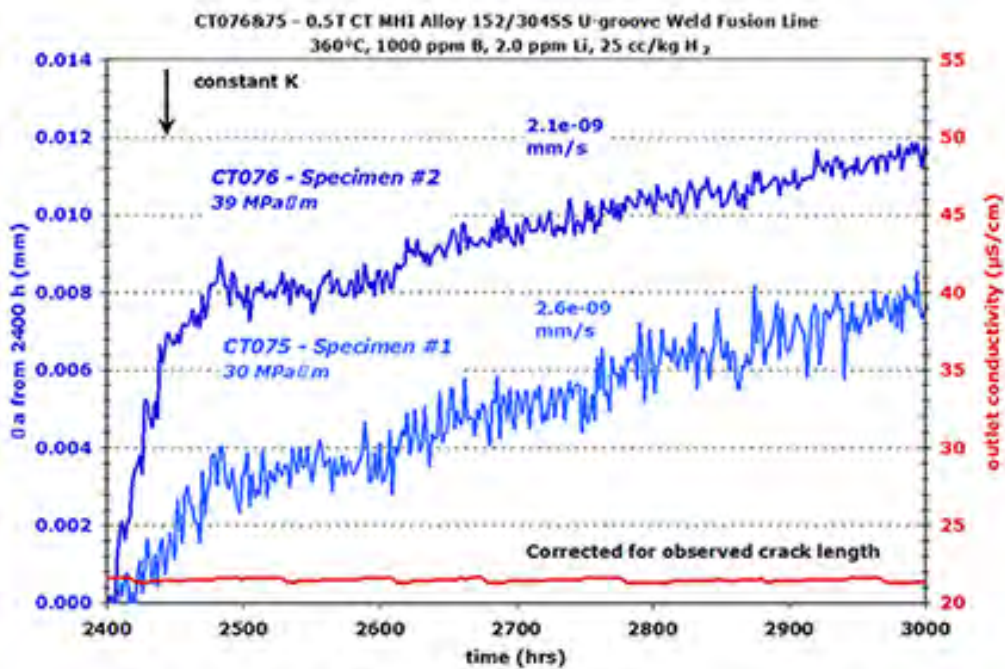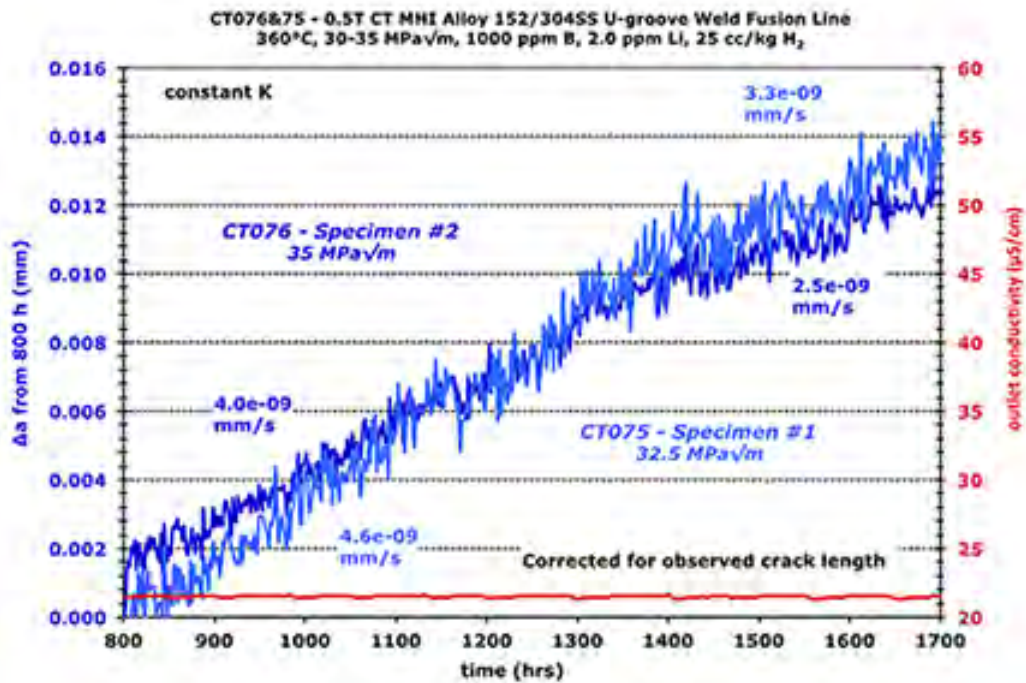
Figure 5-24 Crack Growth During the First and Second Constant K Assessments of the Alloy 152/304SS Fusion Line Specimens (CT075 and CT076)

CT075 - MHI A152 U-Groove Weldment 152/304SS Fusion Line Specimen #1, Side A

alloy 152

approximate constant K location

304SS

0   1   2   3 mm

CT075 - MHI A152 U-Groove Weldment 152/304SS Fusion Line Specimen #1, Side B

alloy 152

approximate constant K location

304SS

0   1   2 mm
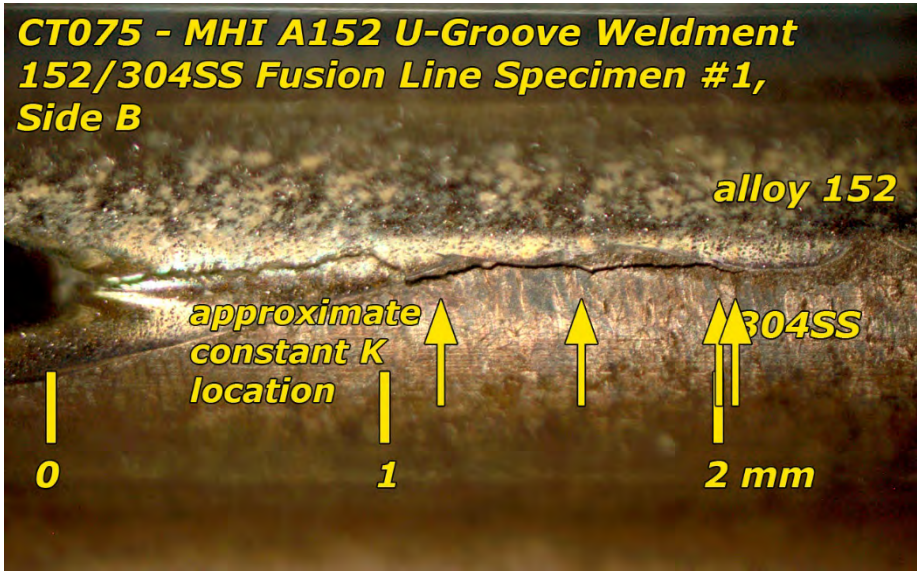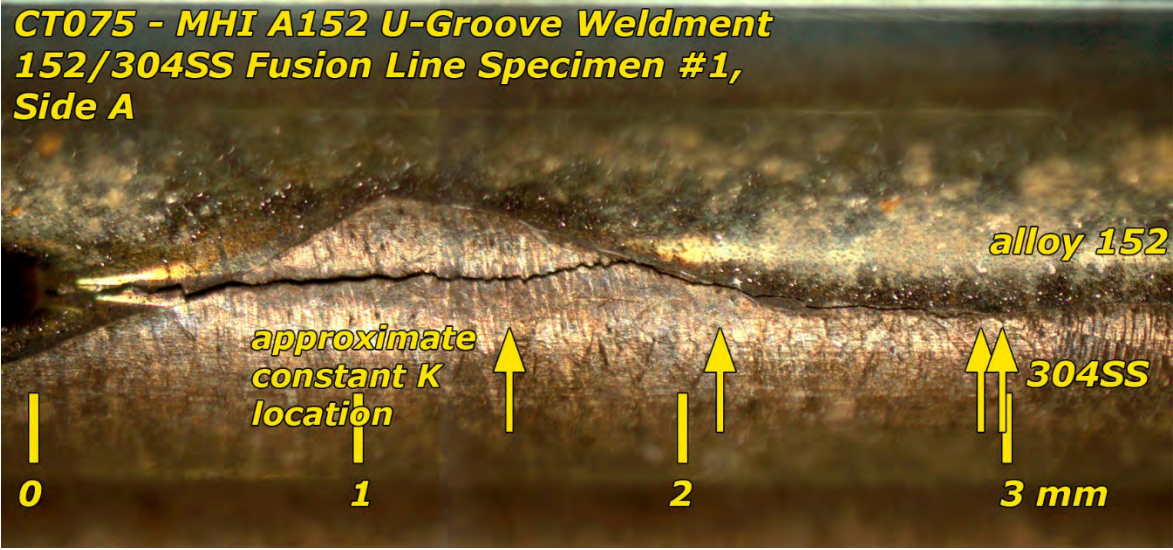
Figure 5-25   Post-Test Optical Images of the Polished and Etched Side Grooves for the First Alloy 152/304SS Fusion Line Specimen (CT075). Approximate Locations for the Constant K or Constant Load Exposures Are Indicated by the Arrows
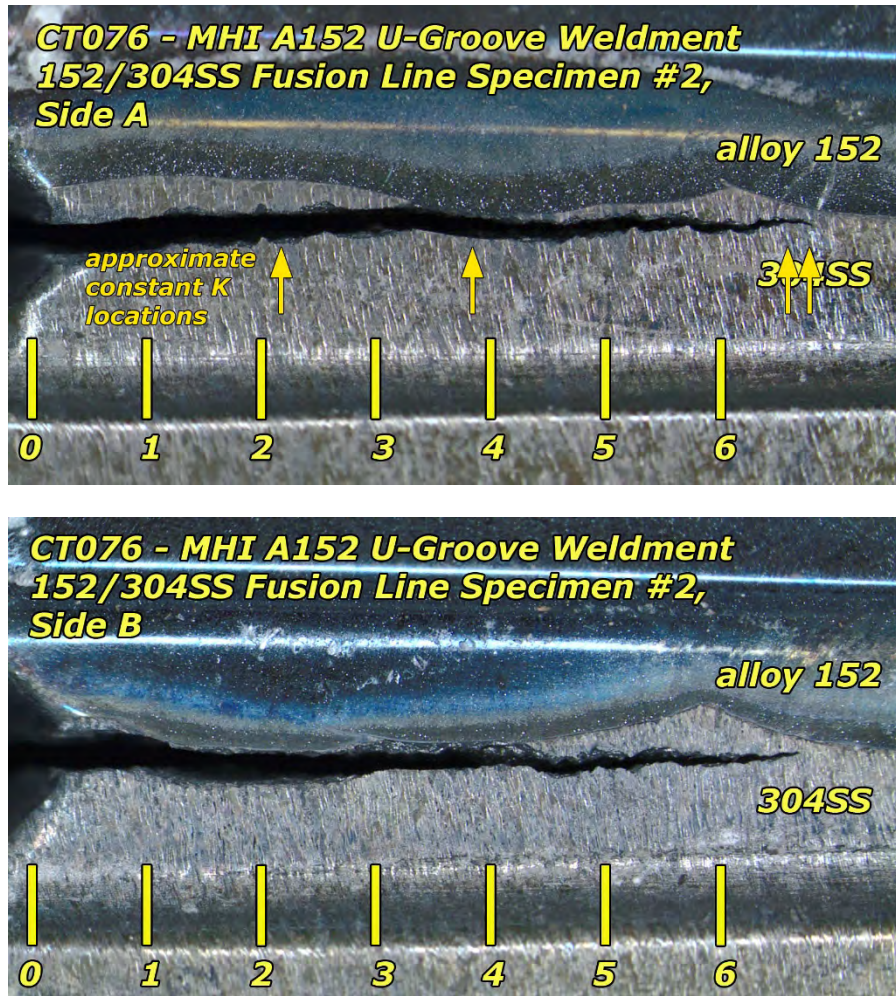
Figure 5-26   Post-Test Optical Images of the Polished and Etched Side Grooves for the Second Alloy 152/304SS Fusion Line Specimen (CT076). Approximate Locations During Constant K or Constant Load Exposures Are Indicated by the Arrows

Next, the specimen was sliced into an 8-mm thick piece and a 4-mm thick piece. The thicker piece was fatigued open for crack growth surface examinations, while the thinner piece was used for crack profile examinations. Images of the crack profile of CT075 and CT076 are shown in Figures 5-27 and 5-28, respectively. The optical image of CT075 shows a highly branched precrack (first ~1.2 mm) driven through the alloy 152 weld metal. In-situ testing begins in the alloy 152, and then the crack passes through the fusion line and stays within 100-200 μm from the fusion line in the 304SS. The fact that the crack did not remain on the fusion line suggests no strong preference for this region. The crack profile for CT076 (SEM images in Figure 5-28) shows the crack growing in the 304SS until the final ~1.5 mm where it meets the fusion line. Instead of following the fusion line, the crack appears to deflect back into the 304SS. When considering all the crack profile images together, there does appear to be a tendency for cracking to take place in the 304SS instead of the alloy 152. SEM-EDS maps did not reveal strong dilution effects in the alloy 152.

Figure 5-27 Optical Image of the Interior Crack Profile of the Alloy 152/304SS Specimen #1 (CT075)
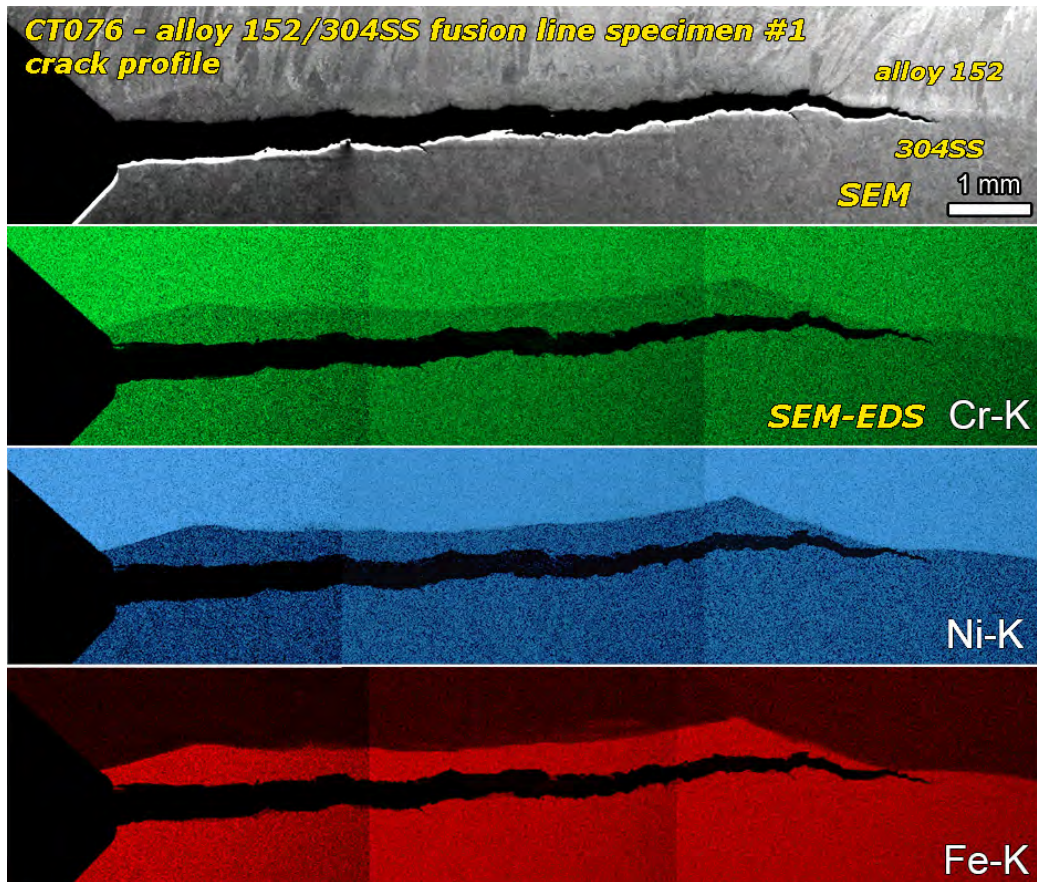
Figure 5-28 SEM-SE and EDS Elemental Maps of the Interior Crack Profile of the Alloy 152/304SS Specimen #2 (CT076)

Optical images of the crack surface for CT075 and CT076 are shown in Figures 5-29 and 5-30, respectively. Notations are written on the images to show how the sides of the specimen correspond to either the crack profile or the side grooves to allow comparison to those images. CT075 has a more undulated crack with a minimum length of ~2 mm in this image and also a minimum length of ~2 mm as observed in side-groove B (Figure 5-25). Some evidence of limited crack extension into the alloy 152 weld metal was observed in CT075 and was confirmed by SEM. A key result from the optical and SEM characterizations of crack-growth surfaces is that no IG cracking was found as illustrated in Figures 5-31 and 5-32. The TG cracking provides confirmation that the alloy 152/304SS weld fusion line is indeed resistant to IGSCC in PWR primary water.
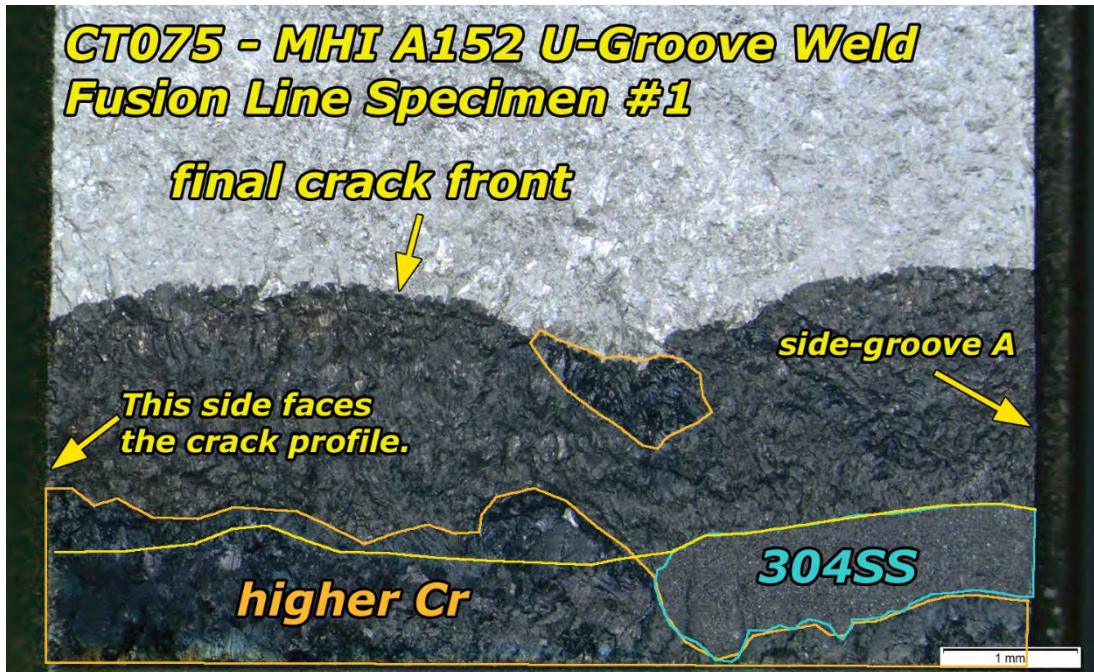
Figure 5-29   Optical Image of the Crack Surface of Alloy 152/304SS Fusion Line Specimen #1 (CT075)
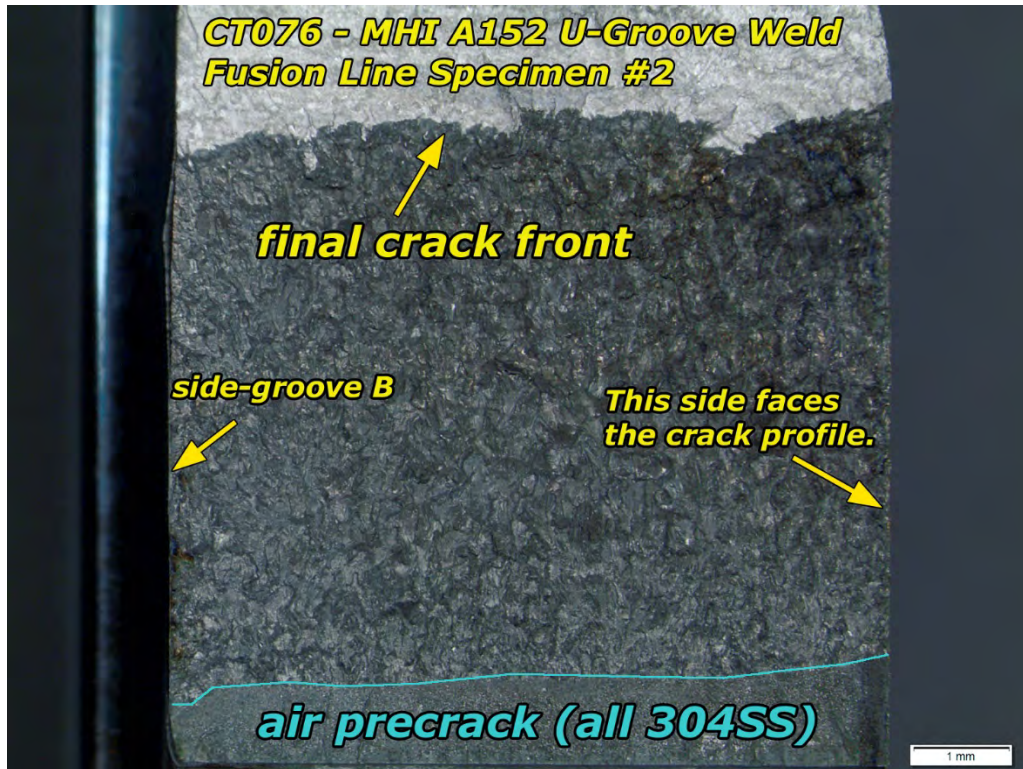
Figure 5-30   Optical Image of the Crack Surface of Alloy 152/304SS Fusion Line Specimen #2 (CT076)
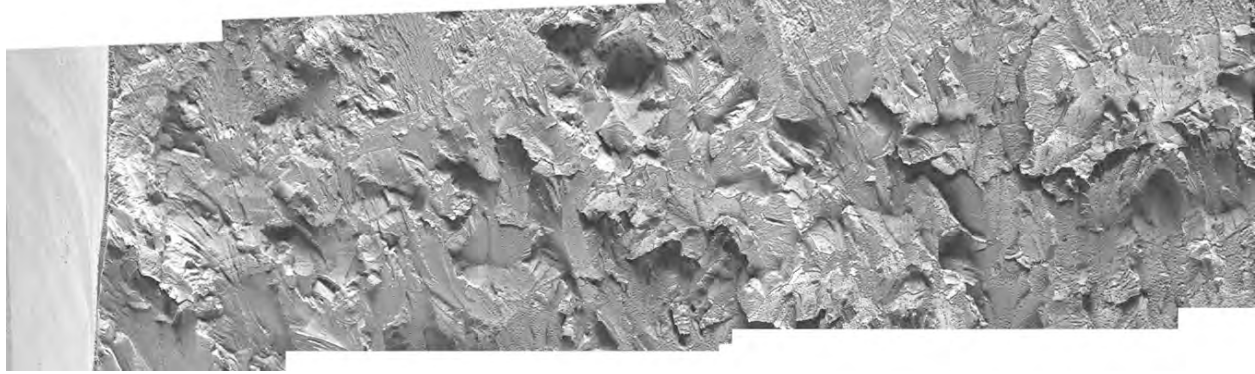
Figure 5-31   SEM-SE Montage of the Crack Surface of Alloy 152/304SS Fusion Line Specimen #2 (CT076) Illustrating TG Cracking Morphology
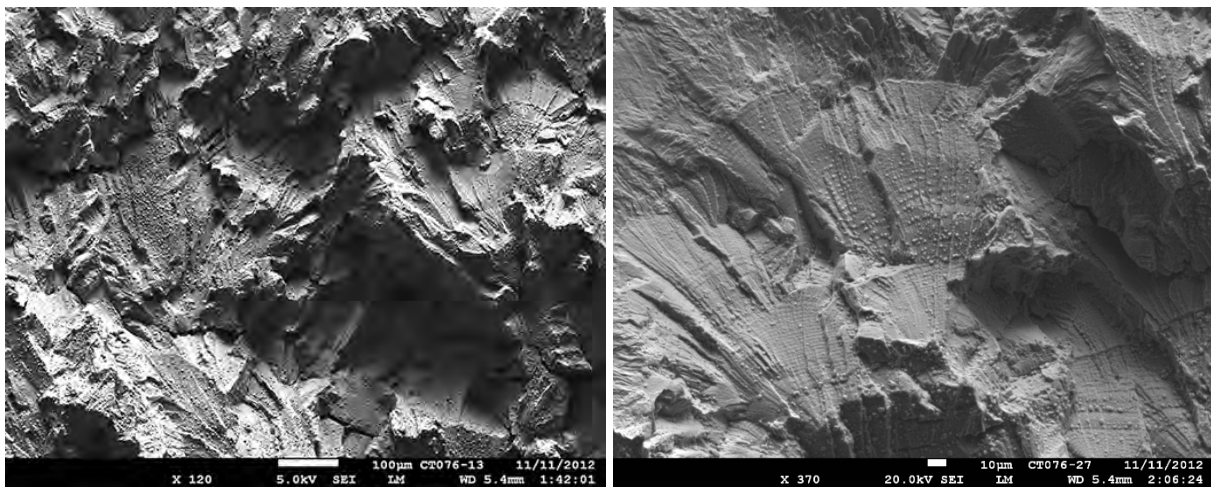
Figure 5-32   SEM-SE Images of the Typical Crack Surface Regions of Alloy 152/304SS Fusion Line Specimen #2 (CT076) Illustrating TG Cracking Morphology

5.3   Alloy 152/52-LAS/CS Interfaces

5.3.1   KAPL 52M/152M-CS DM Weld Interface (CT065 and CT66)

Crack-growth testing was conducted on CS dilution zone specimens from the alloy 52M and alloy 152M dissimilar metal V-groove welds provided by KAPL. As described in section 5.1, the geometric crack plane was positioned ~0.5 mm from the fusion line in the weld metal for both specimens as illustrated in Figures 5-5 and 5-6. An overview crack growth plot of the entire test on these two specimens is shown in Figure 5-33 and a test summary is given in Table 5-3. These two specimens behaved quite similarly during the first transitioning and constant K assessment, and constant K CGRs were found to be very low at ~3×10^{-9} mm/s. However during the second transitioning sequence, the alloy 152M-CS specimen began exhibiting higher and higher cyclic CGRs, and as more gentle load cycling conditions were applied, this response persisted while the alloy 52M-CS specimen continued to exhibit low CGRs. For the second SCC CGR evaluation, constant load was used instead of constant K. As shown in Figure 5-34, the alloy 152M-CS specimen CT066 initially showed a low CGR of ~3×10^{-9} mm/s, but the CGR evolved with time reaching ~2×10^{-6} mm/s after ~1200 h at constant load. The test was ended at this point to examine the specimens.

Because of the differing response between the two specimens and the desire to analyze for weld dilution, the decision was made to section half of each specimen into five crack profile slices, and then fatigue open the other half of the specimen as depicted in Figure 5-35. The side grooves of the specimen were also examined. Specimen characterizations focused first on the alloy 52M-CS specimen (CT065) that exhibited consistently low CGRs throughout the test. Initial observations of the side grooves (Figure 5-36) revealed that the crack followed a straight trajectory staying within the alloy 52M at a distance of no more than ~0.5 mm away from the fusion line. SEM-EDS observations of the crack profile in Figure 5-37 confirmed this trajectory and also showed that the crack did not sample any regions of significant dilution during SCC testing. In particular, the locations of constant K observations are noted. Other crack profile observations showed a similar lack of dilution in the region of SCC testing. Crack surface observations revealed entirely TG crack growth that was not surprising due to the lack of dilution and the ~60° misorientation between the geometric crack path and the weld grain boundaries.
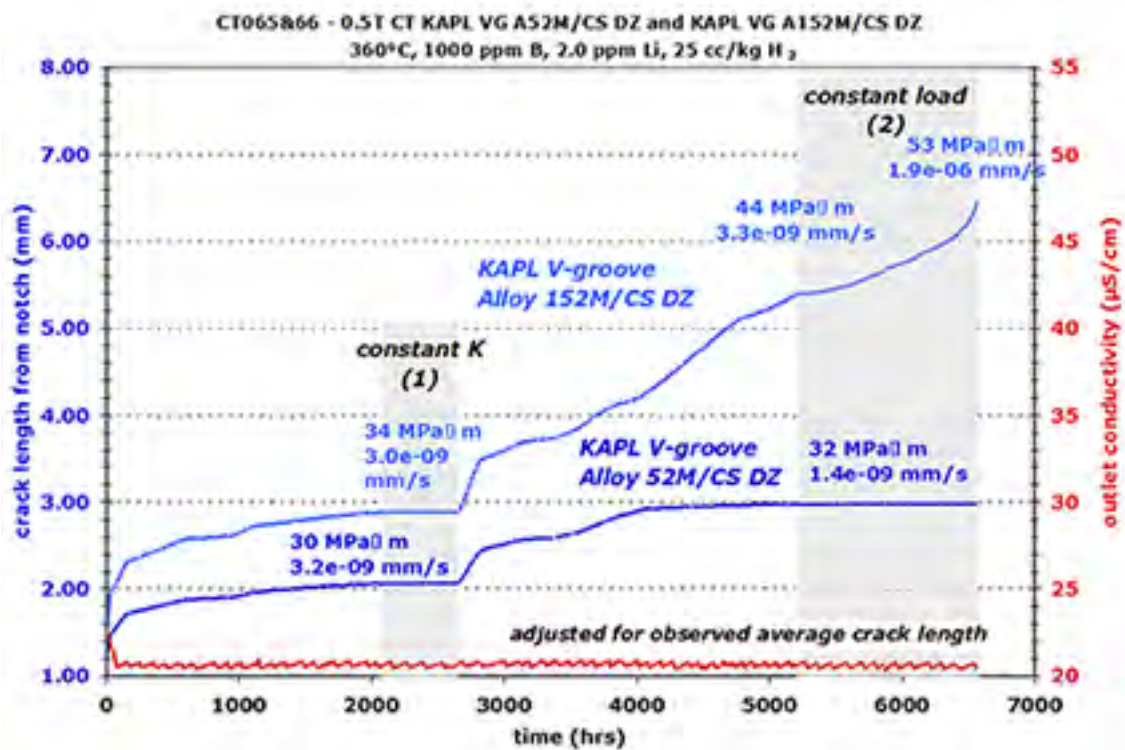
Figure 5-33   Overview of the Entire SCC Test on the Alloy 52M/152M-CS Dilution Zone Specimens (CT065 and CT066)

Table 5-3   Test Summary for KAPL Alloy 52M/CS and Alloy 152M/CS Dilution Zone Specimens CT065 and CT066

Test Phase	Start (h)	Time (h)	R	Freq. (Hz)	Hold (h)	Diss H$_2$ (cc / kg)	Temp (°C)	CT065 KAPL A52M/LAS VG DZ			CT066 KAPL A152M/LAS VG DZ		
								Kmax (MPa√m)	CGR (mm/s)	Crack Exten. (mm)	Kmax (MPa√m)	CGR (mm/s)	Crack Exten. (mm)
1	0	25	0.5	0.1	0	25	360	30	2.6E-06	0.256	32	4.1E-06	0.381
2	25	120	0.5	0.01	0	25	360	30	6.4E-07	0.225	33	9.2E-07	0.351
3	145	440	0.5	0.001	0	25	360	30	9.6E-08	0.152	33	1.7E-07	0.256
4	585	340	0.5	0.001	2.5	25	360	30	1.7E-08	0.012	33	2.4E-08	0.021
5	925	175	0.5	980s/20s	0	25	360	30	1.1E-07	0.063	33	2.1E-07	0.116
6	1100	830	0.5	980s/20s	1	25	360	30	2.0E-08	0.072	34	3.8E-08	0.128
7	1930	179	0.5	980s/20s	2.5	25	360	30	1.6E-08	0.007	34	2.2E-08	0.013
8	2109	550	---	const K	---	25	360	30	3.2E-09	0.006	34	2.9E-09	0.004
9	2659	158	0.5	0.01	0	25	360	31	6.4E-07	0.358	35	1.0E-06	0.549
10	2817	317	0.5	0.001	0	25	360	31	1.1E-07	0.115	35	2.1E-07	0.180
11	3134	243	0.5	0.001	1	25	360	31	1.9E-08	0.018	35	4.5E-08	0.039
12	3377	182	0.5	0.001	0	25	360	31	9.9E-08	0.057	36	1.7E-07	0.093
13	3559	246	0.5	480s/20s	0	25	360	31.5	1.6E-07	0.273	37	1.8E-07	0.404
14	3805	247	0.5	980s/20s	0	25	360	32	1.2E-07	0.111	37	1.4E-07	0.126
15	4052	744	0.5	980s/20s	2.5	25	360	32	1.8E-08	0.053	42	3.5E-07	0.898
16	4796	420	0.5	980s/20s	10	25	360	32	3.7E-09	0.009	44	2.7E-07	0.288
17	5216	1350	---	const K	---	25	360	32	1.5E-09	0.007	53	1.9E-06	1.058
Total	6566									1.791			4.903

CT065&66 – 0.5T CT KAPL VG A52M/CS DZ and KAPL VG A152M/CS DZ
360°C, 1000 ppm B, 2.0 ppm Li, 25 cc/kg H₂

constant load

1.9e-06 mm/s

KAPL V-groove
Alloy 152M/CS DZ
44-53 MPa√m

6e-07 mm/s

KAPL V-groove
Alloy 52M/CS DZ
32 MPa√m

3.3e-09 mm/s

1.4e-09 mm/s
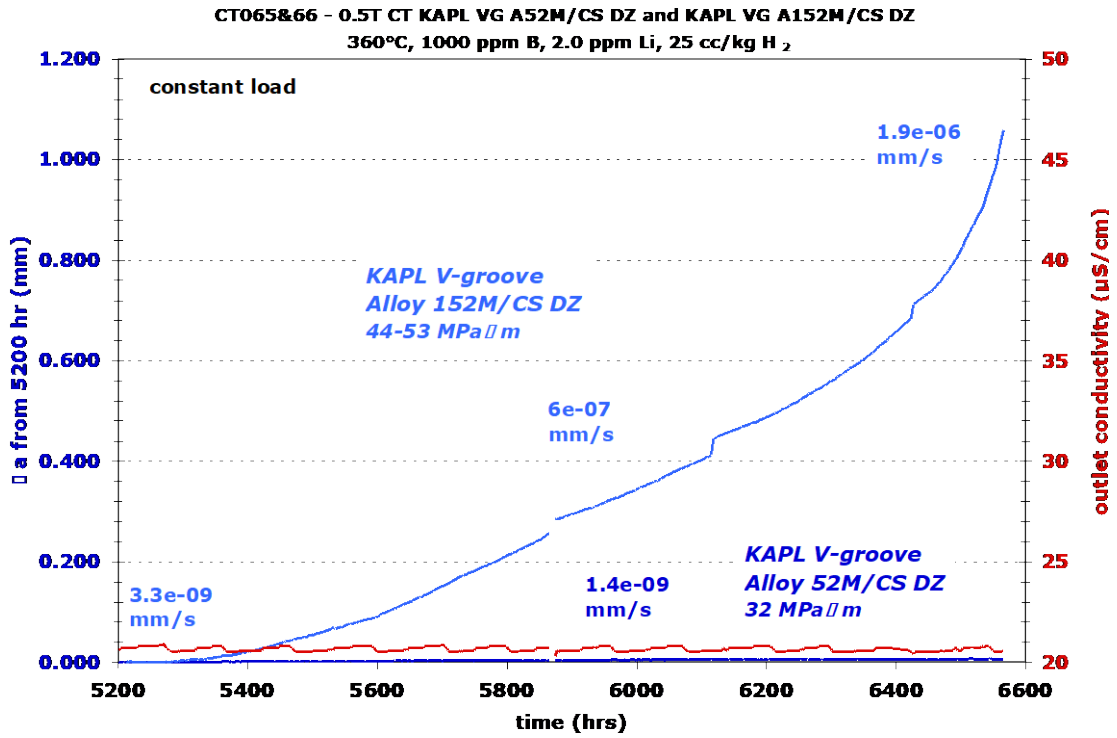
Figure 5-34   Crack Growth of the Alloy 52M/152M-CS Dilution Zone Specimens CT065 and CT066 During the Second SCC Assessment
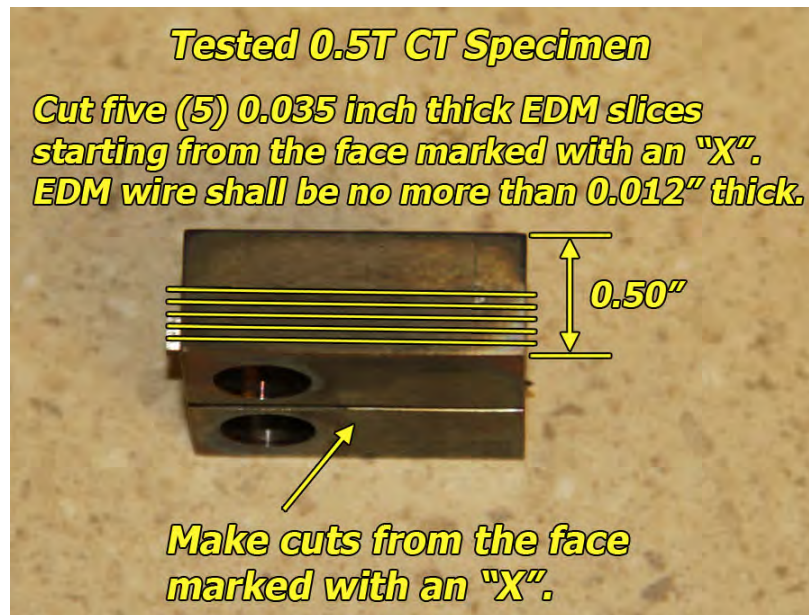
Figure 5-35   Post-Test Specimen Sectioning Plan for the Alloy 52M/152M-CS Dilution Zone Specimens CT065 and CT066
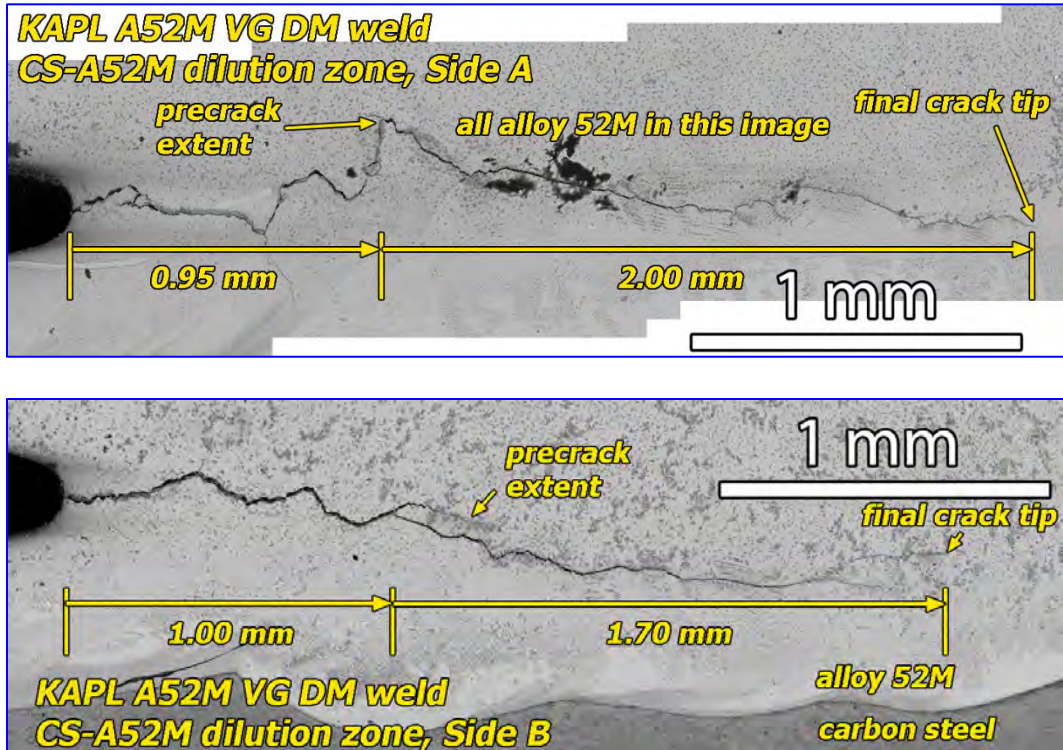
Figure 5-36   SEM-BSE Images of the Side Grooves for the Alloy 52M-CS Dilution Zone Specimen (CT065) After SCC Testing
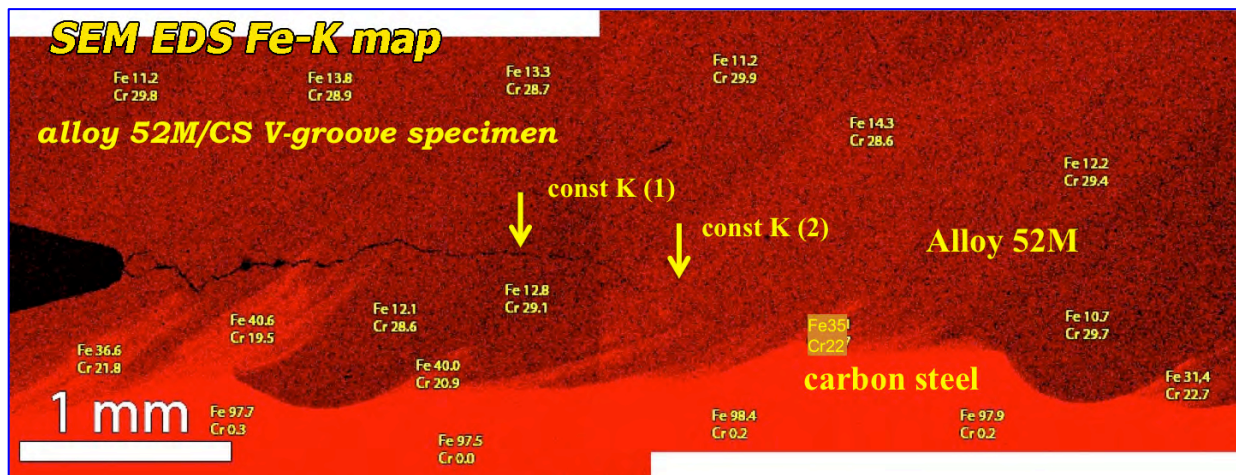
Figure 5-37   SEM-EDS Fe Map of the Alloy 52M-CS Dilution Zone Specimen (CT065) Crack Profile Slice #5 Showing Composition in the Region Around the Crack

Examination of the alloy 152M-CS dilution zone specimen also started with side-groove examinations, however the length of the crack in the side grooves was much shorter than the DCPD crack length indicating that not all the crack was visible in the side grooves. Therefore, characterizations focused on the crack profile and crack-growth surface. The SEM-BSE image of the inner-most slice (slice #5) of the alloy 152M-CS specimen in Figure 5-38 and the corresponding SEM-EDS Fe map in Figure 5-39 provides a good representation of what

microstructures the crack encountered during testing. During the first transitioning and constant K observation, the crack was entirely within the alloy 152M weld metal, and as shown in the EDS map, the crack encountered a region of significant dilution (single pass region shows Cr depletion to ~20 wt% and Fe enrichment to ~40 wt%) during the first constant K assessment. The step-like crack path during the first transitioning suggests some preference for crack growth parallel to the long grain boundaries, however higher resolution images of this slice, the other slices (Figure 5-40) and the crack growth surface (Figure 5-41) revealed that the crack was predominately TG during constant K SCC testing in the ~20 wt% Cr dilution zone.
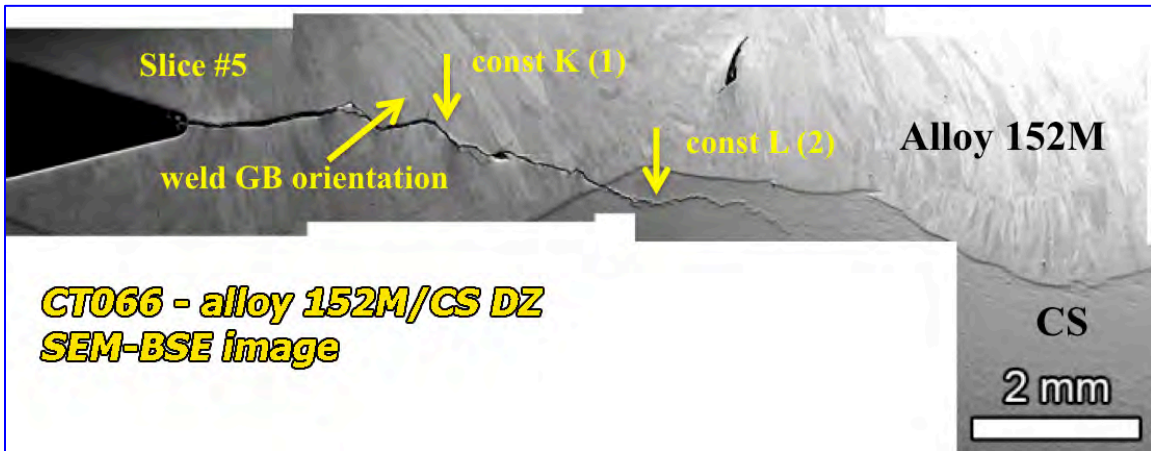
Figure 5-38   SEM-BSE Image of the Inner Most Slice (#5) Cut from the Alloy 152M-CS Dilution Zone Specimen (CT066)
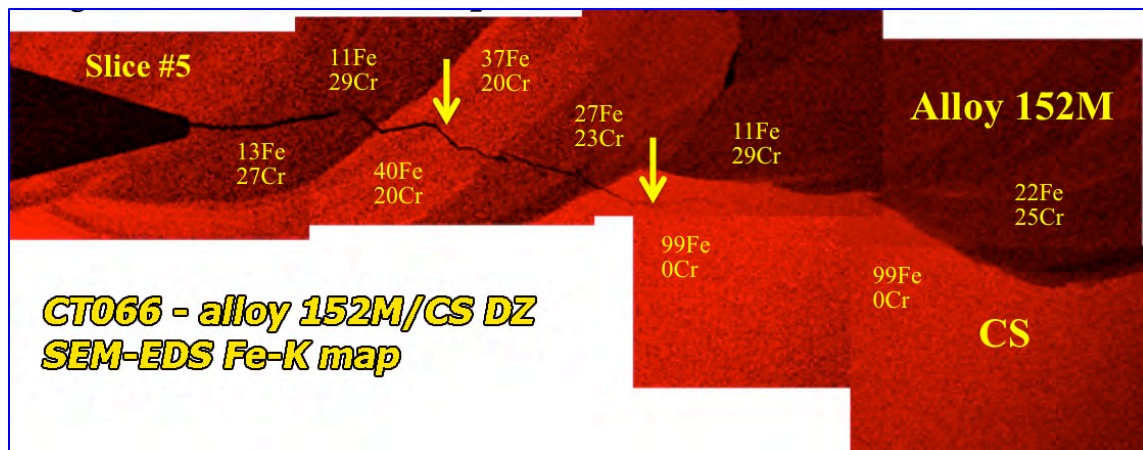
Figure 5-39   Corresponding SEM-EDS Fe-K Map for the SEM-BSE Image in Figure 5-38 of the Alloy 152M-CS Specimen (CT066). Locations of Constant K or Constant Load Evaluations Are Indicated by the Arrows
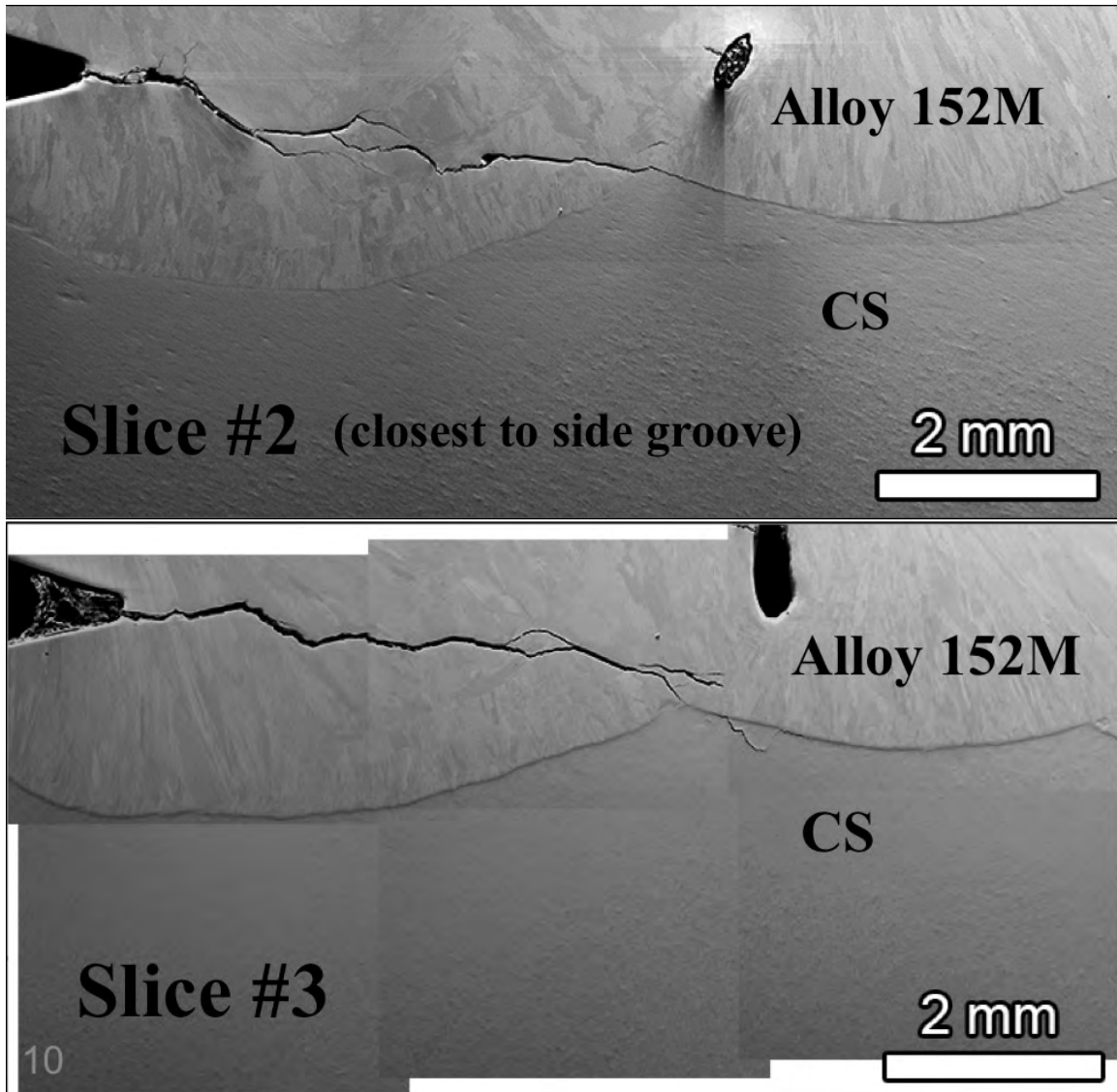
Figure 5-40   SEM-BSE Images of Slices #2 and #3 from the Alloy 152M-CS DZ Specimen. The Crack Can Be Seen to Intersect and Remain on the Fusion Line for a Short Distance in Both Slices

During the second transitioning sequence, the crack continued on a downward trajectory that it had started during the first transitioning sequence and eventually reached the fusion line. Comparison of the crack growth plot to the crack profile and crack surface images indicated that the very high CGRs happened after the crack reached the fusion line and then grew partly on the fusion line and partly in the CS HAZ. Subsequent EBSD examinations of slice #5 (Figure 5-42) showed that the CS has an extremely fine grain size in the immediate vicinity of the fusion line, while microhardness measurements (Figure 5-43) showed correspondingly high Vickers hardness ranging from 200-300 kg/mm^2 in this ~1 mm wide zone along the fusion line. This fine grain, high hardness region was due to a martensitic transformation that occurred during the welding process. In a typical nuclear reactor pressure boundary component that is fabricated by a DM weld involving carbon or low alloy steel, the steel is first buttered and then given a PWHT that tempers the martensite and reduces its strength.
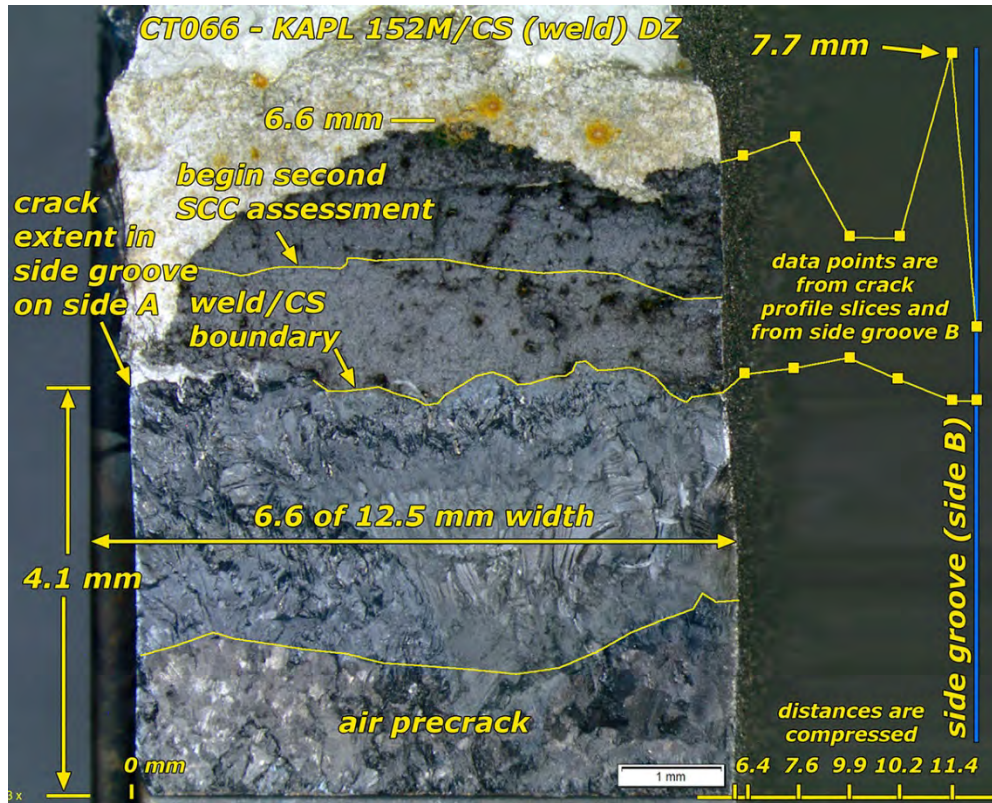
Figure 5-41 Optical Image of a ~6 mm Width of the Crack Growth Surface for the Alloy 152M-CS Specimen CT066. A Reconstruction of the Other Half Is Included Based on Crack Profile Exams
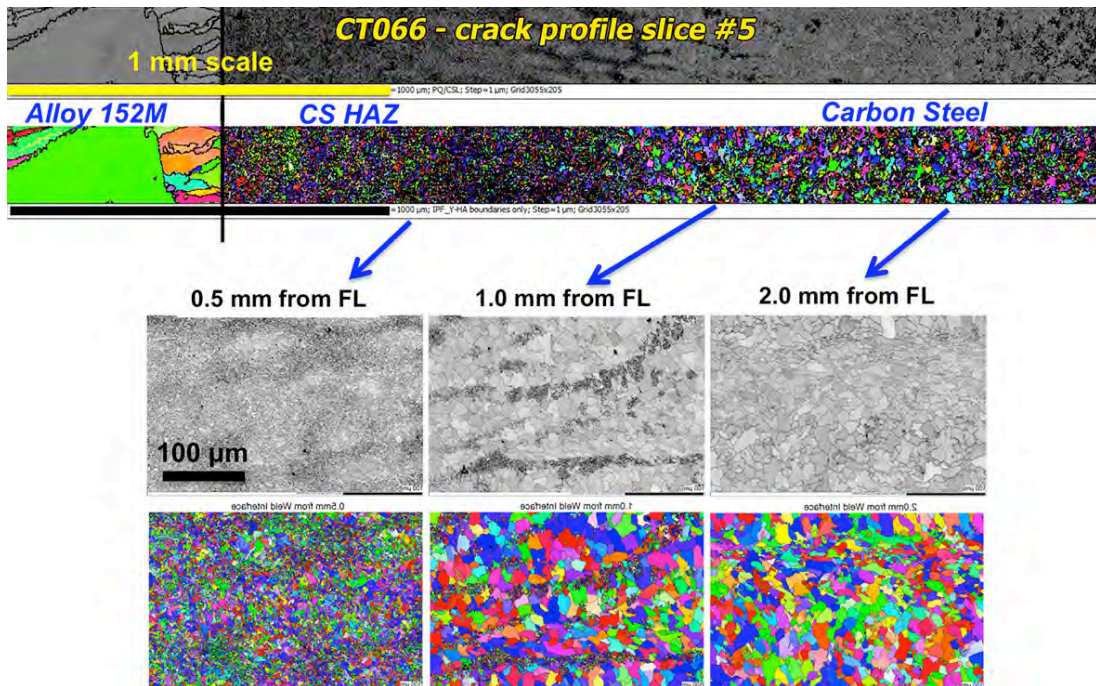
Figure 5-42 SEM-EBSD Analysis of the Alloy 152M-CS Specimen CT066 in the Region of the Fusion Line
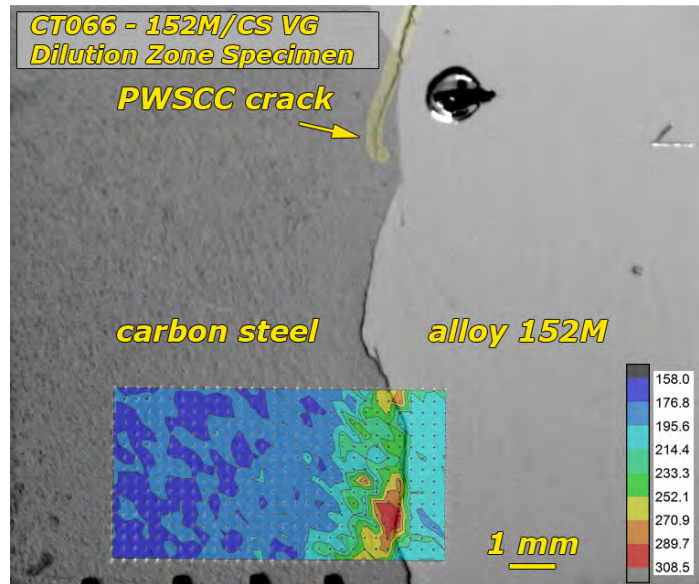
Figure 5-43   Map of Microhardness Measurements Across the CS – Alloy 152M Interface Region in Slice #5 from the Alloy 152-CS DM Weld Specimen CT066.KAPL 52M/152M-CS DM Weld Interface (CT082 and CT083)

A second set of specimens was machined from the KAPL DM welds and tested to assess SCC susceptibility of the fusion line and CS HAZ region including the influence of a PWHT. Side grooves for these specimens were presented in Figures 5-7 and 5-8. As shown in the overview plot in Figure 5-44 and Table 5-4, the first portion of the test was run with the materials in the as-welded condition. Constant K testing in simulated PWR primary water at ~30 MPa√m produced a ~7x10^{-9} mm/s CGR for the alloy 52M-CS fusion line specimen (CT083) but only ~2x10^{-9} mm/s CGR for the alloy 152M-CS fusion line specimen (CT082). Increasing the stress intensity by a dK/da sequence and then re-transitioning to constant K at 36-40 MPa√m resulted in a ~10X CGR increase to ~6x10^{-8} mm/s for the alloy 52M-CS fusion line specimen, but did not affect the CGR of the alloy 152M-CS fusion line specimen (Figure 5-45). Having produced a CGR in the alloy 52M-CS fusion line specimen that was similar to the first test on these V-groove welds, the test was stopped, and the specimens were removed and given a prototypic PWHT of 621°C for 10 hours followed by air cooling. The specimens were reloaded into the autoclave and testing was resumed. After ~200 µm of crack extension during transitioning, constant K conditions were established resulting in ~2x10^{-9} mm/s CGRs for both specimens. Cycle + hold loading was restarted to move the crack forward and test for ligament formation. Steady growth was observed over ~100 µm, and the test was converted to constant K for the last time. Low CGRs were again observed over a period of ~800 h as documented in Figure 5-46. The test was ended and the specimens were sliced up and fatigued open for examinations. The optical and SEM images in Figure 5-47, suggest that the alloy 152M-CS fusion line specimen (CT082) exhibited low crack growth because the geometric crack growth plane was not well aligned with the fusion line. On side-groove side B of the specimen, the fusion line was in the CS, but a considerable distance from the fusion line (~1 mm). On side A, the crack grew primarily in the alloy 152M until reaching the fusion line at the very end of the test. The optical image collage of the alloy 52M-CS fusion line specimen (CT083) in Figure 5-48 reveals that cracking was well aligned with the fusion line and significant growth occurred either on the fusion line or in the CS HAZ region both before and after the PWHT.
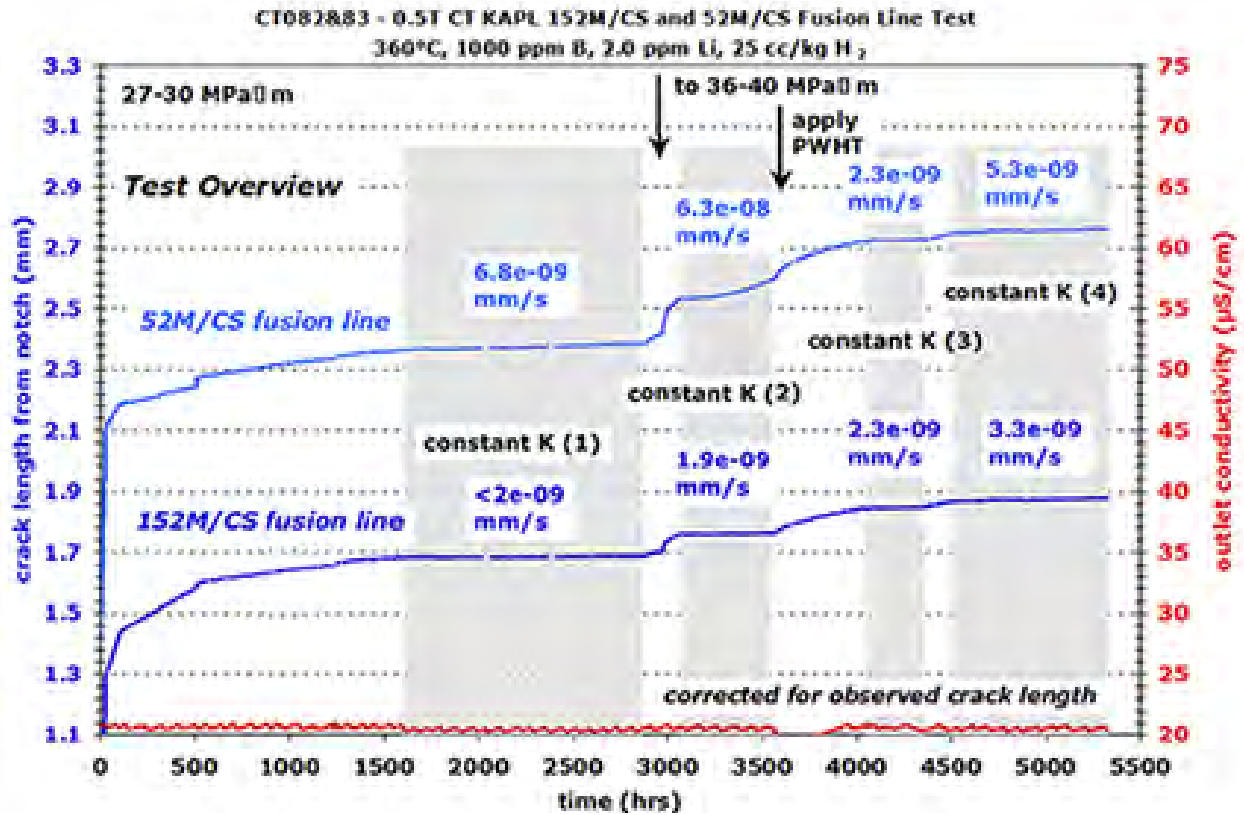
Figure 5-44   Overview Crack Growth Plot of the Entire Test on the Alloy 152M/52M-CS Fusion Line Specimens (CT082 and CT083)

Table 5-4   Test Summary for KAPL Alloy 152M/CS and Alloy 52M/CS Dilution Zone Specimens CT082 and CT083

Test Phase	Start (h)	Time (h)	R	Freq. (Hz)	Hold (h)	Diss H$_2$ cc / kg	Temp (°C)	CT082 KAPL 152M/CS FL test			CT083 KAPL 52M/CS FL test		
								Kmax (MPa√m)	CGR (mm/s)	Crack Exten. (mm)	Kmax (MPa√m)	CGR (mm/s)	Crack Exten. (mm)
1	0	29	0.5	0.1	0	25	360	30	5.5E-06	0.566	32	6.7E-06	0.664
2	29	74	0.5	0.01	0	25	360	30	5.5E-07	0.134	33	2.8E-07	0.069
3	103	209	0.5	0.001	0	25	360	30	9.1E-08	0.076	33	4.0E-08	0.024
4	312	193	0.5	980s/20s	0	25	360	30	9.1E-08	0.067	33	3.0E-08	0.028
5a	505	738	0.5	980s/20s	2.5	25	360	30	2.2E-08	0.074	33	2.4E-08	0.087
5b	1243	123	0.5	980s/20s	2.5	25	360	30	2.4E-08	0.013	33	2.9E-08	0.012
6	1366	333	0.5	980s/20s	10	25	360	30	8.8E-09	0.011	33	1.3E-08	0.015
7	1699	1186	---	const K	---	25	360	30	2.8E-09	0.005	33	7.9E-09	0.020
8	2885	94	0.5	980s/20s	2.5	25	360	30	1.2E-08	0.031	33.5	5.5E-08	0.057
9	2979	90	0.5	980s/20s	2.5	25	360	30->36	8.3E-08	0.038	34->40	1.5E-07	0.075
10	3069	501	---	const K	---	25	360	36	1.9E-09	0.002	40	6.3E-08	0.064
				PWHT				PWHT					
11	3570	468	0.5	980s/20s	2.5	25	360	36	3.7E-08	0.082	40	4.2E-08	0.115
12	4038	338	---	const K	---	25	360	36	1.6E-09	0.005	40	3.4E-09	0.005
13	4376	144	0.5	980s/20s	2.5	25	360	36	3.2E-08	0.019	40	3.7E-08	0.022
14	4520	810	---	const K	---	25	360	36	3.3E-09	0.010	40	5.3E-09	0.012
Total	5330									1.135			1.270
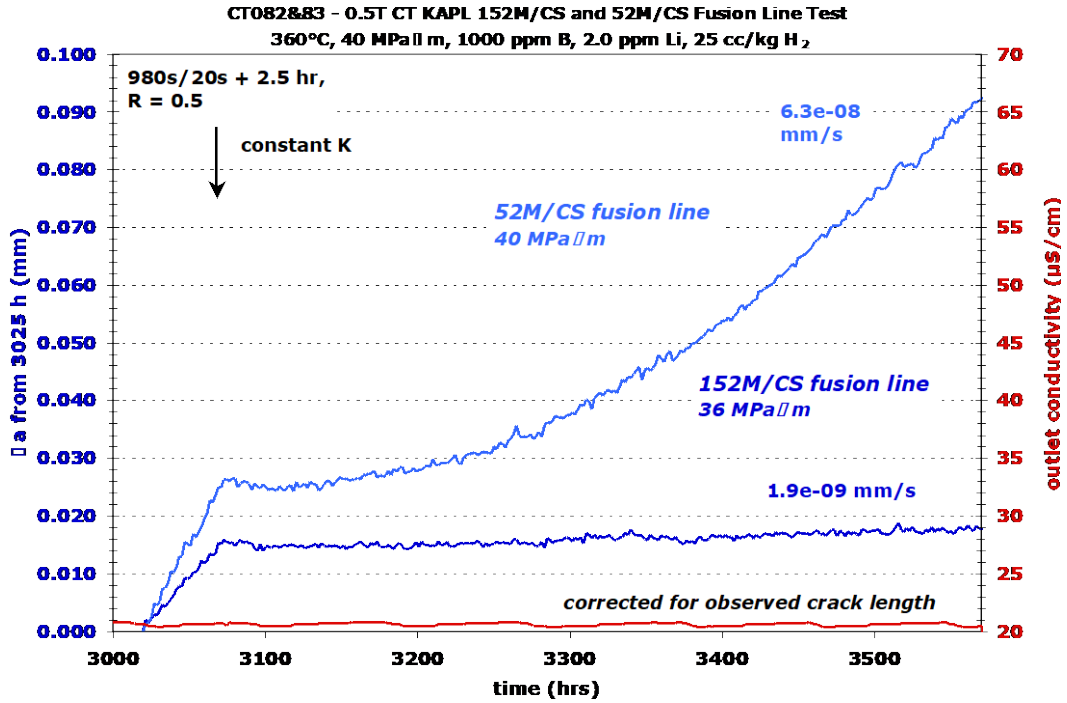
Figure 5-45   Constant K Crack Growth Response at 36-40 MPa√m of the Alloy 152M/52M-CS Fusion Line Specimens _Before_ Application of a Prototypic PWHT
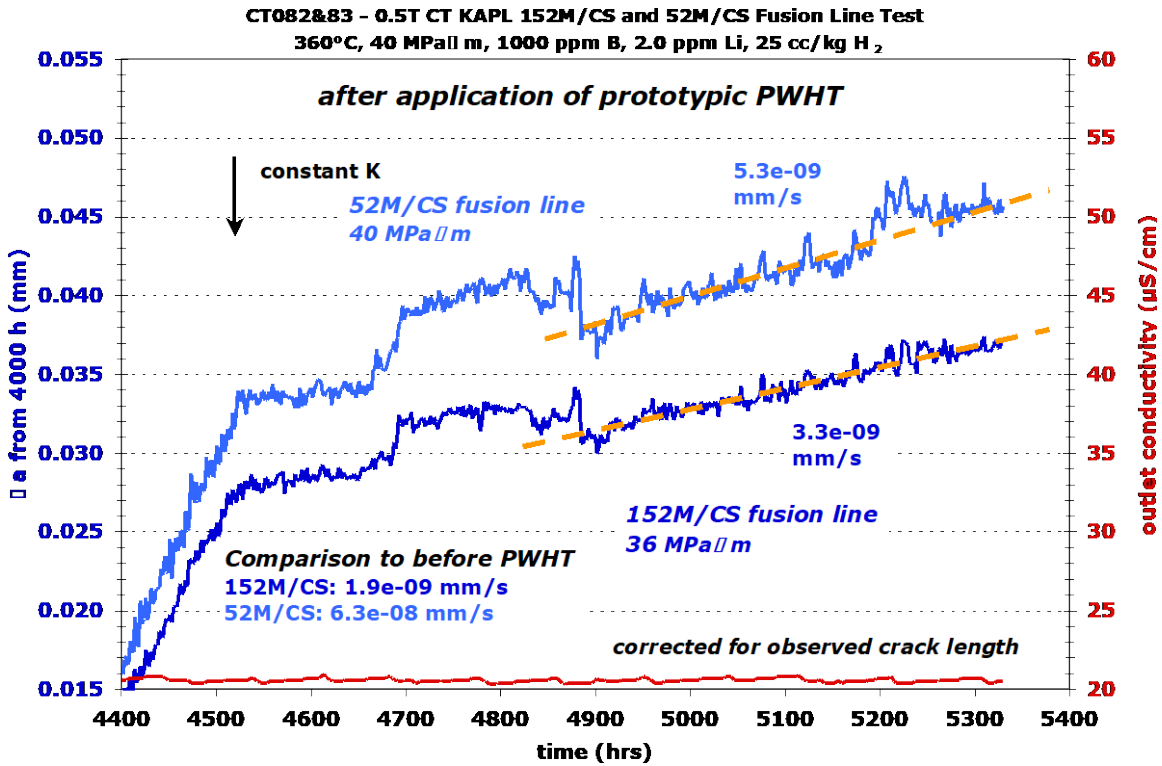
Figure 5-46   Constant K Crack Growth Response at 36-40 MPa√m of the Alloy 152M/52M-CS Fusion Line Specimens _After_ Application of a Prototypic PWHT
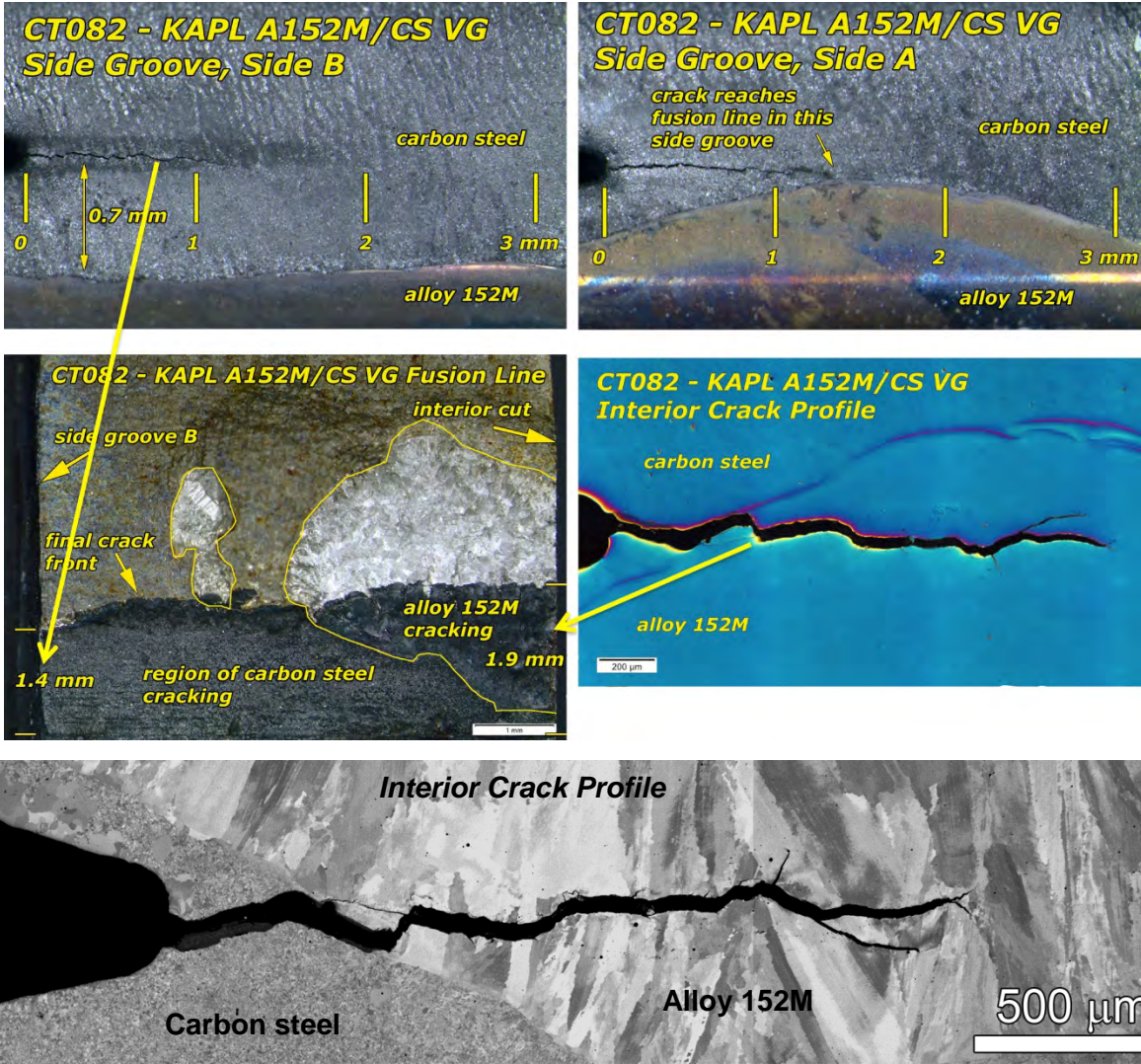
Figure 5-47   Optical (upper four) and SEM-BSE (bottom) Images Showing Cracking in the Alloy 152M-CS Specimen (CT082) That Is Primarily in the Alloy 152M
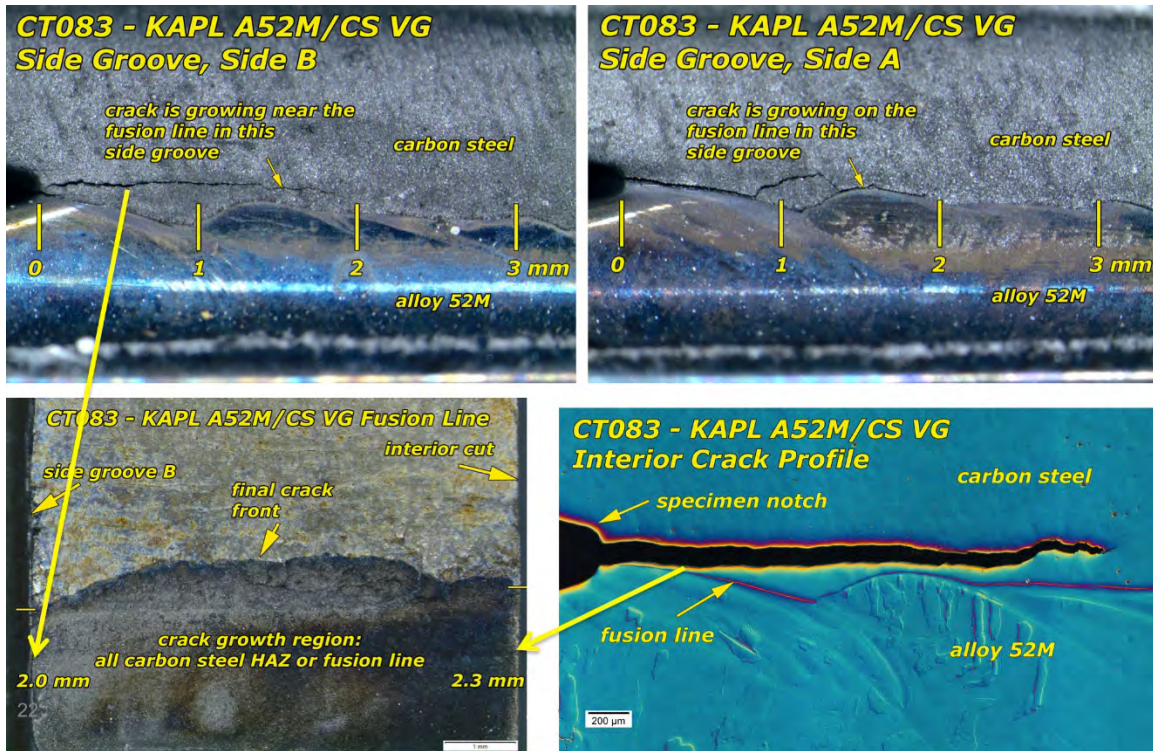
Figure 5-48   Collage of Optical Images of the Cracking in the Alloy 52M-CS Specimen (CT083) Revealing Cracking Either in the CS HAZ or on the Fusion Line

SEM imaging and microhardness measurements were performed on the crack profile slices of the DM weld fusion line specimens CT082 and CT083 (after the PWHT). They confirmed that the PWHT modifies the CS HAZ microstructure as illustrated in Figure 5-49. The alloy 152M-CS specimen CT082 exhibited a significant localized increase in the CS grain size along the fusion line when compared to the non-heat treated CT066 specimen. Hardness mapping on the CT082 specimen in Figure 5-50 revealed a decreased CS hardness (150-170 kg/mm^2) near the fusion line, much lower than before the PWHT (200-300 kg/mm^2). This change in hardness is spatially consistent with the microstructural features and suggests that the reduction in HAZ SCC susceptibility was due to this hardness reduction.
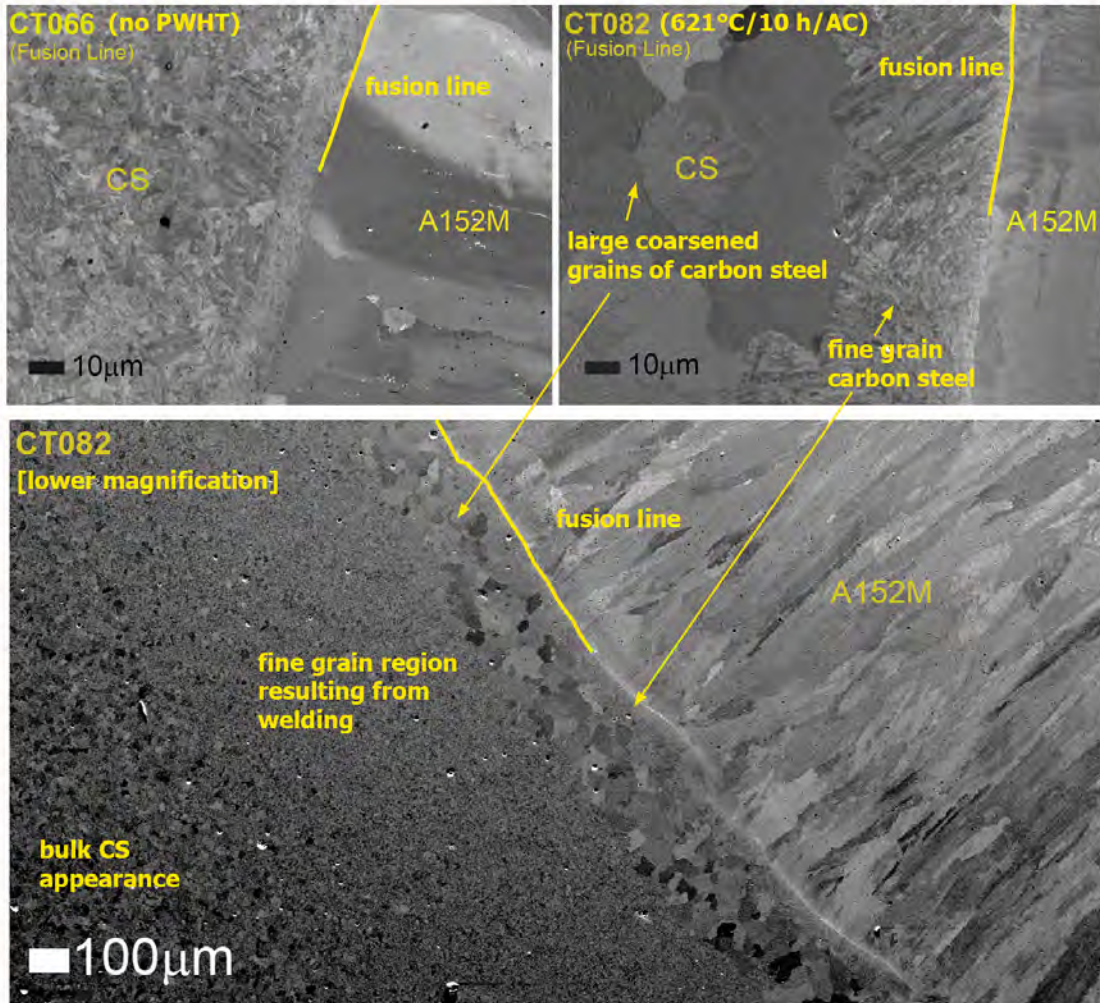
Figure 5-49   Collage of SEM-BSE Images Comparing Microstructural Differences Between the PWHT alloy152M-CS CT082 Specimen and the Non-Heat Treated CT066 Specimen
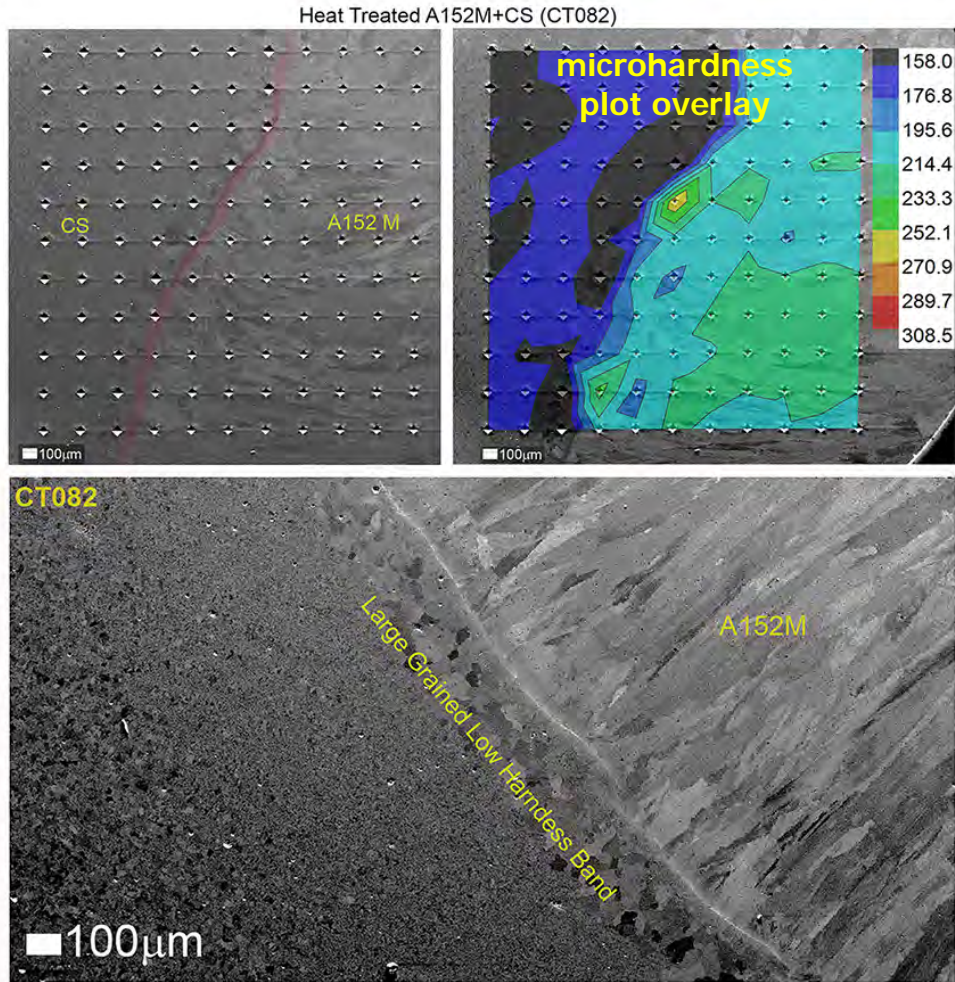
Figure 5-50   **SEM Image of Weld Metal and HAZ (top left) with Overlaid Hardness Contour Plot (top right) of the Alloy 152M-CS Fusion Line Specimen (CT082). The PWHT Had a Significant Effect on the Measured Hardness near the HAZ. The Lowest Measured Hardness Values Are Seen in the Large Grain Region in the CS**

5.3.2   Characterization of ANL 152/LAS Interface DM Weld Specimen (N152-LAS-11)

Post-test analysis of the N152-LAS-11 dilution zone CT specimen was performed in an attempt to better understand the observation of high crack-growth rate of this specimen at constant load. An example of the ANL data is shown in Figure 5-50 with an apparent SCC growth rate of 1-2x10^{-7} mm/s. After testing was completed, the specimen was sectioned into several pieces by ANL. First, both sides of the specimen were machined flat to remove the side grooves. After images were obtained of the cracks on these outer sides, the specimen was fatigued open. One piece (denoted as Piece A) was left intact to allow studying the crack growth surface as a whole, while the other (denoted as Piece B) was cross-sectioned into three slices as shown in Figure 5-51 to enable examinations of crack profile. All four pieces were loaned to PNNL for analysis in support of providing further microchemistry measurements, additional imaging and to assist in determining where to cut DZ specimens from a section of this weldment for PWSCC tests on the identical dilution region at PNNL.
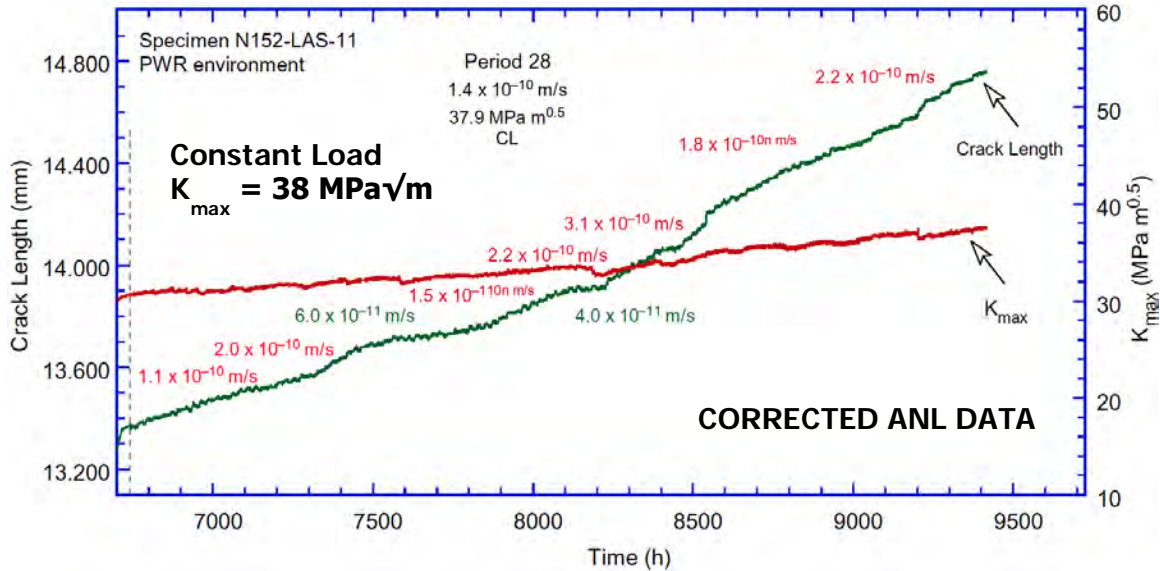
Figure 5-50 Crack-Growth Response Reported for the Alloy 152/LAS Dilution Zone Specimen N152-LAS-11 with SCC Propagation Averaging ~1.4x10^{-10} m/s (1.4x10^{-7} mm/s)
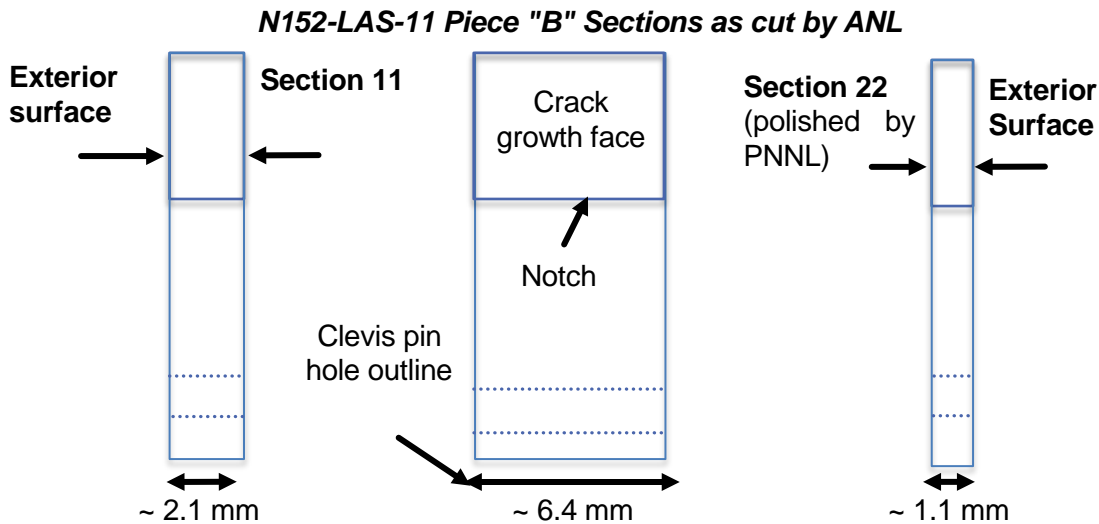
Figure 5-51 Schematic Illustrating the Cross-Section of Face A of the ANL N152-LAS-11 Dilution Zone CT. The Inner Portions of Section 11 and Section 22 Were Analyzed by PNNL

SEM BSE and SE images of the uncut crack-growth face (Face A) of ANL N152-LAS-11 are shown in Figure 5-52. The mass contrast generated by the SEM-BSE imaging provides a generally clear delineation between oxidized regions that were exposed to high temperature water and unoxidized regions that were fatigued open after the test was completed. The Section 11 and Section 22 cuts were performed on Piece B, but the corresponding section planes are also shown here on Face A to provide a relative location to the SCC response across the width of the specimen. Consistent with ANL observations, the region listed as "predominantly cyclic loading" was found to consist of TG cracking with isolated regions of IG

cracking, all of which was in the weld. However beyond that portion of the crack growth surface, the surface morphology changed to either IG cracking in the weld or cracking very near or on the fusion line. Regions of these two types of cracking are illustrated in Figure 5-53.

Higher magnification imaging was performed on these regions of fusion line and IG cracking. An SEM-BSE example of cracking on or near the fusion line is provided in Figure 5-54. IG-like features with a size of ~20-70 µm are apparent in portions of this region. SEM EDS scans of this area revealed >95Fe showing that crack growth was either on the fusion line or slightly into the LAS. A comparison of the cracking on Face A and the (cross) Section 11 view from Piece B is presented in Figure 5-55. The proximity to the fusion line is apparent in the Section 11 view. It appears that the unbroken ligament before the fusion line cracking is a region just prior to reaching the high point in the LAS in that image. SEM EDS maps show it to be weld metal.

SEM-BSE, SE and EDS examinations of Face A corresponding to the IGSCC region near Section 22 are presented in Figures 5-57 to 5-59. The general region of examination is shown in the SEM BSE image in Figure 5-57 with progressively higher magnification images revealing the surface morphology in Figures 5-58 and 5-59. This extensive region of "flat" IG morphology is unexpected and has not been previously observed on crack growth surfaces for alloy 152/52 weld metals. SEM EDS maps were also taken within selected IG regions as documented in Figure 5-60 and indicated compositions of ~23 wt% Cr, ~40 wt% Ni and ~27 wt% Fe.
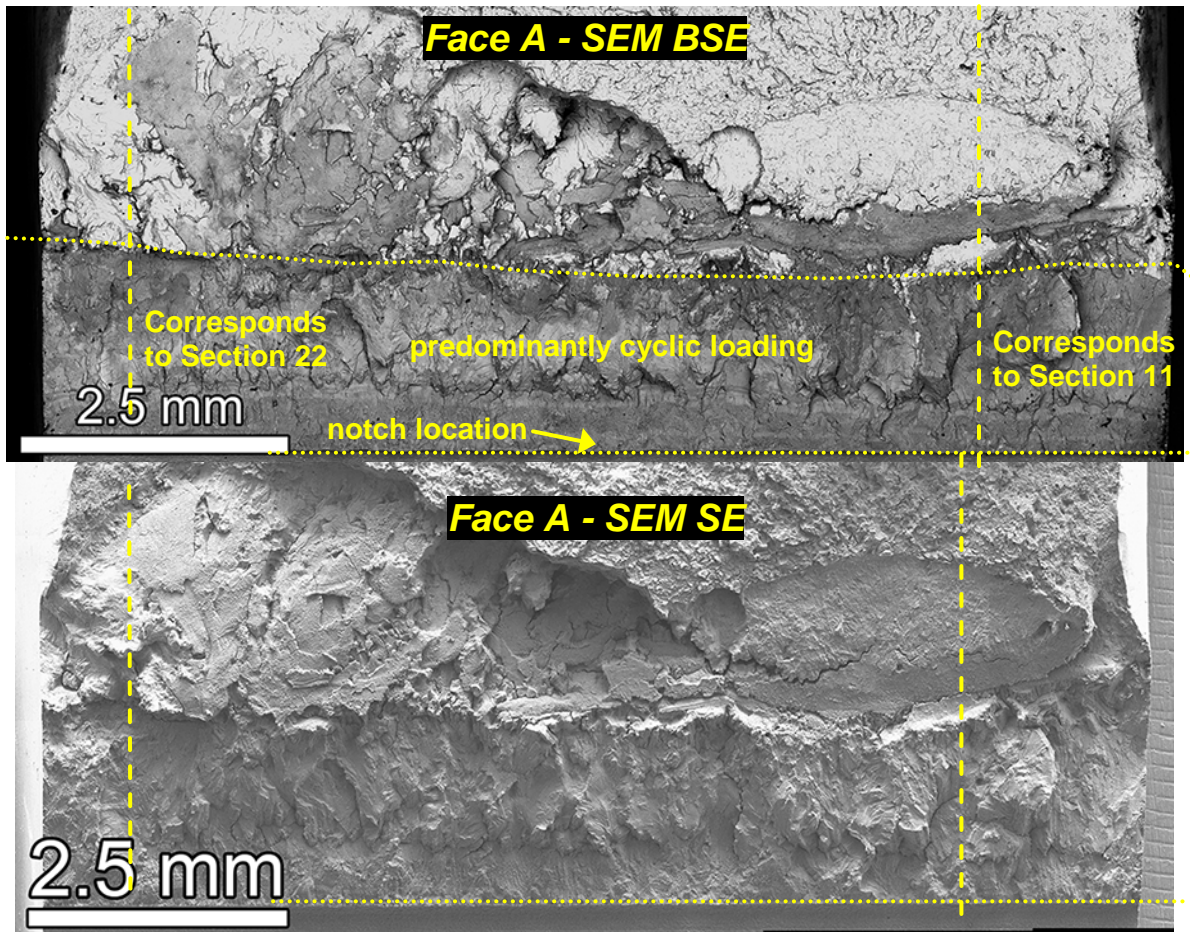
Figure 5-52   SEM-SE Micrographs of the Face A Crack-Growth Surface for the ANL N152-LAS-11 Specimen
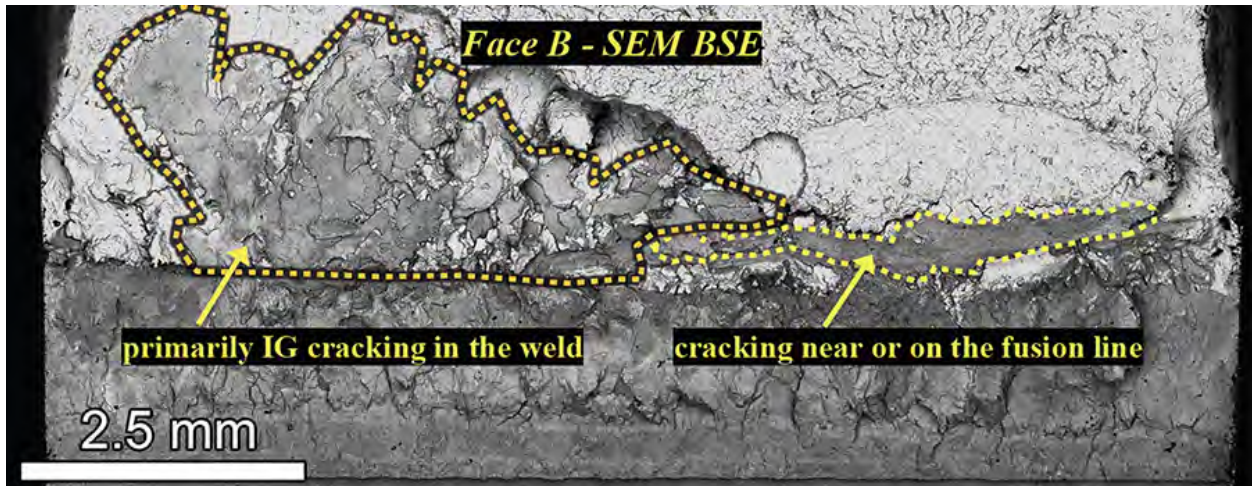
Figure 5-53 Crack-Growth Surface for the Alloy 152/LAS Dilution Zone Specimen N152-LAS-11
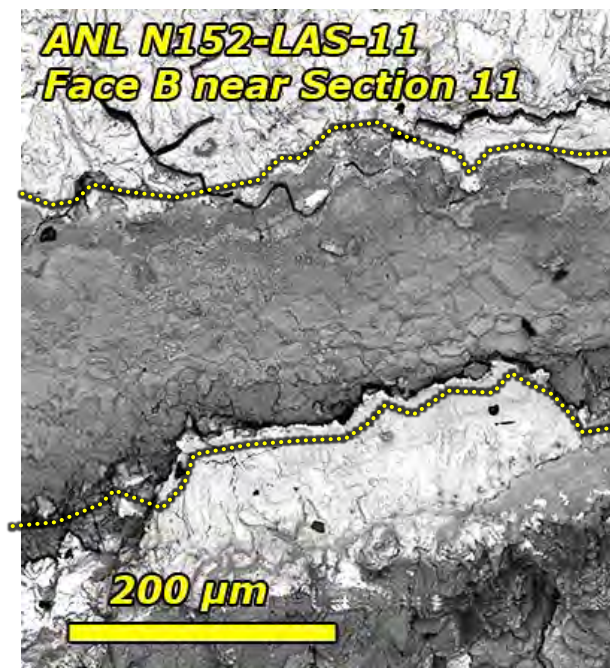
Figure 5-54 Higher Magnification SEM BSE Image of N152-LAS-11 Face A near Section 11 Showing the Cracking Morphology on or near the Fusion Line
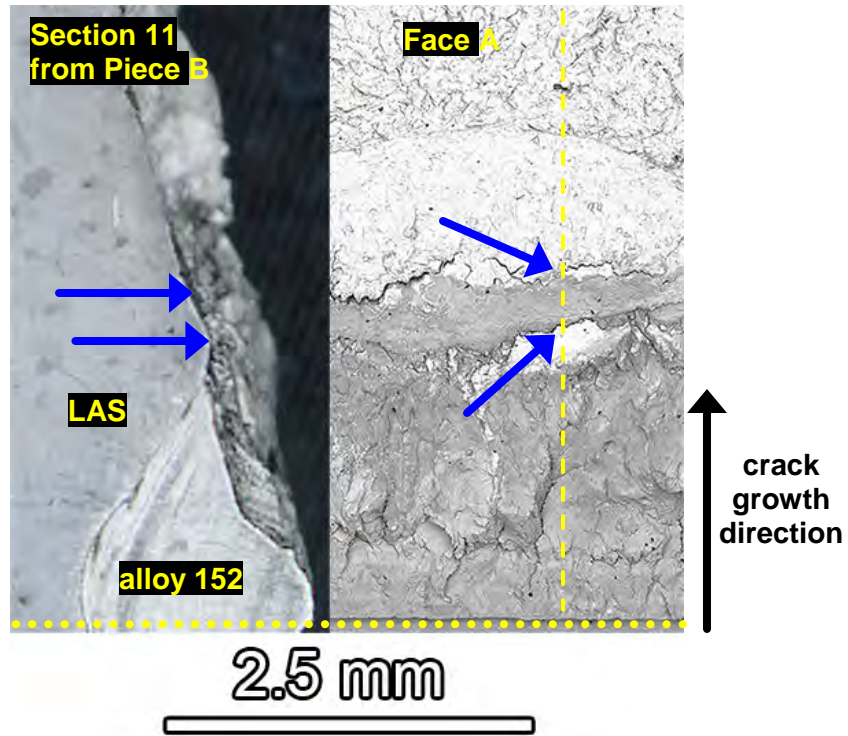
Figure 5-55 Comparison Between the SEM-BSE Crack Appearance on Face A and the Corresponding Cross Section View of the Crack on Section 11 (from Piece B). Cracking on or near the Fusion Line Is Between the Two Blue Arrows
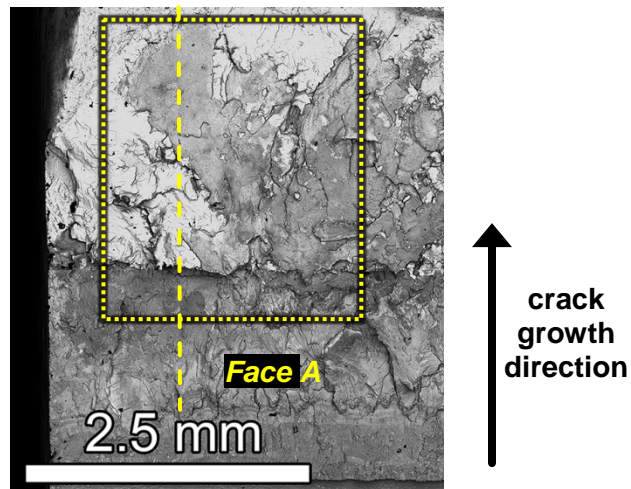
Figure 5-56 SEM-BSE Micrograph of Face A with Dotted Box Showing Where Higher Magnification Imaging Was Performed. The Dotted Line Is a Reminder of the Location of the Section 22 Cut
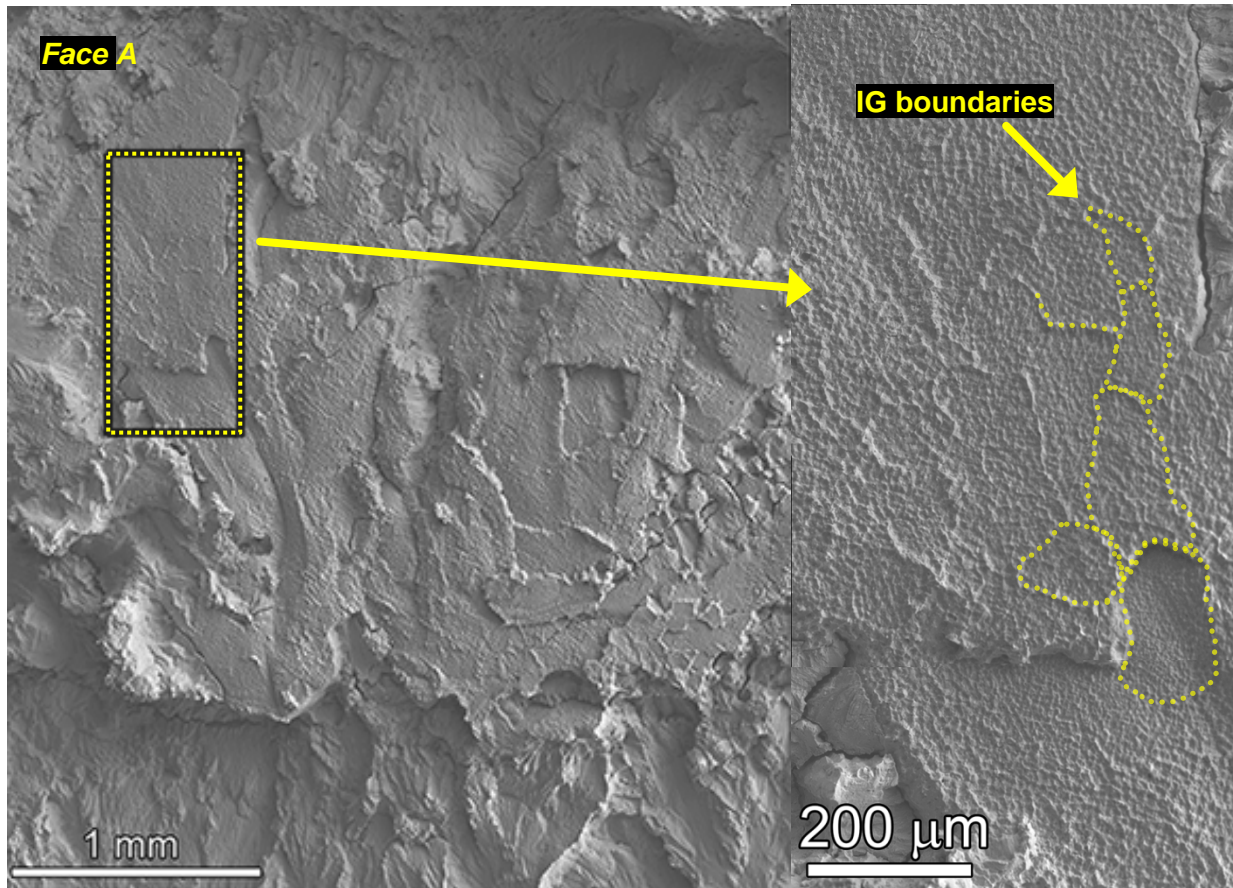
Figure 5-57   SEM-SE Micrographs of the Primary IGSCC Region on Face A Shown in Figure 5-56. Dashed Box Shows Where the Higher Magnification Image Was Taken in the Figure on the Right. Dashed Lines in the Figure on the Right Illustrate Examples of Grain Boundaries
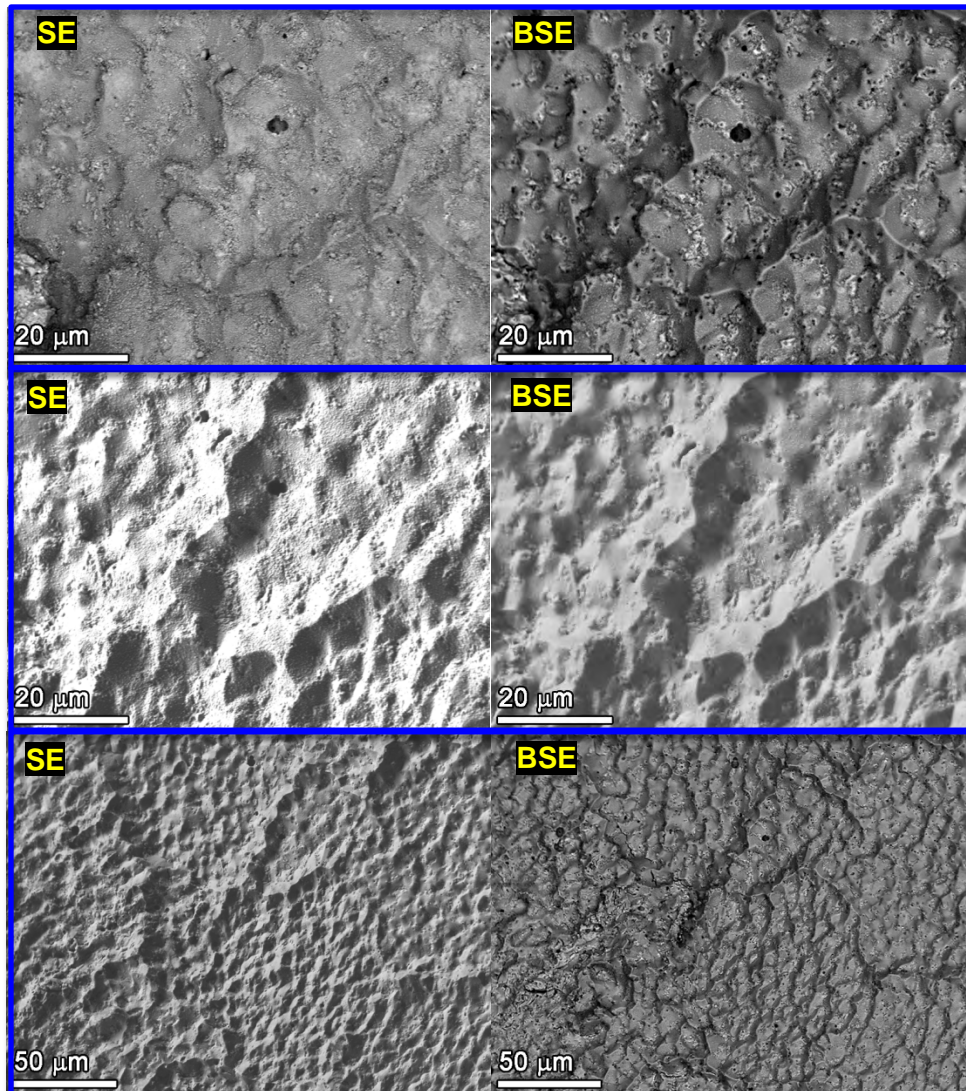
Figure 5-58 SEM (SE and BSE pairs) of Regions on the Face A Crack Growth Face Corresponding to Figures 5-56 and 5-57 Where IGSCC Cracking Occurred
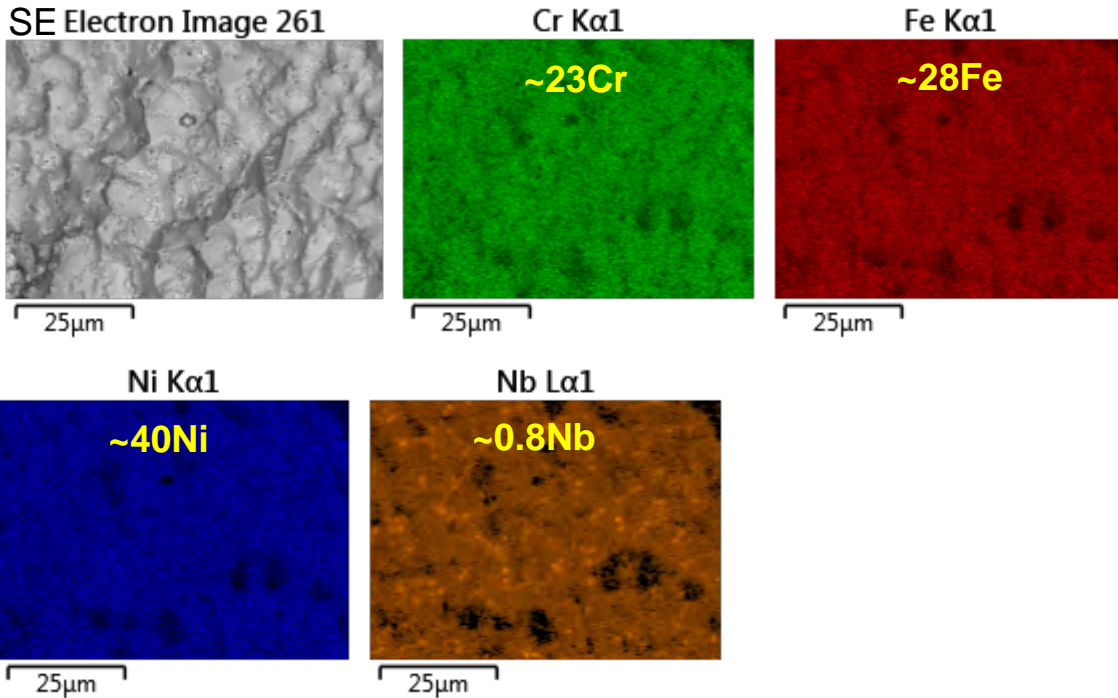
Figure 5-59   SEM-SE Image and Elemental Maps of an IGSCC Region on Face A Similar to That Shown in Figure 5-58

In order to better understand the cracking morphology and the grain structure in the alloy 152 dilution zone region, additional characterizations were performed starting with SEM EDS and EBSD scans on cross-section 22 as shown in Figures 5-60-5-62. An overview SEM SE image of the etched cross-section is presented in Figure 5-60. Cracking is from left to right with the notch position annotated in the image. The crack runs down towards the fusion line and after crossing into the second weld pass, it steps down and then continues across. The region of SCC growth that is documented in Figures 5-57 and 5-58 is denoted with the blue arrows. The etching (performed at ANL) preferentially attacked the lower Cr, making the compositional variations apparent in this secondary electron image.

After documenting the etched surface, the specimen was polished to a colloidal finish for SEM EDS and EBSD examination. SEM EDS mapping of Region 1 in Figure 5-61 shows a relatively uniform composition in the weld away from the fusion line. However, as shown in Figure 5-62, Region 2 with much more compositional variation followed the same contrast trends as in the SE image. The results of SEM EDS area scans are presented in Table 5-5. Areas S2, S4, and S6 all have ≤23 wt% Cr. These compositional streaks are spread throughout the weld pass all the way up to the crack growth surface. Complimentary SEM EBSD orientation imaging of Region 2 shows that with one exception, the composition streaks did not line up with grain boundaries. The grain boundary where this one exception occurred is indicated by the large yellow arrow in Figures 5-62 and 5-63. This grain boundary is very linear in the cross section (aligned with the crack-growth direction) just as with the grain boundary where the IGSCC cracking occurred. It is our belief that such aligned boundaries in the dilution zone are required for significant IGSCC to occur. These measurements also provided important insights into characterizations and specimen machining from the ANL alloy 152/LAS weld slice for PNNL CGR testing that is reported in the next section.
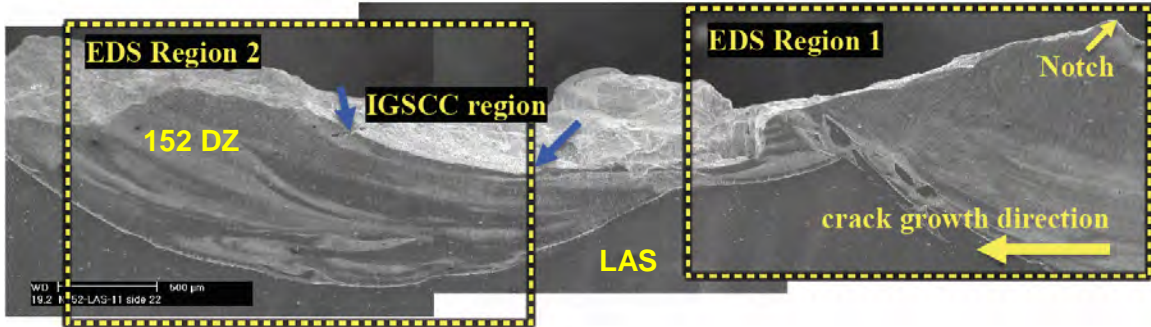
Figure 5-60   SEM-BSE of a Cross-Section Through Crack-Growth Surface for the Alloy 152/LAS Dilution Zone Specimen N152-LAS-11 Revealing Etched Microstructure of the Dilution Zone. Lighter Regions in the Alloy 152 Dilution Zone Indicate Fe-Rich, Cr-Depleted Areas
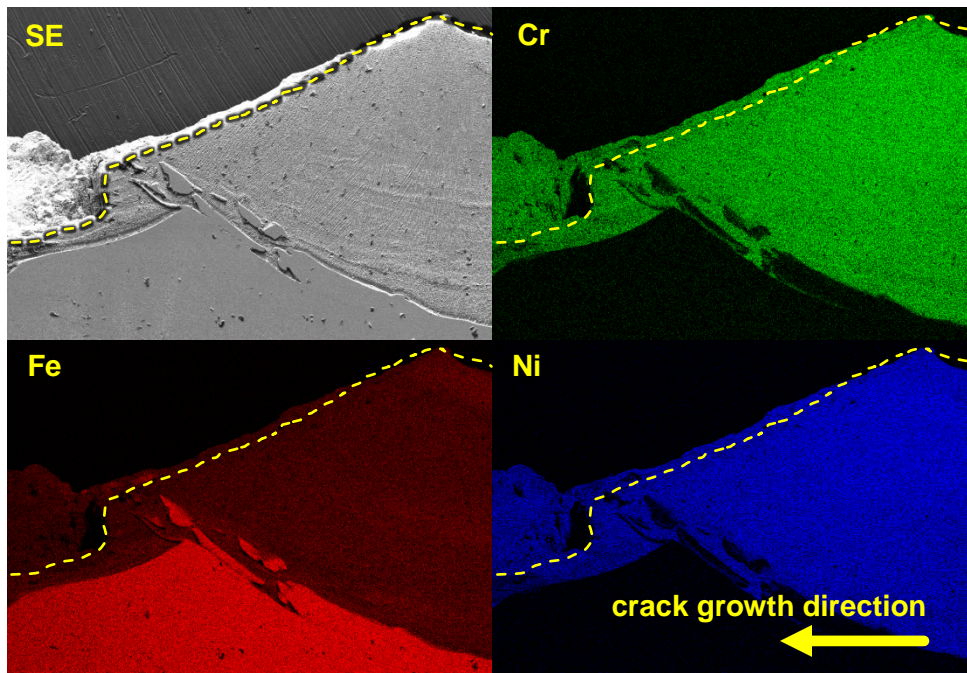
Figure 5-61   SEM-SE and Elemental Maps of EDS Region 1 in Figure 5-60. Dashed Lines Show the Extent of the Cross-Section. Elemental Indications Beyond the Dotted Lines Are Due to X-Ray Signals Detected from the Crack Growth Face Rather than the Cross Section
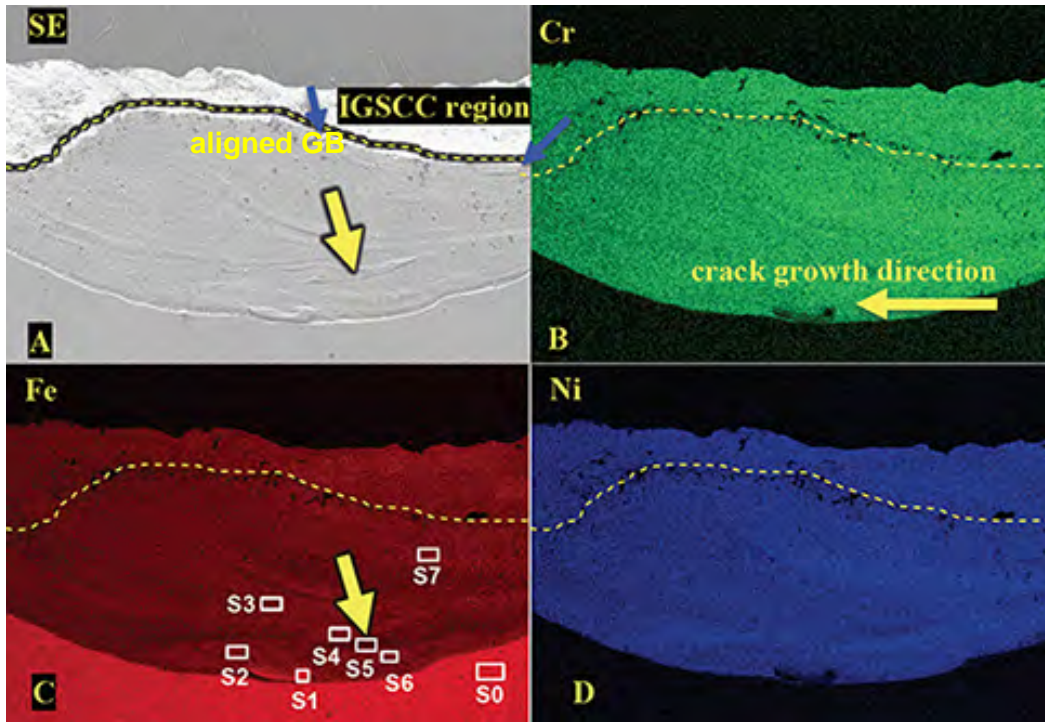
Figure 5-62   SEM EDS Composition Maps in the N152-LAS-11 Cross-Section in Figure 5-60

Table 5-5   SEM EDS Area Scan Composition (wt%) Measurements from Figure 5-62

Area	Cr	Mn	Fe	Ni
S0	0	0.6	98.7	0.2
S1	5.28	2.35	84.07	8.3
S2	21.53	2.72	32.3	41.01
S3	25.26	3.74	27.52	42.77
S4	22.78	4.38	34.17	38.67
S5	29.64	3.93	16.04	50.39
S6	21.9	3.04	35.42	39.64
S7	23.69	3.72	30.85	41.74
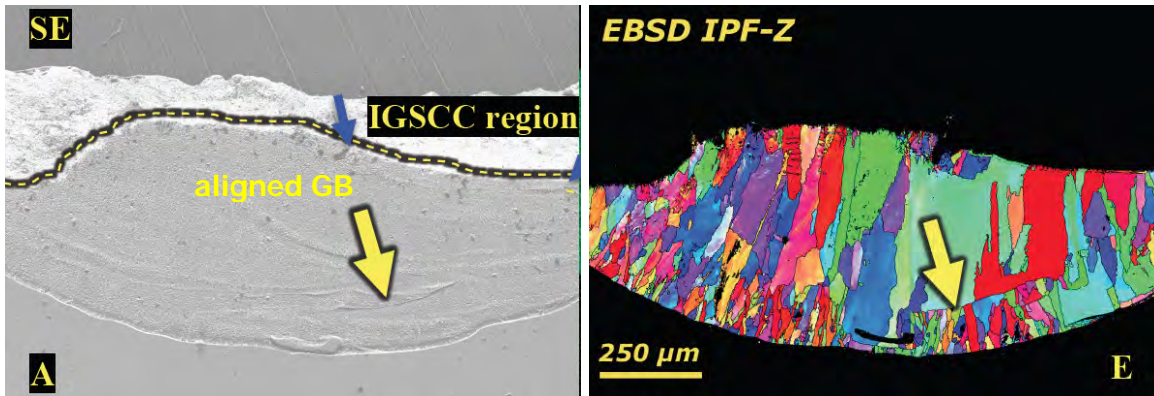
Figure 5-63   SEM-SE and SEM-EBSD IPF-Z Map Revealing Grain Structure in the Alloy 152 Dilution Zone and the Presence of Grain Boundaries Aligned with the Crack Growth Direction in the ANL N152-LAS-11 Specimen Cross-Section (see Figure 5-62)

5.3.3   ANL 152v2 DM Weld: Specimen CT117 - 152/LAS Interface

The two crack-growth tests on the alloy 152 - LAS dilution specimens (CT117 and CT119) turned out to be extremely complex and each ran for >10,000 hours. The CT117 specimen will be described first, since the dilution zone location was selected to match that for the N152-LAS-11 specimen from ANL described in the previous section. The ANL-tested specimen exhibited a high DCPD-measured CGR (~10^{-7} mm/s) at constant load during the test as documented in Figure 5-50 and extensive IG cracking on the crack-growth surface shown in Figures 5-54 and 5-58.

Crack-growth test results will be discussed in two parts separated by a shut down so that the side grooves could be examined and the crack extension estimated. An overview of the first part of the test is summarized in Figure 5-64 and Table 5-6 documenting three evaluations of constant K response and two evaluations during a cycle + 24 h hold loading. Cyclic loading at 0.1, 0.01 and 0.001 Hz (with R=0.5) was applied over the initial ~1000 hours creating a crack extension of   ~1.1 mm before transitioning to a 980s/20 s cycle with and without a 2.5 h hold to investigate whether the propagation response suggested SCC growth. Best SCC CGR results were measured during the first constant K evaluation at ~1345 hours as documented in Figure 5-65. Altering crack growth response was observed over this exposure with SCC CGRs of ~1×10^{-8} mm/s over the first 450 hours before slowing down to ~4×10^{-9} mm/s over the last 100 hours. Subsequent cycle + hold loading response appeared to be promising and produced CGRs of >1×10^{-8} mm/s (Figure 5-66) during a 24h hold, however propagation rates at constant K were quite low as shown in Figure 5-67. In this case, an immediate jump in crack length was observed when switching back to cycle + hold suggesting that ligaments or crack contacts were removed and the actual crack advance was slightly greater. However, the adjusted SCC CGR remained low at 3.3×10^{-9} mm/s.
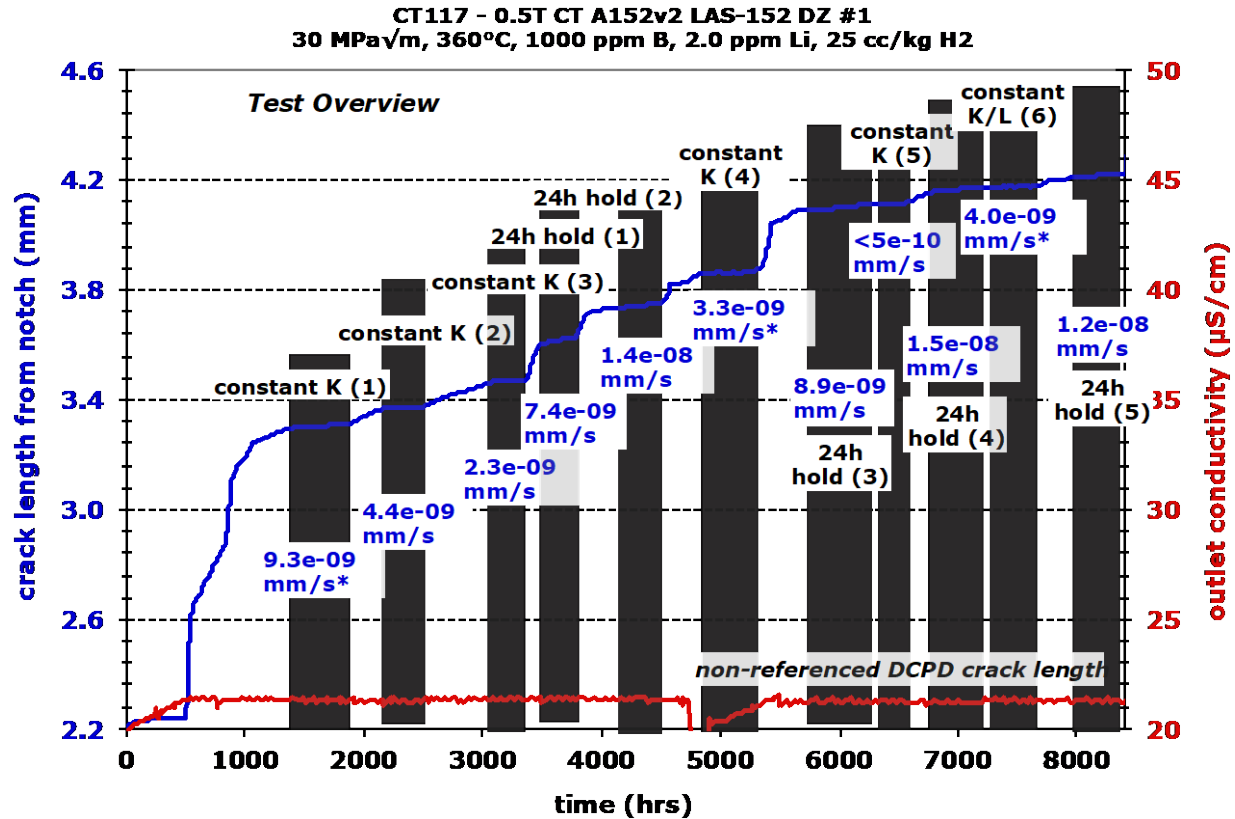
Figure 5-64 Overview Crack Growth Plot of the First Part for Test on the ANL Alloy 152 - LAS Dilution Zone Specimen (CT117)

Several more attempts were made to assess SCC behavior in steps 27-32 as documented in Table 5-6. Response during 980s/20s cycle + hold loading was promising with both the 2.5h (steps 28 and 31) and 24h hold (steps 29 and 32) CGRs similar to previous behavior, but propagation at constant K was limited. The inability to reproduce the higher SCC CGR at constant K in step 7 (Figure 5-65) during the following 5 constant K evaluations prompted a closer examination of cycle + hold response. Indications of ligament formation (steps in crack length during cycle + hold loading) became more pronounced as the test progressed leading to a need to better determine the optimum loading condition to break ligaments. The goal is to break the ligaments while not disturbing SCC engagement and not having the load cycle add significantly to the CGR. This has to be balanced by applying the load cycle frequently enough to keep ligaments from building up.

Table 5-6   Data Summary for the First Part of the Test on the ANL Alloy 152 - LAS Dilution Zone Specimen CT117

Test Phase	Start (h)	Time (h)	R	Freq. (Hz)	Hold (h)	Diss. H_2 (cc / kg)	Temp (°C)	Kmax (MPa√m)	CGR (mm/s)	Crack Exten. (mm)
0	0	505	---	const K	---	25	360	30	---	---
1	505	5	0.5	0.1	0	25	360	30	7.5E-06	0.180
2	510	57	0.5	0.01	0	25	360	30	1.3E-06	0.236
3	567	267	0.5	980s/20s	0	25	360	30	2.1E-07	0.220
4	834	74	0.5	0.01	0	25	360	30	1.2E-06	0.255
5	908	141	0.5	980s/20s	0	25	360	30	2.4E-07	0.101
6	1049	286	0.5	980s/20s	2.5	25	360	30	4.6E-08	0.056
7	1335	555	---	const K	---	25	360	30	9.3E-09	0.019
8	1890	212	0.5	980s/20s	2.5	25	360	30	6.5E-08	0.050
9	2102	392	---	const K	---	25	360	30	4.4E-09	0.005
10	2494	601	0.5	980s/20s	2.5	25	360	30	3.5E-08	0.097
11	3095	261	---	const K	---	25	360	30	2.3E-09	0.003
12	3356	101	0.5	980s/20s	0	25	360	30	3.0E-07	0.120
13	3457	110	0.5	980s/20s	2.5	25	360	30	4.1E-08	0.017
14	3567	191	0.5	980s/20s	24	25	360	30	7.4E-09	0.005
15	3758	79	0.5	980s/20s	0	25	360	30	4.3E-07	0.070
16	3837	89	0.5	980s/20s	2.5	25	360	30	7.2E-08	0.036
17	3926	319	0.5	980s/20s	24	25	360	30	1.4E-08	0.017
18	4245	280	0.5	980s/20s	12	25	360	30	1.6E-08	0.018
19	4525	50	0.5	980s/20s	0	25	360	30	3.4E-07	0.062
20	4575	163	0.5	980s/20s	12	25	360	30	1.4E-08	0.019
21	4738	93	0.5	980s/20s	2.5	25	360	30	6.9E-08	0.032
22	4831	416	---	const K	---	25	360	30	3.3E-09	0.005
23	5247	95	0.5	980s/20s	2.5	25	360	30	4.7E-08	0.014
24	5342	90	0.5	980s/20s	0	25	360	30	6.1E-07	0.159
25	5432	215	0.5	980s/20s	2.5	25	360	30	6.6E-08	0.048
26	5647	768	0.5	980s/20s	24	25	360	30	8.9E-09	0.027
27	6415	150	---	const K	---	25	360	30	<1E-09	0.000
28	6565	191	0.5	980s/20s	2.5	25	360	30	6.7E-08	0.040
29	6756	416	0.5	980s/20s	24	25	360	30	1.5E-08	0.019
30	7172	521	---	const K/L	---	25	360	30	4.0E-09	0.007
31	7693	76	0.5	980s/20s	2.5	25	360	30	7.9E-08	0.022
32	7769	639	0.5	980s/20s	24	25	360	30	1.1E-08	0.026
	8408	*Stop*	*for*	*Exam*						
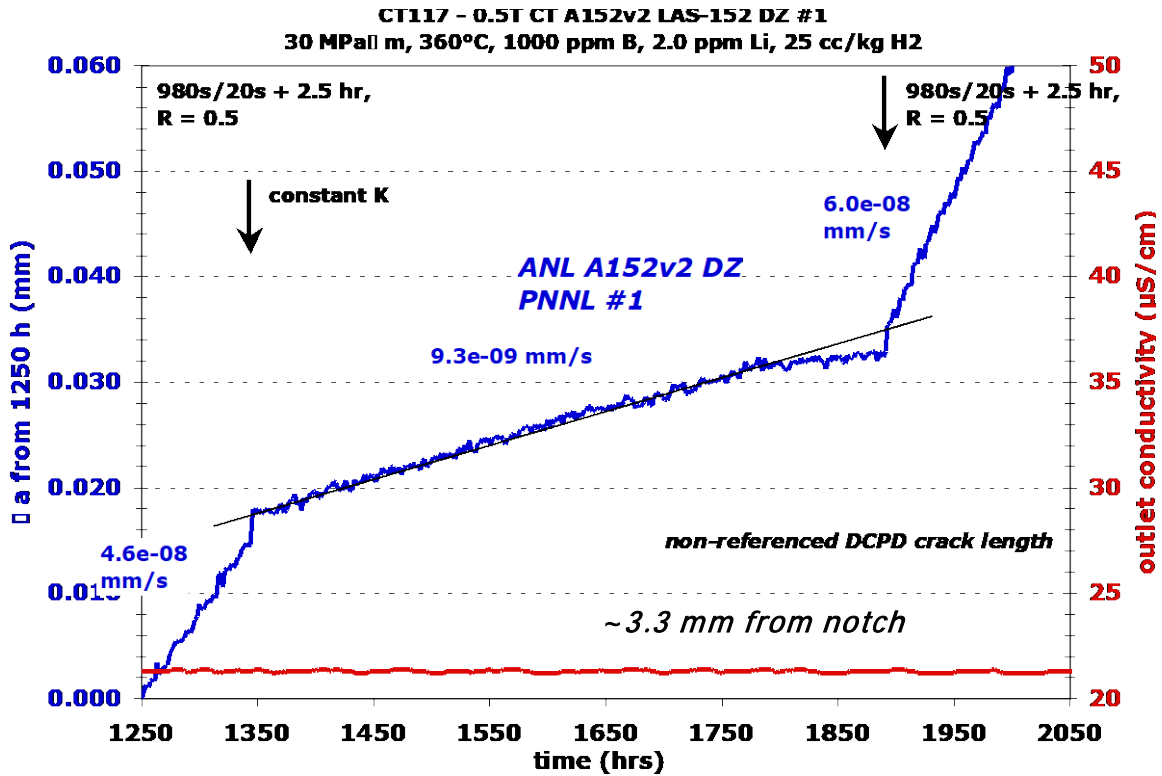
Figure 5-65   First Evaluation of SCC Response at Constant K for Specimen CT117
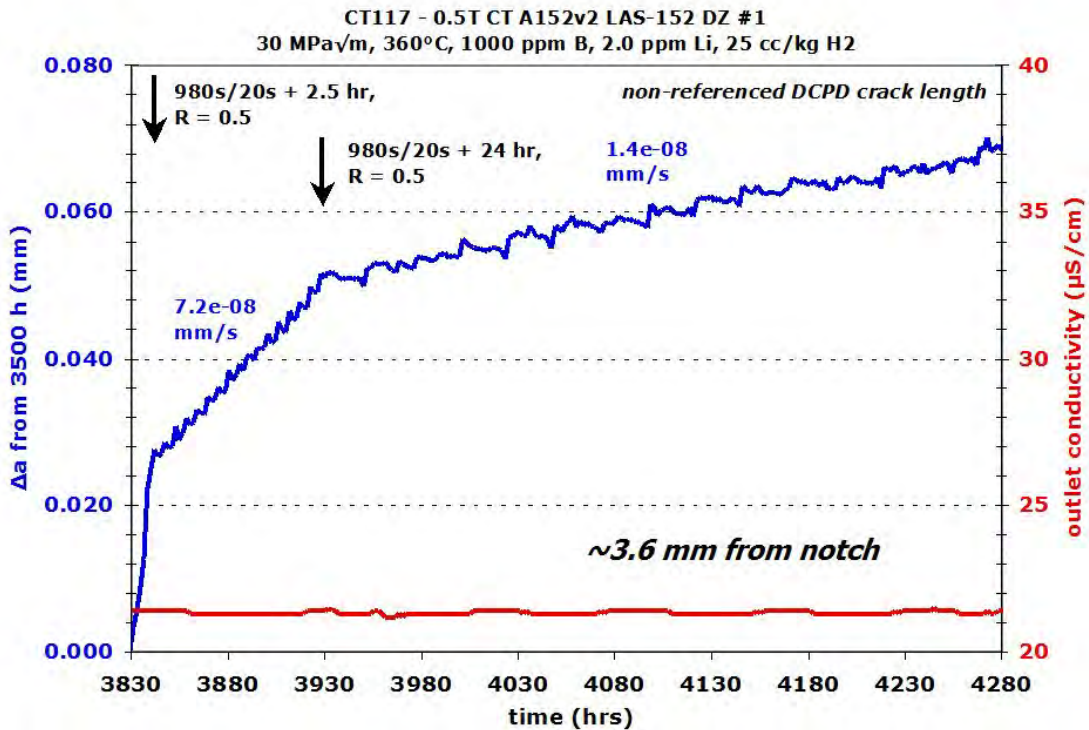
Figure 5-66   Crack-Growth Response at Cycle + 24h Hold Loading for Specimen CT117
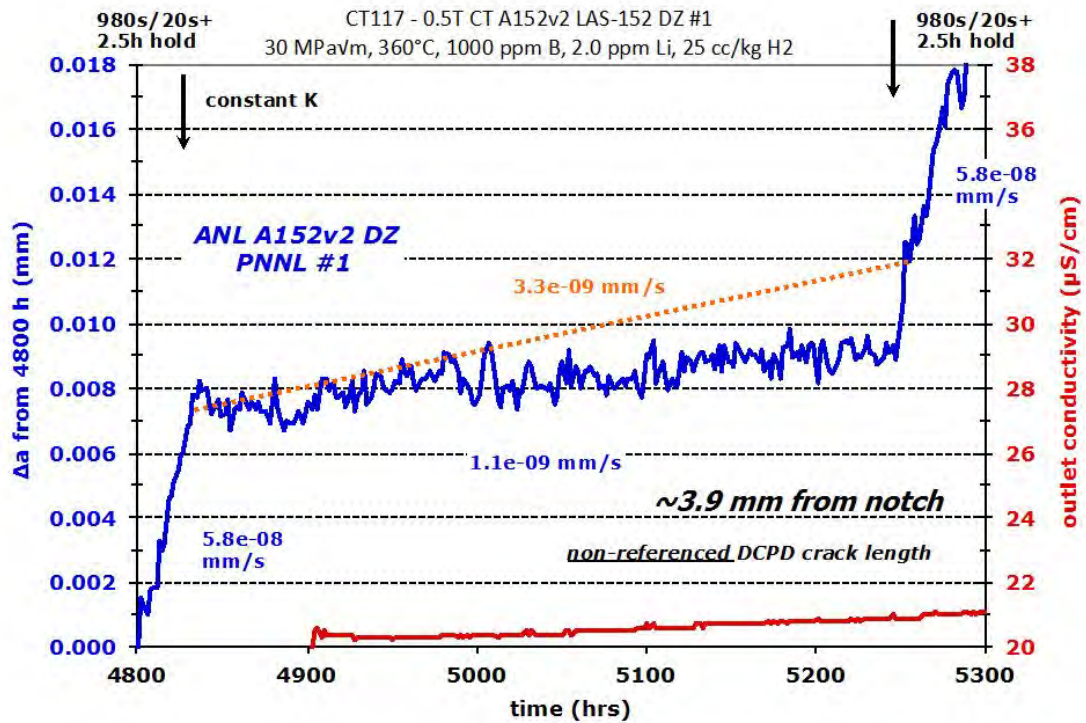
Figure 5-67   Fourth Evaluation of SCC Response at Constant K for Specimen CT117
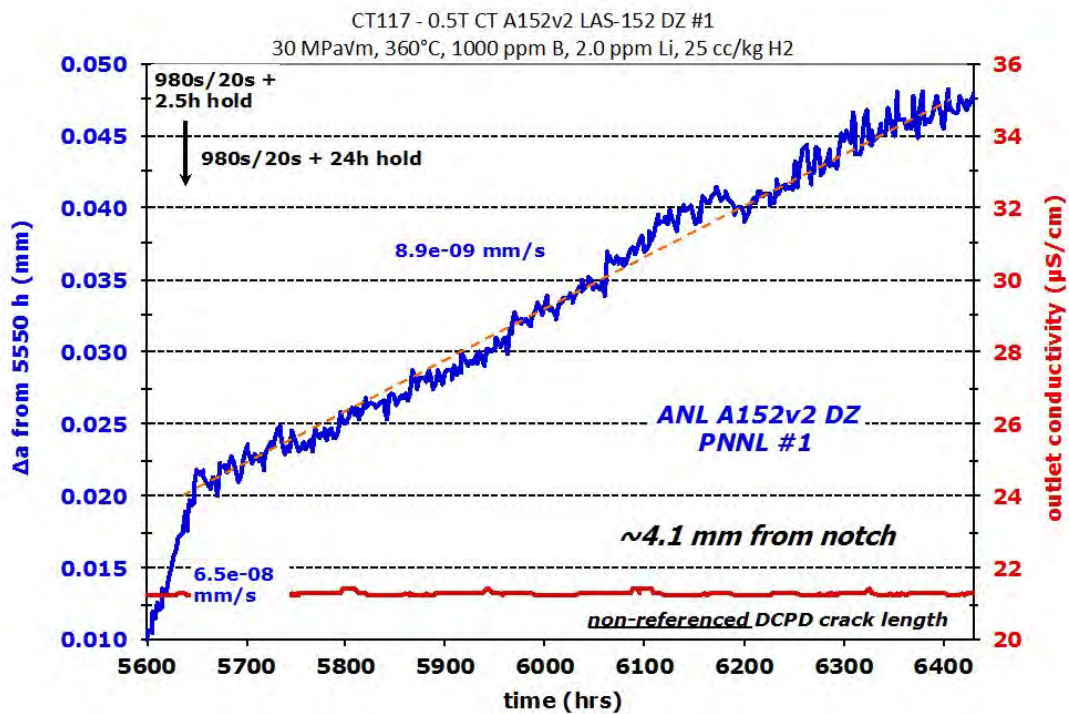
Figure 5-68   Crack-Growth Response at Cycle + 24h Hold Loading for Specimen CT117

An approach used at ANL and elsewhere to estimate SCC response from cycle + hold loading data has been to consider the cycle + hold response as a sum of the cyclic response and the hold time response. The mathematical representation is:

$$\dot{a}_T t_T = \dot{a}_C t_C + \dot{a}_H t_H \tag{5.1}$$

Where $\dot{a}_T$, $\dot{a}_C$ and $\dot{a}_H$ are the CGRs for cycle + hold loading, continuous cyclic loading and for the hold time during cycle + hold loading respectively. t_T, t_C, and t_H are the time period for one cycle + hold load cycle, a continuous load cycle and the hold time, respectively. $\dot{a}_H$ is considered to be an estimate of the constant K SCC CGR response. $\dot{a}_T$, $\dot{a}_C$, t_T, t_C, and t_H are all readily determined from the available data. This method is very sensitive to the CGR measured during pure cyclic loading because this value is typically over an order of magnitude larger than the constant K SCC CGR response of a material. A variation in the measured pure cyclic loading CGR in the first decimal place can cause up to 10X variations in the estimated SCC CGR response ($\dot{a}_H$) and often times can lead to negative estimated SCC CGRs or unrealistically high SCC CGRs. The most reasonable estimates are obtained when the pure cyclic loading value is measured directly before the cycle + hold loading step. Another issue that affects this technique is that the SCC response at the start of a hold is typically elevated due to changes in the crack tip during the load cycle, e.g., oxide film rupture caused by the load cycle. Because of this, short hold times typically produce inflated constant K SCC CGR estimates. Thus, in order for this method to produce reasonable values, a balance needs to be established between having enough load cycles to sufficiently break ligaments while not unduly sampling non-representative propagation behavior during the early portion of the hold time. Related to this is the selection of the load cycle. The load cycle should be aggressive enough to break ligaments while not being so aggressive that it drives IG cracking back to TG cracking. For susceptible materials such as alloy 182, a rapid unload-reload cycle appears to accomplish this. Our judgment for SCC-resistant, high Cr welds is that a more gentle cycle is needed to prevent driving the crack TG and a 980s/20s load cycle with R = 0.5 has been selected.

With these limitations and goals in mind, the estimated constant K CGRs from the cycle + hold loadings are presented in Table 5-7. Five different 980s/20s continuous cycling measurements have been made over many months of testing with each value a little bit different. For the table, five columns have been created to show the estimated constant K rates using the two most recent 980s/20s CGRs for the estimated SCC CGR calculation. In most cases, calculated SCC rates are similar for the two different baseline 980s/20s values. Estimated SCC rates are listed for the most appropriate values based on the behavior of the specimen at that portion of the test. Reviewing the constant K observations reveals that the highest SCC growth was seen early in the test during step 7 at 9.3x10⁻⁹ mm/s. The next two constant K evaluations decreased to 4.4 and 2.3x10⁻⁹ mm/s, somewhat consistent with the decreasing SCC rates calculated from cycle + 2.5h hold CGRs in steps 8 and 10. As the test continued, cycle + hold and constant K values decreased further, but cycle+hold response in steps 16, 17, 18, 20 and 21 suggested some SCC growth may be occurring during the hold time. The final steps from 22 to 32 did not indicate any significant growth at constant K and any estimated SCC growth during cycle + hold was unclear. These results support the observation of lower SCC response over the last section of the test and the decision was made to stop the test and examine the specimen side grooves at 8408 hours.

Table 5-7   Estimated Constant K SCC CGR for CT117 from Cycle+Hold Loading Data Using a 980s/20s Load Cycle

Test Step	Hold Time (h)	CGR for Test Step (mm/s)	Est. SCC CGR Using Step 5 (mm/s)	Est. SCC CGR Using Step 12 (mm/s)	Est. SCC CGR Using Step 15 (mm/s)	Est. SCC CGR Using Step 19 (mm/s)	Est. SCC CGR Using Step 24 (mm/s)
5	*0*	*2.4×10^{-7}*					
6	2.5	4.6×10^{-8}	3.3×10^{-8}				
7	Const K	9.3×10^{-9}					
8	2.5	6.5×10^{-8}	5.2×10^{-8}	4.1×10^{-8}			
9	Const K	4.4×10^{-9}					
10	2.5	3.8×10^{-8}	1.7×10^{-8}	1.2×10^{-8}			
11	Const K	2.3×10^{-9}					
12	*0*	*3.0×10^{-7}*					
13	2.5	4.1×10^{-8}		1.2×10^{-8}	-2.9×10^{-9}		
14	24	7.4×10^{-9}		4.0×10^{-9}	2.5×10^{-9}		
15	*0*	*4.3×10^{-7}*					
16	2.5	7.2×10^{-8}		4.7×10^{-8}	3.2×10^{-8}		
17	24	1.4×10^{-8}		9.7×10^{-9}	8.1×10^{-9}		
18	12	1.6×10^{-8}		9.1×10^{-9}	6.0×10^{-9}		
19	*0*	*3.4×10^{-7}*					
20	12	1.4×10^{-8}			4.5×10^{-9}	6.6×10^{-9}	
21	2.5	6.9×10^{-8}			2.9×10^{-8}	3.8×10^{-8}	
22	Const K	3.3×10^{-9}					
23	2.5	4.7×10^{-8}				1.4×10^{-8}	-1.6×10^{-8}
24	*0*	*6.1×10^{-7}*					
25	2.5	4.4×10^{-8}					-1.9×10^{-8}
26	24	1.3×10^{-8}					6.1×10^{-9}
27	Const K	$<1 \times 10^{-9}$					
28	2.5	6.6×10^{-8}					5.6×10^{-9}
29	24	8.9×10^{-9}					3.1×10^{-9}
30	Const K/L	4.0×10^{-9}					
31	2.5	7.9×10^{-8}					2.0×10^{-8}
32	24	1.1×10^{-8}					4.1×10^{-9}

Optical and SEM examinations were conducted to determine both the crack length on the side surfaces and the morphology of cracking. SEM-BSE images in Figures 5-69 and 5-70 highlight the cracking on side A of the CT117 specimen. The lower magnification montage in Figure 5-69 shows a reasonable straight crack from the notch extending to and beyond the interface between weld passes #1 and #2. The extent of crack propagation into pass #2 is best seen in Figure 5-70 where there is also evidence of deformation and fine secondary cracks at the surface near the crack tip. In order to indicate the dilution zone chemistry along the crack path, EDS elemental composition maps were taken at several magnifications starting with the overall leading crack region shown in Figure 5-71. The Fe and Cr maps illustrate more significant dilution in pass #2 than pass #1 with very little changes near the transition from pass #1 to pass #2 as best seen in Figure 5-72. Figure 5-73 highlights a local region of extremely high Fe and very low Cr, Ni and Mn that corresponds to a complex crack morphology immediately behind the leading crack tip. It appears that the crack is blocked at the high Fe pocket of material and complex secondary cracking is produced before the primary crack emerges beyond the Fe-rich phase. The composition in this region is characterized at higher resolution by the Fe map in Figure 5-74 with local concentrations for the major elements identified in Table 5-8.
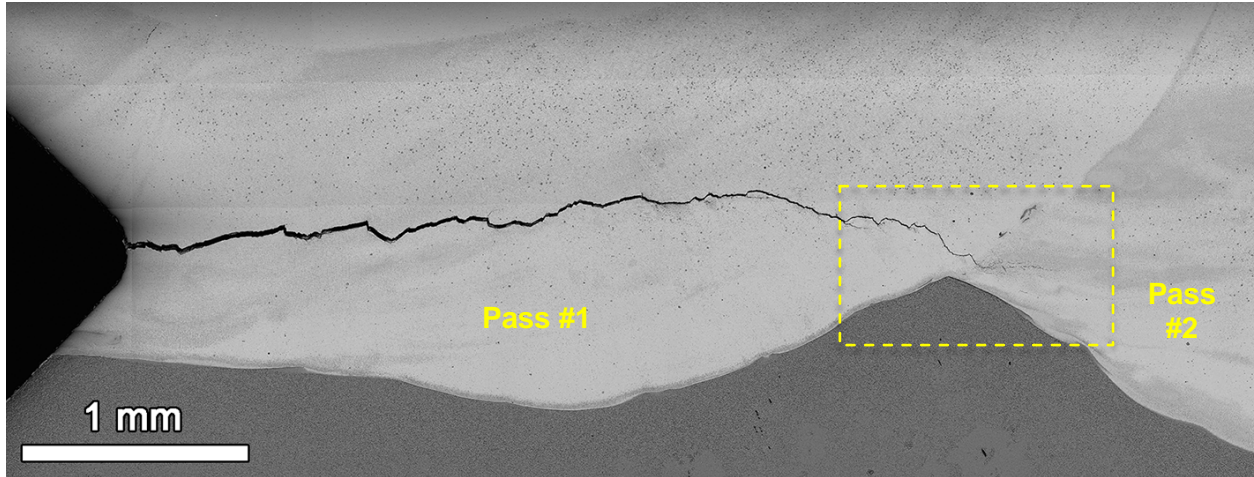
Figure 5-69   SEM-BSE Low Magnification Montage of the Crack in Side Groove A at mid Test
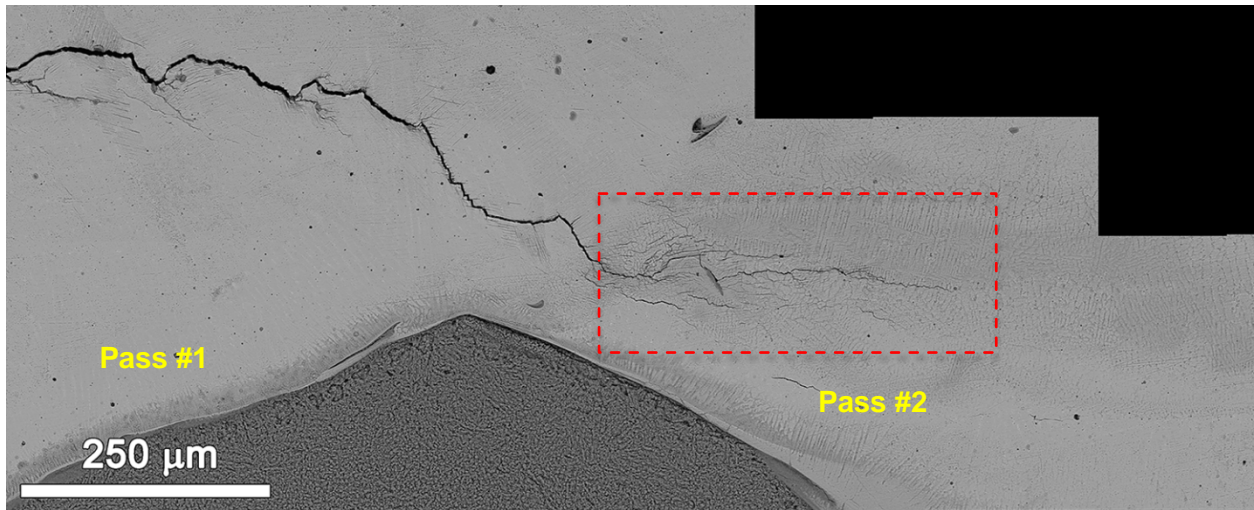
Figure 5-70   SEM-BSE Higher Magnification Image of Leading Crack Region in Side Groove A (area from dashed yellow box in Figure 5-69). Considerable Secondary Cracking Can Be Seen in Pass #2 as Highlighted by Dashed Red Box
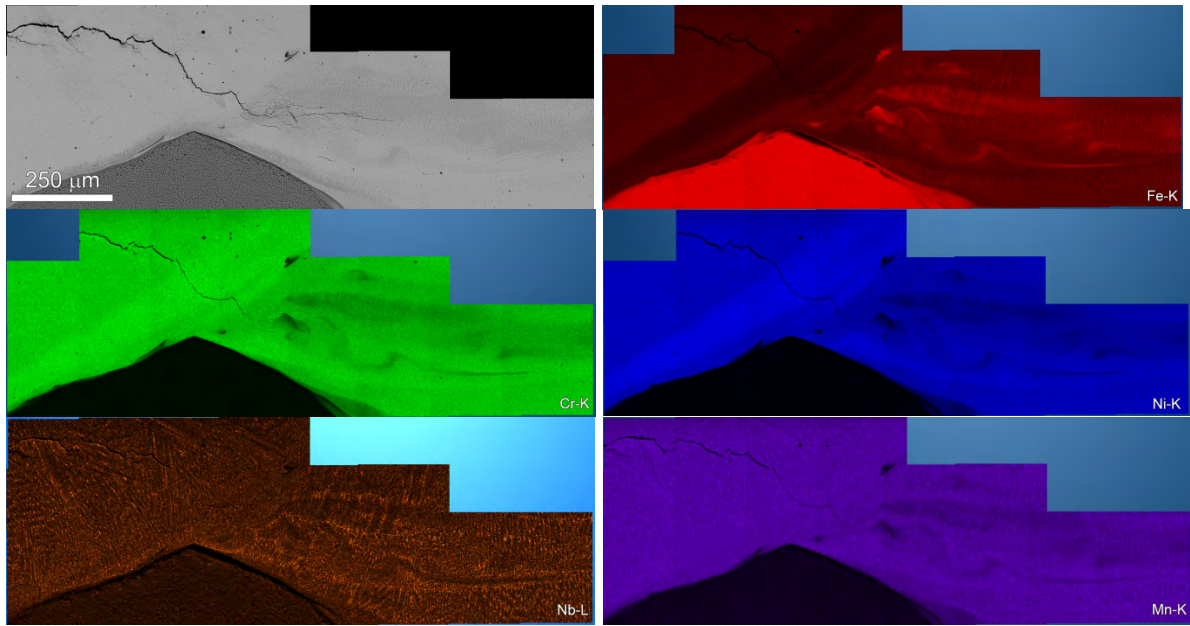
Figure 5-71   SEM-BSE Montage from Figure 5-70 and Corresponding EDS Elemental Maps of the Leading Crack Region in Side Groove A
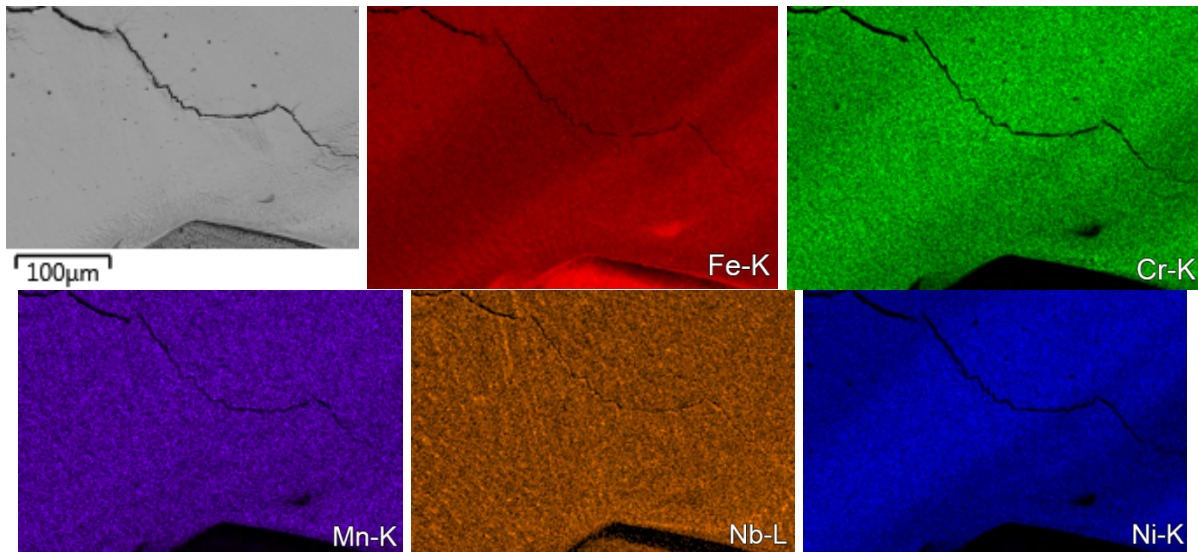
Figure 5-72   SEM-BSE Montage and Corresponding EDS Elemental Maps near the Weld Pass Boundary Behind the Leading Crack Region in Side Groove A
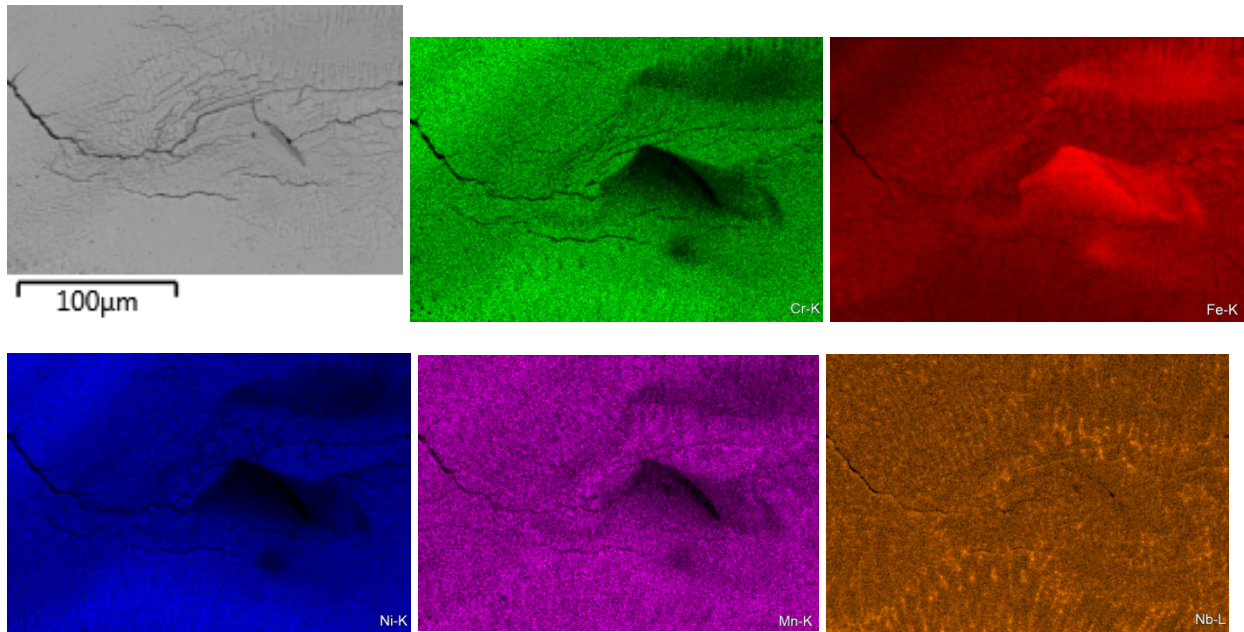
Figure 5-73   SEM-BSE Micrograph and Corresponding EDS Elemental Maps at a Region of Secondary Cracking Just Behind the Leading Crack Tip on Side A
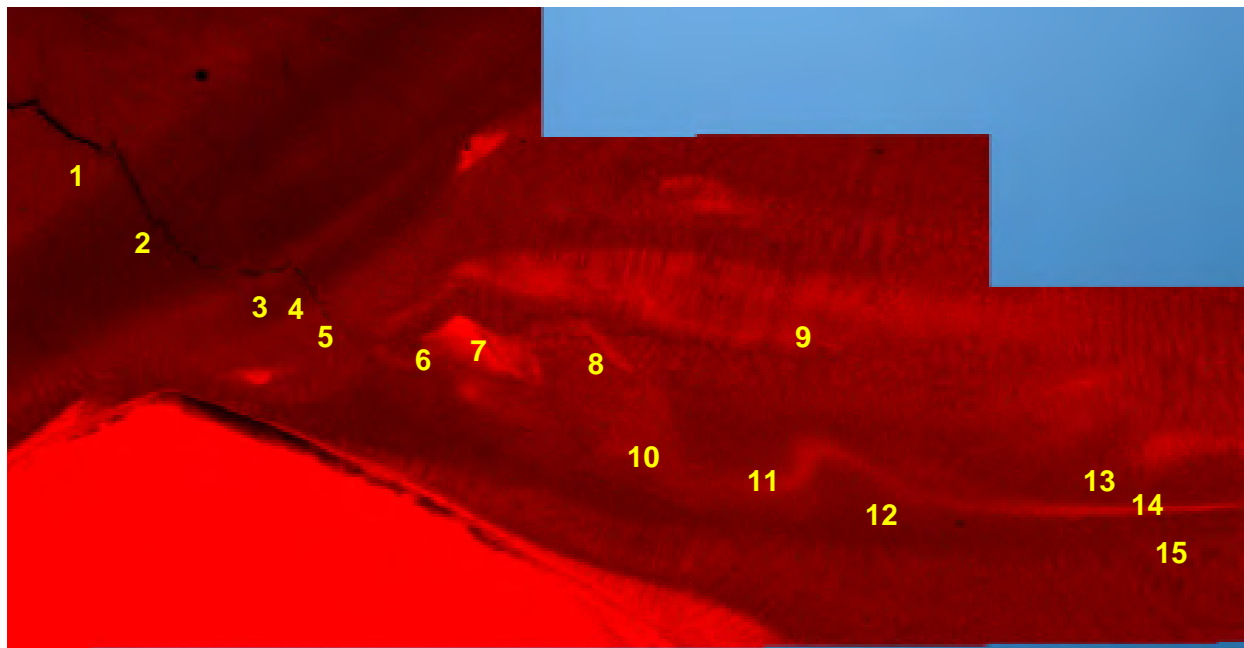
Figure 5-74   SEM-EDS Fe-K Map of the Leading Crack and Crack-Tip Region from the Side Groove on Side A

Table 5-8   Composition of Regions Near Crack Front (wt%) in Figure 5-74

Region	Fe	Cr	Ni
1	25.4	28.9	45.7
2	16.5	31.0	52.5
3	27.0	27.3	45.7
4	22.8	28.9	48.3
5	31.3	26.2	42.6
6	30.4	26.5	43.1
7	66.3	12.5	21.2
8	37.6	23.0	39.4
9	36.2	24.4	39.5
10	25.7	27.7	46.6
11	34.1	24.3	41.6
12	29.6	26.4	44.0
13	29.5	26.6	43.9
14	43.3	21.0	35.7
15	27.7	27.1	45.2

The SEM-EDS measurements in the side groove shown in Table 5-8 should be considered only estimates of the actual concentration due to surface oxide complications leading to higher Cr and Fe with lower Ni. More quantitative measurements of compositions were obtained on polished cross-section samples after the test was completed. However, the current results illustrate the strong Fe enrichment in pass #2 and confirm that the region of extensive secondary cracking surrounds a phase of primarily Fe.

Cracking observed in side groove B (Figure 5-75) was discovered to be quite different. Instead of extending well into pass #2, the crack ends ~0.7 mm before the transition into pass #2 near an interesting microstructural feature as better shown in Figure 5-76. The image contrast for this feature suggests that it may be a LAS "island" that was drawn into the weld metal. This conclusion is supported by the EDS maps in Figure 5-77 where an extensive plume of Fe enrichment is present corresponding to low Ni and Cr concentrations. A very similar microstructure and compositional variation can be seen at the pass #1 – pass #2 boundary. The Fe composition map is highlighted in Figure 5-78 along with locations where local elemental concentrations were determined. Table 5-9 lists these measurements and establishes the extremely high Fe concentration in the region associated with the microstructural feature in front of the crack tip. It appears likely that crack growth on this side of the specimen was restricted during the test due to the presence of the large plume of Fe-rich metal. This is somewhat consistent with complex secondary cracking around the smaller Fe-rich area observed in pass #2 on side A.
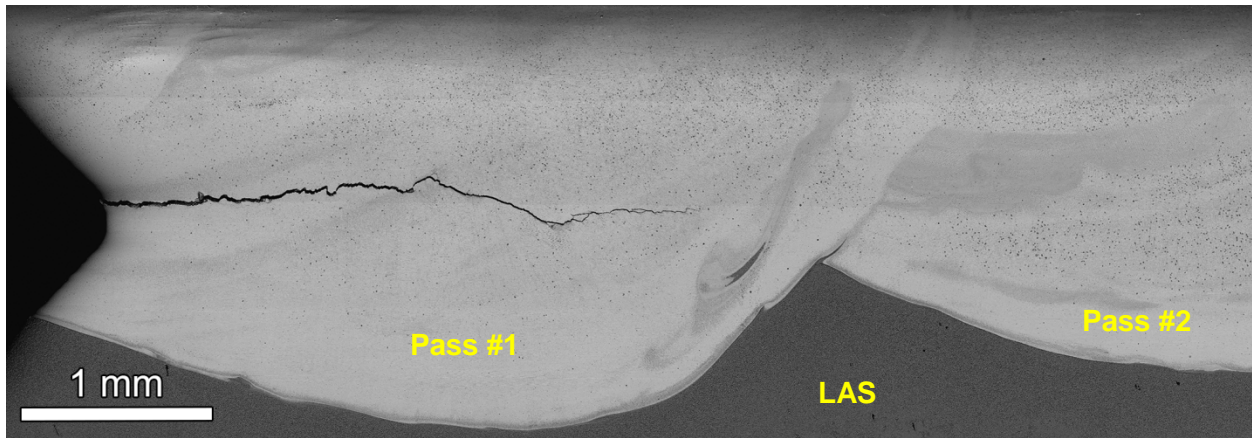
Figure 5-75   SEM-BSE Low Magnification Montage of the CT117 Side Groove on Side B
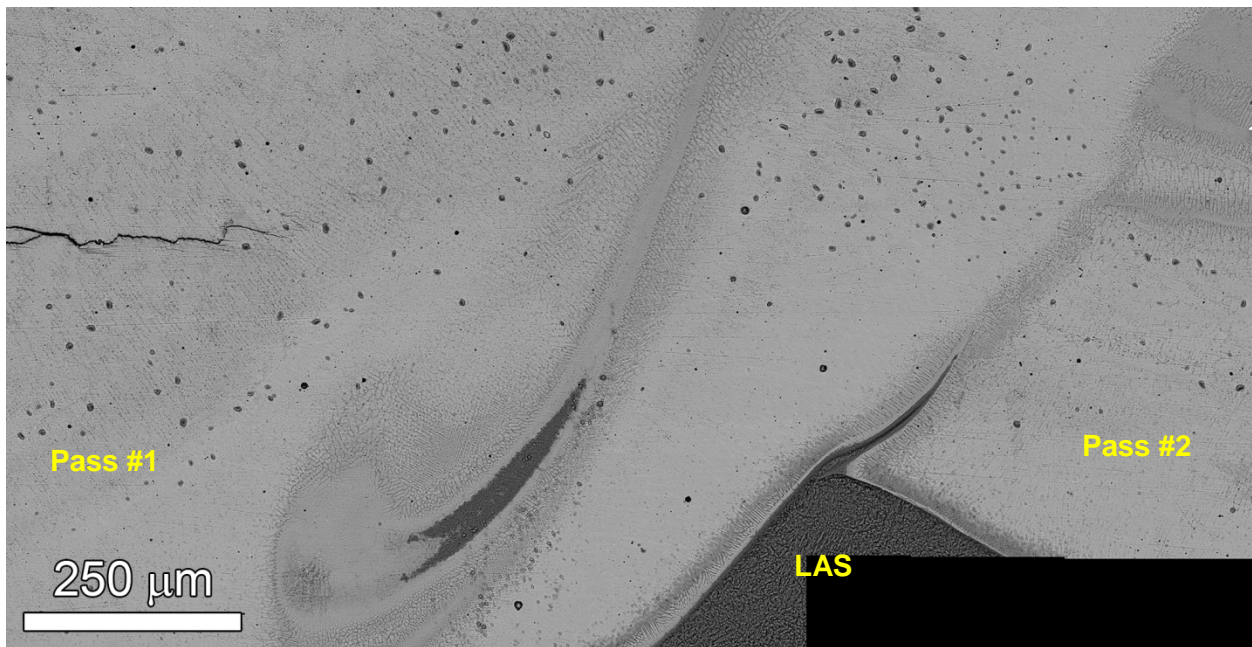
Figure 5-76   SEM-BSE High Magnification Montage Showing the Microstructural Feature Immediately Ahead of Crack Tip in Side Groove B

Two important aspects were discovered by the side grove examinations of the ANL dilution zone specimen CT117. First, the crack length was considerable longer on side A at ~5 mm (well into pass #2) from the notch that on side B at <3 mm from the notch. As a result, the expectation is that we have a highly irregular crack front across the CT117 specimen thickness. The second indication is that regions of extremely high Fe dilution (possible trapped regions of LAS) in the weld may restrict crack growth. As a result, there may be complex microstructure and microchemistry characteristics influencing corrosion fatigue and SCC growth in the weld metal adjacent to the LAS interface. The decision was made to continue crack-growth testing on the CT117 specimen and eventually move the crack front completely into weld pass #2.
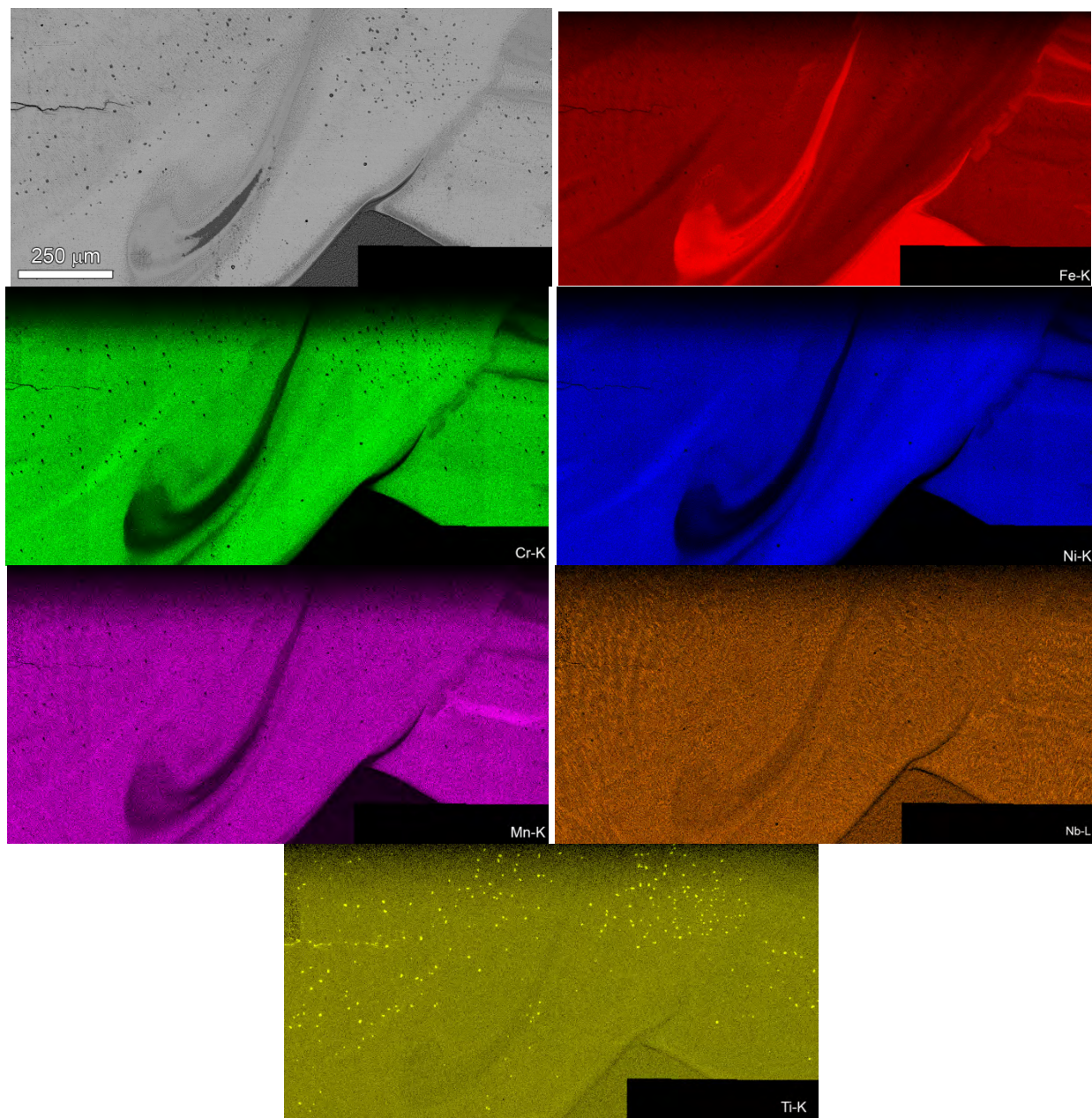
Figure 5-77   SEM-BSE Montage and Corresponding EDS Elemental Maps of the CT117 Leading Crack Region on Side B
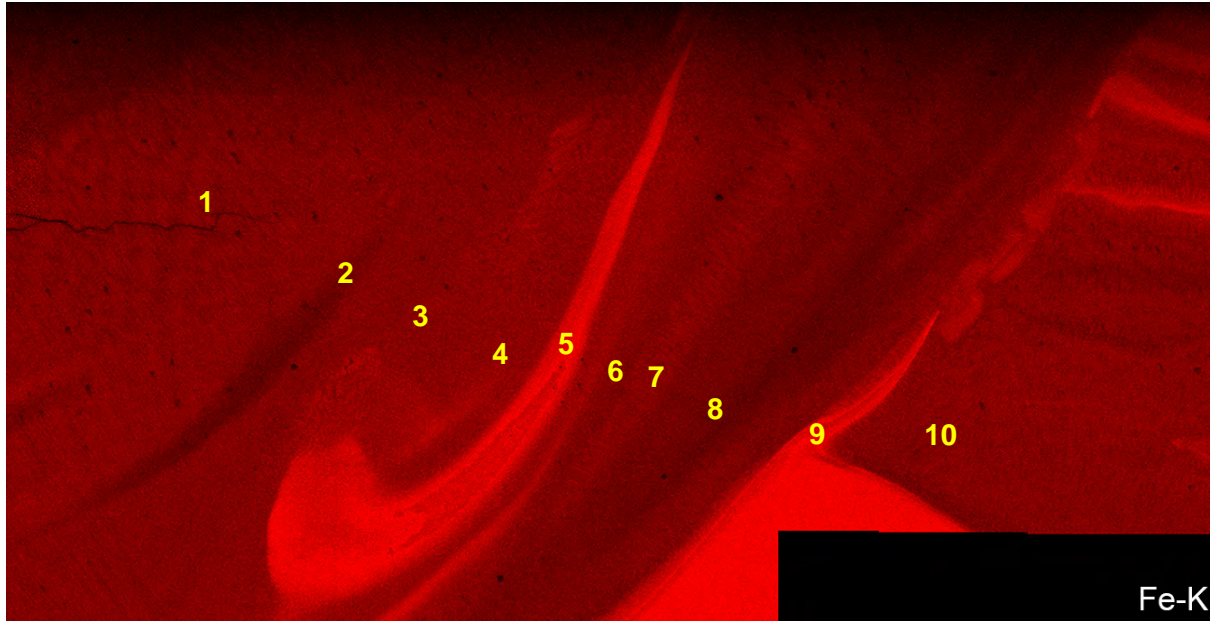
Figure 5-78   SEM-EDS Fe-K Map of the Leading Crack Region for CT117 Side B (Figure 5-77)

Table 5-9   Composition (wt%) near the Leading Crack Region on Side B (Figure 5-78)

Region	Fe	Cr	Ni
1	27.4	28.1	44.5
2	22.3	29.0	48.7
3	30.4	26.5	43.1
4	32.3	25.6	42.2
5	66.7	12.8	20.5
6	29.6	26.5	43.9
7	29.4	26.7	44.0
8	20.4	29.3	50.3
9	69.9	11.2	18.9
10	29.2	27.0	43.8

An overview of the second part of the test is summarized in Figure 5-79 and Table 5-10 documenting four evaluations of constant K response loading. Cyclic loading at a 980 s/20 s cycle with and without a 2.5 h or 24 h hold was again employed to indicate whether the propagation response suggested SCC growth. Steps 33-50 were applied to once again investigate crack-growth response at 30 MPa√m and confirm behavior observed in part 1 testing.
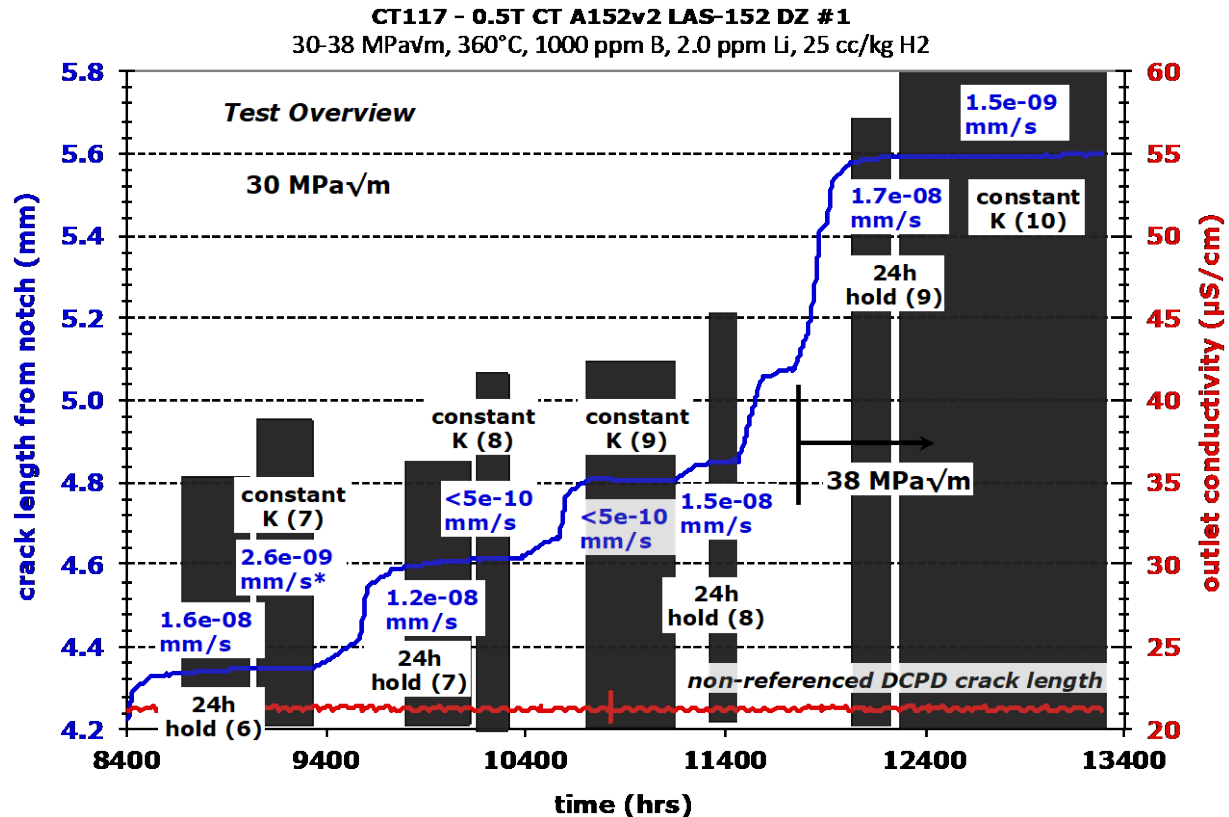
Figure 5-79   Overview Crack Growth Plot of Second Part for Test on the ANL Alloy 152 - LAS Dilution Zone Specimen CT117

Three transitioning sequences to constant K were performed that included evaluations of response during cyclic + 24 h hold loading. Evidence for ligament and/or contact formation in the crack was observed as illustrated in Figures 5-80, 5-81 and 5-82. The first constant K examination (Figure 5-80) after the restart exhibited a small increase in crack length early followed by no growth after ~100 hours. After switching back to cyclic + 2.5 h hold loading, an immediate jump in crack length was seen suggesting additional growth at constant K with an adjusted CGR of 2.6×10^{-9} mm/s. Contact formation was also indicated during a subsequent cyclic + 24h hold loading where DCPD crack length drops during the hold time after each 980s/20s cycle as shown in Figure 5-81. The final example highlighted is a constant K exposure in Figure 5-82 where the crack length decreases throughout. As a result of these issues, the decision was made to advance the crack front forward and increase the applied K level from 30 to 38 MPa√m. This was done in steps 50 and 51 with an increase in the 980s/20s cyclic CGR from 3.6×10^{-7} to 1.1×10^{-6} mm/s. Different response was observed during the cycle + 24h hold loading as documented in Figure 5-83. Although small jumps can be seen at each cycle, the DCPD crack length did not decrease during the 24h hold period. This might suggest some SCC growth during the hold in comparison to the previous response. A final SCC evaluation was then performed as presented in Figure 5-84 revealing a low CGR of 1.5×10^{-9} mm/s over ~1100 hours at constant K.

Table 5-10   Data Summary for the Second Part of the Test on the ANL Alloy 152 - LAS Dilution Zone Specimen CT117

Test Step	Start (h)	Time (h)	R	Freq. (Hz)	Hold (h)	Diss. H_2 (cc / kg)	Temp (°C)	Kmax (MPa√m)	CGR (mm/s)	Crack Exten. (mm)
33	8408	15	0.5	980s/20s	0	25	360	30	5.8E-07	0.058
34	8423	104	0.5	980s/20s	2.5	25	360	30	6.2E-08	0.043
35	8527	456	0.5	980s/20s	24	25	360	30	1.6E-08	0.021
36	8983	366	---	const K	---	25	360	30	2.6E-09	0.003
37	9349	212	0.5	980s/20s	2.5	25	360	30	5.8E-08	0.065
38	9561	40	0.5	980s/20s	0	25	360	30	5.6E-07	0.116
39	9601	125	0.5	980s/20s	2.5	25	360	30	9.4E-08	0.059
40	9726	545	0.5	980s/20s	24	25	360	30	1.2E-08	0.031
41	10271	106	---	const K	---	25	360	30	<5E-10	0.000
42	10377	182	0.5	980s/20s	2.5	25	360	30	7.4E-08	0.051
43	10559	41	0.5	980s/20s	0	25	360	30	6.7E-07	0.083
44	10600	128	0.5	980s/20s	2.5	25	360	30	9.0E-08	0.058
45	10728	433	---	const K	---	25	360	30	<5E-10	0.000
46	11161	96	0.5	980s/20s	2.5	25	360	30	9.2E-08	0.033
47	11257	203	0.5	980s/20s	24	25	360	30	1.5E-08	0.011
48	11460	108	0.5	980s/20s	0	25	360	30	4.9E-07	0.183
49	11568	169	0.5	980s/20s	2.5	25	360	30	9.7E-08	0.037
50	11737	72	0.5	980s/20s	0	25	360	30	3.6E-07	0.087
51	11809	66	0.5	980s/20s	0	25	360	30->38	1.1E-06	0.241
52	11875	28	0.5	980s/20s	2.5	25	360	38	1.7E-07	0.027
53	11903	27	0.5	980s/20s	0	25	360	38	1.1E-06	0.092
54	11930	94	0.5	980s/20s	2.5	25	360	38	1.5E-07	0.061
55	12024	169	0.5	980s/20s	24	25	360	38	1.7E-08	0.010
56	12193	1103	---	const K	---	25	360	38	1.5E-09	0.007
Total	13296									3.385

For comparison purposes, the SCC CGRs were again estimated from the cycle + hold data in Table 5-10 as was done for the part 1 data in Table 5-7. Several higher estimated SCC rates were calculated for the cycle + 2.5 h hold data in steps 32, 39, 42, 44, 46 and 56. In addition, the cycle + 24h data also suggested some SCC growth in steps 35, 40 and 45. Unfortunately, this possible SCC behavior was not confirmed by constant K evaluations in steps 36, 41, 45 and 56. The overall conclusion remained that in-situ DCPD did not revealing any significant crack growth without a periodic unload.
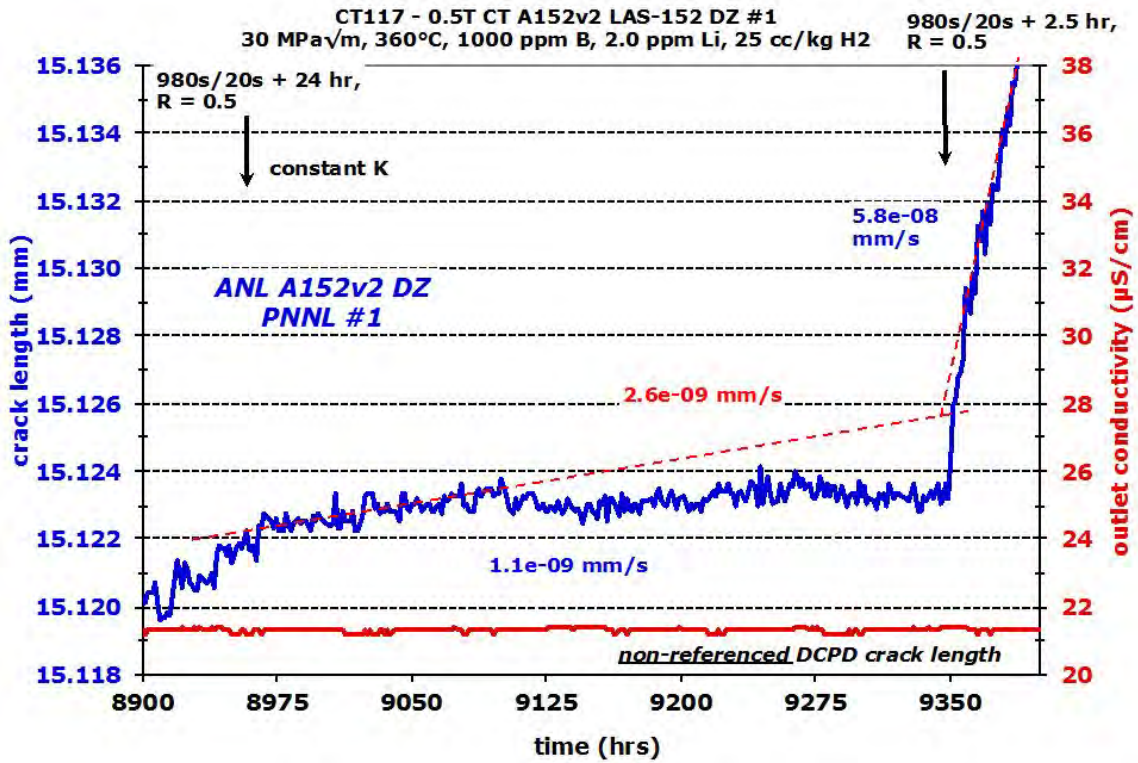
Figure 5-80   Evaluation of SCC Response After Specimen CT117 Restart and Transitioning
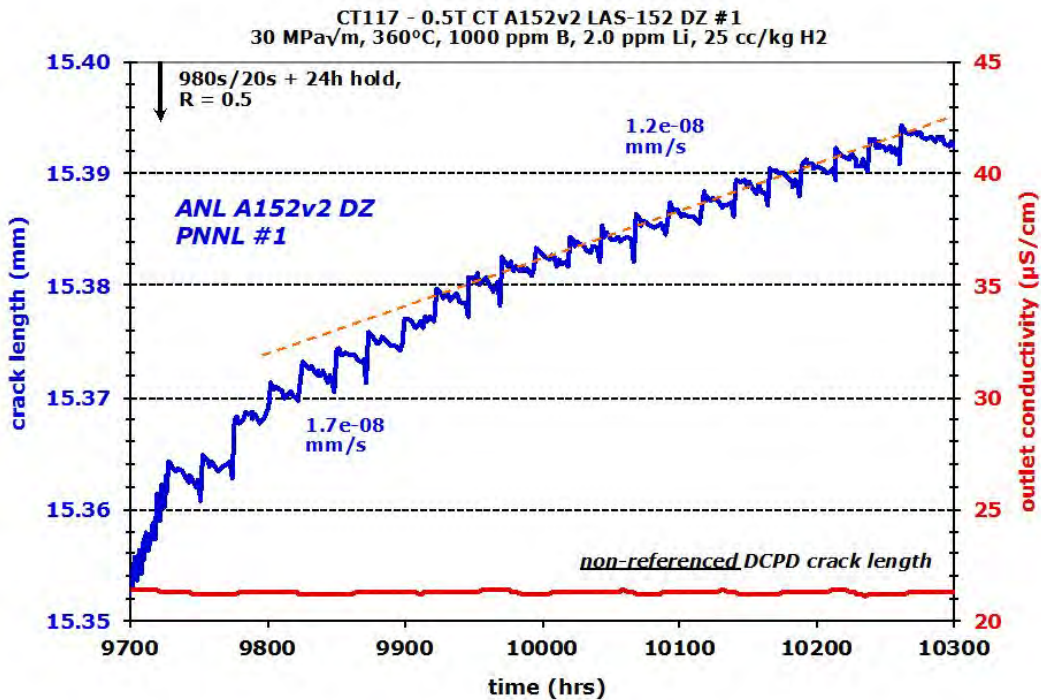
Figure 5-81   Crack-Growth Response at Cycle + 24 H Hold Loading Showing Distinct Jumps During Cycle and Decrease in Crack Length During Hold Time
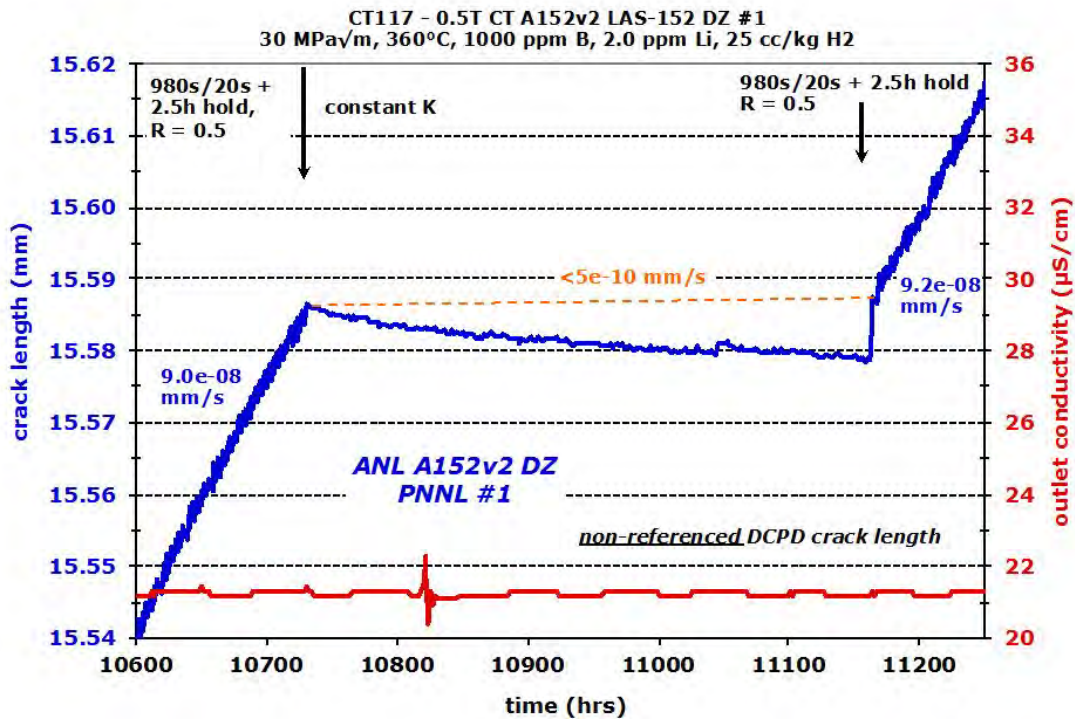
Figure 5-82   Evaluation of SCC Response for Specimen CT117 Showing No Growth at Constant K
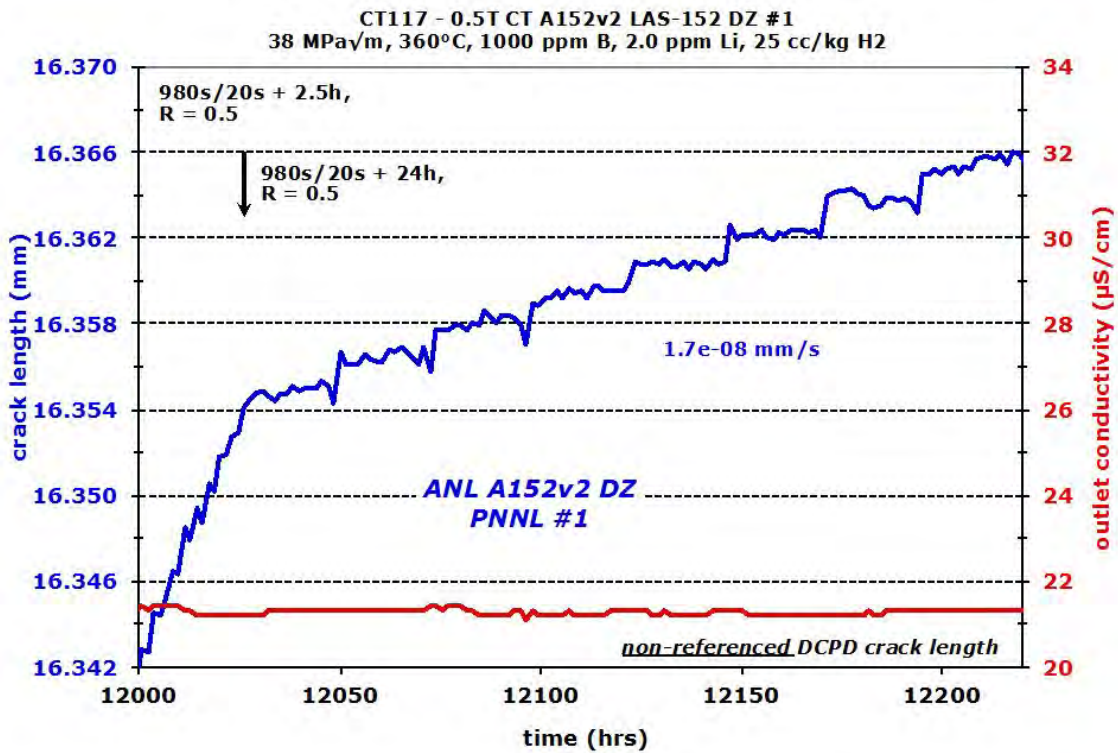
Figure 5-83   Crack-Growth Response at Cycle + 24 H Hold Loading at Higher K Level
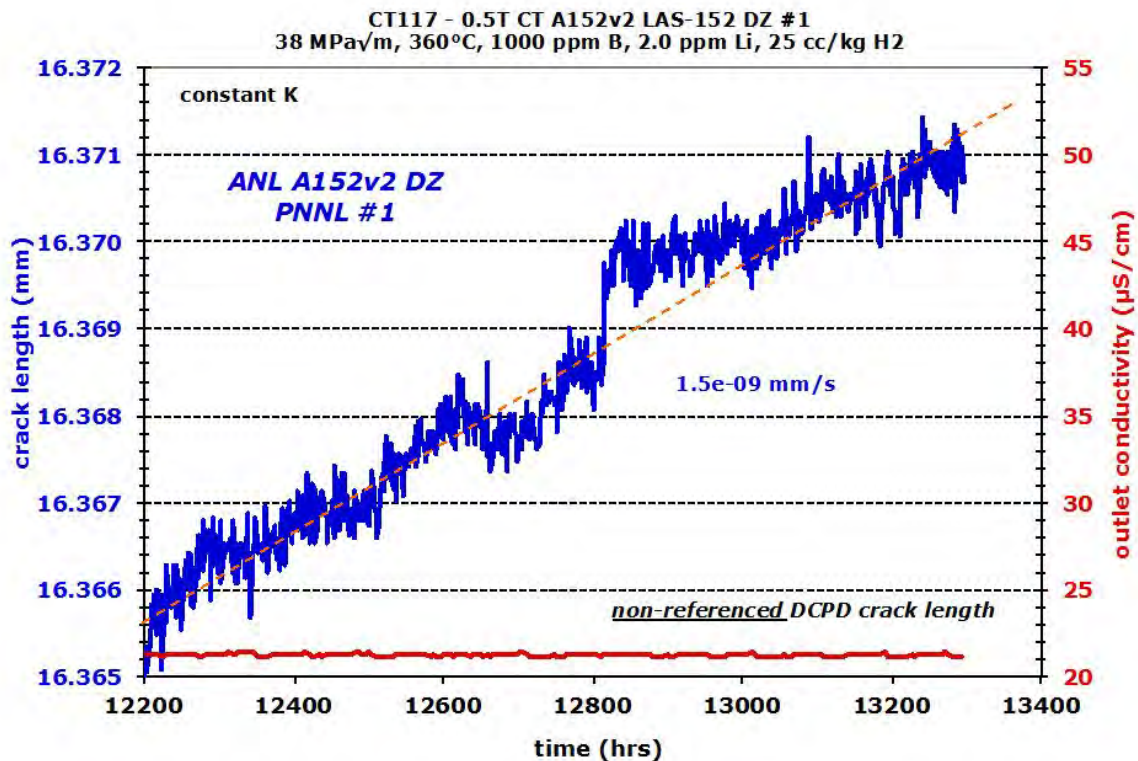
Figure 5-84   Tenth and Final Evaluation of SCC Response at Higher K for Specimen CT117

The decision was made to end the test after this last constant K result showed no indication of enhanced SCC growth. A remaining question for this alloy 152 weld is whether any significant localized SCC propagation occurs at constant K. Since in-situ DCPD does not reveal an answer, more detailed post-test characterizations were required. Ending this test after 13,296 hours made it one of the longest SCC crack-growth tests we have run at PNNL. Consistent with our normal approach to characterize the cracking morphology for our SCC crack-growth tests, the CT117 specimen was sectioned 1/3-2/3 and the 1/3 section was cross-sectioned for detailed examinations while the 2/3 section was fatigued open to document the cracking morphology. Before that was done, the side grooves were documented as shown in Figures 5-85 and 5-86. The biggest difference from the mid-test examination in Figures 5-69 and 5-75 can be seen in Figure 5-86 where cracking has clearly propagated into weld pass #2. A critical next step was to integrate the side groove images with the crack-growth surfaces documented in Figure 5-87. This integration is shown in Figure 5-88 exhibiting the side groove images with the cross-section at ¼ thickness and the remaining ¾ specimen crack growth surface. One aspect that is the most prominent in each image is the transition from weld pass #1 to pass #2 where cracking occurs along the alloy 152 – LAS fusion line.

Table 5-11   Estimated Constant K SCC CGR from Cycle + Hold Loading Data Using a 980s/20s Load Cycle for the Second Part of the Test on CT117

Test Step	Hold Time (h)	CGR for Test Step (mm/s)	Est. Constant K CGR Using Step 33 or 38 (mm/s)	Est. Constant K CGR Using Step 43 (mm/s)	Est. Constant K CGR Using Step 48 (mm/s)	Est. Constant K CGR Using Step 53 (mm/s)
	Restart		$K = 30$ MPa√m			
33	*0*	*$9.7x10^{-7}$*				
34	2.5	$1.1x10^{-7}$	$4.6x10^{-8}$			
35	24	$1.3x10^{-8}$	$6.2x10^{-9}$			
36	Const K	$2.6x10^{-9}$				
37	2.5	$5.8x10^{-8}$	$2.2\text{-}4.2x10^{-9}$			
38	*0*	*$5.6x10^{-7}$*				
39	2.5	$6.0x10^{-8}$	$4.4x10^{-9}$			
40	24	$1.2x10^{-8}$	$6.7x10^{-9}$			
41	Const K	$<5x10^{-10}$				
42	2.5	$7.4x10^{-8}$	$2.0x10^{-8}$	$1.4x10^{-8}$		
43	*0*	*$6.7x10^{-7}$*				
44	2.5	$9.1x10^{-8}$		$2.7x10^{-8}$		
45	Const K	$<5x10^{-10}$				
46	2.5	$9.1x10^{-8}$		$2.7x10^{-8}$	$4.6x10^{-8}$	
47	24	$1.5x10^{-8}$		$7.4x10^{-9}$	$9.4x10^{-9}$	
48	*0*	*$4.7x10^{-7}$*				
49	2.5	$5.0x10^{-8}$			$3.3x10^{-9}$	
50	*0*	*$3.6x10^{-7}$*				
			$K = 38$ MPa√m			
53	*0*	*$1.1x10^{-6}$*				
56	2.5	$1.4x10^{-7}$				$3.3x10^{-8}$
55	24	$1.6x10^{-8}$				$3.5x10^{-9}$
56	Const K	$1.5x10^{-9}$				

SEM-SE imaging was performed to determine the cracking morphology produced in PWR primary water across the fracture surface. An overall montage is presented in Figure 5-89 that reveals TG cracking from precracking and initial transitioning in water (steps 1-6) until the crack front moved beyond the pass #1 to pass #2 boundary. Extensive IG cracking was discovered in weld pass #2 as documented by the dashed yellow lines in the upper montage. Just beyond the pass #1 to pass #2 boundary, the cracking is >80% IG for ~1 mm into pass #2 across most of the CT specimen width. The cracking becomes more complex with a mixture of TG and IG over the next several mm of growth to the final crack front produced in water. In particular, the middle of the specimen became predominately TG while two areas of predominately IG cracking can be seen closer to sides A and B that extended deeper. Examples of the IG morphology are shown at higher magnification in the lower two SE images. The bumpy appearance on the IG facets reflects the dendrite packets intersecting the grain boundary surface.

Although the cracking morphology has now been assessed, it remains difficult to directly relate the measured crack-growth behavior to locations across the fracture surface. The mid-test, side-groove exams (Figures 5-69 and 5-75) clearly revealed that near side A the crack front had propagated well into pass #2 while the crack front near side B was still well within pass #1. These mid-test crack locations are identified on Figure 5-85 and are consistent with the final side-groove exams where the crack length was ~1.1 mm longer on side A than side B.
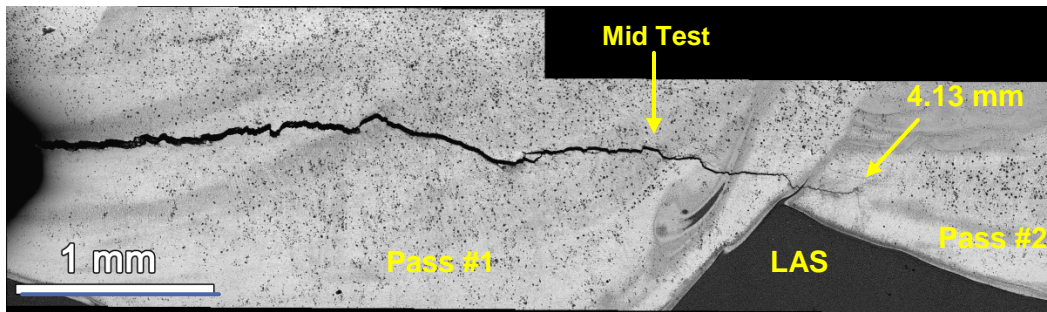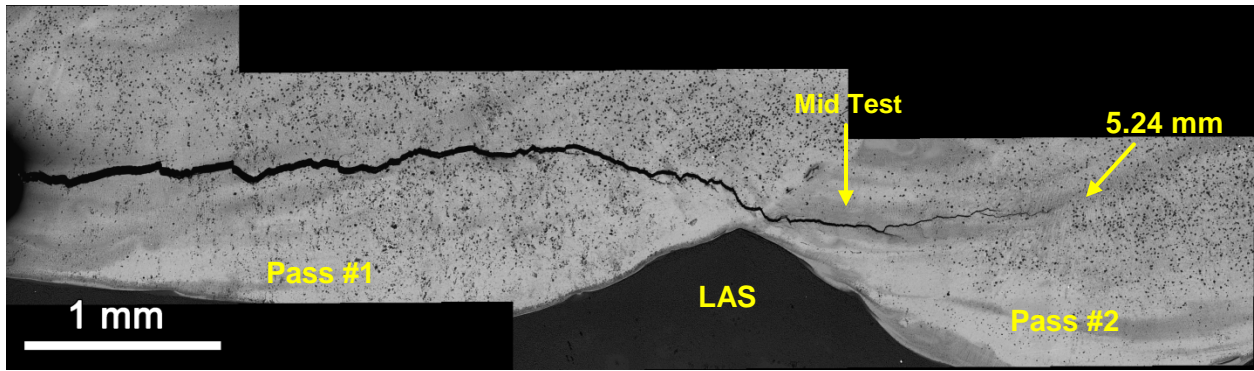
Figure 5-85 Side Groove SEM-BSE Montages Showing the Overall Crack Path on Side A (top) and Side B (bottom)
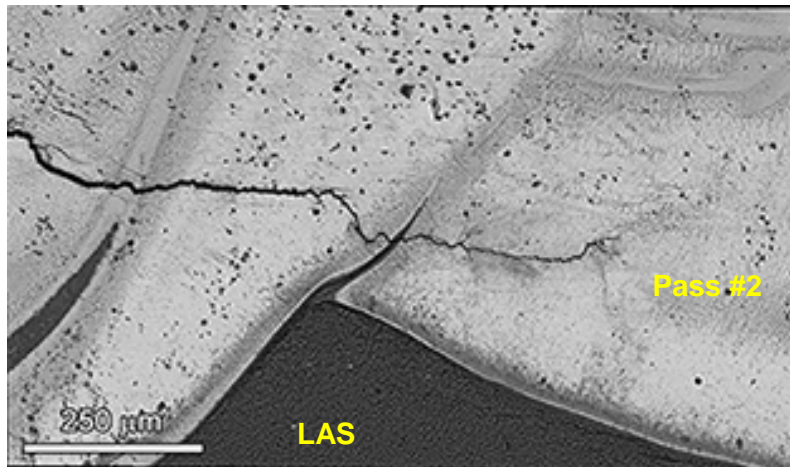
Figure 5-86 Higher Magnification SEM/BSE Image from Side B Showing Crack Has Propagated into Weld Pass #2
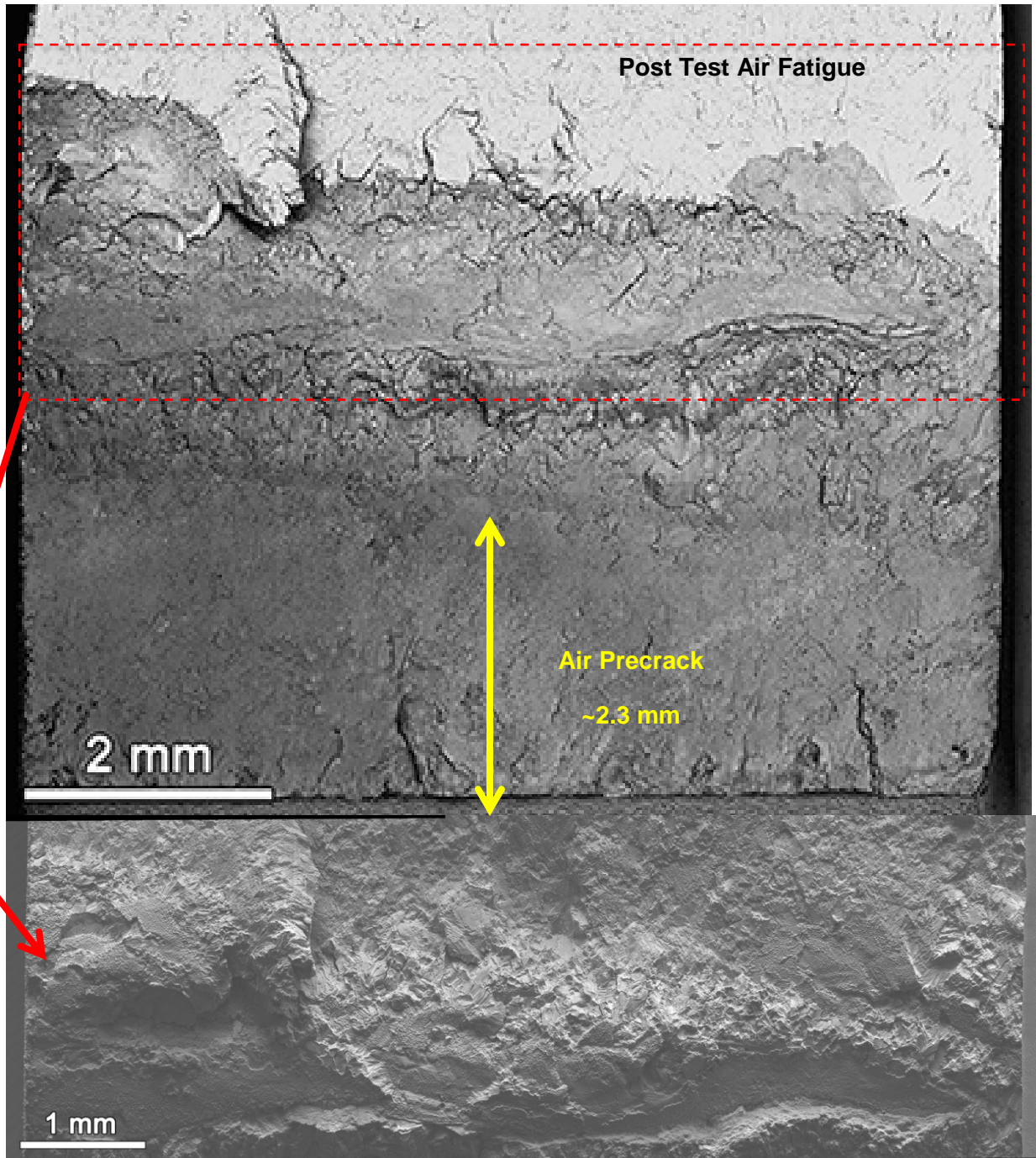
Figure 5-87   **Upper Image Is a SEM-BSE Montage Showing the Entire Crack Growth Surface and Lower Image Is a SEM-SE Montage Revealing the Cracking Morphology in the Dashed Red Box. Darker Contrast in the Crack-Growth Surface BSE Image Identifies Region Exposed to High-Temperature Water with Lighter Upper Area Opened by Fatigue in Air After the SCC Test**
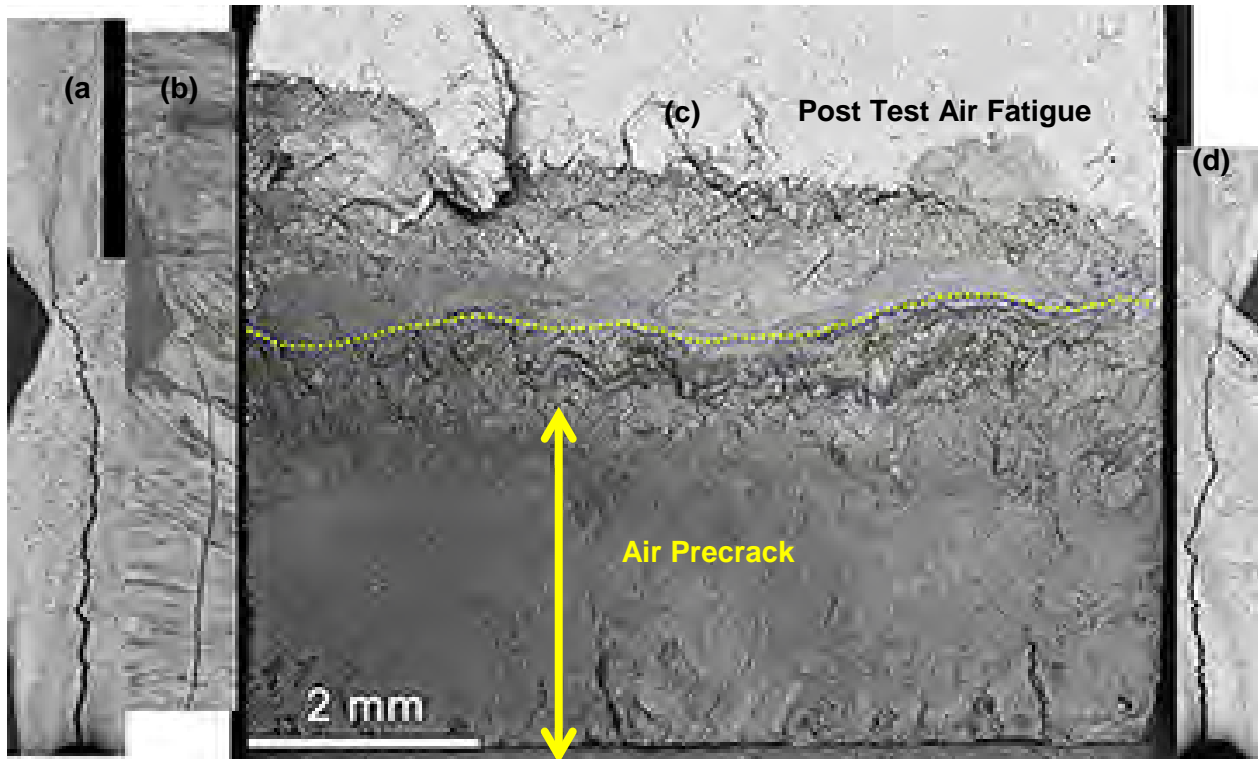
Figure 5-88 **SEM-BSE Images from Left to Right: (a) Side Groove A, (b) Side Surface Cross-Section, (c) Crack-Growth Surface Montage and (d) Right Side Groove B. The Dashed Line in the CGF Image Illustrates Approximate Location of the Boundary Between the Two Weld Passes. Darker Contrast in the Crack-Growth Surface Image Identifies Region Exposed to High-Temperature Water with Lighter Upper Area Opened by Fatigue in Air After the SCC Test**

More detailed characterizations of the cross-section removed from side A are presented in Figures 5-90 and 5-91. The cracking morphology can be identified in Figure 5-90 with TG cracking through large elongated grains in pass #1 of the alloy 152 weld metal that are oriented perpendicular to crack path. As the crack enters pass #2, it follows the LAS – alloy 152 interface for ~0.5 mm before finding grain boundaries better aligned for IG cracking. These aligned grain boundaries are created at the intersection of several large elongated grains with smaller equiaxed grains close to the fusion boundary. The IG crack path is maintained for >1 mm and cracking ends at a region where large elongated grains are again oriented perpendicular to crack path. Not only is the microstructure favorable for IG growth in pass #2, but the aligned grain boundaries also corresponded with an area of Fe-rich, Cr-depleted weld metal. SEM-EDS composition maps are shown in Figure 5-91 and reveal the IG crack path closely follows the dilution region. Along the IG crack, it was estimated that Fe concentrations ranged from ~28-34 wt% and Cr levels ranged from ~21-25 wt%. Therefore, *environment-assisted IG cracking occurred in this cross-section only where aligned grain boundaries and Cr depletion were both present.*
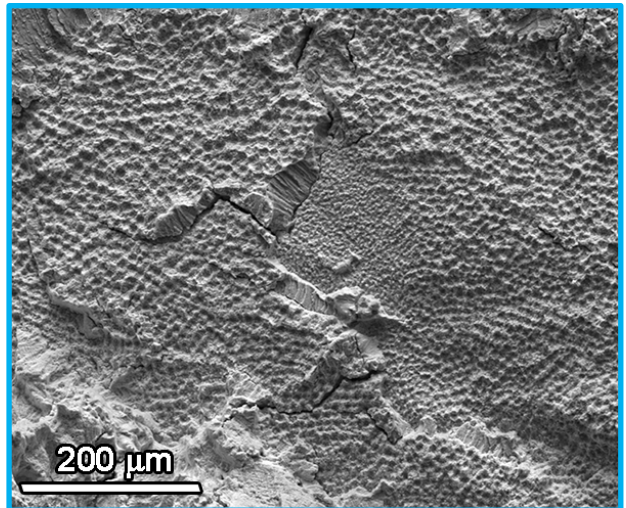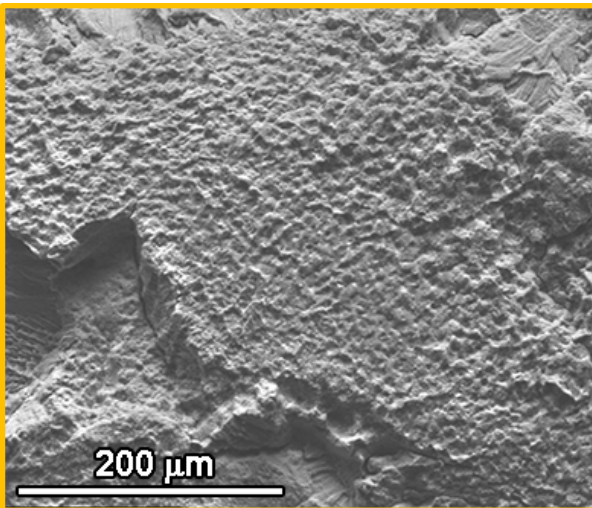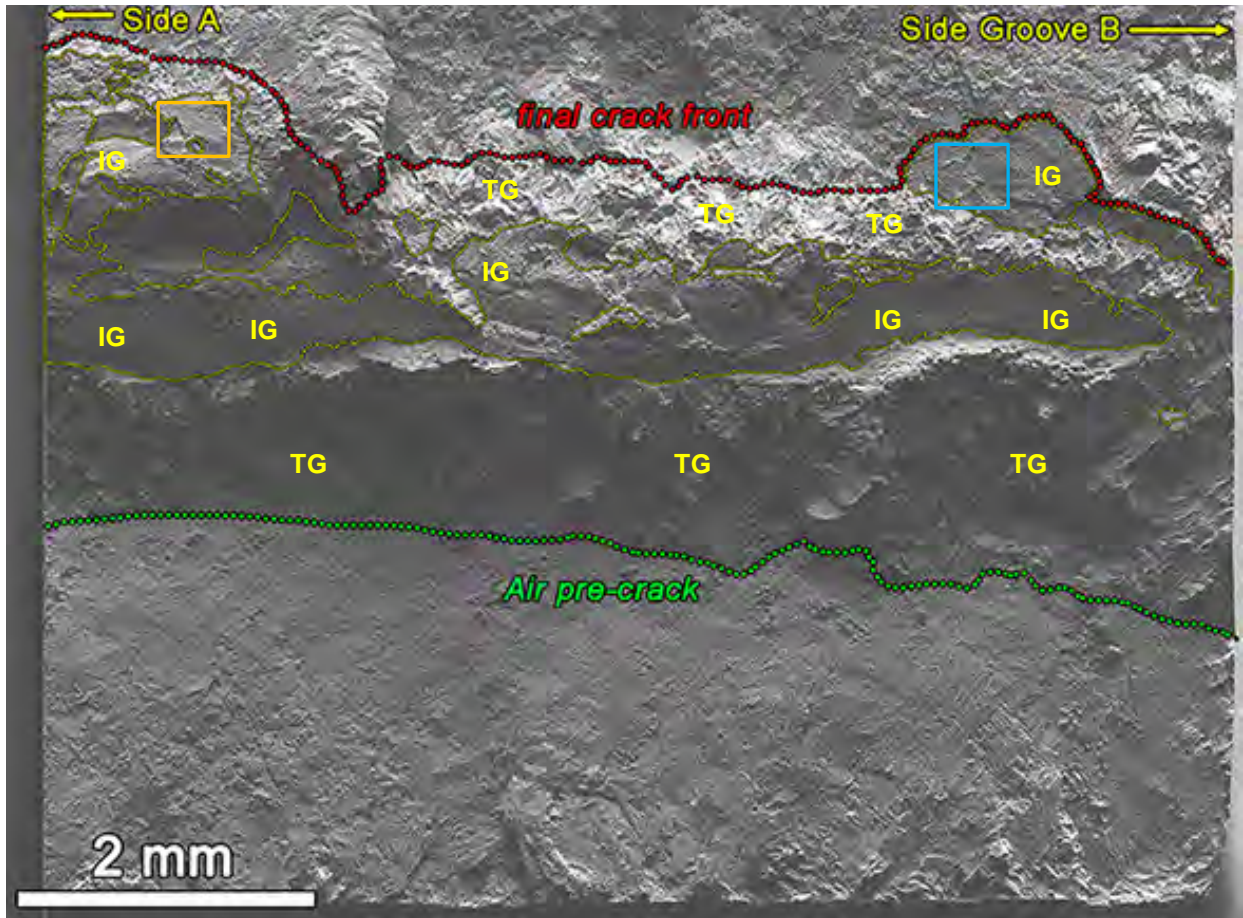
Figure 5-89 Upper SEM-SE Montage Maps the Entire Crack-Growth Surface Area and Identifies IG Regions That Are Surrounded by the Fine Dashed Yellow Lines. Two Typical IG Regions Are Highlighted by Orange and Light Blue Boxes in the Montage and Shown at Higher Magnification in the Lower Images
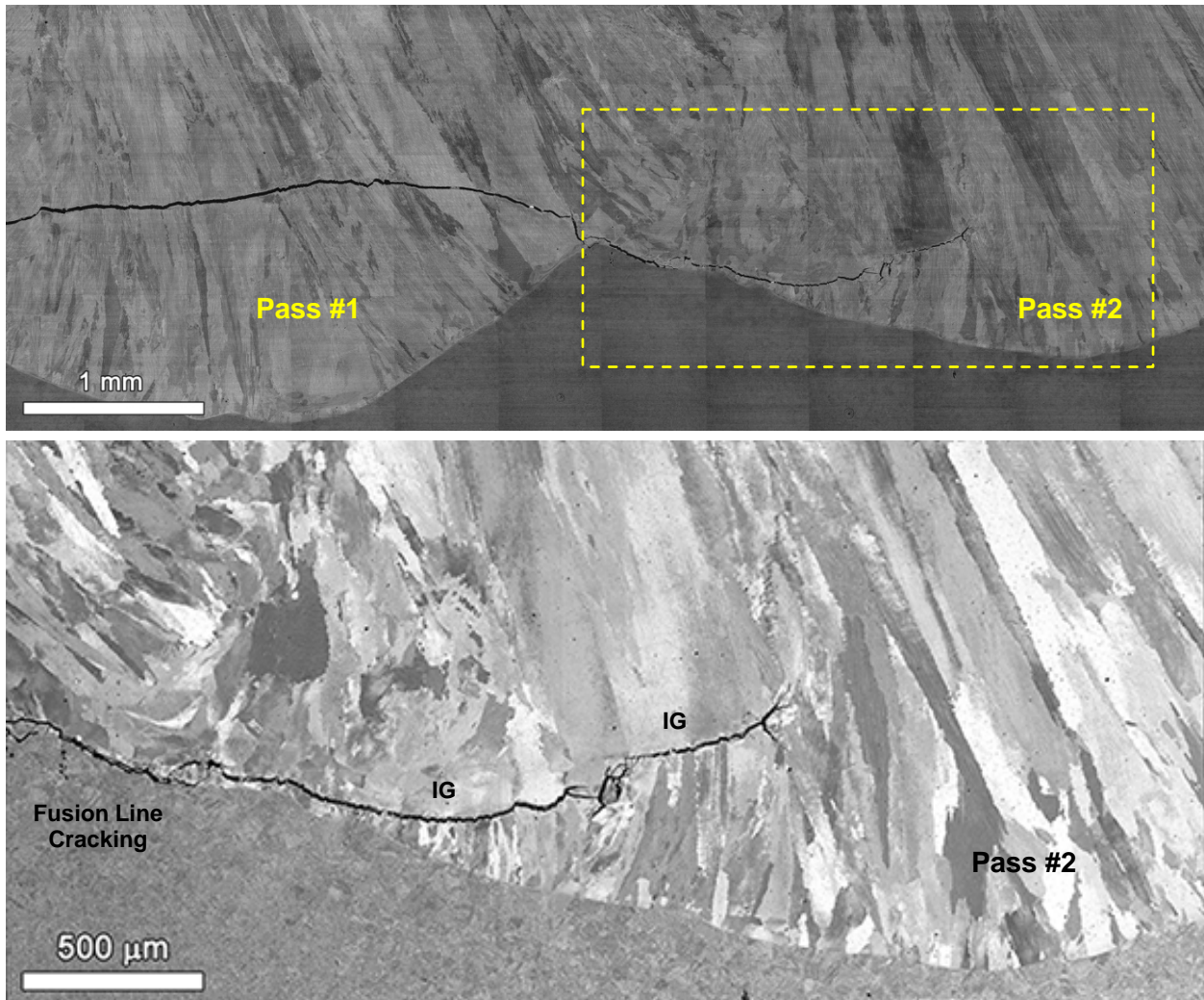
Figure 5-90   Characterization of the Cross-Section Sample off Side A of the Specimen CT117 Showing the Overall Crack Produced in Water (top image) and the Final Crack Path After It Propagated into Weld Pass #2 (below)
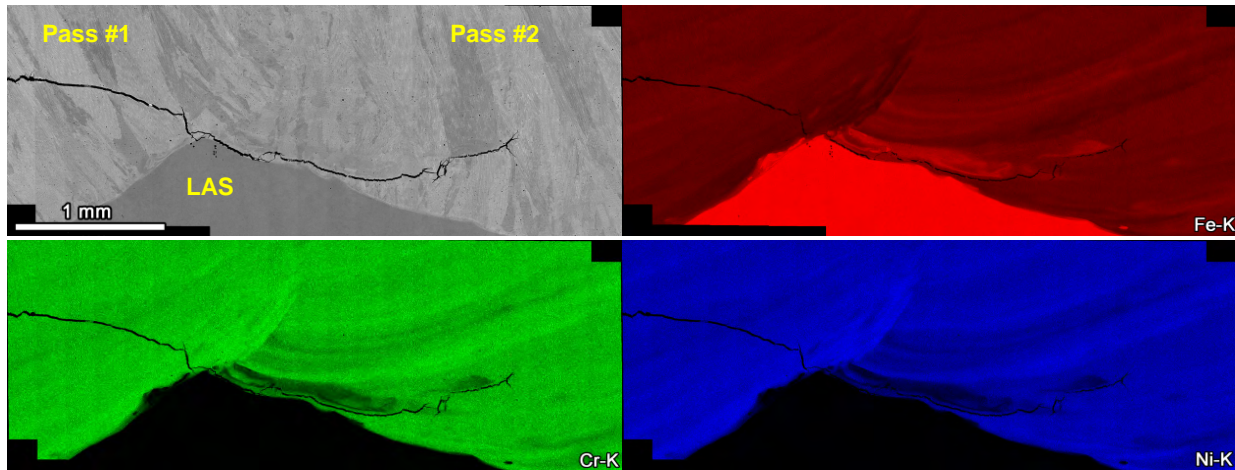
Figure 5-91   SEM-BSE Image and EDS Elemental Maps of the Cross-Section Sample off Side A of the Specimen CT117

5.3.4   ANL 152v2 DM Weld: Specimen CT119 – Alloy 152/LAS Interface

The second crack-growth test on an alloy 152 - LAS dilution specimen (CT119) was conducted in a similar fashion to CT117 with two parts separated by a shut down so that the side grooves could be examined. An overview of the first part of the test is summarized in Figure 5-92 with three evaluations of constant K response and two evaluations during cycle + 24 h hold loading. Details on the initial 31 steps are listed in Table 5-12. Cyclic loading at 0.1, 0.01 and 0.001 Hz (with R=0.5) was applied over the first ~1000 hours creating a crack extension of ~1.1 mm before transitioning to a 980s/20s cycle with and without a 2.5 h hold to indicate whether the propagation response suggested SCC growth. More aggressive cycling at 0.01 Hz was again applied in steps 10 and 12 when low CGRs were observed during cycle + hold loading. Best CGR results for the 2.5 h hold were seen at ~1900 hours in step 16 and constant K was evaluated for ~1200 hours as documented in Figure 5-93. Altered propagation response was observed over this exposure with CGRs reaching ~1×10^{-8} mm/s, then slowing to ~4×10^{-9} mm/s. The decision was made to assess ligament formation at 3340 hours by switching back to cycle + hold and the DCPD-measured crack length jumped by ~35 µm during the first cycles and then settled back to a normal cycle + hold CGR. This indicated unmeasured crack extension at constant K and the actual SCC growth rate is estimated at 1.4×10^{-8} mm/s.
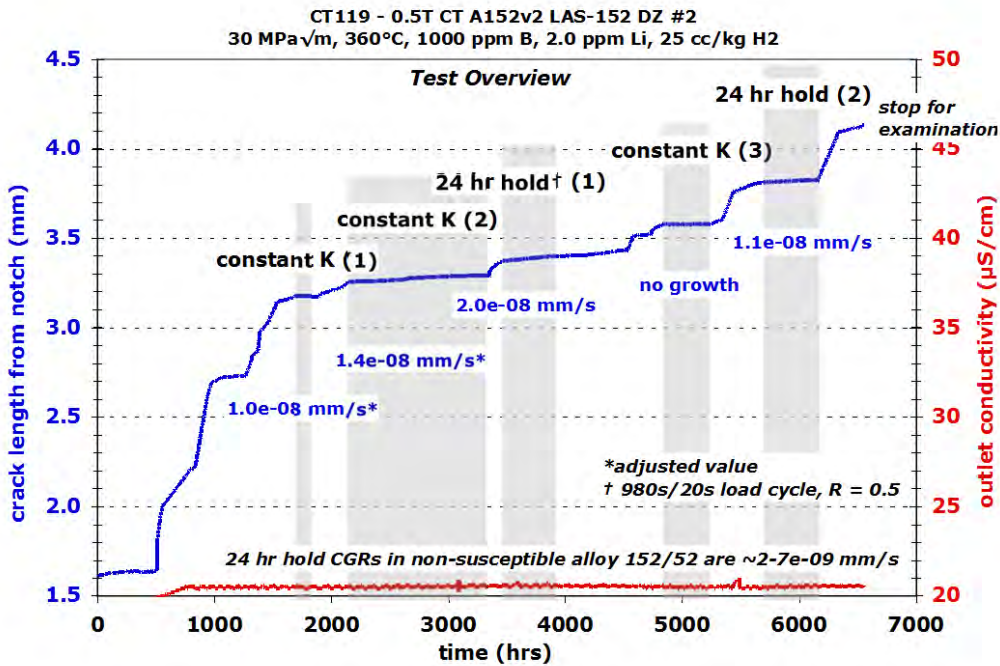
Figure 5-92 Overview Crack Growth Plot of First Part for Test on the ANL Alloy 152 - LAS Dilution Zone Specimen (CT119)
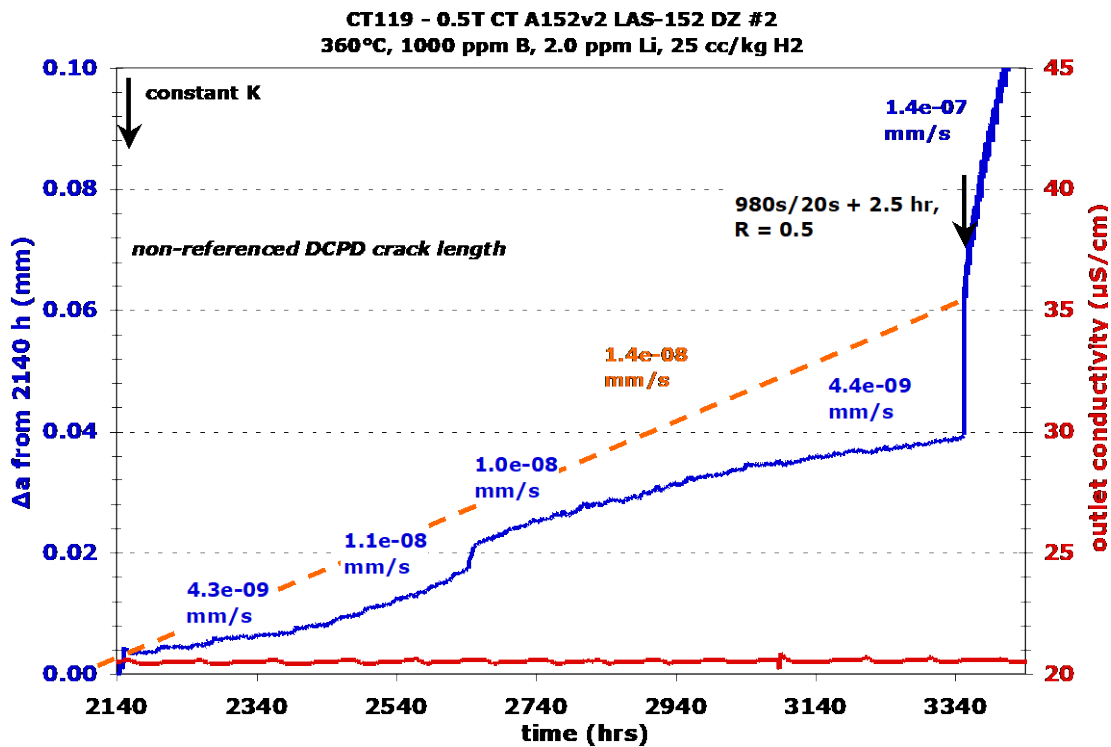
Figure 5-93 Second Evaluation of SCC Response at Constant K Showing Slowing Growth with Time over 1200 Hours. Evidence for Ligament Formation and Unmeasured Crack Extension by DCPD Indicating Higher SCC Propagation Rate

Table 5-12   Data Summary for the First Part of the Test on the ANL Alloy 152 - LAS Dilution Zone Specimen CT119

Test Step	Start (h)	Time (h)	R	Freq. (Hz)	Hold (h)	Diss. H$_2$ (cc / kg)	Temp (°C)	Kmax (MPa√m)	CGR (mm/s)	Crack Exten. (mm)
1	0	505	---	const K	---	25	360	20	---	---
2	505	6	0.5	0.1	0	25	360	30	6.9E-06	0.130
3	511	41	0.5	0.01	0	25	360	30	1.3E-06	0.196
4	552	15	0.5	0.001	0	25	360	30	1.9E-07	0.012
5	567	268	0.5	980s/20 s	0	25	360	30	2.5E-07	0.211
6	835	136	0.5	0.01	0	25	360	30	7.1E-07	0.467
7	971	50	0.5	0.001	0	25	360	30	8.3E-08	0.017
8	1021	28	0.5	980s/20 s	0	25	360	30	7.4E-08	0.008
9	1049	215	0.5	980s/20 s	2.5	25	360	30	1.7E-08	0.019
10	1264	56	0.5	0.01	0	25	360	30	5.1E-07	0.105
11	1320	46	0.5	980s/20 s	0	25	360	30	1.6E-07	0.029
12	1366	22	0.5	0.01	0	25	360	30	1.4E-06	0.108
13	1388	137	0.5	980s/20 s	0	25	360	30	3.8E-07	0.149
14	1525	170	0.5	980s/20 s	2.5	25	360	30	5.2E-08	0.050
15	1695	195	---	const K	---	25	360	30	1.0E-08	0.006
16	1890	257	0.5	980s/20 s	2.5	25	360	30	1.1E-07	0.071
17	2147	1205	---	const K	---	25	360	30	1.4E-08	0.039
18	3352	90	0.5	980s/20 s	2.5	25	360	30	1.4E-07	0.057
19	3442	480	0.5	980s/20 s	24	25	360	30	2.0E-08	0.030
20	3922	319	0.5	980s/20 s	48	25	360	30	8.7E-09	0.010
21	4241	280	0.5	980s/20 s	12	25	360	30	3.1E-08	0.026
22	4521	49	0.5	980s/20 s	0	25	360	30.1	4.1E-07	0.065
23	4570	164	0.5	980s/20 s	12	25	360	30.1	1.5E-08	0.016
24	4734	93	0.5	980s/20 s	2.5	25	360	30.2	7.9E-08	0.052
25	4827	416	---	const K	---	25	360	30.2	~6E-10	0.001
26	5243	95	0.5	980s/20 s	2.5	25	360	30.2	7.2E-08	0.031
27	5338	89	0.5	980s/20 s	0	25	360	30.4	4.6E-07	0.140
28	5427	215	0.5	980s/20 s	2.5	25	360	30.5	6.1E-08	0.065
29	5642	503	0.5	980s/20 s	24	25	360	30.5	1.1E-08	0.014
30	6145	182	0.5	980s/20 s	0	25	360	31.1	3.9E-07	0.259
31	6327	228	0.5	980s/20 s	2.5	25	360	31.1	5.3E-08	0.046
	6555	*Stop*	*for*	*Exam*						

In an attempt to better confirm this SCC propagation behavior and the influence of ligament formation, several different hold times were evaluated. Once stable CGR was observed during the 2.5 h hold, a 24 h hold was applied as documented in Figure 5-94. The stepped DCPD response for crack length again suggests the breaking of ligaments and the overall CGR of $2x10^{-8}$ mm/s supports the previously measured SCC rate at constant K. However, the evaluation of an even longer hold time of 48 hours (Figure 5-95) resulted in a CGR lower than that extrapolated from the constant K response. Apparently a single cycle is not sufficient to completely remove the ligaments/contacts formed during the 48h hold. One additional periodic unload was tried at a 12 h hold time (Figure 5-97) and the CGR increased back to $3.2x10^{-8}$ mm/s. Another evaluation of constant K behavior was performed in step 25 as presented in Figure 5-97. DCPD indicated noisy response with little if any crack growth during the 416-hour exposure. The subsequent cycle + hold loading revealed no evidence for a jump in crack length that would suggest ligament formation. Final attempts were made to find an area of enhanced SCC by switching between 980s/20s cycling to move the crack front forward followed by cycle + hold evaluations. After several attempts showing lower CGRs, the decision was made to stop the tests and examine the crack morphology in the specimen side grooves.
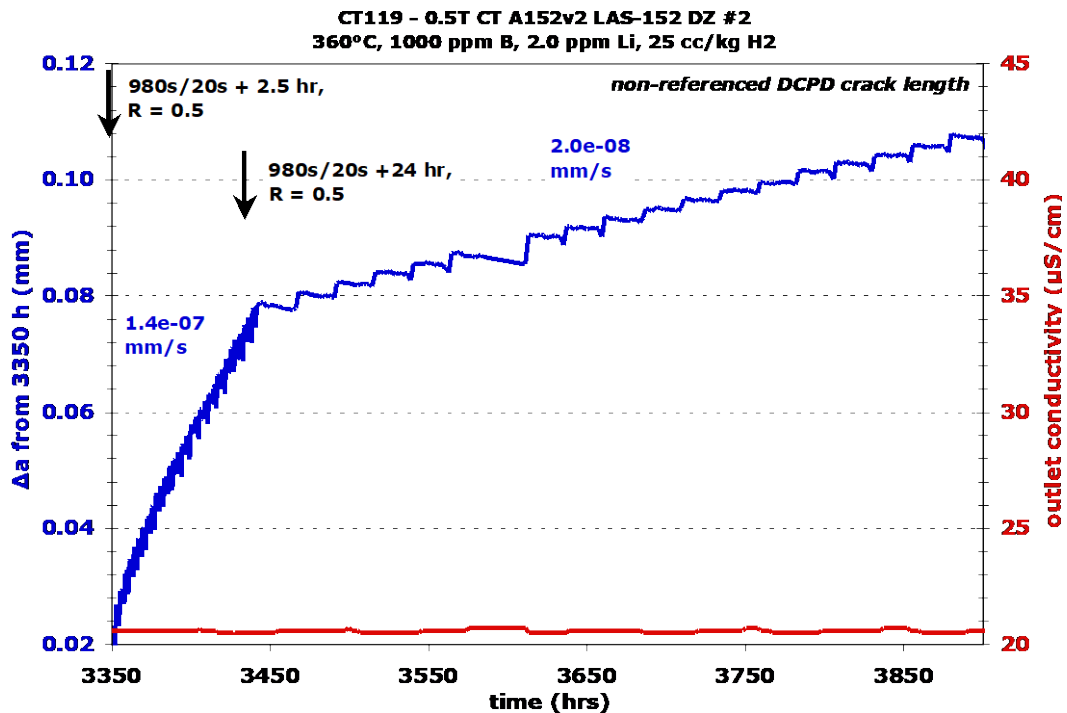
Figure 5-94   Crack Growth Response During Cycle + 24 h Hold Loading
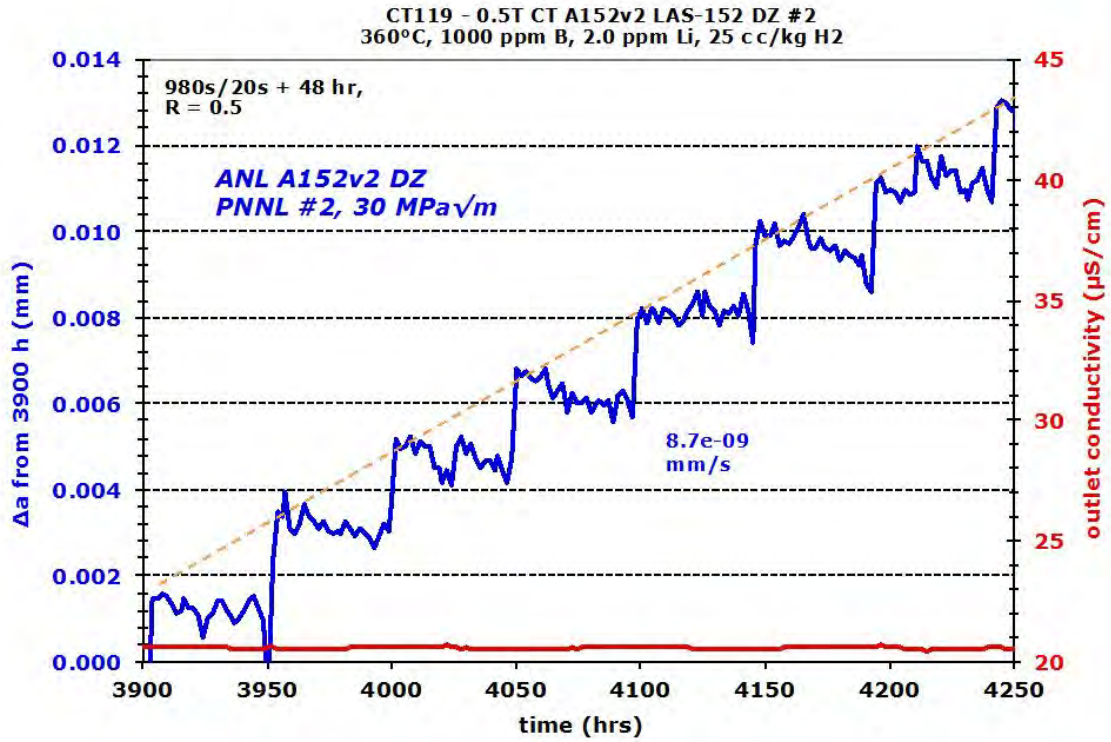
Figure 5-95   Crack Growth Response During Cycle + 48 h Hold Loading
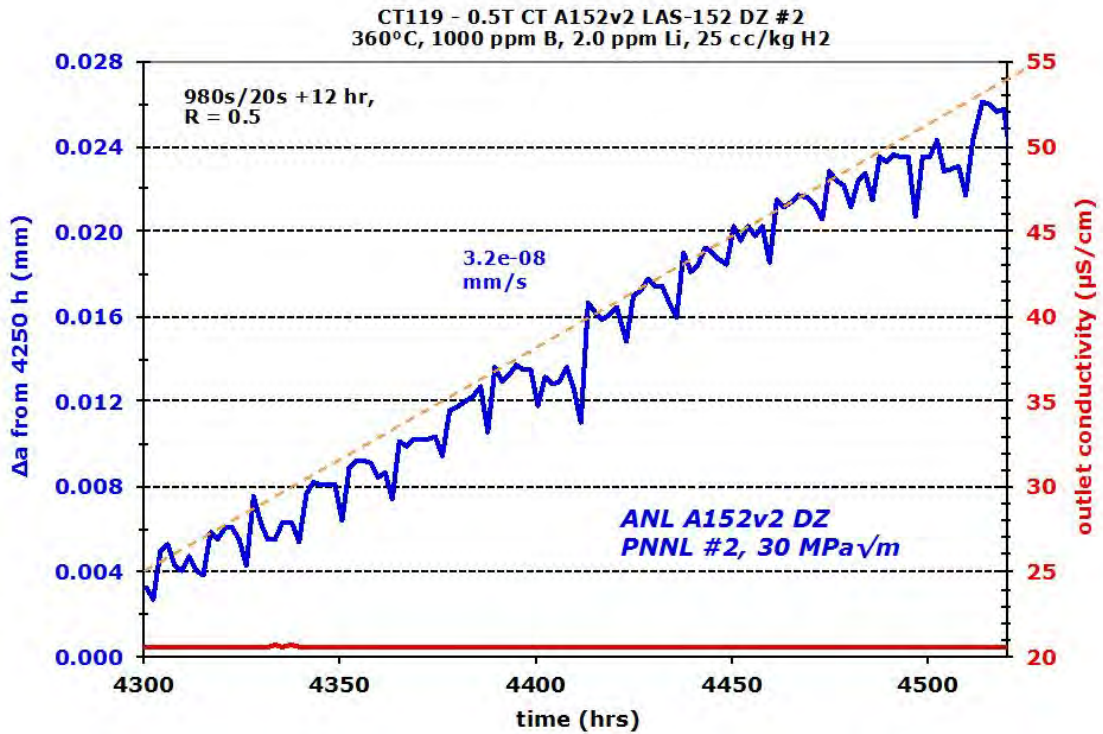
Figure 5-96   Crack Growth Response During Cycle + 12 h Hold Loading
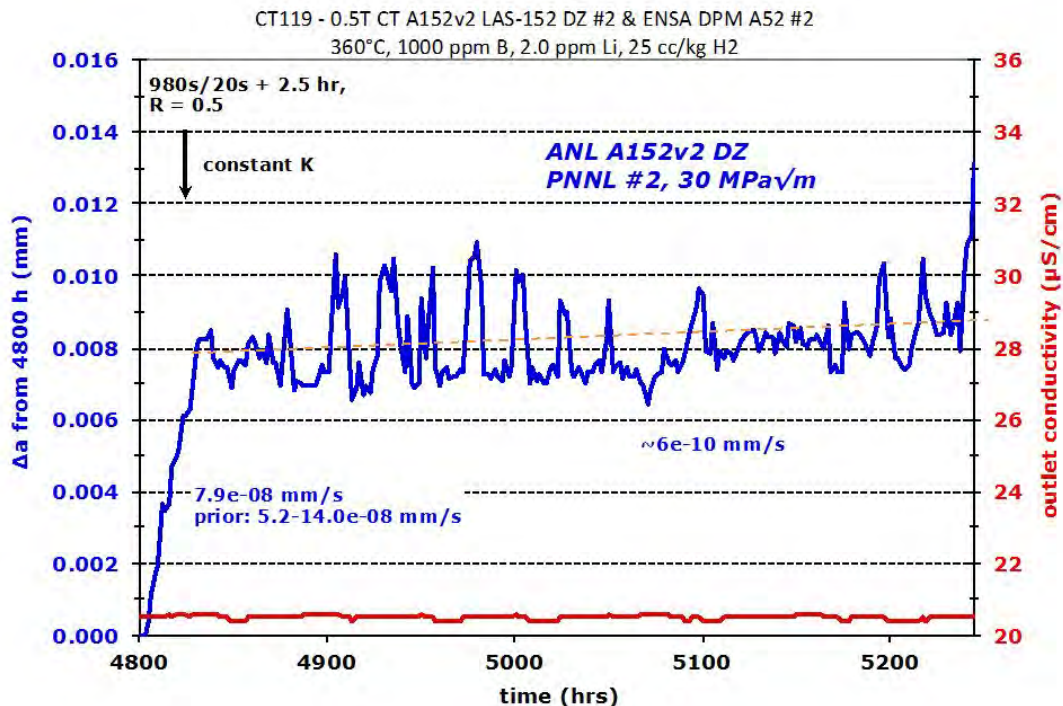
Figure 5-97   Crack Growth Response for the 3rd Constant K Evaluation Showing Little or No Growth

Optical and SEM exams revealed that the crack diverted downward toward the LAS peak at the transition from weld pass #1 to pass #2 in both side groove A and side groove B as illustrated in Figure 5-98. The crack extension in side groove A was slightly greater than in side groove B, but the crack front was clearly into weld pass #2 for both. As was noted during the pre-test side groove exams for CT119 (Figure 5-15), a region of strong Fe enrichment and Cr depletion was present in weld pass #2 including two second phase islands in the alloy 152 weld metal that appeared to be trapped LAS. These two LAS islands are identified in Figure 5-98 and the crack clearly interacted with them causing fine secondary cracks. A higher magnification image of the leading crack in side A is shown in Figure 5-99 and no cracking could be seen in the LAS islands themselves. The leading crack tip with TG and IG components is highlighted in Figure 5-100.

An overview of the second part of the test is summarized in Table 5-13 and Figure 5-101. Cyclic loading at a 980s/20s cycle with and without a 2.5 h or 24 h hold was again employed to indicate whether the propagation response suggested SCC growth. Steps 34-46 were applied to once again investigate crack-growth response at ~31 MPa√m and confirmed behavior observed at the end of part 1 testing with no indication of SCC enhancement. An example of this response is shown in Figure 5-102 for steps 37-40 where the measured CGRs for the 2.5 h hold evaluations remained below previous values. As a result, the decision was made to move the crack front forward into a new microstructure. Aggressive cycling at 0.1 and 0.01 Hz in steps 47 and 48 moved the crack forward by ~2 mm and increased the K level, however a low CGR was seen during 980s/20s cycling in step 49. Transitioning was continued in steps 50-58 with CGRs remaining much lower than previous attempts and the test was then shut down to evaluate the cracking morphology.
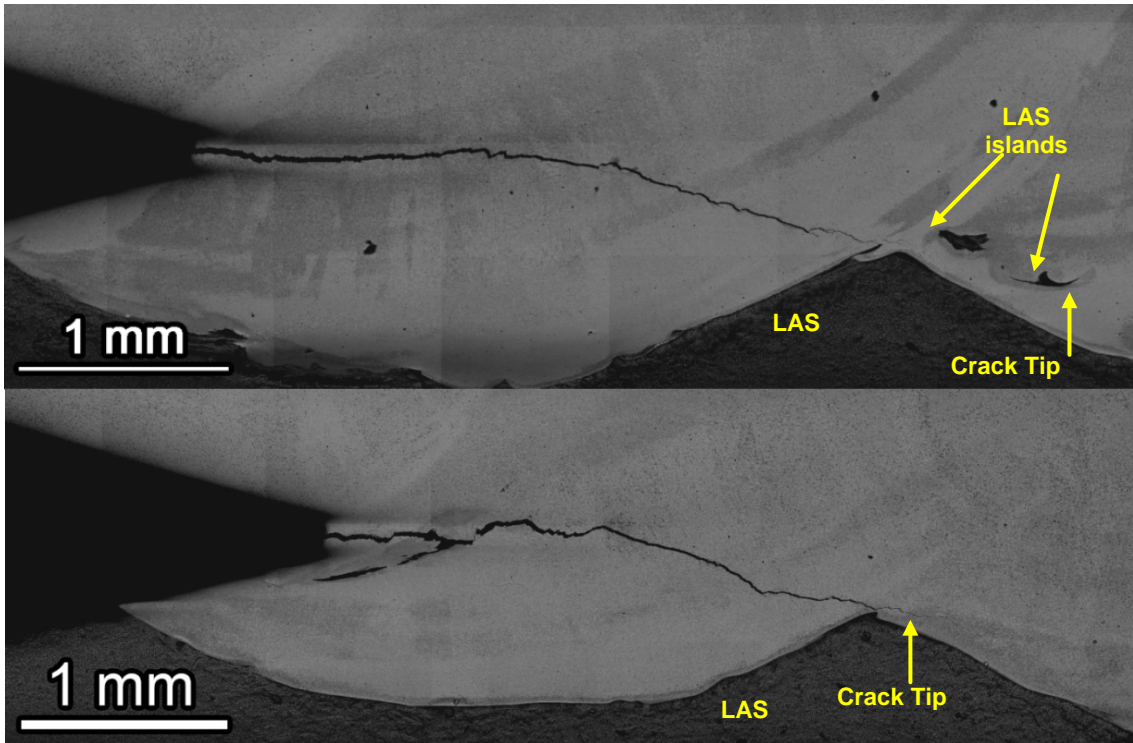
Figure 5-98 **SEM-BSE Images of Side Groove A (top) and Side Groove B (bottom) for Specimen CT119 After 6555 Hours of Testing**
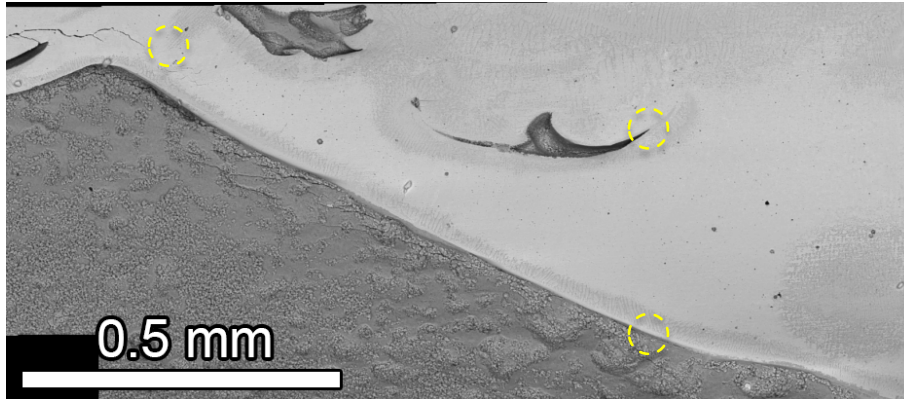
Figure 5-99 Higher Magnification SEM-BSE Image of the Leading Crack Region in Side Groove A with Crack Tips Highlighted in Small Circles
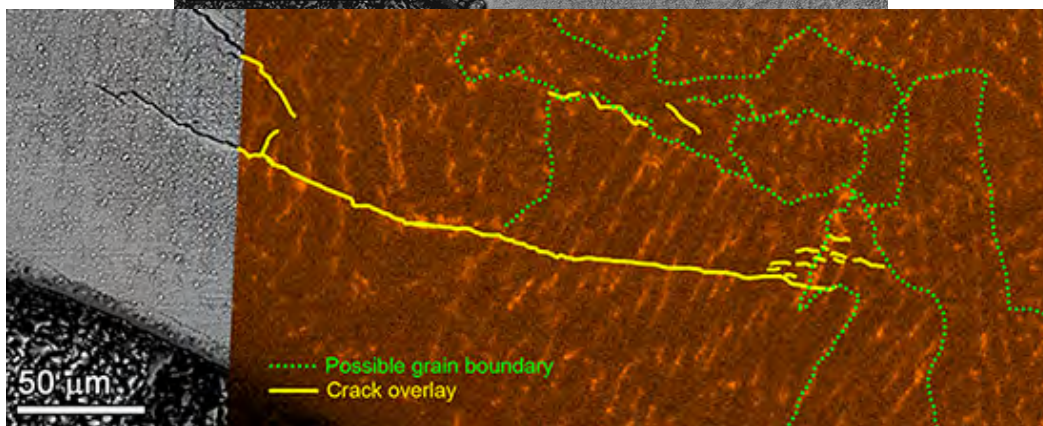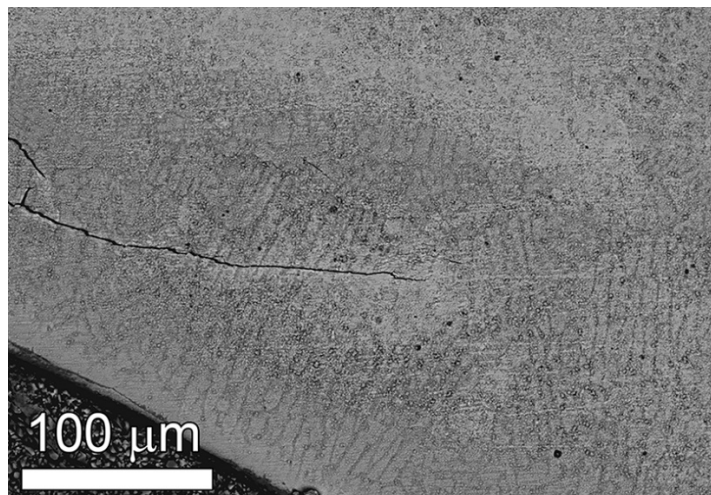
Figure 5-100 Fine Cracks and Leading Crack Tips for the Side Groove B. Cracks Are Shown in Yellow with Apparent Grain Boundaries in Dashed Green Based on the Nb Composition Map

Table 5-13   Data Summary for the Second Part of the Test on the ANL Alloy 152 - LAS Dilution Zone Specimen CT119

Test Step	Start (h)	Time (h)	R	Freq. (Hz)	Hold (h)	Diss. H_2 (cc / kg)	Temp (°C)	Kmax (MPa√m)	CGR (mm/s)	Crack Exten. (mm)
33	6555	154	---	const K	---	25	360	31.1	1.7E-09	0.001
34	6709	85	0.5	980s/20s	2.5	25	360	31.1	8.3E-08	0.022
35	6794	95	0.5	980s/20s	0	25	360	31.1	4.2E-07	0.151
36	6889	185	0.5	980s/20s	2.5	25	360	31.1	4.4E-08	0.033
37	7074	128	0.5	980s/20s	0	25	360	31.1	3.2E-07	0.153
38	7202	87	0.5	980s/20s	2.5	25	360	31.1	5.6E-08	0.021
39	7289	138	0.5	980s/20s	0	25	360	31.2	2.4E-07	0.145
40	7427	419	0.5	980s/20s	2.5	25	360	31.2	3.3E-08	0.055
41	7846	66	0.5	980s/20s	0	25	360	31.3	2.3E-07	0.051
42	7912	72	0.5	980s/20s	0	1	360	31.3	2.8E-07	0.069
43	7984	124	0.5	980s/20s	0	25	360	31.4	3.0E-07	0.117
45	8108	164	0.5	980s/20s	2.5	25	360	31.4	3.1E-08	0.025
46	8272	101	0.5	980s/20s	24	25	360	31.4	1.7E-09	0.001
47	8373	125	0.5	0.1	0	25	360	33.4	4.7E-06	1.889
48	8498	50	0.5	0.01	0	25	360	33.4	5.6E-07	0.092
49	8548	44	0.5	980s/20s	0	25	360	33.4	2.2E-08	0.006
50	8592	25	0.5	0.1	0	25	360	33.5	4.2E-06	0.265
51	8617	95	0.5	0.01	0	25	360	33.5	3.5E-07	0.122
52	8712	143	0.5	980s/20s	0	25	360	33.5	4.4E-08	0.021
53	8855	20	0.5	0.1	0	25	360	33.7	3.7E-06	0.226
54	8875	120	0.5	0.01	0	25	360	33.8	3.5E-07	0.177
55	8995	228	0.5	980s/20s	0	25	360	33.8	1.3E-08	0.024
56	9223	12	0.5	0.1	0	25	360	33.8	3.8E-06	0.152
57	9235	63	0.5	0.01	0	25	360	33.8	4.2E-07	0.106
58	9309	315	0.5	980s/20s	0	25	360	33.8	2.5E-08	0.011
Total	9613									6.424

Post-test side groove images are in Figure 5-103 revealing what appears to be completely TG cracking from the mid-test crack location through all of weld pass #2 with cracks ending in the LAS. The final crack tips propagating into the LAS are highlighted Figure 5-104. One possible reason for the lack of IG cracking during the second phase of this test was the lack of both a favorable microstructure (aligned grain boundaries) and significant dilution. Composition maps for weld pass #2 associated with the crack path are presented in Figures 5-105 and 5-106 revealing no significant dilution zone. Consistent with the observations of some SCC susceptibility early in the test, the crack-growth surface exhibited several areas of IG cracking corresponding to the first part of the test. The overall crack-growth surface is documented in Figure 5-107 and considerable IG regions can be seen closer to side A of the specimen over a depth of ~1.5 mm. This region of IG cracking corresponds to the area in weld pass #2 just beyond the pass #1 to pass #2 transition where aligned grain boundaries were observed along with significant Fe enrichment and Cr depletion. An example of one of these IG regions is shown at higher magnification in Figure 5-108. Although more limited environment-assisted IG cracking was found for the CT119 specimen than the CT117 specimen, the microstructural and microchemical features were similar for areas of IG cracking.
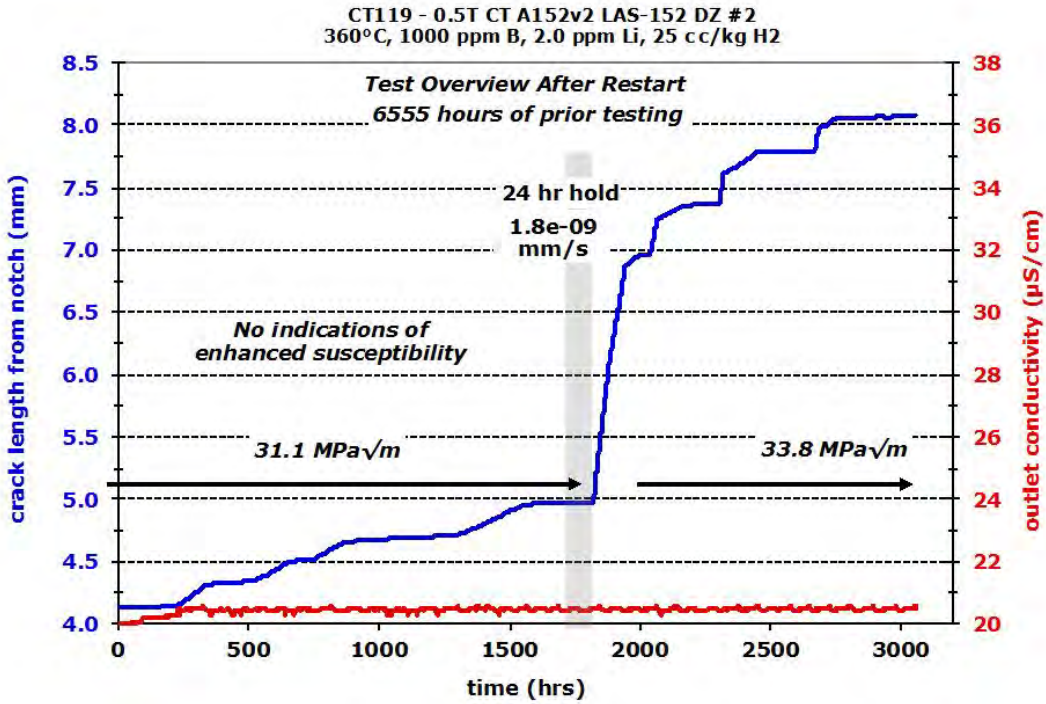
Figure 5-101   Overview Crack Growth Plot of Second Part for CT119 Specimen Test
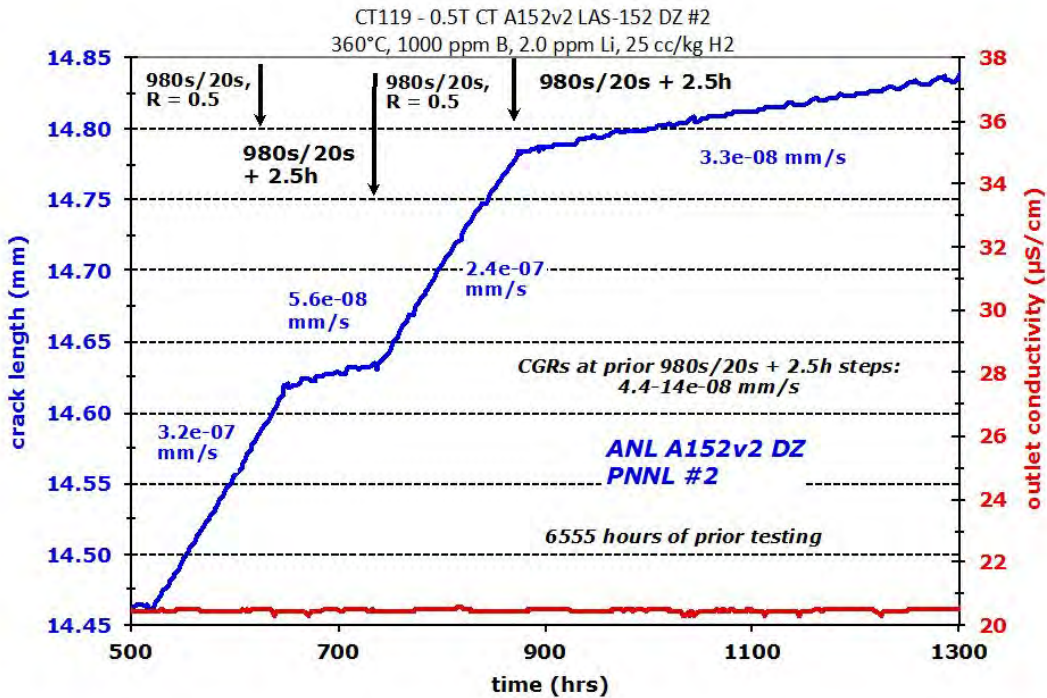
Figure 5-102 Cyclic and Cycle + 2.5 h Hold Response After Restarting Specimen CT119

5-83
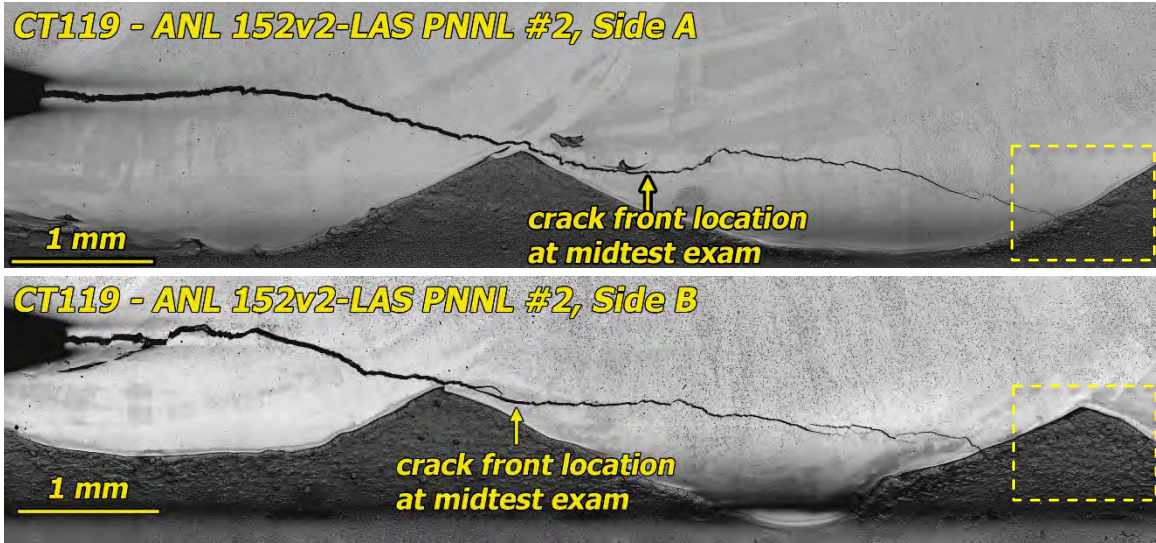
Figure 5-103   Post-Test Side Groove Images for Specimen CT119
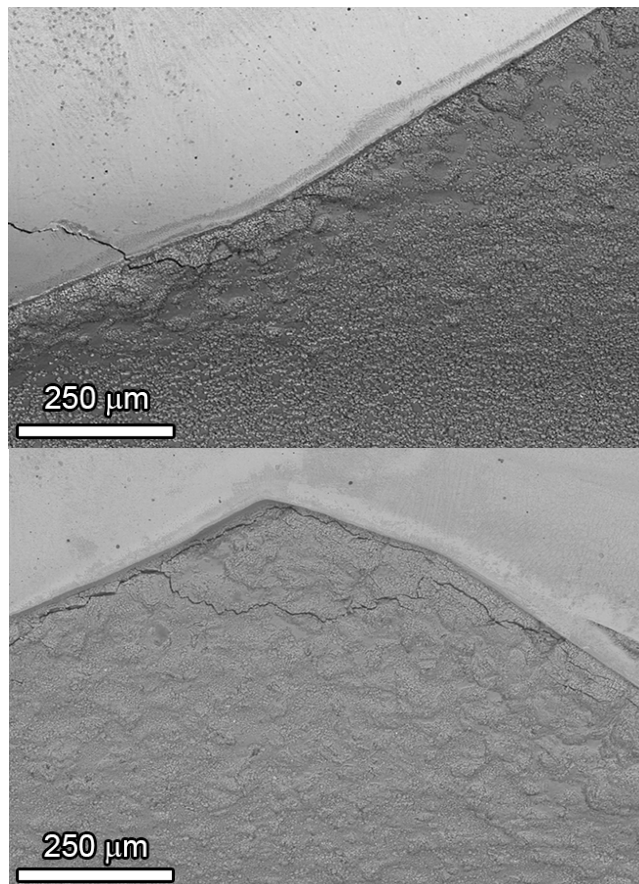
Figure 5-104   Final Crack Tips in the LAS for CT119 in Side Grooves A (top) and B (bottom)
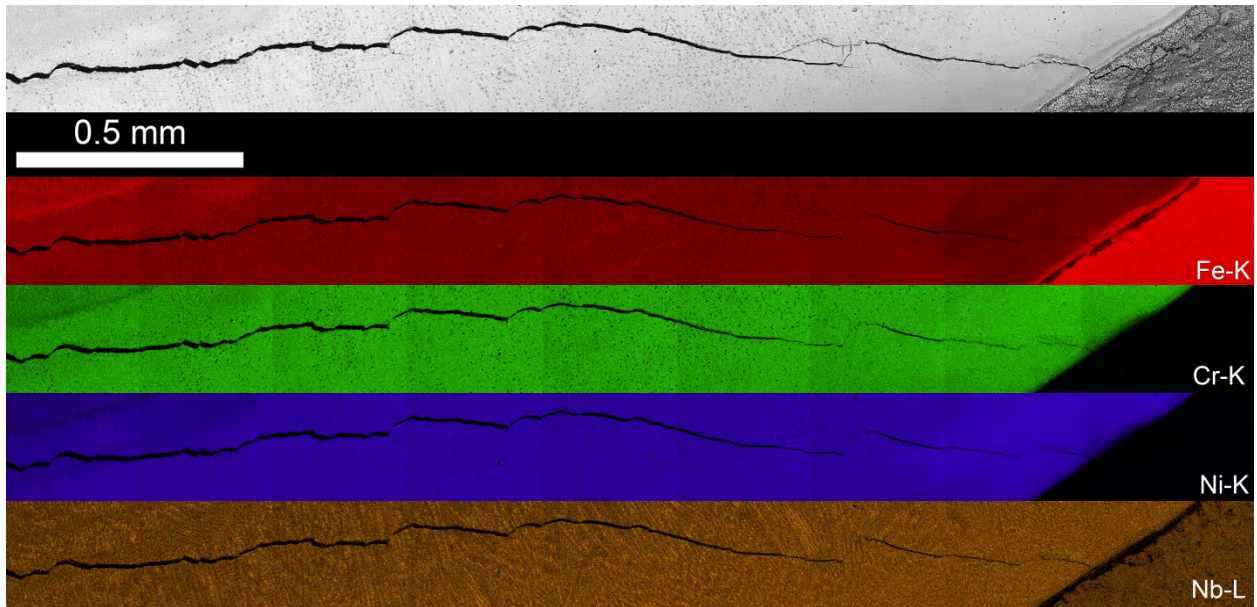
Figure 5-105   Crack Path in Side Groove A Through Weld Pass #2 During Second Part of the Test on CT119 Along with EDS Composition Maps Showing No Significant Dilution in This Region
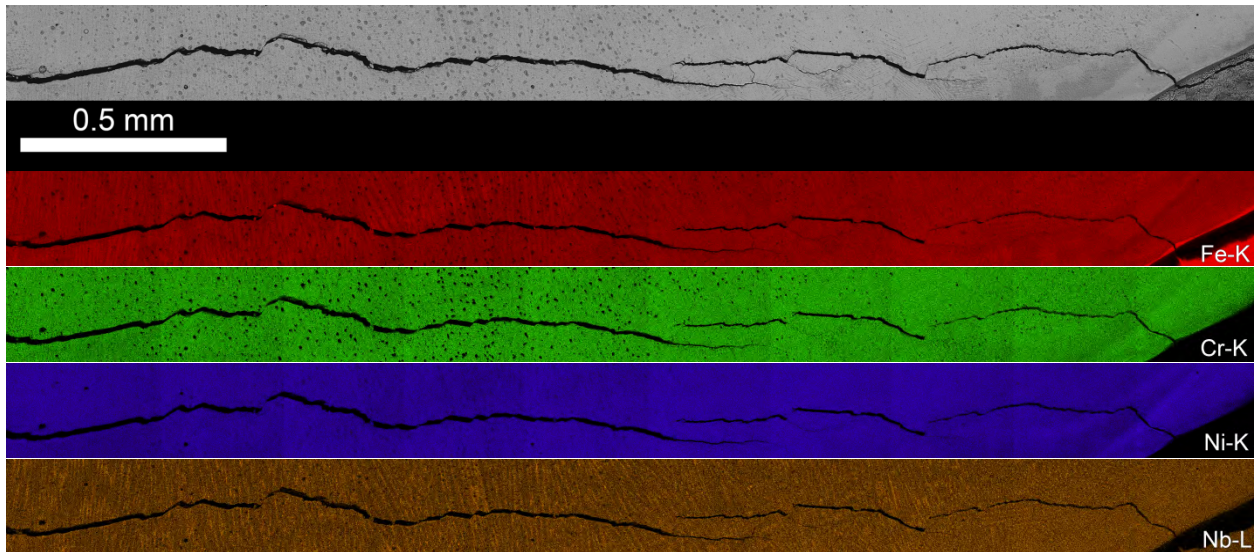
Figure 5-106   Crack Path in Side Groove B Through Weld Pass #2 During Second Part of the Test on CT119 Along with EDS Composition Maps Showing No Significant Dilution in This Region
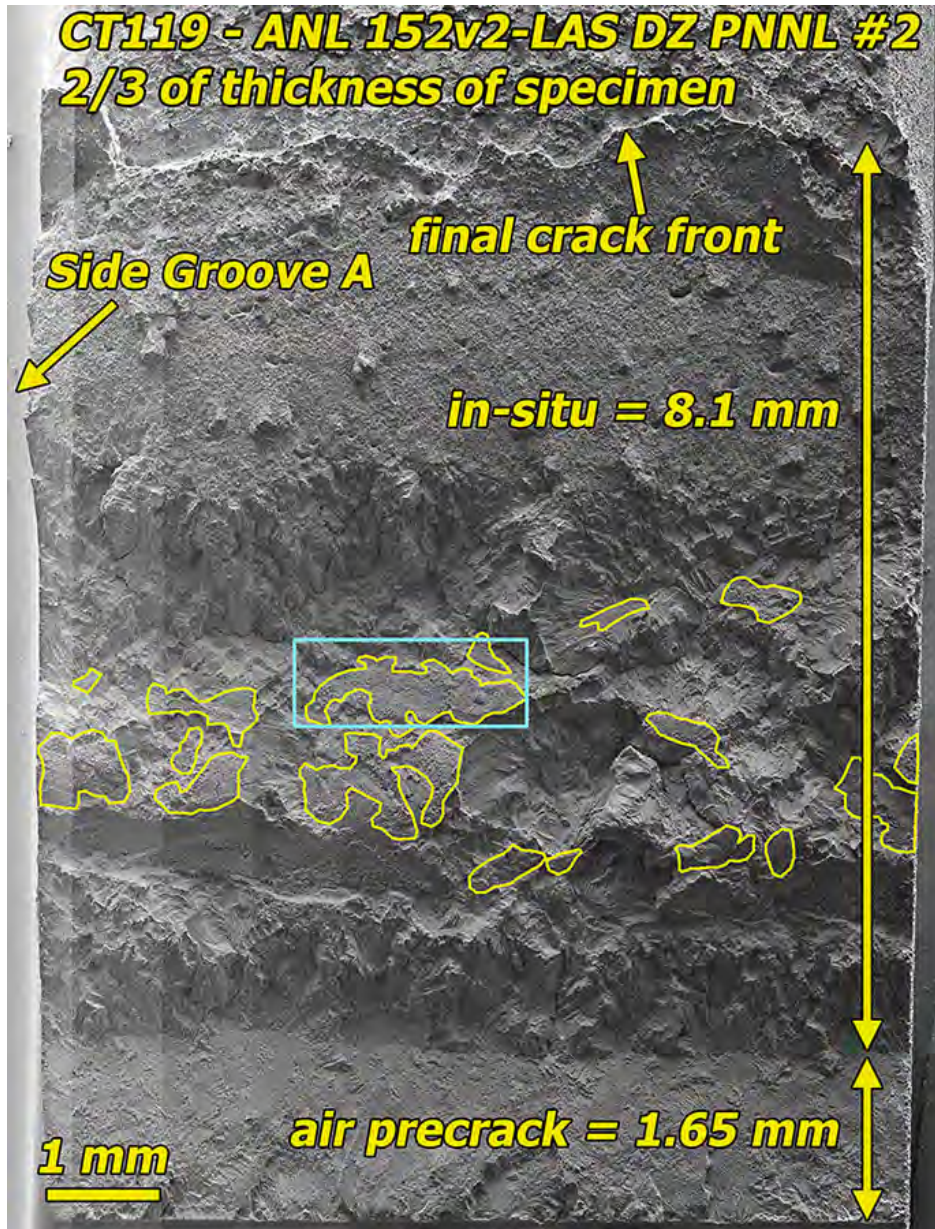
Figure 5-107 SEM-SE Montage Maps the Entire Crack-Growth Surface Area and Identifies IG Regions Outlined in Yellow
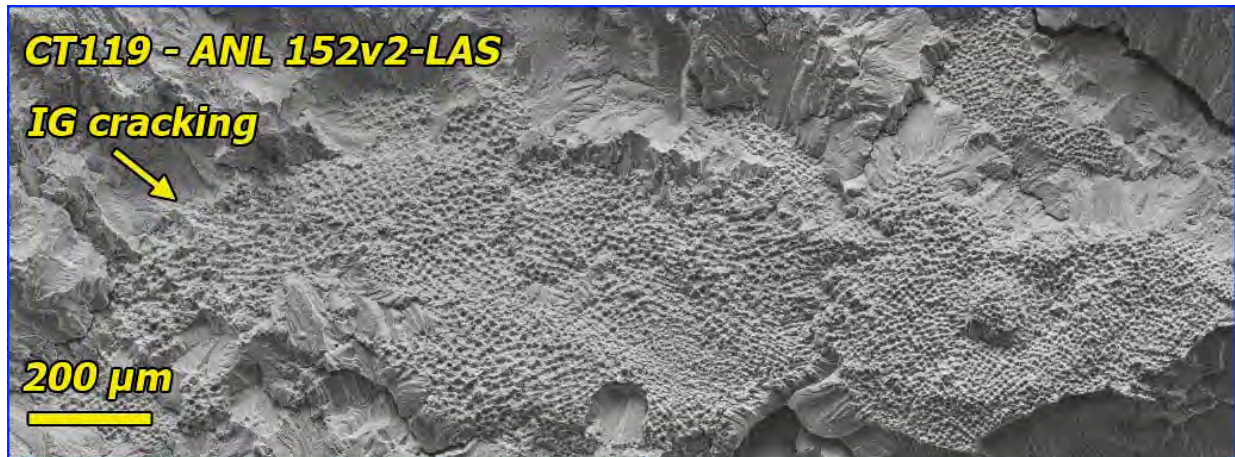
Figure 5-108 A Typical IG Region from Figure 5-107 (blue box), Bumpy Appearance Results from the Termination of Dendrite Packets at the Surface

5.3.5   EPRI Temper Bead DM Repair Weld: Specimen CT136 – Alloy 52M/LAS Interface

The final weld examined within this chapter is the EPRI temper-bead, alloy 690 – alloy 52M – LAS DM repair weld. Characterization and testing on the repair weld will be described in a future report, however crack-growth results for tests on the temper-bead alloy 52M – LAS interface region will be summarized in this section. Pre-test characterizations on the interface and dilution zone regions were presented in section 5.1 and Figures 5-18-5-22. The air pre-crack was extended by aggressive cycling in water (steps 1-4) and transitioning attempts started using 980s/20s cycling with and without a 2.5 h hold time in steps 5-10. This crack length should correspond to an Fe-rich and Cr-depleted region where aligned grain boundary were identified in side groove A. A summary of the test can be observed in Table 5-14 and Figure 5-109. The first attempt to assess SCC propagation was made at a test time of 1514 hours as shown in Figure 5-110. A reasonably steady, but low growth rate of 3.4×10^{-9} mm/s was measured over an exposure time of ~1000 hours. Additional transitioning was attempted (including the use of longer hold times) and the crack front was moved forward approaching and possibly reaching the LOF cracks identified in both side groves at a distance of ~3.5 to 4.3 mm from the notch. The most promising DCPD response was found for the periodic unload with a 24 h hold time (step 25) presented in Figure 5-111 where a CGR of 1.5×10^{-8} mm/s was observed, two times larger than the previous attempt in step 17 suggesting SCC growth during the hold time. However, the subsequent constant K evaluation (step 27) did not reveal a higher CGR as illustrated by the plot in Figure 5-112.

This result and the uncertainty whether the crack front had reached the LOF cracks prompted the decision to shut down the test at 5923 hours and examine the CT136 specimen side grooves. Optical images are shown in Figure 5-113. The crack front on these surfaces has clearly reached the end of LAS plateau and propagated through the preexisting LOF defects. Based on the side groove examinations, DCPD appears to have underestimated the crack length for CT136 by nearly 1 mm and the applied K level by ~10%. Based on this crack front location, it appears that the second and third constant K observations and the second 24 h hold may have all taken place as the crack grew through the LOF region.

Table 5-14   Data Summary for the Test on the EPRI DM Repair Weld Specimen CT136

Test Step	Start (h)	Duration (h)	R	Freq (Hz)	Hold (h)	Water Chem. (cc H_2 / kg)	Temp (°C)	Kmax (MPa√m)	CGR (mm/s)	Approx. Crack Extension (mm)
1	0	16	0.5	0.1	0	25	360	30	3.4E-06	0.182
2	16	84	0.5	0.01	0	25	360	30	7.9E-07	0.205
3	100	262	0.5	0.001	0	25	360	30	1.4E-07	0.119
4	362	63	0.5	0.01	0	25	360	30	8.2E-07	0.167
5	425	271	0.5	980s/20s	0	25	360	30	1.5E-07	0.221
6	696	287	0.5	980s/20s	2.5	25	360	30	2.5E-08	0.024
7	983	98	0.5	980s/20s	0	25	360	30	1.2E-07	0.049
8	1081	235	0.5	980s/20s	2.5	25	360	30	1.5E-08	0.013
9	1316	64	0.5	980s/20s	0	25	360	30	1.1E-07	0.021
10	1380	134	0.5	980s/20s	2.5	25	360	30	2.2E-08	0.008
11	1514	1014	---	const K	---	25	360	30	3.4E-09	0.011
12	2528	262	0.5	980s/20s	2.5	25	360	30	1.6E-08	0.009
13	2790	210	0.5	980s/20s	0	25	360	30	1.1E-07	0.068
14	3000	96	0.5	280/20s	0	25	360	30	3.0E-07	0.118
15	3096	168	0.5	980s/20s	0	25	360	30	1.7E-07	0.096
16	3264	263	0.5	980s/20s	2.5	25	360	30	2.5E-08	0.026
17	3527	384	0.5	980s/20s	24	25	360	30	8.4E-09	0.007
18	3911	107	0.5	280/20s	0	25	360	30	4.9E-07	0.209
19	4018	36	0.5	980s/20s	0	25	360	30	4.0E-07	0.053
20	4054	96	0.5	980s/20s	2.5	25	360	30	5.7E-08	0.026
21	4150	239	---	const K	---	25	360	30	2.4E-09	0.003
22	4389	96	0.5	980s/20s	2.5	25	360	30	4.7E-07	0.017
23	4485	56	0.5	980s/20s	0	25	360	30	1.6E-08	0.127
24	4541	59	0.5	980s/20s	2.5	25	360	30	1.2E-07	0.032
25	4600	421	0.5	980s/20s	24	25	360	30	1.5E-08	0.026
26	5021	259	0.5	980s/20s	2.5	25	360	30	9.4E-08	0.061
27	5280	547	---	const K	---	25	360	30	3.5E-09	0.039
28	5827	96	0.5	980s/20s	2.5	25	360	30	1.0E-07	0.036
Side	Groove	Exams								
29	5923	26	0.5	980s/20s	2.5	25	360	30	2.3E-07	0.017
30a	5949	541	---	const K	---	25	360	34	4.2E-09	0.012
30b	6390	400	---	const K	---	25	360	34	<5E-10	0.001
30	6790	175	0.5	980s/20s	2.5	25	360	34	1.5E-07	0.093
31	6965	806	---	const K	---	25	360	34	3.2E-09	0.011
Total	7771									2.105
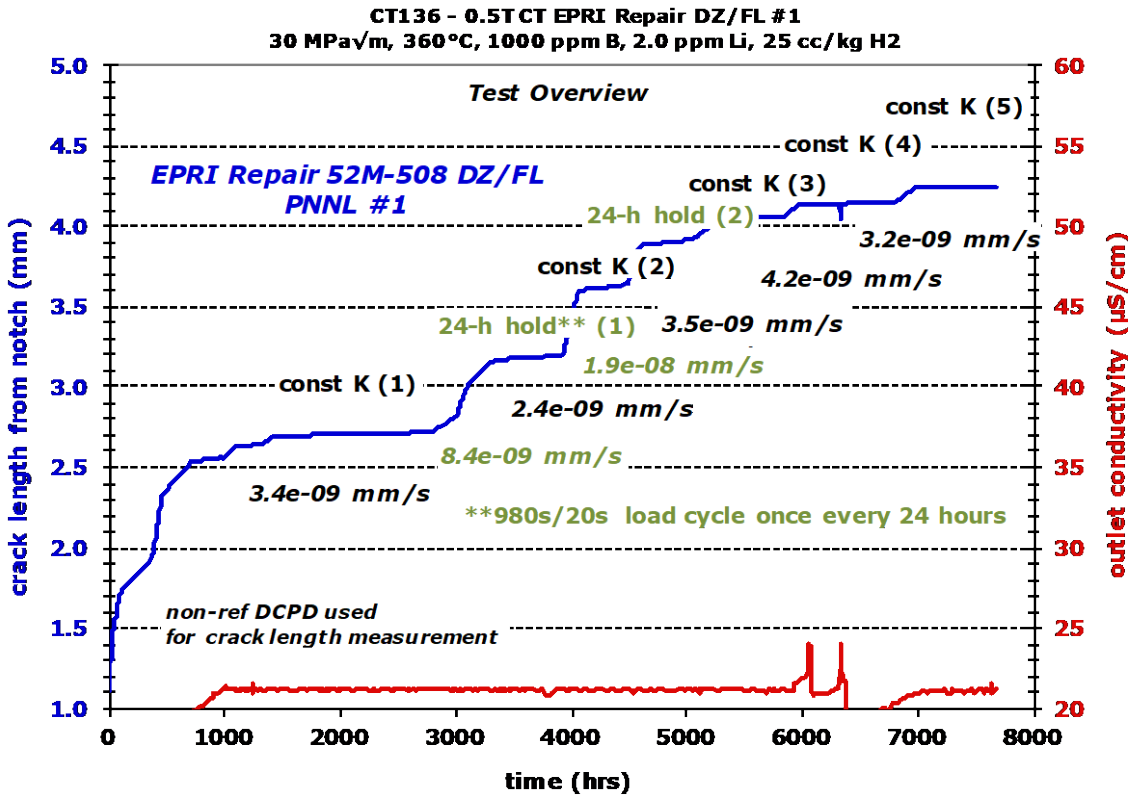
Figure 5-109 Overview Crack Growth Plot for Test on the EPRI Alloy 52M - LAS Interface and Dilution Zone Specimen (CT136)
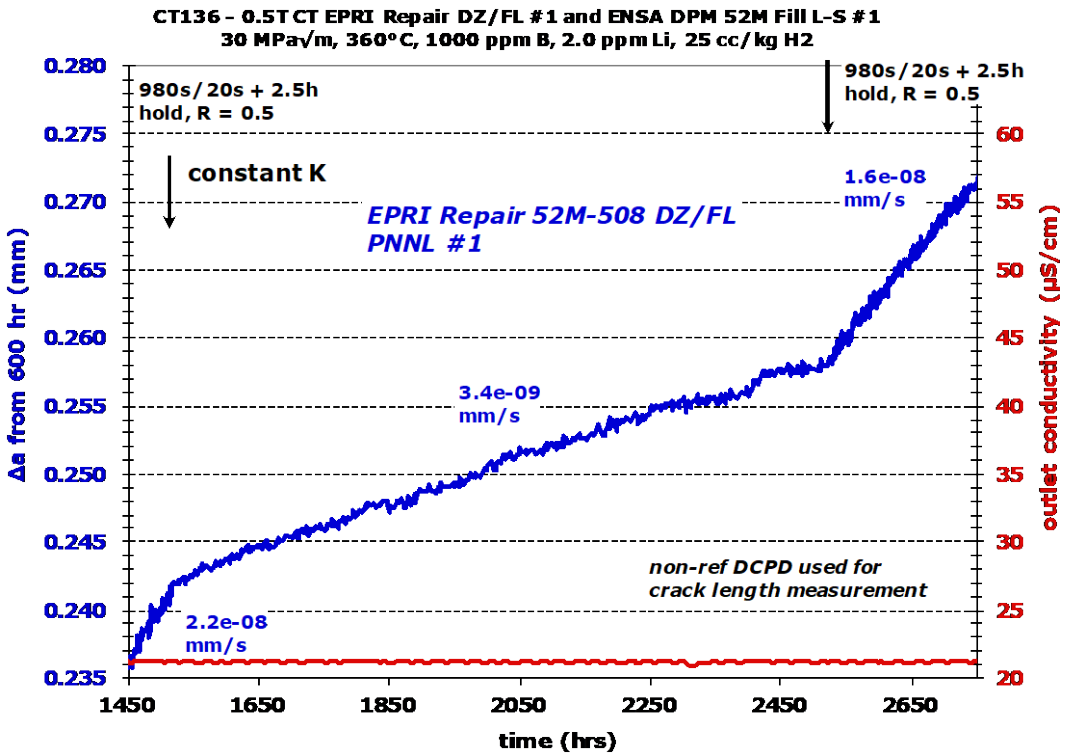
Figure 5-110 First Constant K Evaluation of SCC Response in the CT136 Specimen
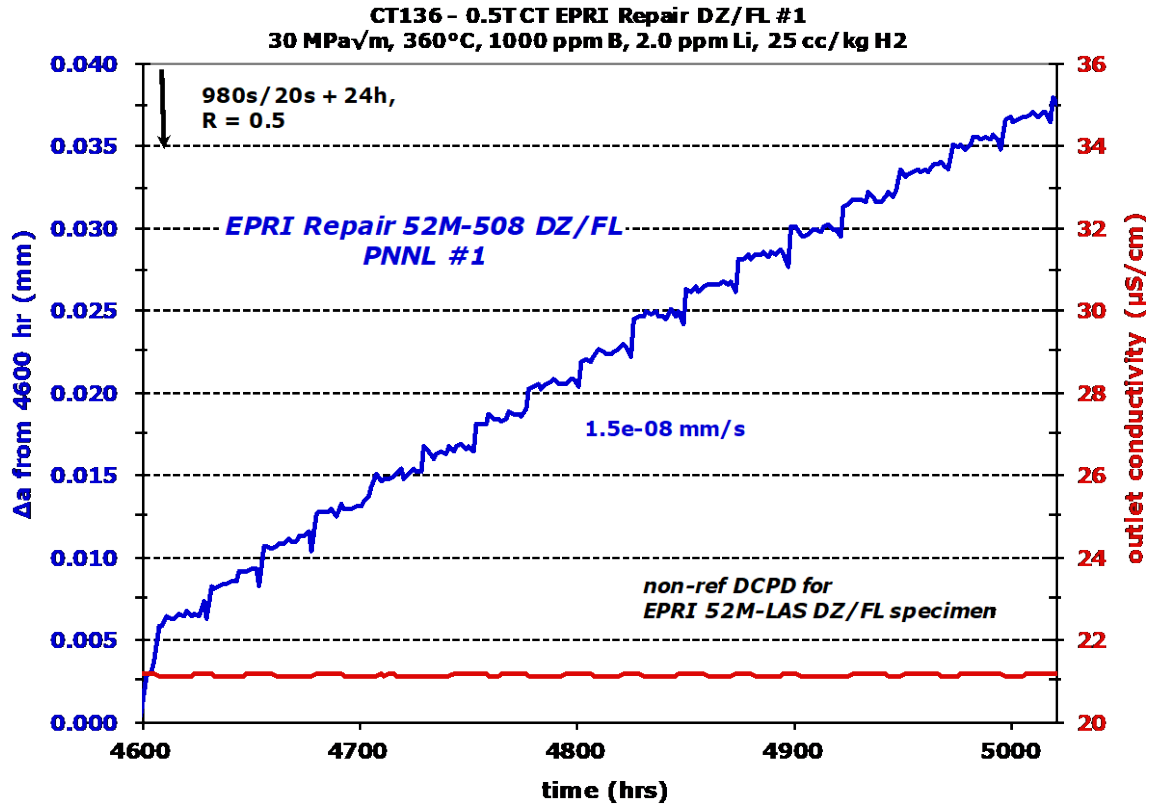
Figure 5-111 Cycle + 24 h Hold CGR Response in the CT136 Specimen
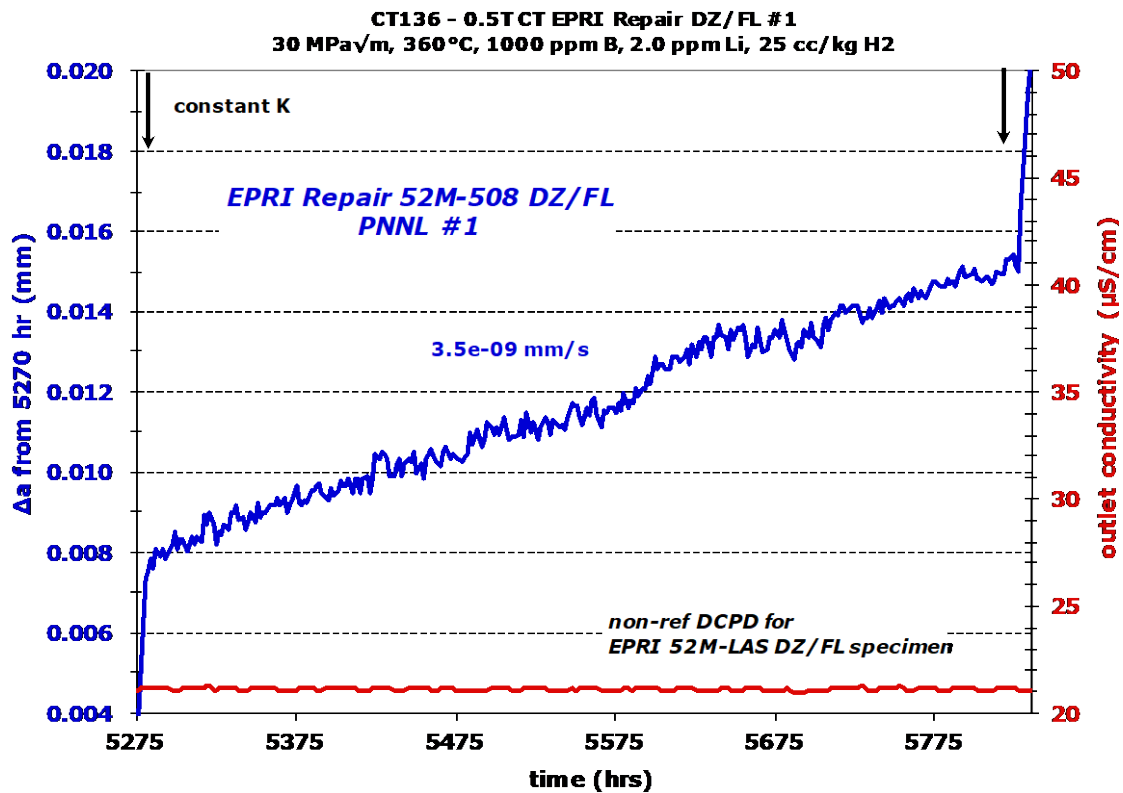
Figure 5-112 Third Constant K Evaluation of SCC Response in the CT136 Specimen

Figure 5-113 Optical Images Showing Cracking in CT136 Side Grooves After a Test Time of 5900 Hours. Crack Front Has Reached the LOF Defects (black arrows) at the LAS Interface on Both Sides and Small Cracks Appear to Extend to the End of the LAS Plateau

The CT136 specimen were then reloaded and testing continued under cycle + 2.5 h hold loading in step 29 exhibiting a somewhat higher CGR of 2.3×10^{-7} mm/s. Since the crack front was near the LOF defects, SCC response was again assessed. The early CGR at constant K was similar to previous measurements at 4.2×10^{-9} mm/s, however the test system experienced water chemistry and flow rate issues that directly impacted DCPD response as shown in Figure 5-114. After a sharp spike in outlet conductivity and DCPD signal at ~6325 hours, corrective actions were taken to restore proper flow rate and adjust water chemistry. After ~100 hours, proper conditions were restored but the DCPD-indicated CGR was quite different. Essentially no SCC growth was measured during the last 400 hours at constant K. Because of this problem and the resulting questionable DCPD behavior, cycle + hold loading was again applied in step 30 before one final attempt to asses SCC. The final constant K evaluation is presented in Figure 5-115 and revealed a low CGR under stable water chemistry conditions similar to prior observations on this specimen. After discussions with the NRC, the decision was made to end this test after 7771 hours and characterize the crack growth morphology.

This CT specimen was cut into 1/3 and 2/3 sections with the cross-section metallography exams performed on the internal surface of the 1/3 piece removed from side A. An SEM-EBSD pattern quality image is presented in Figure 5-116(a) that illustrates the crack path through the alloy 52M grain microstructure. The cracking morphology in this cross-section location appears to be predominately TG with only one region where the cracking may have followed aligned grain boundaries. It is important to note that several fine grain areas are present with better aligned grain boundaries (yellow arrows in Figure 5-116a) in pass #1 consistent with what we observed for side groove A (Figure 5-20). The composition variation measured on the cross-section also matched what was seen for side groove A with a protrusion of Fe-enrichment and Cr/Ni-depletion into the alloy 52M weld metal located where finer grain were present creating the grain boundaries aligned with the CT specimen crack path from the notch. However, it is clear that the crack path did not intersect or preferentially follow the aligned grain boundaries in this cross-section and no significant IG cracking was present.
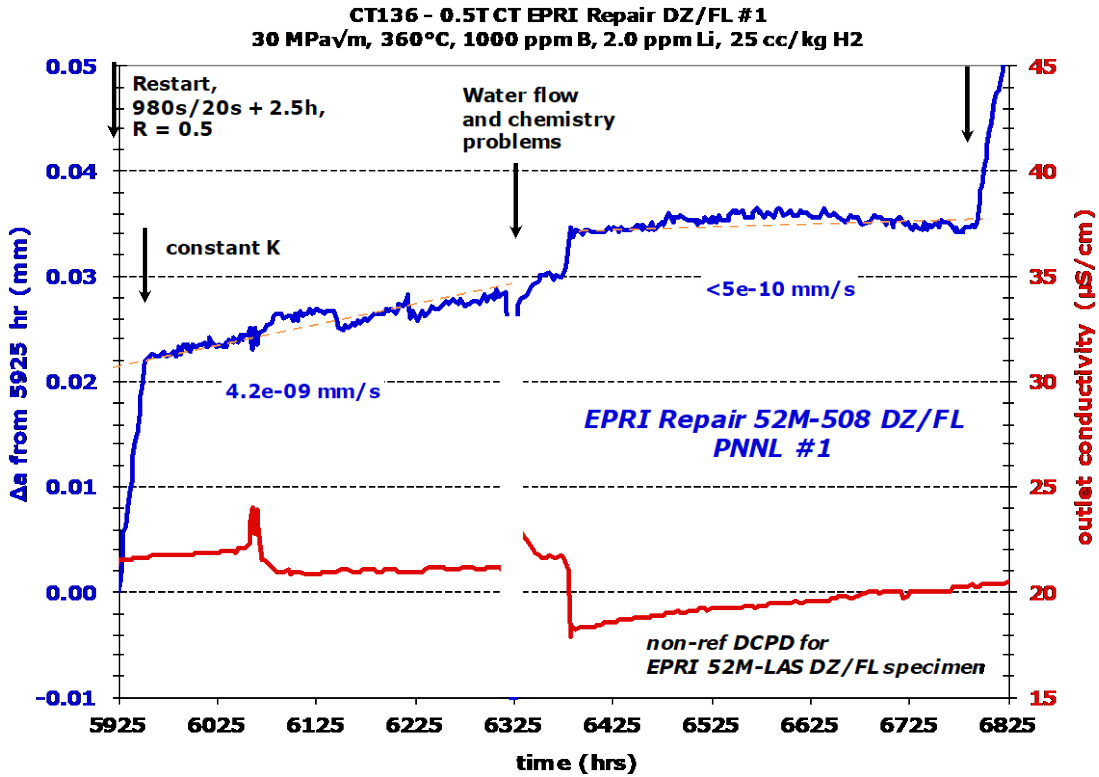
Figure 5-114 Fourth Constant K Evaluation of SCC Response in the CT136 Specimen Immediately After Restart. Problems with Water Flow and Chemistry Impacted DCPD Measurements and Corrective Action Was Taken at ~6325 Hours
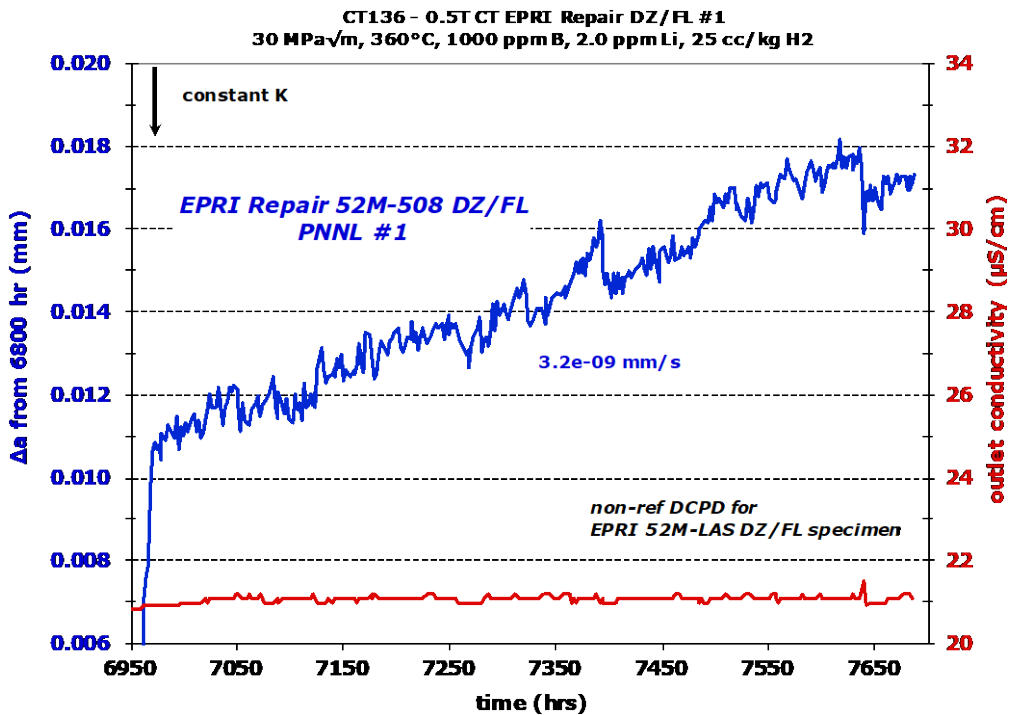
Figure 5-115 Fifth and Final Constant K Evaluation of SCC Response in the CT136 Specimen
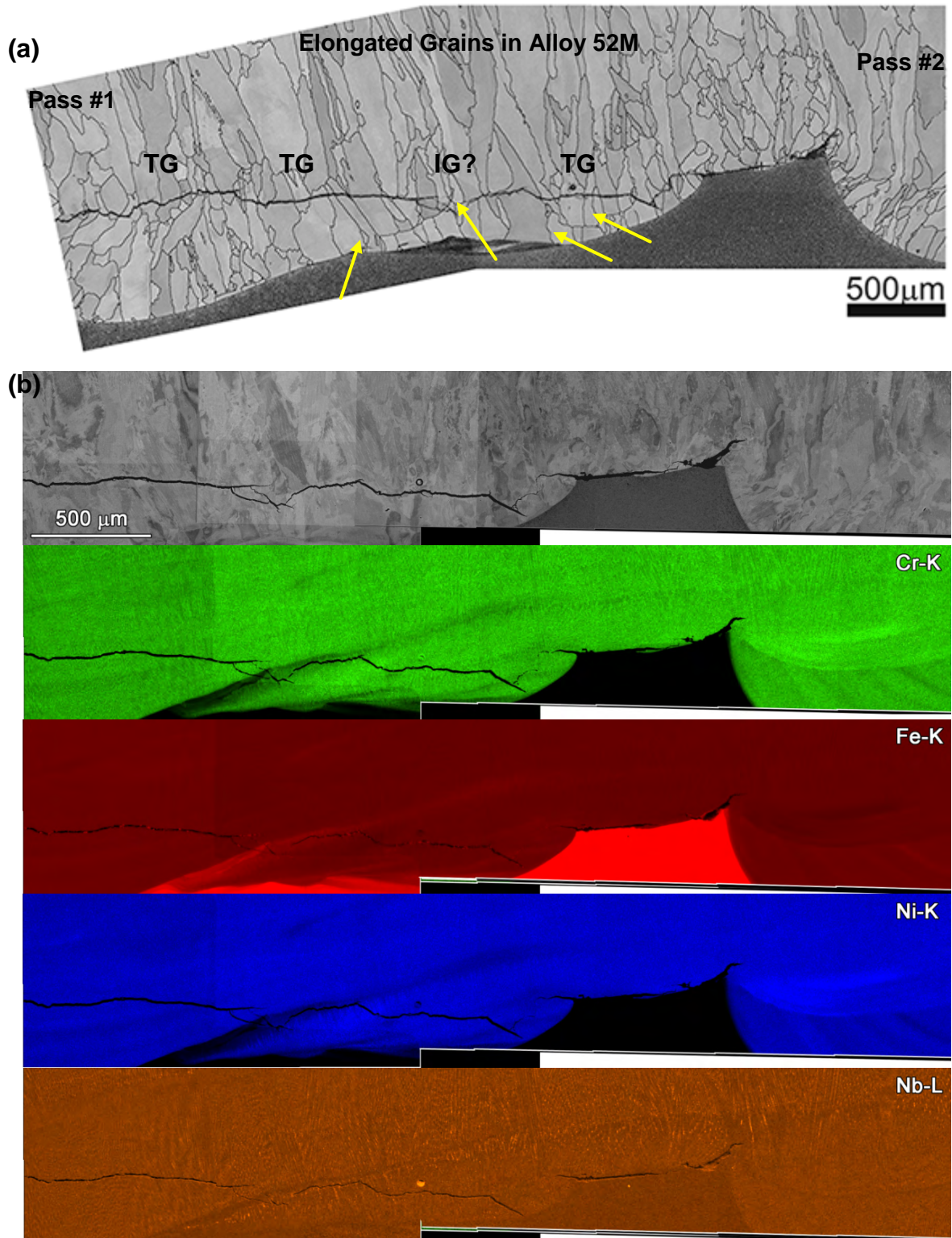
Figure 5-116 SEM-EBSD Pattern Quality Image Showing Crack Path Through the Weld Metal Microstructure (a) and the Corresponding SEM-BSE Image and EDS Compositional Maps (b) from This Region

Additional EBSD examinations were performed to better characterize the alloy 52M microstructure, crack path and local strain misorientations. An IPF map of the crack path matching the pattern quality image in Figure 5-116(a) is shown in Figure 5-117 to better highlight the grain orientations in the alloy 52M weld metal. Large, elongated grains in the weld metal can be easily resolved along with local regions of smaller grains (and aligned grain boundaries) closer to the LAS interface. The one area identified where the crack path may have followed an aligned grain boundary is shown at higher magnification in Figure 5-118 along with an EBSD local misorientation map. Higher misorientation (strain) is present along the crack path and suggests that the crack propagated near the aligned grain boundaries, but remained TG. It also revealed that crack branching likely occurred in this local region.
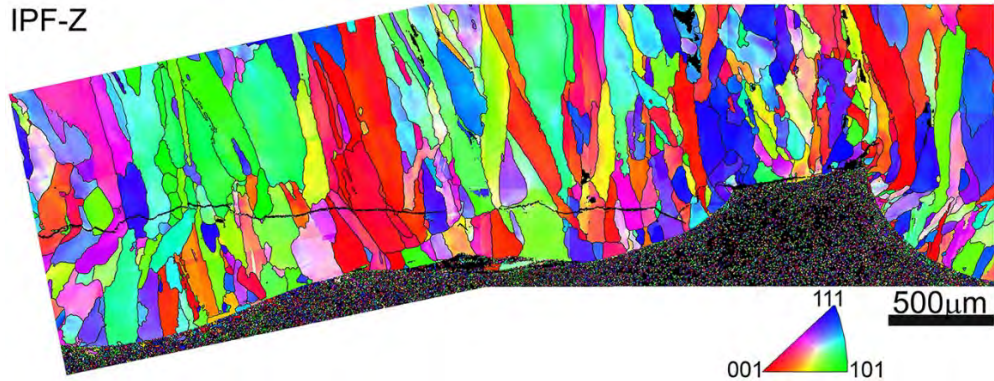
Figure 5-117 EBSD IPF Image of the Alloy 52M Microstructure Along the Crack Path in CT136
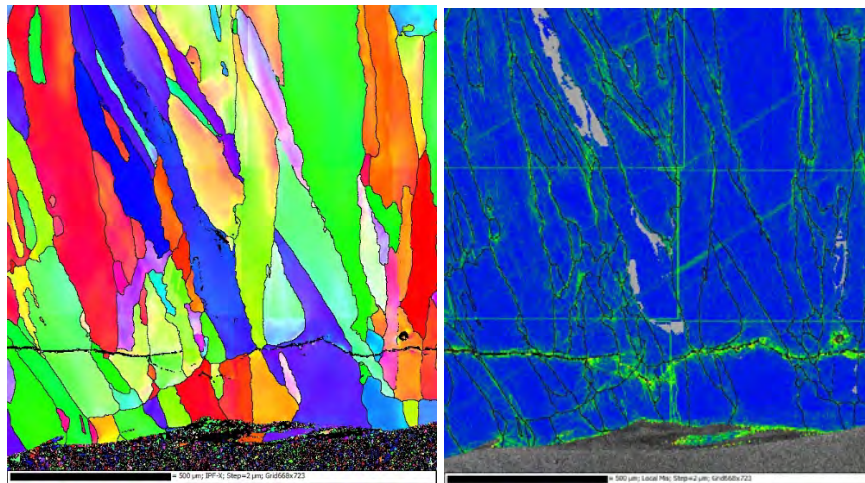
Figure 5-118 EBSD IPF Image and Local Misorientation Map of a Region Along the Crack Path. A Higher Magnification IPF Image of the Plateau Region Is Presented in Figure 5-119 Along with an EBSD Local Misorientation Map
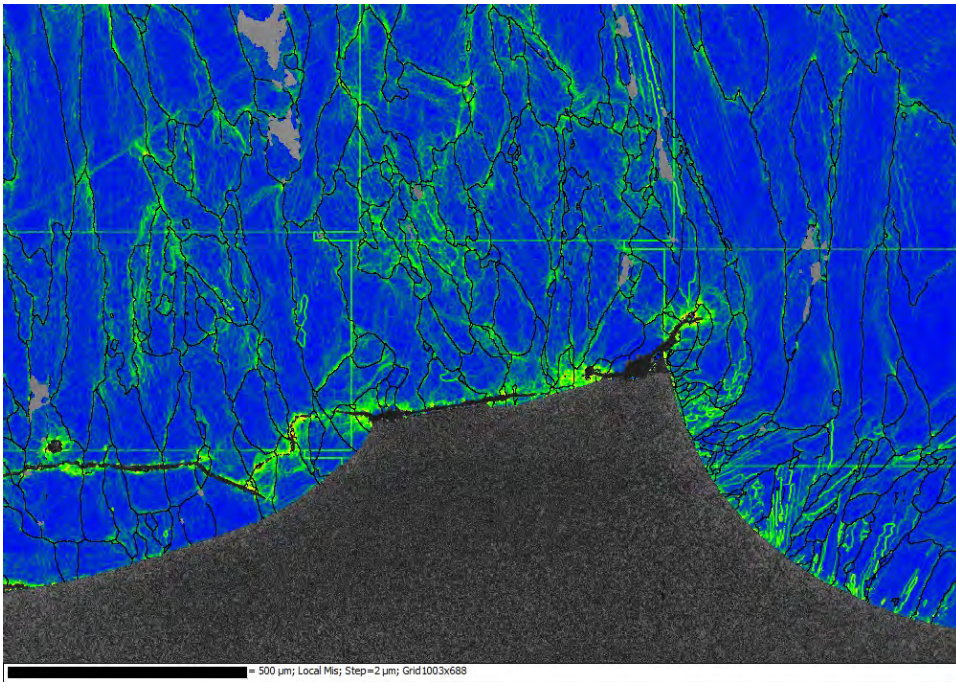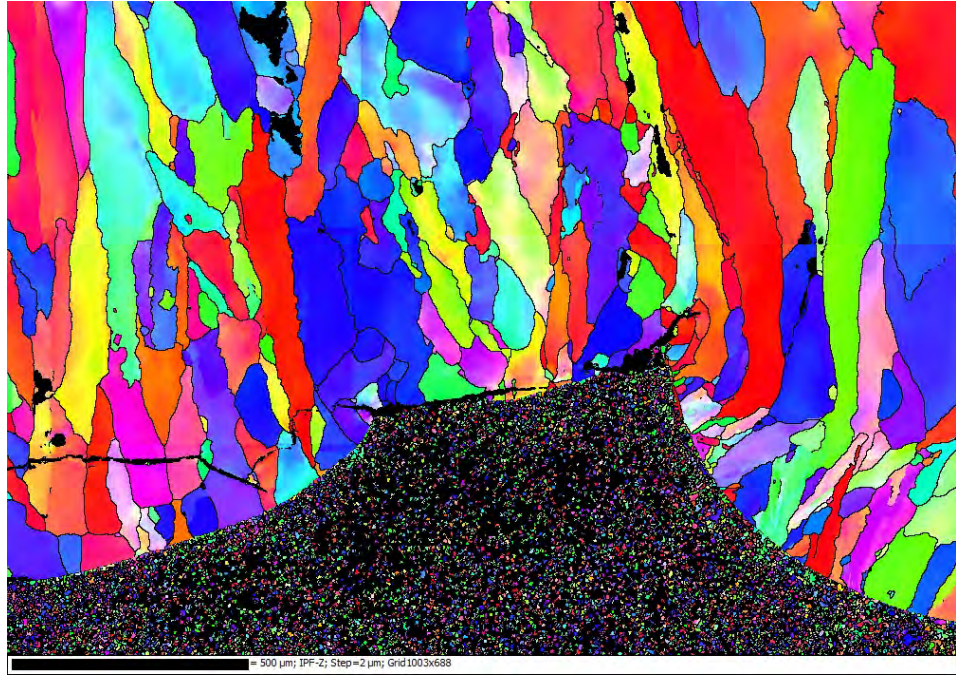
Figure 5-119 EBSD IPF Image and Local Misorientation Map at the LOF Region in CT136

High-resolution SEM characterizations were also performed along the crack path and at the leading crack tip for the cross-section sample. Results for three regions are highlighted and are identified in Figure 5-120. The crack tip region 1 is presented in Figure 5-121 showing a TG crack emanating from the second preexisting LOF defect that intersects with and propagates a short distance along a grain boundary. The boundary in this case is nearly perpendicular to the CT specimen crack path, so a reduced K would be expected for continued IG growth. Region 2 captures the site where the propagating TG crack intersects in Figure 5-122 with the first preexisting LOF defect and an oddly shaped open feature is formed. The crack path appeared to be headed for the alloy 52M – LAS interface in region 3, but instead shifted upward to LOF defect in region 2.
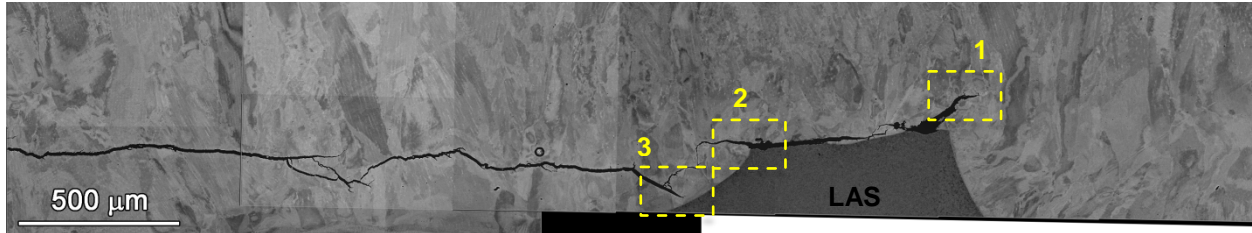
Figure 5-120   SEM-BSE Image of the Crack Path in CT136 with Regions Identified for Exams
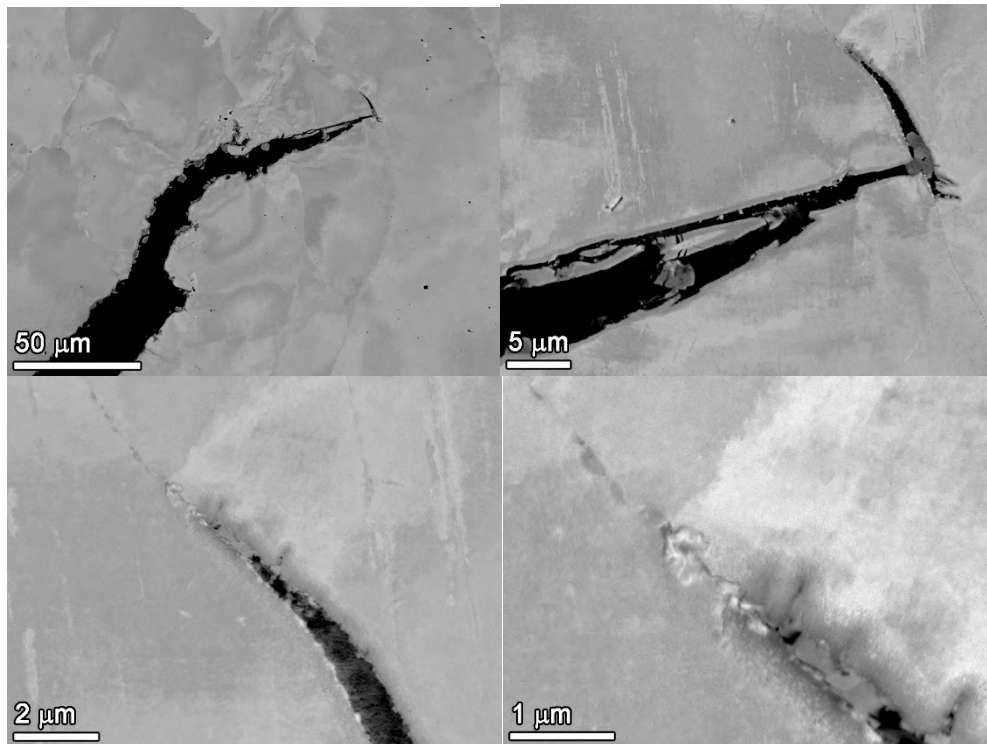
Figure 5-121   SEM-BSE Images Showing the Crack Region 1 from Figure 5-120 at Increasing Magnifications Revealing Short Propagation Along a Grain Boundary off the Main TG Crack Tip
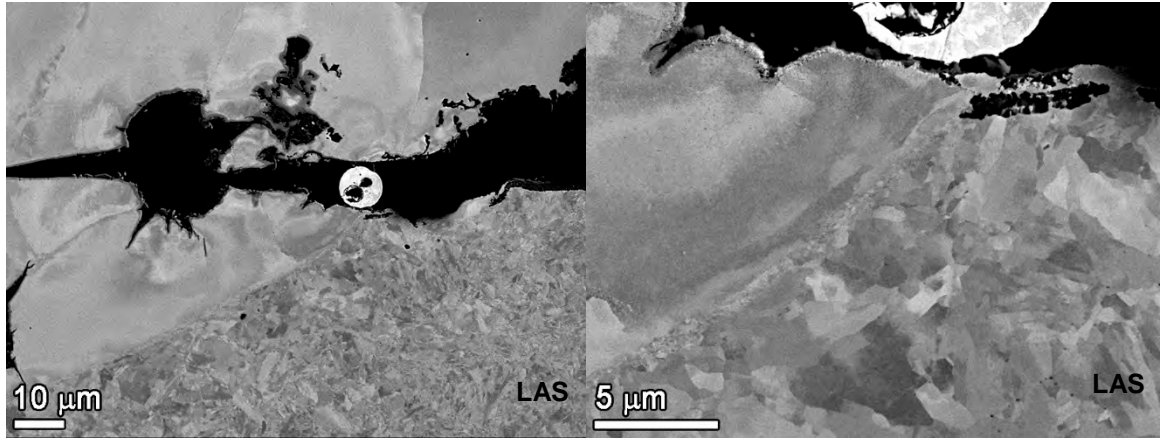
Figure 5-122   SEM-BSE Images Showing the Crack Region 2 from Figure 5-120 Where the Crack Intersected the First Preexisting LOF Defect at the LAS Interface

The final area highlighted is region 3 near the alloy 52 – LAS interface documented in Figure 5-123. Tight cracks can be seen near the interface including what could be growth along a Type 2 boundary and two cracks that reach the LAS. No crack propagation was observed into the LAS at any location in this cross section, which is interesting since temper-bead welding produced a layer of high hardness in the LAS (presented in Figure 5-18). The fact that cracks stopped at the interface and formed pit-like corrosion suggests that the LAS is effectively tempered and resistant to environment-assisted cracking. Figure 5-123 also illustrates the extremely fine-grained microstructure in the LAS except within ~10 µm of the alloy 52 – LAS interface where some grain growth has occurred.
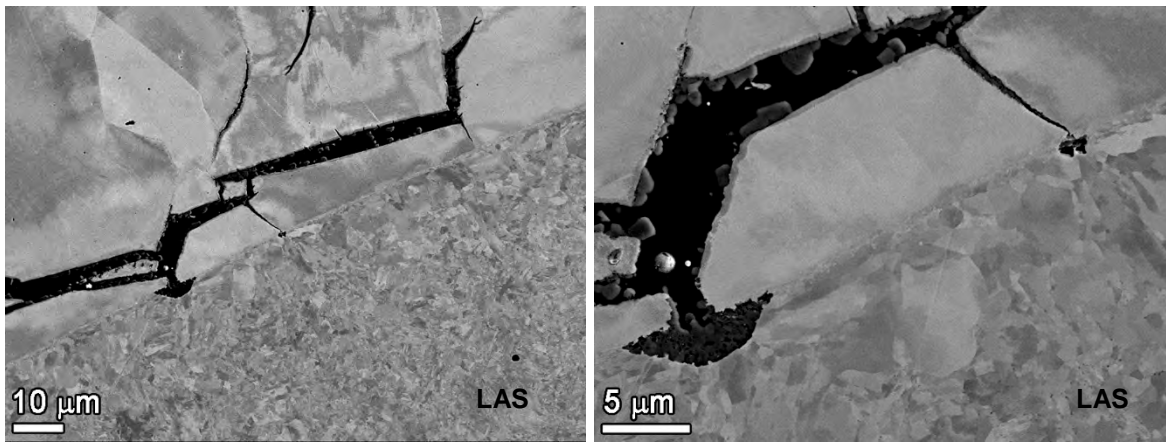
Figure 5-123   SEM-BSE Images Showing the Crack Region 3 from Figure 5-120 at Higher Magnifications Revealing Cracks in the Alloy 52M near the LAS Interface. Two Cracks Are Seen to Reach the Interface and Form Pit-like Corrosion into the LAS

In order to establish the overall crack propagation morphology, the remaining 2/3 specimen was fatigued open in air and the crack-growth surface examined by optical and SEM techniques. An SEM-SE montage is shown in Figure 5-124 documented the cracking morphology across the CT136 specimen. The two preexisting LOF fusion defects present at LAS plateau interface have a flat smooth appearance and extend across the entire fracture surface with a short

section of complex cracking between the two LOF defects. The crack growth during the test in PWR primary water ended near the edge of the second LOF defect as indicated by the horizontal arrows. Morphology of cracking through weld pass #1 (below the LOF defects) was predominately TG with the exception being two islands of predominately IG. These two islands are outlined in yellow and the one on the right is shown at higher magnification in Figure 5-125.
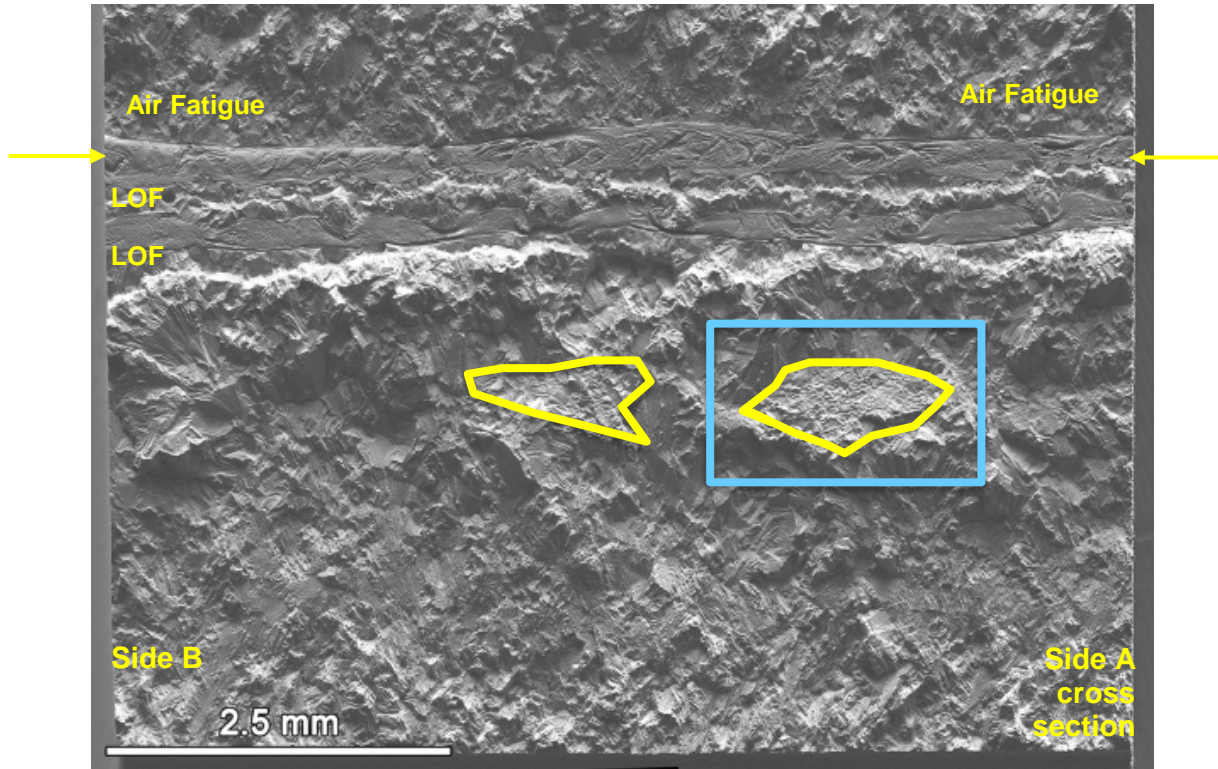
Figure 5-124   SEM-SE Image Montage Revealing the Crack Growth Surface Produced in Water for Specimen CT136. Two Islands of Primarily IG Cracking Were Observed in Pass #1
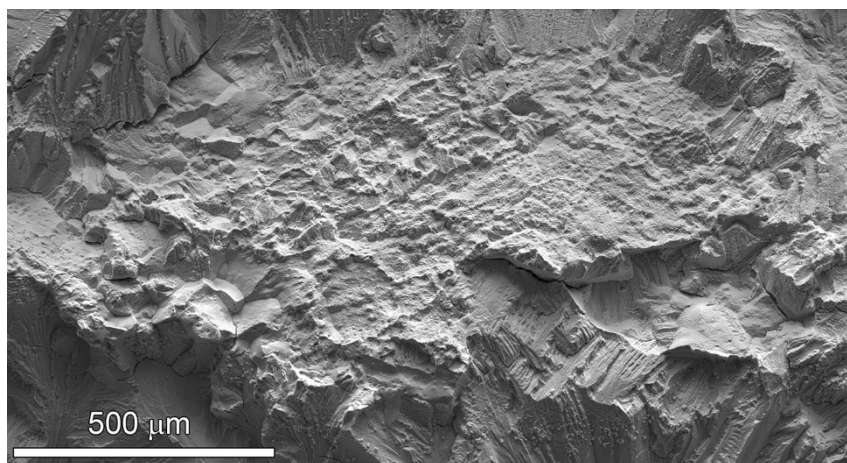
Figure 5-125   SEM-SE Image Highlighting One of the Two IG Islands Present on the CT136 Crack Growth Surface

5.4   Summary of Testing at Alloy 152/152M/52M DM Weld Interfaces

PWSCC testing was performed on five DM welds in the region of the fusion line between alloy 152, 152M or 52M weld metal and either 304SS, CS or LAS. Low constant K SCC CGRs of <$5x10^{-9}$ mm/s were observed during testing on the fusion line of the alloy 152/304SS mockup. The crack growth path in the specimens suggested a preference for crack propagation in the 304SS HAZ. In the as-welded condition without a prototypic PWHT, laboratory-fabricated alloy 152M/52M-CS welds exhibited high constant K SCC CGRs ranging from ~$7x10^{-8}$ mm/s at 40 MPa√m to $2x10^{-6}$ mm/s at 53 MPa√m when the crack path was either on the fusion line or in the CS HAZ. Application of a prototypic PWHT to these materials eliminated the high susceptibility suggesting that the high CGRs were due to substantial hardening in the CS HAZ as a result of a martensitic transformation during the welding process. Finally, PWSCC testing was also performed in the dilution zone region of these alloy 152M/52M-CS DM weldments. When dilution down to ~20 wt% Cr was encountered in weld metal near the fusion line of the alloy 152M-CS specimen, CGRs did not increase, and there was no tendency for the crack to prefer an IG path.

While these tests suggest good PWSCC resistance in materials that are fabricated following acceptable procedures, additional testing was performed on specimens oriented for propagation in the alloy 152 or 52M weld near the fusion line with LAS. The first tests were conducted on a DM weld produced by ANL using different alloy 152 weld wires for the top half and bottom sections of the weld as described in Figure 5-12. Significant constant K rates (up to ~$1.4x10^{-8}$ mm/s) were measured during certain parts of the tests on the ANL DM weld specimens. Post-test analyses indicated that these isolated results showing moderate SCC growth rates corresponded to regions of IG cracking on the crack-growth surface. Microstructural examinations of cross-section samples revealed that the regions of IG cracking and higher growth rates were consistent with the presence of aligned grain boundaries in the alloy 152 dilution zone adjacent to LAS interface. The combination of aligned grain boundaries and some degree of Cr depletion is believed to be important to promote IGSCC. In all cases, the lengths of aligned grain boundaries were limited within individual passes and reasonably match the local regions of IGSCC on the crack growth surface. A final test was performed on an alloy 52M – LAS DM temper bead weld from EPRI. Microstructural and microchemical characterizations in the alloy 52M first layer identified regions of Fe enrichment and Cr depletion along with a few

aligned grain boundaries. In addition, LOF defects were discovered at the alloy 52M/LAS interface between many weld passes. Finally, hardness mapping revealed a continuous band of higher hardness in the LAS HAZ suggesting that the temper bead welding may not have been completely effective. Crack growth testing indicated very low SCC susceptibility along the alloy 52M dilution zone and the alloy 52M/LAS interface. This was consistent with the observation of only a few, small isolated regions of IG cracking on the post-test crack-growth surface. There was no tendency for the crack path to enter the LAS to follow the higher hardness band as was seen previous for the non-tempered CS HAZ.

Although the current results on dissimilar metal welds are limited, we believe they do show that the alloy 152/52M weld interfaces with CS or LAS consistently creates local regions of significant Fe enrichment and Cr depletion in the alloy 152/52M. In our opinion, this dilution zone does increase susceptibility to IGSCC in PWR primary water but crack growth is limited by the availability of properly aligned grain boundaries. The combination of both characteristics is required for significant IGSCC. Additional research is needed and planned to produce and evaluate dissimilar metal welds to better determine whether dilution zones represent a concern for SCC in reactor service.

6   SUMMARY AND FUTURE RESEARCH NEEDS

Stress corrosion crack growth of alloy 690 and its weld metals has been a focus of research at PNNL and several other laboratories over the last decade. Overall results have revealed excellent resistance to SCC and extremely low CGRs in PWR primary water environments in agreement with PWR service experience. This resistance can change with a moderate-to-high degree of cold work as demonstrated for alloy 690 materials [5]. Even though this cold-worked, high-strength condition is not believed to exist for alloy 690 or its weld metals in operating reactor components, it remains critical to understand the limiting material conditions that can promote SCC susceptibility.

The current report has documented SCC results on a large number of industry-made alloy 152, 152M, 52, 52M and 52MSS weld mockups revealing low CGRs (all <5x10^{-9} mm/s and most <2x10^{-9} mm/s) in 360°C simulated PWR primary water. Moreover, specialized tests performed on alloy 52M overlay and inlay mockups supported very low SCC CGRs in the alloy 52M weld metal. The main conclusion from these experiments on alloy 152, 152M, 52, 52M and 52MSS weld metals with typical Cr bulk concentrations (28-30 wt%) is that they are resistant to SCC crack growth.

Some differences were observed for alloy 152 and 52M welds in regions where the local Cr concentration was found to equal to or below ~24 wt%. SCC propagation rates up to ~1.4x10^{-8} mm/s were measured in an alloy 52M weld pass for the Ringhals overlay (CT035) and within DM weld alloy 152 dilution zones adjacent to the LAS interface (CT117 and CT119). The presence of aligned grain boundaries along the crack path were a key requirement for significant SCC growth in the dilution zone specimens and limited the extent of observed IGSCC to local areas. Overall, these results support the excellent SCC resistance of the high Cr welds in the as-welded condition.

Based on our investigations at PNNL over the last decade and interactions with the international community, additional research is recommended in several areas for alloy 690 and its weld metals:

1) Continue to investigate alloy 690 heat-to-heat and alloy 152/52/52M weld-to-weld variability. The early results by Bettis showing high SCC CGRs in moderately cold-worked alloy 690 at low K levels still raise a potential concern that certain heats (and microstructures) may show more significant SCC susceptibility. Attempts should be made to determine what microstructural/microchemical features were responsible for the observed behavior.

2) Improve understanding of strength effects on IGSCC particularly for cold/warm work levels that bound what may exist in existing and planned LWRs. Additional SCC testing is needed in the 10-15% cold work range on additional alloy 690 heats and is also suggested for selected alloy 152/52/52M weld metals.

3) Repairs during installation may have created alloy 152/52/52M welds in reactor service that have a higher degree of residual plastic strain and have regions of much higher strength than for the typical as-welded condition. It is important to better understand what a "worse case" condition might be and produce repair weld mock ups to properly evaluate whether this higher strength condition increases SCC susceptibility. Proper

analysis of effects due to repair welding can help establish levels of cold/warm work that should be applied to simulate the strength change.

4) Weld defects remain an issue of potential concern, since it is difficult to produce pertinent weld mock ups and also to directly assess their effects on SCC initiation and growth using conventional testing approaches. One approach that appears promising for this issue is to machine blunt notch CT specimens where pre-existing weld defects (i.e., DDC and/or solidification cracks) intersect the notch surface, thereby enabling SCC initiation and growth processes to be evaluated from the pre-existing defects.

5) Additional DM weld dilution zones need to be characterized and tested, particularly those produced between alloy 152/52M and LAS. A better understanding of the local composition changes (Fe enrichment, Cr depletion) and its continuity along the interface region is required plus the grain boundary microstructure that would enable IGSCC propagation over significant distances.

6) Long range ordering has been shown to occur in alloy 690 and its weld metals at temperatures slightly higher than PWR service and cause significant hardening. At this time, it is not known whether ordering is a concern for these materials after long-term service. Better quantification of this process at lower temperatures is needed along with the evaluation of its effect on SCC resistance for pertinent materials.

7) For nearly all of the items listed above, characterization and testing of materials removed from PWR service would be extremely helpful. Access to selected alloy 690 components and alloy 152/52/52M welds may become possible due to reactor shutdown. The ability to perform detailed examinations of welds may provide unique insights into variabilities among microstructures, residual plastic strains, local strength, defects and dilution zones. These results would help confirm whether mock-up welds for laboratory testing have been sufficient to address material variations in service and their effects on SCC. Similar assessments of microstructure and SCC behavior for alloy 690 component materials would also help ensure that laboratory studies on many heats have been sufficient and that long-term aging in service does not significantly impact properties.

7   REFERENCES

[1]   "Materials Reliability Program: Resistance of Alloys 690, 152, and 52 to Primary Water Stress Corrosion Cracking (MRP-237, Rev. 1) ", Product ID 1018130, Electric Power Research Institute, August 2008.

[2]   "Materials Reliability Program: Resistance of Alloys 690, 152, and 52 to Primary Water Stress Corrosion Cracking (MRP-237, Rev. 2) Summary of Findings Between 2008 and 2012 from Completed and Ongoing Tests", Product ID 3002000190, Electric Power Research Institute, April 2013.

[3]   S.M. Bruemmer and M.B. Toloczko, "Pacific Northwest National Laboratory Investigation of Stress Corrosion Cracking in Nickel Base Alloys, Volume 2", NUREG/CR-7103, Vol. 1, ML11277A230 and ML11294A228, U.S. NRC, September 2011.

[4]   S.M. Bruemmer, M.B. Toloczko, M.J. Olszta, "Pacific Northwest National Laboratory Investigation of Stress Corrosion Cracking in Nickel Base Alloys, Volume 2", NUREG/CR-7103, Vol. 2, ML12114A011, U.S. NRC, April 2012.

[5]   M.B. Toloczko, N.R. Overman, M.J. Olszta, S.M. Bruemmer, Stress corrosion cracking in nickel-base alloys: stress corrosion cracking of cold worked alloy 690, U.S. Nuclear Regulatory Commission, NUREG/CR-7103, Vol. 3, July 2016.

2. TITLE AND SUBTITLE

Pacific Northwest National Laboratory Investigation of Stress Corrosion Cracking in Nickel-Base Alloys: Behavior of Alloy 152 And 52 Welds

3. DATE REPORT PUBLISHED

MONTH	YEAR
April	2019

4. FIN OR GRANT NUMBER

5. AUTHOR(S)

S. Bruemmer, M. Olszta, R.J. Seffens, R.A. Bouffioux, N.R. Overman, M. Toloczko

6. TYPE OF REPORT

Technical

7. PERIOD COVERED (Inclusive Dates)

8. PERFORMING ORGANIZATION - NAME AND ADDRESS (If NRC, provide Division, Office or Region, U. S. Nuclear Regulatory Commission, and mailing address; if contractor, provide name and mailing address.)

Pacific Northwest National Laboratory, Richland, Washington, 99352

9. SPONSORING ORGANIZATION - NAME AND ADDRESS (If NRC, type "Same as above", if contractor, provide NRC Division, Office or Region, U. S. Nuclear Regulatory Commission, and mailing address.)

Same as above

10. SUPPLEMENTARY NOTES

11. ABSTRACT (200 words or less)

The objective of this program is to evaluate the primary water stress corrosion cracking (PWSCC) susceptibility of high chromium Ni-base weld metals, establish quantitative measurements of crack-growth rates and determine relationships among cracking susceptibility, environmental conditions and metallurgical characteristics. Stress-corrosion, crack-growth rates have been determined for 11 alloy 152/52/52M weld metal specimens, 4 alloy 52M/182 overlay specimens and 2 alloy 52M/82 inlay specimens in simulated PWR primary water environments. Weld metal, overlay and inlay specimens were machined from industry mock ups to provide plant-representative materials for testing. Specimens have been tested for one alloy 152 weld, two alloy 52 welds and three alloy 52M welds. The overlay and inlay specimens were prepared to propagate stress-corrosion cracks from the alloy 182 or 82 material into the more resistant alloy 52M. In all cases, crack extension was monitored in situ by direct current potential drop (DCPD) with length resolution of about ± 1 μm making it possible to measure extremely low growth rates approaching 5×10^{-10} mm/s. Most SCC tests were performed at 325-360°C with hydrogen concentrations from 11-29 cc/kg; however, environmental conditions were modified during a few experiments to evaluate the influence of temperature, water chemistry or electrochemical potential on propagation rates.

12. KEY WORDS/DESCRIPTORS (List words or phrases that will assist researchers in locating the report.)

Alloy 690
Nickel alloys
Cold work
Stress corrosion cracking

13. AVAILABILITY STATEMENT

unlimited

14. SECURITY CLASSIFICATION

(This Page)

unclassified

(This Report)

unclassified

15. NUMBER OF PAGES

16. PRICE